

Foreword

Nuclei are many body quantum systems bound by strong nuclear force, and they exhibit properties characteristic of both single particle and collective nature. The binding of the nucleons inside a nucleus has been described with a mean field potential which has been quite successful in explaining many features of the ground states and excited states of nuclei. With the recent studies on exotic nuclei with large neutron and proton excesses as well as nuclei in the super-heavy mass region, new challenges are being posed to the existing mean field theories. The relativistic mean field theory, based on the exchange of scalar and vector bosons has achieved good success in the understanding of the nuclear phenomena. The applications of this theory in describing the properties of exotic and super-heavy nuclei, neutron stars, nuclear excitations etc. need to be carefully examined and explored.

The present workshop on “*Relativistic Mean Field Theory in Nuclear Physics*” is aimed to bring to the highlight the research that is being carried out in the country in this field. With the availability of new generation Radioactive Ion Beam facilities and accessibility to nuclei in the neutron and proton drip line regions in the coming years, it would be necessary to have a strong base in the theoretical formulations to explain the new phenomena that will be associated in studying them. Organisation of this workshop has provided a platform for the active researchers to discuss the latest ideas in the theoretical developments in this field of research.

March 2005

R K Choudhury
Director
Institute of Physics
Bhubaneswar

Preface

A Workshop on "Relativistic Mean Field Theory in Nuclear Physics" was organised by the Institute of Physics, Bhubaneswar during July 26-31, 2004. The relativistic mean field theory has recently become rather the most successful many-body approach for the description of the ground state properties of all kinds of nuclei - light mass to heavy, spherical to deformed and neutron deficient to neutron rich. The predictive power of this approach is better than any other known non-relativistic theory.

In India there are now a sizable number of practitioners of this approach. The objective of this workshop was to bring all such workers together to a forum to discuss the current and future research problems in nuclear physics.

In this volume, the series of lectures by invited speakers are reproduced. The application of relativistic mean field theory to various nuclear phenomena such as (i) Exotic Nuclei (ii) Nuclear Astrophysics (iii) Giant Resonances (iv) Nuclear Structure and Reactions and (v) Nuclear Matter and Equation of State are discussed. Apart from these, several interesting topics like Triton clustering in nuclei, Giant dipole resonance in hot rotating nuclei, Interacting boson model, Deformed shell model, Double beta decay and Generator coordinate method were also discussed and are included in this volume.

We feel that the present volume represents a comprehensive account of the current status of our understanding of the field of Relativistic mean field formalism in Nuclear Physics and its application to astrophysics and hadron physics. We believe it will be quite useful to beginners as well as to specialists in this field.

We take the opportunity to thank the Director, Institute of Physics, members of the faculty, the scholars, the administrative, library and supporting staff for their cooperation. Dr. P. Arumugam played an invaluable role in bringing the chapters together in a uniform format. We express our gratitude to DAE-BRNS for financial support for publishing these proceedings. Last but not the least we thank Allied Publishers Private Limited and Ms. J Mehrotra for the publication of the book. The Editors are not responsible for the views expressed by the speakers.

February 2005

S K Patra
A Ansari

Table of Contents

A General Introduction to Mean Field Theory	1
<i>Ahmad Ansari</i>	
Salient Features of RMF and its Applications	14
<i>Y. K. Gambhir</i>	
Some questions and new results based on the relativistic mean field model	31
<i>Raj K. Gupta, S.K. Patra</i>	
Application of RMF and RQRPA to Nuclear Structure Studies	46
<i>Ahmad Ansari</i>	
Consistent description of recent RIB measurements of total reaction and charge changing cross sections	56
<i>A. Bhagwat</i>	
Relativistic mean field study of nuclei far from the valley of stability	70
<i>G. Gangopadhyay</i>	
Recent Developments in Relativistic Mean Field Theory	82
<i>S.K. Patra, B.K. Sharma, P. Arumugam, M. Centelles, X. Viñas</i>	
Neutron Stars and Equation of States of Neutron Star Matter- An Overview	107
<i>Somenath Chakrabarty</i>	
Chiral Sigma Model and Neutron Stars	137
<i>P. K. Sahu</i>	
Effect of Relativistic Mean Field Theory on Collective Flow at AGS Energies	153
<i>P. K. Sahu</i>	
Hadronic Properties in Nuclear Medium	162
<i>S.C. Phatak</i>	
Mean Field Models and In-Medium Modification of Hadron Masses	170
<i>Abhijit Bhattacharyya</i>	
Nuclear Structure effects in Nuclear Astrophysics	185
<i>Radhey Shyam, S.K. Dhiman</i>	
Mean-field Approach for Interacting Boson Models: New Applications	194
<i>V.K.B. Kota</i>	
Recent Applications of Deformed Shell Model	209
<i>R. Sahu</i>	

Hartree-Fock-Bogoliubov model application to double beta decay	228
<i>P.K. Raina, A. Shukla, K. Chaturvedi, R. Chandra, J. Singh, P.K. Rath, S.K. Dhiman, J.G. Hirsch</i>	
A new symmetry for triton clustering in nuclei	241
<i>Afsar Abbas</i>	
The Generator Coordinate Method and Role of Pauli Principle in the Structure of Light Nuclei	257
<i>V.K. Sharma</i>	
Nuclear saturation in non-relativistic and relativistic theories	277
<i>L. Satpathy</i>	
Giant Dipole Resonance in Hot and Rotating Nuclei	287
<i>P. Arumugam, A. Ganga Deb, S.K. Patra</i>	
Energy dependence of Lane potential and effective mass splitting	303
<i>T.R. Routray, A. Pradhan, B. Behera</i>	
Author Index	318

A General Introduction to Mean Field Theory

Ahmad Ansari

Institute of Physics, Bhubaneswar 751 005, India

Abstract. An introduction to the concept of an average(mean) one-body potential in which all the nucleons of a nucleus can be assumed to be moving independently(non-interacting) is presented. As an example, expressions for the Hartree-Fock and Hartree-Fock-Bogoliubov potentials are derived in terms of a general non-relativistic two-body potential. Some results illustrating the application of these methods are very briefly discussed.

1 Introduction

An atomic nucleus presents a unique quantal self-bound many-body system with the nucleons following Fermi-Dirac statistics. The interaction amongst these particles is assumed to be only of two-body type, the range of interaction being short, about one to two fermi(10^{-13} cm). The observable properties of such a body and its microscopic structure is a complex function of many degrees of freedom. Therefore, for a systematic study one starts with a rather drastic simplified picture of a nucleus in terms of only a few degrees of freedom. Then one gradually proceeds to unravel the underlying microscopic many-body structure in terms of single particle degrees of freedom.

A most simplified assumption is to treat a nucleus as a collection of non-interacting protons and neutrons moving in an average one-body phenomenological potential, e.g., a harmonic oscillator potential (see fig. 1):

$$V(r) = V_0 + \frac{1}{2}m\omega^2 r^2, \quad (1)$$

where, V_0 is a constant giving the strength of the interaction potential, m is the nucleon mass about 938 MeV and ω the oscillator frequency. A better choice is the Woods-Saxon potential(fig. 1)

$$V(r) = \frac{V_0}{1 + \exp(\frac{r-R}{a})}. \quad (2)$$

Then one adds an attractive spin-orbit term ($\mathbf{l} \cdot \mathbf{s}$) in order to explain the occurrence of the magic numbers 2, 8, 28, 50, 82, 126 etc. Nuclei with such proton and neutron numbers are spherical in shape in the ground state and show relatively excessive binding energy per particle. It is obvious that out of thousands of nuclei in the periodic table only a small number of nuclei can be perfectly spherical even in the ground state. Actually majority of the nuclei are prolate (cigar shaped) in the ground state. For such cases one can take deformed harmonic oscillator or deformed Woods-Saxon potential in the phenomenological approach. However, here we are actually interested to follow

a microscopic approach to derive an average one-body potential using the two-body interaction potential.

Essence of such an approach is the following. One can write a two-body potential as

$$\begin{aligned} \sum_{i,j} V(i,j) &= \sum_i U(i) + \left(\sum_{i,j} V(i,j) - \sum_i U(i) \right) \\ &= \sum_i U(i) + \sum_{i,j} \delta V(i,j) \end{aligned} \quad (3)$$

$$= \sum_i U(i) \quad (if \delta V = 0) \quad (4)$$

So, an interacting many particle system can be replaced, in the zeroth order, by an equivalent non-interacting system provided a correct one-body potential can be guessed or parametrized. In the microscopic approach the mean field theory provides a prescription to achieve this using directly the two-body interaction potential starting with the ansatz that the nuclear many-body wave function is an antisymmetrized product of single particle wave functions, and the expectation value of the Hamiltonian should be minimized with respect to the relevant parameters of the single particle wave functions or the single particle density. Within such a framework we derive Hartree-Fock equations in the next section.

2 Hartree-Fock Formalism

• The General Variational Principle [1]

For a given Hamiltonian the exact Schrödinger equation to be solved is

$$H | \Psi \rangle = E | \Psi \rangle, \quad (5)$$

where

$$E[\Psi] = \frac{\langle \Psi | H | \Psi \rangle}{\langle \Psi | \Psi \rangle}. \quad (6)$$

Using the above expression, the variation $\delta E[\Psi] = 0$, leads to

$$\langle \delta \Psi | H - E | \Psi \rangle + \langle \Psi | H - E | \delta \Psi \rangle = 0. \quad (7)$$

Since $| \Psi \rangle$ is in general complex, the variations $| \delta \Psi \rangle$ and $\langle \delta \Psi |$ can be treated independently, and both the terms should vanish separately. Since the variation $| \delta \Psi \rangle$ is arbitrary, solving for

$$\langle \delta \Psi | H - E | \Psi \rangle = 0 \quad (8)$$

is equivalent to solving the original Schrödinger equation.

Let E_0 denote the exact ground state energy of the system. Then we can see that this is the lower bound for the variational solution. The trial wave function can be written in terms of the exact eigenfunctions of the Hamiltonian

$$| \Psi \rangle = \sum_{n=0}^{\infty} a_n | \Psi_n \rangle, \quad (9)$$

with

$$H | \Psi_n \rangle = E_n | \Psi_n \rangle . \quad (10)$$

We can see that

$$E[\Psi] = \frac{\sum_n |a_n|^2 E_n}{\sum_n |a_n|^2} . \quad (11)$$

The right hand side of the above relation is E_0 if and only if all the states are degenerate to the ground state (which is normally not the case) or all the coefficients a_n vanish for $n \neq 0$. Thus, in practice the variationally determined energy is always higher than the real ground state energy and the determined wave function, say, $|\Phi\rangle$ is only approximately close to the exact ground state wave function $|\Psi_0\rangle$.

• Derivation of the HF Hamiltonian

In second quantized notation the many-body Hamiltonian can be written as

$$H = \sum_{\alpha, \beta} \langle \alpha | t | \beta \rangle c_{\alpha}^{\dagger} c_{\beta} + \frac{1}{4} \sum_{\alpha \beta \gamma \delta} \langle \alpha \beta | v | \gamma \delta \rangle c_{\alpha}^{\dagger} c_{\beta}^{\dagger} c_{\delta} c_{\gamma} , \quad (12)$$

with antisymmetrised two body matrix elements in a basis space $\alpha \equiv (nljm\tau_3)$ etc. in standard notations. With the HF ground state wave function Φ , using the Wick's theorem the total energy can be written as a functional of the single-particle density [1, 2]

$$\begin{aligned} E[\rho] &= \sum_{\alpha \beta} \langle \alpha | t | \beta \rangle \rho_{\beta \alpha} + \frac{1}{2} \sum_{\alpha \beta \gamma \delta} \rho_{\gamma \alpha} \langle \alpha \beta | v | \gamma \delta \rangle \rho_{\delta \beta} \\ &= Tr(t\rho) + \frac{1}{2} Tr_1 Tr_2(\rho v \rho) , \end{aligned} \quad (13)$$

with density matrix defined as

$$\rho_{\beta \alpha} = \langle \Phi | c_{\alpha}^{\dagger} c_{\beta} | \Phi \rangle , \quad (14)$$

and, as obvious, Tr standing for the trace. Tr_1 , and Tr_2 imply traces in the spaces of particles one and two, respectively. The Eq. 13 is independent of the basis space, and we can go to the HF basis space in which the density is diagonal. This basis is defined as

$$|k\rangle = \sum_{\alpha} D_{\alpha k} |\alpha\rangle , \quad (15)$$

and

$$a_k^{\dagger} = \sum_{\alpha} D_{\alpha k} c_{\alpha}^{\dagger} . \quad (16)$$

Now the density matrix becomes

$$\rho_{\beta \alpha} = \sum_{i=1}^A D_{\alpha i}^* D_{\beta i} , \quad (17)$$

where A stands for the number of particles (i.e., sum is only over the occupied HF states, also termed as hole states). This implies that

$$\rho_{kk'} = \delta_{kk'} n_k \quad (18)$$

with $n_k = 1$ for the occupied states(holes) and 0 for unoccupied(particle) states. That is $\rho^2 = \rho$ and $Tr(\rho) = A$, the number of particles. Thus, ρ is a projector on the space of the hole states, and $\sigma = 1 - \rho$ is a projector on the particle space.

Now we can write the HF energy in the HF-basis in which ρ is diagonal,

$$E = \sum_i \langle i|t|i \rangle n_i + \frac{1}{2} \sum_{i,j} \langle ij|v|ij \rangle n_j n_i . \quad (19)$$

• Variation of the Energy

In order to determine the HF-basis (15) we have to minimize the energy (13) with respect to Φ or for all densities ρ with the condition that $\rho^2 = \rho$. Assuming a very small variation $\rho_0 + \delta\rho$ with $(\rho_0 + \delta\rho)^2 = \rho_0 + \delta\rho$, within linear terms in $\delta\rho$ we obtain,

$$\delta\rho = \rho_0 \delta\rho + \delta\rho \rho_0 . \quad (20)$$

In the basis where ρ is diagonal the particle-particle (pp) and hole-hole (hh) matrix elements of $\delta\rho$ vanish, and only (ph) and (hp) matrix elements of $\delta\rho$ are non-zero. With

$$E[\rho_0 + \delta\rho] = E[\rho_0] + \delta\rho \frac{\partial E[\rho]}{\partial \rho} \Big|_{\rho_0} + \dots , \quad (21)$$

the variation of the energy is given by

$$\begin{aligned} \delta E &= E[\rho_0 + \delta\rho] - E[\rho_0] \\ &= \sum_{k,k'} h_{kk'} \delta\rho_{k'k} , \end{aligned} \quad (22)$$

where the hermitian matrix h is defined as

$$h_{kk'} = \frac{\partial E_{HF}[\rho]}{\partial \rho_{k'k}} , \quad (23)$$

and with the use of Eq. 13 this is finally given by

$$h = t + I \quad (24)$$

along with the *mean field*

$$\Gamma_{kk'} = \sum_{ll'} \langle kl|v|k'l' \rangle \rho_{l'l} . \quad (25)$$

Since arbitrary values of $\delta\rho$ are allowed in Eq. 22, the condition $\delta E = 0$ for the HF solution means that the particle-hole(ph) matrix elements of h must vanish,

$$\langle p|h|h \rangle = \langle p|t|h \rangle + \sum_{h'=1}^A \langle ph'|v|hh' \rangle = 0 \quad (26)$$

in the basis where ρ is diagonal. This means h and ρ commute and these can be simultaneously diagonalized. So, we can diagonalize h in the full basis space (Eq. 15) and

construct ρ as well from these solutions. This defines the HF basis along with the HF mean field given by Eq. 25.

$$h_{kk'} = \langle k|t|k' \rangle + \sum_{i=1}^A \langle ki|v|k'i \rangle = \epsilon_k \delta_{kk'} \quad (27)$$

In the basis space the above expression becomes a Hermitian eigenvalue equation (HF equation).

$$\sum_{\gamma} (t_{\alpha\gamma} + \sum_{\beta\delta} \langle \alpha\beta|v|\gamma\delta \rangle \rho_{\delta\beta}) D_{\gamma k} = \epsilon_k D_{\alpha k} \quad (28)$$

It is a highly nonlinear equation in ρ and is to be solved in a self-consistent iterative way.

• HF Equations in Coordinate Space

The above HF equation (28) becomes physically more transparent when written in the space coordinates. Assuming a local two-body potential depending only on space coordinates the above equation becomes [1]

$$-\frac{\hbar^2}{2m} \Delta \phi_k(\mathbf{r}) + \sum_{j=1}^A \int d\mathbf{r}' v(\mathbf{r}, \mathbf{r}') \phi_j^*(\mathbf{r}') \{ \phi_j(\mathbf{r}') \phi_k(\mathbf{r}) - \phi_j(\mathbf{r}) \phi_k(\mathbf{r}') \} = \epsilon_k \phi_k(\mathbf{r}) \quad (29)$$

Now define a local Hartree potential

$$\Gamma_H(\mathbf{r}) = \int d\mathbf{r}' v(\mathbf{r}, \mathbf{r}') \sum_{j=1}^A |\phi_j(\mathbf{r}')|^2 = \int d\mathbf{r}' v(\mathbf{r}, \mathbf{r}') \rho(\mathbf{r}') \quad (30)$$

and a nonlocal or exchange potential

$$\Gamma_{EX}(\mathbf{r}, \mathbf{r}') = -v(\mathbf{r}, \mathbf{r}') \rho(\mathbf{r}, \mathbf{r}'). \quad (31)$$

We find that ϕ_k is the solution of a nonlocal Shrödinger equation

$$\left\{ -\frac{\hbar^2}{2m} \Delta + \Gamma_H(\mathbf{r}) \right\} \phi_k(\mathbf{r}) + \int d\mathbf{r}' \Gamma_{EX}(\mathbf{r}, \mathbf{r}') \phi_k(\mathbf{r}') = \epsilon_k \phi_k(\mathbf{r}). \quad (32)$$

It should be noted that starting with a local two-body interaction, the Fock (exchange) potential is nonlocal. Starting with a nonlocal two-body interaction would make even the Hartree potential as nonlocal.

Before ending this section we may discuss briefly two aspects of this approach in a nonrelativistic calculation. Except in the use of Skyrme type interactions, usually one assumes an inert core of some doubly closed shell spherical nuclei with particle numbers, say, Z_0 and N_0 . Then an effective Hamiltonian is employed corresponding to the number of valence particles, $Z-Z_0$ and $N-N_0$. In this procedure the internucleon interaction between the core particles and the valence particles is ignored. That is polarization of the so called inert core by the valence particles is also ignored. This all is to be accounted for by adjusting the parameters of the effective Hamiltonian and other physical

operators like quadrupole moment operator etc. Thus, one often needs to parametrize the interaction from region to region of the periodic table.

Application of the Wick's theorem to the two-body part of the Hamiltonian (12) not only gives a single-particle density but also gives a two-body pairing density term which is ignored at the HF mean field level. Generalization to include also such terms is achieved in the Hartree-Fock-Bogoliubov(HFB) approach which we discuss in the next section.

2.1 Hartree-Fock-Bogoliubov Formalism

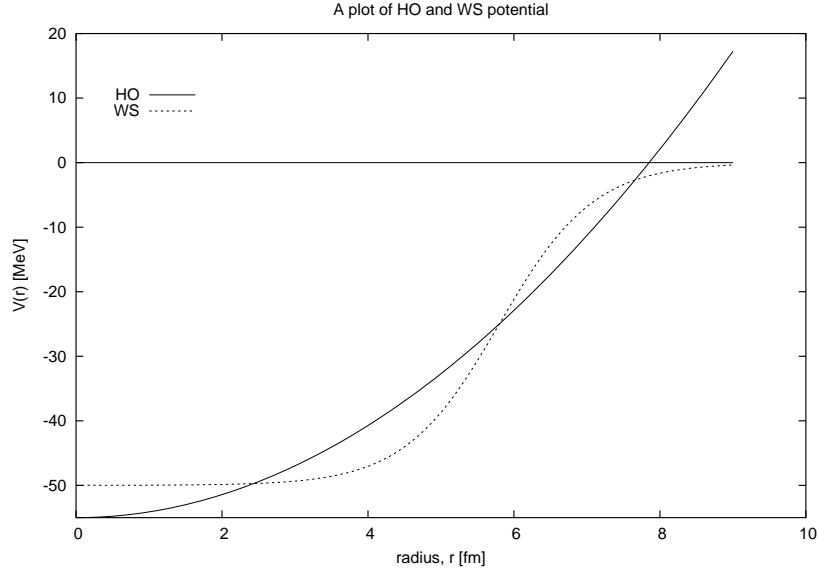


Fig. 1. HO: harmonic oscillator potential with $V_0 = -55$ MeV and $\hbar\omega = 8.6$ MeV. WS: Woods-Saxon potential with $V_0 = -50$ MeV, $R = 5.8$ fm and $a = 0.65$ fm.

After performing a selfconsistent HF calculation for a nucleus, if one finds that the gap above the Fermi surface λ_F is not sufficiently large (compared to the average spacing between single particle levels) leading to a high density of states near the Fermi surface, the short range pairing correlations become important. This is illustrated in fig. 2 for a schematic spectrum for single particle levels of a spherical as well as a deformed system. But then in order to remain still in an independent particle picture the concept of hole and particle states is to be changed to that of quasiparticles through a unitary Bogoliubov transformation. The full Hamiltonian is approximated by

$$H = H_0 + \sum_i E_i b_i^\dagger b_i + H_{int} , \quad (33)$$

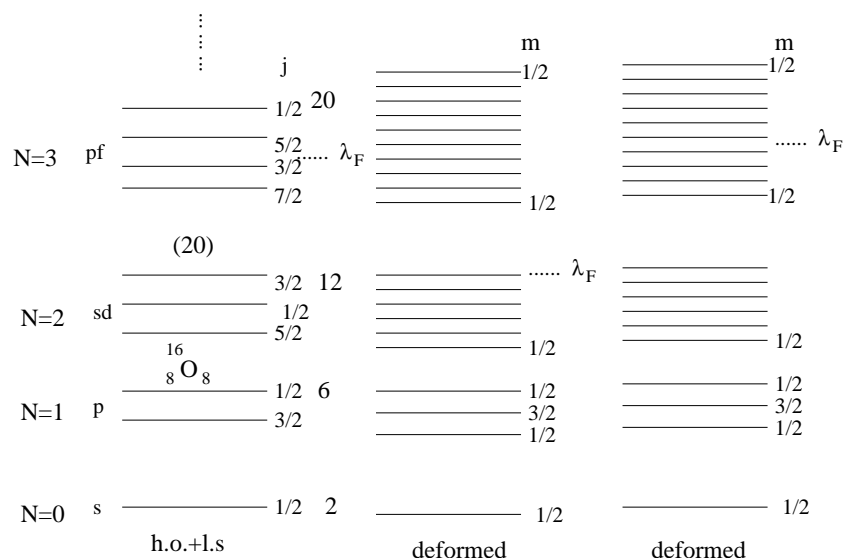


Fig. 2. A schematic single-particle spectrum for spherical as well as deformed single-particle states. The position of the Fermi level λ_F is indicated to illustrate if the pairing correlations would be important.

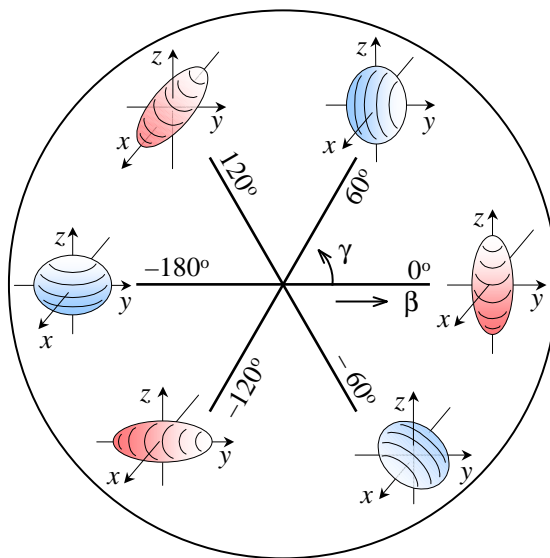


Fig. 3. A schematic picture showing quadrupole shape changes as a function of γ .

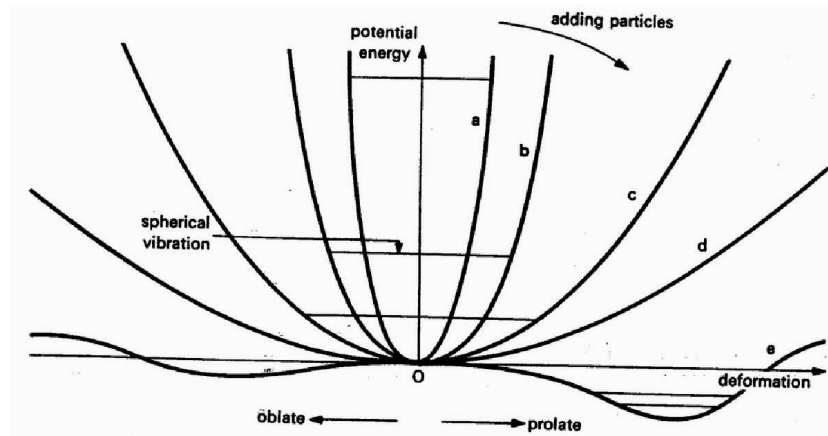


Fig. 4. A schematic potential energy surface plot in the axial quadrupole deformation parameter β space for spherical(a) to well deformed (e) nuclei.

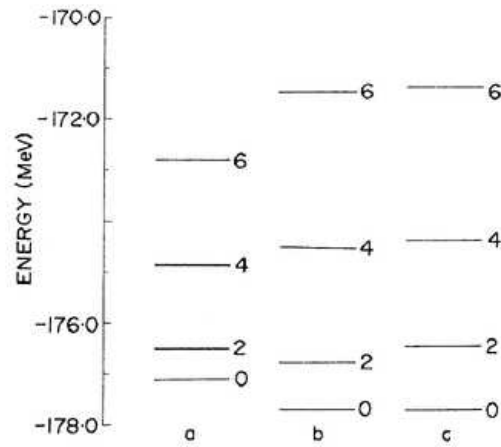


Fig. 5. Ground band spectrum of ^{22}Ne . Column 'c' is the experimental spectrum, whereas columns 'a' and 'b' refer to angular momentum projected results from HF and HFB solutions, respectively [6].

where b_i^\dagger is a quasiparticle creation operator with E_i as the quasiparticle energy. H_0 is the intrinsic ground state energy within this approximation. H_{int} represents the interaction between the quasiparticles.

The quasiparticle operators are defined in terms of the basis space operators as

$$\begin{aligned} b_i^\dagger &= \sum_{\alpha} (A_{\alpha i} c_{\alpha}^\dagger + B_{\alpha i} c_{\alpha}) \\ b_i &= \sum_{\alpha} (B_{\alpha i}^* c_{\alpha}^\dagger + A_{\alpha i}^* c_{\alpha}) \end{aligned} \quad (34)$$

The inverse relations are

$$\begin{aligned} c_{\alpha}^\dagger &= \sum_i (A_{\alpha i}^* b_i^\dagger + B_{\alpha i} b_i) , \\ c_{\alpha} &= \sum_i (B_{\alpha i}^* b_i^\dagger + A_{\alpha i} b_i) \end{aligned} \quad (35)$$

The HFB ground state contains no quasiparticles, and is defined through

$$b_i | HFB \rangle = 0 , \quad (36)$$

with a possible choice of $|HFB\rangle = \prod_i b_i |0\rangle$, $|0\rangle$ being the real vacuum.

It is inherent in the qp transformation that the $|HFB\rangle$ wavefunction is not an eigen-state of the particle number operator.

$$\hat{N} = \sum_{\alpha} c_{\alpha}^\dagger c_{\alpha} \quad (37)$$

However, the particle number can be conserved on the average as a constraint through the use of a Lagrange multiplier, such that the Hamiltonian can be written as

$$\begin{aligned} H' &= H - \lambda \hat{N} \\ &= \sum_{\alpha} (e_{\alpha} - \lambda) c_{\alpha}^\dagger c_{\alpha} + \frac{1}{4} \sum_{\alpha\beta\gamma\delta} \langle \alpha\beta | v | \gamma\delta \rangle c_{\alpha}^\dagger c_{\beta}^\dagger c_{\delta} c_{\gamma} . \end{aligned} \quad (38)$$

The HFB equations can be derived following the above energy density functional procedure taking the total energy to depend on sp density and pairing density $E(\rho, \kappa)$ [2]. However, here we will follow another alternative method as discussed below. To remain within the independent quasiparticle picture the following equation of motion should be satisfied (see Eq. 33).

$$\begin{aligned} [H', b_i^\dagger] &= E_i b_i^\dagger , \\ [H', b_i] &= -E_i b_i . \end{aligned} \quad (39)$$

To evaluate the commutators of the Fermionic operators the following identity is very useful.

$$[AB, C] = A\{B, C\} - \{A, C\}B \quad (40)$$

$$[A, BC] = \{A, B\}C - B\{A, C\} \quad (41)$$

Now we can easily evaluate the one body and two body commutators required in the above equations of motion (Eq. 39).

$$[c_\alpha^\dagger c_\beta, b_i^\dagger] = A_{\beta i} c_\alpha^\dagger - B_{\alpha i} c_\beta \quad (42)$$

$$[c_\alpha^\dagger c_\beta^\dagger c_\delta c_\gamma, b_i^\dagger] = A_{\gamma i} c_\alpha^\dagger c_\beta^\dagger c_\delta - A_{\delta i} c_\alpha^\dagger c_\beta^\dagger c_\gamma + B_{\beta i} c_\alpha^\dagger c_\delta c_\gamma - B_{\alpha i} c_\beta^\dagger c_\delta c_\gamma \quad (43)$$

To simplify the product of three operators we can use the Wick's theorem as seen below for one case:

$$c_\alpha^\dagger c_\beta^\dagger c_\delta =: c_\alpha^\dagger c_\beta^\dagger c_\delta : + \langle c_\alpha^\dagger c_\beta^\dagger \rangle c_\delta + \langle c_\beta^\dagger c_\delta \rangle c_\alpha^\dagger - \langle c_\alpha^\dagger c_\delta \rangle c_\beta^\dagger \quad (44)$$

Next we define one body HF density ρ and pairing density matrix κ

$$\begin{aligned} \rho_{\delta\beta} &= \langle HFB | c_\beta^\dagger c_\delta | HFB \rangle \\ &= (B^* \tilde{B})_{\delta\beta} \\ \kappa_{\delta\gamma} &= \langle HFB | c_\delta c_\gamma | HFB \rangle \\ &= (AB^\dagger)_{\delta\gamma}, \end{aligned} \quad (45)$$

where \tilde{B} stands for the transpose of B . Using the above relations, antisymmetry property of the interaction matrix elements and manipulating with the summation indices one gets the commutator

$$\begin{aligned} [H', b_i^\dagger] &= \sum_{\alpha\gamma} \{ [(e_\alpha - \lambda)\delta_{\alpha\gamma} + \Gamma_{\alpha\gamma}] A_{\gamma i} + \Delta_{\alpha\gamma} B_{\gamma i} \} c_\alpha^\dagger \\ &\quad - [((e_\alpha - \lambda)\delta_{\alpha\gamma} + \Gamma_{\alpha\gamma}^*) B_{\gamma i} + \Delta_{\alpha\gamma}^* A_{\gamma i}] c_\alpha, \end{aligned} \quad (46)$$

where the HF potential Γ and pairing potential Δ are defined as

$$\Gamma_{\alpha\gamma} = \sum_{\beta\delta} \langle \alpha\beta | v | \gamma\delta \rangle \rho_{\delta\beta} \quad (47)$$

$$\Delta_{\alpha\beta} = \frac{1}{2} \sum_{\gamma\delta} \langle \alpha\beta | v | \gamma\delta \rangle \kappa_{\delta\gamma} \quad (48)$$

As per the equation of motion (39) the above Eq. 46 should be equated to $E_i \sum_\alpha (A_{\alpha i} c_\alpha^\dagger + B_{\alpha i} c_\alpha)$ for each value of α . This equality leads to the HFB equations [1, 3].

$$\begin{pmatrix} \bar{\Gamma} & \Delta \\ -\Delta^* & -\bar{\Gamma}^* \end{pmatrix} \begin{pmatrix} A \\ B \end{pmatrix} = E \begin{pmatrix} A \\ B \end{pmatrix}. \quad (49)$$

In the above, $\bar{\Gamma}_{\alpha\gamma} = (e_\alpha - \lambda)\delta_{\alpha\gamma} + \Gamma_{\alpha\gamma}$.

Like HF equations, the HFB equations too have to be solved iteratively. In order to choose a guess value for the Bogoliubov transformation coefficients A and B one may perform a Hartree-BCS or Nilsson-BCS calculation such that $A_{\alpha i} = D_\alpha^i U_i$ and $B_{\alpha i} = D_\alpha^i V_i$, where D are the HF expansion coefficients and U and V are the standard BCS occupation probability parameters.

The total intrinsic ground state energy in HFB theory can be calculated as

$$E_{HFB} = \sum_{\alpha\gamma} (e_\alpha \delta_{\alpha\gamma} + \frac{1}{2} \Gamma_{\alpha\gamma}) \rho_{\gamma\alpha} + \frac{1}{2} \sum_{\alpha\beta} \Delta_{\alpha\beta} \kappa_{\beta\alpha}^*. \quad (50)$$

2.2 Mean Field at Finite Temperature

In heavy ion induced fusion reactions residual compound nuclei can be formed at high intrinsic excitation energies(finite temperature, T). Assuming thermal equilibrium the statistical mechanics can be applied to study the structural properties of such nuclei. Simplest way is to introduce in the Hartree-Fock formalism the occupation probabilities n_i (Eq. 18) through the Fermi distribution function [4]

$$n_i = \frac{1}{1 + \exp(\frac{\epsilon_i - \mu}{T})} \quad (51)$$

This implies that the Fermi surface is now not sharp but diffused. In the above equation μ is the chemical potential and is determined by the constraint that the number of particles is given by

$$\sum_i n_i = N, \quad (52)$$

where N actually stands for protons as well as neutrons. The method is rather straight forward, where the free energy $F = E - TS$ is to be minimized, S being the entropy of the system, calculated as

$$S = - \sum_i \{n_i \ln(n_i) + (1 - n_i) \ln(1 - n_i)\} \quad (53)$$

If the pairing correlations are important, one has to follow HFB method at finite temperature. Goodman [5] has performed several cranked HFB calculations at finite temperature and angular momentum. We will not present this formalism here. But, will like to point out that if typically $T > 0.5$ MeV, thermal fluctuations in the shape degrees of freedom become important. As temperature increases the free energy as a function of the shape parameters becomes increasingly shallower. One can talk only of thermal average values rather than equilibrium values, for all the observables

$$\langle O \rangle_T = Z^{-1} \int D[\alpha] O(\alpha) e^{-\frac{F(\alpha)}{T}}, \quad Z = \int D[\alpha] e^{-\frac{F(\alpha)}{T}}. \quad (54)$$

In the above α stands for the set of shape variables and $D[\alpha]$ stands for the volume element (Haar measure).

3 Some Results and Discussions

In HF or HFB calculations it is always useful to look at the energy surface as a function of the relevant deformation parameters. As a function of the quadrupole asymmetry deformation parameter γ we show in fig. 3 the possible prolate or oblate shapes along with the axis of the axial symmetry. This figure is particularly relevant while studying the evolution of the quadrupole shape with nuclear spin. Now we display in fig. 4 a schematic plot of potential energy surface(PES) as a function of deformation parameter(β) for an axially deformable spheroidal shape. Curves ' a ' to ' e ' demonstrate possible PES shapes for different nuclei, from good (deep minimum) spherical to well

deformed prolate equilibrium shape. In between the minima are shallow and a good description of the ground state of such nuclei will require mixing of various nonorthogonal many-body wavefunctions corresponding to these deformations. The vibrations around a spherical equilibrium shape can be described by the method of random phase approximation(RPA) or quasiparticle RPA in the angular momentum coupled scheme [1,3]. But the microscopic description of rotational bands for the deformed nuclei is more complicated in the sense that one has to follow angular momentum projection techniques.

We show in fig. 5 a result obtained by Gunye and Khadkikar [6] for ^{22}Ne after angular momentum projection from HF and HFB solutions. It is found that the spectrum($J = 0$ to 6) is significantly affected by inclusion of the pairing correlations(HFB) leading to a good agreement with the experimental data.

At this point it may be remarked that the manifestation of the effect of pairing correlations on nuclear properties is best realized by calculation of the moment of inertia. The value gets typically reduced by factors of the order of 2 to 5 in the HFB approach as compared to that of the rigid body and HF value. This can be seen for example, in fig. 4-12 in ref. [7], where experimentally deduced values of the moment of inertia are plotted as a function of the nuclear mass number. The experimental value (in the rotor model approximation) may be computed as $\mathcal{I}/\hbar^2 = (2J - 1)/E_\gamma^J$ and the rigid body value as $0.4 A m R^2(1 + \beta/3)$. In the above m is the nucleon mass and the nuclear radius $R = 1.2A^{1/3}\text{fm}$. As an example, for ^{238}U using the excitation energy of the first 2^+ rotational state as 45 keV and $\beta = 0.3$ the ratio of the rigid body to experimental value is about 2. This is the case for a nucleus which is a very good rotor with the ratio $E_4/E_2 = 3.3$.

In very brief let us mention about some results of Goodman [5] for high spin properties of ^{158}Yb at finite temperatures in the cranked HFB theory. The intrinsic deformed shape obtained in HFB at $T = 0$ becomes spherical at some finite value of T (shape phase transition) and remains so at higher temperatures(a classical result). On the otherhand it never goes to zero if thermal fluctuation effects are included as discussed above. At a high spin $J = 40$ and $T = 0$ the shape of ^{158}Yb becomes oblate($\gamma = -60^\circ$), and remains so at all temperatures with rotation about the symmetry axis. But if the effects of thermal fluctuations are incorporated the shape becomes prolate at $T = 0.8$ MeV, and at $T = 1.6$ MeV γ goes to about $+20^\circ$.

4 Conclusions

We have derived expressions for mean field HF and pairing potentials in terms of the two-body general interaction potential for nuclei. Application of these methods for the study of nuclear structure properties along with some illustrative results have also been discussed.

References

1. P. Ring and P. Schuck, *The Nuclear Many-body Problem*, Springer-Verlag New York Inc. (1980).

2. Jean-Paul Blaizot and Georges Ripka, *Quantum Theory of Finite Systems*, The MIT Press (1986).
3. M.K. Pal, *Theory of Nuclear Structure*, Affiliated East-West Press (1982).
4. A.L. Goodman, Nucl. Phys. **A352** (1981) 30.
5. A.L. Goodman, Phys. Rev. **C 39** (1989) 2008.
6. M.R. Gunye and S.B. Khadkikar, Phys. Rev. Lett. **24** (1970) 910.
7. A. Bohr and B.R. Mottelson, *Nuclear Structure* vol. II, Benjamin, Reading MA. (1975).

Salient Features of RMF and its Applications

Y. K. Gambhir

Department of Physics, I.I.T. Powai, Bombay 400076, India

Abstract. The essentials of the Relativistic Mean Field (RMF) formalism are presented and discussed. We begin with an answer to the standard question “Why the relativistic formulation is required in the description of the nuclear properties?”.

The RMF describes the Dirac spinor nucleons interacting via the electromagnetic (e.m.) and meson fields. The mesons considered are the iso-scalar scalar sigma (σ), iso-scalar vector omega (ω) and iso-vector vector rho (ρ). The variational principle yields the equations of motion. In the mean field approximation, replacing the fields by their expectation values, one ends up with a set of coupled equations:

1. The Dirac equation with potential terms involving meson and e.m. fields describing the nucleon dynamics
2. A set of Klein-Gordon type equations with sources involving nucleonic currents and densities, for mesons and the photon.

This set of equations, known as RMF equations are to be solved self-consistently. The pairing correlations, essential for the description of open shell nuclei, are incorporated either by the simple BCS prescription, or self consistently through the Bogoliubov transformation. The latter leads to the Relativistic Hartree Bogoliubov (RHB) equations.

The RMF/RHB equations are solved in practice either by using the conventional basis expansion technique (spherical / deformed harmonic oscillator basis) or in the coordinate space. The solution in the coordinate space with the right boundary conditions is expected to incorporate the correct asymptotics. Here, we discuss both the techniques of solving the RMF/RHB equations.

Several applications of the RMF/RHB are presented and discussed through a variety of illustrative examples.

1 Introduction

The complex nuclear many body problem can not be solved exactly. Therefore, the major efforts in this context are devoted to develop approximate methods. The mean field has been the most successful and fruitful concept which also provides a first useful step towards the solution of this complex problem. To illustrate this mean field concept, consider the Schroedinger equation for A - nucleons (N -neutrons and Z -protons, $A = N + Z$) interacting only via two-body interaction V :

$$H\Psi = E\Psi ; \quad (1)$$

with,

$$H = \sum_i T_i + \sum_{i<j} V_{ij}. \quad (2)$$

Now add and subtract a one body operator $\boxed{U_i}$, to get

$$H = \sum_i \left(T_i + \boxed{U_i} \right) + \left(\sum_{i < j} V_{ij} - \sum_i \boxed{U_i} \right) \quad (3)$$

$$= \sum_i h_i + h_{int} . \quad (4)$$

The important point to note is that we have the

$\boxed{\text{freedom to choose this one body operator } U_i}$.

We exploit this freedom to our advantage and choose this operator in such a way that it makes the interaction term (h_{int}) as small as possible. As a result the mean field (h_i) dominates. In the first step, the interaction term is ignored (the mean field approximation). This provides the independent particle picture where each nucleon moves independently in this mean field. This average mean field (h_i) is supposed to originate from the overall interaction of this nucleon with all the rest of the nucleons in the nucleus. In the next step this approximation can be improved at various levels by incorporating specific additional correlations arising from the left over effective two body interaction h_{int} . The average field (h_i) can either be introduced phenomenologically (as in the conventional shell model) or can be derived microscopically following the

$\boxed{\text{self-consistent Brueckner - Bethe - Hartree - Fock BBHF procedure}}$

The non-relativistic analysis is known to indicate that the average field in the nucleus has almost Woods-Saxon (WS) radial shape with strength (U) about 50 MeV., while the important spin-orbit interaction term ($l \cdot s$) in the mean field has to be introduced phenomenologically. Notice that

$$U \sim 50 \text{ MeV} \ll mc^2 (\sim 1000 \text{ MeV}).$$

Now the **Question** arises :

$\boxed{\text{Why the relativistic formulation is required?}}$

The answer to this question is affirmative mainly due to the following reasons.

- The availability of the polarised permits to perform experiments with polarized proton beams on a variety of targets at various energies. This enabled accurate measurements of spin observables like analyzing power, spin rotation function and longitudinal and transverse responses etc. Surprisingly, it was found that the conventional (non relativistic) Optical Model (OM) completely fails to describe the measured spin observables like the Analyzing Power (A_y) and the spin Rotation Function (Q) in the intermediate energy ($E \sim 300 \text{ MeV}$) polarized proton - nucleus (p - A) scattering. As the proper description of spin is relativistic, it was therefore, suggested to replace the Schrödinger equation by the Dirac equation with Lorentz scalar (S) and vector (V) (Lorentz time like) potentials. This so called **Dirac Phenomenology** turned out to be remarkably successful in accurately reproducing the measured cross sections (σ) and the spin variables A_y & Q .

Further, the microscopically calculated scalar (S) and vector (V) potentials using the relativistic Brueckner type t-matrix, reproduce the corresponding S and V used

in the **Dirac Phenomenology**. In addition the non-relativistic reduction of the Dirac equation leads to Schrödinger like equation with energy dependent potential. The analysis of this equivalent energy dependent optical model (OM) potential reveals that it changes shape (from Woods-Saxon to Wine Bottle Bottom shape) and even sign (from Attractive to Repulsive) at these intermediate energies. The use of this energy dependent potential in the conventional non-relativistic optical model (OM) reproduces well the observed values of σ , A_y & Q .

It should be added here that it was this phenomenal success of the Dirac Phenomenology which triggered the numerous successful applications of RMF approach to several nuclear properties.

- **The most direct indication** for the need of relativistic description stems from the observed **Large Anomalous nuclear $l \cdot s$ splitting**. We now illustrate this below explicitly:

Notice that in the atomic case $l \cdot s$ interaction is given by the **Thomas Formula**:

$$U_{ls}^{atomic} = \frac{1}{4M^2} \frac{1}{r} \frac{\partial U^{at}}{\partial r} (l \cdot \sigma) \quad (5)$$

$U^{at} \Rightarrow$ Central Potential (Coulomb field of Nucleus + Self- Consistent HF field)

On the other hand the **observed Nuclear $l \cdot s$** is very large (~ 30 times) and is of **opposite sign** as compared to the atomic case. This important term in the non-relativistic description, as mentioned before is introduced in practice, phenomenologically. Explicitly:

$$\frac{\alpha}{r} \frac{\partial \rho}{\partial r} (l \cdot \sigma) , \quad (6)$$

with

$$\frac{\partial U}{\partial r} = - \frac{\partial \rho}{\partial r}. \quad (7)$$

$U \sim -50$ MeV, having **WS Shape**.

We shall now show that these features do emerge from the σ - ω Model of Walecka or from **Dirac Phenomenology**. In this picture the nucleon dynamics is governed by the Dirac Equation with the static Scalar (S) and Vector (V) potentials (fields). It reads:

$$[\alpha \cdot p + \beta (M + S) + V] \Psi_\mu = E_\mu \Psi_\mu \quad (8)$$

Rewriting this equation in terms of ψ_u (ψ_l) the upper (lower) component of the Dirac Spinor (Ψ_μ) and eliminating the lower component ψ_l one ends up with the following second order differential equation (up to an accuracy of order ϵ/M) for the upper component ψ_u :

$$\left[p \frac{1}{2\mathcal{M}} p + \underbrace{(S + V)}_{\uparrow U(r)} + \frac{1}{r} \underbrace{\left(\frac{\partial}{\partial r} \frac{1}{2\mathcal{M}} \right)}_{\uparrow U_{ls}} l \sigma \right] \psi_u = \epsilon \psi_u \quad (9)$$

The energy E is measured relative to nucleon mass M ($E_\mu = M + \epsilon_\mu$; ϵ_μ being negative)

This is Schrödinger like equation with :

- (i) Central Potential $U(r) = \frac{S+V}{2}$; $S - ve$ and $|S| > |V|$.
- (ii) Mass term $\mathcal{M} = M \left(1 + \frac{S-V}{2M}\right)$, $2\mathcal{M} = 2M + S - V$.
- (iii) Spin-Orbit Term: U_{ls} ; $U_{ls} = \frac{1}{r} \frac{\partial}{\partial r} \left(\frac{1}{2\mathcal{M}}\right)$.

NB: U_{ls} is large as (a) $|V - S| \gg U$

and (b) $\mathcal{M} < M$

Notice that it has the correct sign and also the magnitude.

Comparing this with the corresponding non-relativistic (phenomenological) term

$$\frac{1}{r} \frac{\partial}{\partial r} \left(\frac{1}{2\mathcal{M}} \right) = \frac{\alpha}{r} \frac{\partial \rho}{\partial r} \quad (10)$$

yields:

$$\frac{1}{\epsilon \mathcal{M}} = \alpha \rho + \frac{1}{2M} \quad (11)$$

The last term appears because as $r \gg$ nuclear size, $\mathcal{M} \rightarrow M$, $\rho \rightarrow 0$.

Knowing α and ρ one can estimate V and S , as illustrated below:

Phenomenology gives: $\alpha = 85.5 \text{ MeV-fm}^5$ and $\rho = 0.17 \text{ fm}^{-3}$, therefore

$$\frac{\mathcal{M}}{M} = \frac{1}{1 + 2\alpha \rho M} = \frac{1}{1 + 2 \times 85.5 \times 0.17 \frac{Mc^2}{\hbar c}} \approx 0.6 \quad (12)$$

Thus, $\boxed{\mathcal{M} = 0.6 M} \Rightarrow 2M + S - V = 2 \times 0.6M$;

or $\boxed{S - V = -0.8M} \approx -750 \text{ MeV}$.

Shell-Model gives $\boxed{V + S \approx -50 \text{ MeV}}$, yielding, $V \simeq 350 \text{ MeV}$ and $S \simeq -400 \text{ MeV}$

These magnitudes of V and S are Consistent with the Dirac Phenomenology

Thus in spite of the fact that $\epsilon/M \ll 1$, inside the nucleus, the fields acting on the nucleon are not small ($\sim -400 \text{ MeV}$, $+350 \text{ MeV}$) in comparison with its rest mass. So this is the reason why the nucleus is relativistic even though $\epsilon/M \ll 1$. The value $U = -50 \text{ MeV}$ is the result of the delicate cancellation of two big numbers. Now we shall present the a short summary of the Relativistic Mean Field (RMF) formulation.

2 Essentials of RMF

The Relativistic Mean Field still works at the level of Baryons and Mesons. Several variants of this formulation like the extended Walecka model (conventional RMF), Effective Field Theory (EFT) and the Point Coupling Approach (PCA) exist. All these start with the appropriate interaction Lagrangian. The conventional RMF has σ , ω , ρ and e.m. fields along with the Dirac nucleon spinors. It has basically 7 (8) parameters

(if self coupling of ω is included). The EFT, inspired by the QCD based expansion, includes up to quartic meson field terms. Conventionally, it has 13 parameters. On the other hand, the PCA, as the name suggests, avoids completely the meson fields and includes quadratic (including derivatives), cubic and quartic terms of bi-linear spinors. It has 9 (7) parameters (if the iso-vector terms are dropped). The parameters appearing in their respective Lagrangians are seldom derived, but usually are determined phenomenologically by fitting some ground state properties of a few selected nuclei. All the approaches, though having different number of parameters, lead to more or less the results of the same level of accuracy. Even the density dependence of the parameters have been investigated. It is not yet clear, which one to choose. May be, future will have the answer.

Here, we shall confine to the conventional RMF. It starts with a nonlinear (σ , ω , ρ) interaction Lagrangian developed for and widely used in the nuclear structure applications [8, 9]. The classical variation principle yields the equations of motion. At this stage, the mean field approximation is introduced, and accordingly, the fields are replaced by their expectation values (c - numbers). One then ends up with a set of coupled equations: the Dirac equation with potential terms involving meson and e.m. fields describing the nucleon dynamics and a set of Klein-Gordon type equations with sources involving nucleonic currents and densities, for mesons and the photon. The exchange terms are ignored, that is, one works at the Hartree level. These equations can be further simplified by imposing the symmetry requirements like the charge conservation and the time reversal invariance.

The simplified RMF equations of motion are given by [8]:

$$\left(-i\alpha \cdot \nabla + \beta (M + g_\sigma \sigma) + g_\omega \omega^0 + g_\rho \tau_3 \rho_3^0 + e \frac{1 + \tau_3}{2} A^0 \right) \psi_i = \epsilon_i \psi_i. \quad (13)$$

for the nucleon. Here M is the nucleon mass and σ , ω^0 , ρ_3^0 and A^0 are the respective meson and e.m. fields. These fields are to be determined self-consistently from the Klein-Gordon (KG) equations for the mesons and the photon:

$$\{-\nabla^2 + m_\sigma^2\} \sigma = -g_\sigma \rho_s - g_2 \sigma^2 - g_3 \sigma^3 \quad (14)$$

$$\{-\nabla^2 + m_\omega^2\} \omega^0 = g_\omega \rho_v \quad (15)$$

$$\{-\nabla^2 + m_\rho^2\} \rho_3^0 = g_\rho \rho_3 \quad (16)$$

$$-\nabla^2 A^0 = e \rho_c \quad (17)$$

In these equations m_σ (g_σ), m_ω (g_ω), m_ρ (g_ρ) are meson masses (coupling constants); g_2 and g_3 are the coupling constants for the cubic and quartic self-interaction terms for the σ -field [3]. The source terms (nuclear currents and densities) appearing in the above equations are given by [8],

$$\rho_s = \sum_i n_i \bar{\psi}_i \psi_i; \quad \rho_v = \sum_i n_i \psi_i^\dagger \psi_i \quad (18)$$

$$\rho_3 = \sum_i n_i \psi_i^\dagger \tau_3 \psi_i; \quad \rho_c = \sum_i n_i \psi_i^\dagger \left(\frac{1 + \tau_3}{2} \right) \psi_i \quad (19)$$

In practical calculations, the sum in these equations is taken only over the positive energy states (no-sea approximation).

The occupation probabilities n_i for the state i , in the absence of pairing is given by:

$$\begin{aligned} n_i &= 1 \text{ for } \epsilon_i \leq \epsilon_f; \\ &= 0 \text{ for } \epsilon_i > \epsilon_f. \end{aligned}$$

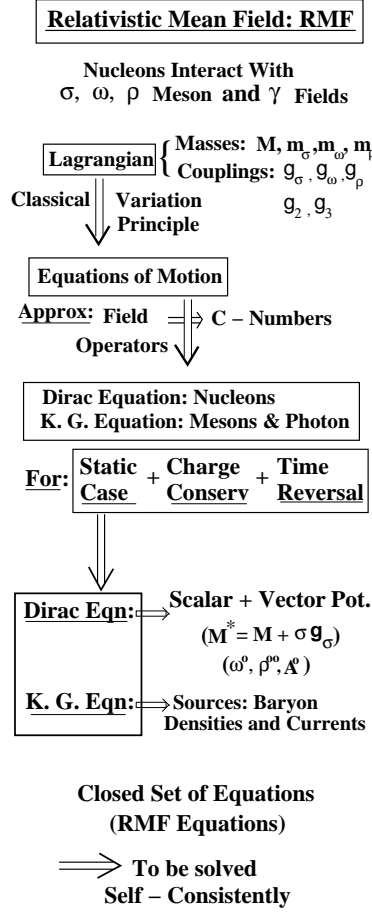


Fig. 1. Schematic picture of RMF framework

Here, ϵ_i is the single particle energy of the state i and ϵ_f is the fermi energy.

The pairing correlations are known to be important for the description of open shell nuclei. The simplest way to incorporate pairing is the frozen gap approximation, where the pairing gap (Δ) is identified with the experimental odd-even mass difference, which in turn can be obtained directly from the known experimental masses [4]. The occupa-

tion probabilities then, are given by the well-known BCS formula:

$$n_i = \frac{1}{2} \left[1 - \frac{\epsilon_i - \epsilon_f}{\sqrt{(\epsilon_i - \epsilon_f)^2 + \Delta^2}} \right] \quad (20)$$

The fermi energy or the chemical potential ϵ_f is fixed by demanding the particle number conservation. This simple prescription (constant Δ) for pairing may work well for nuclei close to the β stability line. However, for consistent and better understanding of the pairing correlations one needs to extend the RMF formulation to the Relativistic Hartree-Bogoliubov theory. The relativistic Hartree-Bogoliubov (RHB) equations have been derived [14] starting from the RMF Lagrangian. The resulting Relativistic Hartree-Bogoliubov (RHB) equations [9] read:

$$\begin{pmatrix} h_D - \lambda & \hat{\Delta} \\ -\hat{\Delta}^* & -h_D^* + \lambda \end{pmatrix} \begin{pmatrix} U \\ V \end{pmatrix}_k = E_k \begin{pmatrix} U \\ V \end{pmatrix}_k. \quad (21)$$

Here, λ is the Lagrange multiplier, E_k is the quasi-particle energy for the state k ; U_k and V_k are properly normalised four dimensional Dirac spinors; h_D is the usual Dirac Hamiltonian (see [9]) given by,

$$h_D = -i\alpha \cdot \nabla + \beta (M + g_\sigma \sigma) + g_\omega \omega^0 + g_\rho \tau_3 \rho_3^0 + e \frac{1 + \tau_3}{2} A^0. \quad (22)$$

The fields σ , ω^0 , ρ_3^0 and A^0 are still given by the Klein-Gordon (KG) equations (14 - 17), where the sources are now given by [9]:

$$\rho_s = \sum_{E_k > 0} V_k^\dagger \gamma^0 V_k; \quad \rho_v = \sum_{E_k > 0} V_k^\dagger V_k \quad (23)$$

$$\rho_3 = \sum_{E_k > 0} V_k^\dagger \tau_3 V_k; \quad \rho_c = \sum_{E_k > 0} V_k^\dagger \frac{1 + \tau_3}{2} V_k. \quad (24)$$

Here also, the sum in Eqs. (23) - (24) is taken only over the positive energy states.

The RHB equations have two distinct parts: the self consistent field (h_D) that describes the long range particle-hole correlations and the pairing field ($\hat{\Delta}$) that accounts for the correlations in the particle-particle (pp) channel. In the coordinate space representation, the kernel of the pairing field $\hat{\Delta}$ is given by,

$$\Delta_{ab}(\mathbf{r}, \mathbf{r}') = \frac{1}{2} \sum_{c,d} V_{abcd}^{pp}(\mathbf{r}, \mathbf{r}') \kappa_{cd}(\mathbf{r}, \mathbf{r}'), \quad (25)$$

where, the roman symbols a,b,c,d denote all the single particle state quantum numbers; $V_{abcd}^{pp}(\mathbf{r}, \mathbf{r}')$ are the matrix elements of the two body nuclear potential or even the one meson exchange potential in the pp -channel. The pairing tensor is given by,

$$\kappa_{cd}(\mathbf{r}, \mathbf{r}') = \sum_{E_k > 0} U_{ck}^*(\mathbf{r}) V_{dk}(\mathbf{r}') \quad (26)$$

The integral operator $\hat{\Delta}$ acts on $V_k(\mathbf{r})$,

$$\hat{\Delta}_a(V_k(\mathbf{r})) = \sum_b \int d^3 r' \Delta_{ab}(\mathbf{r}, \mathbf{r}') V_{bk}(\mathbf{r}'). \quad (27)$$

In the case of the constant gap, $\hat{\Delta}_a (\equiv \Delta)$ becomes diagonal and decouples into a set of 2×2 diagonal matrices resulting in the BCS expressions (Eq. 20) for the occupation probabilities. As a result, the RHB equations (Eq. 1) reduce to the RMF equations with frozen gap.

Reliable and satisfactory derivation of V_{abcd}^{pp} is not yet available in RMF (see [9,14]). Guided by the success of the non-relativistic Hartree-Fock-Bogoliubov (HFB) investigations with phenomenological finite or effective zero range Gogny type interaction in the pp -channel and in the absence of the field theoretic derivation of V_{abcd}^{pp} in the RMF, one adopts a phenomenological approach while solving the RHB equations employing the finite range Gogny-D1S interaction [6, 15] is:

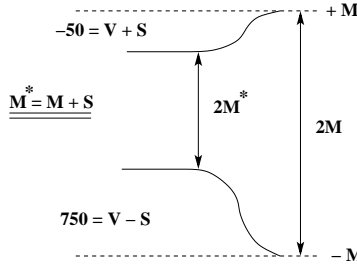
$$V(\mathbf{r}_1, \mathbf{r}_2) = \sum_{i=1,2} e^{-\{(\mathbf{r}_1 - \mathbf{r}_2)/\mu_i\}^2} (W_i + B_i P^\sigma - H_i P^\tau - M_i P^\sigma P^\tau). \quad (28)$$

Factors μ_i , W_i , B_i , H_i & M_i ($i=1,2$) are parameters of the interaction. Alternatively, one may use for V^{pp} , the density dependent, effective two body zero range interaction [16]:

$$V(\mathbf{r}_1, \mathbf{r}_2) = V_o \delta(\mathbf{r}_1 - \mathbf{r}_2) \frac{1}{4} (1 - \sigma_1 \sigma_2) \left(1 - \frac{\rho(r)}{\rho_o} \right); \quad (29)$$

where, V_o is the interaction strength with cutoff energy about 300 MeV [16] and ρ_o ($=0.152 \text{ fm}^{-3}$ [16]) is the nuclear matter density. The strength V_o is fixed [16] so as to reproduce the pairing energy obtained by using the finite range Gogny D1S interaction in RHB framework.

2.1 Saturation Mechanism



The saturation mechanism is built-in, in this relativistic formulation. A glance on any standard Lagrangian parameter set (see, for example, Tab. (1) reveals that m_σ , m_ω are very large. Ignoring the Laplacian in the KG equation, we get for fields:

$$\sigma(\omega) \propto \rho_s(\rho_v).$$

$$\rho_s = \sum (|f_i|^2 - |g_i|^2)$$

$$\rho_s = \sum (|f_i|^2 - |g_i|^2)$$

For collapse, $2M^*$ shrinks, i.e. S becomes large. On the other hand, small components $|g|^2$ become large.

Thus, if $|g|^2$ becomes large, ρ_s becomes small. As ρ_s = source of σ , i.e., S , makes automatically σ or S smaller. This is the mechanism (of preventing collapse) of Saturation in the Relativistic Hartree.

3 Applications

The explicit calculations require the following input information:

- 1) Lagrangian parameter set
- 2) V^{pp} or Δ .

As an output, one obtains, Dirac Spinors / Mesonic Fields; single particle energies; binding energies; radii, etc. Several sets of the parameters appearing in the Lagrangian are available in the literature [9–11, 19]. Some of these widely used parameters are presented in table 1.

Table 1. Lagrangian Parameter Sets

	NL1	NL-SH	NL3
M	938.0	939.0	939.0
m_σ	492.3	526.06	508.2
m_ω	795.4	783.0	782.5
m_ρ	763.0	763.0	763.0
g_σ	10.138	10.444	10.217
g_ω	13.285	12.945	12.868
g_ρ	4.976	4.383	4.474
g_2 (fm $^{-1}$)	-12.172	-6.910	-10.431
g_3	-36.265	-15.834	-28.885

The RMF/RHB equations are solved using the oscillator basis (spherical / deformed) expansion technique [8] or in the coordinate space. Explicitly:

1. Calculations in the oscillator basis for:
 - a. RMF- with frozen gap approximation (corresponding results are denoted by SPH)
 - b. RHB using finite range Gogny DIS interaction (corresponding results being denoted by RHB (ob)).
2. The RHB calculations in the coordinate space with a box size of 25 fm, using the effective zero range density dependent two body interaction [16] (the results obtained for this case are denoted by RHB (c)).
3. To ascertain the effect of deformation the RMF equations with the constant gap approximation in the deformed oscillator basis with axial symmetry have also been solved and the corresponding results are denoted by DEF.

Several applications for the successful description of the nuclear properties have been / still being reported [8–10, 12]. The RMF is very successful in reproducing the ground

state nuclear properties (like total binding energies, deformations, radii, isotope shifts, densities). One of the essential features is, extremely delicate cancellation between the σ and ω contributions. Both are very large, and have opposite signs. This cancellation is responsible for accurate predictions. For example, the total binding energies are reproduced within 0.25% and the calculated charge radii differ from the experiment only in the second place of fermi. The reliability of the calculated densities have been tested by using these in the calculation of total reaction and charge changing cross sections.

In this article, for illustration, we shall present and discuss the results for Gadolinium isotopes (rare earth region) and a few α decay chains of Superheavy Nuclei.

3.1 Ground State Properties

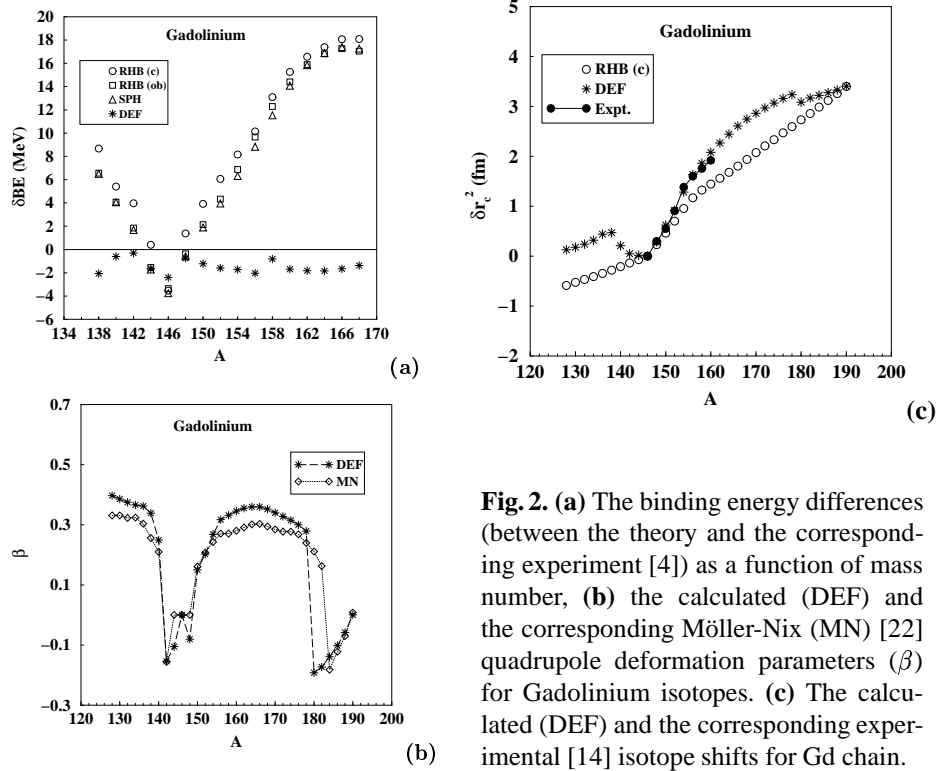


Fig. 2. (a) The binding energy differences (between the theory and the corresponding experiment [4]) as a function of mass number, (b) the calculated (DEF) and the corresponding Möller-Nix (MN) [22] quadrupole deformation parameters (β) for Gadolinium isotopes. (c) The calculated (DEF) and the corresponding experimental [14] isotope shifts for Gd chain.

The difference between the calculated and the corresponding experimental binding energies are plotted in Fig. (2)(a). The calculations reproduce the experiment well. The RHB(c) and RHB(ob) results are found to be very similar, indicating that the inclusion of correct asymptotics has a little effect on the binding energies. Further, the SPH binding energies are also similar to those of the RHB(c) and RHB(ob). This is proba-

bly due to the choice of pairing gaps. Inclusion of deformation is found to improve the agreement between theory and experiment dramatically.

The DEF quadrupole deformation parameters and the corresponding microscopic - macroscopic Möller - Nix values (MN) are next presented in Fig. (2)(b). The DEF results and MN results are very similar. The graph reveals that except for the isotopes in the neighbourhood of mass number 146, and 188 all the other nuclei in the Gd chain are deformed. Prolate to oblate shape transitions are observed between $^{140-142}\text{Gd}$ and also between $^{178-180}\text{Gd}$.

The calculated isotope shifts for Gadolinium isotopes are shown in Fig. (2)(c). The available experimental isotope shifts [14] are also indicated (where available). Clearly, the anomalous behaviour near the neutron shell closure is well reproduced. The calculations predict increase in the charge radius with decrease in the neutron number below the neutron shell closure, but unfortunately, there is no experimental data available to confirm these predictions.

3.2 Superheavy Nuclei

To produce, identify and study the Super Heavy Elements (SHE) has been a cherished dream of nuclear physicists. It is indeed a challenging task and has been the focus of extensive research activity. The earlier attempts achieved a considerable success toward this goal. The cold (hot) fusion with Pb-/Bi- (actinide: $^{235}\text{U}/^{244}\text{Pu}$) targets and suitable projectiles $^{64}\text{Ni}/^{70}\text{Zn}$ (^{48}Ca) have been successfully used for the production of very heavy elements with $Z = 110, 111, 112$ (114, 116) at GSI (Dubna).

The earlier RMF studies (see, for example, [15]) were carried out with the primary aim to predict the combination of neutron number (N) and the proton number (Z), where the spherical shell closure may occur. In these studies, the occurrence of a spherical proton (neutron) shell closure with given Z (N) may change with varying neutron number N (proton number Z). In such studies, the pairing and deformation may play an important role. At the shell closure:

- The pairing energy will vanish or will have a minimum value.
- There should appear a reasonable gap between the occupied and unoccupied levels around the fermi level in the single particle level spectrum.
- The shell corrections should have the maximum negative value.

The calculated neutron pairing energy several isotopic chains and the single particle spectrum for $N = 162$, taken from [15] are shown Figs. (3,4) for illustration.

The neutron number $N=162$ has been predicted [15] to exhibit shell closure at around $Z = 108 - 110$. This is consistent with the findings of [16] about the nucleus $^{273}110$. In addition, the calculated shell corrections (see Tab.5, page 222 of [15]) peak at $N = 166$ for $Z = 112$ indicating the stable structure of $Z = 112$ around $N = 166$. This is consistent with the observation of the Superheavy nucleus $^{277}112$ [17, 18].

As illustrative example, we present and discuss the α decay chains of elements $Z = 110$ and 111 . The calculations proceed in three steps. In the first step, the ground state properties of the relevant nuclei are calculated using the RMF framework. We use both the NL3 as well as NL-SV1 [19] parameter sets for this purpose. The latter caters to the Lagrangian with ω quartic self - coupling.

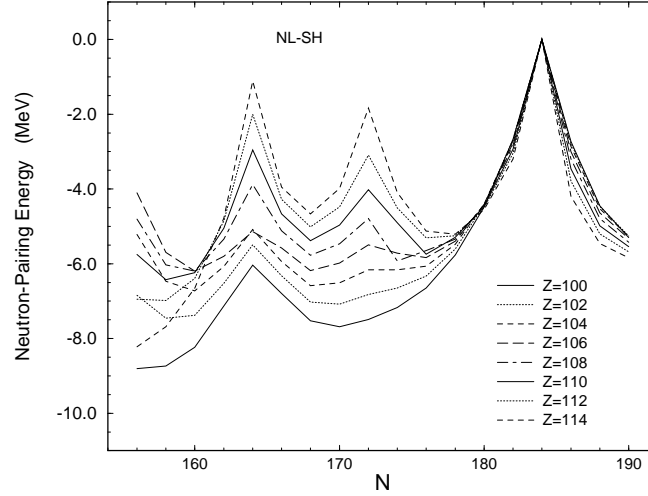


Fig. 3. The calculated neutron pairing energies, taken from [15].

The calculated binding energies for the ^{271}Ds and $^{272}111$ α -decay chain are shown in Fig. 1 along with the corresponding values Audi and Wapstra (Audi03) [4]. All reasonably agree among themselves. Both the calculations are in good agreement with those of Audi and Wapstra [4]. The NL-SV1 binding energies are found to be consistently smaller than the corresponding NL3 values.

The calculated (DEF) deformation parameters (β) shown in Fig. (1) (right hand panel) indicate that all the nuclei belonging to the considered decay chains are prolate deformed. This observation agrees with the findings of Möller and Nix (MN) [22], though the calculated β 's are slightly higher than that of MN. NL3 and NL-SV1 yield almost identical values of the deformation parameters.

Since NL3 and NL-SV1 yield nearly similar binding energies, the Q values are also expected to be similar to each other, and that is what turns out to be the case. Therefore, from here onward, we restrict ourselves to NL3 parameter set only. The calculated Q values for the respective α -decays are shown in Fig. 6 (left hand panel), along with the available experimental [18] values. The calculations agree reasonably well with the experiment. The maximum deviation from the experiment is found to be less than 10%.

Next we calculate the decay half lives for the considered α decay chains within the WKB approximation. This procedure has been applied successfully to describe the decay properties of the $^{277}112$ chain [20]. For this purpose, first, the α -daughter interaction energy is calculated.

Calculation of half lives The calculated $L = 0$ projected and re-normalised DEF densities along with an effective nucleon - nucleon interaction (e.g. M3Y) are used to obtain the total interaction energy of the α -daughter system in the double folding model [21–23]. The density dependent M3Y nucleon - nucleon interaction with pseudo-

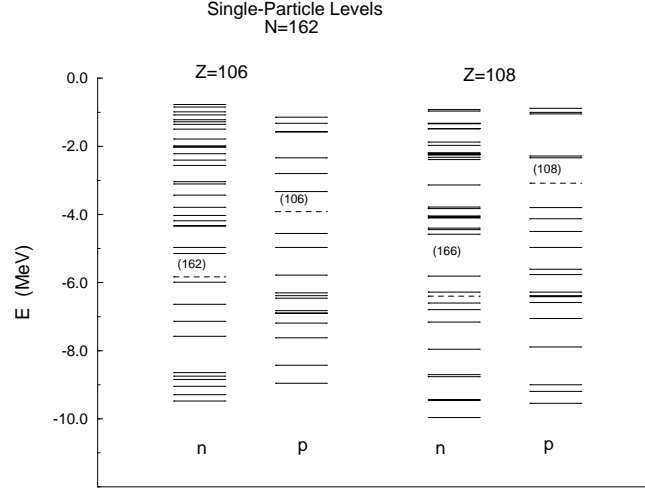


Fig. 4. The calculated single particle level spectrum for $N = 162$ isotones taken from [15].

potential, used in the present work reads:

$$v(s) = \left(7999.0 \frac{e^{-4s}}{4s} - 2134.25 \frac{e^{-2.5s}}{2.5s} - 276\delta(s) \right) (1 - \beta\rho_1^{2/3})(1 - \beta\rho_2^{2/3}) \quad (30)$$

The density dependence is supposed to take into account the higher order exchange effects and the Pauli Blocking. The total double folding potential between the nucleus-nucleus (Projectile: P; Target: T) system is given by:

$$V_{PT}(\mathbf{R}) = \int \rho_P(\mathbf{r}_p) \rho_T(\mathbf{r}_t) v(\mathbf{r}_p - \mathbf{r}_t + \mathbf{R} \equiv \mathbf{s}) d^3\mathbf{r}_p d^3\mathbf{r}_t. \quad (31)$$

The half life time of the nucleus (parent) against the α - decay is given by:

$$T_{1/2} = \frac{\ln(2)}{\nu} (1 + e^K) \quad (32)$$

where, within the WKB approximation, the action integral K appearing in Eq. (32) reads:

$$K = \frac{2}{\hbar} \int_{R_a}^{R_b} \{2\mu (V_{PT}(R) + V_C(R) - Q)\}^{1/2} dR; \quad (33)$$

$V_C(R)$ is the Coulomb potential for the α - daughter system obtained by using the double folding procedure. The Q value for the α - decay can be obtained either from the kinetic energy (corrected for the recoil) of the emerging α - particle or from the binding energies of the α , daughter and the parent nuclei. The R_a and R_b appearing in Eq. (33) are classical turning points determined requiring that the integrand in Eq. (33) should vanish at these points.

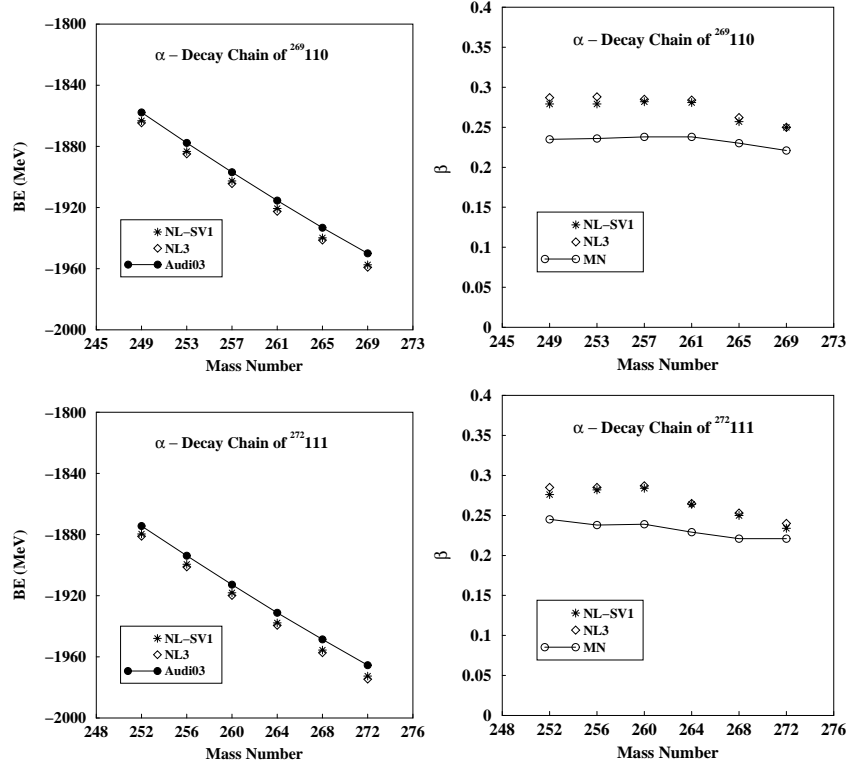


Fig. 5. The binding energies and deformation parameters for the nuclei belonging to α decay chains of ^{271}Ds and $^{272}\text{111}$. The binding energies obtained from systematics (Audi03) [4] and the Möller - Nix values [22] of deformation parameters are also indicated.

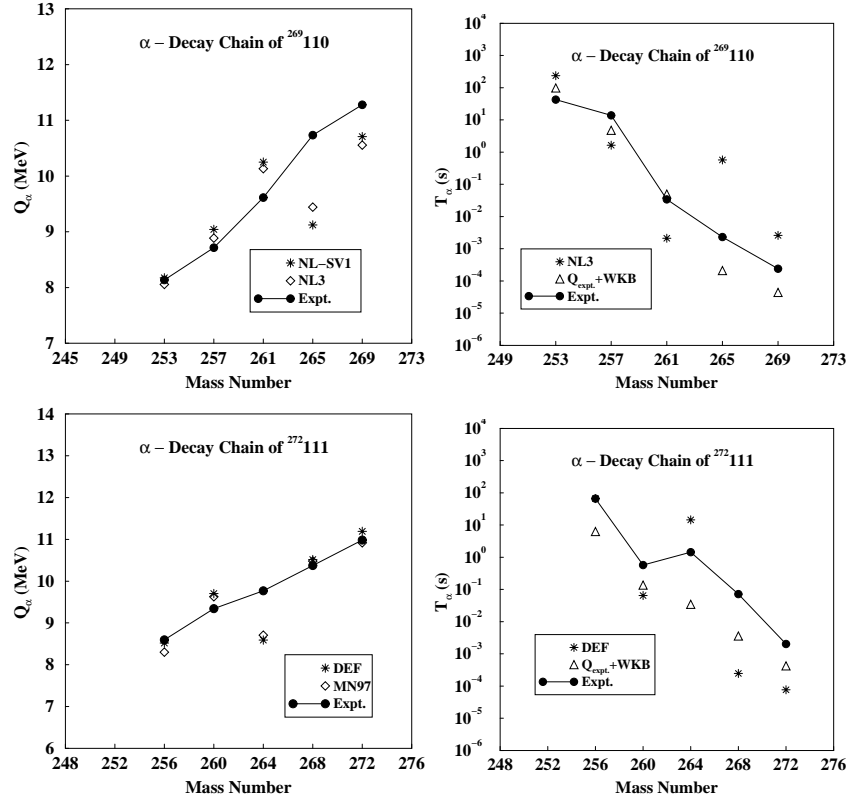


Fig. 6. The calculated and the corresponding experimental Q values (left hand panel) and the calculated and the corresponding experimental half lives (right hand panel) against α decay. See text for details.

The calculated half lives are presented in Fig. (6)(right hand panel). Two sets of calculations are carried out here: 1) using the calculated (DEF) Q values in WKB or 2) using the experimental Q values in WKB. The former are denoted by 'DEF' and the latter are denoted by ' $Q_{Exp.}+WKB$ ' respectively in Fig. (6). Both the calculations reasonably agree with the experiment [18]. However, the ' $Q_{Exp.}+WKB$ ' values are closer to the experiment than the 'DEF' values. A comparison between these two reveals that the half lives are very sensitive to Q values. Even a small change in Q value can impart an order of magnitude change in the corresponding decay half life.

4 Summary and conclusions

The essential features of the Relativistic Mean Field (RMF) theory are presented. The RMF Lagrangian is found to have all the necessary ingredients of the nucleon - nucleon interaction. The mechanism of saturation is explicitly presented. The RMF theory is found to describe accurately the observed ground state properties of the nuclei. The deformation effects are shown to be crucial, especially for the binding energies and anomalous isotope shifts.

The observed Q values for Superheavy nuclei in the α decay chains of ^{271}Ds and $^{272}\text{111}$ are well reproduced. However, the half lives are found to be very sensitive to the Q values. Use of the experimental Q values in WKB approximation along with the α daughter interaction energy is found to reproduce the experiment well. This indicates reliability of the double folding α - daughter potential. Thus, it can be used with confidence in the reaction investigations as the real part of the optical potential.

Acknowledgments

Part of the work presented here has been done in collaboration with A. Bhagwat, M. Gupta and Arun K. Jain. Partial financial support from the Board for Research in Nuclear Sciences (BRNS), Government of India (Proj. No. 2001/37/13/BRNS/485) is gratefully acknowledged.

References

1. Y. K. Gambhir and P. Ring, *Pramana* **32**, 389 (1989) and Y. K. Gambhir, P. Ring and A. Thimet, *Ann. Phys. (NY)*, **198**, 132 (1990).
2. P. Ring, *Prog. Part. Nucl. Phys.*, **37**, 193 (1996) and references cited therein.
3. J. Boguta and A. R. Bodmer, *Nucl. Phys. A* **292**, 413 (1977).
4. G. Audi *et al.*, *Nucl. Phys. A* **729**, 337 (2003).
5. H. Kucharek and P. Ring, *Z. Phys. A* **339**, 23 (1991).
6. J. Decharge and D. Gogny, *Phys. Rev. C* **21**, 1568 (1980).
7. T. Gonzalez-Llarena *et al.*, *Phys. Lett. B* **379**, 13 (1996).
8. J. Meng and P. Ring, *Phys. Rev. Lett.* **77**, 3963 (1996); *Nucl. Phys. A* **635**, 3 (1998).
9. G. A. Lalazissis, J. K'önig and P. Ring, *Phys. Rev. C* **55** 540 (1997).
10. P. G. Reinhardt *et al.*, *Z. Phys. A* **323**, 13 (1986); P. G. Reinhardt, *Rep. Prog. Phys.* **52**, 439 (1989).
11. M. M. Sharma, M. A. Nagarajan and P. Ring, *Phys. Lett. B* **312**, 377 (1993).

12. Y. K. Gambhir, Nuclear Physics at Intermediate Energies p. 89 (1999); ed. S. Pal (Narosa Pub. House); *Pramana* **57**, 545 (2001).
13. P. Möller *et al.*, *At. Data Nucl. Data Tables* **59**, 185 (1995).
14. E. W. Otten, *Treatise on Heavy Ion Science*, vol 8, 517 (ed. D. Allen Bromley, Plenum Press, NY, 1989) and references cited therein.
15. G. A. Lalazissis *et al.*, *Nucl. Phys. A* **608**, 202 (1996).
16. R. Smolanczuk and A. Sobiczewski, *Low Energy Nuclear Dynamics* 313 (1995), World Scientific Publishing Co., Singapore.
17. G. Müntzenberg, The Nuclear Many - Body Problem 2001, 281 (2002), ed. W. Nazarewicz and D. Vretenar, Kluwer Academic Publishers.
18. S. Hofmann, *Z. Phys. A* **358**, 125 (1997).
19. M. M. Sharma, A. R. Farhan and S. Mythili, *Phys. Rev. C* **61**, 054306 (2000).
20. Y. K. Gambhir, A. Bhagwat, M. Gupta and A. K. Jain, *Phys. Rev. C* **68**, 044316 (2003).
21. G. R. Satchler and W. G. Love, *Phys. Reports* **55**, 183 (1979).
22. D. T. Khoa, W. von Oertzen and H. G. Bohlen, *Phys. Rev. C* **49**, 1652 (1994).
23. A. K. Choudhuri, *Nucl. Phys. A* **449**, 243 (1986).

Some questions and new results based on the relativistic mean field model

Raj K. Gupta^{1*} and S.K. Patra¹

¹ Department of Physics, Panjab University, Chandigarh 160 014, India.

² Institute of Physics, Sachivalaya Marg, Bhubaneswar 751 005, India.

Abstract. The relativistic mean field theory is used to calculate the various gross nuclear structure properties of nuclei from light to super-heavy nuclei. In each case, the nuclei considered range from proton drip-line to neutron drip-line, and the calculations made are within the framework of an axially deformed self-consistent relativistic mean field formalism for a number of parameter sets, namely NL1, NL3, NL-SH, TM1, TM2 and NL-RA1. Also, in some cases, the potential energy surfaces are calculated in a quadratic constraint scheme, in particular, for the studies of multiple shape co-existence. Some of the common difficulties with these calculations are the undetermined strength of pairing interaction and the lack of consistent predictions by any one force parameter set. Some of these questions and results are discussed.

1 Introduction

The structural properties of light nuclei near the proton- and neutron-drip lines have attracted considerable experimental and theoretical attention. The radioactive nuclear beam (RNB) facilities at various laboratories in the World have provided many intriguing experimental information on the structure and reactions of nuclei near the proton- and neutron-drip lines. For example, the existence of neutron-halo and neutron-skin in some of the nuclei on the neutron-drip line is by now well established, and the proton-halo nuclei are also observed. One of the primary goals of experiments, as well as of theory, is to determine the changes in nuclear structure near the drip-lines where the binding energies of single particle orbits approach zero [1, 2]. Of particular interest has been the region of β -unstable nuclei near the $N=28$ magic number, because of the observed large deformations for some $Z=16$ nuclei [1, 3–5]. This means the question of possible breaking of spherical major shell gap at $N=28$ for drip-line nuclei. In other words, the basic question is: Do deformed nuclei exist at the drip-lines? Similarly, the magicity of $Z=82$ shell for nuclei at the proton-drip line has been questioned in the study of the structures of neutron-deficient isotopes of Hg and Pb nuclei [6]. Already, a triple shape co-existence (spherical, oblate and prolate shapes of almost identical excitation energies) is observed in ^{186}Pb [7]. This is the best example where the choice of the parameter set and strength of pairing force is found very crucial for predicting the correct ground state deformation in relativistic mean field theory. Similar multiple

* Speaker.

shape co-existence structures are predicted for many light and medium mass $N=Z$ nuclei [9, 35]. Ever since its first observation in ^{72}Se [10], co-existence of two nuclear shapes is now a general phenomenon in $A \approx 80$ mass nuclei [11].

For super-heavy elements, one of the important questions is the next magic shells (for protons and neutrons), beyond $Z=82$ and $N=126$. Though the older studies predict the next magic number at $Z=114$ for protons and at $N=184$ for neutrons, the more recent calculations place the same at $Z=120$ and $N=172$ or 184 [12–14]. Some calculations [15] also predict $Z=126$ as the next proton magic number with $N=184$ as the neutron magic number. Apparently, this requires a systematic study of the structural properties of various nuclei in the super-heavy mass region [13, 14, 16–18].

The relativistic mean field (RMF) model has the advantage that, with the proper relativistic kinematics and with the mesons and their properties already known, or fixed from the properties of nuclear matter and of a small number of known nuclei [19–23], the method gives excellent results for the binding energies, root mean square (rms) radii, quadrupole and hexadecapole deformations and other nuclear properties, not only of spherical-, but also of deformed-nuclei. The same parameter sets also well describe the properties of nuclear matter. One of the major attractive features of the RMF approach is that the spin-orbit interaction and the associated nuclear shell structure automatically arise from meson-nucleon interaction [24]. The inclusion of ρ meson takes care of the neutron-proton asymmetry. The π -meson fields are not included since they do not contribute in RMF approximation for Hartree states having good parity. We can thus expect that the RMF calculations provide useful information about the properties of nuclei up to the neutron-/proton-drip lines.

The paper is organised as follows: Since the details of theory must be discussed in earlier lectures, in Section II, we present only the relativistic Lagrangian density and a very brief description of the method. Section III gives our results for binding energies, rms radii, quadrupole deformation, multiple shape coexistence and shell structures first for the light and then for super-heavy nuclei. Our concluding remarks are given in Section V.

2 Relativistic Mean Field Theory

The relativistic Lagrangian density for a nucleon-meson many-body system:

$$\begin{aligned} \mathcal{L} = & \bar{\psi}_i \{ i \gamma^\mu \partial_\mu - M \} \psi_i + \frac{1}{2} \partial^\mu \sigma \partial_\mu \sigma - \frac{1}{2} m_\sigma^2 \sigma^2 - \frac{1}{3} g_2 \sigma^3 - \frac{1}{4} g_3 \sigma^4 - g_s \bar{\psi}_i \psi_i \sigma \\ & - \frac{1}{4} \Omega^{\mu\nu} \Omega_{\mu\nu} + \frac{1}{2} m_\omega^2 V_\mu V_\mu + \frac{1}{4} C_3 (V_\mu V^\mu)^2 - g_\omega \bar{\psi}_i \gamma^\mu \psi_i V_\mu - \frac{1}{4} B^{\mu\nu} \cdot B_{\mu\nu} \\ & + \frac{1}{2} m_\rho^2 \boldsymbol{\rho}^\mu \cdot \boldsymbol{\rho}_\mu - g_\rho \bar{\psi}_i \gamma^\mu \boldsymbol{\tau} \psi_i \cdot \boldsymbol{\rho}_\mu - \frac{1}{4} F^{\mu\nu} F_{\mu\nu} - e \bar{\psi}_i \gamma^\mu \frac{(1 - \tau_{3i})}{2} \psi_i A_\mu. \end{aligned} \quad (1)$$

Here, the field for the σ -meson is denoted by σ , that of ω -meson by V_μ and of the isovector ρ -meson by $\boldsymbol{\rho}_\mu$. A^μ denotes the electromagnetic field. ψ_i are the Dirac spinors for the nucleons, whose third component of isospin is denoted by τ_{3i} . The g_s , g_ω , g_ρ and $\frac{e^2}{4\pi}$ ($= \frac{1}{137}$) are the coupling constants for σ , ω , ρ mesons and photon, respectively. g_2 and g_3 and C_3 are the parameters for the nonlinear terms of sigma and omega mesons.

M is the nucleon mass and m_σ , m_ω and m_ρ are the σ , ω and ρ -meson masses, respectively. $\Omega^{\mu\nu}$, $B^{\mu\nu}$ and $F^{\mu\nu}$ are the field tensors for the V^μ , ρ^μ and the photon fields, respectively.

From the above relativistic Lagrangian (1), we get the field equations for mesons and nucleons. These equations are solved by expanding the upper and lower components of the Dirac spinors and the boson field wavefunctions with initial deformation β_0 in a sufficiently large deformed harmonic oscillator basis. The set of coupled equations are solved numerically by self-consistent iteration method. The quadrupole deformation parameter β is evaluated from the resulting quadrupole moments of neutron Q_n and proton Q_p , using the formula

$$Q = Q_n + Q_p = \sqrt{\frac{9}{5\pi}} AR^2 \beta, \quad (2)$$

where $R = 1.2A^{1/3}$ fm and Q is the total quadrupole moment.

The total binding energy of the system is given by $-E_{total}$, where

$$E_{total} = E_{part} + E_\sigma + E_\omega + E_\rho + E_c + E_{pair} + E_{CM}, \quad (3)$$

where E_{part} is the sum of the single-particle energies of the nucleons and E_σ , E_ω , E_ρ , E_c , and E_{pair} are, respectively, the contributions of the meson fields, the Coulomb field and the pairing energy. The pairing interaction is added in BCS formalism, with constant pairing gaps [25]. The $E_{CM} (= -\frac{3}{4} 41A^{-\frac{1}{3}})$ is the non-relativistic approximation for center-of-mass energy correction. Finally, the parameter sets used are summarized in Table I. In the parameter sets TM1 and TM2, Sugahara and Toki [26] introduced a nonlinear term $(V_\mu V^\mu)^2$ into the ω vector meson potential, obtaining a correct sign for g_3 . The TM1 set is designed for nuclei with $Z > 20$, whereas the TM2 set is appropriate for $Z \leq 20$.

For computing the potential energy surface, we introduce a quadrupole constraint [27–29], i.e., instead of minimizing $\langle H \rangle$, we minimize $\langle H' \rangle$ where $\hat{H}' = \hat{H} - \mu \hat{Q}_\mu$, with $\hat{Q}_\mu = r^2 Y_{2\mu}(\theta, \phi)$ and the Lagrangian multiplier μ fixed by the constraint $\langle Q \rangle_\mu = Q_0$. Specifically, we have solved the set of RMF equations with two quadratic constraints [27, 30], $\frac{1}{2}C_0(\langle \hat{Q}_0 \rangle - \mu_0)^2 + \frac{1}{2}C_2(\langle \hat{Q}_2 \rangle - \mu_2)^2$, where the constraining operators \hat{Q}_μ are used as the time components of a vector field in Dirac equation and the Lagrangian multipliers are adjusted to fix a definite deformation. The quadratic constraint is used in order to be able to treat also the concave areas of the energy surface [27, 30].

3 Results and Discussion

In this section, we illustrate the successes and failures of the RMF method by presenting some of our results on the gross structural properties of nuclei ranging from light to super-heavy mass regions.

Table 1. Various parameter sets for the Lagrangian density in (1). The constant g_2 is in fm^{-1} and other coupling constants g_x are dimensionless.

	NL1	NL3	NL-SH	TM1	TM2	NL-RA1	Emp. Value
M	938.0	939.0	939.0	938.0	938.0	939.0	938.0
m_σ	492.25	508.1941	526.059	511.198	526.443	515.700	
m_ω	795.359	782.501	783.000	783.0	783.000	783.00	783 ± 5
m_ρ	763.000	763.000	763.000	770.000	770.000	763.00	773 ± 77
g_σ	10.138	10.2169	10.444	10.0289	11.4694	10.36231	
g_ω	13.285	12.8675	12.945	12.6139	14.6377	12.921154	
g_ρ	4.9755	4.4744	4.383	4.6322	4.6783	4.4058795	
g_2	-12.172	-10.4307	-6.9099	-7.2325	-4.4440	-10.059947	
g_3	-36.265	-28.8851	-15.8337	0.6183	4.6076	-27.5565	
C_3	0.000	0.000	0.000	71.3075	84.5318	0.000	

3.1 Binding-energies, Separation-energies and Neutron- and/ Proton-drip Lines [1,2]

Fig. 1 illustrates the binding energies obtained in RMF model calculations for Ne nuclei, using the NL-SH, TM2 and NL2 parameter sets, compared with the finite-range droplet model (FRDM) [31] results and experimental (or extrapolated) data [32]. We notice that the agreement between RMF calculations and the experimental or FRDM results is within $\sim 2\%$ for the TM2 parameter set, and that for NL-SH parameter set is within $< 3\%$. On the other hand, the NL2 parameter set underpredicts the experimental values for both the proton- and neutron-rich nuclei, and also terminates (reaches the neutron-drip line) much earlier than the FRDM or other parameter set results. This shows the complete inability of NL2 parameter set for the light nuclei.

For determining the drip-lines, the quantity that plays a more crucial role is the two neutron/ proton separation energy, $S(N,Z)_{2n} = \text{BE}(N,Z) - \text{BE}(N-2,Z)$ and $S(N,Z)_{2p} = \text{BE}(N,Z) - \text{BE}(N,Z-2)$, respectively. Fig. 2 illustrates S_{2n} values for Ne nuclei. The RMF results for the two parameter sets are nearly similar, agreeing quite well with the experimental and FRDM data. The S_{2n} value decreases with increase of neutron number (so also S_{2p} with proton number, not shown here) and reaches zero (or becomes negative) at the neutron-drip line. The estimated proton- and neutron-drip lines, for the two parameter sets, are shown in Fig. 3. Also plotted in this figure are the most stable nuclei in the isotopic chain, the so-called β -stability line. Note that there are some small differences in the predictions of two parameter sets, and the available experimental data (also shown in the figure) agrees at some points and disagrees at some others which should be settled as more and more data are measured. Similar results are obtained for the lighter $Z < 10$ nuclei (see Table 1 in [2]).

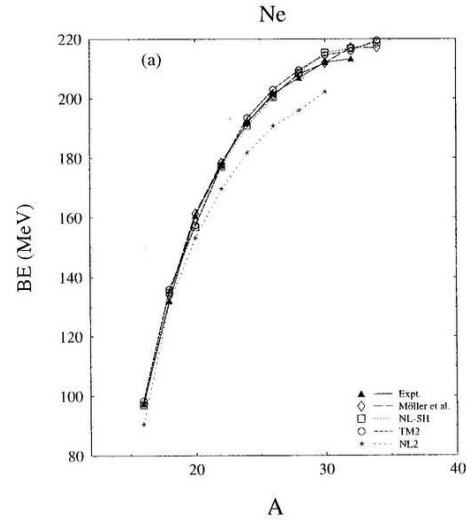


Fig. 1. The RMF calculated binding energies compared with experiments and FRDM results for Ne isotopes, from [1].

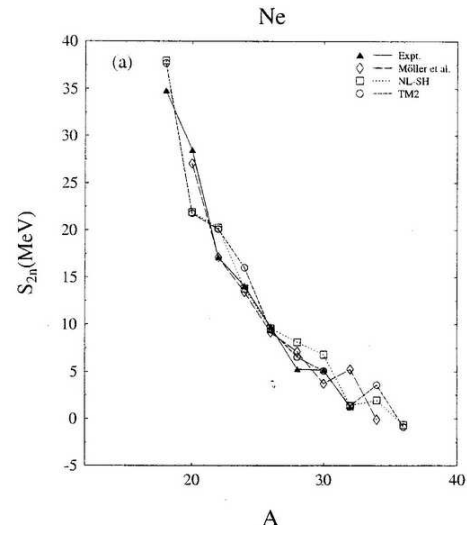


Fig. 2. Same as for Fig. 1, but for two-neutron separation energies, from [1].

3.2 Neutron/Proton radii and Neutron/Proton skin [1]

The systematics of neutron and proton radii give information about the formation of proton/ neutron skin. Fig. 4 shows the neutrons, protons and matter distribution radii r_n , r_p and r_m , respectively, for the illustrative Ne nuclei as a function of A for the TM2 parameter set. The r_m gives the average value of r_n and r_p . We notice that as we go towards the neutron-drip line, the increase in r_n is substantially large and implies the presence of more and more neutrons near the surface. The large difference in the magnitude between r_p and r_n near the proton-/ neutron-drip line means a thick proton/ neutron skin.

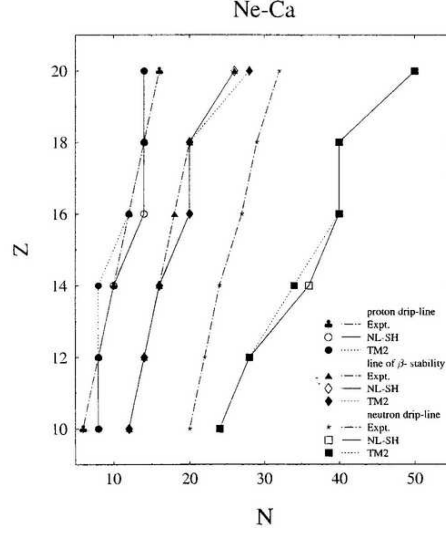


Fig. 3. The neutron- and proton-drip lines and the β -stability line for $Z = 10 - 20$ region using RMF model, compared with the available experimental data, from [1].

3.3 Nuclear shapes [1,4]

Fig. 5 shows a plot of quadrupole deformation parameter $|\beta|$ for the illustrative S nuclei. The spherical shapes for $N=14$, and 20 are evident (more so for the TM2 set). However, the influence of the magic number $N=28$ seems to be weakened since prolate (for NL-SH) or oblate (for TM2) solutions are obtained (^{46}Ar and ^{48}Ca are predicted to be perfectly spherical nuclei). This means that the nature of deformation (prolate / oblate) depends on the choice of force parameter. Interesting enough, the experimental data for S nuclei though indicate the magicity of both $N=20$ and 28, but in a rather strongly diminished way. Note that the RMF predictions are off by a factor of two, at least. However, in the absence of pairing correlations, the predicted $|\beta|$ values are

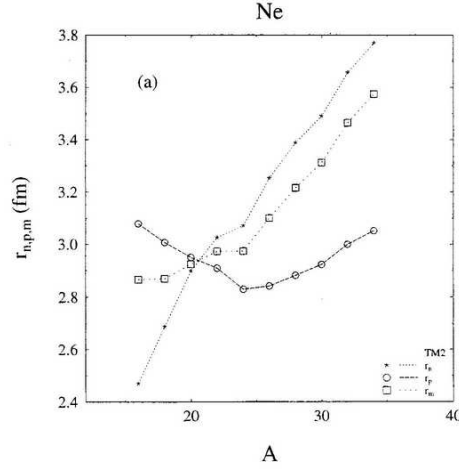


Fig. 4. The calculated rms radii using TM2 parameter set for Ne isotopes, [1].

much closure to the experiments. The role of pairing, however, changes from nucleus to nucleus, and hence has consequences for the shape co-existence, discussed below.

3.4 Shell structures and the spherical shell breaking [1,4,6]

The single particle levels give information about the shell gaps and the shell model configurations. Both the cases of spherical and deformed nuclei are of interest.

Fig. 6 shows the single particle levels for the deformed $N=28$ ^{42}Si nucleus for the TM2 parameter set. In addition to all the occupied levels, one unoccupied level (the top one) is also shown. We notice in this figure that each level is not an eigenstate of J and hence is two-fold degenerate due to m_J i.e., each state is filled with two particles having the quantum numbers m_J and $-m_J$ (both for protons and neutrons). The states are therefore labelled with Nilsson index $[Nn_3A]$. Looking at the Nilsson labels, we find that the shell gap at $N=28$ is **not** due to $0f_{7/2}$ shell alone but mixed due to states from $0f_{5/2}$ and $1p_{1/2}$. Such a breaking of **spherical** shell gap occurs due to the nucleus ^{42}Si being strongly oblate deformed ($\beta=-0.327$) where new magic numbers appear, in addition to the usual ones. The same result is also true for the NL-SH parameter set. Interesting enough, the same phenomenon of spherical shell breaking is also found to occur in the strongly prolate deformed $N=28$ ^{40}Mg nucleus for both the TM2 and NL-SH parameter sets ($\beta=0.45$ and 0.44 , respectively), but in the moderately oblate deformed ^{44}S nucleus only for the NL-SH parameter set ($\beta=-0.182$). For the TM2 parameter set ^{44}S is moderately prolate deformed ($\beta=0.155$) and shows the spherical shell gap $N=28$, purely due to $0f_{7/2}$ orbit. This result is due to the presence of shape coexistence in this nucleus, since the shape of ^{44}S (prolate/ oblate) depends on the strength of pairing. On the other hand, in ^{40}Mg and ^{42}Si the $N=28$ shell is broken under all conditions, independent of pairing strength as well as the choice of parameter set.

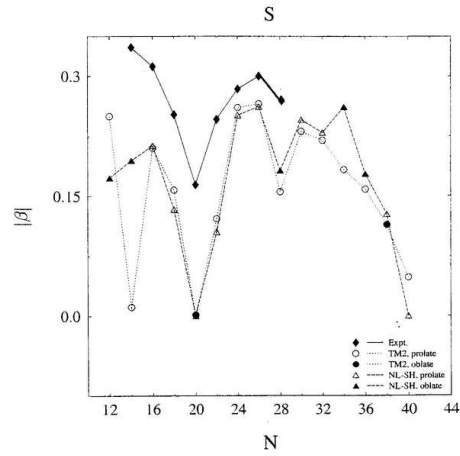


Fig. 5. The RMF calculated quadrupole deformation parameter $|\beta|$ using NL-SH and TM2 parameter sets, compared with experimental data, for S isotopes, from [4].

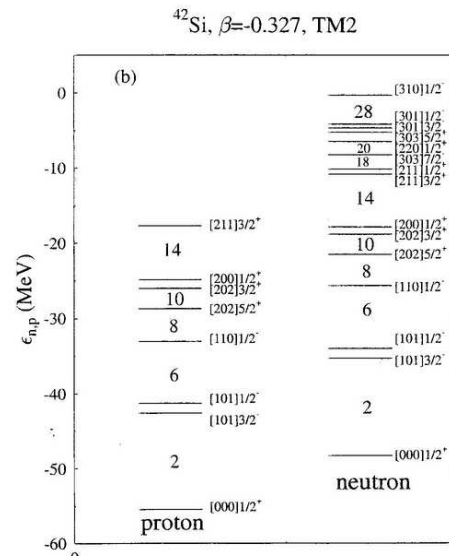


Fig. 6. The ground state single particle levels for oblate deformed ^{42}Si nucleus, using the TM2 parameter set, from [1].

A similar spherical shell breaking is found to occur for $Z=82$, $^{182-190}\text{Pb}$ nuclei for zero/ non-zero, constant BCS-pairing gap case, using various parameter sets (NL1, NL3, NL-SH, NL-RA1 and TM1) [6]. Specifically, ^{186}Pb is prolate deformed ($|\beta| \sim 0.2$), and the shell gap at $Z=82$ is almost zero for NL3 and is considerably reduced for NL1, for both the cases of with and without pairing. However, the quadrupole constraint calculated potential energy surfaces (PES) show only the two deformed (prolate and oblate) shape co-existing solutions, i.e. with no spherical solution. Alternatively, some authors [33] have used the constant strength of pairing interaction G , which restored the $Z=82$ spherical magic shell for Pb nuclei for NL1 parameter set, but then the deformed relativistic Hartree-Bugoliubov (RHB) approach [34], using the NL3 parameter set with finite range Gogny interaction DIS, result in predicting $^{188-194}\text{Pb}$ nuclei as oblate deformed in their ground-states. Perhaps, in this case, one need to go beyond mean-field formalism.

3.5 Multiple shape structures in $N = Z$, $A = 80 \pm 10$ neutron deficient nuclei [9,35].

The phenomenon of multiple shape co-existence, i.e. more than two shapes at about the same binding energy, is predicted in the above said region [35], suggesting a "dynamically" variable nature of the nuclear shapes in the neutron-deficient $N=Z$ exotic nuclei which is in sharp contradiction to the well accepted concept and observation of one permanent deformation of the nucleus. Hence, it is a new result and needs an experimental verification.

The shape co-existence phenomenon provides information regarding the excitation energies of two (or more) neighbouring intrinsic states. Alternatively, this means that if deeper minima in the potential energy surface are not nearly equally deep (i.e. the energy difference between the first two minima $\Delta E > 2-2.5$ MeV), then such states are isomeric states, giving information about the first excited intrinsic state above the ground-state (deepest minimum), and so on for the next minima. Since the first excited intrinsic state for *spherical* nuclei lie very high, it is possible that ΔE contains the information about the magic structure of nuclei and hence allows us to test the validity of model parameters used in, say, the mean field approaches applied to nuclei far away from the valley of β -stability.

Fig. 7 illustrates the potential energy surfaces calculated in the quadratic constraint scheme for $N=Z$ ^{72}Kr to ^{92}Pd nuclei, for use of the two parameter sets NL3 and TM1. Note that no triaxial shapes (γ -deformation) are allowed here, and hence we may get oblate and prolate solutions whose absolute values are similar. Only one of them may be a real (γ -soft) minimum. It is evident from the calculated PES that their shape co-existence nature is nearly independent of the choice of the parameter set i.e. both NL3 and TM1 parameter sets, though have opposite signs for the coupling constant g_3 , produce solutions of similar deformations. However, in this context it is important to add that, in general, although the number of solutions obtained for NL3 and TM1 parameters are almost equal in each case, due to their shape-coexistence nature, the different solutions correspond to different intrinsic states. For example, for ^{72}Kr the second intrinsic state ($\beta_2 = -0.172$) in TM1 corresponds to the solution of third intrinsic state ($\beta_2 = -0.189$) in NL3, and the third intrinsic state ($\beta_2 = 0.396$) of TM1 corresponds to

the second intrinsic state ($\beta_2 = 0.391$) of NL3 set (see Table 1 in [35]). Furthermore, it is interesting to note that these co-existing spherical, deformed (oblate and prolate) and superdeformed shapes include even the cases of exceedingly large super-deformations (see, e.g., $\beta = 0.63$ at 0.15 MeV above the ground-state for ^{84}Mo , using NL3 parameter set).

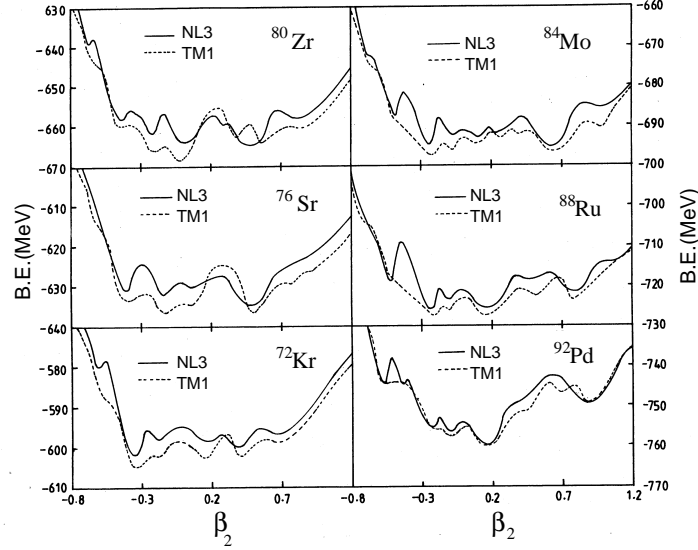


Fig. 7. The PES, i.e. binding energy as a function of quadrupole deformation β , for $N=Z$ ^{72}Kr to ^{92}Pd nuclei using the NL3 and TM1 parameter sets, from [35].

Fig. 8 gives a plot of the difference between the ground state binding energy and the energy of the first excited state, ΔE . The points lying on the zero line means the nuclei having no excited states, i.e. the pairing washes away the excited state minima. Two results are apparent: (i) The shape co-existence region ($\Delta E < 2$ MeV) is confined mainly to deformed $Z=14-16$, $Z=30-44$ and $Z=52-54$ nuclei, in the vicinity of the sub-shell closure ($0d_{5/2}$) and the magic numbers 28 and 50. (ii) For all the parameter sets, the peaking structures occur at all the magic numbers 20, 28 and 50, for both the cases of with and without pairing. Thus, as stated above, ΔE contains the information about the magic structure of nuclei.

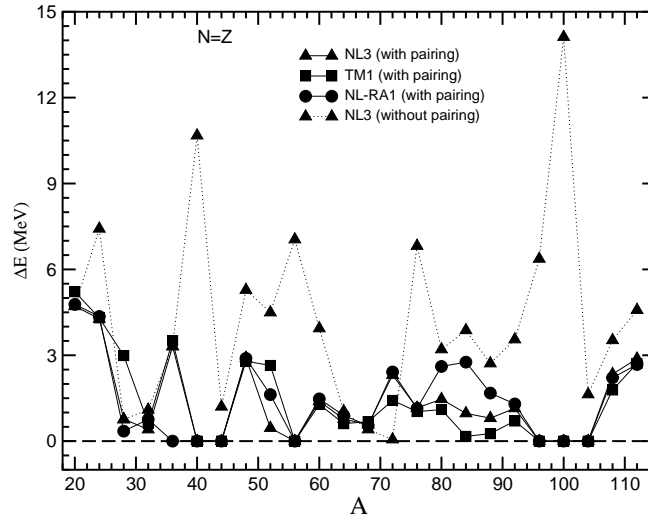


Fig. 8. The difference between ground- and first excited-state binding energies vs. A for $N=Z$ nuclei for three parameter sets for cases of with and without pairing, [9].

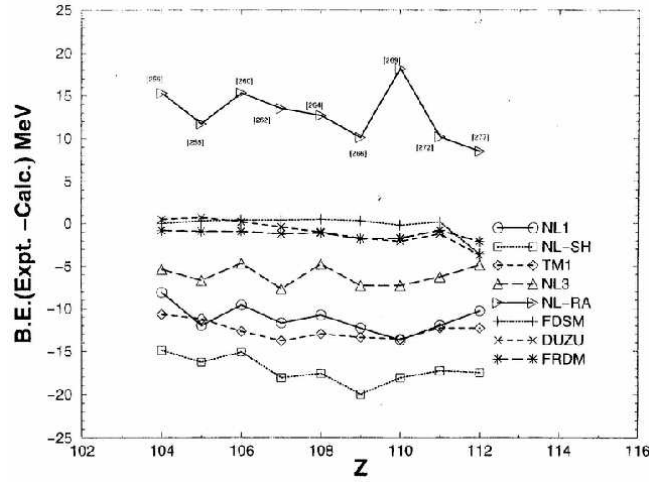


Fig. 9. The difference in experimental and RMF calculated ground state binding energies, using various parameter sets, for $Z=104-112$ super-heavy nuclei, compared with other available theoretical calculations, from [16].

3.6 Super-heavy elements [13, 14, 16–18]

binding energy calculations [13, 14, 16] Fig. 9 shows the difference in experimental and computed binding energies for all the known heavy nuclei from $Z=104$ to 112 , using the various parameter sets. Also, plotted in this figure are the other available theoretical calculations [31, 35, 36], marked FDSM, DUZU and FRDM, which agree very well with the experimental data because of their phenomenological nature. Fig. 9 shows clearly that almost all the parameter sets give an overall (nearly independent of Z) overbinding, except for the lone NL-RA1 parameter set which predicts an underbinding that oscillates with Z . The NL3 parameter set gives the best results, within ~ 5 MeV of experiments for all the observed cases. The other parameter sets differ from the experimental data by different constant energy shifts, which, if subtracted, would make the calculations nearly coincide with the experimental data. Note that the errors in the predicted binding energies are of less than 1% with experiments, which are within the accuracy of the present relativistic mean field approach. Since only the binding energies are known experimentally for the superheavy nuclei, it is difficult to conclude at present about the best parameter set.

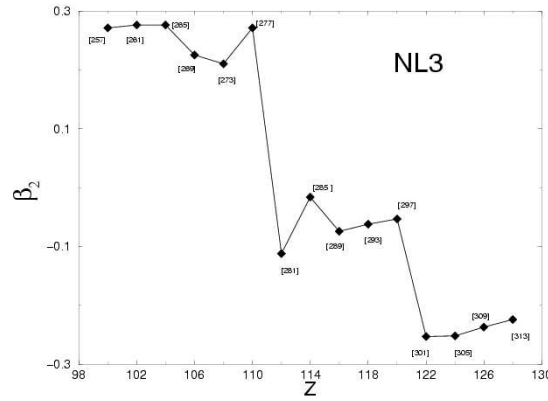


Fig. 10. Quadrupole deformation parameter β_2 vs. Z for various isotopes of $Z=100$ -128, using NL3 parameter set, from [16].

Nuclear Shape calculations [14, 16] Fig. 10 shows the calculated quadrupole deformation parameter using NL3 force parameters for $^{257}_{100}$ to $^{313}_{128}$ nuclei, in steps of α -nucleus mass. An interesting result of this figure is that the shape changes systematically from a prolate to an oblate shape via a definite region of spherical nuclei with

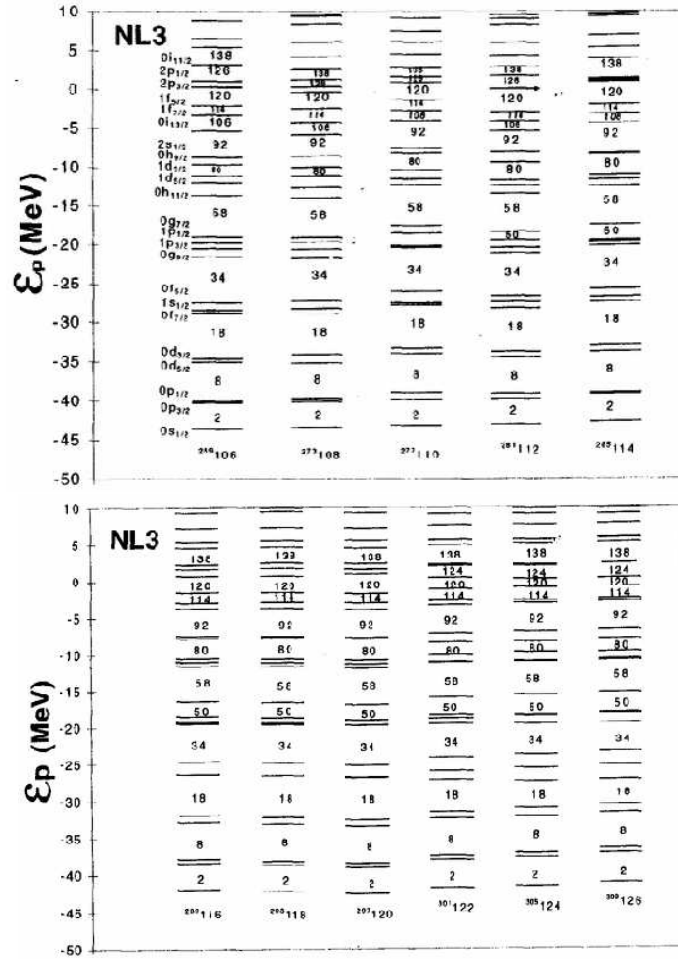


Fig.11. Spherical (not a ground-state) single-particle energy spectra for protons in Z=106-126 nuclei, using NL3 force parameter, from [16].

$Z=116\pm 4$, rather than a single nucleus. This could be considered as the true island of superheavy nuclei, with its centre (i.e. magic numbers for protons and neutrons) lying at one of these nuclei. Note that $Z=114$ and 120 nuclei are the most spherical nuclei.

Shell structure of super-heavy nuclei [13, 16] Fig. 11 gives the calculated single-particle energy spectra for protons in $Z=106$ to 126 and $A=269$ to 309 nuclei, chosen in steps of the α -nucleus mass. Only the spherical solutions are plotted, though the spherical states are not the ground state solutions. We notice in this figure that the known magic numbers at $Z=20, 28$ and 82 are never obtained and even the new proton shell gaps are different for the different regions of the heavier elements. However, the shell gap at $Z=120$ remains significant throughout the considered region of super-heavy nuclei (and is largest for $Z=120$ nucleus), though the other gaps, say, at $Z=138$ could not be ignored. The shell gap at $Z=114$ also starts appearing and increases steadily, but then the shell gap at $Z=120$ starts diminishing and becomes comparable to the gap at $Z=114$ and a new shell gap at $Z=124$ starts competing with the gaps at $Z=114$ and 120 .

Similarly, for neutrons the known shell gap at $N=126$ is never obtained in these calculations, though $N=124$ is reasonably strong. The new result obtained is that the shell gap at $N=172$ competes with the shell gap at $N=184$, and that the next higher shell gaps at $N=198, 228$ and even 258 are large enough not to be ignored. Also, a shell at $N=164$ is equally predominant throughout.

4 Concluding remarks

We have seen that the relativistic mean field theory provides a reasonably good description of the gross properties of nuclei at the two extremes of mass (the light and super-heavy nuclei) and iso-spin (nuclei at the proton and neutron-drip lines). A large amount of data is explained and many new results are obtained. The major difficulty is the strength of pairing interaction which could lead to a difficulty in choosing a consistent force parameter set. It is hoped that in near future it will be possible to improve upon the RMF theory for inclusion of coupling to continuum [37], the projection of good angular momentum states, or go beyond the mean-field by including, say, the effects of π -mesons, etc..

References

1. S.K. Patra, R.K. Gupta and W. Greiner, Int. J. Mod. Phys. **E6** (1997) 641.
2. T.K. Jha, M.S. Mehta, S.K. Patra, B.K. Raj and R.K. Gupta, Pramāna J. Phys. **61** (2003) 517.
3. H. Glasmacher, *et al.*, Phys. Lett. **B395** (1997) 164.
4. R.K. Gupta, S.K. Patra and W. Greiner, Mod. Phys. Lett. **A12** (1997) 1317.
5. T.R. Werner, *et al.*, Phys. Lett. **B335** (1994) 259; Nucl. Phys. **A597** (1996) 327.
6. M.S. Mehta, S.K. Patra and R.K. Gupta, Pramāna J. Phys. (2004)- to be published.
7. A.N. Andreyev, *et al.*, Nature **405** (2000) 430.
8. S.K. Patra, B.K. Raj, M.S. Mehta and R.K. Gupta, Phys. Rev. **C65** (2002) 054323.
9. M.S. Mehta, T.K. Jha, S.K. Patra and R.K. Gupta, Pramāna J. Phys. **62** (2004) 841.

10. J.H. Hamilton, A.V. Ramayya, W.T. Pinkston, R.M. Ronningen, G. Garcia-Bermudez, R.L. Robinson, H.J. Kim, R.O. Sayer, H.K. Carter, Phys. Rev. Lett. **32** (1974) 239; **36** (1976) 340.
11. C. Chandler, *et al.*, Phys. Rev. **C61**, 044309 (2000) and the earlier references there in.
12. K. Rutz, M. Bender, T. B'urvenich, T. Schilling, P.-G. Reinhard, J.A. Maruhn and W. Greiner, Phys. Rev. **C56** (1997) 238.
13. R.K. Gupta, S.K. Patra and W. Greiner, Mod. Phys. Lett. **A12** (1997) 1727.
14. S.K. Patra, C.-L. Wu, C.R. Praharaaj and R.K. Gupta, Nucl. Phys. **A651** (1999) 117.
15. S. Cwiok, J. Dobaczewski, P.-H. Heenen, P. Magierski and W. Nazarewicz, Nucl. Phys. **A611** (1996) 211.
16. S.K. Patra, W. Greiner and R.K. Gupta, J. Phys. G: Nucl. Part. Phys. **26** (2000) L65.
17. S.K. Patra, C.-L. Wu, W. Greiner and R.K. Gupta, J. Phys. G: Nucl. Part. Phys. **26** (2000) 1569.
18. M.S. Mehta, B.K. Raj, S.K. Patra and R.K. Gupta, Phys. Rev. **C66** (2002) 044317.
19. P.-G. Reinhard, M. Rufa, J. Maruhn, W. Greiner and J. Friedrich, Z. Phys. **A323** (1986) 13.
20. M. Rufa, P.-G. Reinhard, J.A. Maruhn, W. Greiner and M.R. Strayer, Phys. Rev. **C38** (1988) 390.
21. P.-G. Reinhard, Z. Phys. **A329** (1988) 257; Rep. Prog. Phys. **52** (1989) 439.
22. Y.K. Gambhir, P. Ring and A. Thimet, Ann. Phys. (N.Y.) **198** (1990) 132.
23. M.M. Sharma, M.A. Nagarajan and P. Ring, Phys. Lett. **B312** (1993) 377.
24. B.D. Serot and J.D. Walecka, Adv. Nucl. Phys. **16** (1986) 1.
25. D.G. Madland and J.R. Nix, Nucl. Phys. **A476** (1988) 1;
P. M'oller, W.D. Myers, W.J. Swiatecki and J. Treiner, At. Data Nucl. Data Tables **39** (1988) 225.
26. Y. Sugahara and H. Toki, Nucl. Phys. **A579** (1994) 557.
27. W. Koepf and P. Ring, Phys. Lett. **B212** (1988) 397.
28. J. Fink, V. Blum, P.-G. Reinhard, J.A. Maruhn and W. Greiner, Phys. Lett. **B218** (1989) 277.
29. D. Hirata, H. Toki, I. Tanihata and P. Ring, Phys. Lett. **B314**(1993) 168.
30. H. Flocard, P. Quentin and D. Vautherin, Phys. Lett. **B46** (1973) 304.
31. P. M'oller, J.R. Nix, W.D. Myers and W.J. Swiatecki, At. Data and Nucl. Data Tables, **59** (1995) 185.
32. G. Audi and A.H. Wapstra, Nucl. Phys. **A565** (1993) 1.
33. S. Yoshida and N. Takigawa, Phys. Rev. **C55** (1997) 1255.
34. T. Nikšić, D. Vretenar, P. Ring and G.A. Lalazissis, Phys. Rev. **C65** (2002) 054320.
35. C.-L. Wu, M. Guidry and D.H. Feng, Phys. Lett. **B387** (1996) 449; X.L. Han, C.-L. Wu, M. Guidry and D.H. Feng, Phys. Rev. **C45** (1992) 1127.
36. J. Duflo and A.P. Zuker, Phys. Rev. **C52** (1995) R23, and ATOMIC MASS DATA CENTER File "du_zu_10.feb96" (1996).
37. J. Meng and P. Ring, Phys. Rev. Lett. **77** (1996) 3963; *ibid* **80** (1998) 460; W. P'oschl, D. Vretenar, G.A. Lalazissis and P. Ring, Phys. Rev. Lett. **79** (1997) 3841; G. A. Lalazissis, D. Vretenar and P. Ring, Phys. Rev. **C57** (1998) 2294.

Application of RMF and RQRPA to Nuclear Structure Studies

Ahmad Ansari

Institute of Physics, Bhubaneswar 751 005, India

Abstract. The relativistic Hartree-Bogoliubov(RHB) theory in coordinate space provides an appropriate framework to study the bulk properties of neutron deficient to neutron-rich all the nuclei in the periodic table. It is found that even the dynamical properties such as the giant resonances and low-lying vibrational states in spherical nuclei are described rather well employing the same Lagrangian in the quasiparticle random phase (QRPA) formalism.

1 Introduction

Usually in a non-relativistic mean field description of a nucleus with A nucleons, an inert core of A_0 nucleons(with magic proton and neutron numbers) is assumed, and a suitable effective Hamiltonian for the $(A - A_0)$ valence particles in a model space is employed which has a few adjustable parameters. Experience shows that for different regions of the periodic table one needs different cores and different effective Hamiltonians. Due to this reason the predictive power of such an approach is very much limited, particularly for very neutron rich or neutron deficient nuclei. In this sense the relativistic mean field theory(RMFT) [1–4] has made a real breakthrough. In RMFT there is no assumption of an inert core and a Lagrangian density is parametrized in terms of about 8 parameters after fitting the nuclear matter properties and binding energies and rms radii of a few selected spherical nuclei.

Following the relativistic mean field theory one is able to reproduce the gross properties in the ground state, like binding energies and radii, quite satisfactorily throughout the periodic table. Now one must go beyond this to understand the dynamic properties, i.e., properties of the excited states. Recently Ring and coworkers [5, 6] have developed the random phase approximation (RPA) and quasiparticle RPA (QRPA) formalism following time-dependent relativistic mean field theory in the *no-sea* approximation. In this approach, the configuration space includes not only the usual ph-states, but also *ah*-configurations formed from occupied states in the Fermi sea and empty negative energy states in the Dirac sea. Dirac sea (see fig. 1). Finally the matrix equations of the RPA are formulated in the canonical single-particle basis of the relativistic Hartree-Bogoliubov(RHB) model employing an effective Lagrangian with non-linear self-interaction terms.

2 Formalism

We present here only an outline of the formalism giving relevant references. For the description of most of the nuclei (spherical as well as deformed) in the ground state

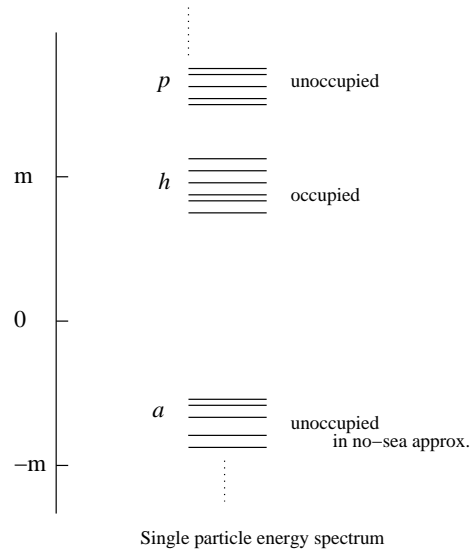


Fig. 1. Schematic diagram to illustrate 'no-sea' approximation.

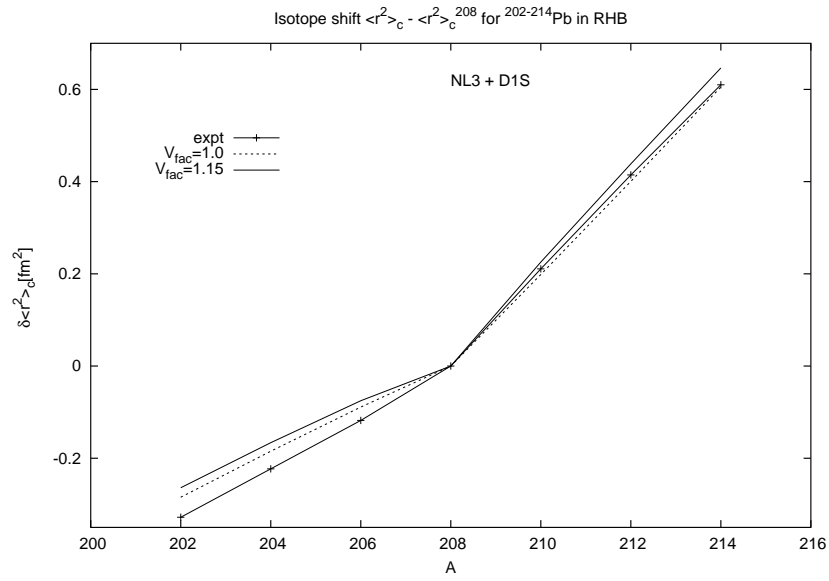


Fig. 2. Isotope shift $\delta \langle r^2 \rangle$ as a function of A in lead isotopes.

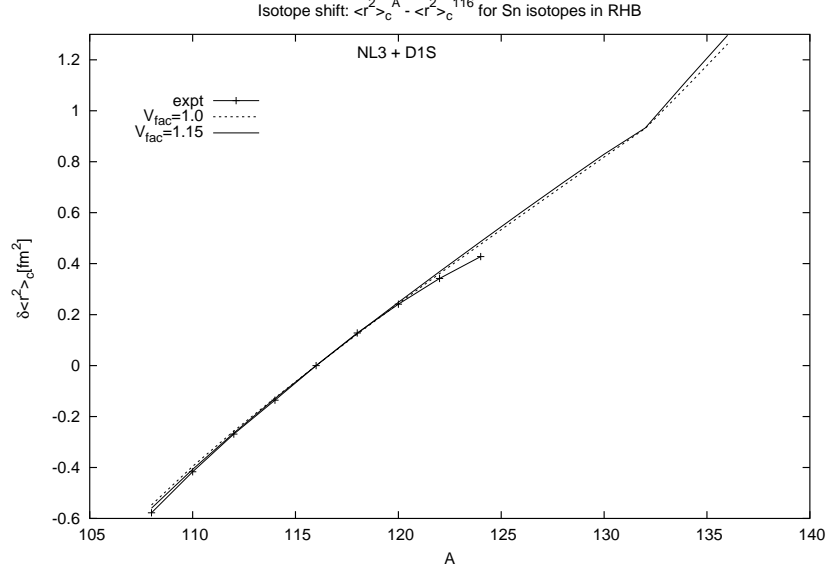


Fig. 3. Isotope shift $\delta \langle r^2 \rangle$ as a function of A in tin isotopes.

and at low excitations the pairing degrees of freedom are important. To incorporate the latter effects the relativistic Hartree theory is generalized to Hartree-Bogoliubov (RHB) theory and the details can easily be found in the literature [4]. The starting point of the relativistic models is to consider a Lagrangian density with Dirac spinors describing the nucleons interacting via the exchange of mesons (e.g. σ , ω , ρ) and the photons. The interaction between nucleons and mesons is given by the minimal coupling

$$\mathcal{L}_{int} = -\bar{\psi}\Gamma_{\sigma}\sigma\psi - \bar{\psi}\Gamma_{\omega}\omega\psi - \bar{\psi}\mathbf{\Gamma}_{\rho}\boldsymbol{\rho}\psi - \bar{\psi}\Gamma_e A\psi, \quad (1)$$

where.

$$\Gamma_{\sigma} = g_{\sigma}, \quad \Gamma_{\omega}^{\mu} = g_{\omega}\gamma^{\mu}, \quad \mathbf{\Gamma}_{\rho}^{\mu} = g_{\rho}\boldsymbol{\tau}\gamma^{\mu}, \quad \Gamma_e^{\mu} = e\frac{1-\tau_3}{2}\gamma^{\mu}, \quad (2)$$

with the coupling constants g_{σ} , g_{ω} , g_{ρ} and e . In non-linear version the mass term of free meson is replaced by a non-linear potential, such as,

$$\frac{1}{2}m_{\sigma}^2\sigma^2 \rightarrow U(\sigma) = \frac{1}{2}m_{\sigma}^2\sigma^2 + \frac{g_2}{3}\sigma^3 + \frac{g_3}{4}\sigma^4. \quad (3)$$

The classical variation principle gives the equations of motion, the Dirac equation for nucleons and the Klein-Gordon equations for the mesons. We will not go into further details on the formalism. However, we just mention that the pairing part is treated non-relativistically taking the pairing part of a finite range Gogny D1S force [7]. The RPA theory provides a convenient method to describe collective excitations of many-fermion systems. In practice two equivalent formalisms are used: one is the configuration space formalism and the other is called a linear response formalism. We shall discuss briefly the former approach in which a non-hermitian matrix

$$\begin{pmatrix} A & B \\ -B^* & -A^* \end{pmatrix}$$

is diagonalized for a given angular momentum state with matrices A and B constructed in the model space of 1 particle - 1 hole(ph) states based on a mean field ground state, like in Hartree-Fock approach. For the open shell spherical nuclei the pairing correlations are included through the Hartree-Fock-Bogoliubov treatment and RPA is generalised to quasiparticle RPA(QRPA). Instead of going into details of the derivation of the QRPA equations and expressions for the matrices A and B we refer to [6].

3 Ground state properties

We present below some RHB results on the ground state properties to illustrate the level of the successes of this approach. Besides many results available in the literature, we will take a few examples from the publications of Ring and coworkers only [8–11].

(a). Neutron halo in light nuclei.

Employing NL2 set of parameters for the RMF Lagrangian and density dependent zero range interaction for the pairing correlations Meng and Ring [8] have analysed the formation of the neutron halo in Li isotopes. The computed neutron densities are plotted in fig.2 of ref. [8] for ^9Li and ^{11}Li . The formation of halo in the latter nucleus is clearly seen by a sudden increase of the density as compared to ^9Li beyond 4 fm. A delicate balance between the selfconsistent mean-field and pairing field is found to be the microscopic origin of halo formation. In agreement with the experimental data ^{10}Li is found to be unbound with odd number of neutrons. Similar halo effects have been predicted in heavier nuclei [9].

(b). Ground state properties.

The ground state properties of Ni and Sn isotopic chains have been studied in ref. [10] using the NL3 set of Lagrangian parameters and Gogny D1S interaction [7] in the pairing channel. In these two very different mass regions the binding energies and rms radii are described very well. The total binding energies for Ni and Sn isotopes are compared with experimental values in fig.3 of ref. [10] whereas neutron densities are plotted in fig.4 of the same reference. Except for the region around ^{60}Ni and $^{100-102}\text{Sn}$ the absolute differences between the calculated and experimental values is less than 2 MeV. The density profiles display shell effects in the central region and a gradual increase of the neutron radii with the increase of neutron number.

We very briefly discuss about isotopic shift of charge radii in Pb and Sn isotopes. No non-relativistic mean field approach was able to explain a sudden kink in the relative charge radii $\delta \langle r^2 \rangle_A = \langle r^2 \rangle_A - \langle r^2 \rangle_{208}$ of Pb isotopes found experimentally at $A = 208$, but for the RMF approach [12]. Below in fig. 2 we display this for the NL3 parameter set of the Lagrangian with Gogny D1S pairing interaction. The pairing matrix elements are renormalized by an over all multiplicative factor $V_{fac} = 1.15$ and 1.0, the latter value implying actually no renormalization. The figure shows that the theory produces even a more drastic kink than the experimental one, and $V_{fac} = 1.0$ curve is closer to the experimental one [13].

In fig. 3 we show a similar plot for the tin isotopes, where mean square charge radii are measured relative to ^{116}Sn . The experimental curve does not exhibit any kink here,

but the curve has a parabolic shape. Between the two theoretical curves, the one with $V_{fac} = 1.0$ is again in somewhat better agreement with the data (but not showing a good parabolic behaviour). However, like in case of Pb isotopes the calculation predicts a kink at $N = 82$ magic number. The experimental data may show even a more pronounced kink if the measurements can be extended to $A > 132$.

(c). Sizes and shapes of $A = 20$ isobars.

A description of ground state properties of an isobaric sequence of nuclei tests the isovector channel of effective nuclear interaction. A Correct description of such nuclei ensures the use of such forces to study and predict the properties of nuclei far from the line of β - stability. Lalazissis et al [11] have analysed the sequence of $A = 20$ nuclei with mass number $Z = 7 - 12$. Experimental data [14] provide evidence of a proton skin in ^{20}Mg and a neutron skin in ^{20}N . For the mirror nuclei ^{20}O and ^{20}Mg the difference in radii of about 0.2 fm has been reported. In fig.1 of ref. [11] the binding energies of $A = 20$ nuclei(N, O, F, Ne, Na and Mg) calculated in RHB theory with NL3 + D1S parameter sets has been compared with experimental values, and the agreement is very good. The difference in neutron and proton radii is also in very good agreement with the data.

After the above very brief discussion on study of the ground state properties in the RHB theory, we would like to see as to how well the dynamic properties of excited states are described by the use of the same Lagrangian parameters.

4 Collective excitations

With progress on experimental measurements towards neutron drip line, it is of interest to make theoretical spectroscopic studies of isotopic chains over large range of neutron and proton numbers. Recently Terasaki *et al* [15] have calculated the lowest excited E_2 and $B(E2)$ decay rates of some isotopic chains around ^{132}Sn in a non-relativistic QRPA approach using quadrupole + pairing model Hamiltonian. In their scheme of calculation they predict an increase of $B(E2)$ value at $A = 132$ for Sn, but it is found to disappear when Nilsson single particle energies are used for the one-body part of the Hamiltonian.

As already mentioned above, Ring *et al* [5, 6] have derived fully self-consistent (ground and excited state properties calculated in the same framework) relativistic RPA and QRPA equations based on the relativistic Hartree-Bogoliubov(RHB) mean field within the ‘no-sea’ approximation. So far these have been applied mainly to the study of the collective multipole excitations in some neutron-rich isotopes like that of oxygen and tin etc. For example, fig. 2 in ref. [6] shows the dipole response in neutron-rich oxygen isotope ^{22}O calculated in a fully self-consistent RHB+RRPA formalism. It also predicts the so-called *pygmy* resonances at low collective excitations besides a giant resonance at about 20 MeV peak energy. Recently the search for pygmy resonances has attracted considerable interest. Similarly the fig. 10 in ref. [6] shows a good agreement between calculated isovector giant dipole resonance(GDR) energies and the available experimental values for Sn isotopes. Encouraged with good results on multipole resonances, we now apply it to study the low lying vibrational states in spherical nuclei. Tin isotopes seem to provide almost the longest chain of isotopes to study the structural properties as a function of the neutron number. So, we have chosen for the present

study Sn isotopes with $A = 100-138$ employing NL3 + D1S Lagrangian parameters. RMF calculations [16] show that Sn isotopes heavier than $A = 138$ may be deformed in the ground state, and then the present formalism can not be applied.

It may be good to check if the pairing interaction Gogny D1S as such is satisfactory or some renormalization is desirable. For this purpose we have compared the binding energy per particle (B/A) with experimental data and that of Gogny in tables (1) and (2) for Pb and Sn, respectively after renormalizing the D1S matrix elements by an overall multiplicative factor V_{fac} . The values of pairing energy calculated in the present RHB approach and that by Gogny are also compared.

Table 1. RHB results on binding energy per particle and pairing energy, for Pb isotopes with two values of V_{fac} .

A	BE/A[MeV]				E_{pair} [MeV]		
	Expt.	Gogny	$V_{fac}=1.0$	$V_{fac}=1.1$	Gogny	$V_{fac}=1.0$	$V_{fac}=1.1$
202	7.882	7.811	7.895	7.901	14.41	10.87	16.83
204	7.880	7.813	7.895	7.899	10.49	7.32	12.13
206	7.876	7.813	7.892	7.895	5.74	3.51	6.58
208	7.868	7.815	7.886	7.886	0.0	0.0	0.0
210	7.836	7.769	7.849	7.852	4.19	5.54	8.66
212	7.805	7.730	7.812	7.818	8.64	9.98	15.23
214	7.772	7.692	7.775	7.783	12.89	13.56	20.51

Table 2. As in table 1, for Sn isotopes.

A	BE/A[MeV]				E_{pair} [MeV]		
	Expt.	Gogny	$V_{fac}=1.0$	$V_{fac}=1.1$	Gogny	$V_{fac}=1.0$	$V_{fac}=1.1$
112	8.513	8.419	8.505	8.518	19.04	11.49	18.13
114	8.523	8.433	8.515	8.527	19.29	11.74	18.90
116	8.523	8.437	8.516	8.530	19.39	12.87	19.90
118	8.517	8.431	8.512	8.526	19.15	14.09	20.79
120	8.505	8.417	8.502	8.516	17.92	14.77	21.14
122	8.489	8.400	8.488	8.502	16.76	14.73	20.70
124	8.467	8.378	8.471	8.484	14.94	13.86	19.32
126	8.444	8.353	8.450	8.461	12.50	12.10	16.87
128	8.418	8.326	8.426	8.435	9.45	9.34	13.16
130	8.388	8.300	8.399	8.404	5.48	5.41	7.83
132	8.355	8.283	8.369	8.369	0.00	0.00	0.00

Clearly $V_{fac} = 1.1$, just a 10% enhancement, seems rather strong for the considered Pb isotopes. On the otherhand, for Sn $V_{fac} = 1.1$ seems good for the lighter isotopes, and 1.0 favourable for the heavier end.

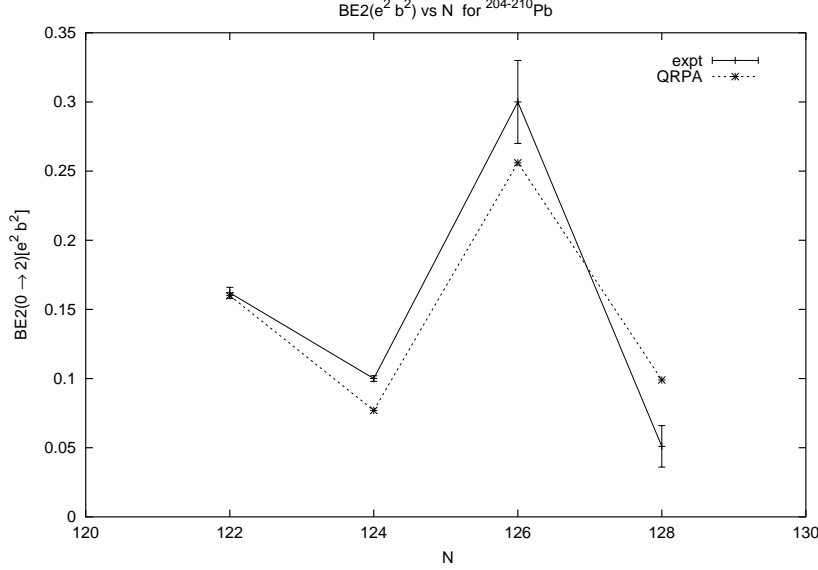


Fig. 4. $BE2 \uparrow$ values for $^{204-210}\text{Pb}$ isotopes.

Before proceeding for results on Sn isotopes, we have checked it for $^{204-210}\text{Pb}$ isotopes. Normally a large value of $B(E2)$ is a measure of collectivity, and at and near a shell closure the collectivity vanishes. However, it is known since long that in case of ^{208}Pb the E_2 energy becomes suddenly large (4.085 MeV) accompanied by an enhancement of $BE2 \uparrow$ as well [17]. In fig. 4 we see that our calculation reproduces this behaviour very well. The calculated values of E_2 energies come out to be 1.25, 1.26, 5.08, 1.13 MeV as compared to the experimental values of 0.90, 0.80, 4.08, 0.80 MeV for $^{204-210}\text{Pb}$, respectively.

In Fig. 5 we compare our calculated E_2 values for Sn isotopes with the available experimental data [17]. At $A = 132$ pairing collapses and we obtain $E_2 = 4.487$ MeV as compared to the experimental value 4.041 MeV. Our predicted value for E_2 at $A = 100$ is 5.1 MeV. A close inspection of the table 2 reveals that the calculated B/A for the tin isotopes are in better agreement with the experimental data if $V_{fac} = 1.1$ is used for the lighter end and 1.0 is used for the other end (heavy ones). So, in this figure the theoretical values are plotted for three values of the scaling factor V_{fac} as the labels on the figure indicate, with $x = 1.0 - (N - Z)/2$ in $V_{fac} = 1.15x$. To appreciate further the quality of these results let us compare, for example, our numbers for ^{120}Sn with recent results of Hagino and Sagawa [18] computed in 'continuum QRPA in coordinate space representation'. We get $E_2 = 1.43$ MeV, $B(E2) \uparrow = 0.157e^2b^2$,

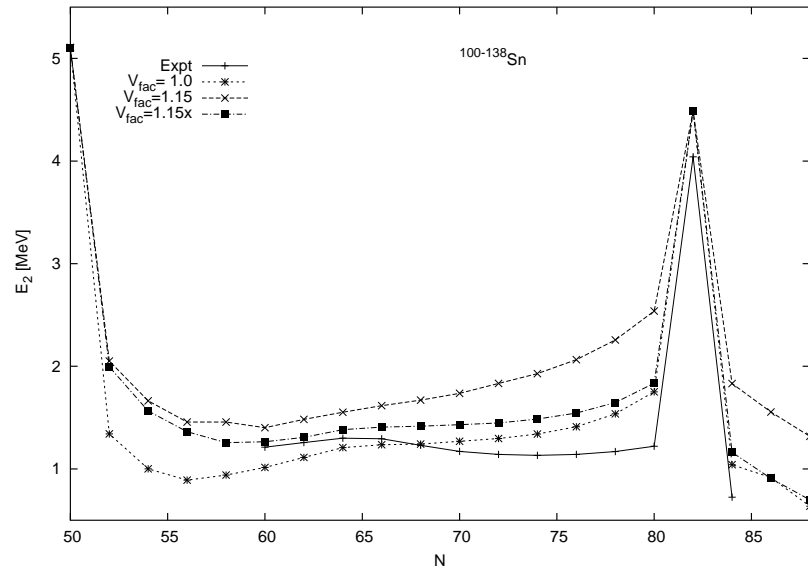


Fig. 5. Dependence of E_2 on N for Sn isotopes.

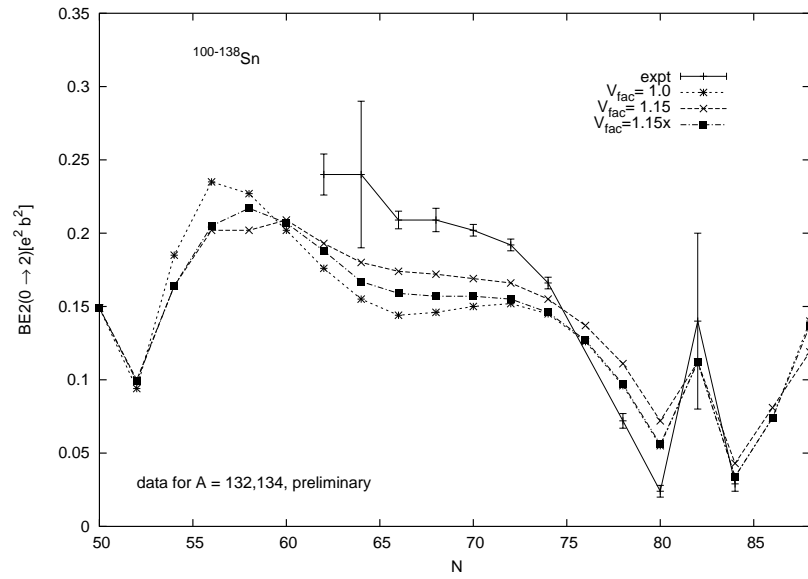


Fig. 6. Dependence of $BE2 \uparrow$ on N for Sn isotopes. Experimental data for $A = 132$ and 134 are still preliminary [20].

$E_{3-} \uparrow = 2.1$ MeV, $B(E3) = 0.166e^2b^3$ which should be compared with that of Ref. [18]: $E_2 = 2.3$ MeV, $B(E2) \uparrow = 0.105e^2b^2$, $E_{3-} = 3.0$ MeV, $B(E3) \uparrow = 0.077e^2b^3$, the experimental values being $E_2 = 1.17$ MeV, $B(E2) \uparrow = 0.202e^2b^2$, $E_{3-} = 2.4$ MeV, and $B(E3) \uparrow = 0.09e^2b^3$. It is clear that our results are very satisfactory.

At $A = 132$, neutron as well as proton hole-particle(h-p) excitations compete. The lowest neutron h-p energy is 6.20 MeV, while for protons it is 6.16 MeV. In Fig. 6 we compare our RQRPA results (for the three values of V_{fac} as discussed above) with the available experimental data [17, 19]. In view of a fully microscopic calculation without any adjustable free parameter, the agreement with data is very good. The most important feature is the increase of $B(E2) \uparrow$ at the magic number $N = 82$ and 50 compared to the immediate neighboring isotopes. For the lowest value of E_2 in ^{132}Sn we may elaborate in a bit details about the RPA wavefunction components X, Y (in conventional notations). Corresponding to neutrons the lowest **two** h-p configurations are $(1h_{11/2}, 2f_{7/2})$ and $(1h_{11/2}, 1h_{9/2})$ with h-p energies as 6.20 and 7.16 MeV, and (X, Y) components as (0.78, 0.07) and (-0.23, -0.03), respectively. Similarly for protons the lowest two h-p configurations are $(1g_{9/2}, 1g_{7/2})$ and $(1g_{9/2}, 2d_{5/2})$ with h-p energies as 6.16 and 8.99 MeV and the (X, Y) components as (-0.36, -0.03) and (0.36, 0.07), respectively. Such proton (X, Y) components are much smaller in case of the neighboring isotopes which lead to smaller $B(E2)$ values. The behaviour of E_2 as well as $B(E2)$ at the doubly magic mass number $A = 100$ is predicted to be quite similar to that near $A = 132$.

5 Conclusions

From these studies we would like to draw the following conclusions:

1. In RHB approach using only a global parameter set(NL3) for the Lagrangian along with Gogny's pairing interaction (D1S) the ground state properties of almost all nuclei are reproduced very well.
- In the isotope shift plot for the Sn isotopes we predict a kink at $N = 82$, like that for lead isotopes at $N = 126$.
2. Also the multipole resonances and excitation energies of the first 2^+ states along with the $B(E2)$ decay rates for several Pb and Sn isotopes are reproduced quite well following the relativistic QRPA theory.
3. Ours is the first calculation to predict a rise of the $B(E2)$ transition rates at the neutron magic numbers $N = 50$ and 82 compared to the neighbouring isotopes in tin.
4. Though it is not desirable, it seems that for certain dynamical properties, an isospin dependent V_{fac} should be employed.

This is to acknowledge that the calculations are carried out using a code developed in collaboration with Peter Ring.

References

1. B.B. Serot and J.D. Walecka, Adv. Nucl. Phys. **16** (1986) 1.
2. Y.K. Gambhir, P. Ring and A. Thimet, Ann. Phys. (N.Y.) **198** (1990) 132.
3. P.-G. Reinhard, Rep. Prog. Phys. **52** (1989) 439.

4. P. Ring, Prog. Part. Nucl. Phys. **37** (1996) 193.
5. P. Ring, Zhong-yu Ma, Nguyen Van Giai, D. Vretenar, A. Wandelt, and Li-gang Cao, Nucl. Phys. **A694**, 249 (2001).
6. N. Paar, P. Ring, T. Niksic, and D. Vretenar, Phys. Rev. **C 67**, 034312 (2003).
7. J.F. Berger, M. Girod and D. Gogny, Nucl. Phys. **A428** (1984) 32.
8. J. Meng and P. Ring, Phys. Rev. Lett. **77** (1996) 3963.
9. J. Meng and P. Ring, Phys. Rev. Lett. **80** (1998) 460.
10. G.A. Lalazissis, D. Vretenar and P. Ring, Phys. Rev. **C 57** (1998) 2294.
11. G.A. Lalazissis, D. Vretenar and P. Ring, Phys. Rev. **C 63** (2001) 034305.
12. T. Gonzalez-Llaren, J.L. Egido, G.A. Lalazissis, and P. Ring, Phys. Lett. B **379**, 13 (1996).
13. E.W. Otten in *Treatise on Heavy Ion Science*, vol. 8, ed: D. Allan Bromley (Plenum Press, New York and London, 1989)pp. 517.
14. L. Chulkov, Nucl. Phys. **A603** (1996) 219.
15. J. Terasaki, J. Engel, W. Nazarewicz, and M. Stoitsov, Phys. Rev. **C 66**, 054313 (2002).
16. G.A. Lalazissis, S. Raman and P. Ring, At. Data Nucl. Data Tables **71** (1999) 1.
17. S. Raman, C.W. Nestor, Jr., and P. Tikkanen, At. Data Nucl. Data Tables **78**, 1 (2001).
18. K. Hagino, and H. Sagawa, Nucl. Phys. **A695**, 82 (2001).
19. D.C. Radford *et al*, Phys. Rev. Lett. **88**, 222501 (2002); and to be published.
20. J. Beene, private communication.

Consistent description of recent RIB measurements of total reaction and charge changing cross sections

A. Bhagwat*

Department of Physics, I.I.T. Powai, Bombay 400076, India

Abstract. Extensive experimental data on the charge changing cross sections for several nuclei, near the β stability line exist in the literature. The currently available Radioactive Ion Beam (RIB) facilities help to produce, accelerate and then use the beams of these radioactive nuclei as projectiles in further experimentation. Recently, extensive measurements of reaction (σ_R) and charge changing (σ_{cc}) cross sections for exotic nuclei using the Radioactive Ion Beams have been reported. The σ_R (σ_{cc}) is defined as the total cross section for change in the mass (charge) number of the projectile. The σ_{cc} reveals the information about the proton distribution in the presence of neutrons in the nucleus. The measured σ_R have been frequently used to extract the neutron radii of the exotic nuclei within the Glauber model. Here we present the simultaneous analysis of σ_R and σ_{cc} , measured recently using the RIB facilities. The calculations are carried out in two steps. As a first step, the ground state properties of these exotic nuclei are calculated using the well established Relativistic Mean Field (RMF) theory. The RMF calculations reproduce well the experimental binding energies, radii, etc., as expected. The Glauber model is then employed to calculate both σ_R and σ_{cc} using the calculated RMF densities. Explicit results for the exotic nuclei incident on ^{12}C targets are presented. The theory is found to give an excellent account of the experiment.

1 Introduction

Production, acceleration and subsequent use of the beams of unstable nuclei in further experimentation is of current interest. This is achieved in the Radioactive Ion Beam (RIB) facilities. In such facilities, a primary beam of stable nuclei is made to undergo fragmentation. The desired nuclei are extracted from the projectile fragments and then accelerated again for further experimentation. Some of these nuclei have large neutron excess / deficiency. They may lie far from the line of β stability. In such cases, the last neutron / proton has small single particle separation energy. As a result, the corresponding density distribution possesses long tail. The long protruding tail in the density distribution of such nuclei influences some of the observables like the reaction cross sections.

Careful investigations of such loosely bound nuclei have lead to a number of new and exciting discoveries in Nuclear Physics, such as the existence of neutron / proton halos, thick skins, disappearance of conventional magic numbers, appearance of new magic numbers etc. [1].

* In collaboration with Prof. Y. K. Gambhir

In the RIB experiments, the quantity that is generally measured is the total reaction or the mass changing cross section (σ_R). It is defined as the cross section for change in mass number of the projectile. Extensive measurements of σ_R have been reported in the literature [1]. The measured σ_R values are used to *deduce* the total matter radii of the unstable projectiles. Well - known Glauber model [2] is employed for this purpose. The Glauber model requires neutron and proton densities of both the target and the projectile as input. Generally, in RIB experiments, stable targets like ^{12}C or ^{28}Si are used, for which the experimental charge densities are known. Therefore, the only unknown quantity remains is the density distribution for the projectile. For this purpose, a particular form is *assumed*, like, the Saxon - Woods form or even the Gaussian form. The projectile density parameter is tuned to reproduce the experimentally observed reaction cross section. The matter radii thus obtained are generally called the ‘experimental matter radii’ of the unstable nuclei. It should be noted that such so - called experimental matter radii are model dependent. In fact, the discovery of neutron halo in ^{11}Li [3] has been due to such analysis, which was further substantiated by the transverse momentum distribution of the last neutrons in ^{11}Li [4].

Another related and important observable is the charge changing cross section (σ_{cc}), defined as the total cross section for change in the charge number of the projectile. Extensive measurements for the charge changing cross sections for a number of stable and unstable nuclei have been reported in the literature [5, 6]. It has been pointed out [6, 7] that a combined analysis of the total reaction cross sections and the corresponding charge changing cross sections may help in drawing definite conclusions on the differences in proton and neutron densities of the neutron rich nuclei. Further, the charge changing cross section may set an ‘upper limit’ over the *rms* charge radius of the nucleus [7].

Here, we present a systematic and consistent description of the total reaction and charge changing cross sections. The calculations proceed in two steps. In the first step, the ground state properties, like, the binding energies, point proton and neutron densities, *rms* radii, etc. of the projectile nuclei are determined within the framework of the well - established Relativistic Mean Field (RMF) / Relativistic Hartree Bogoliubov (RHB) theories. In the next step, the calculated RMF / RHB spherical densities are used in the Glauber model to obtain the reaction and the charge changing cross sections. For the present purpose, we use the zero range Glauber model [4]. The Glauber model in the zero range approximation, is applicable only for the higher projectile energies. For lower projectile energies, the zero range Glauber model is known to be inadequate, and it should be replaced by the finite range Glauber model. Towards the end of this article, a few preliminary results of the finite range Glauber model calculations are also presented.

A discussion on the essentials of the RMF / RHB models is now in order.

2 Essentials of RMF

It is now believed that the Relativistic Mean Field (RMF) theory provides one of the most successful description of the nuclear structure properties [8–13]. The RMF theory successfully reproduces the nuclear matter properties as well as the ground state prop-

erties of finite nuclei spread over the entire periodic table including those away from the β stability line [8, 9]. The RMF still works at the level of nucleons and mesons. It starts with the standard (nonlinear- σ , ω , ρ) interaction Lagrangian, developed for the nuclear-physics applications. The equations of motion are obtained by employing the Euler - Lagrange variational principle. These are further simplified by using different symmetry requirements. This yields the Dirac type equation with potential terms describing the nucleon dynamics and a set of Klein-Gordon type equations with sources for mesons and the photon. In the mean field approximation, replacing the fields by their expectation values, one ends up with a set of coupled equations, the so called RMF equations, that are to be solved self consistently.

The pairing correlations, important for open shell nuclei, can be taken into account in a phenomenological way, using occupation numbers of the BCS type based on experimental pairing gap deduced from odd-even mass differences (see e.g. [8]). This simple procedure (constant gap approximation) may work well in the valley of beta-stability, where experimental masses are known. Conceptually, for the proper treatment of pairing correlations, it is required to extend the present RMF formulation to a relativistic Hartree - Bogoliubov theory. The relativistic Hartree-Bogoliubov (RHB) equations have been derived [14] starting from the RMF Lagrangian. The resulting Relativistic Hartree-Bogoliubov (RHB) equations [9] read:

$$\begin{pmatrix} h_D - \lambda & \hat{\Delta} \\ -\hat{\Delta}^* & -h_D^* + \lambda \end{pmatrix} \begin{pmatrix} U \\ V \end{pmatrix}_k = E_k \begin{pmatrix} U \\ V \end{pmatrix}_k. \quad (1)$$

Here, λ is the Lagrange multiplier, E_k is the quasi-particle energy and U_k and V_k are properly normalised four dimensional Dirac spinors, h_D is the usual RMF Dirac Hamiltonian [9]:

$$h_D = -i\alpha \cdot \nabla + \beta (M + g_\sigma \sigma) + g_\omega \omega^0 + g_\rho \tau_3 \rho_3^0 + e \frac{1 - \tau_3}{2} A^0. \quad (2)$$

Here M is the nucleon mass, σ is the scalar field and ω^0 , ρ_3^0 and A^0 are the Lorentz time like components of the meson and e.m. fields. These fields are to be determined self-consistently from the Klein-Gordon (KG) equations with sources (nuclear currents and densities) involving super spinors (U (V)) [9].

The RHB equations have two distinct parts: the self consistent field (h_D) that describes the long range particle-hole correlations and the pairing field ($\hat{\Delta}$) that accounts for the correlations in the particle-particle (pp) channel. The pairing field $\hat{\Delta}$ is expressed in terms of the matrix elements of the two body nuclear potential V^{pp} in the pp -channel and the pairing tensor involving the super-spinors (U, V). In the case of the constant gap, $\hat{\Delta}$ ($\equiv \Delta$) becomes diagonal, resulting in the BCS type expressions for the occupation probabilities. As a result, the RHB equations (Eq. 1) reduce to the RMF equations with constant gap.

Reliable and satisfactory derivation of V^{pp} is not yet achieved in RMF [9]. Therefore, in practical calculations, it is customary to adopt a phenomenological approach while solving the RHB equations. Thus, one often uses for V^{pp} , the finite range Gogny-D1S [15] interaction, which is known to have the right content of pairing. It is given

by [15]:

$$V(\mathbf{r}_1, \mathbf{r}_2) = \sum_{i=1,2} e^{-\{(\mathbf{r}_1 - \mathbf{r}_2)/\mu_i\}^2} (W_i + B_i P^\sigma - H_i P^\tau - M_i P^\sigma P^\tau), \quad (3)$$

where, μ_i , W_i , B_i , H_i & M_i ($i=1,2$) are parameters of the interaction. Alternatively, one may use for V^{pp} , the density dependent, effective two body zero range interaction [16]:

$$V(\mathbf{r}_1, \mathbf{r}_2) = V_o \delta(\mathbf{r}_1 - \mathbf{r}_2) \frac{1}{4} (1 - \sigma_1 \sigma_2) \left(1 - \frac{\rho(r)}{\rho_o} \right); \quad (4)$$

where, V_o is the interaction strength with cutoff energy about 300 MeV [16] and ρ_o ($=0.152 \text{ fm}^{-3}$ [16]) is the nuclear matter density. The strength V_o is fixed [16] so as to reproduce the pairing energy obtained by using the finite range Gogny D1S interaction in RHB framework.

2.1 Ground State Properties

When the RMF/RHB equations are solved either using the oscillator basis expansion technique or in the coordinate space itself, the explicit calculations require the following input information:

- ★ Parameters appearing in the Lagrangian
- ★ V^{pp} or the experimental gap parameters Δ for the calculation of v_k^2 .

The pairing gaps can be calculated from the observed odd even mass differences [17]. Alternatively, these can be fixed so as to reproduce the pairing energy obtained from Gogny D1S interaction. For example, Δ_p (Δ_n) calculated from the observed odd-even mass differences is finite for $Z > 9$ ($N > 9$). The pairing energies obtained with the constant gap in the spherical oscillator basis, differ in several cases from the corresponding RHB values obtained in the spherical oscillator basis or in the coordinate space. Also, the use of the constant gaps may yield different occupation probabilities as compared to the corresponding RHB values with the Gogny D1S interaction for pairing. To be consistent with the RHB results, the constant gaps (independent of the particle level) are fixed so that the calculated pairing energy is almost identical to the corresponding D1S pairing energy. In fact, the gaps with this prescription are found to be more realistic than the corresponding experimental pairing gaps [18].

Several sets of the Lagrangian parameters are available in the literature. In the present work, one of the recent and the most successful Lagrangian parameter set, NL3 [19] has been used. The results obtained by using the other successful Lagrangian parameter sets (e.g. NL1 [8, 20], NL-SH [21]) exhibit identical systematics. Therefore, the conclusions/inferences presented here will generally remain valid.

The RMF/RHB calculations yield the following results:

The single particle energies (ε_i), nucleon spinors (Ψ_i), the fields (σ , ω° , ρ_3° & A°), the occupancies, binding energy, root mean square radii, densities and moments and so on.

In the present work, the RMF/RHB calculations have been carried out, using different prescriptions described earlier. Explicitly:

1. Calculations in the oscillator basis for:
 - a. RMF- with frozen gap approximation (corresponding results are denoted by SPH)
 - b. RHB using finite range Gogny DIS interaction (corresponding results being denoted by RHB (ob)).
2. The RHB calculations in the coordinate space with a box size of 25 fm, using the effective zero range density dependent two body interaction [16] (the results obtained for this case are denoted by RHB (c)).
3. To ascertain the effect of deformation the RMF equations with the constant gap approximation in the deformed oscillator basis with axial symmetry have also been solved and the corresponding results are denoted by DEF.

For odd - A nuclei, the last odd nucleon does not have a partner to occupy its time reversed state. As a result, the mean field ground state wave function does not have time reversal symmetry. For this purpose, we follow the tagged Hartree - Fock procedure, satisfactorily used in the non relativistic calculations.

The explicit calculations have been carried out for series of nuclei spanning the entire periodic table. Here, the results for the Neon (isotopic), A = 17 (isobaric) and N = 12 (isotonic) chains are presented and discussed as illustrative examples.

2.2 Binding Energies and Deformations

All the calculations are found to qualitatively reproduce the experimental binding energies [17] well. To examine the quantitative agreement of the different calculations with the corresponding experiment, the difference between the calculated and the experimental [17] binding energies is presented in Fig. (1) (left hand panel) as a function of the third component of isospin $T_z (= (N - Z)/2)$. The RHB(c) and the RHB(ob) results are almost identical, indicating that the inclusion of the correct asymptotics does not have a significant effect on the binding energies. Further, the SPH and RHB(ob) results are also found to be similar to each other. This is probably due to the right choice of the pairing gaps. The inclusion of deformation is found to bring the calculations closer to the experiment. This effect is seen most dramatically in the case of the Neon isotopes. Therefore, henceforth, only the RHB(c) and the DEF results are presented.

The quadrupole deformation parameter, β is a quantitative measure of the deformation of the nucleus. In practice, β is extracted from the proton (Q_p) and neutron (Q_n) quadrupole moments through:

$$Q = Q_n + Q_p = \sqrt{\frac{16\pi}{5}} \frac{3}{4\pi} A R_o^2 \beta \quad \text{with } R_o = 1.2 A^{1/3}. \quad (5)$$

The calculated (DEF) quadrupole deformation parameters (β) are shown in Fig. (1) (right hand panel) along with the corresponding Möller - Nix (MN) [22] values (where available). The calculated β values are found to be reasonable and also consistent with the corresponding MN values. The Neon isotopes close to N = Z are found to have strong prolate deformation. The present calculation indicates shape transition between ^{22}Ne and ^{23}Ne , which is in accordance with that of Möller - Nix [22]. The deformation parameters obtained for A = 17 and N = 12 chains are also reasonable. The only exception is ^{17}B , which seems to be very heavily deform (~ 0.6).

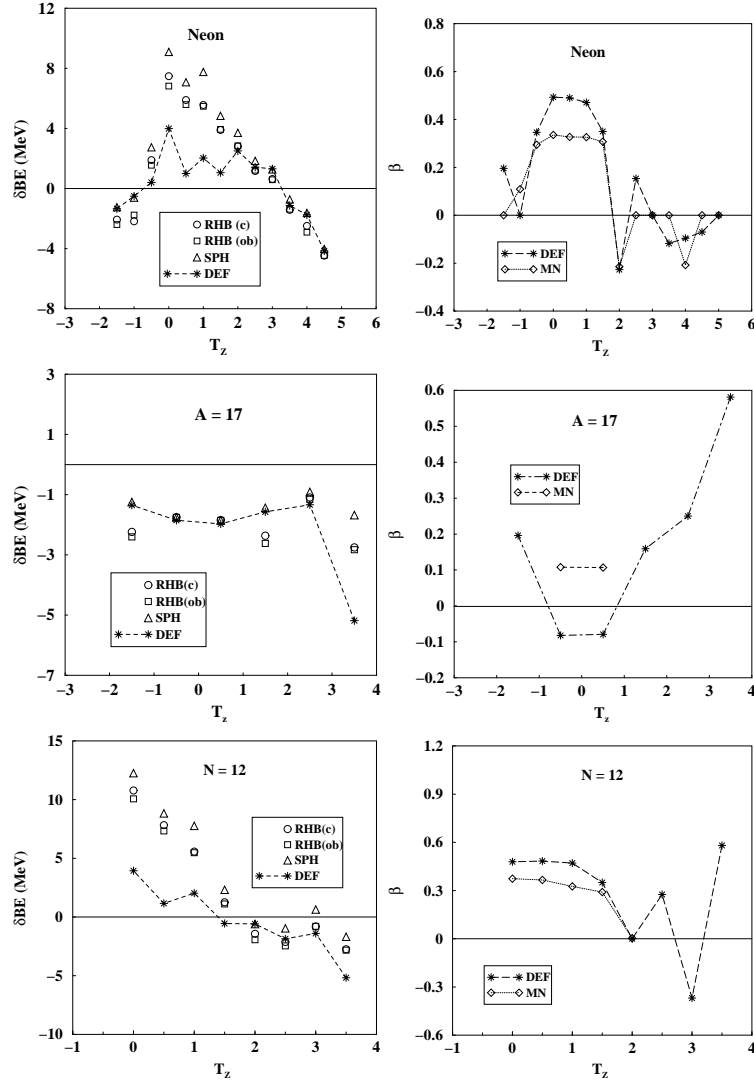


Fig. 1. The binding differences between the results obtained by different prescriptions of solving the RMF/RHB equations and the corresponding experiment [17] for Ne (isotopic), $A = 17$ (isobaric) and $N = 12$ (isotonic) chains. The quadrupole deformation parameters (β) are also shown (right hand panel) along with the corresponding Möller - Nix (MN) values (where available).

2.3 Radii

The charge radii (r_c) can be obtained from the calculated point proton root mean square (rms) radii (r_p) through the relation:

$$r_c^2 = r_p^2 + 0.64, \quad (6)$$

where, the factor 0.64 accounts for the finite size of proton. The calculated (RHB(c) and DEF) rms charge radii (r_c) along with the corresponding experimental values [6,23–26] are shown in Fig. (2) (left hand panel). The calculations reproduce the experiment very well. The deformation is found to improve the agreement between the calculations and the experiment, especially for the Neon isotopes.

The charge radii of Neon, deduced from the recent isotopic shift measurements [26] (knowing the charge radius of ^{20}Ne [23]), exhibit rich structure. The charge radius is maximum for ^{28}Ne on the neutron rich side, and for ^{17}Ne for the neutron deficient side. It goes through a minimum at ^{24}Ne . Thus, with addition or removal of neutrons from ^{24}Ne , the charge radius is found to *increase*. In addition, a mild odd - even staggering is clearly observed in the neutron rich as well as deficient isotopes. The calculated (DEF) charge radii are found to be in perfect harmony with the experiment. The anomalous behaviour (departure from the expected $r_o A^{1/3}$ behaviour) is nicely reproduced. The RHB(c) results, on the other hand, do not reproduce this trend, indicating that the deformation effects are crucial for describing the anomalous behaviour in the isotopic shifts.

For the case of $A = 17$ and $N = 12$ isobaric and isotonic chains as well, both the RHB(c) and DEF calculations describe the observed charge radii well. The r_c for the $A = 17$ and $N = 12$ chains are found to decrease monotonically with the T_z , which is in tune with the experimental trend. The departures from the corresponding experimental values are observed at some places, but these are found to be small.

The rms matter radii (r_m) are next presented in Fig. (2) (right hand panel). The corresponding so-called experimental r_m values [1] are also shown (where available). Both the calculations reproduce the experimental trend well.

The matter radii for the chain of Neon isotopes reflect a trend similar to that in the case charge radii. Both (RHB(c) and DEF) the theoretical calculations reproduce the experimental r_m very well, apart from a prominent dip at ^{19}Ne . The r_m for the $A = 17$ and $N = 12$ chains are found to be approximately a constant. This observation is consistent with the experimental trend, within the limits of the error bar.

3 Glauber Model

In the Glauber model, the reaction cross section is expressed as:

$$\sigma_R = 2\pi \int_0^\infty b [1 - T(b)] db. \quad (7)$$

$T(b)$ is the transparency function for impact parameter ' b '. In the optical limit for the zero range approximation, it is expressed as:

$$T(b) = \exp \left[- \sum_{i,j} \bar{\sigma}_{ij} \int d\mathbf{s} \bar{\rho}_{ti}(s) \bar{\rho}_{pj}(|\mathbf{b} - \mathbf{s}|) \right]; \quad (8)$$

Here, the summation indices i, j run over protons and neutrons and the subscript 'p' ('t') refers to the projectile (target). $\bar{\sigma}_{ij}$ is the experimental nucleon - nucleon cross section at the relevant energy (corrected for the medium effects). The z-integrated densities ($\bar{\rho}$) appearing in Eq. 8 are defined as:

$$\bar{\rho}(w) = \int_{-\infty}^{+\infty} \rho(\sqrt{w^2 + z^2}) dz, \quad (9)$$

with $w^2 = x^2 + y^2$.

This version of the Glauber model is applicable only in the case of high energy projectiles. The zero range Glauber model is required to be modified when the projectile energies are small. The modifications are twofold: 1) the finite range effects in the profile function and 2) Coulomb modified trajectories.

Within the finite range approximation the transparency function is written as:

$$T(b) = \exp \left\{ - \int_P \int_T \sum_{ij} [\Gamma_{ij}(\mathbf{b} - \mathbf{s} + \mathbf{t}) \bar{\rho}_{Pi}(\mathbf{t}) \bar{\rho}_{Tj}(\mathbf{s})] ds dt \right\} \quad (10)$$

Here, the profile function is given by [27, 28]:

$$\Gamma_{ij}(b_{eff}) = \frac{1}{2\pi\beta_{NN}^2} \sigma_{ij} \exp \left(- \frac{b_{eff}^2}{2\beta_{NN}^2} \right) \quad (11)$$

In this expression,

$$b_{eff} = |\mathbf{b} - \mathbf{s} + \mathbf{t}|. \quad (12)$$

\mathbf{b} is the impact parameter and \mathbf{s} and \mathbf{t} are just the dummy variables for integration over the z - projected target and projectile densities. The range parameter β_{NN} is given by,

$$\beta_{NN} = 0.996 \times \exp \left(- \frac{E}{106.679} \right) + 0.089, \quad (13)$$

where, E is the projectile energy. This range parameter is obtained by fitting ^{12}C on ^{12}C cross sections from 30A MeV to 1A GeV energies [28]. The nucleon - nucleon cross section at the specified projectile energy E is determined from the experimental nucleon - nucleon cross sections (by interpolation) or taken from some empirical fit to the experimental nucleon-nucleon cross sections (see, for example, [29]).

Especially for the lower energies, apart from the finite range effect, another important aspect is required to be taken into account: the effect of Coulomb interaction. The straight line trajectories assumed in the Glauber model, get distorted since the Coulomb force becomes significant at lower energies. This effect can be incorporated in the Glauber model through the classical perihelion. Under this assumption, the Coulomb modified impact parameter (b') can be written as [30]:

$$b' = \frac{1}{k} \left[\eta + (\eta^2 + k^2 b^2)^{1/2} \right], \quad (14)$$

where, η is the usual Sommerfeld parameter and k is the wave number of projectile. With this correction, the total reaction cross section is expressed as:

$$\sigma_R = 2\pi \int_{2\eta/k}^{\infty} b' \left(1 - \frac{\eta}{kb'} \right) [1 - T(b')] db'. \quad (15)$$

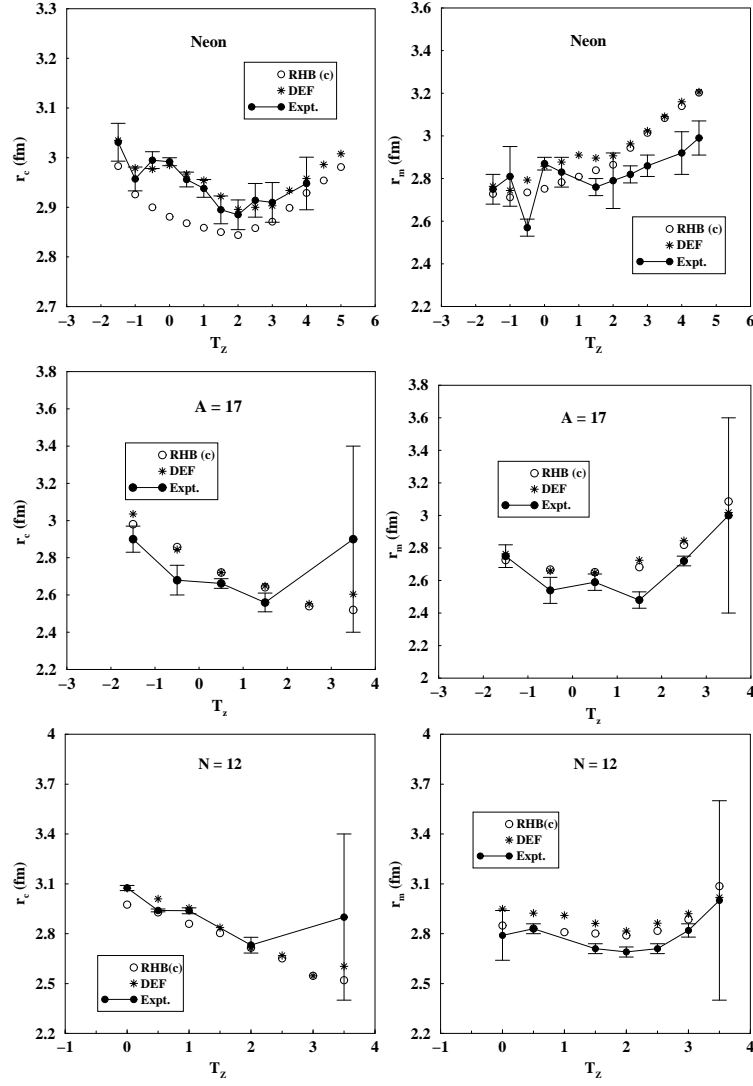


Fig. 2. The calculated (RHB(c) and DEF) charge and matter radii for Ne (isotopic), $A = 17$ (isobaric) and $N = 12$ (isotonic) chains. The corresponding experimental values [1, 6, 23–25] are also shown (where available).

3.1 Charge Changing Cross Sections

To derive an expression for the charge changing cross section, let us consider again, the zero range Glauber model.

Suppressing the explicit coordinate dependence in the z-integrated densities and writing all the terms appearing in the summation, the exponent of Eq. 8 is expressed as:

$$\begin{aligned} \sum_{i,j} \bar{\sigma}_{ij} \int d\mathbf{s} \bar{\rho}_{ti} \bar{\rho}_{pj} &= \bar{\sigma}_{pp} \int d\mathbf{s} \bar{\rho}_{tp} \bar{\rho}_{pp} + \bar{\sigma}_{pn} \int d\mathbf{s} \bar{\rho}_{tp} \bar{\rho}_{pn} \\ &+ \bar{\sigma}_{np} \int d\mathbf{s} \bar{\rho}_{tn} \bar{\rho}_{pp} + \bar{\sigma}_{nn} \int d\mathbf{s} \bar{\rho}_{tn} \bar{\rho}_{pn} \end{aligned} \quad (16)$$

Re-grouping the terms appearing in Eq. 16, the transparency function ($T(b)$) can be factorised as:

$$T(b) = T^p(b) T^n(b),$$

with,

$$T^p(b) = \exp \left[-(\bar{\sigma}_{pp} \int d\mathbf{s} \bar{\rho}_{tp} \bar{\rho}_{pp} + \bar{\sigma}_{np} \int d\mathbf{s} \bar{\rho}_{tn} \bar{\rho}_{pp}) \right] \quad (17)$$

$$T^n(b) = \exp \left[-(\bar{\sigma}_{pn} \int d\mathbf{s} \bar{\rho}_{tp} \bar{\rho}_{pn} + \bar{\sigma}_{nn} \int d\mathbf{s} \bar{\rho}_{tn} \bar{\rho}_{pn}) \right]. \quad (18)$$

Notice that the first term ($T^p(b)$) contains full target density and only the proton density of the projectile while the second term ($T^n(b)$) also involves the full target density but only the neutron density of the projectile. The reaction cross section now reads:

$$\begin{aligned} \sigma_R &= 2\pi \int_0^\infty b [1 - T^p(b) T^n(b)] db \\ &= 2\pi \int_0^\infty b [1 - T^p(b)] db + 2\pi \int_0^\infty b [T^p(b) (1 - T^n(b))] db. \end{aligned} \quad (19)$$

Intuitively, one may think that the charge changing cross section may involve only the proton density of the projectile. The first term in Eq. (19) represents such a mechanism for the charge changing cross sections. We denote this term by σ_{cc}^{free} , signifying that the neutrons in the projectile have no role to play in the charge changing process. The second term in Eq. (19) is denoted by σ_{cc}^I , leading to:

$$\sigma_R = \sigma_{cc}^{free} + \sigma_{cc}^I. \quad (20)$$

Considering the fact that the projectile neutrons may also contribute to the charge changing cross sections, we write σ_{cc} as a sum of two terms:

$$\sigma_{cc} = \sigma_{cc}^{free} + \mathcal{F} \sigma_{cc}^I. \quad (21)$$

The factor \mathcal{F} is deduced from the systematic analysis of the results of the present calculations. It is observed that [31]:

$$\begin{aligned} \mathcal{F} &= 0.8 \frac{Z^2}{N^2} \text{ for } N \geq Z \\ &= 0.8 \text{ for } N < Z; \end{aligned} \quad (22)$$

where, N (Z) denotes the neutron (proton) number of the projectile.

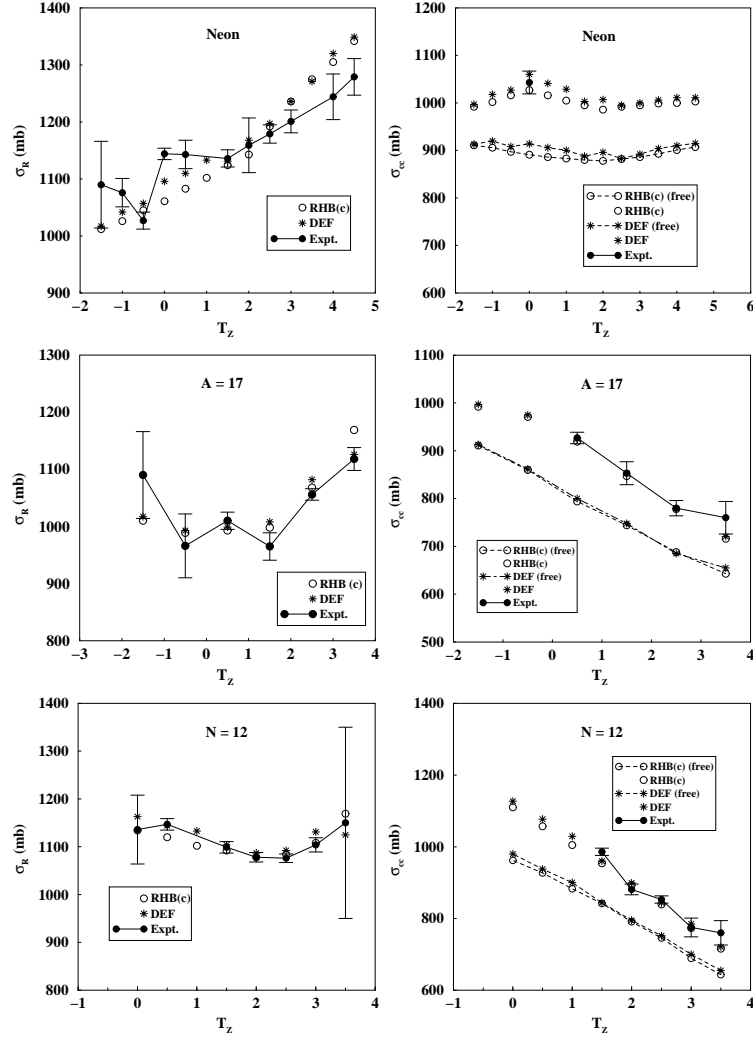


Fig. 3. The calculated (RHB(c) and DEF) reaction and total charge changing cross sections, along with the corresponding experimental values [1, 6] (where available).

3.2 Results of the Glauber Model Calculations

The Glauber calculations for the cross sections require both the target and the projectile density distributions. All the projectile densities are obtained in the relativistic mean field framework. In the case of the deformed densities, the $L = 0$ component (spherical) is projected out and then renormalised, separately for the protons and the neutrons. The resulting nucleon density distributions closely agree with the experiment (where available). The density of the ^{12}C target has been taken from an earlier work [32].

The Glauber model calculations also require an additional phenomenological parameter, which is the ratio of the experimental free nucleon-nucleon cross section to the in-medium nucleon-nucleon ($N - N$) cross section. This means that the in-medium $N - N$ cross sections may be less than the corresponding free $N - N$ cross sections. This is reasonable, since the medium poses additional restrictions due to complicated effects like the Pauli blocking and Fermi motion. In almost all the Glauber model analysis, this parameter is assumed to have a fixed value, 0.8 [3]. However, in order to reproduce σ_{cc} with only the first term of Eq. 21 (as assumed in [33]), this parameter turns out to be atleast 1.3, which may be unphysical.

The RHB(c) and DEF reaction cross sections calculated using the zero range Glauber model for Neon isotopes, $A = 17$ isobars and $N = 12$ isotones as projectiles, incident on ^{12}C target are presented in Fig. (3) (left hand panel). The corresponding experimental values [1] are also shown (where available). Clearly, the calculations reproduce the experiment well. The deformation is found to have only marginal effect on the reaction cross sections. It is interesting to note that the σ_R and r_m for all these cases follow a similar trend.

The total charge changing cross sections for the Neon, $A = 17$ and $N = 12$ chains are presented in Fig. (3) (right hand panel). The corresponding experimental values [6, 7] are also shown. The model for the charge changing cross sections is found to be satisfactory. The projectile proton contribution to the total charge changing cross sections is found to be around 80 to 90 % (as indicated by the ‘free’ cross sections in Fig. (3)).

3.3 Reaction cross sections at low projectile energies

We now present some of the preliminary results of the finite range Glauber model calculations. A significant amount of experimental data for the low energy reaction cross section measurements, for stable as well as unstable projectiles exists in the literature [34–36]. As illustrative examples, we have chosen two cases: 1) ^{12}C on 12 reactions (energy dependence) and 2) cross sections for chain of neutron deficient Selenium isotopes as projectiles, incident on ^{28}Si target at low energies (~ 50 A MeV).

The calculated Glauber model reaction cross sections for ^{12}C projectile incident on ^{12}C target at different energies are shown in Fig. (3.3) (left hand panel). It can be clearly seen that at energies below around 150 A MeV, the finite range Glauber model (FRGM) results are in excellent agreement with the experiment [28, 34], in comparison with the corresponding zero range (ZRGM) results. At higher projectile energies, the difference between the two models decreases. Both of these are in good agreement with the experiment at the higher projectile energies.

Next, the calculated (DEF) reaction cross sections for neutron deficient Selenium isotopes are presented in Fig. (3.3) (right hand panel), along with the corresponding experimental values [36]. The agreement between the calculations and the experiment is found to be excellent within the limits of the experimental error bars.

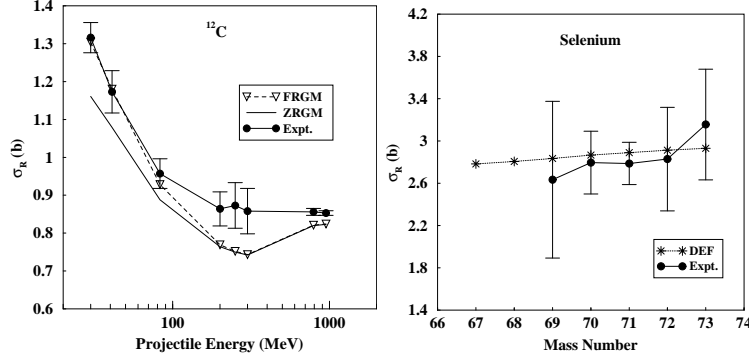


Fig. 4. The calculated and the experimental reaction cross sections for 1) ^{12}C projectiles on ^{12}C target (energy dependence) and 2) Selenium projectiles on ^{28}Si target. See text for details.

4 Summary

The total mass and charge changing cross sections are investigated systematically using the Glauber model. The calculations proceed in two steps. In the first step, the ground state properties of the relevant nuclei are obtained within the structural framework on the Relativistic Mean Field (RMF) / Relativistic Hartree - Bogoliubov (RHB) theories. The calculated ground state properties are found to be in good agreement with the corresponding experiment. The deformation effects are found to be crucial for binding energies as well as the charge radii, especially for the Neon isotopes. In the next step, the calculated point proton and neutron densities of the relevant nuclei are used in the zero range Glauber model to calculate the reaction cross sections. The charge changing cross sections are shown to be separable from the Glauber's expression for the reaction cross sections. The calculated reaction and charge changing cross sections are in excellent agreement with the experiment. Few preliminary results for the finite range Glauber model with Coulomb modified trajectories, which is expected to be good for low projectile energies are further presented. The calculated reaction cross sections for low energy (~ 50 MeV) Selenium projectiles are found to be in tune with the experimental data.

References

1. A. Ozawa, T. Suzuki and I. Tanihata, Nucl. Phys. A **693**, 32 (2001) and references cited therein.

2. R. J. Glauber, *Lectures in Theoretical Physics*, vol. 1 p. 315; ed. W. Brittin and L. Dunham (Interscience Publishers Inc. 1959)
3. I. Tanihata *et al.*, Phys. Rev. Lett. **55**, 2676 (1985).
4. I. Tanihata, J. Phys. G: Nucl. Part. Phys. **22**, 157 (1996); Prog. Part. & Nucl. Phys. **35**, 505 (1995) and references cited therein.
5. T. Brohm *et al.*, Nucl. Phys. A **585**, 565 (1995).
6. L. V. Chulkov *et al.*, Nucl. Phys. A **674**, 330 (2000).
7. O. V. Bochkarev *et al.*, Eur. Phys. J. A **1**, 15 (1998).
8. Y. K. Gambhir, P. Ring and A. Thimet, Ann. Phys. (NY), **198**, 132 (1990).
9. P. Ring, Prog. Part. Nucl. Phys. **37**, 193 (1996) and references cited therein.
10. Y. K. Gambhir and P. Ring, Pramana **32**, 389 (1989).
11. A. Bouyssy, J. F. Mathiot, N. van Giai and S. Markos, Phys. Rev. C **36**, 380 (1987).
12. B. D. Serot and J. D. Walecka, Adv. Nucl. Phys. **16**, 1 (1986).
13. B. D. Serot, Rep. Prog. Phys. **55**, 1855 (1992).
14. H. Kucharek and P. Ring, Z. Phys. A **339**, 23 (1991).
15. T. Gonzalez-Llarena, J. L. Egido, G. A. Lalazissis and P. Ring, Phys. Lett. B **379**, 13 (1996).
16. J. Meng and P. Ring, Phys. Rev. Lett. **77**, 3963 (1996); Nucl. Phys. A **635**, 3 (1998).
17. G. Audi, and A. H. Wapstra, Nucl. Phys. A **565** 1 (1993); *ibid* **565**, 66 (1993).
18. Y. K. Gambhir and A. Bhagwat, Phys. Rev. C **66**, 034306 (2002).
19. G. A. Lalazissis, J. Konig and P. Ring, Phys. Rev. C **55**, 540 (1997).
20. P. -G. Reinhardt, Rep. Prog. Phys. **52**, 439 (1989) and references cited therein.
21. M. M. Sharma, M. A. Nagarajan and P. Ring, Phys. Lett. B **312**, 377 (1993).
22. P. Moller *et al.*, At. Data Nucl. Data Tables **59**, 185 (1995).
23. C. W. de Jager, H. de Vries, and C. de Vries, At. Data Nucl. Data Tables **36**, 495 (1987).
24. A. Ozawa *et al.*, Phys. Lett. B **334**, 18 (1994).
25. L. Chulkov *et al.*, Nucl. Phys. A **603**, 219 (1996).
26. W. Geithner, Ph.D. Dissertation, CERN-THESIS-2002-030, 14.07.2002; and references cited therein.
27. Y. Ogawa, K. Yabana and Y. Suzuki, Nucl. Phys. A **543**, 722 (1992).
28. T. Zheng *et al.*, Nucl. Phys. **709**, 103 (2003) and references cited therein.
29. S. K. Charagi and S. K. Gupta, Phys. Rev. C **41**, 1616 (1990) and references cited therein.
30. A. Vitturi and F. Zardi, Phys. Rev. C **36**, 1404 (1987).
31. A. Bhagwat and Y. K. Gambhir, Phys. Rev. C **69**, 014315 (2004).
32. A. Bhagwat, Y. K. Gambhir and S. H. Patil, Eur. Phys. J. A **8**, 511 (2000) and J. Phys. G: Nucl. Part. Phys. **27**, B1 (2001).
33. J. Meng, S. -G. Zhou and I. Tanihata, Phys. Lett. B **532**, 209 (2002).
34. S. Kox *et al.*, Phys. Rev. C **35**, 1678 (1987) and references cited therein.
35. D. Q. Fang *et al.*, Phys. Rev. C **61**, 064311 (2000).
36. G. F. Lima *et al.*, Nucl. Phys. A **735**, 303 (2004).

Relativistic mean field study of nuclei far from the valley of stability

G. Gangopadhyay

Department of Physics, University of Calcutta, 92 Acharya Prafulla Chandra Road, Kolkata 700 009, India

Abstract. Advances in accelerator technology and detection systems, particularly the availability of radioactive ion beams, have made it possible to produce and study a number of exotic nuclei far from the valley of stability. The structure of these nuclei is a matter of intense ongoing research. New phenomena like proton and neutron halo, new magic numbers and level inversion emerge out of these studies. Relativistic structure calculations in exotic nuclei, particularly Hartree Bogoliubov approach, role of continuum coupling, and importance of calculation in co-ordinate space will be discussed. Results in different mass regions starting from very light systems to superheavy elements will be presented to illustrate the different features. Importance of studying low and medium energy elastic scattering involving the newly discovered exotic nuclei will be emphasized.

1 Introduction

The last fifteen years have been an exciting time for nuclear physics. With the giant leaps in detection systems and accelerator technologies, particularly with the availability of radioactive ion beams, the old theories have been severely tested as never before. The limits of nuclear stability are now being probed yielding surprising results.

One of the major surprises in low energy nuclear structure is the emergence of new magic numbers along with the disappearance of the normal shell closures observed near the stability valley. In some neutron rich (and at least one proton rich) nuclei, wave functions of the last one or two nucleons extend outside the core to a large distance creating halo states. These states are very weakly bound and interaction with the continuum may play a major role. In some neutron rich nuclei, the ground state is a multiparticle-hole state, giving rise to large deformation near a conventional shell closure. Finally, with the production of superheavy nuclei, theoretical models now face another challenge—to explain the structure and stability of nuclei in regions where the liquid drop barrier is absent. How far the Relativistic Mean Field (RMF) theories succeed in this regard is the subject of this talk.

2 Theory

RMF calculation is now a standard tool to investigate the structure of the nucleus [1]. The starting point is the relativistic Lagrangian density for point nucleons interacting

via exchange of the scalar-isoscalar meson σ , the vector-isoscalar meson ω , the vector-isovector meson ρ and the photon. One version of the Lagrangian density is

$$\begin{aligned}\mathcal{L} = & \bar{\psi}(i\gamma_\mu\partial^\mu + g_\sigma\sigma - g_\omega\omega^\mu\gamma_\mu - \frac{1}{2}g_\rho\gamma^\mu\boldsymbol{\tau}\cdot\rho_\mu - e\frac{1+\tau_3}{2}A^\mu\gamma_\mu - M)\psi \\ & + \frac{1}{2}(\partial_\mu\sigma\partial^\mu\sigma - m_\sigma^2\sigma^2) - \frac{1}{3}g_3\sigma^3 - \frac{1}{4}g_4\sigma^4 - \frac{1}{4}\omega_{\mu\nu}\omega^{\mu\nu} + \frac{1}{2}m_\omega^2\omega_\mu\omega^\mu \\ & - \frac{1}{4}\rho_{\mu\nu}\rho^{\mu\nu} + \frac{1}{2}m_\rho^2\rho_\mu\rho^\mu - \frac{1}{4}A_{\mu\nu}A^{\mu\nu}\end{aligned}\quad (1)$$

Other possible meson self interactions and couplings have also been considered.

In the conventional RMF+BCS approach the Euler-Lagrange equations obtained are solved under the usual approximations, *i.e.* classical meson fields, time reversal symmetry, no-sea contribution, etc. Pairing is introduced under the BCS approximation. Both constant gap and constant strength as well as other methods have been used in different works. Very often the resulting equations are solved in a harmonic oscillator basis [2]. In exotic nuclei, the basis expansion method using harmonic oscillator, because of its incorrect asymptotic properties, faces problems in describing the weakly bound halo states. A solution of the Dirac and Klein Gordon equations in co-ordinate space may be preferable to describe the weakly bound states. This approach has been modified to study deformed nuclei also [3]. The states in the continuum, which are very important in exotic nuclei, are usually discretized by applying the box normalization condition. Recently, contribution of the continuum has been estimated by including resonant states [4]. The energy and width of the resonant states have been calculated by solving the Dirac equations for the positive energy states with appropriate scattering boundary conditions and finding out the energy for which the phase shift is $\pi/2$. Pairing has been included with appropriate modification for resonance states. Expansion in a Woods-Saxon basis has also been applied for halo nuclei [5].

In the Relativistic Hartree Bogoliubov (RHB) approach [6–8] the independent quasi-particles are introduced by the usual unitary Bogoliubov transformation of the single nucleon operators. A pairing field is used, in most cases it being a phenomenological nonrelativistic interaction like the pairing part of the Gogny force. However, it has been pointed out that very often, the use of a pairing gap calculated from odd-even mass difference in RMF+BCS approach is sufficient to reproduce results practically indistinct from the more sophisticated and much more time consuming RHB calculation [9]. Relativistic continuum Hartree Bogoliubov equations have also been solved recently [10].

Calculation for odd or odd-odd nuclei is difficult as the odd nucleon breaks the time-reversal symmetry of the mean field and the spacelike components of the meson fields are expected to contribute to the mean field. However, it is well known that these contributions are relatively unimportant for bulk properties like binding energy or deformation. The blocking mechanism in BCS theory is sometimes applied for treatment of the odd particle, thus restoring the symmetry.

RMF calculations employ a number of forces with different values for the coupling constants and the meson masses and in some cases different interactions. Sharma *et al.* [9] have pointed out that a vector meson self coupling may help in describing the exotic nuclei. Among the various forces that have been used, the forces NL-Z, NL3,

NL-SV1 NL-SH, NL-VT1 and TMA may be mentioned. The last force has a mass dependence of the parameters.

The usual method for measuring the density in stable nuclei is electron scattering. However, this method is difficult to apply in nuclei far away from the valley of stability. One alternative approach uses the density calculated from theory in a semimicroscopic approach to generate an optical model potential and uses that to study elastic scattering [11]. Experimental differential cross sections in inverse reactions using proton target and beams of exotic nuclei may be compared with theory. We discuss this approach in a little more detail.

A semi-microscopic optical model potential (OMP) using density from a mean field theory was first obtained by Jeukenne *et al.* [12] The OMP in nuclear matter was obtained for a given nucleon density with a given set of global parameters. The final nuclear matter (NM) potential for a given matter density $\rho = \rho_n + \rho_p$ and asymmetry $\alpha = (\rho_n - \rho_p)/\rho$ reads

$$U_{NM}(E)_{\rho,\alpha} = \lambda_V(E) \left[V_0(\tilde{E}) \pm \lambda_{V1}(E)\alpha V_1(\tilde{E}) \right] + i\lambda_W(E) \left[W_0(\tilde{E}) \pm \lambda_{W1}(E)\alpha W_1(\tilde{E}) \right], \quad (2)$$

with E being the incident nucleon energy, $\tilde{E} = E - V_c$ (where V_c is the Coulomb field), V_0 , V_1 , W_0 , and W_1 the real isoscalar, real isovector, imaginary isoscalar, and imaginary isovector OMP components, respectively, and λ_V , λ_{V1} , λ_W , and λ_{W1} the real (isoscalar+isovector), real isovector, imaginary, and imaginary isovector normalization factors, respectively in NM. The values of λ_V , λ_{V1} , λ_W , and λ_{W1} used [11] are

$$\lambda_V(E) = 0.951 + 0.0008 \ln(1000E) + 0.00018 [\ln(1000E)]^2 \quad (3)$$

$$\lambda_W(E) = \left[1.24 - \left[1 + e^{\left(\frac{E-4.5}{2.9}\right)} \right]^{-1} \right] \left[1 + 0.06 e^{-\left(\frac{E-14}{3.7}\right)^2} \right] \times \left[1 - 0.09 e^{-\left(\frac{E-80}{78}\right)^2} \right] \left[1 + \left(\frac{E-80}{400} \right) \Theta(E-80) \right] \quad (4)$$

$$\lambda_{V1}(E) = 1.5 - 0.65 \left[1 + e^{\frac{E-1.3}{3}} \right]^{-1} \quad (5)$$

$$\lambda_{W1}(E) = \left[1.1 + 0.44 \left[1 + \left(e^{\frac{E-40}{50.9}} \right)^4 \right]^{-1} \right] \times \left[1 - 0.065 e^{-\left(\frac{E-40}{13}\right)^2} \right] \left[1 - 0.083 e^{-\left(\frac{E-200}{80}\right)^2} \right]. \quad (6)$$

with the energy E expressed in MeV.

To obtain the OMP in finite nuclei, Local Density Approximation is used, that is the local value of the potential at \mathbf{r} is taken to be equal to the nuclear matter potential for the density $\rho(\mathbf{r})$. This is also improved by applying a form factor

$$U_{FN}(r, E) = (t\sqrt{\pi})^{-3} \int \frac{U_{NM}(\rho(r'), E)}{\rho(r')} \exp(-|\mathbf{r} - \mathbf{r}'|^2/t_r^2) \rho(r') d\mathbf{r}', \quad (7)$$

with t the range of the Gaussian form factor. The values $t_r = 1.25$ fm and $t_i = 1.25$ fm were found [11] to be global optimal values for the real and imaginary ranges, respectively.

A spin orbit potential between the nucleus and the nucleon along with complex potential depths $\lambda_{v_{so}}$, and $\lambda_{w_{so}}$ [13] is used

$$U_{n(p)}^{so}(r) = (\lambda_{v_{so}}(E) + i\lambda_{w_{so}}(E)) \frac{1}{r} \frac{d}{dr} \left(\frac{2}{3}\rho_{p(n)} + \frac{1}{3}\rho_{n(p)} \right), \quad (8)$$

with $\lambda_{v_{so}} = 130 \exp(-0.013 E) + 40$ and $\lambda_{w_{so}} = -0.2 (E - 20)$.

3 Results

3.1 Light nuclei: drip line and halo states

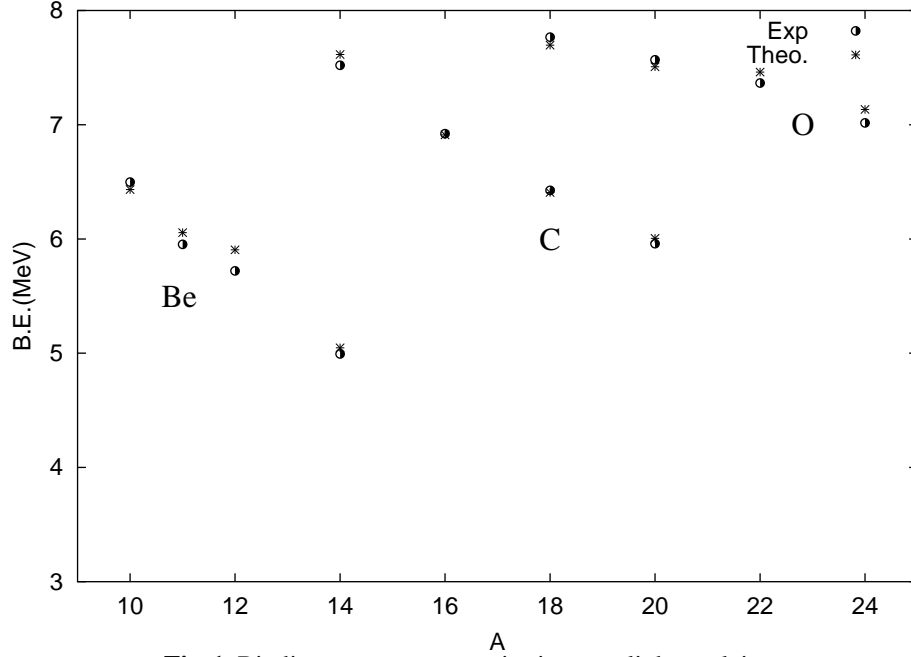


Fig. 1. Binding energy systematics in some light nuclei.

With the present experimental setups the neutron drip line can be reached only in very light nuclei. It all started fifteen years ago when the halo in ^{11}Li was discovered. Since then, one neutron halo has been observed in ^{11}Be and ^{19}C , two neutron halo in ^6He , ^{14}Be , ^{17}B and possibly in ^{22}C , one proton halo in ^8B and possibly in ^{17}F and ^{17}Ne . The nucleus ^8He has been described as $^4\text{He}+4n$ configuration.

The first success in describing the large radius and binding energy in ^{11}Li was achieved using RHB methods with the NL2 force [7, 10]. We have applied the NLSH force in the co-ordinate space RMF approach to calculate the binding energy in Be, C and O nuclei. Our results are compared with experimental values in Fig. 1. We find that the effect of pairing is very small in these nuclei. In our calculation, $^{12,14}\text{Be}$ and all the C nuclei come out to be either weakly deformed or spherical. A level inversion occurs with the $2s_{1/2}$ level coming down below the $1d_{5/2}$ level and becomes weakly bound in $^{12,14}\text{Be}$. In ^{14}Be , its binding energy is only 300 Kev and consequently a neutron halo appears. In Fig. 2, we plot the nucleon density in $^{12,14}\text{Be}$ for a spherical calculation in co-ordinate space and the neutron s.p. states in ^{12}Be . Co-ordinate space (and RHB) calculation indicates that ^{14}Be has a neutron halo and the corresponding neutrons are just bound. In Carbon nuclei, the neutron single particle structure is slightly different. There is no level inversion and in the drip line nucleus ^{22}C the last filled level is bound by more than 3 MeV. The neutron number $N=16$ becomes the new magic number and there is no sign of a two neutron halo in our calculation. However, our calculation fails to predict the spin of the ground state in ^{11}Be . Besides, the present calculation predicts that ^{28}O is the drip line nucleus, a fact at variance with experimental observation. Results of calculation on even-even neutron rich Be and C nuclei using the force NLSH are compared with experimental measurements in table 1.

Table 1. Binding energy, deformation and radius in Be and C isotopes. Exp. binding energy values are from the compilation [14]. Experimental r.m.s. radii values are from [15] and are results of Glauber model analysis in the optical limit. Experimental neutron radii for C isotopes are from [16].

AZ	B.E.(MeV)			Radius					
	Exp.	Theo.	β_2 Theo.	Exp.			Theo.		
				r_n	r_{rms}	r_p	r_n	r_{rms}	
^{10}Be	6.498	6.407	0.35		2.30(2)	2.21	2.45	2.36	
^{12}Be	5.721	5.874	0.11		2.59(6)	2.26	2.73	2.58	
^{14}Be	4.994	5.014	0.12		3.16(38)	2.27	4.42	3.93	
^{14}C	7.520	7.642	0.00	2.70(10)	2.30(7)	2.37	2.56	2.48	
^{16}C	6.922	6.897	0.06	2.89(9)	2.70(3)	2.40	3.01	2.80	
^{18}C	6.426	6.375	-0.10	3.06(29)	2.82(4)	2.42	3.23	2.99	
^{20}C	5.959	5.978	-0.10		2.98(5)	2.44	3.32	3.08	
^{22}C	5.440 ¹	5.568	0.00			2.45	3.39	3.16	

¹ Estimated value

3.2 Ni isotopes: From proton to neutron drip line

Ni isotopes have been studied extensively in mean field theories. Experimentally, they have been observed from the proton drip line nucleus ^{48}Ni to the $N=50$ nucleus ^{78}Ni .

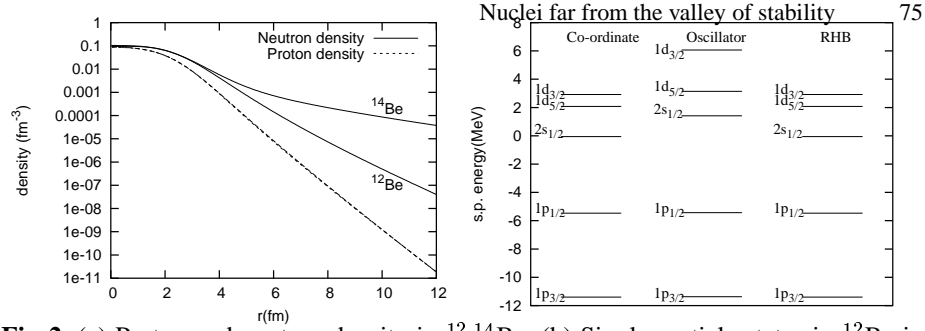


Fig. 2. (a) Proton and neutron density in ^{12,14}Be. (b) Single particle states in ¹²Be in co-ordinate calculation, oscillator basis expansion and RHB.

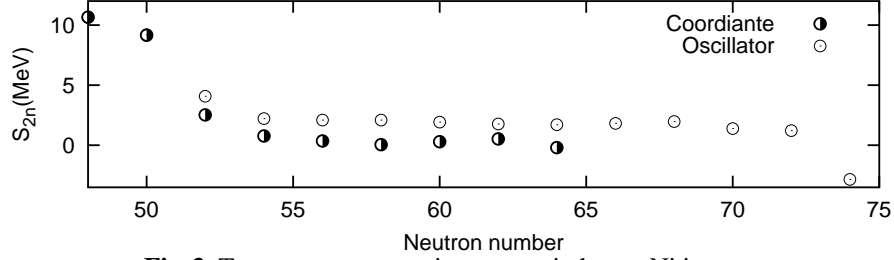


Fig. 3. Two neutron separation energy in heavy Ni isotopes

We have studied Ni isotopes using the NLSH force in the spherical RMF+BCS formalism in co-ordinate space in the constant gap approach. The pairing gap for neutrons is taken from odd-even mass difference, if known, or estimated by the prescription $\Delta = 11.2/\sqrt{A}$. Proton number is taken to be magic. Earlier Sharma *et al.* [9] have studied Ni and Sn isotopes in RMF+BCS formalism using a basis expansion method as well as RHB formalism using a number of forces, including NLSH. The calculations correctly predict the proton drip line to be beyond ⁴⁸Ni. There is a substantial difference between the basis expansion method and the co-ordinate space calculation. Fig. 3 shows the two neutron separation energy in heavier Ni isotopes. The shell gap at N=50 comes out to be less in oscillator expansion. This, in turn, leads to completely different predictions for the drip line. The study also shows that the spin-orbit splitting in large l states gets quenched for large neutron excess.

3.3 Zr and Ni isotopes : Resonant continuum

As already pointed out, the s.p. states in the continuum play a vital role near drip line as some of the nucleons are very weakly bound. Centrifugal barrier for both types of nucleons and Coulomb barrier for protons tend to localize the wave function of the resonant states.

Sandulescu *et al.* [4] have investigated the structure of ground state of Zr nuclei while Cao *et al.* [17] have studied Ni isotopes using the resonant continuum states. Their conclusion is that simple RMF+BCS method can describe the drip line nuclei

quite well if one includes the resonant states properly. Sandulescu *et al.* [4] have shown that their results compare favourably with a much more involved RHB calculation.

3.4 RHB : Proton drip line

A lot of work has been done in the RHB approach and some of them have been cited earlier. Here we mention only a work [18] on deformed ground state proton emitters in the rare earth region. RHB equations obtained using the pairing part of the Gogny force are solved assuming axial symmetry. The proton separation energies at the drip line of ^{131}Eu , ^{141}Ho and ^{147}Tm have been nicely reproduced. In another work, the binding energy of nuclei near the proton drip line for $N=18, 20$ and 22 was investigated in a spherical RHB calculation [19]. The binding energy was reproduced and the location of the drip line correctly predicted.

3.5 Elastic scattering

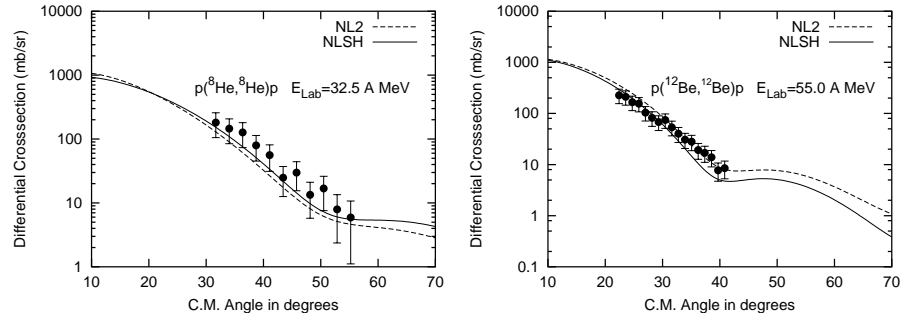


Fig. 4. Elastic scattering cross section for proton scattering of exotic nuclei in inverse kinematics.

The density of exotic nuclei can be probed using elastic proton scattering in inverse kinematics. We have calculated the elastic scattering cross section of two exotic nuclei and compared them with experiment in Fig. 4. The experimental data are taken from [20]. The theoretical values are for two forces, NL2 and NLSH. The RMF equations have been solved in the co-ordinate space assuming spherical symmetry. One can see that both the forces explain the available data very well. It is difficult to comment on the relative accuracy of the two forces and more data with better accuracy is required to resolve the issue.

3.6 Island of inversion: The disappearance of magicity at $N=20$

In neutron rich nuclei near ^{32}Mg , a pair of neutrons may be excited across the $N=20$ shell gap resulting in the $2\hbar\omega$ configurations. In the Nilsson model picture, the shell gap vanishes at large deformation for neutrons. This so called ‘island of inversion’

where the $2\hbar\omega$ states lie below the normal states has been extensively investigated both theoretically and experimentally.

We have investigated the particle-hole states in neutron rich nuclei around ^{32}Mg in the fixed configuration approach with the force NL3 using an axially deformed harmonic oscillator basis. The BCS calculation assumes $\Delta_n = \Delta_p = 1.0$ MeV. At large deformation, the levels coming from the higher fp shell cross the upper levels of the sd shell giving rise to the configuration of these states. The solutions obtained are of course intrinsic solutions. The energy of the 0^+ state has been obtained by using the cranking model formula $E(0^+) = E_{in} - \langle J_\perp^2 \rangle / 2I_{cr}$ with I_{cr} being the moment of inertia.

Table 2. Theoretical results in the island of inversion. See text for details. Configurations denoted normal are $0\hbar\omega$ solutions.

Nucleus	Config.	E_{in} MeV	J_\perp^2/\hbar^2	I_{cr}/\hbar^2 MeV $^{-1}$	$E.(0^+)$ MeV	β_C	β_A
^{32}Mg	normal	-250.97			-250.97	0.000	0.000
	$\nu^2 - \nu^{-2}$	-248.93	33.67	4.73	-252.50	0.457	0.492
^{30}Mg	normal	-240.68	10.95	1.84	-243.66	0.285	0.230
	$\nu^2 - \nu^{-4}$	-237.75	36.93	4.18	-242.17	0.522	0.601
^{34}Mg	normal	-257.62	21.53	3.77	-260.48	0.345	0.327
	$\nu^4 - \nu^{-2}$	-255.81	45.20	4.91	-260.42	0.511	0.562
^{30}Ne	normal	-215.93			-215.93	0.000	0.000
	$\nu^2 - \nu^{-2}$	-213.06	27.62	3.88	-216.62	0.444	0.502
^{28}Ne	normal	-208.61	5.32	1.35	-210.57	0.202	0.162
	$\nu^2 - \nu^{-4}$	-204.72	29.35	3.58	-208.82	0.499	0.619

The predicted value of charge quadrupole moment in ^{32}Mg compares favourably with experimental value from Coulomb excitation, $\beta_C = 0.438 \pm 0.046$. In ^{34}Mg , same reaction provides a upper value $\beta_C < 0.599$. Our conclusion is that the the nuclei ^{32}Mg , ^{30}Ne , and possibly ^{34}Mg belong to the island of inversion.

3.7 Superheavy elements(SHE)

The very existence of SHE is a quantum effect as the liquid drop barrier is negligible in this region. The nuclear models have to be pushed beyond their familiar grounds to describe such nuclei. So this mass region provides a testing ground for theories. The binding energy systematics in Fig. 5 indicate new forces like TMA which have a mass dependence of the parameters may be useful. Among the conventional forces, NL3 seems to be the best. Some of the theoretical values are taken from [21]- [26].

In any study of odd mass nuclei in the superheavy region the most important quantities are the binding energy and the Q_α value. In many cases, the binding energy is known from the Q_α values of the decays of the chain when the mass of any member of the chain is known previously, assuming the decay to be between the ground states of

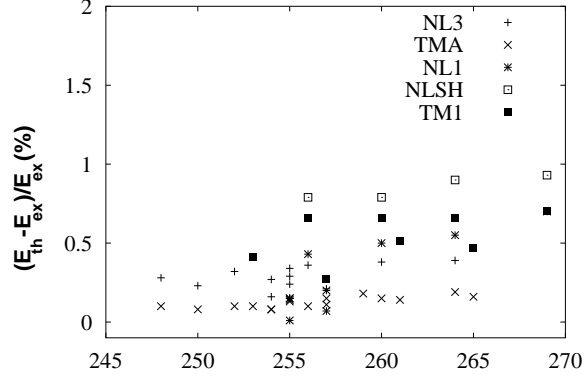


Fig. 5. The percentage error in binding energy of superheavy nuclei using different RMF forces.

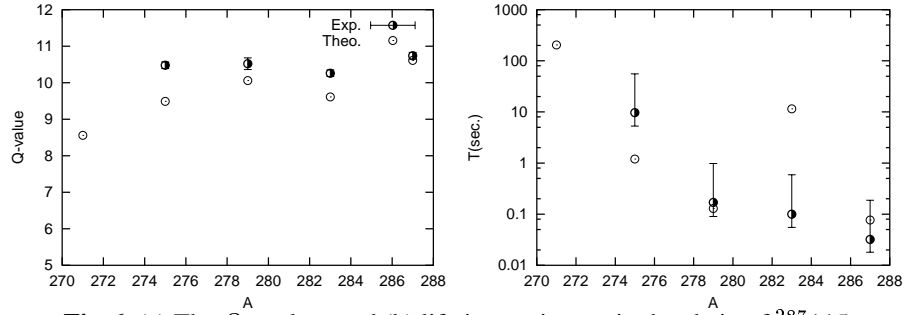


Fig. 6. (a) The Q_α values and (b) lifetime estimates in the chain of $^{287}115$.

the parent and the daughter nuclei. However, decay from ground state to ground state may be hindered or forbidden due to spin-parity selection rules. Thus it is important to study the one quasiparticle states near the ground state for possible decay paths. We have calculated [28] energy and the deformation of the one quasiparticle states and the Q_α -value for the newly discovered chain of $^{287}115$ using the blocking approximation in deformed harmonic oscillator basis and obtained the lifetime estimates using the Viola-Seaborg formula [29]. The results for Q_α values and lifetime using the force NL3 are shown Fig. 6

One interesting feature in SHE is the observation of symmetric fission around ^{260}Fm . This can be traced to the disappearance of the double humped fission barrier in symmetric fission around ^{260}Fm because of the shell closure in the symmetric fragments. Fig. 7 shows that a constrained RMF calculation can reproduce this characteristic of the fission barrier.

We have calculated the first barrier beyond $\beta \sim 0.5$ in some of the nuclei with $Z \geq 98$ and $A \geq 248$ using the force NL3. The barrier height and the experimental half life values are given in table 2. In nuclei with $A > 256$, where there is no second

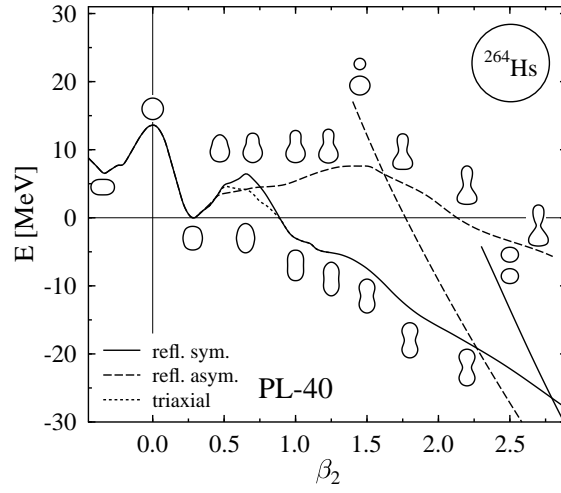


Fig. 7. The PES of ^{264}Hs drawn using the force PL-40. The mass density contours at $\rho_0 = 0.07 \text{ fm}^{-3}$ are drawn near the corresponding curves. Taken from [27].

Table 3. Calculated first barrier height (S) in some of the nuclei and the measured half life (τ) for spontaneous fission. All the half life values are from [30] unless otherwise indicated.

Nucleus	S(MeV)	τ	Nucleus	S(MeV)	τ
$^{284}_{112}$	9.60	98 ms ¹	^{256}Rf	14.00	6.4 ms
$^{282}_{112}$	9.10	1.0 ms ¹	^{256}No	14.09	549 s
^{272}Ds	9.97	8.6 ms	^{256}Fm	12.27	2.89 hr
^{264}Hs	10.84	1.6 ms	^{254}No	15.84	7.9 hr
^{262}Rf	12.42	2.3 s	^{252}No	13.00	12 s
^{262}No	11.74	5 ms	^{252}Fm	12.84	126 Yr
^{260}Sg	11.34	7.2 ms	^{252}Cf	12.25	85.6 Yr
^{260}Rf	14.40	21 ms	^{250}Fm	12.73	323 d
^{260}No	10.21	106 ms	^{250}Cf	12.47	16350 Yr
^{260}Fm	10.21	4 ms	^{248}Fm	12.48	10 hr
^{258}Sg	11.32	2.9 ms	^{248}Cf	12.94	3.15X10 ⁴ Yr
^{258}Rf	11.86	14 ms			
^{258}No	12.17	1.2 ms			
^{258}Fm	10.91	370 μs			

¹ Taken from [31]

barrier, we expect symmetric fission to take place. Because the barrier in these nuclei is much narrower, the fission lifetime is very short.

4 Conclusions

The ground state of nuclei away from the valley of stability shows many interesting phenomena. As we have seen, relativistic calculations have been able to reproduce a number of these newly observed features. Though a lot of work has been done, we have reviewed only a few representative calculations. Reaction studies, including charge changing transition presented in this workshop [32], RPA and other features are also very important. Another important field that has not been discussed is Effective Field Theory. Exotic nuclei are still a matter of active research. As experiments get more advanced, newer facts will be discovered. We expect relativistic calculations to succeed in interpreting them, but only with novel approaches.

Acknowledgment

The author wishes to thank his collaborators S. Das and S. Bhowal for their help in doing the work. He gratefully acknowledges the contribution of Dr. Subinit Roy in the calculation of elastic scattering cross section.

References

1. H.-P. Duerr, Phys. Rev. **103**, 469 (1955); J. Boguta and A.R. Bodmer, Nucl. Phys. **A292**, 413 (1977); B.D. Serot and J.D. Walecka, Phys. Lett. **87B**, 172 (1979).
2. Y.K. Gambhir, P. Ring and A. Thimet, Ann. Phys. (N.Y.) **198**, 132 (1990).
3. G. Gangopadhyay, Phys. Rev. C **59**, 2541 (1999).
4. N. Sandulescu, L.S. Geng, H. Toki and G. Hillhouse, Phys. Rev. C **66**, 024311 (2002).
5. S-G Zhou, J. Meng and P. Ring, Phys.Rev. C **68**, 034323 (2003).
6. T. Gonzalez-Llarena, J.L. Egido, G.A. Lalazissis and P. Ring, Phys. Lett **379B**, 13 (1996).
7. J. Meng and P. Ring, Phys. Rev. Lett. **77**, 3963 (1996).
8. W. P'oschl, D. Vretenar and P. Ring, Comput. Phys. Commun. **103**, 217 (1997).
9. M.M. Sharma, A.R. Farhan and S. Mythili, Phys. Rev. C **61**, 054306 (2000); M.M. Sharma and A.R. Farhan, Nucl. Phys **A688**, 150C (2001).
10. J. Meng, W. P'oschl and P. Ring, Z. Phys. A **358**, 123 (1997).
11. E. Bauge, J.P. Delaroche and M. Girod, Phys. Rev. C **63**, 024607 (2001).
12. J.P. Jeukenne, A. Lejeune, and C. Mahaux, Phys. Rev. C **14**, 1391 (1974).
13. R.R. Scheerbaum, Nucl. Phys. **A257**, 77 (1976).
14. G. Audi, A.H. Wapstra and C. Thibault, Nucl. Phys. **A729**, 337 (2003).
15. A. Osawa, T. Suzuki and I. Tanihata, Nucl. Phys. **A 693**, 32 (2002).
16. E. Liatard *et al.*, Europhys. Lett. **13**, 401 (1990).
17. Li-Geng Cao and Zhong-Yu Ma, Nucl-th/0307016 (2003).
18. D. Vretenar, G.A. Lalazissis and P. Ring, Phys. Rev. Lett. **82**, 4595 (1999).
19. D. Vretenar, G.A. Lalazissis and P. Ring, Phys. Rev. C **57**, 3971 (1998).
20. A.A. Korshennikov *et al.*, Phys. Lett. **343B**, 53 (1995).
21. G.A. Lalazissis, M.M. Sharma, P. Ring and Y.K. Gambhir, Nucl. Phys. **A608**, 202 (1996).
22. Z. Ren and H. Toki, Nucl. Phys. **A689**, 691 (2001); Z. Ren, Z.T. Zhu, Y.H. Cai, and G. Xu, J. Phys. G **22**, 1793 (1996); Z. Ren, Phys. Rev. C **65**, 051304(R), 2002.
23. J. Meng and N. Takigawa, Phys. Rev. C **61**, 064319 (2000).

24. S.K. Patra and C.R. Praharaj, J. Phys. G **23**, 939 (1997); S.K. Patra, C.L. Wu, W. Greiner and R.K. Gupta, J. Phys. G **26**, 1569 (2000).
25. T. B'urvenich *et al.*, Eur. Phys. J. **A3**, 139 (1998).
26. G. Gangopadhyay, Invited talk in the DAE-BRNS Symposium on Nuclear Physics, BARC Mumbai.
27. M. Bender *et al.*, Phys. Rev. C **58**, 2126 (1998).
28. Sankha Das and G. Gangopadhyay, J. Phys. G. **30**, 957 (2003).
29. V.E. Viola and G.T. Seaborg, J. Inorg. Nucl. Chem. **28**, 741 (1966).
30. J.K. Tuli, *Nuclear Wallet Cards*, National Nuclear Data Center, Brookhaven National Laboratory (2000).
31. Yu. Ts. Oganessian *et al.*, Phys. Rev. C **69** 054607 (2004).
32. A Bhagwat and Y K Gambhir, J.Phys. G **30**, B13 (2004) and Proceedings of this Workshop.

Recent Developments in Relativistic Mean Field Theory

S.K. Patra¹, B.K. Sharma¹, P. Arumugam¹, M. Centelles², and X. Viñas²

¹ Institute of Physics, Sachivalaya Marg, Bhubaneswar 751 005, India.

² Departament d'Estructura i Constituents de la Matèria, Facultat de Física, Universitat de Barcelona, Diagonal 647, 08028 Barcelona, Spain

Abstract. We discuss the developments in semiclassical approaches and the recent effective field theory motivated generalization (E-RMF) of relativistic mean field (RMF) theory. In the first part of our discussions, we emphasize the study of giant resonances in the standard RMF formalism. Here, we derive the analytical expressions for the excitation energy by using the scaling method and the extended Thomas-Fermi approach. We study the ability of several non-linear $\sigma - \omega$ parameter sets of common use in reproducing the experimental data for monopole and quadrupole oscillations. The semiclassical results compare satisfactorily with those obtained in relativistic random phase approximation (RRPA) and time-dependent mean field calculations.

In the second part, we use the standard mean field model and the E-RMF model. We first apply it to study the breathing mode energy in a constrained approach. Next we explore the superheavy region and predict $Z = 120$ and $N = 172, 184$ as the magic numbers for this mass region. Then we show quantitatively that the inclusion of vector meson self interaction and scalar-vector cross-interactions in the effective field theory explains naturally the recent experimental observations of the softness of nuclear equation of state (EOS), without losing the advantages of the standard relativistic model for finite nuclei. As a further application of the E-RMF formalism, we apply the EOS to estimate the neutron star properties. The quality of the E-RMF results suggests that E-RMF is a significant step towards a unified description of finite nuclei and infinite nuclear matter.

1 Introduction

Finite nuclei are complex many-body systems. The conventional approach to understand their properties in terms of their constituents i.e. nucleons, is based on a non-relativistic formalism [1–3]. Relativistic effects were considered as being negligible although it always was clear that nucleons are in principle Dirac particles. Despite the remarkable success achieved by these sophisticated non-relativistic calculations [1–3], discrepancies still remain with experimental data indicating that such a traditional treatment is reaching its limits. All of these shortcomings stimulated the investigation of alternative approaches.

One of these approaches is quantum hadrodynamics (QHD), a relativistic quantum field theory for the nuclear many-body problem developed by Walecka [4] and coworkers [7]. It was originally conceived to describe the behaviour of the equation of state (EOS) for dense nuclear matter [4]. In the formalism of QHD, baryonic and mesonic degrees of freedom are treated on an equal footing. Nucleons interact through

the exchange of virtual mesons, so that static potentials need not be introduced and effects of relativistic propagation are naturally incorporated [4]. In the simplest version, which is known as linear $\sigma - \omega$ model, only a vector field accounting for short-range repulsion and a scalar field responsible for attraction are needed to describe saturation in nuclear matter. The scalar and vector fields may be associated with the σ and ω meson, respectively [4, 7].

However, in the linear $\sigma - \omega$ model the nuclear matter incompressibility K_{nm} , is unreasonably high (~ 550 MeV), which is a serious drawback for a precise description of some properties of finite nuclei and of collective excitations such as the breathing mode (isoscalar giant monopole resonance). The problem can be cured by introducing cubic and quartic self-interactions of the σ -meson, which in particular have the effect of lowering the incompressibility, and the model is refined by adding an isovector ρ meson. This model, i.e., the linear $\sigma - \omega$ model plus self-interaction of σ -meson and addition of ρ meson is known as non-linear relativistic mean field (RMF) model [6], which is commonly used in the literature [7–9] and termed as the standard RMF or non-linear $\sigma - \omega$ model, or simply RMF formalism.

The full theory of QHD is highly complex and suitable approximations are needed. In practice, one also deals with a phenomenological approach. The coupling constants and some meson masses of the effective meson-nucleon lagrangian are taken as input for both nuclear matter and finite nuclei [7]. Most calculations have been done in mean field approximation without including any contribution from antiparticles (no-sea approximation) [8]. It may be stated that the RMF models of reasonable sophistication achieve about the same agreement with experiment compared with the more elaborated density-dependent interactions in the non-relativistic Hartree-Fock (HF) approximation, with the conceptual advantage of being fully relativistic and thus automatically incorporating the spin-orbit force, which has fundamental importance in nuclear structure physics.

The RMF model has been applied to describe dynamical collective motions as well as ground state properties of finite nuclei along the periodic table. To calculate the ground-state properties, the relativistic Hartree approximation is commonly used. It is to be noted that pairing correlations cannot be taken in an *ab-initio* manner in the RMF Lagrangian. To take into account the pairing effects, an external pairing correction can be evaluated following methods like BCS [7] or quasi-BCS [10, 11] or Hartree-Bogoliubov [12]. The basic theory of vibrational states in nuclei, the random-phase approximation (RPA) [3] has been generalized to the relativistic domain (RRPA) [14–16] and it has been used in calculations of isoscalar giant resonances, to obtain response functions and mean energies for several magic nuclei. Small-amplitude collective motions such as the isovector dipole, isoscalar and isovector quadrupole and the isoscalar and isovector monopole oscillations have been studied in the time-dependent RMF approach. Another approach is based on constrained RMF calculations [17]. It has been applied to obtain breathing-mode energies and incompressibilities in linear and RMF models. Other calculations of breathing-mode energies in the relativistic framework have relied on the scaling method [18, 19] in combination with the leptodermous expansion of finite nucleus incompressibility [34].

In non-relativistic nuclear physics, semiclassical methods like the Thomas-Fermi (TF) theory, have proven to be very useful for dealing with nuclear properties of global character that vary smoothly with the particle number A [3, 21–23]. The success of these methods stems from the fact that the shell corrections (quantal effects) are small as compared to the smooth part given by the semiclassical calculation. Semiclassical techniques like nuclear fluid dynamics and the extended Thomas-Fermi (ETF) method have been applied to study giant resonances in non-relativistic models. In the relativistic context, the nuclear fluid dynamics approach has been utilized. The authors of Refs. [24, 25] resorted to a local Lorentz boost and the scaling method to study isoscalar giant monopole and quadrupole states in the linear $\sigma - \omega$ model.

The relativistic extended Thomas-Fermi (RETF) method [26–29] is a refinement of the relativistic Thomas-Fermi (RTF) method, which incorporates gradient corrections of order \hbar^2 to the pure RTF approximation. It was derived only a few years ago and it has since been applied in calculations of ground-state binding energies and radii of finite nuclei and in investigations of nuclear surface properties [27, 29]. In the present article we shall use the RTF and RETF approaches to calculate the excitation energies of the isoscalar giant monopole and quadrupole resonances in spherical nuclei. This will be done by means of a scaling method, within the framework of non-linear $\sigma - \omega$ model (i.e., RMF theory).

Despite the success of RMF formalism in many aspects, this model has some limitations as it gives a very stiff equation of state (EOS) for infinite nuclear matter at baryonic densities above the saturation point. To overcome this problem, first Gmuca [30] and later Sugahara and Toki [31] suggested a quartic self-coupling for the vector meson and soften the EOS. It is to be noted that the free non-linear $\sigma - \omega$ model Lagrangian is renormalizable and hence the scalar self-interactions were limited to a quartic polynomial and scalar-vector or vector-vector interactions are not allowed.

Recently, inspired by effective field theory (EFT), Furnstahl, Serot and Tang [16] abandoned the idea of renormalizability and extended the RMF theory by including other non-linear scalar-vector and vector-vector self interactions as well as tensor couplings. This model is known as effective field theory motivated RMF (E-RMF). The E-RMF lagrangian has an infinite number of terms, since it contains all the non-renormalizable couplings, consistent with the underlying QCD symmetries. Therefore it is mandatory to develop a suitable scheme of expansion and truncation. Ref. [16] have shown that it suffice to go to fourth order in expansion. At this level one recovers the standard non-linear $\sigma - \omega$ model (RMF) plus a few additional couplings with thirteen free parameters in all. These parameters have been fitted (parameter sets G1 and G2) to reproduce some observables of few selected nuclei. The fits display naturalness (i.e., all coupling constants are of the order of unity when written in appropriate dimensionless form), and results are not dominated by the last terms retained. This evidence confirms the utility of EFT concepts and justifies the truncation of the effective lagrangian at the first lower orders.

Developments in the theoretical framework and applications of RMF theory are diverse. We have mentioned many of them in the above text. However, we limit further discussions to outline the developments and applications of semiclassical methods and the E-RMF theory. In the first part of this article we give the semiclassical treatment

of the relativistic mean field and obtain the expression for isoscalar giant monopole and quadrupole resonances in finite nuclei, by using scaling method and the extended Thomas-Fermi approach within the standard $\sigma - \omega$ model. In the second part, we discuss the generalization of RMF model i.e., the E-RMF formalism and use it to obtain breathing mode energies of exotic nuclei, the ground-state properties of doubly closed shell superheavy nuclei, the EOS for infinite nuclear matter and neutron star properties. Section 2 comprises the formalism corresponding to both the parts and the results are discussed in Section 3. The conclusions are laid in the last section.

2 Formalism

2.1 Semiclassical approach

In non-relativistic nuclear physics, there are several methods and formalisms to deal with the nuclear many-body problem and allow us to explain an enormous number of experimental facts. In actual numerical calculations, where we want to treat realistic situations the implementation of formalism such as Hartree-Fock (HF), Random Phase Approximation (RPA) or time-dependent Hartree-Fock (TDHF) [3,33] leads to an enormous amount of work. It is therefore desirable to have qualitatively correct but quick estimates of such quantities as the nuclear ground state energy, density and giant resonance frequencies.

A method capable of providing such estimates is very well known from atomic physics, where the self-consistent TF method yields surprisingly good results. But in non-relativistic nuclear physics, TF approach was not exploited much because, it is not well suited to handle many-body systems with very short-ranged two body forces in its primitive form. However, there have been some further developments of TF theory which make its application to nuclear physics possible, by taking into account the quantal corrections, which is popularly known as ETF theory.

In this section we review the formal structure of the semiclassical expansion for the relativistic case [27]. It is derived from the propagator in the Wigner representation. The method is based on the Wigner transform of operators [34] to perform the \hbar -expansion of the propagator for Hamiltonians which have a matrix structure. We focus our attention on the relativistic nuclear problem, and apply the method to a Dirac Hamiltonian which contains a scalar field and the time-like component of a four-vector field. The propagator is related to the density matrix, which in turn is connected with the ground-state averages of physical quantities, viz particle and energy densities. Starting from the Wigner-Kirkwood expansion of these quantities to order \hbar^2 , one substitutes in favour of the particle density in the Wigner-Kirkwood expression for the energy density to obtain the corresponding \hbar^2 -order energy density functional, which we shall refer to as constituting the RETF method.

Relativistic Wigner-Kirkwood Density Matrix The generalized density matrix \hat{R} is obtained from the propagator \hat{G} by an inverse Laplace transform [3]

$$\hat{R}(\lambda) = \frac{1}{2\pi i} \int_{c-i\infty}^{c+i\infty} d\eta \exp(\eta\lambda) \frac{\hat{G}(\eta)}{\eta} = L_{\eta \rightarrow \lambda}^{-1} \left[\frac{\hat{G}(\eta)}{\eta} \right], \quad (1)$$

where λ is the chemical potential and we have made explicit the dependence of \hat{R} and \hat{G} on λ and η respectively. Inserting the \hbar expansion of the propagator into (1), one finds the expression of the corresponding Wigner-Kirkwood density matrix:

$$R_W = L_{\eta \rightarrow \lambda}^{-1} \left[\frac{\hat{G}(\eta)}{\eta} \right] = R_0 + \hbar R_1 + \hbar^2 R_2 + \dots \quad (2)$$

From the definition of the Laplace transform, one formally gets

$$L_{\eta \rightarrow \lambda}^{-1} \left[\eta^n \frac{\exp\{-\eta(V \pm \varepsilon)\}}{\eta} \right] = \frac{\partial^n}{\partial \lambda^n} \Theta(\lambda - V \mp \varepsilon) . \quad (3)$$

Therefore, the 4×4 relativistic density matrix R_W will contain the step function, the delta function and its derivatives. As happens in the non-relativistic problem, R_W has to be considered as a distribution rather than as a function, in the sense that it is only meaningful if used under an integral sign to compute expectation values of one-body operators. For instance, the expression of the zero-order term of the density matrix for positive energy states is

$$R_0 = \frac{\Theta(\lambda - V - \varepsilon)}{2} \left[I + \frac{1}{\varepsilon} (\boldsymbol{\alpha} \cdot \mathbf{p} + \beta m^*) \right] \quad (4)$$

Using Eqs. (2) and (3), R_1 and R_2 are obtained from the contributions G_1 and G_2 to the \hbar expansion of the propagator, respectively, according to the method developed in Refs. [26, 27].

Semiclassical Relativistic Particle and Energy Densities Let us now apply the semiclassical relativistic density matrix to calculate the \hbar expansion of the particle and energy densities, in both the WK approach and the energy density (RETF) formalism. For a given single particle operator \hat{O} , we define its expectation value as

$$\hat{O} = \frac{1}{(2\pi)^3} \int dr \int dp \text{Tr}^+ \left[\hat{O}(r, \hat{p}) \hat{R}(r, \hat{p}) \right]_W , \quad (5)$$

where Tr^+ means that the trace is taken disregarding the negative energy terms. Thus, here and in the following we only consider the positive energy solutions, i.e. we restrict ourselves to the positive energy part of the spectrum and neglect any contribution from antiparticles, as is currently done in most applications of relativistic mean field theory. The semiclassical expectation value corresponding to Eq. (5) reduces to

$$\langle \hat{O} \rangle_{SC} = \frac{1}{(2\pi)^3} \int dr \int dp \text{Tr}^+ [O_W(R_0 + \hbar^2 R_2)] \quad (6)$$

up to order \hbar^2 , since the other terms which in principle could contribute turn out to be zero or vanish after angular average in momentum space.

Density Functionals To obtain the RETF density functional, we have to write ∇V and ΔV as a function of the particle density, the effective mass and their gradients and insert them into the \hbar^2 terms of WK expansions. In the mean field approximation the meson fields are replaced with their ground-state expectation values (classical fields). The relativistic energy density of a finite nucleus in Thomas-Fermi approximation can be written as [7, 35]

$$\mathcal{H} = \mathcal{E} + \frac{1}{2}g_s\phi\rho_s^{\text{eff}} + \frac{1}{3}b\phi^3 + \frac{1}{4}c\phi^4 + \frac{1}{2}g_v V\rho + \frac{1}{2}g_\rho R\rho_3 + \frac{1}{2}e\mathcal{A}\rho_p, \quad (7)$$

in terms of the nucleon energy density

$$\mathcal{E} = \sum_q \frac{1}{8\pi^2} \left[k_{Fq}^3 \epsilon_{Fq}^3 + k_{Fq}^3 \epsilon_{Fq} - m^{*4} \ln \frac{k_{Fq} + \epsilon_{Fq}}{m^*} \right], \quad (8)$$

where $g_s\rho_s^{\text{eff}} = g_s\rho_s - b\phi^2 - c\phi^3$,

$$\rho_s = \frac{\partial \mathcal{E}}{\partial m^*} = \sum_q \frac{m^*}{2\pi^2} \left[k_{Fq} \epsilon_{Fq} - m^{*2} \ln \frac{k_{Fq} + \epsilon_{Fq}}{m^*} \right] \quad (9)$$

is the scalar density and $m^* = m - g_s\phi$ is the nucleon effective mass. For each kind of nucleon ($q = n, p$) the local Fermi momentum k_{Fq} is defined by $k_{Fq} = (3\pi^2\rho_q)^{1/3}$, while $\epsilon_{Fq} = \sqrt{k_{Fq}^2 + m^{*2}}$. ϕ , V , R , \mathcal{A} are the expectation values of the fields of isoscalar scalar σ meson, isoscalar vector ω meson, isovector vector ρ meson ($R \equiv g_\rho b_0(\mathbf{r})$), and photons respectively. g_s, b, c, g_v, g_ρ and e are the corresponding coupling constants.

Scaling The virial theorem relates the kinetic and potential energy components of the energy in certain circumstances. This theorem results from homogeneity properties of the kinetic and potential energy components of \mathcal{H} with respect to a scaling transformation that preserves the normalization. One such normalized scaled version of the baryon density is

$$\rho_\lambda(\mathbf{r}) = \lambda^3 \rho(\lambda\mathbf{r}), \quad (10)$$

where λ is an arbitrary scaling parameter. Accordingly, the local Fermi momentum changes as

$$k_{Fq\lambda}(\mathbf{r}) = [3\pi^2\rho_{q\lambda}(\mathbf{r})]^{1/3} = \lambda k_{Fq}(\lambda\mathbf{r}). \quad (11)$$

The meson fields and the Coulomb field are also modified by the scaling due to the self-consistent equations, which will relate the scaled fields to the scaled densities. Unfortunately, the meson fields do not scale according to simple power laws of λ because of the finite-range character of the meson interactions. This is most apparent for the scalar field ϕ , since the scalar density in the source term of the field equations transforms not only due to the scaling of k_{Fq} but also of ϕ itself (or m^*), see Eq. (9) for ρ_s . For reasons that will become clear immediately, we shall write the scaled effective mass $m_\lambda^*(\mathbf{r}) = m - g_s\phi_\lambda(\mathbf{r})$ in the form

$$m_\lambda^*(\mathbf{r}) \equiv \lambda \tilde{m}^*(\lambda\mathbf{r}). \quad (12)$$

The quantity \tilde{m}^* carries an implicit dependence on λ apart from the parametric dependence on $\lambda \mathbf{r}$.

On account of Eqs. (11) and (12) the scaled form of \mathcal{E} reads $\mathcal{E}_\lambda(\mathbf{r}) = \lambda^4 \mathcal{E}[k_{Fq}(\lambda \mathbf{r}), \tilde{m}^*(\lambda \mathbf{r})] \equiv \lambda^4 \tilde{\mathcal{E}}(\lambda \mathbf{r})$, while the scaled scalar density reads $\rho_{s\lambda}(\mathbf{r}) = \lambda^3 \rho_s[k_{Fq}(\lambda \mathbf{r}), \tilde{m}^*(\lambda \mathbf{r})] \equiv \lambda^3 \tilde{\rho}_s(\lambda \mathbf{r})$. The tilded quantities $\tilde{\mathcal{E}}$ and $\tilde{\rho}_s$ are given by Eqs. (8) and (9) after replacing m^* by \tilde{m}^* . Note the usefulness of (12) to be able to put the transformed densities \mathcal{E}_λ and $\rho_{s\lambda}$ into the above compact form. This way, for the scaled total energy density \mathcal{H}_λ we obtain

$$\mathcal{H}_\lambda = \lambda^3 \left[\lambda \tilde{\mathcal{E}} + \frac{1}{2} g_s \phi_\lambda \tilde{\rho}_s^{\text{eff}} + \frac{1}{3} \frac{b}{\lambda^3} \phi_\lambda^3 + \frac{1}{4} \frac{c}{\lambda^3} \phi_\lambda^4 + \frac{1}{2} g_v V_\lambda \rho + \frac{1}{2} g_\rho R_\lambda \rho_3 + \frac{1}{2} e \mathcal{A}_\lambda \rho_p \right], \quad (13)$$

with the definition $g_s \tilde{\rho}_s^{\text{eff}} = g_s \tilde{\rho}_s - b \phi_\lambda^2 / \lambda^3 - c \phi_\lambda^3 / \lambda^3$.

The scaled energy is stationary for $\lambda = 1$ (which leads to the virial theorem):

$$0 = \left[\frac{\partial}{\partial \lambda} \int \frac{d(\lambda \mathbf{r})}{\lambda^3} \mathcal{H}_\lambda(\mathbf{r}) \right]_{\lambda=1} \quad (14)$$

Let us exemplify the calculation of the derivatives of the scaled fields with respect to λ with the omega field V_λ . It fulfils the scaled Klein-Gordon equation $(\Delta_{\mathbf{u}} - m_v^2 / \lambda^2) V_\lambda(\mathbf{u}) = -\lambda g_v \rho(\mathbf{u})$, where we have used Eq. (10) for ρ_λ and have switched to the coordinate $\mathbf{u} = \lambda \mathbf{r}$. On differentiating this equation with respect to λ we have

$$\left(\Delta_{\mathbf{u}} - \frac{m_v^2}{\lambda^2} \right) \frac{\partial V_\lambda}{\partial \lambda} = -g_v \rho - \frac{2m_v^2}{\lambda^3} V_\lambda. \quad (15)$$

If one now sets $\lambda = 1$ the solution of this equation provides $\partial V_\lambda / \partial \lambda|_{\lambda=1}$. In the case of the scalar field additional terms appear due to the fact that the scalar density itself is a function of the scalar field. Following the same steps as above, from the scaled field equation $(\Delta_{\mathbf{u}} - m_s^2 / \lambda^2) \phi_\lambda(\mathbf{u}) = -\lambda g_s \tilde{\rho}_s^{\text{eff}}(\mathbf{u})$ one easily arrives at

$$\left(\Delta_{\mathbf{u}} - \frac{m_s^2}{\lambda^2} \right) \frac{\partial \phi_\lambda}{\partial \lambda} = -g_s \tilde{\rho}_s^{\text{eff}} - \lambda g_s \frac{\partial \tilde{\rho}_s^{\text{eff}}}{\partial \lambda} - \frac{2m_s^2}{\lambda^3} \phi_\lambda. \quad (16)$$

Using these expressions (and of the corresponding results for the rho and Coulomb fields) into Eq. (14) the virial theorem for the non-linear $\sigma - \omega$ is derived [35]. The detail calculations can be found in ref. [35]. As a further application of the method we shall use it in calculations of the isoscalar giant monopole resonance (ISGMR) and isoscalar giant quadrupole resonance (ISGQR).

Isoscalar giant monopole It is customary to write the excitation energy of the ISGMR as

$$E_M = \sqrt{\frac{C_M}{B_M}}, \quad (17)$$

where C_M and B_M are called, respectively, the restoring force (or incompressibility of the finite nucleus) and the mass parameter of the monopole vibration. To study E_M in

the RMF the authors of Refs. [24, 25] resorted to a local Lorentz boost and the scaling method. Following these works one has

$$C_M = \left[\frac{\partial^2}{\partial \lambda^2} \int d\mathbf{r} \mathcal{H}_\lambda(\mathbf{r}) \right]_{\lambda=1}, \quad (18)$$

where the scaling parameter λ now plays the role of the collective coordinate of the monopole vibration, and

$$B_M = \frac{1}{A} \int d\mathbf{r} r^2 \mathcal{H}(\mathbf{r}), \quad (19)$$

with A being the mass number of the nucleus.

Isoscalar giant quadrupole In the quadrupole vibration the particle density scales as [33]

$$\rho_\lambda(\mathbf{r}) = \rho(x/\lambda, y/\lambda, \lambda^2 z). \quad (20)$$

While the volume element is conserved in both coordinate and momentum space, the momentum distribution, which remained spherically symmetric in the monopole oscillation, becomes highly deformed in the quadrupole case [3, 36]:

$$\mathbf{p}_\lambda = (\lambda p_x, \lambda p_y, p_z / \lambda^2). \quad (21)$$

One has to note that the spherically averaged form of the distribution function $\mathcal{R}(\mathbf{r}, \mathbf{p})$ cannot be employed in the quadrupole scaling calculations due to the deformation of the Fermi sphere [36]. Since the final magnitude of the contribution of the \hbar^2 -order corrections in the semiclassical calculation of the excitation energy of giant resonances is not very significant, we will work at the Thomas-Fermi level in the present study of the giant quadrupole resonance for simplicity. The detailed calculations for the quadrupole excitation energy can be found in Ref. [35]. The final expression is written as

$$\bar{E}_Q^s = \sqrt{\frac{C_Q}{B_Q}}, \quad (22)$$

where C_Q and B_Q are the restoring force and mass parameter for the quadrupole resonance, respectively. We refer [35] for the readers to see the explicit expressions for C_Q and B_Q .

2.2 Effective Field Theory motivated RMF (E-RMF)

Finite Nuclei The developments in the E-RMF model used here have been reported in Refs. [16, 37], where one can find the details of the construction of the effective Lagrangian with a non-linear realization of chiral symmetry. To solve the equations of motion one applies the Hartree approximation. In such an approach the pseudoscalar field of the pions does not contribute explicitly because it has a vanishing expectation value. The quantum structure is introduced by expanding the nucleon field on a single-particle basis. For systems with time reversal symmetry, as there can be no currents,

only the time-like component of the vector meson and photon fields contributes. Charge conservation implies that only the third component of the isovector rho-meson field does not vanish. As a final product, one obtains the energy density functional of the E-RMF model for finite nuclei as [16, 38]:

$$\begin{aligned}
\mathcal{E}(\mathbf{r}) = & \sum_{\alpha} \varphi_{\alpha}^{\dagger} \left\{ -i \boldsymbol{\alpha} \cdot \boldsymbol{\nabla} + \beta(M - \Phi) + W + \frac{1}{2} \tau_3 R + \frac{1 + \tau_3}{2} \mathcal{A} \right. \\
& - \frac{i}{2M} \beta \boldsymbol{\alpha} \cdot \left(f_v \boldsymbol{\nabla} W + \frac{1}{2} f_{\rho} \tau_3 \boldsymbol{\nabla} R + \lambda \boldsymbol{\nabla} \mathcal{A} \right) + \frac{1}{2M^2} (\beta_s + \beta_v \tau_3) \Delta \mathcal{A} \left. \right\} \varphi_{\alpha} \\
& + \left(\frac{1}{2} + \frac{\kappa_3}{3!} \frac{\Phi}{M} + \frac{\kappa_4}{4!} \frac{\Phi^2}{M^2} \right) \frac{m_s^2}{g_s^2} \Phi^2 - \frac{\zeta_0}{4!} \frac{1}{g_v^2} W^4 \\
& + \frac{1}{2g_s^2} \left(1 + \alpha_1 \frac{\Phi}{M} \right) (\boldsymbol{\nabla} \Phi)^2 - \frac{1}{2g_v^2} \left(1 + \alpha_2 \frac{\Phi}{M} \right) (\boldsymbol{\nabla} W)^2 \\
& - \frac{1}{2} \left(1 + \eta_1 \frac{\Phi}{M} + \frac{\eta_2}{2} \frac{\Phi^2}{M^2} \right) \frac{m_v^2}{g_v^2} W^2 - \frac{1}{2g_{\rho}^2} (\boldsymbol{\nabla} R)^2 - \frac{1}{2} \left(1 + \eta_{\rho} \frac{\Phi}{M} \right) \frac{m_{\rho}^2}{g_{\rho}^2} R^2 \\
& - \frac{1}{2e^2} (\boldsymbol{\nabla} \mathcal{A})^2 + \frac{1}{3g_{\gamma} g_v} \mathcal{A} \Delta W + \frac{1}{g_{\gamma} g_{\rho}} \mathcal{A} \Delta R, \tag{23}
\end{aligned}$$

where τ_3 is the third component of the isospin operator. The index α runs over all occupied nucleon states $\varphi_{\alpha}(\mathbf{r})$ of the positive energy spectrum. The meson fields are $\Phi \equiv g_s \phi_0(\mathbf{r})$ (isoscalar scalar σ meson), $W \equiv g_v V_0(\mathbf{r})$ (isoscalar vector ω meson), and $R \equiv g_{\rho} b_0(\mathbf{r})$ (isovector vector ρ meson), and the photon field is $\mathcal{A} \equiv e \mathcal{A}_0(\mathbf{r})$.

From Eq. (23) one derives the field equations for the nucleons and the mesons. The expressions for the densities and the field equations of the E-RMF model can be found in previous works [10, 16, 38, 39]. We solve the Dirac equation in coordinate space by transforming it into a Schrödinger-like equation and iterate numerically the final set of coupled equations till consistency is reached.

In the applications to be presented below, we employ the E-RMF parameter sets G1 and G2 of Refs. [16]. The masses of the nucleon and of the ω and ρ mesons are $M = 939$ MeV, $m_v = 782$ MeV, and $m_{\rho} = 770$ MeV, respectively. The parameters $m_s, g_s, g_v, g_{\rho}, \eta_1, \eta_2, \eta_{\rho}, \kappa_3, \kappa_4, \zeta_0, f_v, \alpha_1$, and α_2 of G1 and G2 were fitted by a least-squares optimization procedure to 29 observables (binding energies, charge form factors and spin-orbit splittings near the Fermi surface) of the nuclei ^{16}O , ^{40}Ca , ^{48}Ca , ^{88}Sr and ^{208}Pb , as described in Refs. [16]. The constants β_s, β_v and f_{ρ} were then chosen to reproduce the experimental charge radii of the nucleon. We report in Table 1 the values of the parameters and the saturation properties of the sets G1 and G2 as well as those of the NL3 set. An interesting feature is that the set G2 has a positive κ_4 coupling, as opposed to G1 and to most of the successful RMF parametrizations such as NL1 and NL3. Formally, a negative value of κ_4 is not acceptable because the energy spectrum then has no lower bound. The larger effective mass M_{∞}^*/M at saturation in

the E-RMF sets is due to the presence of the tensor coupling f_v of the ω meson to the nucleon.

Table 1. The E-RMF (G1 and G2) and RMF (NL3) parameters in dimensionless form, and their saturation properties in nuclear matter (energy per particle, density, incompressibility, effective mass, and symmetry energy coefficient).

Parameter	G1	G2	NL3	Parameter	G1	G2	NL3
m_s/M	0.540	0.554	0.541	α_2	1.788	-1.580	0.0
$g_s/4\pi$	0.785	0.835	0.813	$f_v/4$	0.108	0.173	0.0
$g_v/4\pi$	0.965	1.016	1.024	$f_\rho/4$	1.039	0.962	0.0
$g_\rho/4\pi$	0.698	0.755	0.712	β_s	0.028	-0.093	0.0
κ_3	2.207	3.247	1.465	β_v	-0.250	-0.460	0.0
κ_4	-10.090	0.632	-5.668	a_v (MeV)	-16.14	-16.07	-16.24
ζ_0	3.525	2.642	0.0	ρ_0 (fm $^{-3}$)	0.153	0.153	0.148
η_1	0.071	0.650	0.0	K (MeV)	215.0	215.0	271.5
η_2	-0.962	0.110	0.0	M_∞^*/M	0.634	0.664	0.595
η_ρ	-0.272	0.390	0.0	J (MeV)	38.5	36.4	37.40
α_1	1.855	1.723	0.0				

Nuclear and Neutron Matter In an infinite medium of uniform nuclear matter all of the terms with gradients in the energy density \mathcal{E} and in the field equations vanish. In this limit the nucleon density is given by

$$\rho = \frac{\gamma}{(2\pi)^3} \int_0^{k_F} d^3k = \frac{\gamma}{6\pi^2} k_F^3, \quad (24)$$

where k_F is the Fermi momentum, and the degeneracy factor γ is 4 for symmetric nuclear matter and 2 for pure neutron matter. The pressure P follows from the derivative of the energy density with respect to the nucleon density:

$$P = \rho^2 \frac{\partial}{\partial \rho} (\mathcal{E}/\rho). \quad (25)$$

We give the final expressions for pressure P and energy density ϵ [40]:

$$P = \frac{\gamma}{3(2\pi)^3} \int d^3k \frac{k^2}{E^*(k)} + \frac{1}{4!} \zeta_0 g_v^2 V_0^4 + \frac{1}{2} \left(1 + \eta_1 \frac{g_\Phi \Phi}{M} + \frac{\eta_2}{2} \frac{g_s^2 \Phi_0^2}{M^2} \right) m_\omega^2 V_0^2 \\ - m_\sigma^2 \sigma^2 \left(\frac{1}{2} + \frac{\kappa_3 g_s \Phi_0}{3!M} + \frac{\kappa_4 g_s^2 \Phi_0^2}{4!M^2} \right) + \frac{1}{2} \left(1 + \eta_\rho \frac{g_s \Phi_0}{M} \right) m_\rho^2 b_0^2, \quad (26)$$

$$\epsilon = \frac{\gamma}{(2\pi)^3} \int d^3k E^*(k) - \frac{1}{4!} \zeta_0 g_w^2 V_0^4 - \frac{1}{2} \left(1 + \eta_1 \frac{g_s \Phi_0}{M} + \frac{\eta_2}{2} \frac{g_s^2 \Phi_0^2}{M^2} \right) m_\omega^2 V_0^2 + \frac{1}{2} g_\rho b_0 (\rho_p - \rho_n) \\ + m_\sigma^2 \sigma^2 \left(\frac{1}{2} + \frac{\kappa_3 g_s \Phi_0}{3!M} + \frac{\kappa_4 g_s^2 \Phi_0^2}{4!M^2} \right) + \frac{1}{2} \left(1 + \eta_\rho \frac{g_{\Phi_0} \Phi_0}{M} \right) m_\rho^2 b_0^2 + g_\omega V_0 (\rho_p + \rho_n). \quad (27)$$

In order to describe the asymmetric nuclear matter, one can introduce the asymmetric parameter α which is defined as $\alpha = \frac{(\rho_n - \rho_p)}{(\rho_n + \rho_p)}$. For the symmetric matter, $\alpha=0$ and for the neutron matter, $\alpha=1$.

3 Results and Discussions

3.1 Giant Resonances

The derivatives of the scaled meson fields with respect to λ are computed by solving Eqs. (15) and (16) at $\lambda = 1$. We have found C_M to be positive for all of the (linear and non-linear) parameter sets we have tested in the Thomas–Fermi calculations. A large part of the final value of C_M (usually far more than a half) is due to the contribution of the term $\partial \tilde{\rho}_s / \partial \lambda|_{\lambda=1}$.

Table 2. Excitation energy of the monopole state (in MeV) obtained in the scaling approach by using various relativistic parameter sets (in order of increasing value of the compression modulus K_{nm}). The energies of the main peaks found in the time-dependent RMF (TDRMF) calculations are also shown for ^{90}Zr and ^{208}Pb .

Nucleus	NL-Z2	NL1	NL3	NL-SH	NL2	$80A^{-1/3}$	Expt.
^{40}Ca	20.5	21.2	23.5	26.6	29.5	23.4	19.2 ± 0.4
^{90}Zr	16.4	17.2	19.2	21.9	24.0	17.9	17.9 ± 0.2
(TDRMF)		15.7	~ 18				
^{116}Sn	15.1	15.9	17.7	20.3	22.3	16.4	16.1 ± 0.1
^{144}Sm	14.1	14.9	16.6	19.0	20.8	15.3	15.4 ± 0.3
^{208}Pb	12.3	12.9	14.5	16.6	18.1	13.5	14.2 ± 0.3
(TDRMF)		12.4	14.1	16.1	17.8		

Monopole In Table 2 we display the calculated Thomas-Fermi excitation energies of the ISGMR, together with the empirical estimate $E_M \sim 80/A^{1/3}$ MeV [41], for ^{40}Ca , ^{90}Zr , ^{116}Sn , ^{144}Sm and ^{208}Pb . Recent experimental data on the centroid energy of the ISGMR are available for these nuclei [42]. We have employed the non-linear parameter sets (see ref. [35] for their origin) NL-Z2 ($K_{nm} = 172$ MeV), NL1 ($K_{nm} = 212$

MeV), NL3 ($K_{\text{nm}} = 272$ MeV), NL-SH ($K_{\text{nm}} = 355$ MeV) and NL2 ($K_{\text{nm}} = 399$ MeV). From the table one can see that the smaller the mass number, the larger is the monopole energy. The energy of the ISGMR increases with increasing K_{nm} in the various parameter sets. For example, the monopole energy in ^{208}Pb is 12.3 MeV for NL-Z2 while it is 17.8 MeV for NL2. The dependence on K_{nm} is roughly linear for each nucleus.

The ISGMR has been studied in the time-dependent RMF (TDRMF) theory by Vretenar et al. [43]. We include in Table 2 their results for the energy of the main peaks that appear in the monopole strength distributions of ^{90}Zr and ^{208}Pb . Our scaling results compare very well in the case of ^{208}Pb for all parameter sets, but give somewhat larger excitation energies for ^{90}Zr . It should be mentioned that the Fourier spectrum of ^{90}Zr in the TDRMF calculation is considerably fragmented (specially for the sets with higher K_{nm}) and then the determination of the centroid energy is more uncertain [43]. Recently, it has been demonstrated that the relativistic random phase approximation (RRPA) is equivalent to the small amplitude limit of the TDRMF theory in the no-sea approximation, when pairs formed from the empty Dirac sea states and the occupied Fermi sea states are included in the RRPA [44].

Quadrupole As we have indicated, our calculations for the quadrupole mode are restricted to the RTF approximation. We collect in Table 3 the calculated excitation energy of the quadrupole oscillation for ^{16}O , ^{40}Ca , ^{48}Ca , ^{90}Zr and ^{208}Pb , along with the empirical law $E_x \sim 65/A^{1/3}$ MeV and some experimental data taken from Ref. [45]. The theoretical results shown in this table correspond to the non-linear sets NL1, NL3, NL-SH and NL2, and to the set LZ ($K_{\text{nm}} = 586$ MeV, $m_{\text{nm}}^*/m = 0.53$) which we take as a representative of the linear sets.

Table 3. Excitation energy of the quadrupole vibration (in MeV) obtained in the scaling approach. The experimental values are from Ref. [45].

Nucleus	NL1	NL3	NL-SH	NL2	LZ	$65A^{-1/3}$	Exp.
^{16}O	21.6	22.9	24.0	24.7	25.8	25.8	22.0
^{40}Ca	17.9	18.6	19.2	19.4	20.8	19.0	18.0
^{48}Ca	16.9	17.5	18.1	18.1	19.5	17.9	
^{90}Zr	14.4	14.8	15.2	15.1	16.4	14.5	14.5
^{208}Pb	10.9	11.2	11.5	11.3	12.4	11.0	10.5

One can see that the four non-linear $\sigma - \omega$ parametrizations reproduce the empirical trend and that, contrary to the situation found in the monopole case, they give rather similar results for each nucleus. This is due to the fact that the energy of the quadrupole vibration is basically independent of the bulk compression modulus of the effective force. Nevertheless, the comparison with experiment favours the NL3 set and, especially, the NL1 set (i.e., those sets with a lower incompressibility). In fact, if the incompressibility of the force is very large (set LZ) the theoretical predictions clearly over-

estimate the experimental values. The relativistic results of the non-linear sets compare well with those obtained in non-relativistic Hartree-Fock and extended Thomas-Fermi calculations using Skyrme forces [46]. Calculations of the isoscalar giant quadrupole resonance are rather scarce in the relativistic domain. Time-dependent RMF calculations of this mode have been carried out in Ref. [47] using the NL-SH parameter set. Our relativistic Thomas-Fermi calculation is in good agreement with the excitation energies of 23.6, 17.7 and 17.7 MeV for ^{16}O , ^{40}Ca and ^{48}Ca , respectively, reported in that work.

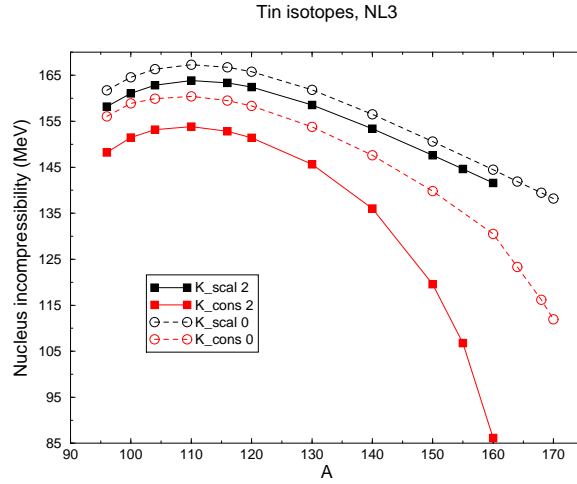


Fig. 1. The incompressibility obtained by scaling K_{scal} and constrained K_{cons} calculations with RTF and RETF methods for Sn isotopes.

Application to drip-line nuclei: In our exploratory analysis of the behaviour of the excitation energies of the giant monopole and quadrupole resonances in nuclei near the drip lines, we have studied the isotones of Ca, Zr, Sn and Pb from the proton drip line up to the neutron drip line. We have performed semiclassical TF and ETF calculations in the relativistic frame with the NL3 parameter set. This force reproduces with a reasonable good agreement the experimental excitations of the GMR in the stable nuclei ^{40}Ca , ^{90}Zr , ^{116}Sn and ^{208}Pb which have been recently reanalyzed [42]. Here we have reported only the results of Sn and Pb isotopes and the extended results will be published in ref. [48].

The two main ingredients that determine the average excitation energies of the giant resonances in our semiclassical description are the restoring force and the mass denominator. The key ingredient that determines the mass denominator is the mass rms radius.

From our calculations [48] we see that the neutron rms radius increases almost linearly with increasing number of neutrons. The rms radius of the proton distribution also increases roughly linearly with increasing number of particles but its slope is smaller than the one corresponding to the neutron distribution.

Let us now discuss the restoring force for the monopole resonances. In this case the restoring force C_M is directly related with the finite nucleus incompressibility ($C_M = AK_A$). Figure 1 displays the scaled (K_A^S) and constrained (K_A^C) incompressibilities obtained with the RTF and RETF approaches for the chain of isotopes of tin between the proton and neutron drip lines. In both semiclassical approximations the scaled incompressibility K_A^S is roughly constant in the region corresponding to stable nuclei and smoothly decreases with the mass number when A approaches the drip lines. This behaviour can be qualitatively understood through the leptodermous expansion of the finite nucleus incompressibility [34]:

$$K_A = K_{nm} + K_{sf}A^{-1/3} + K_{vs}I^2 + K_{coul}Z^2A^{-4/3} + \dots, \quad (28)$$

where K_{nm} is the nuclear matter incompressibility and K_{sf} , K_{vs} and K_{coul} are the surface, symmetry and Coulomb corrections which in the scaling model are negative [34]. Although the surface and Coulomb contributions will decrease with the increasing

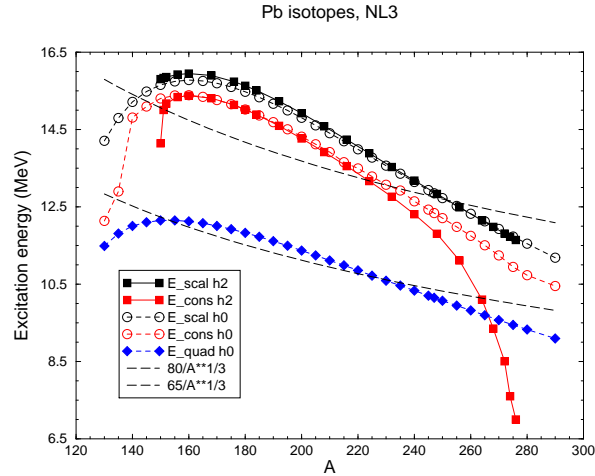


Fig. 2. The monopole (E_{scal} , E_{cons}) and quadrupole (E_{quad0}) excitation energies obtained by RTF and RETF calculations for Pb isotopes. The empirical results for monopole ($80A^{1/3}$ MeV) and quadrupole ($65A^{1/3}$ MeV) excitations are also plotted.

mass number, the symmetry term (that usually is large) will reduce the finite nucleus incompressibility when the number of neutrons increases. The calculated semiclassical

K_A^C is always smaller than K_A^S . Again it is roughly constant for stable nuclei but it is strongly reduced when the mass number A approaches the neutron drip line. This effect is much more pronounced if the calculation is performed in the RETF approximation instead of the simpler RTF approach [48].

Finally, the excitation energy of the GMR has been obtained with RTF and RETF methods and GQR is calculated only with the scaling method and the RTF approach for simplicity. This excitation energy is also computed with the relativistic NL3 parameter set and it is displayed in Figure 2 for Pb isotopes. The results for other nuclei will be published in ref. [48]. The semiclassical scaled RTF excitation energy of the GQR decreases almost linearly with increasing mass number, for Pb isotopes. When one approaches to the proton drip line (i.e when A decreases) the scalar excitation energy of the GQR becomes almost constant.

3.2 E-RMF Results for Finite Nuclei

Breathing mode energy in exotic nuclei Properties very different from the normal nuclei are expected to be found as soon as one leaves the β -stability region and approaches the drip lines. Neutron-rich nuclei near the drip line and the occurrence of closed shells are very important in nuclear astrophysics as their properties strongly influence how stable are the neutron-rich nuclei formed through the r-process. One expects that in very neutron-rich nuclei the shell structure to be strongly modified, with some of the traditional shell gaps disappearing and with new ones appearing. Another interesting

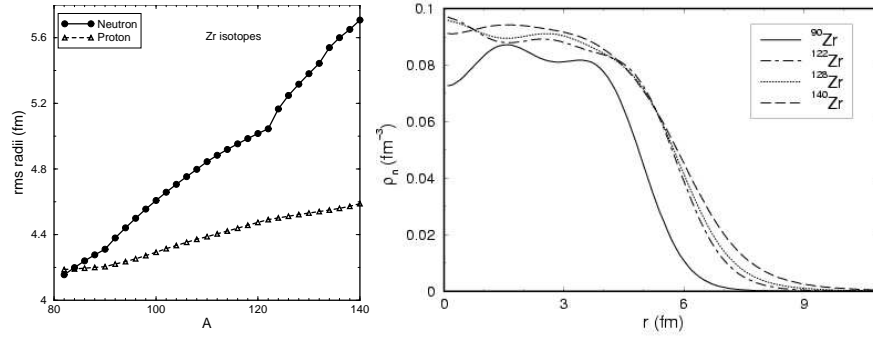


Fig. 3. Left: Neutron and proton rms radii calculated with the G2 set for the Zr isotopic chain as a function of the mass number. Right: Radial dependence of the neutron densities of Zr isotopes.

feature of some exotic nuclei is the appearance of a halo structure which was first experimentally discovered in ^{11}Li and later on observed in $^{11,14}\text{Be}$ and ^{17}B [49].

In RMF calculations [12], it is predicted that Zr isotopes near the drip-line has a giant neutron halo. Therefore, it is interesting to see such effect using our E-RMF formalism [37]. Fig. 3 displays the neutron and proton rms radii for the Zr isotopic chain from $A = 80$ to $A = 120$ obtained using our pairing approach [11, 37] with

the G2 parameter set. One can clearly appreciate the kink at $A = 122$ as a signature of giant halo. In Fig. 3 we display also the calculated neutron densities of some selected Zr isotopes. When the neutron number is significantly above the $N = 82$ core the central density starts to progressively decrease, while a halo develops in the outer region. Some neutrons of the core are scattered by the pairing correlations to the states beyond the Fermi level, resulting in larger rms radii with the increasing number of the neutrons in the outer part of the density distribution of the nuclei beyond ^{122}Zr .

In giant halo nuclei, the excitation energy of collective modes can get strongly modified as compared with stable nuclei. This can be seen, for example in Zr isotopes, where beyond $A = 122$ the last filled levels are weakly bound [37]. Thus, particle-hole excitations from the occupied $2f_{7/2}$, $3p_{3/2}$, $3p_{1/2}$ and $2f_{5/2}$ states to the continuum will give important contributions to the low-energy part of the RPA strength. Constrained calculations are one of the means to estimate the average energy of the breathing mode. Such calculations have been performed in RMF with different parameter sets to obtain the excitation energies of the GMR of some selected nuclei in Ref. [35]. A reasonably good agreement has been found between the results of these calculations with the results from more sophisticated approaches such as the time-dependent RMF formalism or the relativistic RPA.

Here we have followed the method of Ref. [35] and have performed the constrained calculations in E-RMF approach without the pairing correlations, as in the non-relativistic studies of giant resonances in nuclei near the drip lines [50]. Our estimate of the excitation energy of the GMR of the nucleus ^{90}Zr from the constrained calculation with the E-RMF set G2 is 17.2 MeV [37]. It agrees fairly well with the experimental centroid energy 17.9 ± 0.2 MeV. In Fig. 4 we display the finite nucleus incompressibility K_A^c

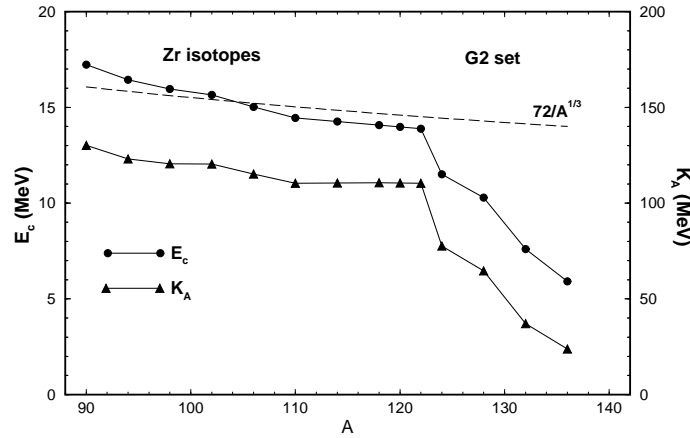


Fig. 4. Average energy E_c of the isoscalar giant monopole resonance and finite nucleus incompressibility K_A obtained from constrained calculations with the G2 set for Zr isotopes.

and average energy E_c of the isoscalar giant monopole resonance calculated using the G2 set for even Zr isotopes ranging from $A = 90$ to $A = 138$. The values of K_A^c are roughly constant from $A = 90$ up to $A = 122$, when the $1h_{11/2}$ level is completely filled. From $A = 122$ on, K_A^c decreases quite fast till the neutron drip line is reached.

Due to the fact that the Zr nuclei beyond $A = 122$ have a large rms radius, the mass denominator [37] also increases when one moves from $A = 122$ towards the neutron drip line. This fact together with the decreasing of the finite nucleus incompressibility reduces strongly the excitation energy of the GMR beyond $A = 122$, as evidenced in Fig. 4. It is known that the experimental GMR excitation energies roughly follow the empirical law $E_{\text{GMR}} \sim 80A^{1/3}$ MeV. The excitation energy of the GMR of the Zr isotopes from $A = 90$ to $A = 122$ can be nicely fitted by an $A^{1/3}$ law, as indicated by the dashed line in Fig. 4. This behaviour breaks down for the isotopes with $A > 122$ pointing out again that for these nuclei the neutrons which occupy the weakly bound levels above the $1h_{11/2}$ orbit are softer than the neutrons belonging to the $A = 122$ core.

Superheavy elements In this section, we concentrate on finding out where the next double shell closures beyond $N = 126$ and $Z = 82$ are located according to the E-RMF model with spherical symmetry. In the non-relativistic framework, the macroscopic-microscopic models predict spherical shell closures at $Z = 114$ and $N = 184$ [51]. The Hartree-Fock calculations with Skyrme forces show, in general, the most pronounced shell effects at $Z = 124$, $Z = 126$ and $N = 184$ [52]. However, the conventional RMF theory typically prefers $Z = 120$ and $N = 172$ as the best candidates for spherical shell closures [52]. In view of these discrepancies in the predicted shell closures for super heavy elements (SHE), it is interesting to reinvestigate them using the more general E-RMF model.

In normal nuclei a large gap in the single-particle spectrum is interpreted as the indication of a shell closure. We start by inspecting the neutron single-particle spectra of the $^{292}120$, $^{304}120$ and $^{378}120$ nuclei, using the G1, G2 and NL3 parameter sets, shown in Fig. 5. As mentioned above, $Z = 120$ is found to be a magic number as it was in many other RMF calculations [52]. The three parameter sets show a large gap at $N = 172$ and $N = 258$. However, for $N = 184$ a moderate gap is found mainly for the E-RMF sets, G1 and G2, which is smaller for NL3. In the level spectrum of the system with $N = 258$ and $Z = 120$, one can again find appreciable energy gaps across the neutron numbers $N = 198$ ($1j_{13/2}$ level) and $N = 228$ ($1k_{17/2}$ level) in all the considered parameter sets. By comparing the spectra for the three systems with $N = 172$, 184 and 258 , it can be noticed that the gap between two particular levels is strongly modified along the isotopic chain. However, the level gaps are not as distinct as in lighter nuclei. In SHE the level spectra become complicated due to the presence of levels with a high degree of degeneracy. Therefore, it is imperative to look for other quantities to reliably identify the shell closures and magic numbers of SHE, apart from the analysis of the single-particle level structure.

We next consider three energy indicators for locating the nucleon shell closures. First, a sudden jump in the two-neutron (two-proton) separation energies of even-even nuclei, defined as $S_{2q} = E(N_q - 2) - E(N_q)$, where N_q is the number of neutrons

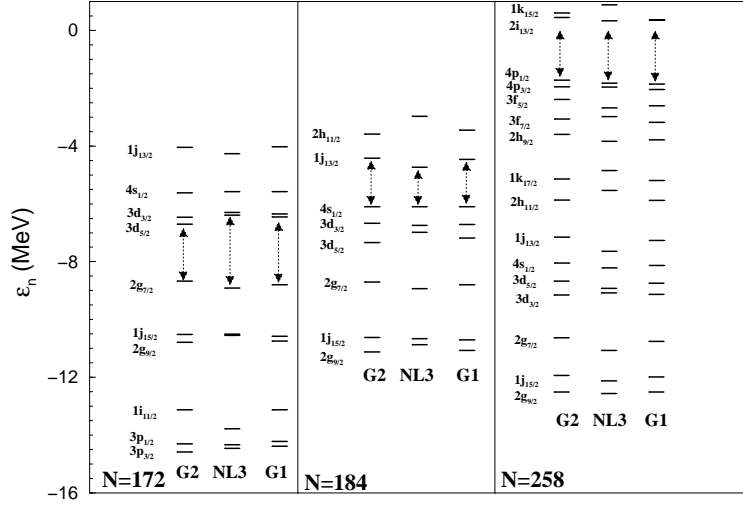


Fig. 5. Single-particle neutron spectra for $Z = 120$ isotopes with $N = 172, 184$ and 258 , evaluated using the parameter sets $G2$, $NL3$ and $G1$. The shell gaps are denoted by arrows. (After [53]).

(protons) in the nucleus for $q = n$ (p). Second, the two-neutron (two-proton) shell gap defined as the second difference of the binding energy: $\delta_{2q}(N_q) = E(N_q + 2) - 2E(N_q) + E(N_q - 2)$. This quantity measures the size of the step found in the two-nucleon separation energy and, therefore, it is strongly peaked at magic shell closures. Third, for closed shell nuclei the pairing gaps Δ_q obtained in the constant strength calculations should vanish or be minimum.

Taking into account the above three energy indicators, it is shown in Ref. [53] that the E-RMF parameter sets $G1$, $G2$ and the RMF set $NL3$ clearly point out towards the robust double magic character of the combinations $(N = 172, Z = 120)$ and $(N = 258, Z = 120)$. Also, for the particular case of the new set $G2$, the combinations $Z = 114$ and $Z = 120$ with $N = 184$ show evidences of a shell closure, although less strong than in the previous cases. A double shell closure in the $(Z = 114, N = 184)$ nucleus has been traditionally predicted by the macroscopic-microscopic models.

We show in Fig. 6 the total (neutron-plus-proton) shell correction energies calculated employing the Strutinsky smoothing procedure [53] for the $Z = 114$ and $Z = 120$ isotopic chains, using the parameter sets $G2$ and $NL3$. Looking at the results for $Z = 114$, it can be realized that the shell corrections in the $Z = 114$ isotopes are weaker than those of the $Z = 120$ chain indicating lesser stability of the former. Two dips are found at $N = 172$ and $N = 184$, with the minimum at $N = 184$ deeper than the one at $N = 172$. The study of the shell correction energy reveals that the shell stabilized regions of SHE are in good agreement with the previous predictions for shell closures derived from the analysis of the energy indicators.

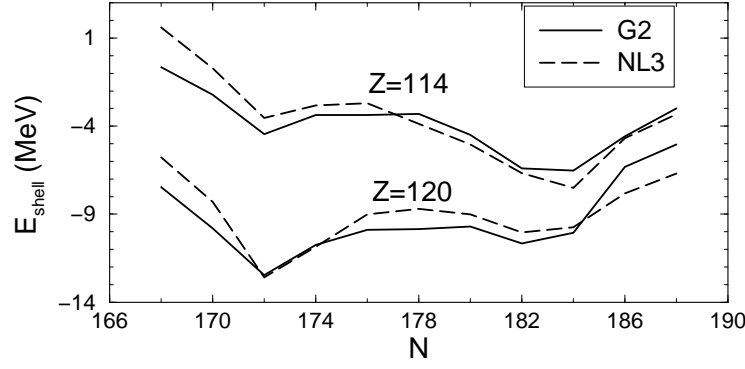


Fig. 6. Shell correction energies for the $Z = 114$ and $Z = 120$ isotopes evaluated by Strutinsky procedure using the energies evaluated with the parameter sets G2 and NL3.

3.3 E-RMF Results for Nuclear Matter

In Fig. 7(a) we present the density dependence of the nuclear matter scalar and vector self-energies calculated with G1, G2, NL1 and NL3 versus the DBHF result. While G2 follows the nature of the DBHF self-energies quite remarkably, at densities only slightly above saturation the NL3 results soon depart from the DBHF behaviour. Thus,

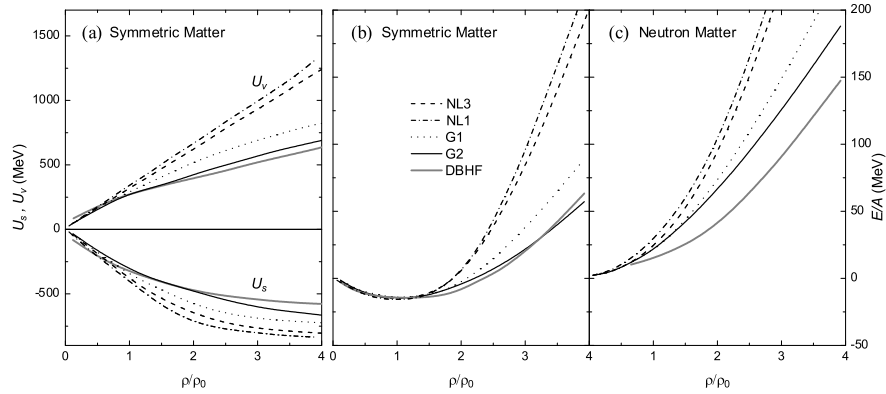


Fig. 7. (a) The density dependence of the scalar (U_s) and vector (U_v) self-energies using the relativistic parameter sets NL1, NL3, G1 and G2, in comparison with the result of the DBHF theory [59]. (b) Energy per particle of symmetric nuclear matter for the same cases as in (a). (c) Energy per particle of neutron matter for the same cases as in (a).

the success of the usual RMF model with only scalar self-interactions for describing the saturation point and the data for finite nuclei is not followed by a proper description of the microscopic DBHF calculations at densities above saturation. This is caused

importantly by a too restrictive treatment of the ω -meson term [10]. While in the standard RMF model the vector potential increases linearly with density and gets stronger, in DBHF it bends down with density. Moreover, the scalar potential overestimates the DBHF result at high density in order to compensate for the strong repulsion in the vector channel. The additional self- and cross-interactions ζ_0 , η_1 , and η_2 included in the E-RMF sets result in a richer density dependence of the mesonic mean fields which brings about the improvement in comparison with the DBHF calculations [10]. It has to be noted that relativistic models which resort to density-dependent couplings are also consistent with the DBHF calculations [54].

The features observed in Fig. 7(a) are further supported by Fig. 7(b) in which the variation of the binding energy per particle is plotted as a function of the density. We can see that the calculations of dense matter based on the RMF sets NL1 and NL3 deviate largely from DBHF, while the E-RMF calculations with G1 and, specially, G2 agree better with the density dependence of the EOS of the DBHF theory. One can realize that in spite of the fact that the incompressibility of NL1 is within the empirical boundaries ($K_{nm} = 212$ MeV with $\rho_0 = 0.154$ fm $^{-3}$), the EOS of this set soon becomes stiff with increasing density and does not follow the DBHF trend. The E-RMF parameter sets give a soft EOS both around saturation and at high densities. A similar situation prevails in the EOS of neutron matter (Fig. 7(c)), though the agreement of G1 and G2 with the DBHF calculation is not as remarkable as in the case of symmetric matter. From the point of view of the comparison with DBHF, this would indicate that the present E-RMF model still needs an improvement in the treatment of the isovector sector, like consideration of additional cross couplings involving the rho-meson field or the introduction of an isovector scalar meson.

The average densities of terrestrial nuclei are not very far from the values around the saturation point of the nuclear EOS, where the E-RMF sets produce similar results to NL3. Hence, one can expect that in finite nuclei the G1 and G2 interactions also will yield results in par with the celebrated NL3 parametrization. This is indeed illustrated in the previous section for the bulk properties of finite nuclei near and away from the β -stability valley.

The recent experimental observations [55,56] rule out any strongly repulsive nuclear EOS. The constraints on the EOS of symmetric nuclear matter at zero temperature, derived experimentally by analyzing elliptic and transverse flow observables in nuclear collisions, are shown in Fig. 8(a) along with the predictions from different RMF and E-RMF sets [57]. We can see that the calculations of dense matter based on NL1 [52] and NL3 [58] deviate drastically from experiment, while the E-RMF calculations with G1 (to some extent) and G2 (to a better extent) agree more with the allowed region. A similar situation prevails in the EOS of neutron matter (Fig. 8(b)). The figures show that conventional sets such as NL1 and NL3 are not well suited for describing the EOS of dense matter, principally due to the fact that without the additional self- and cross-interactions the density dependence of the mesonic mean fields is too poor [10, 31]. Notice that although the incompressibility of NL1 is $K_{nm} = 212$ MeV, which is within the empirical limit, the resulting EOS is stiff at higher densities and does not follow the experimental trend with increasing density. On the other hand, the E-RMF calculations explain better the situation without any forced changes in the fitted parameters or

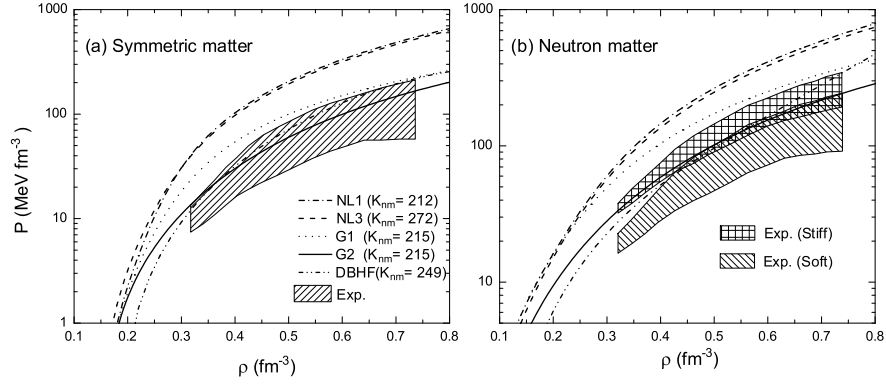


Fig. 8. (a) Zero temperature EOS for symmetric nuclear matter. The shaded area represents the region consistent with the experimental data [55]. The nuclear matter incompressibility of each interaction is expressed in MeV. (b) Zero temperature EOS for neutron matter. The upper and lower shaded areas depict the regions compatible with experiment after inclusion of the pressure from asymmetry terms with, respectively, strong and weak density dependences [55].

the formalism, and the consistency of G2 with experiment is outstanding. As depicted in Fig. 8, the microscopic Dirac-Brueckner-Hartree-Fock (DBHF) theory [59], which starts from the NN interaction in free space, also suggests an EOS for dense matter much softer than in the usual RMF approach. One notices that the DBHF results, for both nuclear and neutron matter, lie within the regions of the EOS compatible with the boundaries extracted from experiment.

The success of G2 in nuclear matter is possible owing to the bulk couplings ζ_0 , η_1 , and η_2 which confer an extra density dependence to the scalar and vector self-energies. If using the functional form one attempts to get a soft EOS for dense matter with vanishing η_1 and η_2 , for realistic saturation conditions, this tends to enforce large unnatural values of ζ_0 . If with $\eta_1 = \eta_2 = 0$ one keeps ζ_0 at acceptable values, then κ_4 tends to become negative. With inclusion of the additional parameters ζ_0 , η_1 and η_2 one can agree better with experiment, have $\kappa_4 > 0$ and a not very large ζ_0 value, as in the case of G2. The experimental data of Fig. 8 also are explained reasonably well [55] by the calculations of Akmal *et al* [60] which employ the Argonne v_{18} interaction, though the use of this interaction for finite nuclei is still limited.

In Table 4 we present the results for the mass and radius of a neutron star. The structure of the neutron star is determined through the Tolman-Oppenheimer-Volkov equation, which follows from hydrostatic equilibrium in strong gravitational fields and general relativity [61], combined with the EOS for $P(\rho)$. One sees that the neutron star properties computed with G2 are very much in accord with the available experimental information. The critical temperatures for the liquid-gas phase transition from our calculations of nuclear matter at finite temperature are also displayed in Table 4. These values are governed by the EOS around saturation where the E-RMF sets produce similar results to NL3. Hence, one expects that in the finite nuclei regime G1 and G2 yield

results in par with the celebrated NL3 parametrization. That this is indeed the case has been proven in previous works and therefore we shall not attempt to present more results in this respect here. We rather refer the reader to the literature [10, 11, 16, 39, 53, 62] where it has been shown that the bulk and single-particle properties of finite nuclei are well described by the E-RMF model with a similar quality to the standard RMF parametrizations, not only for stable isotopes but also for exotic isospin-rich nuclei far from the valley of β stability.

Table 4. The radius R (in km) and the mass ratio M/M_\odot of a neutron star, and the critical temperature T_c (in MeV) for the liquid-gas phase transition in nuclear matter and in asymmetric matter with asymmetry $\alpha = (\rho_n - \rho_p)/(\rho_n + \rho_p) = 0.2$.

	NL1	NL3	G1	G2	Exp.
R	16.94	15.47	13.88	10.08	10–12
M/M_\odot	2.93	2.78	2.15	2.05	1.5–2.5
T_c (Sym.)	13.5	14.3	14.3	14.2	13–20
T_c (Asym.)	12.9	13.7	13.8	13.7	

In choosing between the parameter sets G1 and G2 for further calculations we prefer G2. It is worth noting that G2 presents a positive value of the Φ^4 coupling constant (κ_4), as opposed to G1 and to most of the successful RMF parametrizations, such as NL3. Though the energy spectrum strictly has no lower bound with a negative κ_4 [63], such negative value is necessary in the standard RMF model to get the results closer to experiment. On the other hand, to have a positive κ_4 it is not indispensable to make two parameter sets (one for light and one for heavy nuclei) as in Ref. [31].

4 Summary and Conclusions

Among the various developments in RMF theory, we have presented here the details of the semiclassical approach to the relativistic model and to the E-RMF theory. In the first part of this report, we have discussed the semi classical approach. We have derived the virial theorem for the relativistic nuclear mean field model on the basis of the scaling method and the Thomas–Fermi approximation. In this approach we have calculated for realistic parameter sets of the RMF theory the breathing-mode energy of finite nuclei fully self-consistently (i.e., we did not use a leptodermous expansion of the finite nucleus incompressibility as in some previous studies with the scaling method).

The excitation energies of the monopole and quadrupole oscillation turn out to be in good agreement with the outcome of dynamical time-dependent RMF calculations. It has been shown recently that the relativistic RPA, with the inclusion of Dirac sea states, amounts to the limit of small amplitude oscillations of the TDRMF theory. From the present Thomas-Fermi analysis one can thus conclude that, similarly to the non-relativistic case, also in the relativistic framework the excitation energies obtained with the scaling method simulate the results of the random phase approximation.

We extended the calculations to dripline nuclei for the whole mass region of the periodic table. We analyze the mass-number dependence of the energy and width of the ISGMR and of the energy of the ISGQR from the proton to the neutron dripline. In neutron-rich nuclei near the dripline there is a substantial decrease of the energies which in the monopole case is accompanied by a visible enhancement of the resonance width, more pronounced in the lighter isotopic chains [48]. Similar features were recognized at the proton dripline, but they were hindered owing to the Coulomb barrier.

In the second part of our report, we have outlined the formalism of recently developed E-RMF. We have presented our E-RMF results for breathing mode energy of exotic nuclei, prediction of magic numbers in superheavy region and the EOS of symmetric and asymmetric nuclear matter. We predict $Z = 120$ and $N = 172, 184$ as the proton and neutron magic numbers respectively. We have also shown that the E-RMF parameter sets give a soft EOS both around saturation and at high densities which is consistent with the measurements of kaon production [56] and the flow of matter [55] in energetic heavy-ion collisions, and with the observed neutron star masses and radii. The results thus suggest that in the quest for a unified mean field description of finite nuclei, even in exotic regions of the nuclear landscape, as well as of nuclear and neutron matter up to densities several times above the saturation density, the relativistic mean field model motivated by effective field theory is one reliable candidate. Surely, this is not the only way of obtaining such a unified description. Other implementations of effective field theory for the nuclear many-body problem, formulations of the relativistic model with inclusion of other mesons, or with density-dependent coupling vertices, may also probably deliver a consistent description similar to the E-RMF model. Nevertheless, with the present findings we hope to have illustrated the plausibility of the application of effective field theory methods to the nuclear structure problem.

Acknowledgement

We thank Dr. P.K. Sahu and Dr. Tapas Sil for enlightening discussions and for their contributions in some parts of this work.

References

1. E. Chabanat, P. Bonche, P. Haensel, J. Meyer, and R. Schaeffer, Nucl. Phys. **A635**, 231 (1998).
2. N. Tajima, P. Bonche, H. Flocard, P. -H. Heenen, and M. S. Weiss, Nucl. Phys. **A551**, 434 (1993).
3. J. Dobaczewski, T. R. Werner, J. F. Berger, C. R. Chenn, and J. Decharge, Phys. Rev. C **53**, 2809 (1996); J. Terasaki, P. -H. Heenen, H. Flocard, and P. Bonche, Nucl. Phys. **A600**, 371 (1996).
4. J. D. Walecka, Ann. Phys. (N.Y.) **83**, 491 (1974).
5. B.D. Serot and J.D. Walecka, Adv. Nucl. Phys. **16**, 1 (1986).
6. J. Boguta and A. R. Bodmer, Nucl. Phys. **A292**, 413 (1977).
7. S. K. Patra and C. R. Praharaj, Phys. Rev. **C44**, 2552 (1991).
8. P. -G. Reinhard, M. Rufa, J. Maruhn, W. Greiner, and J. Friedrich, Z. Phys. A **323**, 13 (1986).
9. P. Ring, Prog. Part. Nucl. Phys. **37**, 193 (1996).

10. M. Del Estal, M. Centelles, X. Viñas, and S. K. Patra, Phys. Rev. C **63**, 024314 (2001).
11. M. Del Estal, M. Centelles, X. Viñas, and S. K. Patra, Phys. Rev. C **63**, 044321 (2001).
12. J. Meng and P. Ring, Phys. Rev. Lett. **80**, 460 (1998).
13. P. Ring and P. Schuck, The Nuclear Many-Body Problem, Springer-Verlag, Berlin, 1980.
14. M. L'Huillier and Nguyen Van Giai, Phys. Rev. **C39**, 2022 (1989).
15. J.F. Dawson and R.J. Furnstahl, Phys. Rev. **C42**, 2009 (1990); C.J. Horowitz and J. Piekarewicz, Nucl. Phys. **A511**, 461 (1990); J. Piekarewicz, Phys. Rev. **C62**, 051304 (2000).
16. Zhong-yu Ma, Nguyen Van Giai, H. Toki and M. L'Huillier, Phys. Rev. **C55**, 2385 (1997); Zhong-yu Ma, H. Toki and Nguyen Van Giai, Nucl. Phys. **A627**, 1 (1997).
17. T. Maruyama and T. Suzuki, Phys. Lett. **B219**, 43 (1989).
18. M.V. Stoitsov, M.L. Cescato, P. Ring and M.M. Sharma, J. Phys. **G20**, L149 (1994).
19. T. v. Chossy and W. Stocker Phys. Rev. **C56**, 2518 (1997).
20. J.P. Blaizot, Phys. Rep. **64**, 171 (1980).
21. R.M. Dreizler, J. da Providência (Eds.), Density Functional Methods in Physics, Vol. 123 NATO ASI Series B, Plenum, New York, 1985; E.K.U. Gross, R.M. Dreizler (Eds.), Density Functional Theory, Vol. 337 NATO ASI Series B, Plenum, New York, 1995.
22. R. Arvieu, M. Durand, P. Schuck and E. Suraud (Eds.), 'International Workshop on Semi-classical and Phase Space Approaches to the Dynamics of the Nucleus', J. Phys. Colloq. **C2** (1987).
23. I.Zh. Petkov, M.V. Stoitsov, Nuclear Density Functional Theory, Clarendon Press, Oxford, 1991.
24. S. Nishizaki, H. Kurasawa and T. Suzuki, Nucl. Phys. **A462**, 689 (1987).
25. Chaoyuan Zhu and Xi-Jun Qiu, J. Phys. **G17**, L11 (1991).
26. M. Centelles, X. Viñas, M. Barranco and P. Schuck, Nucl. Phys. **A519**, 73c (1990).
27. M. Centelles, X. Viñas, M. Barranco and P. Schuck, Ann. of Phys. (N.Y.) **221**, 165 (1993).
28. M.K. Weigel, S. Haddad and F. Weber, J. Phys. **G17**, 619 (1991).
29. C. Speicher, R.M. Dreizler and E. Engel, Ann of Phys. (N.Y.) **213**, 312 (1992).
30. S. Gmuca, J. Phys. G **17**, 1115 (1991); S. Gmuca, Z. Phys. A **342**, 387 (1992); Nucl. Phys. **A547**, 447 (1992).
31. Y. Sugahara and H. Toki, Nucl. Phys. **A579**, 557 (1994).
32. R. J. Furnstahl, B. D. Serot, and H. B. Tang, Nucl. Phys. **A598**, 539 (1996); *ibid* **A615**, 441 (1997); *ibid* **A640**, 505 (1998).
33. O. Bohigas, A. Lane and J. Martorell, Phys. Rep. **51**, 267 (1979).
34. B. Grammaticos and A. Voros, Ann. Phys. **123**, 359 (1979); **129**, 153 (1980).
35. S.K. Patra, X. Viñas, M. Centelles and M. Del Estal, Nucl. Phys. **A703**, 240 (2002); *ibid* Phys. Lett. **B523**, 67 (2001) and references therein.
36. B.K. Jennings, Phys. Lett. **B96**, 1 (1980).
37. Tapas Sil, S. K. Patra, B. K. Sharma, M. Centelles, and X. Viñas, *Progress in Field Theory Research*, Nova Science Publishers Inc., (in press).
38. B. D. Serot and J. D. Walecka, Int. J. Mod. Phys. **E6**, 515 (1997).
39. M. A. Huertas, Phys. Rev. C **66**, 024318 (2002).
40. P. Wang, Phys. Rev. C **61**, 054904 (2000).
41. A. van der Woude, Prog. Part. Nucl. Phys. **18**, 217 (1987).
42. D.H. Youngblood, H.L. Clark and Y.-W. Lui, Phys. Rev. Lett. **82**, 691 (1999); D.H. Youngblood, Y.-W. Lui and H.L. Clark, Phys. Rev. **C63**, 067301 (2001).
43. D. Vretenar, G.A. Lalazissis, R. Behnsch, W. Pöschl and P. Ring, Nucl. Phys. **A621**, 853 (1997).
44. Zhong-yu Ma, Nguyen Van Giai, A. Wandelt, D. Vretenar and P. Ring, Nucl. Phys. **A686**, 173 (2001).

45. F.E. Bertrand, Ann. Rev. Nucl. Part. Sci. **26**, 457 (1976); J. Speth and A. Van der Woude, Rep. Prog. Phys. **44**, 719 (1981); K. Goeke and J. Speth, Ann. Rev. Nucl. Part. Sci. **32**, 65 (1982).
46. M. Centelles, M. Pi, X. Viñas, F. Garcias and M. Barranco, Nucl. Phys. **A510**, 397 (1990).
47. D. Vretenar, H. Berghammer and P. Ring, Nucl. Phys. **A581**, 679 (1995).
48. S.K. Patra, X. Viñas, M. Centelles and J.N. De (to be published).
49. I. Tanihata, J. Phys. **G22**, 157 (1996).
50. H. Hamamoto, H. Sagawa, and X. Z. Zhang, Phys. Rev. C **56**, 3121 (1997).
51. P. Möller, and J. R. Nix, Nucl. Phys. **A549**, 84 (1992); J. Phys. **G20**, 1681 (1994).
52. P. -G. Reinhard, M. Bender, and J. A. Maruhn, Comm. Mod. Phys. **2**, A177 (2002).
53. Tapas Sil, S. K. Patra, B. K. Sharma, M. Centelles, and X. Viñas, **C69**, 044315 (2004).
54. S. Typel and B. A. Brown, Phys. Rev. C **67**, 034313 (2003).
55. P. Danielewicz, R. Lacey, and W. G. Lynch, Science **298**, 1592 (2002).
56. C. Sturm *et al*, Phys. Rev. Lett. **86**, 39 (2001); C. Fuchs, A. Faessler, E. Zabrodin, and Yu-Ming Zheng, Phys. Rev. Lett. **86**, 1974 (2001).
57. P. Arumugam, B.K. Sharma, S.K. Patra, Tapas Sil, M. Centelles and X. Viñas, Phys. Lett. **601**, 51 (2004).
58. G.A. Lalazissis, J. König and P. Ring, Phys. Rev. **C55**, 540 (1997).
59. G. Q. Li, R. Machleidt, and R. Brockmann, Phys. Rev. C **45**, 2782 (1992).
60. A. Akmal, V. R. Pandharipande, and D. G. Ravenhall, Phys. Rev. C **58**, 1804 (1998).
61. S. Weinberg, *Gravitation and Cosmology*, (Wiley, New York, 1972).
62. M. Del Estal, M. Centelles, and X. Viñas, Nucl. Phys. **A650**, 443 (1999).
63. G. Baym, Phys. Rev. **117**, 886 (1960).

Neutron Stars and Equation of States of Neutron Star Matter- An Overview

Somenath Chakrabarty*

Department of Physics, University of Kalyani, Kalyani 741 235, India.

Abstract. In these two lectures we shall review i) the formation and some of the gross properties of neutron stars and ii) the neutron star matter equation of states. In the neutron star part, we shall discuss the general relativistic hydrostatic equilibrium equation, known as Tolman, Oppenheimer-Volkoff (TOV or OV) equation. We shall also very briefly explain how to solve and mention a few significant features of the Newtonian form of this equation using uniform matter density as well as the polytropic form of equation of state. Hence we shall obtain the Lane-Emden equation with polytropic form of equation of state and discuss the numerical techniques to solve this equation. We shall discuss the importance of this non-relativistic equation in the case of neutron stars. We shall also briefly mention some of the issues related to the stability criteria from the minimization of total energy of neutron stars in the Newtonian model and show the necessary corrections needed from general relativity. On the discussion part of equation of states we shall consider both non-magnetic and strongly magnetized neutron star matter of various chemical compositions. In the non-magnetic case we shall concentrate on the relativistic mean field type approximation with $\sigma - \omega$ boson exchange. In the strongly magnetized case we shall give a formalism based on relativistic version of Landau theory of Fermi liquid with $\sigma - \omega$ boson exchange.

1 Introduction

From the time a star is formed it goes through a long and complex succession of evolutionary changes [1]. The knowledge of how a star is formed from hot gases and interstellar matter is not yet well understood. The very first stage is the condensation of dense stellar gas (mainly hydrogen) and a protostar is formed. If the gravitational field of the protostar is strong enough, causes a contraction and its further evolution starts. Because of strong gravitational force it will continue to contract. Owing to various dissipative processes inside the matter, a part of the macroscopic motion is converted into thermal energy. The temperature in the central regions of the protostar steadily rises, and when it reaches $\sim 10^7$ K, hydrogen is ignited. The star enters the main sequence on the Hertzsprung-Russell diagram (H-R diagram) from the Hayashi line. H-R diagram shows the relationship between temperature and luminosity (see fig.1). The rate of thermonuclear reactions inside the star and its course of evolution depend on the initial mass and chemical composition (which is homogeneous in a protostar). For massive star, the rate of hydrogen burning is very fast, which implies the temperature at the central region is very high. The reverse is true for low mass star. For example, stars of mass $\sim M_{\odot}$, the burning of hydrogen is very low and lasts for 10^{10} years.

* E-Mail: somenath@klyuniv.ernet.in

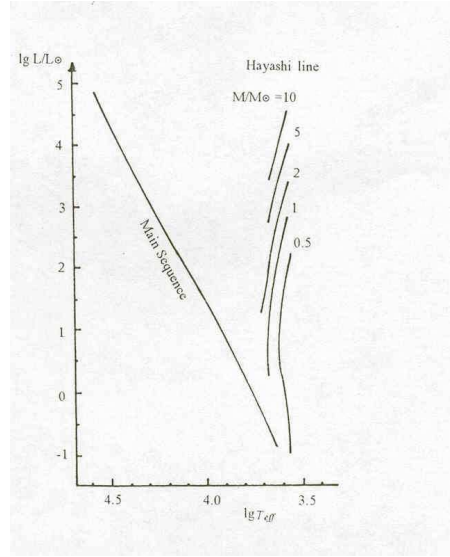


Fig. 1. H-R and Hayashi line.

With the progress of hydrogen burning, its amount at the core region of the star decreases and the chemical composition becomes more and more heterogeneous. With all hydrogen exhausted at the centre, the burning of hydrogen is confined within a thin layer surrounding a helium core. Since the temperature at the core is still too low to ignite helium, the star contracts further, temperature rises slowly. When the temperature reaches $\sim 10^8\text{K}$, the helium begins to burn, while the combustion of hydrogen still continues in the surrounding layer. The central core is now mainly a mixture of carbon and oxygen. If the mass of the core is $< 6M_{\odot}$, the temperature of this region becomes isothermal and at this stage the star suffers an extensive loss of mass. The core shrinks while the outer part expand. The outer envelope of the star may be blown off and forms a planetary nebula. The mass loss may become so effective that at the final stages of the evolution the mass of the star becomes $\sim 1.4M_{\odot}$, and the core region reduces to a white dwarf- the thermo-nuclear reactions come to a halt.

If the mass of the star is in the interval $6M_{\odot} < M \leq 9M_{\odot}$, the stellar evolution follows a somewhat different course. In this case, in order to produce a temperature gradient at the core region, it should shrink. The thermo-nuclear processes continue as in the case of low mass stars until a carbon oxygen core is formed. In this case because of mass loss, which is most effective during the burning of helium in the layer surrounding the carbon-oxygen core, the mass of the core reaches $1.4M_{\odot}$. Its own energy exhausted, the core region loses its stability and implodes. The temperature and density of the core region grow so rapidly that there will be a violent ignition of carbon nuclei. In this violent process, most of the mass of the star are ejected and the star becomes a supernova (energy released $\sim 10^{51}\text{erg}$). The remaining core becomes either a

neutron star or a white dwarf (for more detailed discussion see the review by Sugimoto and Nomoto [2]).

For star masses in the interval $9M_{\odot} < M \leq 40M_{\odot}$, the initial stages of stellar evolution are similar to those of low mass stars, but the rates of thermo-nuclear reactions are much faster. In this range of masses, the ignition of carbon at the core region starts quietly compared to lighter stars and the evolution through further nuclear processes eventually lead to the formation of a core composed of mostly iron. Since iron is the most stable nucleus, the thermo-nuclear reaction at the core come to a halt. As the core mass increases, the density and temperature also rise, the core becomes unstable. The stability sets in when the core density reaches $\sim 10^9 \text{ gm/cc}$ and the process of neutronization begins- the capture of electrons by iron nuclei with the simultaneous conversion of protons into neutrons and emission of neutrinos, or photo-disintegration of iron nuclei. The central pressure decreases, core collapses. The neutrinos escaping from the central core are absorbed by the outer layers, the additional transmission of energy results in the expulsion of envelope, or in other words, triggers a supernova explosion. The energy released in photo-disintegration of iron nuclei is so high that it results total fragmentation of the whole star. Energy emission in the supernova explosion is $\sim 10^{53} \text{ erg}$. The stars with initial masses $> 40M_{\odot}$ evolve still faster and finally become black holes with a release of energy $\sim 10^{54} - 10^{55} \text{ erg}$.

The type of stellar evolution described here is for an isolated main sequence star. Evolution of stars in binary systems is somewhat different. In general, they evolve much faster than single stars [3]. Although the end product of stellar evolution leads to the formation of either a white dwarf, neutron star or a black hole, however, in these lectures we are only interested in the formation of neutron stars and review some of the gross properties of such objects.

2 Chemical Compositions of Neutron Stars

In 1934 Baade and Zwicky [4] proposed the idea of neutron stars. Their radius is very small ($\approx 10 \text{ km}$), mass is \sim a few times M_{\odot} , density of matter inside is very high and more strongly bound by gravitational force than the ordinary stars. In spite of much theoretical effort, most physicists and astronomers did not take the possibility of neutron stars very seriously (although the possibility of black holes was established by general relativity). Only after the discovery of pulsars during 1967 [5], the proposal of neutron star was accepted. Since the only explanation of periodic pulsar emission is by a rotating magnetized neutron star, the existence of neutron stars is now accepted by the physics and astrophysics community. We shall briefly discuss the issue of pulsar emission at the end of this review.

We have discussed in the introduction that the central part of supernova remnant will be a neutron star if the mass of the progenitor is high enough. The density of matter at the core region in such objects is $\sim 10^{15} - 10^{16} \text{ gm/cc}$. To describe the chemical composition of a typical neutron star, let us start with an initial system, which we shall gradually compress to increase the density, consists of fully ionized ^{56}Fe and a degenerate electron gas. Now as the density increase by the gravitational contraction of the system, electrons are captured by the protons of iron nuclei and more and more neutron

rich nuclei are produced, which are unstable under normal condition (β active nuclei). However, under such extreme condition (density $\sim 10^9 \text{ gm/cc}$) they are stable as most of the energy levels of degenerate electrons are already filled up. At matter density $\sim 10^{11} \text{ gm/cc}$, the binding energy of neutrons becomes zero. Neutrons begin to come out from the neutron rich nuclei (neutron drip)- free neutrons now appear as a new component of the gas. As the compression proceed further, at about density $\sim 10^{13} \text{ gm/cc}$, the density of neutrons in between nuclei increases, and eventually equals the density of neutrons in nuclei. The nuclei then merge to form a uniform fluid consisting mainly of neutrons with a few percent of protons and enough electrons to ensure electrical neutrality ($n_p = n_e$). This is the neutron matter from which neutron stars are mostly made. The stability of a neutron star is governed by the degeneracy pressure of dense neutron matter (this is repulsive in nature). However, in the case of white dwarfs, the corresponding repulsive pressure comes from the degenerate electron gas. In a typical neutron star, the central density $> 10^{14} \text{ gm/cc}$, and almost all the electrons have combined with protons to make neutrons; $n_e = n_p \approx 0.03 n_n$, hence the name *neutron star*. These stars are very compact, with masses \sim a few times M_\odot and radii $R \sim 10 \text{ km}$.

Now at still higher densities, when the magnitude of electron Fermi momentum exceeds the muon rest mass, it becomes energetically favorable to produce negatively charged muons instead of electrons. In this case, the charge neutrality condition demands $n_p = n_e + n_\mu$ [6, 7].

With the further increase of matter density, the chemical potential of nucleons become comparable with the masses of hyperons. In that case more and more massive hyperons are produced in dense neutron star matter. It is also likely to have superfluid neutron matter with the droplets of superconducting proton matter. A bit exotic phenomena, e.g., pion and kaon condensation are also expected in such dense neutron star matter. In the extreme case, if the density of matter at the core exceeds a few times normal nuclear density, it is possible that the hadrons (neutrons, protons, etc) merge together and form an infinite cluster of quark matter- which gives rise to quark stars, strange stars or hybrid stars [7]. Some people believe that charge neutral and color neutral multi-quark cluster, known as color flavor locked (CFL) states are more favorable energetically than quark matter or strange quark matter (we will not discuss these exotic phenomena in these lectures and only concentrate on normal interacting neutron star matter). We can not hope to review the range of physics necessary for a complete understanding of evolution and the gross properties of neutron stars in these lectures. However, we can isolate the essential role of gravity and the equation of states to investigate some of the gross features of neutron stars.

3 Structure of Neutron Stars

3.1 Hydrostatic Equilibrium

In the case of a white dwarf, the mass will be maximum for $\rho_c \approx 10^9 \text{ gm/cc}$, and is $\sim 1.46 M_\odot$, the radius $R \sim 3.1 \times 10^8 \text{ cm}$. Then it is very easy to show that the ratio of gravitational potential to the square of velocity of light at the surface is given by $\epsilon = GM/(c^2 R) \approx 10^{-4}$ and this value is typical throughout the star. Thus, general relativity is of little relevance to the structure of white dwarfs. On the other hand, in the

case of a neutron star of mass $\sim 1.4M_\odot$, radius $\sim 10\text{km}$, the ratio $\epsilon \approx 0.1$, relativistic gravity is therefore important for the structure of neutron stars. Now the usual simplest structure of a neutron star is spherically symmetric, static and out side is considered to be vacuum (density of radiation if any is extremely low compared to matter density). If we therefore consider gravitational field in vacuum produced by a centrally symmetric distribution of mass (the mass distribution may be static or there may exist motion along the radial direction, e.g., radial contraction, expansion or vibration, but no rotation), the line element is given by

$$ds^2 = \left(1 - \frac{2M}{r}\right) dt^2 - \left(1 - \frac{2M}{r}\right)^{-1} dr^2 - r^2(d\theta^2 + \sin^2\theta d\phi^2) \quad (1)$$

and is called Schwarzschild exterior line element, obtained by K. Schwarzschild in 1916 (published in German from Berlin). Here M is the total mass of the star. The interior line element is given by

$$ds^2 = e^{2\Phi} dt^2 - e^{2\lambda} dr^2 + r^2 d\Omega^2 \quad (2)$$

where Φ and λ are functions of r and t and $d\Omega^2 \equiv d\theta^2 + \sin^2\theta d\phi^2$ [9].

Geometrical Units

It is extremely convenient in general theory of relativity to choose units so that $c = G = 1$. In this choice of units, time is measured in cm: $1\text{cm} = 3 \times 10^{10}\text{cm}$. The mass is also expressed in length unit, e.g., $1\text{g} = 0.7425 \times 10^{-28}\text{cm}$. With this convention $M_\odot = 1.4766\text{km}$. The reason for choosing such system is that, the mass of the sun in km. is more accurately known than its mass in gms. These kind of choice of units is called geometrized units

The general relativistic version of hydrostatic stability equation for a spherically symmetric non-rotating neutron star can be obtained from the Einstein equation, given by

$$R_{\mu\nu} = 8\pi \left(T_{\mu\nu} - \frac{1}{2} g_{\mu\nu} T^\lambda_\lambda \right) \quad (3)$$

where the metric $g_{\mu\nu}$ is given by

$$g_{\mu\nu} = \begin{pmatrix} (1 - 2M/r) & 0 & 0 & 0 \\ 0 & -(1 - 2M/r)^{-1} & 0 & 0 \\ 0 & 0 & -r^2 & 0 \\ 0 & 0 & 0 & -r^2 \sin^2\theta \end{pmatrix} \quad (4)$$

The energy momentum tensor $T_{\mu\nu}$ is given by

$$T_{\mu\nu} = -Pg_{\mu\nu} + (P + \rho)u_\mu u_\nu \quad (5)$$

where $u_\mu u^\mu = 1$, P and ρ are kinetic pressure and matter density respectively. The components of Ricci tensor $R_{\mu\nu}$ are obtained with the Schwarzschild metric elements as defined above. Then we get from the Einstein's equation

$$\frac{dm}{dr} = 4\pi r^2 \rho(r) \quad (6)$$

$$\frac{dP}{dr} = -\frac{\rho(r)P(r)}{r^2} \left(1 + \frac{P(r)}{\rho(r)}\right), \left(1 + \frac{4\pi P(r)r^2}{m(r)}\right) \left(1 - \frac{2m(r)}{r}\right)^{-1}, \quad (7)$$

$$\frac{d\Phi}{dr} = -\frac{1}{\rho(r)} \frac{dP}{dr} \left(1 + \frac{P(r)}{\rho(r)}\right)^{-1} \quad (8)$$

eqn.(6) is called the Oppenheimer-Volkoff or Tolman, Oppenheimer-Volkoff equation (OV or TOV equation) [6, 8], the complementary mass equation has the interpretation of $m(r)$, mass inside radius r , Φ is the gravitational potential in the Newtonian limit. As it is evident that the Newtonian limit is recovered by taking $P \ll \rho$ and $m \ll r$, then we have after putting back the factors G and c , i.e., $m \rightarrow Gm/c^2$, $\rho \rightarrow G\rho/c^2$ and $P \rightarrow GP/c^2$

$$\frac{dm}{dr} = 4\pi r^2 \rho_0(r), \quad (9)$$

$$\frac{dP}{dr} = -\rho_0(r) \frac{Gm(r)}{r^2}, \quad (10)$$

$$\frac{d\Phi}{dr} = -\frac{1}{\rho_0} \frac{dP}{dr} = \frac{Gm(r)}{r^2} \quad (11)$$

where ρ_0 is the rest mass density, dominates in the Newtonian limit.

To solve numerically the TOV equation along with the supplementary mass equation, we follow the following steps:

- a) Choose a central density ρ_c . From the equation of state obtain P_c , the central pressure. Further $m(r=0) = 0$.
- b) Integrate eqns.(6) and (7) numerically from the centre ($r=0$) to the surface. During integration, each time a new value of P and from the equation of state ρ are obtained.
- c) Since pressure vanishes at the star's surface, the value $r=R$, the radius of the star is obtained for $P=0$, and the corresponding $m(r=R) = M$, the mass of the star.

The quantity $m(R)$ must equal M so that the interior metric coefficient

$$e^{2\lambda} \equiv \left(1 - \frac{2m}{r}\right)^{-1} \quad (12)$$

will match smoothly to the exterior Schwarzschild metric coefficient

$$e^{2\lambda} \equiv \left(1 - \frac{2M}{R}\right)^{-1} \quad (13)$$

We will further elaborate this issue, including the detailed numerical techniques and results in the discussion on the equation of states of neutron star matter. However, an

analytical solution of structure equations and some important results of neutron star gross properties can be obtained for the simplest case, the uniform matter density approximation, i.e., $\rho = \text{constant}$. In this case

$$M = M(R) = \frac{4\pi}{3}\rho R^3 \quad (14)$$

and

$$P(r) = \frac{3M}{4\pi R^2} \frac{\left(1 - \frac{2M}{R}\right)^{1/2} - \left(1 - \frac{2Mr^2}{R^3}\right)^{1/2}}{\left(1 - \frac{2Mr^2}{R^3}\right)^{1/2} - 3\left(1 - \frac{2M}{R}\right)^{1/2}} \quad (15)$$

with the boundary condition $P(r = R) = 0$. The most important feature of the above solution is that it necessarily imposes a constraint connecting the star's mass and radius. To obtain the constraint, we notice that the pressure at the centre (say at $r = r_0$) can be infinity provided

$$r_0^2 = 9R^2 - \frac{4R^3}{M} \quad (16)$$

and the only way to remove this unphysical result we need r_0 as given above be imaginary, i.e.,

$$\frac{M}{R} < \frac{4}{9} \quad (17)$$

This constraint is actually true for any equation of state. The same constraint can also be obtained directly from the Einstein field equation. The physical meaning of this constraint is that if you pack more mass for a star of fixed radius or contract a star of fixed mass so that the above inequality breaks, will destroy the hydrostatic equilibrium condition (due to increased gravitational attraction). The above constraint can be rewritten as

$$M^2 < \frac{16}{243\pi\rho} \quad (18)$$

Before we go over to the discussion of polytropic solution of neutron stars, let us go back to the Schwarzschild's exterior metric (eqn.(1)). There is obviously something interesting happening at the radii $r = 0$ and $r = R_s = 2M$. The latter is called the Schwarzschild radius. It is the characteristic length scale for curvature in the Schwarzschild geometry. Now in the case of normal stars and neutron stars, it has very little importance. In the case of sun $2M_\odot \approx 2.95\text{km}$, $\ll 6.96 \times 10^5\text{km}$, the solar radius, whereas in the case of a typical neutron star of radius 10km and $M \sim 1.4M_\odot$, this quantity ≈ 4 , which is about $2/5$ th of its radius. However, both $r = 0$ and $r = R_s$ are extremely important in the case of black holes. To show the importance of Schwarzschild radius in the case of black holes, we define the gravitational red shift in the form

$$\nu' = \nu \left(1 - \frac{2M}{R}\right)^{1/2} \quad (19)$$

where ν is the original frequency and ν' is the red shifted frequency of light. It is obvious that $\nu' = \nu$ for either M is very small or R is very large. Let us consider a star which is shrinking continuously because of its own gravity. As the radius R becomes

R_s , ν' goes to identically zero. Below this radius it is imaginary, which is unphysical. Therefore, R_s , the event horizon plays an extremely important role in this case. Now if we identify frequency with energy or mass of matter instead of ordinary radiation, the expression for red shift indicates even the matter (or mass) can not come out of a star whose radius $R \leq R_s$, called Schwarzschild black hole (of course Hawking radiation is there in the case of black holes. Which is purely quantum mechanical effect at the black hole surface). The quantity $r = 0$ is called the real physical singularity.

3.2 Newtonian Neutron Stars with Polytropic Equation of State

In the Newtonian limit, the energy density $\rho(r)$ is dominated by the rest mass density $\rho_0(r)$ of stellar matter. Moreover, the gravitational potential, defined by $2GM/r$ is everywhere small enough. Under such condition combining eqns.(9) and (10), the hydrostatic stability equation reduces to

$$\frac{1}{r^2} \frac{d}{dr} \left(\frac{r^2}{\rho_0} \frac{dP}{dr} \right) = -4\pi G \rho_0 \quad (20)$$

Now the polytropic equation of state is the simplest form of equation of state for stellar matter, given by

$$P = K \rho_0^\Gamma \quad (21)$$

which is nothing but the adiabatic equation of state with K and Γ are constants. Writing $\Gamma = 1 + 1/n$, where n is called the polytropic index, the equation can be reduced to dimensionless form by writing

$$\rho_0 = \rho_c \theta^n \quad (22)$$

$$r = a \xi \quad (23)$$

$$a = \left[\frac{(n+1)K \rho_c^{(1/n-1)}}{4\pi G} \right]^{1/2} \quad (24)$$

where $\rho_c = \rho_0(r = 0)$ is the central density. Then we have the hydrostatic stability equation

$$\frac{1}{\xi^2} \frac{d}{d\xi} \xi^2 \frac{d\theta}{d\xi} = -\theta^n \quad (25)$$

this equation is also called the Lane-Emden equation for the structure of a polytrope of index n . Since it is a second order differential equation, for the unique solution we need two boundary conditions. For the polytropic star they are given by $\theta(0) = 1$ and $\theta'(0) = 0$

This differential equation can very easily be integrated numerically with the initial conditions as mentioned above, starting from $\xi = 0$. It is easy to check that only for $n < 5$ ($\Gamma > 6/5$), the solution decreases monotonically and go to zero at a finite value $\xi = \xi_1$ (say). The point corresponds to the stars surface where $\rho_0 = P = 0$. Hence the radius of the star is given by

$$R = \left[\frac{(n+1)K}{4\pi G} \right]^{1/2} \rho_c^{(1-n)/2} \xi_1 \quad (26)$$

and the mass is given by

$$M = 4\pi \left[\frac{(n+1)K}{4\pi G} \right]^{1/2} \rho_c^{(3-n)/2} \xi_1^2 | \theta'(\xi_1) | \quad (27)$$

Then by eliminating the central density ρ_c from the above two equations, we get the mass-radius relation

$$M = 4\pi R^{(3-n)/(1-n)} \left[\frac{(n+1)K}{4\pi G} \right]^{n/(n-1)} \xi_1^{(3-n)/(1-n)} \xi_1^2 | \theta'(\xi_1) | \quad (28)$$

The special solutions are for low density non-relativistic and high density ultra-relativistic cases, given by

$$1. \quad \Gamma = \frac{5}{3}, \quad n = \frac{3}{2}, \quad \xi_1 = 3.65375, \quad \xi_1^2 | \theta'(\xi_1) | = 2.71406, \quad (29)$$

$$2. \quad \Gamma = \frac{4}{3}, \quad n = 3, \quad \xi_1 = 6.89685, \quad \xi_1^2 | \theta'(\xi_1) | = 2.01824 \quad (30)$$

respectively. From these two equations we get for white dwarfs

$$R \approx 1.22 \times 10^4 \left(\frac{\rho_c}{10^6 \text{ gm cm}^{-3}} \right)^{-1/6} \text{ km} \quad (31)$$

$$M \approx 0.7011 \left(\frac{R}{10^4 \text{ km}} \right)^{-3} M_\odot \quad (32)$$

and for neutron stars

$$R \approx 3.347 \times 10^4 \left(\frac{\rho_c}{10^6 \text{ gm cm}^{-3}} \right)^{-1/3} \text{ km} \quad (33)$$

$$M \approx 1.457 M_\odot \quad (34)$$

In this case the maximum mass is independent of ρ_c and R . This limiting value of neutron star mass is the well known Chandrasekhar mass.

Now it is very easy to find that the total gravitational energy E_g of the system is given by

$$E_g = -\frac{3}{5-n} \frac{GM^2}{R} \quad (35)$$

and the total internal energy E_i is expressed by the formula

$$E_i = \frac{n}{5-n} \frac{GM^2}{R} \quad (36)$$

Therefore, the total energy of the system, $E = E_i + E_g$, is

$$E = \frac{n-3}{5-n} \frac{GM^2}{R} = -\frac{3\Gamma-4}{5\Gamma-6} \frac{GM^2}{R} \quad (37)$$

Hence the systems with $\Gamma > 4/3$ are energetically stable, while those with $\Gamma < 4/3$ are unstable. The stability criterion as mentioned is obtained from Newtonian gravity.

In the case of Newtonian theory of radial pulsation against small radial perturbation, the study of normal mode vibration of the star's surface, the fundamental frequency ω is given by

$$\omega^2 \approx \overline{(3\Gamma - 4)} \frac{E_g}{I} \quad (38)$$

where \overline{X} denotes the average over the whole volume and I is the moment of inertia of the star with respect to the centre. The system is therefore dynamically stable when $\omega^2 > 0$, i.e., when $\overline{\Gamma} > 4/3$. However, the general relativistic criterion is different and was discovered by Chandrasekhar and Fowler [10]. According to their calculation a star becomes unstable with respect to radial oscillation when its radius R falls below the critical value R_{cr} , with

$$R_{cr} = \frac{\alpha M}{\Gamma - \frac{4}{3}} \quad (39)$$

when $\alpha \approx 1$ a numerical constant and obtained from the Newtonian structure of the star. Therefore, in general relativity a star can become unstable even where $\Gamma > 4/3$, the stability criterion for the Newtonian gravity. These conclusions are valid for all kinds of equation of states.

Therefore, the adiabatic index Γ is important so far the stability against radial pulsation is concerned. The prediction is of course purely Newtonian in nature. The inclusion of general relativity changes the result significantly. As we will see in the next section on the discussion of equation of states, that in general relativity a neutron star can become unstable against collapse beyond some central density. The derivative $dM/d\rho_c$ is in general a positive quantity (M increase with ρ_c), but beyond some maximum value (which of course depends on the type of equation of state), say $\rho_c^{(\max)}$ it becomes negative. Such bending in $M - \rho_c$ curve is not observed in the Newtonian gravity. It can also be shown in general relativity that instability can appear long before a star can approach its theoretically permitted radius (the event horizon radius or Schwarzschild radius), which is 9/8 times the Schwarzschild radius and is because of purely general relativistic effect.

4 Equation of States of Neutron Star Matter

The relation between kinetic pressure and energy density or mass density is known as the equation of state of matter. This is the main input necessary to study gross properties of neutron stars. We have already introduced the simplest form of equation of state for dense stellar matter in eq.(21), known as polytropic equation, which is nothing but the adiabatic form of equation of state of matter. In this lecture note although we shall concentrate mainly on the equation of state of dense neutron star matter, however, for the sake of completeness, we shall first briefly discuss various kinds of equation of states for different values of matter density. First we shall discuss the types of equation of states used for matter densities below neutron drip. The simplest form is the Chandrasekhar's ideal electron gas equation of state, valid for the matter density range $0 \leq \rho \leq \infty$, where ρ is expressed in gm/cc. The constituents are fully ionized atoms and free electrons of chemical potential μ_e , fixed by the density of electrons [11]. Feynman-Metropolis-Teller equation of state is used for the density range

$7.9 \leq \rho \leq 10^4$. The ingredients are e^- and ^{56}Fe nuclei. The model used is Thomas-Fermi-Dirac model [12]. Harrison and Wheeler proposed the equations of state for the density ranges a) $7.9 \leq \rho \leq 10^4$, same as ref. [12] with the same matter composition as mentioned above, b) for $10^4 \leq \rho \leq 10^7$ with e^- and ^{56}Fe nuclei in equilibrium. The model used is non-interacting electrons in presence of positive background of iron nuclei and finally c) for $10^7 \leq \rho \leq 10^{11}$ with e^- and heavy nuclei in equilibrium, the model used is *Semi-empirical mass formula; and matter is in equilibrium* [13]. The equations of state proposed by Baym-Pethick-Sutherland: density ranges a) $7.9 \leq \rho \leq 10^4$ is same as ref [12], b) for $10^4 \leq \rho \leq 8 \times 10^6$, with ingredients e^- and ^{56}Fe nuclei, the theory used is ideal electron gas with Coulomb lattice corrections and finally c) for $8 \times 10^6 \leq \rho \leq 4.3 \times 10^{11}$, the ingredients are e^- and equilibrium nuclide, the theory used is the extrapolation of laboratory nuclear energies and the inclusion of Coulomb lattice energy correction for matter in equilibrium [14]. Now above neutron drip, the Harrison-Wheeler equation of state is used based on the theory of non-interacting electron gas, semi-empirical mass formula for the matter in equilibrium. Before we go to the detailed discussions on the mean field type equation of state for dense neutron star matter, we shall now briefly introduce the type of equation of states along with the many body theory used for dense stellar matter above neutron drip. Baym-Bethe-Pethick equation of state is used for the density range $4.3 \times 10^{11} \leq \rho \leq 5 \times 10^{14}$ with the composition, e^- , neutrons and nuclide in equilibrium. The Reid soft core interaction is used. The many body theory is based on *mass formula for nuclei constructed from compressible liquid-drop model* [15]. Pandharipande used reid soft core interaction adapted to nuclear matter to obtain equation of state for stellar matter of density $\rho > 7 \times 10^{14}$. The constituents are mainly neutrons and the many body theory is based on the *Variational principle applied to correlation function* [16]. The famous Bethe-Johnson equation of state is used for the density range $1.7 \times 10^{14} \leq \rho \leq 3.2 \times 10^{16}$ with modified Reid soft core interaction and *Constrained variational method* type mean field model. The constituents are $n, p, e^-, \Lambda, \Sigma^{\pm,0}, \Delta^{\pm,0}$ and Δ^{++} [17]. Using pion exchange tensor interaction model in dense neutron star matter the equation of state was obtained by Pandharipande and Smith [18] and is applicable for $\rho > 8.4 \times 10^{13}$. The many body technique used is also constrained variational method. Using three nucleon interaction the equation of state for dense neutron star matter was obtained by Friedman and Pandharipande for $\rho > 1.7 \times 10^{14}$ with the same many body technique as mentioned above [19]. Pandharipande and Smith also obtained an equation of state for dense neutron star matter with nuclear attraction due to scalar exchange and is valid for $\rho > 4.4 \times 10^{11}$. The many body technique used is called mean field approximation for scalar with variational method [20]. Finally the most successful model for neutron matter equation of state was obtained by Walecka and is known as relativistic mean field approximation model or Walecka model [21]. In this model scalar boson σ and vector boson ω exchange is considered. Later the model was successful modified by including ρ mesons and pions. The mean field model is also used for more exotic type neutron star matter, viz., pion and kaon condensed matter, quark matter etc.

4.1 Simplest Model

Now before we go into the detailed discussion on mean field theory of (normal) neutron star, we consider the most simplest, the ideal Fermi gas model of neutron star matter. This model will help us to explain how to solve TOV equation numerically using some equation of state. For more realistic models, however, the numerical technique to solve TOV equation does not change much. This simple Fermi gas model was used by Oppenheimer and Volkoff and obtained neutron star mass and radius numerically. To explain how to get these values, let us assume that the neutron star matter contains only free neutrons. Then the matter density is given by

$$\rho = \frac{1}{\pi^2} \int_0^{k_F} (k^2 + m^2)^{1/2} k^2 dk \quad (40)$$

where k_F is the neutron Fermi momentum in MeV related to the number density n_N by the relation

$$k_F = (3\pi^2 n_N)^{1/3} \quad (41)$$

and the choice of units ($\hbar = c = 1$) gives ρ in MeV^4 . Similarly the pressure is given by

$$P = \frac{1}{3\pi^2} \int_0^{k_F} \frac{k^2}{(k^2 + M_N^2)^{1/2}} k^2 dk \quad (42)$$

where M_N is the neutron mass expressed in MeV.

To solve TOV equation (eqns.(6) and (7)) numerically we proceed in the following manner:

- a) Choose some neutron matter density (which is several times normal nuclear density) and obtained k_F .
- b) Evaluate ρ and P .
- c) Repeat it for a large number of densities upto some sub-nuclear value.
- d) Express ρ and P in erg and dyne/cc respectively.
- e) Obtain the tabulated form of P vs ρ after multiplying each number by G/c^2 . Which will convert them into proper units ($G = c = 1$).
- f) Obtain an extrapolated or some functional form of $P = P(\rho)$
- g) Choose some central density (within the extrapolated range) and obtain P .
- h) Choose the initial condition $m = 0$ for $r = 0$ and use Runge-Kutta method to solve the differential equations eqns.(6) and (7) simultaneously in small steps of r , the radius parameter. Obtain ρ (and then P from the equation of state) and m for the next step. Repeat the same numerical technique by replacing the initial conditions by the second step values. Continue the step by step numerical integration unless P becomes zero (in actual numerical calculation, depending on the type of equation of state, the pressure may not become zero, in that case it is necessary to introduce some cut off value for kinetic pressure). When P becomes zero, the value of radius parameter $r = R$ (say) will be the radius of neutron star and $m = M$ (say) will be the corresponding mass. In the units chosen, both R and M are expressed in km.
- i) Repeat the step h) for a number of central densities (from several times normal nuclear density to sub-nuclear density) and plot M/M_\odot against ρ_c , the central density.

A typical variation is shown in Fig. 2. It is obvious from the figure that initially the mass M increases with ρ_c ($dM/d\rho_c > 0$), but beyond some maximum value, say ρ_c^{\max} $dm/d\rho_c < 0$. The value ρ_c^{\max} is the maximum allowed central density for the type of equation of state considered. For the central density $> \rho_c^{\max}$, the system becomes gravitationally unstable. This is true for TOV equation only and does not show such behavior in the Newtonian approximation.

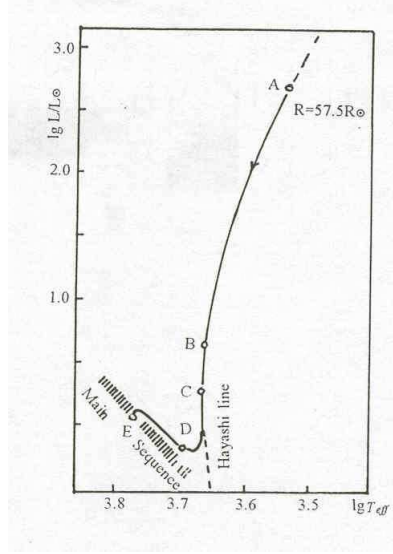


Fig. 2. H-R and Hayashi line.

4.2 n-p-e in β -Equilibrium

Now in reality the neutron star matter can not be a pure neutron matter. In the simplified picture, we assume it to be a mixture of neutron (n), proton (p) and electron (e) in dynamic equilibrium, governed by the equations

$$n \rightarrow p + e + \bar{\nu}_e \quad p + e \rightarrow n + \nu_e \quad (43)$$

where ν_e and $\bar{\nu}_e$ are electron type neutrinos and anti-neutrinos respectively, which are assumed to be non-degenerate, i.e., they leave the system as soon as they are produced (These weak interaction processes are called URCA processes). Then the chemical equilibrium condition gives

$$\mu_n = \mu_p + \mu_e \quad (44)$$

where μ_i 's are the chemical potentials. Under such circumstances, the system is called in β -equilibrium. In the case of trapped neutrinos inside neutron star matter, the chemical potentials of neutrinos and anti-neutrinos will also contribute (with $\mu_{\nu_e} = -\mu_{\bar{\nu}_e}$).

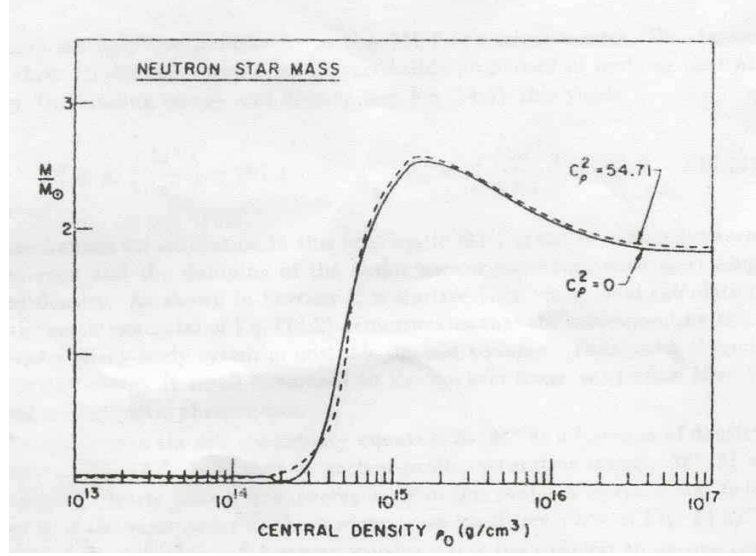


Fig. 3. $M - \rho_c$ Diagram.

The other conditions which are satisfied are charge neutrality and baryon number conservation, given by

$$n_p = n_e \quad n_B = n_n + n_p \quad (45)$$

respectively. Solving these three equations numerically one can get the chemical potentials and hence the equation of states. The rest of the calculations remain same as mentioned above.

4.3 Relativistic Mean Field Model

So far we have considered only free neutron star matter. To obtain the equation of state of interacting neutron star matter at zero temperature (since the actual temperature $\approx 10\text{MeV} \ll$ the degeneracy temperature of the system, we can safely assume it to be at zero temperature) we start with the following field:

- i) A baryon field $\psi(x)$ for the neutrons and protons (presence of other massive hyperons will be discussed briefly latter).
- ii) A neutral scalar field $\sigma(x)$ coupled with the scalar density $n_s = \bar{\psi}\psi$.
- ii) A neutral vector field $\omega^\mu(x)$ coupled to the conserved vector field $j^\mu = \bar{\psi}\gamma^\mu\psi$ (isovector field ρ will be discussed at the end of this section).

The total Lagrangian of the system is then given by

$$\begin{aligned} \mathcal{L} = & \bar{\psi} [i\gamma_\mu (\partial^\mu + ig_\omega \omega^\mu) - (m - g_\sigma \sigma)] \psi \\ & + \frac{1}{2} (\partial_\mu \sigma \partial^\mu \sigma - m_\sigma^2 \sigma^2) - \frac{1}{4} \omega_{\mu\nu} \omega^{\mu\nu} + \frac{1}{2} m_\omega^2 \omega_\mu \omega^\mu \end{aligned} \quad (46)$$

where $\omega_{\mu\nu} = \partial_\mu \omega_\nu - \partial_\nu \omega_\mu$ as in classical electrodynamics. Then we have from the Euler-Lagrange equations

$$(\square + m_\sigma^2)\sigma = g_\sigma \bar{\psi}\psi \quad (47)$$

$$(\square + m_\omega^2)\omega_\mu = g_\omega \bar{\psi}\gamma_\mu\psi \quad (48)$$

and

$$[\gamma_\mu(i\partial^\mu - g_\omega\omega^\mu) - (m - g_\sigma\sigma)]\psi = 0 \quad (49)$$

We now make an approximation, known as the *relativistic mean-field approximation*. The matter is assumed to be static, uniform and in the ground state. Then we replace the fields by their average values, given by

$$m_\sigma^2 \langle \sigma \rangle = g_\sigma \langle \bar{\psi}\psi \rangle, \quad (50)$$

$$m_\omega^2 \langle \omega_0 \rangle = g_\omega \langle \psi^\dagger\psi \rangle, \quad (51)$$

$$m_\omega^2 \langle \omega_k \rangle = g_\omega \langle \bar{\psi}\gamma_k\psi \rangle \quad (52)$$

In the momentum space, the Dirac equation reduces to

$$(\gamma^\mu K_\mu - m^*)\psi(K) = 0 \quad (53)$$

where

$$k^\mu \rightarrow K^\mu = k^\mu - g_\omega\omega^\mu \text{ and } m^* = m - g_\sigma\sigma \quad (54)$$

the canonical four momentum and the effective baryon mass. Then we can write

$$K_0 = E(\mathbf{k}) = (\mathbf{K}^2 + m^{*2})^{1/2} \quad (55)$$

$$k_0(\mathbf{k}) = \varepsilon(\mathbf{k}) = E(\mathbf{k}) + g_\omega\omega_0 \quad (56)$$

$$E(\mathbf{k}) = ((\mathbf{k} - g_\omega\boldsymbol{\omega})^2 + (m - g_\sigma\sigma)^2)^{1/2} \quad (57)$$

Since we are dealing with the ground state of uniform static matter, it is obvious from the equation of motion of the vector field ω^μ that the spatial components ω^i should vanish every where in the system. Then

$$\varepsilon(\mathbf{k}) = E(\mathbf{k}) + g_\omega\omega_0 = (\mathbf{k}^2 + (m - g_\sigma\sigma)^2)^{1/2} \quad (58)$$

Then

$$g_\sigma\sigma = \left(\frac{g_\sigma}{m_\sigma}\right)^2 n_s \quad (59)$$

$$= \left(\frac{g_\sigma}{m_\sigma}\right)^2 \sum_{i=n}^p \frac{g_i}{2\pi^2} m^* \int_0^{k_{F_i}} k^2 dk \frac{1}{(k^2 + m^{*2})^{1/2}} \quad (60)$$

$$g_\omega\omega_0 = \left(\frac{g_\omega}{m_\omega}\right)^2 n_B \quad (61)$$

$$= \left(\frac{g_\omega}{m_\omega}\right)^2 \sum_{i=n}^p \frac{g_i}{2\pi^2} \int_0^{k_{F_i}} k^2 dk \quad (62)$$

$$\omega_k = 0 \quad (63)$$

Using all these results, we have the energy density

$$\epsilon = \sum_{i=n,p,e} \epsilon_i + \epsilon_\sigma + \epsilon_\omega \quad (64)$$

where

$$\epsilon_i = \frac{g_i}{2\pi^2} \int_0^{k_{Fi}} k^2 dk (k^2 + m^{*2})^{1/2} \quad (65)$$

here $i = n$ and p . For freely moving electrons

$$\epsilon_e = \frac{g_e}{2\pi^2} \int_0^{k_{Fe}} k^2 dk (k^2 + m_e^2)^{1/2} \quad (66)$$

and

$$\epsilon_\sigma = \frac{1}{2} m_\sigma^2 \sigma^2, \quad \epsilon_\omega = \frac{1}{2} m_\omega^2 \omega_0^2 \quad (67)$$

Similarly the pressure is given by

$$\begin{aligned} P = & -\frac{1}{2} m_\sigma^2 \sigma^2 + \frac{1}{2} m_\omega^2 \omega_0^2 + \frac{g_e}{6\pi^2} \int_0^{k_{Fe}} \frac{k^2}{(k^2 + m_e^2)^{1/2}} k^2 dk \\ & + \sum_{i=n,p} \frac{g_i}{6\pi^2} \int_0^{k_{Fi}} \frac{k^2}{(k^2 + m^{*2})^{1/2}} \end{aligned} \quad (68)$$

These two expressions can also be written in the following form

$$\epsilon = \frac{g_\omega^2}{2m_\omega^2} n_B^2 + \frac{m_\sigma^2}{2g_\sigma^2} (m - m^*)^2 + \sum_{i=n,p} \frac{g_i}{2\pi^2} \int_0^{k_{Fi}} k^2 dk (k^2 + m^{*2})^{1/2} + \epsilon_e \quad (69)$$

and

$$P = \frac{g_\omega^2}{2m_\omega^2} n_B^2 - \frac{m_\sigma^2}{2g_\sigma^2} (m - m^*)^2 + \sum_{i=n,p} \frac{g_i}{6\pi^2} \int_0^{k_{Fi}} \frac{k^4 dk}{(k^2 + m^{*2})^{1/2}} + P_e \quad (70)$$

The equations for m^* along with the conservation of baryon number n_B , the charge neutrality condition (eqn.(45)) and the chemical equilibrium conditions among the constituents (eqn.(44)) ($n - p - e$, assuming neutrinos / anti-neutrinos are non-degenerate) are solved self-consistently to obtain $\mu_i, i = n, p$ and e and m^* , using the constants $g_\sigma^2(m^2/m_\sigma^2) = 267.1$ and $g_\omega^2(m^2/m_\omega^2) = 195.9$. With these quantities if we evaluate energy density and pressure of neutron star matter for various baryon densities, we get the relativistic mean field equation of state with $\sigma - \omega$ meson exchange. Now following the same method as discussed for the free neutron star matter, it is possible to solve numerically the TOV equation and study the gross properties of neutron stars.

4.4 Iso-Vector Interaction

We shall now introduce the iso-vector (ρ_μ) meson exchange- a triplet of mesons of the same mass and charges ($0, \pm 1$), they couple to the iso-spin current of the nucleon, given by

$$I_\tau^\mu = \frac{1}{2} \bar{\psi} \gamma^\mu \boldsymbol{\tau} \psi \quad (71)$$

Here in the matrix representation, the components of $\boldsymbol{\tau}$, the iso-spin three vector are given by standard 2×2 -Pauli matrices. The corresponding interaction part of the Lagrangian is given by

$$\mathcal{L} = -g_\rho \rho_\mu \cdot \mathbf{I}^\mu \quad (72)$$

Now only those components of ρ_μ in the iso-spin space will exist as iso-vector field which have non-zero mean values in the ground state of matter at a given baryon density. The first two components of the iso-spin vector $\boldsymbol{\rho}$ can be expressed as a combination of raising and lowering operators of charged ρ -mesons, therefore, their ground state expectation values vanish. Hence only $\rho_3^\mu \neq 0$. Now by the same argument with which only $\omega_0 \neq 0$, leaving only ρ_3^0 non-vanishing. Then the equation of motions are

$$g_\rho \rho_3^0 = \frac{1}{2} \left(\frac{g_\rho}{m_\rho} \right)^2 \langle \bar{\psi} \gamma^0 \tau_3 \psi \rangle = \left(\frac{g_\rho}{m_\rho} \right)^2 \frac{1}{2} (n_p - n_n) \quad (73)$$

$$g_\rho \rho_3^k = \frac{1}{2} \left(\frac{g_\rho}{m_\rho} \right)^2 \langle \bar{\psi} \gamma^k \tau_3 \psi \rangle = 0 \quad (74)$$

and

$$[\gamma_\mu (k^\mu - g_\omega \omega^\mu - \frac{1}{2} g_\rho \tau_3 \rho_3^\mu) - (m - g_\sigma \sigma)] \psi = 0 \quad (75)$$

Then the energy eigen values

$$\begin{aligned} \varepsilon_{I_3} &= g_\omega \omega^0 + g_\rho \rho_3^0 I_3 + E \\ E &= [k^2 + (m - g_\sigma \sigma)^2]^{1/2} \end{aligned} \quad (76)$$

where $I_3 = +1/2$ for proton and $-1/2$ for neutron. The energy density and pressure will also be modified due to the presence of ρ -meson exchange, a term $1/2(m_\rho^2 \rho_{03}^2)$ has to be added in both the expressions (eqns.(64) and (68)).

Now at very high density, if $\mu_{n,p}$ exceeds the masses of hyperons, then it is energetically favorable to produce new hyperons in the system through strong interaction processes. In presence of many baryons (indicated by B), we have

$$m_\omega^2 \omega_0 = \sum_B g_{\omega B} n_B \quad (77)$$

$$m_\rho^2 \rho_{03} = \sum_B g_{\rho B} I_{3B} \rho_B \quad (78)$$

$$m_\sigma^2 \sigma = \sum_B \frac{g_B}{2\pi^2} g_{\sigma B} \int_0^{k_{FB}} \frac{m_B - g_{\sigma B} \sigma}{[k^2 + (m_B - g_{\sigma B} \sigma)^2]^{1/2}} k^2 dk \quad (79)$$

and

$$[\gamma_\mu (k^\mu - g_{\omega B} \omega^\mu - \frac{1}{2} g_{\rho B} \boldsymbol{\tau} \cdot \boldsymbol{\rho}^\mu) - (m_B - g_{\sigma B} \sigma)] \psi_B = 0 \quad (80)$$

In this case the expressions for pressure and energy density have to be properly modified. The sum over $i = n, p$ in both the expressions have to be replaced by the sum over B - all the baryons present in the system. The conserved quantities are now *baryon number*, *charge* and *strangeness content in strong interaction processes*. The modified form of β -equilibrium condition has to be considered along with the conserved quantities as mentioned above to solve self-consistently for σ , m_B 's and μ_B , for all possible B . In this case the equilibrium among the baryons produced / destroyed through strong interaction processes along with the possible weak decay / reaction processes have to be taken into account to setup constraint equations connecting the chemical potentials (μ_B) and solve them numerically. Hence obtain the equation of states and use it to solve TOV equation with such complex chemical composition.

5 Pulsars- Rotating Magnetized Neutron Stars

For the sake of completeness, let us now consider rotating magnetized neutron stars, known as pulsars. The first pulsar was discovered by Hewish et. al. in 1967 [22] (see also [6]) and since then a large number of them have been discovered through various kinds of astronomical observations. Pulsars are emitters of radio signals in pulses with time period ranging from a few second to a few mill-second. One of the pulsar with period 0.033 sec is the crab pulsar, situated at the centre of crab nebula, expanding gas cloud and is the remnant of supernova explosion observed by Chinese astronomer in the year 1053 A.D.

There are theoretical proof that the pulsars are rotating neutron stars, not the rotating white dwarfs. The emitted radio signals are originated from the rotation of magnetized neutron stars. During the formation of neutron stars by supernova explosion, the conservation of magnetic flux can produce a neutron star magnetic field whose strength at the surface can be as large as $\sim 10^{12}\text{G}$. Therefore, for a distant observer, the rotating magnetized neutron star is just like a rotating magnetic moment. Now if the magnetic axis is not aligned with the rotation axis, by Synchrotron mechanism electromagnetic waves will be emitted along the specific direction. The interpretation of pulsars as rotating, magnetized neutron stars was given by Gold [23]. Let us therefore assume that each pulse is a bunch of electromagnetic waves and the direction of emission is rigidly fixed with the body of rotating neutron star (rigid rotor). Then as the star rotates, so does the beam and every time it sweeps past the observatory on the earth's surface and we observe a periodic pulse of electromagnetic radiation. The interval between successive pulses is equal to the rotational period of a pulsar. Therefore, before we switch over to the discussion on strongly magnetized neutron stars, we may conclude that neutron stars are one of the natural laboratory for many branches of physics at extreme condition.

6 Strongly Magnetized Neutron Stars

6.1 Introduction

The study of dense stellar matter under ultra-strong magnetic field has gotten a new life after the discovery of a few magnetars [24–27] (also see [28]). These stellar objects are

believed to be strongly magnetized young neutron stars. The surface magnetic fields are observed to be $\geq 10^{15}\text{G}$. Then it is quite possible that the field at the core region may go up to 10^{18}G . The exact source of this strong magnetic field is not known. These objects are also supposed to be the possible sources of anomalous X-ray and soft gamma emissions (AXP and SGR). If the magnetic field is really so strong, in particular at the core region, they must affect most of the important physical properties of such stellar objects. The elementary processes, e.g., weak and electromagnetic processes taking place at the core region should also change significantly.

The strong magnetic field affects the equation of state of dense neutron star matter and as a consequence the gross-properties of neutron stars [29–32], e.g., mass-radius relation, moment of inertia, rotational frequency etc. should change significantly. In the case of compact neutron stars, the phase transition from neutron matter to quark matter at the core region is also affected by strong quantizing magnetic field. It has been shown that a first order phase transition initiated by the nucleation of quark matter droplets is absolutely forbidden if the magnetic field $\sim 10^{15}\text{G}$ at the core region [33, 34]. However a second order phase transition is allowed, provided the magnetic field strength $< 10^{20}\text{G}$. This is of course too high to achieve at the core region.

The elementary processes, in particular, the weak and the electromagnetic processes taking place at the core region of a neutron star are strongly affected by such ultra-strong magnetic field [35, 36]. Since the cooling of neutron stars are mainly controlled by neutrino/anti-neutrino emission, the presence of strong quantizing magnetic field should affect the thermal history of strongly magnetized neutron stars. Further, the electrical conductivity of neutron star matter which directly controls the evolution of neutron star magnetic field will also change significantly.

In another kind of work, the stability of such strongly magnetized rotating objects are studied. It has been observed from the detailed general relativistic calculation that there are possibility of some form of geometrical deformation of these objects from their usual spherical shapes [37–39]. In the extreme case such objects may either become black strings or black disks. In the non-extreme case, however, it is also possible to detect gravity waves from these rotating objects.

In a recent study of microscopic model of dense neutron star matter, we have observed that if most of the electrons occupy the zeroth Landau level, with spin anti-parallel to the direction of magnetic field and very few of them are with spin along the direction of magnetic field and Landau quantum number > 0 , then either such strongly magnetized system can not exist or such a strong magnetic field can not be realized at the core region of a neutron star [40]. We have shown in that work that since the electrical conductivity of the medium becomes extremely low in presence of ultra-strong magnetic field, the magnetic field at the core region must therefore decay very rapidly. Hence we have argued that the second possibility is more feasible, i.e., strong magnetic field can not exist at the core of a magnetar.

So far most of the calculations on the equation of states of dense stellar matter in presence of strong magnetic field are either based on some kind of mean field approximation or non-relativistic potential model [30, 41]. In this paper we shall derive an exact formalism of relativistic version of Landau theory of Fermi liquid in presence of strong quantizing magnetic field and obtain the quasi-particle energy for both scalar and vector

coupling cases. We shall consider a typical many body fermionic system in presence of strong magnetic field interacting via some kind of scalar and vector bosons exchange. Therefore from this investigation it is very easy to obtain equation of state of a real fermion system in presence of strong magnetic field, e.g., high density electron gas (with photon exchange), dense neutron star matter (with $\sigma - \omega - \rho$ meson exchange) or even dense quark matter produced at the core region as a result of quark-hadron phase transition (exchange of color gluons). Not only that, one can study the magnetic as well as the non-equilibrium properties of such dense fermionic system as mentioned above. The relativistic version of this model without magnetic field was developed long ago by Baym and Chin [42]. So far most of the scattering or reaction or decay rates/cross-sections are evaluated either with very low magnetic field approximation or in presence of ultra-strong magnetic field. To the best of our knowledge the present article is the first attempt to develop an exact theoretical formalism to obtain the two-body scattering matrix element (both direct and exchange) for all possible strengths of external magnetic field. In a completely different type of work we have used this formalism to obtain the rates of weak and electro-magnetic processes. We have investigated the effect of strong magnetic field on the emissivities and mean free paths of neutrinos / anti-neutrinos and electrical conductivity of dense electron gas in neutron star matter. These quantities play significant role in thermal evolution and the evolution of magnetic fields of neutron stars respectively.

Now similar to the conventional non-relativistic case, the relativistic version also deals with normal Fermi liquid and applicable only for the low-lying excited states of the system, which are made of superpositions of quasi-particle excitations close to the Fermi surface. The relativistic version is therefore applicable to high density electron gas, dense neutron star matter and also to dense quark matter which may present at the core region of compact neutron stars. For the applicability of this model the temperature of the systems are therefore assumed to be low enough compared to the chemical potential of the constituents.

The paper is organized in the following manner. In the next section we shall develop an exact formalism for the relativistic version of Landau theory of Fermi liquid considering a typical many body fermionic system interacting via some kind of scalar and vector boson exchange field. In the last section we have discussed the results and future prospects of the work.

6.2 Formalism

We have considered a dense relativistic fermionic system at zero temperature ($T \ll \mu_f$, the chemical potential of the fermions) and interacting via scalar and vector boson fields represented by ϕ and V^μ respectively with masses ζ and η respectively. The corresponding coupling constants with the fermionic field are g_s and g_v respectively. Then the basic Lagrangian density is given by

$$\begin{aligned} \mathcal{L} = & \frac{i}{2} \bar{\psi} \gamma^\mu (\mathbf{D}_\mu - \overleftarrow{\mathbf{D}}_\mu) \psi - m \bar{\psi} \psi \\ & - g_v \bar{\psi} \gamma^\mu V_\mu \psi - g_s \bar{\psi} \phi \psi + \mathcal{L}_v + \mathcal{L}_s + \mathcal{L}_{\text{em}} \end{aligned} \quad (81)$$

Where $D^\mu = \partial^\mu + iqA^\mu$ with q is the magnitude of electric charge, m is the rest mass of the fermions and $A^\mu \equiv (0, 0, xB_m, 0)$, the electro magnetic field vector. Here the gauge choice is such that the constant external magnetic field B_m is along Z-axis, \mathcal{L}_v , \mathcal{L}_s and \mathcal{L}_{em} are the free Lagrangian densities for the vector, scalar and the electromagnetic fields respectively. Therefore, in this particular case, \mathcal{L}_{em} is the Lagrangian density corresponding to the constant magnetic field B_m . We now adiabatically turn on the interaction between the fermions. Therefore, the normal Fermi liquid system will evolve from the non-interacting ground state into the interacting ground state and there will be a one-to-one correspondence between the bare particle states of the original system and the dressed or quasi-particle states of the interacting system.

Next to obtain f the Landau Fermi liquid interaction, which is also called the quasi-particle interaction function, we have considered both direct and exchange type interaction. The exchanged bosons are either scalar or vector type. The Landau Fermi liquid interaction f is related to the two-particle forward scattering amplitude. Therefore, it is essential to compute transition matrix element for two-particle direct as well as exchange interaction forward scattering via the exchanged scalar and vector bosons. We further assume that the constant magnetic field acts as a background field and is present throughout the system. We further assume that the strength of magnetic field is such that in the relativistic case the Landau levels are populated for the charged fermions, i.e., $B_m \geq B_m^{(c)(f)}$, the quantum mechanical limit, given by $qB_m^{(c)(f)} = m^2$.

Then the modified form of spinor solutions of charged fermions in presence of strong quantizing magnetic field is given by

$$\psi = \frac{1}{(L_y L_z)^{1/2}} \exp\{-iE_\nu t + ip_y y + ip_z z\} u^{\uparrow\downarrow} \quad (82)$$

where

$$u^\uparrow = \frac{1}{[2E_\nu(E_\nu + 1)]^{1/2}} \begin{pmatrix} (E_\nu + m)I_{\nu;p_y}(x) \\ 0 \\ p_z I_{\nu;p_y}(x) \\ -i(2\nu qB_m)^{1/2} I_{\nu-1;p_y}(x) \end{pmatrix} \quad (83)$$

and

$$u^\downarrow = \frac{1}{[2E_\nu(E_\nu + 1)]^{1/2}} \begin{pmatrix} 0 \\ (E_\nu + m)I_{\nu-1;p_y}(x) \\ i(2\nu qB_m)^{1/2} I_{\nu;p_y}(x) \\ -p_z I_{\nu-1;p_y}(x) \end{pmatrix} \quad (84)$$

where the symbols \uparrow and \downarrow indicates up and down spin states.

$$I_\nu = \left(\frac{qB_m}{\pi}\right)^{1/4} \frac{1}{(\nu!)^{1/2}} 2^{-\nu/2} \exp\left[-\frac{1}{2}qB_m \left(x - \frac{p_y}{qB_m}\right)^2\right] H_\nu \left[(qB_m)^{1/2} \left(x - \frac{p_y}{qB_m}\right)\right] \quad (85)$$

with H_ν the well known Hermite polynomial of order ν , $E_\nu = (p_z^2 + m^2 + 2\nu qB_m)^{1/2}$, the single particle energy eigen value with $\nu = 0, 1, 2, \dots$, the Landau quantum numbers and L_y, L_z are length scales along Y and Z directions respectively.

In presence of strong quantizing magnetic field along Z-axis (as specified by the choice of gauge) the momentum in the orthogonal plane gets quantized and is given by $p_{\perp} = (2\nu q B_m)^{1/2}$, whereas, the component along Z-axis varies continuously from $-\infty$ to ∞ . Further the phase space volume integral in momentum space in this condition is given by

$$\frac{1}{(2\pi)^3} \int d^3 p f(p) = \frac{1}{(2\pi)^3} \int dp_z d^2 p_{\perp} f(p) = \frac{q B_m}{4\pi^2} \sum_{\nu} (2 - \delta_{\nu 0}) \int_{-p_f}^{+p_f} dp_z f(\nu, p_z) \quad (86)$$

here we have assumed $c = \hbar = 1$ and p_f is the Fermi momentum.

To compute the Landau Fermi liquid interaction function f from two particle forward scattering matrix, we first derive from the first principle the general form of two fermion transition matrix element. We calculate for both scalar and vector coupling with direct and exchange type interactions. Therefore, we have the two particle transition matrix corresponding to scalar and vector boson exchange interactions

$$T_{fi} = i \int j_{fi}^0(x) \phi(x) d^4 x \quad (87)$$

$$T_{fi} = i \int j_{fi}^{\mu}(x) V^{\mu}(x) d^4 x \quad (88)$$

where the fermion four-current is given by $j_{fi}^{\mu}(x) = g_k \bar{\psi}_f(x) \gamma^{\mu} \psi_i(x) \equiv (\rho(x), \mathbf{j}(x))$, with the spinors given by eqns.(3) and (4) and $k = s$ and $k = v$ corresponding to scalar and vector coupling cases respectively. The scalar and vector fields can very easily be obtained from the well known Greens function solutions of Klein-Gordon equations

$$(\partial^2 + m^2)\phi, V^{\mu} = \rho, j^{\mu}$$

and are given by

$$\phi(x) = - \int \frac{d^4 q}{(2\pi)^4} \frac{\exp[-iQ \cdot (x - x')]}{Q^2 - \zeta^2} \rho(x') d^4 x' \quad (89)$$

$$V^{\mu}(x) = - \int \frac{d^4 q}{(2\pi)^4} \frac{\exp[-iQ \cdot (x - x')]}{Q^2 - \eta^2} j^{\mu}(x') d^4 x' \quad (90)$$

where Q is the transferred four momentum ($Q^{\mu} \equiv (q_0, q_x, q_y, q_z)$). Let us first compute the transition matrix element for scalar interaction case. Substituting for the Fermi spinors (eqns.(3) and (4)), we have

$$\rho(x') = \frac{g_s}{L_y L_z} \exp[-i\{(E_{\nu_1} - E_{\nu_2}) - (p_{1y} - k_{1y}) - (p_{1z} - k_{1z})\}][\rho] \quad (91)$$

where

$$[\rho] = \frac{1}{2} \sum_{\text{spin}} \bar{u}(x', \nu_2, k_1) \gamma^0 u(x', \nu_1, p_1) = \frac{1}{2} \text{Tr}(A(x', \nu_1, \nu_2, p_1, k_1) \gamma^0) \quad (92)$$

Then we have after putting for $\rho(x')$ and integrating over t' , y' and z' , the direct part of two-particle transition matrix element with scalar coupling interaction

$$T_{fi}^{(d,s)} = -i \int \frac{d^4 q}{(2\pi)} \delta(q^0 - E_{\nu_1} + E_{\nu_2}) \delta(q_y - p_{1y} + k_{1y}) \delta(q_z - p_{1z} + k_{1z}) \frac{\exp(-iQ \cdot x)}{Q^2 - \zeta^2} [\rho(x')] \frac{g_s}{L_y L_z} \exp(iq_x x') dx' \frac{g_s}{L_y L_z} [\rho(x)] d^4 x \exp[-i\{(E_{\nu'_1} - E_{\nu'_2}) - (p_{2y} - k_{2y}) - (p_{2z} - k_{2z})\}] \quad (93)$$

Integrating over t , y , z and q^0 , q_y , q_z , we get

$$T_{fi}^{(d,s)} = -i(2\pi)^3 \delta(E) \delta(p_y) \delta(p_z) \frac{g_s^2}{L_y^2 L_z^2} \int \frac{dq_x}{2\pi} [\rho(x)] [\rho(x')] \exp[-iq_x(x-x')] \frac{1}{Q^2 - \zeta^2} dx dx' \quad (94)$$

where the δ -functions indicate the abbreviated form of energy, y and z components of momentum conservation. In the derivation of eqn.(14) and the computation of subsequent matrix elements for direct case with vector boson exchange, we have assumed the two body process in the form

$$1(p_1) + 2(p_2) \rightarrow 1'(k_1) + 2'(k_2) \quad (95)$$

In this case the forward scattering amplitude can be obtained if we put $E_{\nu_1} = E_{\nu_2} = E_\nu$ (say), $E_{\nu'_1} = E_{\nu'_2} = E_{\nu'}$ (say), $p_{1y} = k_{1y} = p_y$ (say), $p_{2y} = k_{2y} = p'_y$ (say), $p_{1z} = k_{1z} = p_z$ (say) and $p_{2z} = k_{2z} = p'_z$ (say). Then after evaluating the contour integral over q_x , given by

$$I_{q_x} = \int_{-\infty}^{+\infty} \frac{dq_x}{2\pi} \frac{1}{Q^2 - \zeta^2} \exp[-iq_x(x-x')] = -\frac{\exp[-\zeta |x-x'|]}{2\zeta} \quad (96)$$

and substituting in two-body forward scattering matrix element given by eqn.(14), we have the Landau Fermi liquid interaction function corresponding to direct term for scalar coupling case

$$f_{\text{Dir.}}^{(s)} = \frac{g_s^2}{8\zeta} \int \exp[-\zeta |x-x'|] [\rho(x)] [\rho(x')] dx dx' \quad (97)$$

After evaluating the quantities within [] (see Appendix A) we finally get

$$f_{\text{Dir.}}^{(s)} = \frac{g_s^2}{32\zeta E_\nu E_{\nu'} (E_\nu + m)(E_{\nu'} + m)} \int \exp[-\zeta |x-x'|] dx dx' \{2E_\nu(E_\nu + m)(I_{\nu;p_y}^2(x) + I_{\nu-1;p_y}^2(x)) + 2\nu q B_m(I_{\nu;p_y}^2(x) - I_{\nu-1;p_y}^2(x))\} \{2E_{\nu'}(E_{\nu'} + m)(I_{\nu';p'_y}^2(x') + I_{\nu'-1;p'_y}^2(x')) + 2\nu' q B_m(I_{\nu';p'_y}^2(x') - I_{\nu'-1;p'_y}^2(x'))\} \quad (98)$$

Then the quasi-particle energy is given by

$$\begin{aligned} \varepsilon_\nu(p_z) &= E_\nu(p_z) + \frac{1}{(2\pi)^2} \sum_{\nu'=0}^{[\nu_{\max}]} (2 - \delta_{\nu'0}) \int_{x,x'=-\infty}^{\infty} \int_{p_{y'}=-\infty}^{\infty} \int_{p_{z'}=-p_f}^{p_f} dx dx' dp_{y'} dp_{z'} f_{\text{Dir.}}^{(s)}(p, p'; \nu, \nu') \\ &= E_\nu(p_z) + \Delta E_{\nu;\text{Dir.}}^{(s)}(p_z) \end{aligned} \quad (99)$$

where $[\nu_{\max}] = (\mu_f^2 - m^2)/(2qB_m)$, the integer part of right hand side. In the case of ultra-strong magnetic field, $\nu = \nu' = 0$, then

$$\varepsilon_0(p_z) = E_0(p_z) + \frac{g_s^2}{\zeta^2} n_f \quad (100)$$

where

$$n_f = \frac{qB_m}{2\pi^2} p_f \quad (101)$$

the number density of fermions. The form of the result given in eqn.(20) is identical with that of zero field case [42]. The energy density is then given by

$$\epsilon = \frac{qB_m}{4\pi^2} \sum_{\nu=0}^{[\nu_{\max}]} (2 - \delta_{\nu 0}) \int_{-p_f}^{p_f} dp_z \varepsilon_\nu(p_z) \quad (102)$$

Let us now compute the exchange part for scalar coupling case. In this case we substitute $E_{\nu_1} = E_{\nu'_2} = E_\nu$, $E_{\nu'_1} = E_{\nu_2} = E_{\nu'}$, $p_{1y} = k_{2y} = p_y$, $p_{1z} = k_{2z} = p_z$, $p_{2y} = k_{1y} = p'_y$, $p_{2z} = k_{1z} = p'_z$, to obtain the two-body forward scattering amplitude. In this particular example, the basic process is

$$1(p_1) + 2(p_2) \rightarrow 1'(k_2) + 2'(k_1) \quad (103)$$

and the q_x contour integral is given by

$$I_{q_x} = -\frac{\exp[-K |x - x'|]}{2K} \quad (104)$$

where $K \approx (q_y^2 + q_z^2 + \zeta^2)^{1/2}$ and $q_i = (p_i - p'_i)$, with $i = y$ and z . Then evaluating $[\rho(x)\rho(x')]$ (see Appendix A), we get

$$f_{\text{ex}}^{(s)} = \frac{g_s^2 m}{32E_\nu E_{\nu'}} \int dx dx' \frac{\exp[-K |x - x'|]}{K} \quad (105)$$

$$[(E_\nu E_{\nu'} + p_z p'_z + m^2) \text{Tr}(AA') - \mathbf{p}_\perp \cdot \mathbf{p}'_\perp \text{Tr}(BB')]$$

where

$$\text{Tr}(AA') = 2(I_\nu(x)I_\nu(x')I_{\nu'}(x)I_{\nu'}(x') + I_{\nu-1}(x)I_{\nu-1}(x')I_{\nu'-1}(x)I_{\nu'-1}(x')) \quad (106)$$

and

$$\text{Tr}(BB') = 2(I_{\nu-1}(x)I_\nu(x')I_{\nu'-1}(x)I_{\nu'}(x') + I_\nu(x)I_{\nu-1}(x')I_{\nu'}(x)I_{\nu'-1}(x')) \quad (107)$$

Then as before

$$\Delta E_{\nu;\text{ex}}^{(s)} = \frac{1}{(2\pi)^2} \sum_{\nu'=0}^{[\nu_{\max}]} (2 - \delta_{\nu' 0}) \int_{x,x'=-\infty}^{\infty} \int_{p_{y'}=-\infty}^{\infty} \int_{p_{z'}=-p_f}^{p_f} dx dx' dp_{y'} dp_{z'} f_{\text{ex}}^{(s)}(p, p'; \mathbf{p}_\perp, \mathbf{p}'_\perp)$$

For $\nu = \nu' = 0$,

$$\Delta E_{\nu; \text{ex}}^{(s)} = \frac{g_s^2}{8\pi^2} \int_{-p_f}^{p_f} dp'_z \exp\left(\frac{v'^2}{qB_m}\right) \frac{(E_0 E'_0 + p_z p'_z + m^2)}{E_0 E'_0} \int_0^{\pi/2} \text{erfc}\left(\frac{v'}{(2qB_m)^{1/2}} \sec \theta\right) \sec \theta d\theta \quad (109)$$

where $v' \approx |p_z - p'_z|$. In the zero field case

$$f_{\text{ex}}^{(s)} = \frac{g_s^2}{4E_0(p)E_0(p')} \frac{m^2 - p \cdot p'}{(p' - p)^2 + \zeta^2} \quad (110)$$

We next consider the vector coupling case. The current four vector in the direct case is given by

$$j^\mu(x) = g_v \frac{\exp[-i\{(E_{\nu_1} - E_{\nu_2}) - (p_{1y} - k_{1y}) - (p_{1z} - k_{1z})\}]}{L_y L_z} [j^\mu(x, p_1, k_1)] \quad (111)$$

where

$$[j^\mu] = \frac{1}{2} \sum_{\text{spin}} \bar{u} \gamma^\mu u = \frac{1}{2} \text{Tr}(\Lambda(x, \nu_1, \nu_2, p_1, k_1) \gamma^\mu) \quad (112)$$

Then it is very easy to show that the Landau Fermi liquid interaction function is given by

$$f_{\text{Dir}}^{(v)} = \frac{g_v^2}{32\eta E_\nu E_{\nu'}} \int dx dx' \exp[-\eta |x - x'|] [(E_\nu E_{\nu'} - p_z p_{z'}) \text{Tr} A \text{Tr} A' + \mathbf{p}_\perp \cdot \mathbf{p}'_\perp \text{Tr} B \text{Tr} B'] \quad (113)$$

where we have used the same kind of substitutions as has been done for the scalar case and further the relation,

$$\text{Tr}(\Lambda(x, \nu, p) \gamma^\mu) = \frac{1}{2E_\nu} (\text{Tr} A + \text{Tr} B) p^\mu \quad (114)$$

(see Appendix B) is used to obtain this expression.

The exchange term corresponding to vector coupling case is similarly given by (see Appendix B for brief derivation)

$$f_{\text{Ex}}^{(v)} = \frac{g_v^2}{32E_\nu E_{\nu'}} \int dx dx' \frac{\exp[-K |x - x'|]}{K} [(p_z p_{z'} - E_\nu E_{\nu'} + 3m^2) \text{Tr}(AA') - \mathbf{p}_\perp \cdot \mathbf{p}'_\perp \text{Tr}(BB')] \quad (115)$$

Then energy density of the system is given by (including all the terms)

$$\epsilon = \frac{qB_m}{4\pi^2} \sum_{\nu=0}^{[\nu_{\text{max}}]} (2 - \delta_{\nu 0}) \left\{ \int_{-p_f}^{+p_f} dp_z E_\nu(p_z) + \sum_{k,l} \int_{-p_f}^{+p_f} dp_z \Delta E_{\nu;(l)}^{(k)}(p_z) \right\} \quad (116)$$

where $k = s$ or v and $l = \text{Dir}$ or ex . The kinetic pressure is then given by

$$P = \mu_f n_f - \epsilon \quad (117)$$

The chemical potential or the Fermi energy is given by

$$\begin{aligned}\mu_f = \varepsilon_\nu(p_z = p_f) &= E_\nu(p_f) + \sum_{k,l} \Delta E_{\nu;l}^{(k)}(p_f) \\ &= \mu_0 + \Delta\mu\end{aligned}\quad (118)$$

Therefore knowing the modified form of single particle energy or the quasi-particle energy, it is possible to obtain all the thermodynamic quantities of the system from standard definitions.

To obtain equation of state of dense neutron star matter or dense electron gas, since both direct and exchange terms contribute in the case of $e + e \rightarrow e + e$ scattering, it is necessary to screen $e - e$ and $e - p$ interactions in the direct case (in the case of $e - p$ scattering, of course, only the direct term exists). To get the screening mass of electron, we proceed in the following manner. We assume protons as the positively charged background. Then assuming local charge fluctuation we have

$$\begin{aligned}n^+ &= n_0^+ + n_1^+ \\ n_e &= n_0^+ + n_e'\end{aligned}\quad (119)$$

In the case positive lattice background, we have to replace n_0 by Zn_0 , where Z is the atomic number of the lattice ions. Then in the case of proton background, the well known Poisson equation is given by

$$\nabla^2\psi = -4\pi n_1^+e + 4\pi n_e'e \quad (120)$$

where ψ is the electrostatic potential produced in the system because of local charge fluctuation. Then we have from eqn.(21) after substituting for p_f in terms of chemical potential μ_f and electrostatic potential ψ ,

$$n_e = n_0^+ + \frac{eB_m}{2\pi^2} \sum_\nu (2 - \delta_{\nu 0}) \frac{\mu_f e \psi}{(\mu_f^2 - m^2 - 2\nu e B_m)^{1/2}} \quad (121)$$

The last term is the perturbed part (n_e') as mentioned in the second line of eqn.(39). Then we have

$$\nabla^2\psi = -4\pi n_1^+e + \frac{2e^2 B_m \mu_f}{\pi} \sum_\nu (2 - \delta_{\nu 0}) \frac{1}{(\mu_f^2 - m^2 - 2\nu e B_m)^{1/2}} \psi \quad (122)$$

which may be re-written in the form

$$[\nabla^2 - k_{sc}^2] \psi = -4\pi n_1^+e \quad (123)$$

where k_{sc} is the screening mass and is given by

$$k_{sc} = \left[\frac{2e^2 B_m \mu_f}{\pi} \sum_\nu (2 - \delta_{\nu 0}) \frac{1}{(\mu_f^2 - m^2 - 2\nu e B_m)^{1/2}} \right]^{1/2} \quad (124)$$

and the screening length $r_D = 1/k_{sc}$

In the case of quark matter, however, only the exchange term contributes, we therefore do not need quark-quark screening. Since colorless gluons do not exist, the direct term has no significance.

6.3 Conclusion

In this article we have developed an exact formalism to obtain two-body scattering matrix element for an wide range of magnetic field strength. Although the result has been used to formulate an exact relativistic version of Landau theory of Fermi liquid, is also applicable to study weak and electromagnetic processes in presence of strong magnetic field.

The formalism developed in this paper to compute Landau Fermi liquid interaction f can also be used to study magnetic properties of fermionic system. The calculations (both theoretical and numerical) are of course quite complicated in the relativistic region (we shall report the result in some future publication). The other interesting property-the transport theory of normal Fermi liquid can very easily be studied with the help of present formalism and obtain various kinetic coefficients along with their dependences on the strength of magnetic field.

A

In the direct case we need

$$\Lambda(\nu, x, x', k_y) = \sum_{\text{spin}} u(\nu, x, k) \bar{u}(\nu, x', k) \quad (125)$$

Substituting for the up and down spin solutions of Dirac equation (eqns.(3) and (4)), we get

$$\Lambda = \frac{1}{2E_\nu} (A k_\mu \gamma^\mu (\mu = 0 \text{ and } z) + mA + B k_\mu \gamma^\mu (\mu = y \text{ and } p_y = p_\perp)) \quad (126)$$

The matrices A and B are given by

$$A = \begin{pmatrix} I_\nu I'_\nu & 0 & 0 & 0 \\ 0 & I_{\nu-1} I'_{\nu-1} & 0 & 0 \\ 0 & 0 & I_\nu I'_\nu & 0 \\ 0 & 0 & 0 & I_{\nu-1} I'_{\nu-1} \end{pmatrix} \quad (127)$$

$$B = \begin{pmatrix} I_{\nu-1} I'_\nu & 0 & 0 & 0 \\ 0 & I_\nu I'_{\nu-1} & 0 & 0 \\ 0 & 0 & I_{\nu-1} I'_\nu & 0 \\ 0 & 0 & 0 & I_\nu I'_{\nu-1} \end{pmatrix} \quad (128)$$

where the primes indicate the functions of x' .

Eqn.(A2) is an entirely new result and to the best of our knowledge it has not been reported earlier. Further, this result plays the key role in all kind of calculations related with electromagnetic and weak interactions in presence of strong quantizing magnetic field.

Since γ matrices are traceless and both A and B matrices are diagonal with identical blocks, it is very easy to evaluate the traces of the product of γ -matrices multiplied with any number of A and/or B , from any side with any order e.g.,

$$\text{Tr}(\gamma^\mu \gamma^\nu A_1 A_2 \dots B_1 B_2 \dots) = \text{Tr}(A_1 A_2 \dots B_1 B_2 \dots) g^{\mu\nu}, \quad (129)$$

$$\text{Tr}(\gamma^\mu \gamma^\nu \gamma^\lambda \gamma^\sigma A_1 A_2 \dots B_1 B_2 \dots) = \text{Tr}(A_1 A_2 \dots B_1 B_2 \dots)(g^{\mu\nu} g^{\sigma\lambda} - g^{\mu\lambda} g^{\nu\sigma} + g^{\mu\lambda} g^{\nu\sigma}), \quad (130)$$

$\text{Tr}(\text{product of odd } \gamma\text{'s with } A \text{ and/or } B) = 0$ etc. The other interesting aspects of A and B matrices are:

- i) $k_{1\mu} k^{2\mu} \text{Tr}(A_1 A_2) = (E_1 E_2 - k_{1z} k_{2z}) \text{Tr}(A_1 A_2)$
- ii) $k_{1\mu} k^{2\mu} \text{Tr}(B_1 B_2) = \mathbf{k}_{1\perp} \cdot \mathbf{k}_{2\perp} \text{Tr}(B_1 B_2)$
- iii) $k_{1\mu} k^{2\mu} \text{Tr}(A_1 B_2) = k_{1\mu} k^{2\mu} \text{Tr}(B_1 A_2) = 0$
- iv) $p_{1\mu} k^{1\mu} p_{2\nu} k^{2\nu} \text{Tr}(A_1 B_2) \neq 0 = (E_{\nu_1} E_{\nu'_2} - p_{1z} k_{1z}) \mathbf{p}_{2\perp} \cdot \mathbf{k}_{2\perp} \text{Tr}(A_1 B_2)$ These set of relations are also totally new results and have not been reported before.

To compute the direct part for scalar coupling case, we need

$$\text{Tr}(\bar{u}(x, \nu, p) u(x, \nu, p) \gamma^0) = \text{Tr}(\Lambda(x, \nu, p) \gamma^0) \quad (131)$$

Using the expression for Λ , it is very easy to show that the above trace is given by

$$\frac{1}{2E_\nu(E_\nu + m)} [2E_\nu(E_\nu + m)(I_{\nu; p_y}^2(x) + I_{\nu-1; p_y}^2(x)) + 2\nu q B(I_{\nu; p_y}^2(x) - I_{\nu-1; p_y}^2(x))] \quad (132)$$

To compute the exchange part for this case, we need

$$\text{Tr}[(\bar{u}(x, \nu, p) \gamma^0 u(\nu', x, p'))(\bar{u}(x', \nu', p') \gamma^0 u(\nu, x', p))] = \text{Tr}[\Lambda(x, x', p, \nu) \gamma^0 \Lambda(x, x', p', \nu') \gamma^0] \quad (133)$$

Then by simple algebraic manipulation it is trivial to show that the above trace is given by

$$\frac{1}{4E_\nu E_{\nu'}} [(E_\nu E_{\nu'} + p_z p'_z + m^2) \text{Tr}(AA') - \mathbf{p}_\perp \cdot \mathbf{p}'_\perp \text{Tr}(BB')] \quad (134)$$

where

$$\text{Tr}(AA') = 2(I_\nu(x) I_\nu(x') I_{\nu'}(x) I_{\nu'}(x') + I_{\nu-1}(x) I_{\nu-1}(x') I_{\nu'-1}(x) I_{\nu'-1}(x')) \quad (135)$$

$$\text{Tr}(BB') = 2(I_{\nu-1}(x) I_\nu(x') I_{\nu'-1}(x) I_{\nu'}(x') + I_\nu(x) I_{\nu-1}(x') I_{\nu'}(x) I_{\nu'-1}(x')) \quad (136)$$

B

Now to compute two-particle forward scattering matrix element for vector boson exchange case we need

$$\text{Tr}(u(x, \nu, p) \bar{u}(x, \nu, p) \gamma^\mu) \quad (137)$$

for direct case. It is trivial to show that the trace is given by

$$\frac{1}{2E_\nu} \text{Tr}[(Ap_\sigma \gamma^\sigma + mA + Bp_\sigma \gamma^\sigma) \gamma^\mu] = \frac{1}{2E_\nu} [p^\mu (\text{Tr} A + \text{Tr} B)] \quad (138)$$

Then

$$[j^\mu(x)][j_\mu(x')] = \frac{1}{4E_\mu E_{\mu'}} [(E_\nu E_{\nu'} - p_z p'_z) \text{Tr} A \text{Tr} A' + p_\perp p'_\perp \text{Tr} B \text{Tr} B'] \quad (139)$$

In this case the terms $\text{Tr}A\text{Tr}B'$ and $\text{Tr}A'\text{Tr}B$ do not contribute. In the exchange interaction for vector coupling case, we need

$$\text{Tr}[\Lambda(x, x', p, \nu)\gamma^\mu \Lambda(x, x', p', \nu')\gamma^\mu] \quad (140)$$

By some trivial algebra, we can very easily show that this expression is given by

$$\frac{1}{4E_\nu E_{\nu'}} \text{Tr}[AA'p_\sigma p'_\lambda (\gamma^\sigma \gamma^\mu \gamma^\lambda \gamma_\mu) + m^2 AA' \gamma^\mu \gamma_\mu + p_\sigma p'_\lambda BB' (\gamma^\sigma \gamma^\mu \gamma^\lambda \gamma_\mu)] \quad (141)$$

Then using the well known formula for the product of four γ -matrices, we have the final form of the above expression

$$\frac{1}{4E_\nu E_{\nu'}} [(p_z p'_z - E_\nu E_{\nu'}) \text{Tr}(AA') + 3m^2 \text{Tr}(AA') - \mathbf{p}_\perp \cdot \mathbf{p}'_\perp \text{Tr}(BB')] \quad (142)$$

References

1. For detailed discussion see the book by S. Chandrasekhar, *An Introduction to Study of Stellar Structure*, Dover, N.Y., 1957.
2. D. Sugimoto and K. Nomoto, *Space Sci. Rev.* **25** (1980) 155.
3. B. Paczynski, *Stellar Evolution and Close Binaries*, in *Highlights of Astronomy*, **Vol. 5**, D. Reidel Publ. Co. (1980).
4. W. Baade and F. Zwicky, *Phys. Rev.* **45** (1934) 138.
5. See for example, *Pulsars*, R.N. Manchester and J.H. Taylor, Freeman and Comp., San Francisco, 1973.
6. S.L. Shapiro and S.A. Teukolsky, *Black Holes, White Dwarfs and Neutron Stars*, John Wiley & Sons, New York, 1983.
7. N.K. Glendenning, *Compact Stars*, Springer, New York, 2000.
8. J.R. Oppenheimer and G.M. Volkoff, *Phys. Rev.* **55** (1939) 374.
9. See for example S.K. Bose, *An Introduction to General Relativity*, Wiley Eastern Limited, New Delhi, 1980.
10. S. Chandrasekhar, *Phys. Rev. Lett* **12** (1964) 114; **12** (1964) 437; W.A. Fowler, *Rev. Mod. Phys.* **36** (1964) 545.
11. S. Chandrasekhar, *Phil. Mag.* **11** (1931) 592; *Astrophys. Jour.* **74** (1931) 81.
12. R.P. Feynman, N. Metropolis and E. Teller, *Phys. Rev.* **75** (1949) 1561.
13. B.K. Harrison, M. Wakano and J.A. Wheeler, *Matter-Energy at High Density; End Point of Thermonuclear Evolution*, in *La Structure et l'évolution de l'univers, Onzième Conseil de Physique* Solvay, Stoops, Brussels, Belgium, (1958) p. 124.
14. G. baym, C.J. Pethick and P. Sutherland, *Astrophys. Jour.* **170** (1971) 299.
15. G. Baym, H.A. Bethe and C.J. Pethick, *Nucl. Phys.* **A175** (1971) 225.
16. V.R. Pandharipande, *Nucl. Phys.* **A178** (1971) 123.
17. H.A. Bethe and M.B. Johnson, *Nucl. Phys.* **A230** (1974) 1.
18. V.R. Pandharipande and R.A. Smith, *Nucl. Phys.* **A237** (1975) 507.
19. B. Friedman and V.R. Pandharipande, *Nucl. Phys.* **A361** (1981) 502.
20. V.R. Pandharipande and R.A. Smith, *Phys. Lett.* **B59** (1975) 15.
21. J. D. Walecka, *Ann. Phys.* **83** (1974) 491, see also J.D. Walecka, *Theoretical Nuclear and Sub-Nuclear Physics*, Oxford Univ. Press, New York, 1995.
22. A. Hewish, J. Bell, J.D.H. Pilkington, P.F. Scoti and R. A. Collins, *Nature* **217** (1968) 709.
23. T. Gold, *Nature*. **218** (1968) 731.

24. R.C. Duncan and C. Thompson, *Astrophys. J. Lett.* **392**, L9 (1992); C. Thompson and R.C. Duncan, *Astrophys. J.* **408**, 194 (1993); C. Thompson and R.C. Duncan, *MNRAS* **275**, 255 (1995); C. Thompson and R.C. Duncan, *Astrophys. J.* **473**, 322 (1996).
25. P.M. Woods et al., *Astrophys. J. Lett.* **519**, L139 (1999); C. Kouveliotou, et al., *Nature* **391**, 235 (1999).
26. K. Hurley, et al., *Astrophys. Jour.* **442**, L111 (1999).
27. S. Mereghetti and L. Stella, *Astrophys. Jour.* **442**, L17 (1999); J. van Paradijs, R.E. Taam and E.P.J. van den Heuvel, *Astron. Astrophys.* **299**, L41 (1995); S. Mereghetti, astro-ph/99111252; see also A. Reisenegger, astro-ph/01003010.
28. M. Ruderman, Matter in Superstrong Magnetic Field, in *Physics of Dense Matter*, ed. C.T. Hansen, Reidel Publ. Co., Dordrecht.
29. D. Bandopadhyaya, S. Chakrabarty, P. Dey and S. Pal, *Phys. Rev.* **D58**, 121301 (1998).
30. S. Chakrabarty, D. Bandopadhyay and S. Pal, *Phys. Rev. Lett.* **78**, 2898 (1997); D. Bandopadhyay, S. Chakrabarty and S. Pal, *Phys. Rev. Lett.* **79**, 2176 (1997).
31. C.Y. Cardall, M. Prakash and J.M. Lattimer, astro-ph/0011148 and references therein; E. Roulet, Astro-ph/9711206; L.B. Leinson and A. Pérez, Astro-ph/9711216; D.G. Yakovlev and A.D. Kaminkar, *The Equation of States in Astrophysics*, eds. G. Chabrier and E. Schatzman P.214, Cambridge Univ.
32. S. Chakrabarty and P.K. Sahu, *Phys. Rev.* **D53**, 4687 (1996).
33. S. Chakrabarty, *Phys. Rev.* **D51**, 4591 (1995); Chakrabarty, *Phys. Rev.* **D54**, 1306 (1996).
34. T. Ghosh and S. Chakrabarty, *Phys. Rev.* **D63**, 0403006 (2001); T. Ghosh and S. Chakrabarty, *Int. Jour. Mod. Phys.* **D10**, 89 (2001).
35. V.G. Bezchastrov and P. haensel, Astro-ph/9608090.
36. S. Mandal and S. Chakrabarty (two papers on weak and electromagnetic processes to be published).
37. A. Melatos, *Astrophys. Jour.* **519**, L77 (1999); A. Melatos, *MNRAS* **313**, 217 (2000).
38. S. Bonazzola et al, *Astron. & Astrophysics.* **278**, 421 (1993); M. Bocquet et al, *Astron. & Astrophysics.* **301**, 757 (1995).
39. B. Bertotti and A.M. Anile, *Astron. & Astrophysics.* **28**, 429 (1973); C. Cutler and D.I. Jones, gr-qc/0008021; K. Konno, T. Obata and Y. Kojima, gr-qc/9910038; A.P. Martinez et al, hep-ph/0011399; M. Chaichian et al, *Phys. Rev. Lett.* **84**, 5261 (2000); Guangjun Mao, Akira Iwamoto and Zhuxia Li, astro-ph/0109221; A. Melatos, *Astrophys. Jour.* **519**, L77 (1999); A. Melatos, *MNRAS* **313**, 217 (2000); R. González Felipe et al, astro-ph/0207150 and references therein.
40. S. Mandal and S. Chakrabarty (submitted).
41. Issac Vidaña and Ignazio Bombaci, nucl-th/0203061.
42. G. Baym and S.A. Chin, *Nucl. Phys.* **A262**, 527 (1976).

Chiral Sigma Model and Neutron Stars

P. K. Sahu

Institute of Physics, Sachivalaya Marg, Bhubaneswar 751 005, India

Abstract. In the frame work of SU(2) chiral sigma model, the nuclear matter equation of state at zero and finite temperature have been investigated. We have analyzed this by varying different parameters, which agrees well with the one derived from the heavy-ion collision experiment at extreme densities. We have derived the neutron star matter equation of state and estimated the maximum masses ($\sim 2M_{\odot}$) of neutron star. These masses lie in the range of observational limit. We have then calculated the temperature dependent asymmetric nuclear matter, also investigated the critical temperature of liquid gas phase transition and compared with the experimental data. We found that the critical temperature is in the range of 14 – 20 MeV.

A Introduction

The nuclear equation of states (EOS) play a crucial role to study the quark gluon plasma (QGP) at extreme densities and temperatures ([1]- [3]) and also it is a main ingredient for the evolution of stellar systems, and the global properties of neutron star and supernova [2,4,5]. To derive the EOS theoretically, many body approaches have been adopted such as Hartree-Fock, Thomas-Fermi and mean-field theory type procedures [6,7]. One of them, the relativistic mean-field (RMF) formalism is of great success in the theoretical calculation of finite nuclei and infinite nuclear matter [1, 2, 7, 8]. The original Walecka RMF model [9] has been modified to a great extent due to its unrealistic meson nucleon interactions. For example by adding the non-linear self-interaction of scalar mesons in the RMF model [1, 8, 10], one can describe desirable values of saturation properties of nuclear matter such as incompressibility, binding energy, saturation density and effective nucleon mass. Though the non-linear RMF describe well the finite nuclei and the nuclear matter properties at normal density, it deviates from the relativistic Dirac Brueckner Hartree Fock (DBHF) equation of state [11]. Because, the DBHF is considered to be the most realistic EOS in the non-relativistic approach in the low density range. Therefore, there are attempts to include vector meson self-coupling to reproduce the EOS, compatible to DBHF. However, one can not take arbitrarily the vector-scalar and vector-vector interactions for the model to be renormalized. But, these interactions can be included in the RMF model, inspired by the effective field theory(EFT) approach [16].

The chiral sigma (CH) model plays a significant role in the high density matter, because chiral symmetry is a good hadron symmetry [13]. Therefore, it is desirable to have chiral symmetry in any theory of dense hadronic matter. At the same time, the theory should be capable of describing the bulk properties of nuclear matter.

A chiral Lagrangian using a scalar (sigma) field was originally introduced by Gell-Mann and Levy, [14] and later the importance of chiral symmetry in nuclear matter was emphasized by Lee and Wick. [15] The usual theory of pions does not possess the empirically desirable saturation properties for nuclear matter. For this reason, an isoscalar vector field with a dynamically generated mass was introduced via the Higgs mechanism into the theory of nuclear matter and it enabled us to have a saturation density in nuclear matter equation of state. [16] In the standard sigma model, the value of the incompressibility parameter of nuclear matter turns out to be quite large — several times the desirable value — and can be reduced only by introducing the scalar field self-interactions with adjustable coefficients.

Several papers [17, 18] have attempted to derive the chiral sigma model equation of state at high matter density with normal nuclear matter saturation as well as a desirable incompressibility value. One of these is derived by Glendenning [39] in 1986, the equation of state based on the mean field approximation, where the equation of motion for the mean fields is derived in the general case for the chiral sigma model supplemented by a gauge massless vector meson in interaction with the other hadrons, including baryon resonances. This theory has two parameters, which are determined from the saturation density and binding energy per nucleon in normal symmetric matter. The value of the incompressibility is rather very large *i.e.*, $K = 650 \text{ MeV}$. In a subsequent paper, the chiral sigma model based on the mean field approximation was extended by Glendenning [18], where the ω -meson does not have a dynamically generated mass. In this model, the parameters are fitted to obtain two equation of state corresponding to two compression moduli, a ‘stiff’ ($K = 300 \text{ MeV}$) and a ‘soft’ ($K = 200 \text{ MeV}$), by reproducing correct nuclear matter properties.

However, in these theories, the mass of the isoscalar vector field is not generated dynamically. This fact can be considered a shortcoming of the chiral symmetry model. The CH model is very similar to the RMF approach, where meson fields are treated in the mean-field approximation. The important point of this model is that its non-linear terms simulate the three body forces and is essential to reproduce the nuclear matter saturation properties. A decade ago we formulated a SU(2) CH model, where the mass of the isoscalar vector field is generated dynamically [13]. The main problem of this theory was unrealistic high incompressibility. To overcome this shortcoming, recently [20, 21] we made an attempt to introduce the higher order terms of scalar meson field. In this way, we can reproduce the empirical values of incompressibility, effective mass, binding energy and saturation density. Using the same SU(2) CH model we calculate here the EOS for symmetric and asymmetric nuclear matter at zero and finite temperature. In this calculation, we choose the incompressibility 210, 300 and 380 MeV and the effective masses, 0.8, 0.85 and 0.9 of nucleon mass and discuss their applicability to the various heavy-ion collision experiments and properties of neutron star matter.

This lecture is organized as follows: In section II, we present a brief formalism of the CH model. We derive the EOS with zero temperature for symmetric nuclear matter, the neutron star matter and finite temperature in the section III. The corresponding results and discussions are presented in the Section IV. The summary and conclusion follow in section V.

B The Formalism of SU(2) Chiral Sigma Model

The $SU(2)$ chiral sigma Lagrangian can be written as [13, 20, 21]

$$\begin{aligned}\mathcal{L} = & \frac{1}{2}(\partial_\mu \pi \cdot \partial^\mu \pi + \partial_\mu \sigma \partial^\mu \sigma) - \frac{1}{4}F_{\mu\nu}F_{\mu\nu} \\ & - \frac{\lambda}{4}(x^2 - x_o^2)^2 - \frac{\lambda b}{6m^2}(x^2 - x_o^2)^3 - \frac{\lambda c}{8m^4}(x^2 - x_o^2)^4 \\ & - g_\sigma \bar{\psi}(\sigma + i\gamma_5 \tau \cdot \pi)\psi + \bar{\psi}(i\gamma_\mu \partial^\mu - g_\omega \gamma_\mu \omega^\mu)\psi \\ & + \frac{1}{2}g_\omega^2 x^2 \omega_\mu \omega^\mu + \frac{1}{24}\xi g_\omega^4 (\omega_\mu \omega^\mu)^2 - D\sigma.\end{aligned}\quad (1)$$

Here $F_{\mu\nu} \equiv \partial_\mu \omega_\nu - \partial_\nu \omega_\mu$ and $x^2 = \pi^2 + \sigma^2$, ψ is the nucleon isospin doublet, π is the pseudoscalar-isovector pion field, σ is the scalar field, and D is a constant. We work in natural units with $\hbar = c = k_B = 1$.

The Lagrangian includes a dynamically generated mass of the isoscalar vector field, ω_μ , that couples to the conserved baryonic current $j_\mu = \bar{\psi}\gamma_\mu\psi$. The constant parameters b and c are included in the higher-order self-interaction of the scalar field to describe the desirable values of nuclear matter properties at saturation point. Henceforth, we define our model as modified non-linear CH model (MCH) in our successive discussions. In the fourth order term of the omega fields, the quantity ξ is a constant parameter. Throughout our calculations, for simplicity, we set ξ to zero. In this model the pion mass m_π is zero without symmetry breaking. Thus the last term, $D\sigma$ in the Lagrangian is zero in our present calculation. The interaction of the scalar and the pseudoscalar mesons with the vector boson generate a mass for the latter through the spontaneous breaking of the chiral symmetry. The masses of the nucleon, scalar and vector meson are respectively given by

$$m = g_\sigma x_o, \quad m_\sigma = \sqrt{2\lambda}x_o, \quad m_\omega = g_\omega x_o, \quad (2)$$

where x_o is the vacuum expectation value of the σ field, $\lambda = (m_\sigma^2 - m_\pi^2)/(2f_\pi^2)$, with m_π , the pion mass and f_π the pion decay coupling constant, and g_ω and g_σ are the coupling constants for the vector and scalar fields, respectively. In the mean-field treatment we ignore the explicit role of π mesons.

By adopting mean-field approximation, the equation of motion of fields are obtained. This approach has been used extensively to evaluate the EOS [1, 8, 10] in any theoretical models for high density matter. Using the ansatz of the mean-field, the equation of motion for the scalar field (σ_0) in terms of $m^*/m \equiv x/x_o$ is

$$\begin{aligned}(1 - Y^2) - \frac{b}{m^2 c_\omega}(1 - Y^2)^2 + \frac{c}{m^4 c_\omega^2}(1 - Y^2)^3 \\ + \frac{2c_\sigma c_\omega n_B^2}{m^2 Y^4} - \frac{2c_\sigma n_S}{mY} = 0,\end{aligned}\quad (3)$$

where $m^* \equiv Ym$ is the effective mass of the nucleon and $c_\sigma \equiv g_\sigma^2/m_\sigma^2$ and $c_\omega \equiv g_\omega^2/m_\omega^2$ are scalar and vector coupling constants respectively. n_S is the scalar density defined in equation (7)

The equation of motion for the isoscalar vector field is

$$\omega_0 = \frac{n_B}{g_\omega x^2}, \quad (4)$$

where in the mean-field limit $\omega = \omega_0$. The quantity k_F is the Fermi momentum and γ is the nucleon spin degeneracy factor and n_B is the baryon density defined in the next section.

C Equation of state

C.1 Equation of state at zero temperature

The EOS is calculated from the diagonal components of the conserved total stress tensor corresponding to the Lagrangian together with the mean-field equation of motion for the Fermion field and a mean-field approximation for the meson fields. The total energy density, ε , and pressure, P , of the many-nucleon system are the following:

$$\begin{aligned} \varepsilon &= \frac{m^2(1-Y^2)^2}{8c_\sigma} - \frac{b}{12c_\omega c_\sigma}(1-Y^2)^3 + \frac{c}{16m^2 c_\omega^2 c_\sigma}(1-Y^2)^4 \\ &\quad + \frac{c_\omega n_B^2}{2Y^2} + \frac{\gamma}{2\pi^2} \int_0^{k_F} k^2 dk \sqrt{k^2 + m^{*2}}, \\ P &= -\frac{m^2(1-Y^2)^2}{8c_\sigma} + \frac{b}{12c_\omega c_\sigma}(1-Y^2)^3 - \frac{c}{16m^2 c_\omega^2 c_\sigma}(1-Y^2)^4 \\ &\quad + \frac{c_\omega n_B^2}{2Y^2} + \frac{\gamma}{6\pi^2} \int_0^{k_F} \frac{k^4 dk}{\sqrt{k^2 + m^{*2}}}. \end{aligned} \quad (5)$$

The energy per nucleon is $E/A = \varepsilon/n_B$, where $\gamma = 4$ for symmetric nuclear matter and $\gamma = 2$ for neutron matter.

Also we introduce the asymmetric parameter, α to describe the asymmetric nuclear matter. This is defined as

$$\alpha = \frac{n_n - n_p}{n_n + n_p}, \quad (6)$$

where $\alpha=0$ for symmetric matter nuclear matter ($\gamma = 4$) and $\alpha=1$ for the pure neutron matter ($\gamma = 2$).

The baryon density n_B and scalar density n_S are defined as

$$n_B = \frac{\gamma}{(2\pi)^3} \int_0^{k_F} d^3k, \quad (7)$$

and

$$n_S = \frac{\gamma}{(2\pi)^3} \int_0^{k_F} \frac{m^* d^3k}{\sqrt{k^2 + m^{*2}}}, \quad (8)$$

respectively, which are used in eq.(3).

C.2 Equation of state in neutron star matter

In the interior of neutron star is supposed to be very high density, where the neutron chemical potential exceeds the combined mass of the proton and electron. Therefore, the asymmetric matter with an admixture of electrons rather than pure neutron matter is a more likely composition of matter in neutron star interiors. The concentrations of neutrons, protons and electrons can be determined from the condition of beta equilibrium ($n \leftrightarrow p + e + \bar{\nu}$) and from charge neutrality, assuming that neutrinos are not degenerate. We have

$$\mu_n = \mu_p + \mu_e, \quad n_p = n_e, \quad (9)$$

where μ_i is the chemical potential of particle species i . For the description of neutron-rich matter, we include the interaction due to the isospin triplet ρ meson in the Lagrangian (1). The following terms are included in the Lagrangian:

$$-\frac{1}{4}G_{\mu\nu} \cdot G^{\mu\nu} + \frac{1}{2}m_\rho^2\rho_\mu \cdot \rho^\mu - \frac{1}{2}g_\rho\bar{\psi}(\rho_\mu \cdot \tau\gamma^\mu)\psi. \quad (10)$$

Here $G_{\mu\nu} \equiv \partial_\mu\rho_\nu - \partial_\nu\rho_\mu$. Using the mean-field approximation in the equation of motion for ρ , the following density dependence equation is obtained:

$$\rho_o^3 = \frac{g_\rho}{2m_\rho^2}(n_p - n_n). \quad (11)$$

From the semi-empirical nuclear mass formula, the symmetric energy coefficient is

$$a_{\text{sym}} = \frac{c_\rho k_F^3}{12\pi^2} + \frac{k_F^2}{6\sqrt{(k_F^2 + M^{*2})}}, \quad (12)$$

where $c_\rho \equiv g_\rho^2/m_\rho^2$ and $k_F = (6\pi^2 n_B/\gamma)^{1/3}$ ($n_B = n_p + n_n$). We fix the coupling constant c_ρ by requiring that a_{sym} to be the empirical value, 32 MeV [22]. This gives $c_\rho = 4.66 \text{ fm}^2$. The inclusion of the ρ meson in the Lagrangian will contribute the term $m_\rho^2(\rho_o^3)^2/2$ to the energy density and pressure. The chemical potential is defined as $\nu = \mu - g_w w_o + \tau^3 g_\rho \rho_o^3$, due to presence of asymmetric nuclear matter, where τ^3 is $+1/2$ for neutron and $-1/2$ for proton. In the equation of state, the relativistic non-interacting energy density and pressure of the baryons (with effective masses) and electrons will be included.

The mass and radius of a neutron star are characterized by its structure. These are determined from the equations that describe the hydrostatic equilibrium of degenerate stars without rotation in general relativity, the Tolman-Oppenheimer-Volkoff (TOV) equations: [23, 24]

$$\frac{dp}{dr} = -\frac{G(\epsilon + p/c^2)(m + 4\pi r^3 p/c^2)}{r^2(1 - 2Gm/rc^2)}, \quad \frac{dm}{dr} = 4\pi r^2 \epsilon. \quad (13)$$

Here p and ϵ are the pressure and total mass-energy density, and $m(r)$ is the mass contained in a volume of radius r . The quantity G is the gravitational constant, and c

is the velocity of light. To integrate the TOV equations, one needs to know the equation of state for the entire expected density range of the neutron star, starting from the high density at the center to the surface densities. Therefore, we construct a composite equation of state for the entire neutron star density span by joining our equation of state for high density neutron rich matter to those with (i) 10^{14} to $5 \times 10^{10} \text{ g cm}^{-3}$ [25], (ii) $5 \times 10^{10} \text{ g cm}^{-3}$ to 10^3 g cm^{-3} [26], and (iii) less than 10^3 g cm^{-3} [27]. Thus we integrate the TOV equations for the newly constructed equation of state and given central density $\epsilon(r=0) = \epsilon_c$ with the boundary condition $m(r=0) = 0$ to give R and M . The radius R is defined by the point where $P \sim 0$, or, equivalently, $\epsilon = \epsilon_s$, where ϵ_s (7.8 g cm^{-3}) is the density expected at the star surface. The total mass is then given by $M = m(R)$.

C.3 Equation of state at finite temperature

The main interest to study finite temperature nuclear EOS is to observe the liquid gas phase transition [28] near normal nuclear matter density. It is also required to estimate the critical temperature at liquid gas coexistence point. This feature is very much noticeable, because in the medium energy heavy-ion collisions, one of the theoretical studies of dynamics is the liquid gas phase transition. In this direction much works have been carried out using relativistic [29] formalisms. The liquid gas phase transition and the critical temperature were studied extensively based on the non-relativistic theory [30]- [32]. The estimated critical temperature is found to be in the range of 15-20 MeV.

The liquid gas phase also has been studied by many authors based on the RMF theory [29, 33]. In the original Walecka model, the critical temperature in the symmetric nuclear matter is estimated to be 18.3 MeV [7]. This value was brought down to 14.2 MeV, if the non-linear terms were included in the model. However, the recent experiments in heavy-ion collisions for dilute warm nuclear matter report a small liquid gas phase region and low critical temperature $\sim 13.1 \pm 0.6 \text{ MeV}$ [28]. It has been noticed that the different critical temperature are extracted by various theories. This is because, each theory has its own type of treatments of the nuclear interactions. Therefore, our motivation is to see such properties in the present modified CH sigma model.

The EOS for finite temperature can be defined in the same manner as zero temperature, these are as follows:

$$\begin{aligned}
 \epsilon(T) &= \frac{m^2(1-Y^2)^2}{8c_\sigma} - \frac{b}{12c_\omega c_\sigma}(1-Y^2)^3 + \frac{c}{16m^2 c_\omega^2 c_\sigma}(1-Y^2)^4 \\
 &\quad + \frac{c_\omega n_B^2}{2Y^2} + \frac{\gamma}{2\pi^2} \int_0^\infty k^2 dk \sqrt{k^2 + m^{*2}} (f(T) + \bar{f}(T)) , \\
 P(T) &= -\frac{m^2(1-Y^2)^2}{8c_\sigma} + \frac{b}{12c_\omega c_\sigma}(1-Y^2)^3 - \frac{c}{16m^2 c_\omega^2 c_\sigma}(1-Y^2)^4 \\
 &\quad + \frac{c_\omega n_B^2}{2Y^2} + \frac{\gamma}{6\pi^2} \int_0^\infty \frac{k^4 dk}{\sqrt{k^2 + m^{*2}}} (f(T) + \bar{f}(T)) .
 \end{aligned} \tag{14}$$

The baryon and scalar density at finite temperature are respectively modified as

$$n_B(T) = \frac{\gamma}{(2\pi)^3} \int_0^\infty d^3k (f(T) - \bar{f}(T)), \quad (15)$$

and

$$n_S(T) = \frac{\gamma}{(2\pi)^3} \int_0^\infty \frac{m^* d^3k}{\sqrt{k^2 + m^{*2}}} (f(T) + \bar{f}(T)). \quad (16)$$

The nucleon and anti-nucleon distribution functions $f(T)$ and $\bar{f}(T)$, are respectively, expressed as

$$f(T) = \frac{1}{\exp[(E^* + \nu)/T] + 1} \quad (17)$$

and

$$\bar{f}(T) = \frac{1}{\exp[(E^* - \nu)/T] + 1}. \quad (18)$$

where $E^* = \sqrt{k^2 + m^{*2}}$, T is temperature and the chemical potential $\nu = \mu - g_w w_o$. These distribution functions are used in eq.(14-16).

Table 1. Different parameter sets for the MCH model.

set	c_σ (fm^2)	c_ω (fm^2)	b/m^2 (fm^2)	c/m^4 (fm^4)	K (MeV)	m^*/m
I	8.86	1.99	-12.24	-31.59	210	0.85
II	6.79	1.99	-4.32	0.165	300	0.85
III	5.36	1.99	1.13	22.01	380	0.85
IV	8.5	2.71	-9.26	-40.73	300	0.8
V	2.33	1.04	9.59	46.99	300	0.9

D Results and discussions

In the EOS eqs.(5-14) for both zero and finite temperature, the four parameters are: the nucleon coupling to the scalar and the vector fields, c_σ and c_ω , and the coefficients in the scalar potential terms, b and c . These are obtained by fitting at the saturation point: the binding energy/nucleon ($B/A = -16.3$ MeV), baryon density ($n_0 = 0.153 \text{ fm}^{-3}$), incompressibility ($K = 300$ MeV) and effective (Landau) mass ($m^* = 0.85M$) [22]. In our calculation we have chosen the effective mass from $0.8 - 0.9M$, to observe the sensitivity of EOS at high density region. Another interesting point we note that by changing the effective mass, the EOS can be compared well with the recent one which has been extracted from the heavy-ion collisions data [35]. We will discuss this below.

The nuclear incompressibility is somewhat uncertain at saturation and therefore we take in the range of 210–380 MeV. The desirable values of effective mass and nuclear matter incompressibility are chosen in accordance with recent heavy-ion collision data [8,35]. These parameters are listed in Table I.

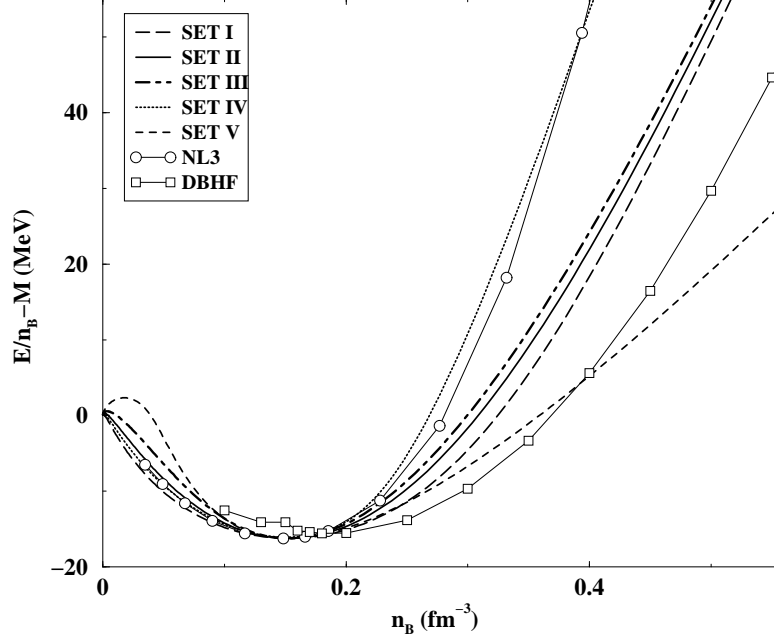


Fig. 1. Energy per particle with a function of baryon density

D.1 At zero temperature

We compare the EOS with the NL3 [8] and DBHF [11] models in Fig. 1. Here we find that sets IV and V match with NL3 and DBHF, respectively up to three times the nuclear matter density. It is to be noted that the EOS obtained by DBHF is trusted up to two times of nuclear matter density [36,37]. The difference between the two sets IV (stiff) and V (soft) is only due to the different effective mass for the same incompressibility ($K = 300$ MeV). The all other three sets namely, I ($K=210$ MeV), II ($K=300$ MeV) and III ($K=380$ MeV) are having same effective mass with different EOS incompressibilities. From this graph, we note that the stiffness or softness of EOS is insignificant with incompressibilities in comparison to NL3 and DBHF.

In Fig. 2 we verify the EOS with the predicted experimental values obtained from the heavy-ion collisions data [35]. The overall EOS are good fit to experimental data. If we consider more vividly, then we notice that the EOS having incompressibility,

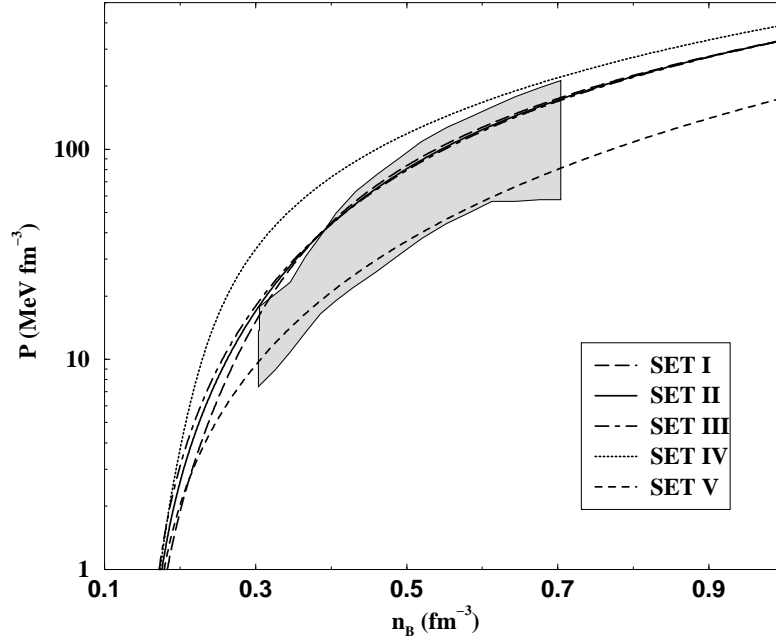


Fig.2. The pressure versus baryon density for different sets of MCH model. The bounded curve represents the experimental values obtained from Ref. [35].

$K=300$ MeV and $m^*/m=0.9$ (set V) fits well. However, $K=210$ (set I) and 300 (set II) MeV with $m^*/m=0.85$ also agree, but slightly deviate from the data at low density. In addition, $K=300$ MeV and $m^*/m=0.8$ (set IV) shows more stiffer EOS. In general, the set II ($K=300$ MeV and $m^*/m=0.85$) explains EOS fairly well and hence could be the ideal parameterization (set II). In our preceding sections we will be considering this parameter set II (model MCH). Note that the value for EOS predicted by experiment may change due to the momentum dependent potential as given in Ref. [8].

D.2 Structure of Neutron Stars

Figure 3, displays the pressure versus the total mass-energy density for neutron-rich matter in beta equilibrium. The solid curve corresponds to the modified chiral sigma model MCH. Inclusion of the two parameters, b and c in the potential term, gives a reasonable value for the incompressibility at the saturation density of nuclear matter. Hence, the MCH model is much softer than the original CH model with regard to the neutron star matter equation of state. The physics behind this is that the pressure generated by the self-interaction of scalar fields at high density is less; i.e., the pressure with density decreases more than that for the CH model. The dashed curve (NL3 [15]) represents the neutron rich equation of state, which was derived from the heavy-ion collision data. [2] From Fig. 3, we note, in comparison with the NL3 model, that the

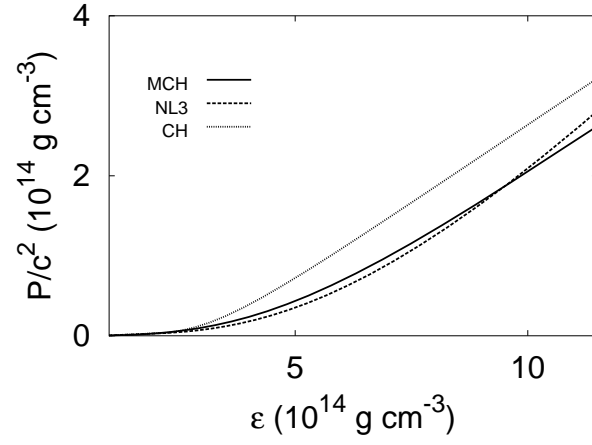


Fig. 3. The neutron star matter pressure as a function of the energy density.

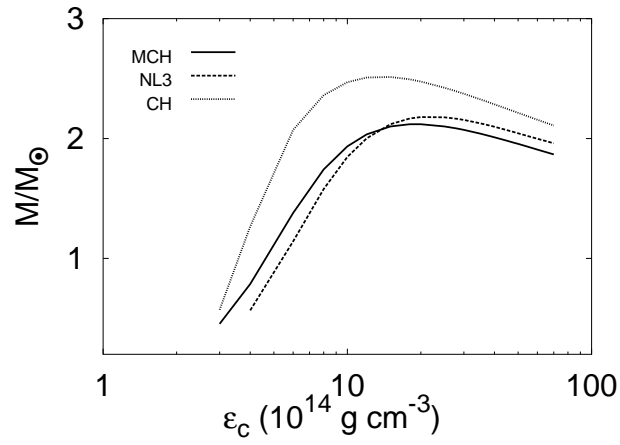


Fig. 4. The maximum mass as a function of the central energy density.

MCH model is stiffer in the low density range and becomes softer above three times the normal nuclear matter density.

Table 2. Neutron star structure parameters in the maximum mass limit.

ε_c (g cm^{-3})	R (km)	M/M_\odot	z	I (g cm^2)	
2.0×10^{15}	12.11	2.12	0.44	2.57×10^{45}	MCH
2.0×10^{15}	11.56	2.18	0.50	2.56×10^{45}	NL3
1.5×10^{15}	13.77	2.51	0.47	4.19×10^{45}	CH

The results for the star structure parameters are listed in Table 2 and displayed in Fig. 4 using equation [13]. This figure plots the mass as a function of the central density. The models are the same as in Fig. 3. In Table 2, we also list additional parameters of interest. These are the moment of inertia I , and the surface redshift $z = \frac{1}{\sqrt{1-2GM/Rc^2}} - 1$ as a function of the central density of the star. (For details, see Ref. [13]) These are important for the dynamics and transport properties of pulsars. From Fig. 4 and Table 2, we see that the maximum masses of the stable neutron stars are $2.1M_\odot$, $2.2M_\odot$ and $2.5M_\odot$ and corresponding radii are 12.1 km, 11.6 km and 13.8 km for MCH, NL3 and CH equation of states, respectively. The corresponding central densities are $2.0 \times 10^{15} \text{ g cm}^{-3}$ (> 7 times nuclear matter density, where the nuclear matter density is $2.8 \times 10^{14} \text{ g cm}^{-3}$), $2.0 \times 10^{15} \text{ g cm}^{-3}$ (> 7 times nuclear matter density) and $1.5 \times 10^{15} \text{ g cm}^{-3}$ (> 5 times nuclear matter density) for MCH, NL3 and CH, respectively, at the maximum neutron star masses. From the neutron star structure point of view, the model MCH is comparable to that of the NL3 [15] model, which was constructed using recent heavy-ion collision data. [2] The maximum masses calculated using our models are in the range of recent observations, [39–42] where the observational consequences are given below.

Very recently, it has been observed that the best determined neutron star masses [43] are found in binary pulsars, and they all lie in the range $1.35 \pm 0.04 M_\odot$, except for those of the non-relativistic pulsars PSR J1012+5307, for which $M = (2.1 \pm 0.8) M_\odot$. [39] There are several measured X-ray binary masses, and the heaviest among them are Vela X-1 with $M = (1.9 \pm 0.2) M_\odot$ [40] and Cygnus X-2 with $M = (1.8 \pm 0.4) M_\odot$. [41] From the recent discovery of high-frequency brightness oscillations in low-mass X-ray binaries, the large masses of the neutron stars are around $M = 2.3 M_\odot$, $M = 2.1 M_\odot$ and $M = 1.9 M_\odot$ in QPO 4U 1820-30, QPO 4U 1608-52 and QPO 4U 1636-536, respectively. [42] This provides a new method to determine the masses and radii of the neutron stars. Our results lie in the range of those predicted by the observational limits. [39–42]

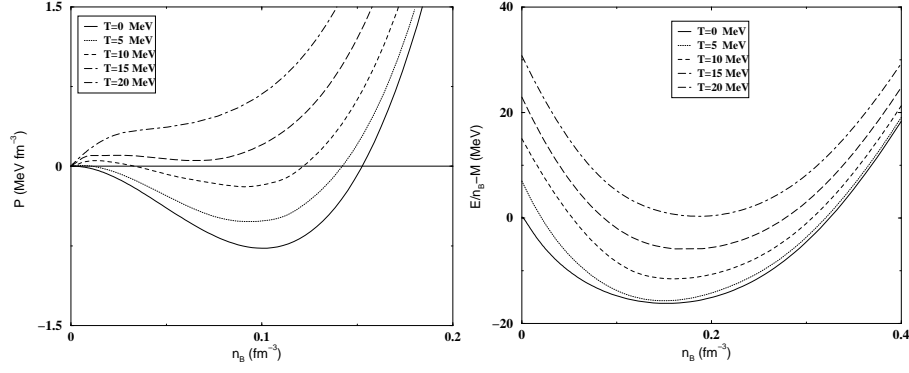


Fig. 5. The left panel of figure represents pressure versus baryon density and the right panel shows the energy per particle as a function of baryon density for the set II (MCH) for different temperature.

D.3 At finite temperature

Here we analyze the effect of temperature on the MCH EOS (set II), explicitly near the nuclear matter density, such as liquid gas phase transition. The pressure versus baryon density is plotted to show the liquid gas phase transition for various temperature ranging from 0 to 20 MeV in left panel of Fig. 5(a). At zero temperature, there is a nice pocket (isotherm), which means that the liquid and gas phase are well separated with each other by an unphysical region, where the pressure is negative. One can make a smooth transition from liquid to gas state by making a Maxwell construction [44]. This pocket gradually decreases with increasing temperature. At a particular temperature, the pocket vanishes and is marked as the pure gas state. At this point the pressure gradient with respect to density (inflection point) is zero ($\partial P / \partial n_B|_{T_c} = \partial^2 P / \partial n_B^2|_{T_c} = 0$) and is noted as the critical point for liquid gas phase transition. In other words, the point where the two phases can not be distinguished from each other for a particular temperature is called the critical point. In this figure, the critical temperature $T_c = 16.8$ MeV which corresponds to pressure $P_c = 0.22$ MeV/fm³ and density $n_c = 0.044$ fm⁻³.

The critical temperature obtained by the density dependent relativistic mean-field theory [33] ($T_c = 12.66$ MeV) and the experimental value ($T_c = 13.1 \pm 0.6$ MeV) [28] are close to the T_c . If one consider the original Walecka model [7] (no non-linear terms), the critical temperature is $T_c \approx 18.3$. This can be reduced to $T_c \approx 14.2$ MeV [45], when one introduces the non-linear terms in the scalar field. The critical temperature extracted by DBHF approach is 15.0 MeV [11]. Also, it is reported by Baldo et al [46] that a very low T_c of about 8 – 9 MeV is obtained in relativistic Dirac-Brueckner calculation. Therefore, it can be concluded from the above models that the critical temperature varies from 8 – 19 MeV depending on the formalisms and the parameters used. In our present investigation, we also find a large range of T_c from 14 – 20 MeV depending on the parameter sets (I, II, III). Thus our model is compatible with the other relativistic and non-relativistic models.

The right panel of Fig. 5(b) displays the energy per particle versus baryon density for the symmetric matter with set II (MCH). With increasing temperature, the system becomes less bound in comparison to zero temperature. At $T = T_c$, the energy per particle is -4.8 MeV.

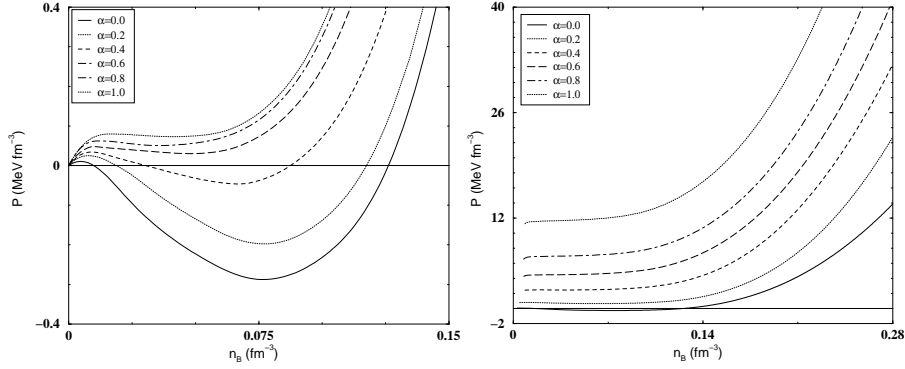


Fig. 6. The pressure as a function of the baryon density for fixed $T=10$ MeV with various asymmetric parameter α . The left panel is without ρ -meson and the right panel is with ρ -meson inclusion for set II (MCH).

In our further discussions, we study the asymmetric, α dependence of the system for a fixed temperature, say for example $T = 10$ MeV. Moreover in this section, we analyzed the effect of ρ -meson on the nuclear system. Also, the behavior of effective mass with temperature and the critical temperature T_c as a function of asymmetric parameter α are studied.

In Fig. 6(a), the pressure versus baryon density for different α at a fixed temperature $T=10$ MeV using parameter set II (MCH) is displayed. In this case, we have not included the effect of ρ -meson. The liquid gas phase transition disappears at $\alpha > \sim 0.6$, below which the pressure shows a minimum with respect to density, that means there is a phase boundary between two phases as shown in Fig. 6(a). Also for different α , we plot pressure versus baryon density for fixed $T=10$ MeV with inclusion of ρ -mesons in the nuclear matter for parameter set II. The graph (Fig. 6(b)) looks very similar to Fig. 6(a), but the pressure rapidly increases as the extra repulsive force generated from the ρ -mesons and hence, the liquid gas phase transition vanishes at $\alpha > \sim 0.2$.

The asymmetric parameter, α versus T_c is displayed in Fig. 7 for the set II (MCH) without considering ρ -meson. The value of critical temperature T_c reduces from nuclear matter $\alpha=0$ ($T_c=16.8$ MeV) to neutron matter $\alpha=1$ ($T_c=11.2$ MeV). It shows that the liquid gas phase transition is more probable in neutron matter than the pure symmetric nuclear matter. The similar behavior has been reported in Ref. [29] within the effective nuclear model based on the mean-field approximation. That means the pressure generated from repulsive saturation force plays vital role to undergo early phase transition.

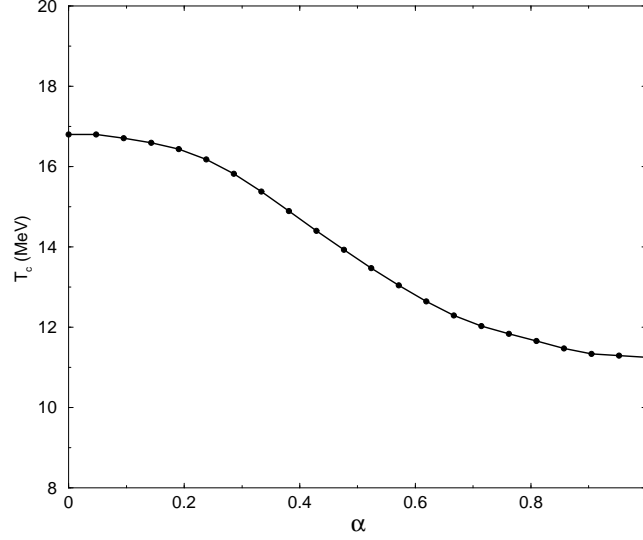


Fig. 7. The T_c as a function of asymmetric parameter α for the set II (MCH).

E Summary and conclusions

We presented a microscopic calculation of EOS in a relativistic framework based on the modified SU(2) chiral sigma model with different parameter sets. In this model, we adopted an approach in which the mass of the isoscalar vector field is generated dynamically. To ensure the empirical value of incompressibility at saturation, we added higher-order terms of scalar meson field. Thus the nucleon effective mass acquires a self-consistent density dependence on the scalar and vector meson fields. Based on this model, we studied the effect of incompressibility ($K = 210 - 380$ MeV) and effective mass ($m^*/m = 0.8 - 9$) on EOS near three times the nuclear matter density. We compared our results with the realistic EOS, prediction at low density region and also with the recently extracted EOS from the heavy-ion collisions [35] at high density. The EOS obtained by MCH models overall agreed well with the experimental data and realistic potential DBHF model. Among these models, we found that the sets I and II (MCH) are in agreement with the predicted EOS. In our discussions, we considered set II, MCH EOS for the analysis of warm asymmetric nuclear system. The reason is that it is compatible with recent heavy-ion collisions data [8].

The same MCH EOS had been applied to the neutron star matter with an admixture of electrons, protons and neutrons. The results for the structure parameters such as masses and radii are calculated. These are in the range of recent observations [39–42].

The liquid gas phase transition is studied within models MCH (set II). We found that the critical temperature is 16.8 MeV. The corresponding P_c and n_c are 0.22 MeV fm⁻³ and 0.044 fm⁻³, respectively. This is close to the recent experimental observation, 13.1 ± 0.6 [28]. Precisely, set I is very close to this value [21]. The binding energy per

particle is also discussed with various temperature up to 20 MeV. We observed that the system becomes less bound with increasing temperature.

The EOS is also shown with variation of asymmetric parameter, α for a fixed temperature, with and without ρ -meson contribution. The critical point decreased due to increase of α . With inclusion of ρ -meson along with α , it is reduced further. This decrease in critical temperature in presence of ρ -meson is because of the strong repulsive force. This model worked well at low density region such as liquid gas phase transition. The success of this model could be revisited for the study of finite nuclei and at extreme densities and temperature.

This work is done in collaboration with A. Ohnishi and S. K. Patra.

References

1. G.F. Burgio, M. Baldo, P.K. Sahu and H.J. Schulze, Phys. Rev.C **66**, (2002) 025802.
2. P. K. Sahu, Phys. Rev. C **62**, (2000) 045801.
3. J. Letessier and J. Rafelski, Phys. Rev. C **67**, (2003) 031902.
4. H. Shen, H. Toki, K. Oyamatsu and K. Sumiyoshi, Nucl. Phys. A **637**, (1998) 435.
5. G. Brown, H. Bethe and G. Bayam, Nucl. Phys. A **375**, (1982) 481.
6. P. Bonche and D. Vautherin, Nucl. Phys. A **372**, (1981) 496.
7. B. D. Serot and J. D. Walecka, Adv. Nucl. Phys. **16**, (1986) 1; Int. J. Mod. Phys. E **6**, (1997) 515.
8. S. K. Patra, M. Del Estal, M. Centelles, X. Vinas, Phys. Rev. C **63**, (2001) 024311.
9. J. D. Walecka, Ann. Phys. **83**, (1974) 491.
10. J. Boguta and A. R. Bodmer, Nucl. Phys. A **292**, (1977) 413.
11. B. ter Haar and R. Malfliet, Phys. Rep. **149**, (1987) 207; R. Brockman and R. Malfliet, Phys. Rev. C **42**, (1990) 1965.
12. R. J. Furnstahl, B. D. Serot and H. -B. Tang, Nucl. Phys. A **598**, (1996) 539.
13. P. K. Sahu, R. Basu and B. Datta, Astrophys. J. **416**, (1993) 267.
14. M. Gell-Mann and M. Levy, Nuovo Cim. **16** (1960) 705.
15. T. D. Lee and G. C. Wick, Phys. Rev. D **9** (1974) 2291.
16. J. Boguta, Phys. Lett. **B120** (1983), 34; **B128** (1983) 19.
17. M. Prakash and T. L. Ainsworth, Phys. Rev. C **36** (1987) 346.
18. N. K. Glendenning, Nucl. Phys. A **480** (1988) 597.
19. N. K. Glendenning, Ann. Phys. **168**, (1986) 246.
20. P. K. Sahu and A. Ohnishi, Prog. Theo. Phys. **104**, (2000) 1163.
21. P. K. Sahu, et al, Nucl. Phys. A **733**, (2004) 169.
22. P. Moller, W. D. Myers, W. J. Swiatecki and J. Treiner, Atomic Data Nucl. Data Tables **39**, (1988) 225.
23. C. W. Misner, K. S. Thorne and J. A. Wheeler, *Gravitation* (San Francisco. Freeman) (1970).
24. J. B. Hartle, Astrophys. J. **150** (1967), 1005.
25. J. W. Negle and D. Vautherin, Nucl. Phys. A **207**, (1973) 298.
26. G. Baym, C. J. Pethick and P. G. Sutherland, Astrophys. J. **170**, (1971) 299.
27. R. P. Feynmann, N. Metropolis and E. Teller, Phys. Rev. **75**, (1949) 308.
28. T. Li *et al.*, Phys. Rev. C **49**, (1994) 1630.
29. P. Wang, Phys. Rev. C **61**, (2000) 054904.
30. H. R. Jaqaman, A. Z. Mekjian and L. Zamick, Phys. Rev. C **29**, (1984) 2067; R. K. Su, S. D. Yang and T. T. S. Kuo, Phys. Rev. C **35**, (1987) 1539.
31. J. Heyer, T. T. S. Kuo, J. P. Shen and S. S. Wu, Phys. Lett. B **202**, (1988) 465. L. Satpathy, M. Mishra and R. Nayak, Phys. Rev. C **39**, (1989) 162.

32. J. M. Lattimer and D. G. Ravenhall, *Astrophys. J.* **223**, (1978) 314; J. M. Lattimer, C. J. Pethick, D. G. Ravenhall and D. Q. Lamb, *Nucl. Phys. A* **432**, (1985) 646.
33. G. Hua, L. Bo and M. Di Toro, *Phys. Rev. C* **62**, (2000) 035203.
34. P. K. Sahu and W. Cassing, *Nucl. Phys. A* **712**, (2002) 357; P. K. Sahu, W. Cassing, U. Mosel and A. Ohnishi, *Nucl. Phys. A* **672**, (2000) 376; P. K. Sahu, A. Hombach, W. Cassing, M. Effenberger and U. Mosel, *Nucl. Phys. A* **640**, (1998) 493.
35. P. Danielewicz, R. Lacey and W. G. Lynch, *Science* **298**, (2002) 1592.
36. Y. Sugahara and H. Toki, *Nucl. Phys. A* **579**, (1994) 557.
37. M. Del Estal, M. Centelles, X. Viñas and S.K. Patra, *Phys. Rev C* **63**, 024314 (2001) 024314.
38. A. Lang, B. Blättel, W. Cassing, V. Koch, U. Mosel and K. Weber, *Z. Phys. A* **340** (1991) 287.
39. J. van Paradijs, *The many faces of neutron stars*, ed. R. Buccheri, J. van Paradijs and M. A. Alpar, (Kluwer Academic Publishers, 1998).
40. M. H. van Kerkwijk, J. van Paradijs and E. J. Zuiderwijk, *Astron. Astrophys.* **303**, (1995) 497.
41. J. A. Orosz and E. Kuulkers, *Mon. Not. Ro. Astron. Soc.* **305**, (1999) 132.
42. M. C. Miller, F. K. Lamb and P. Psaltis, *Astrophys. J.* **508**, (1998) 791; H. Heiselberg, *Proc. of the 10th Int. Conf. on Recent Progress in ManyBody Theories*, World Scientific, (1999).
43. S. E. Thorsett and D. Chakrabarty, *Astrophys. J.* **512**, (1999) 288.
44. H. Muller and B. D. Serot, *Phys. Rev. C* **52**, (1995) 2072.
45. R. J. Furnstahl and B. D. Serot, *Phys. Rev. C* **55**, (1997) 1499.
46. M. Baldo, et al, *Nucl. Phys. A* **583**, (1995) 559c.

Effect of Relativistic Mean Field Theory on Collective Flow at AGS Energies

P. K. Sahu

Institute of Physics, Sachivalaya Marg, Bhubaneswar 751 005, India

Abstract. We study the transverse in-plane (sideward) and elliptic flow at AGS energies in a relativistic dynamical simulation model. In order to study the sensitivity of different relativistic mean-field equation of state (EOS) we use three NL2(soft), NL23(medium) and NL3(hard) momenta dependence mean-field equation of state in the transport model and these are fitted with Schrödinger equivalent potential up to 1 GeV kinetic energy. We calculate the sideward excitation function and elliptic flow within these models and compare with data as a function of beam energies, impact parameters and transverse momentum, respectively. We find that to describe data both sideward and elliptic flow, NL23 model is the better choice at AGS (4–8 A·GeV) with respect to data. However, at higher energies, the differences of three models become rather less significant because all models deal similar reduction of vector potential.

A Introduction

The most interesting observables in ultra-relativistic heavy-ion collisions are the collective motion of the particles. These particles are produced when two heavy-nuclei collide each other with a relativistic beam energies of the order of A·GeV. For example, when two Au + Au nuclei collide at beam energy is more than 2 A·GeV, a huge number of particles are produced and they move collectively. The collective motion of these particles is called flow and is identified according to behavior of the particles: the radial motion of the particles is called radial flow, the bounce off of compressed particles in the reaction plane is called sideward flow and the squeeze-out and enhance of the particles out of the reaction plane are called elliptic flow. The last two flow are important, because these two flow give good insight of understanding the high density nuclear matter, created in the heavy-ion collisions experiments. Also, the side ward and elliptic flow are attributed to the better understanding of nuclear EOS as well as quark-gluon plasma formation, since these are produced at the early stage of collisions and hence depend on the early pressure gradient in the collisions.

The sideward flow is a deflection of forward and backward moving particles away from the beam axis within the reaction plane. This flow has more potential than radial flow in the determination of EOS. Because in the transport model, it has been observed directly that the production of sideward flow is shifted toward the high density phase. On the other hand, the elliptic flow is equally important at very high energies. Specially at SIS to AGS energies, the elliptic flow generates from the early squeeze-out of compressed matter and tries to move out in the direction perpendicular to the reaction

plane. It is associated with the shape of the participant zone in the late stage of in-plane emission. The elliptic flow has two signs: the negative out-of plane elliptic flow contribution comes from the squeeze-out and the positive elliptic flow indicates as in-plane enhancement. The later one is seen at higher AGS energies and results from the asymmetric shape of the overlap volume of the two nuclei. The elliptic flow may play crucial role in the determination of EOS than sideward flow, because it involves almost no opposition of stream of matter moving past each other due to its motion is out-of reaction plane.

In the recent years both, the directed sideward flow and the elliptic flow, have been measured [1–4] for heavy-ion ($Au + Au$) collisions at AGS energies in the incident energy range of $1 \text{ A}\cdot\text{GeV} \leq E_{inc} \leq 11 \text{ A}\cdot\text{GeV}$. Very recently, also differential flow data are available from the E985 Collaboration [5] which allow for more severe constraints on the EOS.

The sideward and elliptic flow of nucleons have been studied [6–8] for various nucleus-nucleus collisions as a function of beam energy from $0.5 \text{ A}\cdot\text{GeV}$ to $11 \text{ A}\cdot\text{GeV}$ employing a relativistic transport model with hadronic and string degrees of freedom. In the AGS energy regime, however, our calculations have been performed only with a ‘stiff’ EOS based on momentum-dependent scalar and vector self energies for the nucleons. Here we continue our calculations within the same transport approach using, furthermore, different equations of state with incompressibilities of 210 MeV (soft), 300 MeV (medium), and 380 MeV (hard) as a function of beam energies, impact parameter and transverse momentum.

We divide this lecture in the following sections: In Section 2 we briefly describe the relativistic transport model and fix the parameter sets for the scalar and vector self energies in comparison to the ‘experimental’ optical potential from Ref. [9]. In Section 3 we will systematically study the transverse in-plane and elliptic flow for $Au + Au$ collisions from 2–8 A·GeV. Section 4 concludes this study with a summary and discussion.

B Description of model

In this work, we analyze both the sideward and elliptic flow as function of energies as well as impact parameters and transverse momenta at AGS energies using a dynamical hadron-string simulation model RBUU [7,8]. The RBUU model has two parts: part one is based on a coupled set of covariant transport equations for the phase-space distributions of a hadron (see for more detail in Ref. [7]) and the second part is the collision term that describe the scattering and hadron production/absorption rates. In the second part, we employ the in-medium cross sections as given in Ref. [10] that are parameterized with the corresponding experimental data for $\sqrt{s} \leq 3.5 \text{ GeV}$. The choice of this parameter $\sqrt{s} \leq 3.5 \text{ GeV}$ imply that it fits the transverse mass spectra of protons in central Au+Au collisions at AGS energies. For higher energies the Lund string formation and fragmentation model [11] are employed, this is similar to the approach of Hadron-String-Dynamics (HSD) model [12, 13], which has been used extensively for the description of particle production in nucleus-nucleus collisions from SIS to SPS energies [12]. Concerning the first part of the relativistic transport model RBUU, it is fully specified by the scalar and vector potentials, which determined the mean-field propa-

gation of the hadrons. The scalar and vector potentials are input from the relativistic mean-field EOS.

In this calculation, we use a similar Lagrangian density as proposed by Walecka [14] for the description of nuclear matter, which has been used in the relativistic BUU model before [15]. This Lagrangian contains nonlinear self-interactions of the scalar field $U(\sigma) = \frac{1}{2}m_\sigma^2\sigma^2 + \frac{1}{3}B\sigma^3 + \frac{1}{4}C\sigma^4$ where the parameters m_σ, B, C are calculated by fitting the saturation density, binding energy, effective nucleon mass as well as the compression modulus at nuclear matter density (cf. NL3 parameter set from Table 1 in Ref. [15]). An additional coupling between the vector and scalar fields in the Lagrangian leads to a relatively soft EOS [16, 17] which, however, does not yield enough repulsion to describe the flow data below 1 AGeV.

The energy density in mean-field theory (for nuclear matter) in this model can be written as [15]

$$\begin{aligned} \varepsilon(m^*, n_b) = & g_v U_0 n_b - \frac{1}{2} m_v^2 U_0^2 + \frac{m_\sigma^2}{2g_s^2} (m - m^*)^2 + \frac{B}{3g_s^3} (m - m^*)^3 \\ & + \frac{C}{4g_s^4} (m - m^*)^4 + \gamma \int_0^{k_f} \frac{d^3 p}{(2\pi)^3} \sqrt{p^2 + m^*}, \end{aligned} \quad (1)$$

where $m^* = m - g_s \sigma$ is the effective nucleon mass, n_b is the baryon density and the spin and isospin degeneracy is $\gamma = 4$. σ and U_0 are the scalar and vector fields with mass m_σ and m_v , which couple to nucleons with coupling constants g_s and g_v , respectively. The quantities B and C are constant parameters and p is the nucleon momentum which has to be integrated up to the Fermi momentum k_f . The vector and scalar potentials are density dependent, however, the vector potential increases only linearly with density. The parameter sets are denoted by NL2 (compression modulus, K=210 MeV, soft), NL23 (K=300 MeV, medium) and NL3 (K=380 MeV, hard) according to stiffness of the equation of states respectively [15, 18].

For all these EOS, the scalar and vector form factors at the vertices are taken into account in the form [7, 8]

$$f_s(\mathbf{p}) = \frac{\Lambda_s^2 - a\mathbf{p}^2}{\Lambda_s^2 + \mathbf{p}^2} \quad \text{and} \quad f_v(\mathbf{p}) = \frac{\Lambda_v^2 - b\mathbf{p}^2}{\Lambda_v^2 + \mathbf{p}^2}. \quad (2)$$

The cut-off parameters Λ_s and Λ_v and constant parameters a and b are obtained by fitting the Schrödinger equivalent potential,

$$U_{sep}(E_{kin}) = U_s + U_0 + \frac{1}{2M}(U_s^2 - U_0^2) + \frac{U_0}{M}E_{kin}, \quad (3)$$

to Dirac phenomenology for intermediate energy proton-nucleus scattering [9]. These parameters Λ_s, Λ_v, a and b are 1.05 GeV, 1.52 GeV, 1/3 and 1/4 for NL2, 1.0 GeV, 1.35 GeV, 1/3 and 1/4 for NL23 and 1.0 GeV, 0.9 GeV, 1/2 and 1/6 for NL3 models, respectively. Figure 1 displays the resulting Schrödinger equivalent potential as a function of the nucleon kinetic energy with respect to the nuclear matter at rest for all three models NL2, NL23 and NL3. The Schrödinger equivalent potentials with function of kinetic energy upto $E_{kin} = 1$ GeV are described well with the data from Hama et al. [9] in all three models. Above the kinetic energy $E_{kin} > 1$ GeV, the potentials decrease and

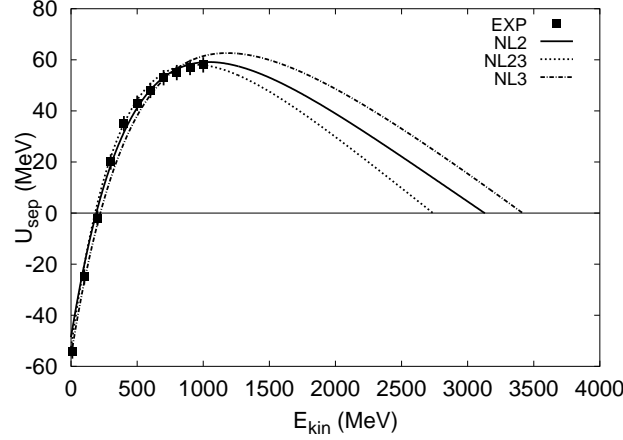


Fig. 1. The Schrödinger equivalent potential (2) at density ρ_0 as a function of kinetic energy in comparison to the data are from [9] (full squares). The solid line results from the parameter set NL2 (soft) while the dotted and dot-dashed lines correspond to NL23 (medium) and NL3 (stiff), respectively.

are set to zero above 3.2 GeV, 2.8 GeV and 3.5 GeV for NL2(solid), NL23(dashed) and NL3(dot-dashed) models, respectively, to prevent the negative optical potential, which is unphysical. The energy per nucleon E/A - as resulting from the 3 parameter sets - is shown in the upper left part of Fig. 2 as a function of the density ρ , where the free nucleon rest mass has been subtracted. The shorthand notations 'soft', 'medium' and 'stiff' become obvious from this figure. It is of further importance, how the optical potentials look like as a function of the baryon momentum p with respect to the nuclear matter at rest for densities of 2, 3, and 5 ρ_0 which are encountered in nucleus-nucleus collisions at AGS energies. This information is also displayed in Fig. 2 for NL2 (solid lines), NL23 (dotted lines) and NL3 (dot-dashed lines). Whereas for low momentum p the optical potential U_{sep} becomes more repulsive with increasing stiffness K (and density ρ), it is of roughly the same size for $p \approx 1$ GeV/c at all densities and even most repulsive for the 'soft' parameter set NL2 above ~ 1.5 GeV/c. Thus the energy per particle E/A in the upper left part of Fig. 2 is somewhat misleading since it only reflects the momentum dependence of the potentials up to the Fermi momentum

$$p_F = \left(\frac{3}{2}\pi^2\rho\right)^{1/3}, \quad (4)$$

which is less than 0.5 GeV/c even at 6 ρ_0 .

C Transverse and elliptic flow

In this Section we discuss the transverse in-plane $\langle p_x \rangle (y)$ and elliptic $v_2(b, p_t)$ flow for mid-peripheral $Au + Au$ collisions from 2–8 A·GeV. The shape of the average proton in-plane momentum $\langle p_x(y') \rangle$ as a function of the normalized rapidity

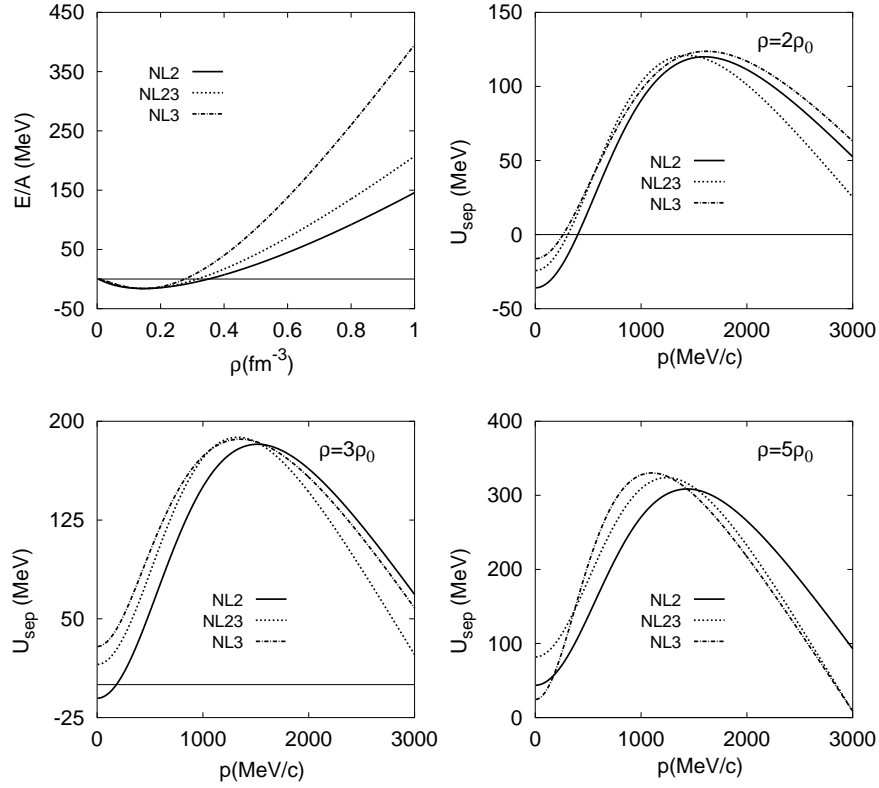


Fig. 2. The energy per nucleon E/A as a function of density ρ is shown in the upper left part for the parameter sets NL2 (solid line), NL23 (dotted line) and NL3 (dot-dashed line). The optical potential (2) as a function of the baryon momentum p with respect to the nuclear matter at rest frame is displayed in the upper right and lower parts for densities of $2\rho_0$, $3\rho_0$ and $5\rho_0$, respectively.

$y' = y_{cm}/y_{proj}$ normally fitted by a polynomial function ($Fy' + Ky'^3$) around midrapidity. The linear coefficient F is represented as sideward flow. This quantity is displayed in Fig. 3 for the parameter sets NL2 (solid line), NL23 (dotted line) and NL3 (dot-dashed line). These sets are compared to the data from Ref. [1] (full squares). From

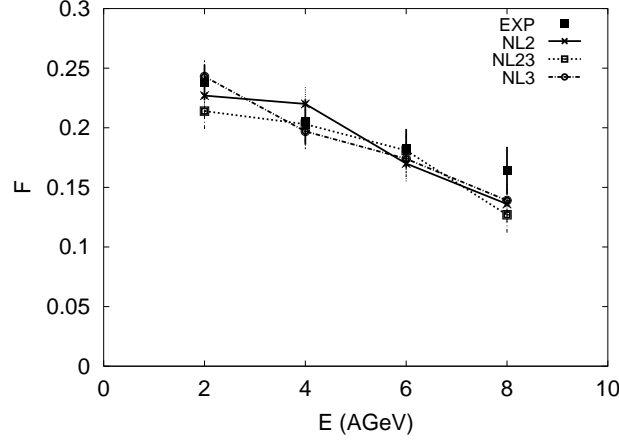


Fig. 3. The flow F as a function of beam energy for $Au + Au$ collisions at $b=6$ fm for the parameter sets NL2 (solid line), NL23 (dotted line) and NL3 (dot-dashed line). The experimental data (full squares) are from the E895 collaboration [1].

this figure we notice that all parameter sets are roughly compatible with the data such that the transverse flow observable F does not qualify very much for a determination of the stiffness of the EOS as pointed out in Ref. [19] more than a decade ago. Only at 2 A·GeV the data more clearly favor a 'stiff' EOS as denoted by NL3. The reasonable description of the transverse flow F at 4-8 A·GeV by all parameter sets is attributed to the fact that the momentum dependence of the scalar and vector mean fields is roughly the same (cf. Fig. 1), which is enforced by the fit to the experimental data from Hama et al. [9]. The significant decrease in F at high energies is due to the reduction of vector potential with momentum as pointed out before in Ref. [7]. According to our understanding the reduction of the vector coupling with density and momentum is a genuine phenomenon of nuclear many-body physics and points toward a restoration of chiral symmetry with increasing density as advocated by Brown and Rho [20]; it not necessarily has to be interpreted as a signature for a phase transition to a QGP.

We now consider the calculations for the elliptic flow $v_2(b, p_t)$. The elliptic flow can be measured by the second Fourier coefficient of the azimuthal distribution of particles with respect to the reaction plane and is characterized by the expectation value [21], $v_2 = \langle (p_x^2 - p_y^2) / (p_x^2 + p_y^2) \rangle$. In Fig. 4 we show the impact parameter b dependence of the elliptic flow for $Au + Au$ collisions at energies of 2 and 6 A·GeV without any cut on the transverse momentum p_t of the protons (a) and (b). Like before similarly, the solid lines display the results from the set NL2, the dotted lines those from NL23

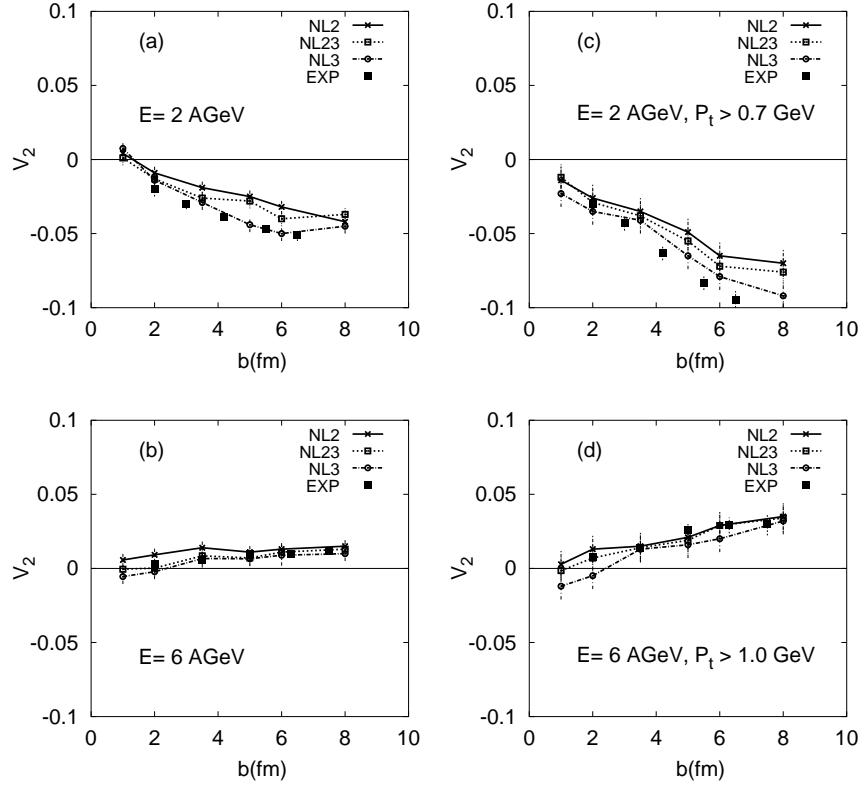


Fig. 4. Elliptic flow v_2 as a function of impact parameter b and transverse momentum p_t for $Au + Au$ collisions at 2 and 6 A·GeV. In this figure (a) and (b) are for $p_t \geq 0$, however, (c) is for $p_t \geq 0.7$ GeV/c and (d) is for $p_t \geq 1.0$ GeV/c, respectively. The experimental data (full squares) are from the E895 Collaboration [5].

and the dot-dashed lines those from NL3. The experimental data (full squares) have been taken from Ref. [5]. At 2 A·GeV we observe a clear sensitivity to the stiffness of the EOS; only the set NL3 (stiff) describes the large negative elliptic flow as a function of b correctly, whereas the other parameter sets turn out too low in v_2 . This finding agrees with that from Danielewicz [22] that the 2 A·GeV data for $Au + Au$ 'need' a stiff EOS. However, contrary to Ref. [22] we do not find the softening of the EOS at higher bombarding energy significantly. The χ^2 fits to the data in Fig. 4 give only a tiny preference to the results from NL23 (medium) at 6 A·GeV.

The situation might be different when comparing to the elliptic flow at high transverse momentum p_t . In Fig. 4 we thus display (c) and (d) our calculations on the elliptic flow as a function of impact parameter b with the corresponding data from Ref. [5] for a cut in $p_t \geq 0.7$ GeV/c at 2 A·GeV and a high p_t cut of 1 GeV/c at 6 A·GeV for $Au + Au$. Again clearly the best description at 2 A·GeV is given by NL3 (stiff) now even slightly underestimating the magnitude of v_2 . On the other hand, the elliptic flow at 6 A·GeV within experimental error bars for all parameter sets is compatible with the data. A χ^2 analysis gives a slight preference for NL23 (medium) followed by NL2 (soft), whereas the χ^2 is higher for NL3 (stiff). However, these differences are still within the statistical accuracy of the transport calculations which becomes poor for high transverse momentum protons. We attribute this approximate insensitivity to the stiffness of the EOS to the fact, that the optical potentials at high density and momenta are roughly the same and that multi-meson production channels from string decays start to dominate the reaction dynamics above 4 A·GeV as pointed out before in Ref. [7].

D Summary and Conclusions

In summary, we have analyzed the sideward and elliptic flow from $Au + Au$ at beam energies ranging from 2 A·GeV to 8 A·GeV using the different nuclear forces starting from soft, medium and stiff equation of states in the microscopic relativistic transport simulation model.

The transverse flow F as a function of energy can be rather good described in the dynamical transport model by all parameter sets in turn is attributed to the fact that the momentum dependence of the scalar and vector mean fields is roughly the same (cf. Fig. 1), which is enforced by the fit to the experimental data from Hama et al. [9]. A χ^2 analysis here favors a 'stiff' EOS at 2 A·GeV while the 4-8 A·GeV data are best reproduced by the 'medium' parameter set NL23. However, the significance for this trend is very low.

Our calculations for the elliptic flow v_2 show a clear sensitivity to the stiffness of the EOS at 2 A·GeV; only the set NL3 (stiff) describes the large negative elliptic flow seen by E895 [5] as a function of b correctly, whereas the other parameter sets turn out too low. This finding agrees with that from Danielewicz [22] that the 2 A·GeV data for $Au + Au$ call for a stiff EOS. However, contrary to Ref. [22] we do not find convincing indications for a softening of the EOS at higher bombarding energy even at high transverse momenta ($p_t \geq 0.7$ GeV/c or 1 GeV/c, respectively). A χ^2 analysis favors again the 'medium' EOS (given by the set NL23) at 4-6 A·GeV in line with the analysis of the transverse flow, but with rather low significance. For bombarding

energies ≥ 6 A-GeV our calculations turn out to be almost insensitive to the stiffness of the EOS, which is likely due to the fact that the optical potentials at high density and momenta (in the transport approach) are roughly the same and that multi-meson production channels from string decays start to dominate the reaction dynamics above 4 A-GeV [7, 8].

Here we remark that our transport calculations – involving all hadrons up to a mass of 2 GeV and strings for the hadronic continuum – give a good description of the differential sideward and elliptic flow data, does not imply that the proper degrees of freedom are employed. On the other hand, we can turn the argument around and conclude, that the differential flow data do not necessarily indicate the presence of a new state of matter such as the QGP. Electromagnetic signals should provide complementary information to the collective observables studied here.

This work is done in collaboration with W. Cassing.

References

1. E895 Collaboration, H. Liu et al., Phys. Rev. Lett. **84** (2000) 5488.
2. N. Herrmann et al., Nucl. Phys. **A 610** (1996) 49c.
3. E895 Collaboration, P. Chung et al., Phys. Rev. Lett. **86** (2001) 2533.
4. E895 Collaboration, J. L. Klay et al., Phys. Rev. Lett. **88** (2002) 102301.
5. E895 Collaboration, P.Chung et al., nucl-ex/0112002 (2002).
6. P. K. Sahu, A. Hombach, W. Cassing, M. Effenberger and U. Mosel, Nucl. Phys. **A 640** (1998) 493.
7. P.K. Sahu, W. Cassing, U. Mosel and A. Ohnishi, Nucl. Phys. **A 672** (2000) 376.
8. P.K. Sahu and W. Cassing, Nucl. Phys. **A712** (2002) 357.
9. S. Hama, B. C. Clark, E. D. Cooper, H. S. Sherif and R. L. Mercer, Phys. Rev. **C 41** (1990) 2737.
10. M. Effenberger, E. L. Bratkovskaya and U. Mosel, Phys. Rev. **C 60** (1999) 044614.
11. B. Nilsson-Almqvist and E. Stenlund, Comp. Phys. Comm. **43** (1987) 387; B. Anderson, G. Gustafson and Hong Pi, Z. Phys. **C 57** (1993) 485.
12. W. Cassing and E. L. Bratkovskaya, Phys. Rep. **308** (1999) 65.
13. W. Ehehalt and W. Cassing, Nucl. Phys. **A 602** (1996) 449; J. Geiss, W. Cassing and C. Greiner, Nucl. Phys. **A 644** (1998) 107.
14. B. D. Serot and J. D. Walecka, Adv. Nucl. Phys. **16** (1986) 1.
15. A. Lang, B. Bl'attel, W. Cassing, V. Koch, U. Mosel and K. Weber, Z. Phys. **A 340** (1991) 287.
16. R. J. Furnstahl, B. D. Serot and Hua-Bin Tang, Nucl. Phys. **A 598** (1996) 539.
17. R. J. Furnstahl and B. D. Serot, Phys. Rev. **C 47** (1993) 2338.
18. S. K. Ghosh, S. C. Phatak and P. K. Sahu, Z. Phys. **A352** (1996) 457.
19. W. Cassing and U. Mosel, Prog. Part. Nucl. Phys. **25** (1990) 235.
20. G. E Brown and M. Rho, Phys. Rep. **363** (2002) 85.
21. STAR collaboration, K. H. Ackermann et al., Phys. Rev. Lett. **86** (2001) 402.
22. P. Danielewicz et al., Phys. Rev. Lett. **81** (1998) 2438; P. Danielewicz, Nucl. Phys. **A 673** (2000) 34; P. Danielewicz, Nucl. Phys. **A 685** (2001) 368.

Hadronic Properties in Nuclear Medium

S.C. Phatak*

Institute of Physics, Sachivalaya Marg, Bhubaneswar 751 005.

Abstract. We shall discuss the modification of properties of hadrons in nuclear medium. In particular we shall consider how the masses and decay widths of hadrons change when they are placed in dense and hot medium. We shall argue that this modification is essentially a many body effect. One should be careful while attributing these changes to effects such as restoration of chiral symmetry etc before accounting for the many body contribution.

A Introduction

The change in the properties of objects when they are placed in a medium is a well-observed and common phenomenon. One of the striking example of this phenomenon is the Archimedes principle, known to us from school days. We know that when an object is immersed in fluids, the weight of the object decreases. So, if one defines the mass of the object as measured by using gravitational field of earth (say, using a spring balance) one would observe that the mass decreases in the medium. Of course, this decrease is now understood in terms of the hydrostatic pressure of the fluid and general principles of statics. Never the less, this change in the weight is due to the interaction of the object with the matter in the fluid. The change of hadronic properties in nuclear medium is also of similar nature in that, the interaction of a hadron with the particles in the medium gives rise to an apparent change in the mass of the hadron.

The presence of the nuclear medium alters many properties of hadrons. Some of these being the mass, decay width, magnetic moment and so on. In this talk, we shall be considering the mass and the decay width only. The interest in these two properties is that this is likely to have observable consequences. For example, if we consider an unstable particle (say a ρ meson), the change in the mass of the particle will give rise to specific characteristic signals depending on whether it decays in medium or in a free state. For example, if the particle decays into another particle (or particles), the energy-momentum carried by these particle(s) will depend on whether the decay took place in the medium or outside. Similarly, the change in the decay width will change the life time of the particle and that will decide whether the decay occurs in the medium or outside (as generally the life of the medium itself is usually not infinite). The subject of mass and decay width modification has got a boost in recent times because of these observable consequences particularly in the relativistic heavy ion collisions [1]. There has also been theoretical conjectures, arising from the restoration of chiral symmetry near QGP phase transition that the masses of chiral doublets would become equal at

* Email:phatak@iopb.res.in

phase transition. This may imply that the masses get modified significantly near the phase transition point.

One may be wondering what the mass modification has to do with the methodology of relativistic mean field [2] (RMF) which is the theme of the workshop. The thing is, the RMF is used in theoretical computation of the properties of nuclear medium at zero or nonzero temperatures as well as high nuclear densities. As a natural consequence, one can also compute the hadronic properties in nuclear medium in RMF approach. Of course, one must note that the RMF approach is one approach and the results obtained in RMF approach must be checked in other approaches and in experiments. In this particular talk, we shall deal with the subject in a pedagogical fashion. We shall not go into detailed RMF calculations and how the masses and widths get modified in the medium. But we shall discuss the problem in a general frame work, considering how one can define the mass change, how can one expect to observe it etc. Some of the results of actual calculations will be presented by Dr. Abhijit Bhattacharjee.

In order to study the change in the masses in medium theoretically, one must have a definition of what one means by mass of a particle in the medium. One must also have a corresponding experimental definition. That is, one must have a method of measuring the mass when the particle is in the medium. Let us consider the experimental issue first. One of the methods, which works for unstable particles, is to detect the decay particles and measure the (four) momenta of the decaying particles. As a concrete example, consider the decay of a ρ meson into a $\mu^+ - \mu^-$ pair. If the four momenta of the two muons are p_1^μ and p_2^μ respectively, the rest mass of ρ meson is $\sqrt{(p_1^\mu + p_2^\mu)^2}$. This quantity is called the invariant mass of a pair of particles. In an experiment, the invariant mass of the pair of muons (one having +ve charge and the other having -ve charge) are measured. The plot of number of pairs v/s the invariant mass would have a nice peak at ρ mass with the width of the peak being the decay width of ρ meson. Now, if the ρ mass and/or decay width is different in the medium and if it decays in the medium, the peak will appear at a mass which is different from the free ρ mass. This is how one would plan to measure the ρ mass in medium. Further, the width of the peak is the decay width of the particle and any change would indicate the change in the decay width in the medium. Please note that this argument works if the decaying particles (in this case muons) are themselves not affected by the nuclear medium and get out of the medium without many interactions. In case of muons, this is indeed the case since muons do not have strong interaction and interact only with electromagnetic and weak interactions. We shall consider the theoretical definition of masses and widths in the following section. Later, in section 3 we shall compute the Green's function in the medium and consider few applications of these definitions to some model systems. Section 4 is devoted to general discussions and conclusions.

B Masses and Widths in Medium

For classical systems, the mass of an object is defined as a ratio of force and acceleration [3]. In Newtonian mechanics, this is called as the inertial mass*. We cannot use this

* Newton also defines another quantity called as the gravitational mass which enters the definition of gravitational force. The inertial and gravitational masses need not be same but Newton

definition to define the hadron mass since, for one, the hadrons cannot be treated by classical mechanics and the definition of force in quantum mechanics is ambiguous. A definition which is applicable to quantum mechanical particles is the relation between the energy and momentum of these particles. For a relativistic particles, the energy momentum relationship is

$$E = \sqrt{p^2 + m^2} \quad (1)$$

so knowing the energy as a function of momentum defines the mass. The same definition can be applied to the hadrons in the medium. However, when the hadron is in a medium, the energy-momentum relation (also called as the dispersion relation) is altered and need not be of the form given in eq(1) above but the energy may have a complex functional dependence on the momentum. One then defines the mass in the limit of vanishing momentum. That is, one defines the mass to be

$$m = \frac{1}{2 \frac{\partial E}{\partial p}} \quad (2)$$

evaluated in the limit $p \rightarrow 0$. Experimentally, one can measure the energy and momentum of a particle in the medium and hence the determine the in-medium mass is possible.

Now the question is, how does one theoretically compute the dispersion relation of hadrons in a medium. The method is to use Green's function which is essentially the inverse of the wave equation. Consider a spin-zero particle in free space. The wave function of this particle is obtained by solving the Klein-Gordon equation

$$\begin{aligned} \square \Psi - m^2 \Psi &= 0 \\ \frac{\partial^2}{\partial t^2} \Psi - \nabla^2 \Psi - m^2 \Psi &= 0. \end{aligned} \quad (3)$$

In momentum space, this equation is $(E^2 - p^2 - m^2)\Psi = 0$. The free particle Green's function is the inverse of the Klein-Gordon operator,

$$G_0^+(E) = \frac{1}{E^2 - p^2 - m^2 + i\eta} \quad (4)$$

where η is an infinitesimal positive quantity added to move the singularity away from the real energy axis. The subscript 0 in the definition of the Green's function stands for free Green's function. Clearly, the Green's function has a pole at $E = \sqrt{p^2 + m^2}$ in the limit of vanishing η and this in fact gives the dispersion relation for a free Klein-Gordon particle. We can therefore define the mass of the particle from the pole of the Green's function. Similar definitions exist particles with spin-1/2 (Dirac) or larger values of spin. What this means is that the definition of the mass in terms of Green's function agrees with the 'kinetic' definition of mass, at least for a free particle.

assumed these to be same(or strictly speaking, the ratio is same for all objects.). Experimentally, one could try to detect the deviation from this assumption. It has been found that this ratio is same for all bodies (within experimental error). This was found to be very profound by Einstein and this led him to formulate the principle of equivalence. [4]

So, now the idea is, to extend this definition for a particle in nuclear medium. Thus, one has to define the Green's function for a hadron in the medium and compute the poles of the function which would give the dispersion relation. From this dispersion relation one can compute the mass of the hadron in the medium by using the definition given in eq(2). Sounds very simple. Actually, all the difficulty lies in the computation of the Green's function to the desired level of accuracy in some approximation scheme.

We may mention here that it may not always be necessary to compute the Green's function to obtain the dispersion relation. In case of nucleons in RMF approximation, one can deduce the dispersion relation of nucleons in the medium from the Dirac equation itself and this directly determines the effective mass. But that is possible essentially because of the mean field approximation.

For unstable particles, the pole of the Green's function is no more on the real axis and it moves away from the real axis. This happens because of the coupling to the decay channels leads to complex self energy(see later for the details). The imaginary part of the pole gives the decay width of the particle and is related to the half life of the particle. It can be shown that the imaginary part leads to loss of flux or equivalently the decay of the particle. The position of the pole of the Green's function does not remain at the same position but can get shifted in the medium and this would lead to the change in the masses as well as the decay widths of particles. It may be noted that, even for stable particles, the in-medium Green's function has poles at non-zero imaginary values. This happens because the particle can excite particle-hole pairs in the medium, thus losing flux from elastic channel. This is an example of a stable particle becoming unstable in the medium. It may also happen that the decay of a particle is prevented in the medium. One common reason is because of Pauli blocking. In that case, the free Green's function pole, which had an imaginary part, moves to the real axis in the medium. This then makes the particle stable in the medium.

C The Green's Function In Medium

We shall now come to the computation of the in-medium (or full) Green's function. There is a full-fledged field theoretic formalism for doing these computations. The formalism can handle the medium at zero as well as finite temperature. Because of lack of time, we will not go into the formalism but quote the results and qualitatively understand these using physical arguments. As a concrete example, consider a hadron in nuclear matter interacting with the nucleons by some two-body interaction potential V_i^{**} where i stands for i^{th} nucleon in nuclear matter.

To compute the Green's function of the hadron in the medium, one has to solve the many body problem involving the hadron and all the nucleons and a general solution is not available , One can however evaluate the Green's function in various levels of approximations and we shall consider some such schemes. The often-used approximation is to assume that the nuclear matter provides the average or effective potential U and the hadron moves in this effective potential. For this case, the equation for the Green's

** We are considering the hadron to be not a nucleon to avoid complications arising from exchange terms and Pauli principle

function in the medium is

$$\begin{aligned}
 G(E) &= G_0(E) + G_0(E)UG(E) \\
 &= G_0(E) + G_0(E)UG_0(E) + G_0(E)UG_0(E)UG_0(E) \cdots \\
 &= \frac{1}{G_0^{-1}(E) - U}
 \end{aligned} \tag{5}$$

The Green's function is computed analytically in case of nuclear matter since the effective potential is independent of position. The Green's function equation is depicted diagrammatically in Fig(1). In the last line above, the integral equation for the Green's function has been formally solved. Thus, the result is

$$G(E) = \frac{1}{E^2 - p^2 - m^2 - U + i\eta}.$$

and the pole of the Green's function is at

$$E = \sqrt{p^2 + m^2 + U}.$$

Therefore the mass of the hadron in the medium is

$$m^* = \sqrt{m^2 + U} \sim m + \frac{U}{2m} \tag{6}$$

Fig. 1. The diagram depicts the integral equation for the Green's function in the medium. The double and single lines represent the full (G) and free (G_0) Green's functions respectively and the interaction of the particle with the medium, U , is represented by a line with a cross at the end.

There are some technical details about which comments are in order.

1. Strictly speaking, the Green's function defined above is correct for scalar (spin-zero) particles. For particles having nonzero spin, things are more complex but the basic arguments presented above are valid.
2. We have assumed that the effective potential is a scalar object. It need not be so and in that case, the scalar part of the effective potential should go in the definition of the effective mass.
3. Depending on the sign of the effective potential, the mass of a particle in the medium increases or decreases.
4. If the effective potential is complex, the effective mass also becomes complex and the imaginary part of the effective mass gives the decay width of the particle.

There are a number of ways of computing the effective potential for the motion of the hadron in medium. The simplest approximation is to consider it to be a coherent sum of individual hadron-nucleon potentials. Then the potential is

$$U = \sum_i V_i \quad (7)$$

where the summation is over all the nucleons. For short ranged potentials, the potential in this approximation is proportional to nuclear density and is real. If one allows for excitations of nucleons, the hadron-nucleon potential gets replaced by in-medium hadron-nucleon scattering matrix in the equation above. This scattering matrix differs from the usual hadron-nucleon scattering matrix because many possible states to which a nucleon can get excited are occupied by other nucleons and Pauli principle forbids the scattering of the nucleon to these states. Never the less, unlike the hadron-nucleon potential, the in-medium scattering matrix is complex and therefore the effective mass becomes complex.

D Computation of Masses and Widths

D.1 Nucleons in RMF

We have already seen the mean field equations for nucleons in presence of σ and ω mesons. For the sake of completeness, let me repeat these. The equations are the Dirac equation for nucleons

$$\left[i\boldsymbol{\gamma} \cdot \boldsymbol{\nabla} - \left(m - g_\sigma \sigma_0(\mathbf{r}) \right) \right] \Psi(\mathbf{r}) = \left(E + g_\omega \omega_0(\mathbf{r}) \right) \Psi(\mathbf{r}) \quad (8)$$

where Ψ is the Dirac spinor, σ_0 and ω_0 are the mean field values of the scalar σ and (time component) of the vector field respectively, g_σ and g_ω are the nucleon-meson coupling constants and E is the energy of the particle. The mean fields satisfy the equations

$$(\nabla^2 + m_\sigma^2) \sigma_0(\mathbf{r}) = g_\sigma \rho_s(\mathbf{r}) \quad (9)$$

$$(\nabla^2 + m_\omega^2) \omega_0(\mathbf{r}) = g_\omega \rho_v(\mathbf{r}) \quad (10)$$

where $\rho_s = \sum_i \bar{\Psi}(\mathbf{r}) \Psi(\mathbf{r})$ and $\rho_v = \sum_i \bar{\Psi}(\mathbf{r}) \gamma_0 \Psi(\mathbf{r})$ are the scalar and vector baryon densities. As you know, these equations are to be solved self consistently. The meaning of these equations is as follows. The nucleons satisfy the Dirac equation with a scalar and a vector potential. These potentials are actually generated by the scalar and vector mesons and, in fact, these are proportional to the mean field values (also called as the vacuum expectation values). The nucleon scalar and vector densities, in turn, act as source terms for scalar and vector mean fields. We can consider that the vector and scalar potentials are generated by the exchange of corresponding mesons between nucleons. In fact, these potentials given in eq(8) are the potentials generated in Hartree approximation. So, the RMF is just the relativistic Hartree theory.

Now, we can define the nucleon mass, also called as the effective mass, in the medium as

$$m^* = m - g_\sigma \sigma_0 \quad (11)$$

because, indeed, m^* enters into the energy-momentum relation for nucleons in presence of other nucleons. Note that, in mean field approximation, the scalar potential, and therefore the in-medium mass is independent of nucleon momentum and there is no need of computing the derivative of the energy in the limit of vanishing momentum. In general this need not be so. Also, in RMF approximation, the effective mass m^* is real so the nucleons don't develop decay width. The reason for this is that the excitation of nucleons is not permitted in RMF. In more technical language, the RMF is a tree level approximation where particle-hole loops are not included. When one includes those, the effective mass would develop imaginary part.

D.2 Effective Mass in Impulse Approximation

In section III above, the effective mass was defined in terms of the effective potential. The effective potential itself arises from the interaction of the particle with the particles in the medium. Exact calculation of the effective potential is generally not possible and a number of schemes are used to compute it. Let us assume that the introduced particle interacts with the particles in the medium by two-body interactions v_i where i stands for i^{th} particle in the medium. In that case, the average potential seen by the introduced particle is $U_{ave} = \sum_i v_i$. Note that the interaction could be scalar or vector. The scalar part of U_{ave} is then the first approximation for the change in the mass of the particle in the medium. So, if the interaction is attractive, the effective, in-medium, mass of the introduced particle would decrease. Further, if v_i is short ranged and the particle density of the medium does not change very much over the range of the potential, one can show that U_{ave} follows the density profile of the medium and, in fact, it is proportional to the particle density of the medium. In coherent scattering approximation, the scattering amplitudes of scattering of the projectile from each nucleon is added coherently and the potential seen by the projectile is

$$\begin{aligned} U_{ave} &= \sum_j \int \Pi_{i \neq j} d^3 r_i < \Psi(r_1, \dots, r_A) | t_{pN} | \Psi(r_1, \dots, r_A) > \\ &= t_{pN} \rho_N \end{aligned} \quad (12)$$

This approximation ignores the interaction of the nucleons and works reasonably well at high energies. Note that the scattering amplitude t_{pN} , and therefore the potential seen by the projectile is generally complex. This means that the effective mass of the projectile becomes complex. This implies that the particle has a 'decay width' in the medium. This needs to be understood carefully in terms of the meaning of the imaginary part of the potential. Recall that the imaginary part of the scattering amplitude gives the total scattering cross section. Now, when the projectile scatters from a nucleon in the nucleus, it imparts some energy and momentum to it. This amounts to the excitation of the nucleus. Thus, the imaginary part of the projectile potential is because of the excitations of the nucleus (by particle-hole production). Thus, it is not that the projectile decays (like pion decays in the free space) in the medium but it loses energy and momentum in excitation of the nucleus. Never the less, this is considered as the 'decay' in the sense that the flux is removed from elastic channel.

Sometimes a particle in medium may become stable. An example is the motion of Δ particle in nuclear medium. In free space Δ decays into a nucleon and a pion. The mass of Δ is 1236 MeV, which is larger than the mass of pion and nucleon ($938 + 139 = 1077$ MeV). The decay width of Δ is 60 MeV or its life time is $\sim 10^{-23}$ sec. In the rest frame of Δ one can determine the momentum carried by the nucleon (or pion) by using energy-momentum conservation. It turns out that the nucleon momentum is about 230 MeV/c. Note that this is comparable with the momentum of nucleons in a nucleus. Thus, when Δ decays in the nucleus, the momentum states of the produced nucleon may already be occupied by nucleons in the medium. Thus the decay of Δ will be blocked by Pauli principle and this would lead to decrease in the Δ width in the medium. In fact, at large enough nuclear densities, the Δ may become a stable particle.

E Summary

We have discussed some aspects of the masses of particles in nuclear medium. We have shown that the mass of a particle needs to be defined and it can be done by using the dispersion relation (energy-momentum relation) of the particle in the medium. Theoretically the dispersion relation is derived by means of the Green's function technique. We have shown that the mass of a particle in medium may decrease or increase, depending on whether the interaction is attractive or repulsive. We have shown that the mass in the medium may be complex and the imaginary part of the mass is related to the decay width of the particle in the medium. We have found that the in-medium decay width may increase (due to nuclear excitations) or sometimes may decrease (due to Pauli blocking).

References

1. B. Lenkeit, CERES Collaboration, *Nucl. Phys.***A661**,23(1999), R. Rapp and J. Wambach, *Adv. Nucl. Phys.***25**,1(2000)
2. B. D. Serot and J. D. Walecka, *Adv. Nucl. Phys.***16**,1 (1986)
3. I. Newton's *Philosophie Naturalis Principia Mathematica* (Univ. of California Press, 1966)
4. See e.g. "Gravitation And Cosmology : Principles And Applications of The General Theory of Relativity, Chapter 3, S. Weinberg, (J. Wiley, N.Y., 1972)

Mean Field Models and In-Medium Modification of Hadron Masses

Abhijit Bhattacharyya

Department of Physics, Scottish Church College, 1 & 3, Urquhart Square, Kolkata - 700 006,
INDIA

Abstract. Some of the in-medium properties of hadrons have been calculated using two types of effective models. Within the framework of Walecka model the ρ -mass has been found to decrease with density. The $\rho - \omega$ mixing amplitude increases with density. The non-linear σ -model predicts that the pseudo-scalar meson masses decrease with temperature.

A Introduction

In the realm of high energy and nuclear physics, the past few decades have seen tremendous progress. It is almost universally accepted that Quantum Chromodynamics (QCD) [1], described by the $SU(3)$ interaction in the internal colour space, is the microscopic theory of strong interaction. Quarks and gluons [2] are the fundamental constituents of hadronic matter. They interact strongly and QCD successfully describes the interactions of these quarks and gluons at high momentum. However, due to colour confinement, it is not possible to look at the interactions of hadrons within the framework of QCD. Hence one has to look at different effective models in order to understand hadronic properties.

One of the most vibrant areas of research, in the context of QCD and hadronic matter, is the strongly interacting matter at high temperature and density. In reality, one can produce a hot and dense strongly interacting matter in ultra relativistic collisions of heavy ions [3]. On the other hand, it is expected that the early universe existed in a quark matter phase till a few microseconds after the big Bang [4]. A dense quark and/or hadronic matter also exists in the core of the neutron star [5], where the baryon density is very high.

Here I will review some of the in-medium (finite temperature/density) properties of hadrons. I understand that most of the speakers, in this workshop, will discuss the in-medium properties at the Mean Field (MF) level. So in this talk I will discuss some of the properties which arise only beyond MF level. I will divide my discussion into two parts. In section 2 the in-medium modification of ρ -meson mass will be calculated within the framework of Walecka model. We will also calculate the in-medium modification of the $\rho - \omega$ mixing amplitude from the same model. Section 3 will be devoted to a completely different approach to the effective models. The temperature dependence of the meson masses will be calculated from the non-linear σ -model, which is derived from the low energy symmetries of QCD. In section 4 we will have a brief summary.

B Relativistic Mean Field Models

In this section we will study the medium modification of ρ -meson mass and also the $\rho - \omega$ mixing amplitude. For both the purposes we will use a Relativistic Mean Field (RMF) model known as Walecka model [6, 7]. In this workshop most of the speakers have reviewed this model. So, I will briefly mention it.

Walecka model was proposed first in 1974 and has been greatly modified over the years by a number of authors; for a recent comparative study among the various versions, see [8]. The Lagrangian density for this model is given by [6, 7, 9]:

$$\begin{aligned} \mathcal{L} = & \sum_B \bar{\psi}_B (\gamma^\mu p_\mu - m_B + g_{\sigma B} \sigma - g_{\omega B} \gamma^\mu \omega_\mu + g_{\rho B} \gamma^\mu \tau \cdot \rho_\mu + f_\rho \sigma^{\mu\nu} \tau \cdot \frac{\partial_\mu}{2m} \rho_\nu) \psi_B \\ & + \frac{1}{2} (\partial^\mu \sigma \partial_\mu \sigma - m_\sigma^2 \sigma^2) - \frac{1}{4} F_{\mu\nu} F^{\mu\nu} + \frac{1}{2} m_\omega^2 \omega^2 - \frac{1}{4} G_{\mu\nu} G^{\mu\nu} + \frac{1}{2} m_\rho^2 \rho^2 \end{aligned} \quad (1)$$

In the above equation ψ_B , σ , ω^μ and ρ^μ are, respectively, the baryon, the σ , the ω and the ρ meson fields; m_B , m_σ , m_ω and m_ρ are the corresponding masses; $g_{\sigma B}$ and $g_{\omega B}$ are the couplings of the baryon to σ and ω mesons, respectively; $g_{\rho B}$ and $f_{\rho B}$ are the vector and tensor couplings of rho meson; $G_{\mu\nu} = \partial_\mu \omega_\nu - \partial_\nu \omega_\mu$ and $F_{\mu\nu} = \partial_\mu \rho_\nu - \partial_\nu \rho_\mu + i g_\rho [\rho_\mu, \rho_\nu]$.

B.1 Medium Dependence of ρ -meson mass

The recent observation of enhanced dilepton production in the low invariant mass domain in heavy ion collider experiments [10–12] has triggered speculation [13] that the effective ρ -meson mass in the nuclear medium is decreased. Simultaneously, theoretical studies based on chiral perturbation theory (χPT) have led to the expectation that even at finite densities (at or above nuclear density) there may be a partial restoration of chiral symmetry, leading to the decrease of vector meson masses from their free values [14]. The evidence (or more appropriately, indication) of the ρ mass renormalization, referred to above, is indirect. Very recently, however, a direct measurement of the invariant ρ mass in photoproduction of ρ^0 on He^3 has been reported in the literature [15, 16]. The decrease in the ρ mass found by these authors is quite substantial ($\delta m_{\rho^0} \sim 280 \pm 40$ MeV). These experimental findings triggered a large number of theoretical calculations to look at the density dependence of ρ -meson mass. Here we will calculate the in-medium ρ -mass within the framework of Walecka model.

In general, for medium and heavy nuclei one uses the mean field approximation (MFA) and then a set of coupled differential equations is solved self-consistently to get the field values as a function of r [17]. But for a light nucleus like He^3 , the MFA may not be reliable. Therefore, a simple approach, *a la* Saito *et al.* [18], will be used here to calculate the effective ρ mass in helium.

Here we will use a simple Gaussian form for the density distribution of He^3 , in which the width parameter β_3 is fitted to reproduce the rms charge radius of He^3 *i.e.* 1.88 fm [18]. The density profile is given in figure 1. So once we know the density distribution of He^3 , one can easily calculate the effective ρ mass, m_ρ^* , as a function of radius, all the fields being known as a function of baryon density [19].

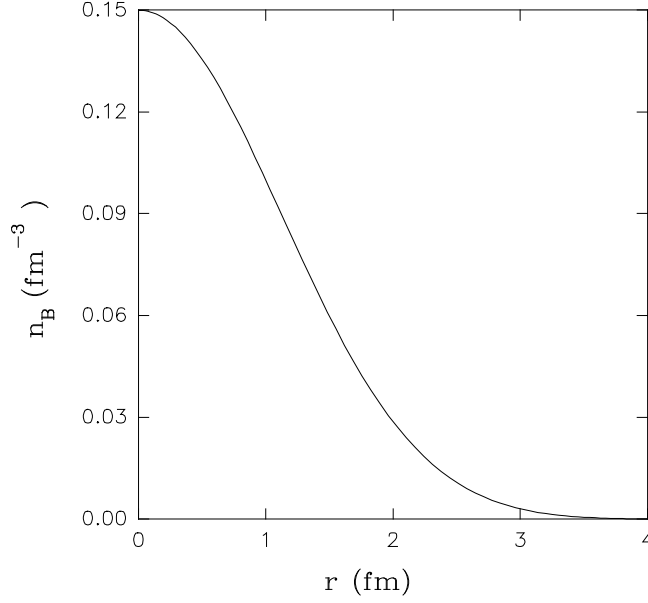


Fig. 1. Density profile of He^3

The ρ mass has been calculated, in the usual manner, at the one loop level. The expression for the ρ -mass is given by [19]

$$m_\rho^{*2} = m_\rho^2 + \Pi_{vac} + \Pi_{med} \quad (2)$$

where

$$\begin{aligned} \Pi_{med} = & \sum_{B=n,p} \frac{8g_\rho^2}{\pi^2} \int_0^{k_{FB}} \frac{p^2 dp}{E_p (m_\rho^{*2} - 4E_p^2)} \\ & \times \left[\frac{2}{3} (2p^2 + 3m_n^{*2}) + m_\rho^{*2} \left\{ 2m_n^* \left(\frac{c_\rho}{2m_n} \right) - \frac{2}{3} \left(\frac{c_\rho}{2m_n} \right)^2 (p^2 + 3m_n^{*2}) \right\} \right] \quad (3) \end{aligned}$$

$$\Pi_{vac} = \frac{g_\rho^2}{\pi^2} m_\rho^{*2} \left[I_1 + m_n^* \left(\frac{c_\rho}{2m_n} \right) I_2 + \frac{1}{2} \left(\frac{c_\rho}{2m_n} \right)^2 (m_\rho^{*2} I_1 + m_n^{*2} I_2) \right] \quad (4)$$

$$I_1 = \int_0^1 dx x(1-x) \ln \left[\frac{m_n^{*2} - m_\rho^{*2} x(1-x)}{m_n^2 - m_\rho^2 x(1-x)} \right]; I_2 = \int_0^1 \ln \left[\frac{m_n^{*2} - m_\rho^{*2} x(1-x)}{m_n^2 - m_\rho^2 x(1-x)} \right] \quad (5)$$

In the above set of equations $c_\rho \equiv f_\rho/g_\rho$. There are two coupling constants involved here. One is the vector coupling of the ρ -meson g_ρ and the other is the tensor coupling

f_ρ (or equivalently c_ρ). This is where the difference between this approach and the earlier works arises; previous authors [18] neglected the tensor coupling of the ρ to the nucleon.

We have used three sets of coupling constants. The density dependence of the ρ -meson mass, for these three sets of parameters, has been shown in figure 2. In order to compare the results for the effective ρ mass with the experimental values, we calculate the average mass of the ρ -meson in the He^3 nucleus. The average mass is defined as

$$\langle m_\rho^* \rangle = \frac{\int d^3r m_\rho^*(r) \rho_B(r)}{\int d^3r \rho_B(r)} \quad (6)$$

In table 2, we show the parameter values and the corresponding average ρ -mass for the three sets.

There have been two recent papers [15, 16] on the density variation of ρ -mass inside the He^3 nucleus. Both of them are the results from the ρ^0 photoproduction experiment of He^3 . The first one is in the energy range $E_\gamma = 800 - 1120 MeV$ and the second for $E_\gamma = 380 - 700 MeV$. The first paper finds a drop in the ρ -mass of $160 \pm 35 MeV$, i.e. m_ρ^* is in the range $575 - 645 MeV$. The other study finds an effective ρ -mass in the range $450 - 530 MeV$.

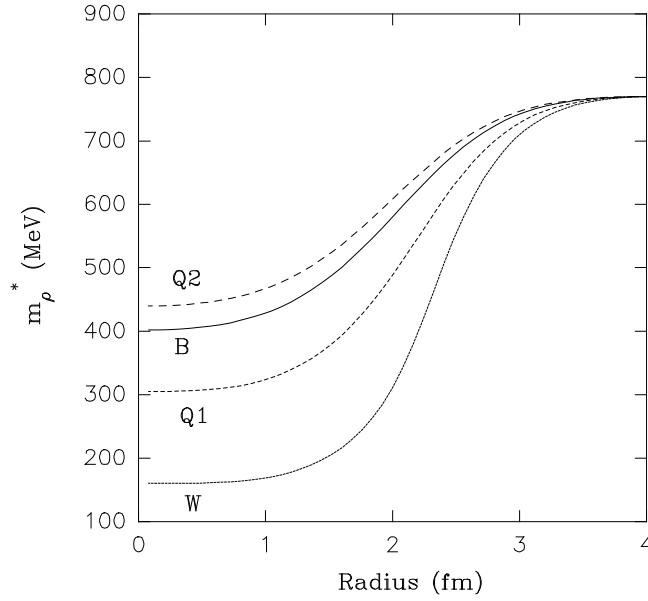


Fig. 2. Density dependence of rho mass, Q1 and Q2 are the upper and lower mass limits for the QCD sum rule parameter set, B for Bonn potential parameters and W is for parameters derived from nuclear matter properties.

In almost all the previous studies of the ρ -meson inside a light nucleus from the mean field approach, the tensor coupling of the ρ -meson to the nucleon [17, 18] was not included, as already mentioned. As a result, the variation of ρ -mass was rather soft in all the previous cases. Here, the incorporation of the tensor coupling leads to a change in the ρ -meson mass which is much larger and we get results which are very close to the experimental findings. For example, the Bonn potential parameter set [20] yields $\langle m_\rho^* \rangle = 536 \text{ MeV}$. For the parameter set suggested by the QCD sum rule case [21] we get $\langle m_\rho^* \rangle = 449 - 565 \text{ MeV}$. For the W parameter set, the value of $\langle m_\rho^* \rangle$ is somewhat lower.

B.2 In-medium $\rho - \omega$ mixing

In this section we will discuss the in-medium modification of the $\rho - \omega$ mixing amplitude. Let us first discuss about the importance of $\rho - \omega$ mixing. The cross section for the process $e^+e^- \rightarrow \pi^+\pi^-$, in the $\rho - \omega$ resonance region, reveals an interference shoulder which results from the superposition of the narrow resonant ω and broad resonant ρ amplitudes [22–24]. Thus a G-parity violating process $\omega \rightarrow \pi^+\pi^-$ is observed which suggests that there is an isospin breaking $\rho - \omega$ mixing. In vacuum the mixing amplitude is found to be proportional to the mass difference of neutron and proton. However, in the medium, as we will see, an additional mixing mechanism comes into play. The mixing amplitude also depends very strongly on the difference of the chemical potential or the Fermi momenta. Thus the $\rho - \omega$ mixing may be important in the context of hot and dense hadronic matter. So it is interesting to calculate the in-medium modification of this amplitude.

In order to calculate the mixing amplitude we will use the same Walecka model. The different parameters are given by: $m_\rho = 770.0 \text{ MeV}$, $m_\omega = 783.0 \text{ MeV}$, $g_\rho^2/4\pi = 0.74$, $g_\omega^2/4\pi = 5.48$, $g_\sigma^2/4\pi = 5.35$ and $C_\rho = f_\rho/g_\rho = 6.1$ [8, 9].

In ref. [9] similar interactions of ρ and ω have been used to calculate the momentum dependence of the $\rho - \omega$ mixing amplitude. The advantage of using this prescription, as pointed out in ref. [9], is that one can write down the contribution of the $\rho - \omega$ mixing to the NN potential in a parameter free form:

$$V_{NN}^{\rho\omega}(q) = -\frac{g_\rho g_\omega \langle \rho | H | \omega \rangle}{(q^2 - m_\rho^2)(q^2 - m_\omega^2)} \quad (7)$$

model	g_ρ	c_ρ	$\langle m_\rho^* \rangle$ (MeV)
Bonn Potential [20]	2.63	6.1	536
QCD Sum rule [21]	2.5 ± 0.2	8.0 ± 2.0	449 – 565
Nuclear Matter	8.912	6.1	304

Table 1. Parameter values and the corresponding average ρ -mass.

where the $\rho - \omega$ mixing amplitude is given by $\langle \rho | H | \omega \rangle = g_\rho g_\omega \Pi(q)$.

In the above equation $\Pi(q)$ is the transverse part of the polarisation function at finite temperature/density. The task ahead is now to calculate $\Pi(q)$ keeping in mind that the ρ -meson has both vector and tensor coupling to the nucleons. So one has [9]

$$\Pi^{\mu\nu}(q, T) = \Pi_{vv}^{\mu\nu}(q, T) + C_\rho \Pi_{vt}^{\mu\nu}(q, t) \quad (8)$$

where

$$\begin{aligned} i\Pi_{vv}^{\mu\nu} &= \int \frac{d^4k}{(2\pi)^4} \text{Tr} [\gamma^\mu G(k+q) \gamma^\nu \tau_z G(k)] \\ i\Pi_{vt}^{\mu\nu} &= \int \frac{d^4k}{(2\pi)^4} \text{Tr} \left[\gamma^\mu G(k+q) \frac{i\sigma^{\nu\lambda} q_\lambda}{2m} \tau_z G(k) \right] \end{aligned} \quad (9)$$

where G is the finite temperature nucleon propagator.

The nucleon propagator can be splitted into isoscalar and isovector components as:

$$G(k) = \frac{1}{2} G_p(k)(1 + \tau_z) + \frac{1}{2} G_n(k)(1 - \tau_z) \quad (10)$$

Once this splitting is introduced in the polarisation function and the isospin trace is carried out one can easily see that the $\rho - \omega$ mixing amplitude is proportional to the difference between the proton and the neutron polarisations [9] *i.e.*

$$\Pi_{\mu\nu}(q) = \Pi_{\mu\nu}^{(p)}(q) - \Pi_{\mu\nu}^{(n)}(q) \quad (11)$$

In the above set of equations the propagator for the baryons can be given by

$$G_B(p) = (\gamma^\mu p_\mu + m_B^*) \left[\frac{1}{(p^2 - m_B^{*2} + i\epsilon)} + 2\pi i \delta(p^2 - m_B^{*2}) \sin^2 \phi_{p_0} \right] \quad (12)$$

where

$$\begin{aligned} \sin \phi_{p_0} &= \frac{e^{-x/2} \theta(p_0)}{(1 + e^{-x})^{\frac{1}{2}}} - \frac{e^{x/2} \theta(-p_0)}{(1 + e^x)^{\frac{1}{2}}} \\ x &= (p_0 - \mu_B)/T \end{aligned} \quad (13)$$

B is either p or n , T is the temperature and μ_B is the chemical potential.

Once we use this propagator the calculation of the polarisation function is really straight forward and we have [9, 25, 26]

$$\begin{aligned} \Pi_{vv}^{(p)}(q) &= -\frac{q^2}{2\pi^2} \left[\frac{1}{6\epsilon} - \frac{\gamma}{6} - \int dx x(1-x) \left[\frac{m_p^2 - x(1-x)q^2}{\Lambda^2} \right] \right] \\ &\quad - 16q^2 \int \frac{d^3k}{(2\pi)^3} \frac{[f_p^+(E_p) + f_p^-(E_p)]}{2E_p(k)} \left[\frac{(E_p^2(k) - |k|^2(1 - \cos^2 \theta)/2)}{q^4 - 4(k \cdot q)^2} \right] \\ \Pi_{vt}^{(p)}(q) &= -\frac{q^2}{8\pi^2} \left[\frac{1}{\epsilon} - \gamma - \int dx \left[\frac{m_p^2 - x(1-x)q^2}{\Lambda^2} \right] \right] \\ &\quad + 8q^4 \int \frac{d^3k}{(2\pi)^3} \frac{[f_p^+(E_p) + f_p^-(E_p)]}{2E_p(k)} \left[\frac{1}{q^4 - 4(k \cdot q)^2} \right] \end{aligned} \quad (14)$$

where $f_B^\pm(E_B) = \frac{1}{1+exp((E_B \mp \mu_B)/T)}$ is the thermal distribution function, Λ is an arbitrary renormalisation cutoff and γ is the Euler-Mascheroni constant. Similar expressions may be obtained for the neutron loops. Since we need to have the difference between the p and n loop contributions we get

$$\begin{aligned}
\Pi_{vv}(q) &= \Pi_{vv}^{(p)} - \Pi_{vv}^{(n)} \\
&= q^2 \frac{1}{2\pi^2} \int dx x(1-x) \left[\frac{m_p^2 - x(1-x)q^2}{m_n^2 - x(1-x)q^2} \right] \\
&\quad - 16q^2 \int \frac{d^3k}{(2\pi)^3} \left[\frac{[f_p^+ + f_p^-]}{2E_p} \times \frac{(E_p^2 - |k|^2(1 - \cos^2\theta)/2)}{q^4 - 4(k \cdot q)^2} \right. \\
&\quad \left. - \frac{[f_n^+ + f_n^-]}{2E_n} \times \frac{(E_n^2 - |k|^2(1 - \cos^2\theta)/2)}{q^4 - 4(k \cdot q)^2} \right] \\
\Pi_{vt}(q) &= \Pi_{vt}^{(p)} - \Pi_{vt}^{(n)} \\
&= q^2 \frac{1}{8\pi^2} \int dx \left[\frac{m_p^2 - x(1-x)q^2}{m_n^2 - x(1-x)q^2} \right] \\
&\quad + 8q^4 \int \frac{d^3k}{(2\pi)^3} \left[\frac{[f_p^+ + f_p^-]}{2E_p} - \frac{[f_n^+ + f_n^-]}{2E_n} \right] \times \frac{1}{q^4 - 4(k \cdot q)^2} \quad (15)
\end{aligned}$$

where $E_B = \sqrt{k^2 + m_B^{*2}}$ is the effective energy of the baryon.

In both Π_{vv} and Π_{vt} the first term is the vacuum contribution and the second term is the contribution arising from the difference in the chemical potentials. From equation (15) it is clear that the mixing amplitude depends on the in-medium baryon masses and chemical potentials. In the MFA the effective baryon masses are : $m_B^* = m_B - g_\sigma \sigma_0$. The baryon number conservation gives $\rho = n_n + n_p$ where ρ is the total baryon number density and n_n and n_p are the number densities of the neutrons and protons respectively. The asymmetry in the numbers of neutrons and protons is given by $x = (n_n - n_p)/(n_n + n_p)$ where x is the asymmetry factor. In this paper, where a $Pb - Pb$ system has been considered, the asymmetry is 44/208. From the above relations one can find out the medium dependence of the baryon masses and chemical potentials.

We can now feed these in-medium baryon masses and chemical potentials in equation (15). After calculating the total polarisation function numerically we have plotted the absolute value of the mixing amplitude $|\langle \rho | H | \omega \rangle|$ at $q^2 = m_\omega^2$ as a function of density, for different temperatures, in figure 3. The amplitude increases sharply with density. But, with increase in temperature it decreases. The dominant contribution to the mixing amplitude, at low densities, comes from the vacuum part of the polarisation function which depends on temperature/density through the baryon masses only. At higher densities it comes from the part of the polarisation function which directly depends on temperature/density through the distribution functions.

C Low Energy Structure of QCD

In the previous section we have used the RMF approach to calculate some of the in-medium properties. Here we will use a completely different approach [27–29]. In the

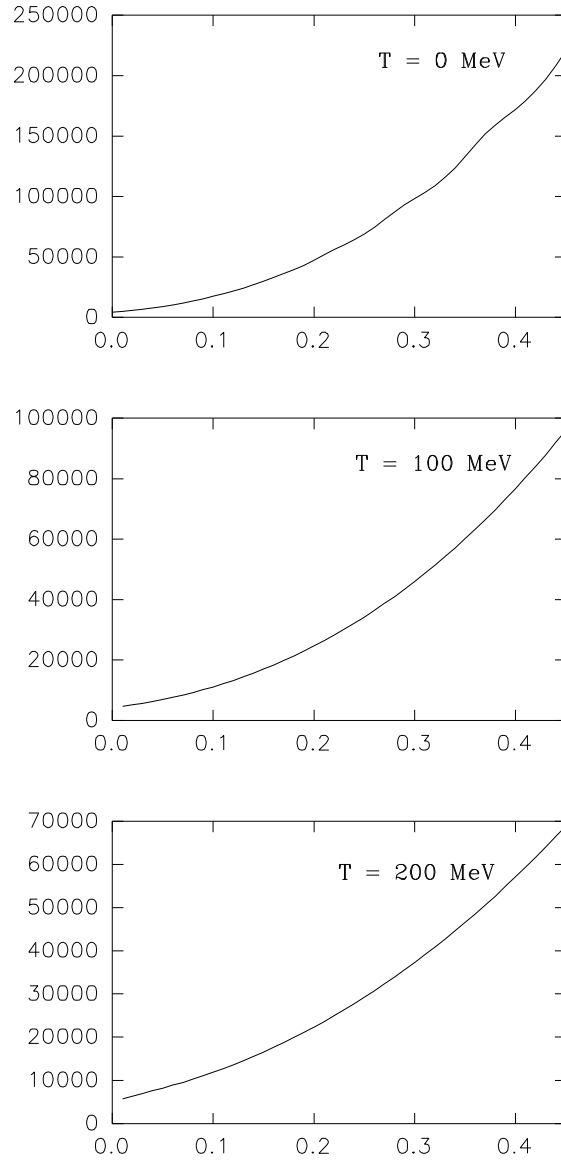


Fig. 3. Density dependence of the modulus of the $\rho - \omega$ mixing amplitude ($|\langle \rho | H | \omega \rangle|$).

large N_c limit QCD reduces to a non-linear effective theory of interacting mesons [30, 31]. The power of this approach lies in the fact that it embodies the symmetries of the QCD Lagrangian. To first order one simply works with the pseudoscalar Goldstone bosons related to the spontaneous breakdown of the $SU(N_f) \times SU(N_f)$ to $SU(N_f)_V$. Here N_f is the number of flavours. The pertinent Goldstone bosons may be pion, kaon and eta. As first pointed out by Skyrme [32, 33], baryons emerge as the topological solitons of the mesonic Lagrangian. Witten [34] demonstrated the link of this model to QCD by investigating the underlying symmetries and connecting the anomalies of QCD to the Wess-Zumino [35] term. If one is interested in the higher energy ranges then one should stretch the mesonic sector to include vector and axial vector mesons. The Lagrangian density for such a model can be written as [36–38]

$$\mathcal{L} = \mathcal{L}_A + a\mathcal{L}_V \quad (16)$$

with

$$\begin{aligned} \mathcal{L}_A &= -\frac{1}{8}f_\pi^2 \text{Tr} \cdot (D_\mu \xi_L \cdot \xi_L^\dagger - D_\mu \xi_R \cdot \xi_R^\dagger)^2 \\ \mathcal{L}_V &= -\frac{1}{8}f_\pi^2 \text{Tr} \cdot (D_\mu \xi_L \cdot \xi_L^\dagger + D_\mu \xi_R \cdot \xi_R^\dagger)^2 \end{aligned} \quad (17)$$

where

$$D_\mu \xi_{L(R)} = (\partial_\mu - igV_\mu) \xi_{L(R)}; \quad \xi_{L(R)} = \exp[\mp iP/f_\pi] \quad (18)$$

g is the gauge coupling constant, V_μ is the vector meson nonet and P is the pseudoscalar meson octet. Here V and P are 3×3 matrices which can be written as

$$\begin{aligned} V_\mu &= \begin{bmatrix} \frac{\rho_\mu^0 + \omega_\mu}{\sqrt{2}} & \rho_\mu^+ & K_\mu^{*+} \\ \rho_\mu^- & \frac{-\rho_\mu^0 + \omega_\mu}{\sqrt{2}} & K_\mu^{*0} \\ K_\mu^{*-} & \bar{K}_\mu^{*0} & \phi_\mu \end{bmatrix} \\ P &= \begin{bmatrix} \frac{\pi^0}{\sqrt{2}} + \frac{\eta}{\sqrt{6}} & \pi^+ & K^+ \\ \pi^- & \frac{-\pi^0}{\sqrt{2}} + \frac{\eta}{\sqrt{6}} & K^0 \\ K^- & \bar{K}^0 & -\frac{2\eta}{\sqrt{6}} \end{bmatrix} \end{aligned}$$

where ρ , ω , ϕ and K^* represent the corresponding vector-meson fields and π , K and η represent the corresponding pseudoscalar meson fields.

It is well known that the $SU(3)_V$ symmetry is not exact in reality. This is reflected by the fact that the masses of K^* and ϕ are different from those of ρ and ω . The explicit breaking of $SU(3)_V$ symmetry can be mediated by a term proportional to $(\xi_R \epsilon_{\xi_L}^\dagger + \xi_L \epsilon_{\xi_R}^\dagger)$. So the \mathcal{L}_A and \mathcal{L}_V are modified now and are given by [36–38]

$$\begin{aligned} \mathcal{L}_A + \Delta\mathcal{L}_A &= -\frac{1}{8}f_\pi^2 \text{Tr} \cdot (D_\mu \xi_L \cdot \xi_L^\dagger - D_\mu \xi_R \cdot \xi_R^\dagger)^2 \\ &\quad \times [1 + (\xi_L \epsilon_A \xi_R^\dagger + \xi_R \epsilon_A \xi_L^\dagger)] \\ \mathcal{L}_V + \Delta\mathcal{L}_V &= -\frac{1}{8}f_\pi^2 \text{Tr} \cdot (D_\mu \xi_L \cdot \xi_L^\dagger + D_\mu \xi_R \cdot \xi_R^\dagger)^2 \\ &\quad \times [1 + (\xi_L \epsilon_V \xi_R^\dagger + \xi_R \epsilon_V \xi_L^\dagger)] \end{aligned} \quad (19)$$

The matrix $\epsilon_{A(V)}$ is taken to be $\epsilon_{A(V)} = \text{diag}(0, 0, c_{A(V)})$ where $c_{A(V)}$ are the $SU(3)_V$ breaking real parameters. These parameters give the mass splitting of the vector mesons and also the split in the pseudoscalar decay constants giving

$$m_\rho^2 = m_\omega^2 = ag^2 f_\pi^2; \quad m_{K^*}^2 = m_\rho^2(1 + c_V); \quad m_\phi^2 = m_\rho^2(1 + 2c_V) \\ f_K = \sqrt{1 + c_A} f_\pi; \quad f_\eta = \sqrt{1 + 4c_A/3} f_\pi \quad (20)$$

where $m_\rho, m_\omega, m_{K^*}$ and m_ϕ are the masses of the corresponding vector mesons and f_π, f_K and f_η are the corresponding decay constants of the pseudoscalar mesons.

The required part of the Wess-Zumino anomaly term with $SU(3)_V$ breaking can be written as [36–39]:

$$\mathcal{L}_{WZ} + \Delta\mathcal{L}_{WZ} = 2g_{WZ}\epsilon^{\mu\nu\alpha\beta}\text{Tr}[\partial_\mu V_\nu(1 + \epsilon_{WZ})\partial_\alpha V_\beta P] \quad (21)$$

with

$$g_{WZ} = -\frac{3g^2}{8\pi^2 f_P} \quad (22)$$

where f_P can be f_π, f_K or f_η and $\epsilon_{WZ} = \text{diag}(0, 0, c_{WZ})$; c_{WZ} is the symmetry breaking parameter in the anomalous sector.

Two other terms contributing to the total Lagrangian are the mass term of the pseudoscalar mesons and the kinetic term for the spin-1 mesons. They are given by

$$\mathcal{L}_M = \frac{f_\pi^2}{2}\text{Tr}[M(\xi + \xi^\dagger - 2)]; \quad \mathcal{L}_k = -\frac{1}{4}F_{\mu\nu}F^{\mu\nu} \quad (23)$$

where $M = \frac{2}{3}(m_K^2 - \frac{1}{2}m_\pi^2)\mathbf{I} - \frac{2}{\sqrt{3}}(m_K^2 - m_\pi^2)\lambda_8$, \mathbf{I} and λ_8 being the identity and the Gell-Mann matrices, respectively and $F_{\mu\nu} = \partial_\mu V_\nu - \partial_\nu V_\mu - ig[V_\mu, V_\nu]$.

So the total Lagrangian is

$$\mathcal{L} = \mathcal{L}_A + \Delta\mathcal{L}_A + a[\mathcal{L}_V + \Delta\mathcal{L}_V] + \mathcal{L}_{WZ} + \Delta\mathcal{L}_{WZ} + \mathcal{L}_M + \mathcal{L}_k \quad (24)$$

This Lagrangian has five parameters: a, g, c_A, c_V and c_{WZ} . They are determined as follows. The parameter a is determined by reproducing the universality *i.e.* $g_{\rho\pi\pi} = g$ and the KSFR relation [40] $m_\rho^2 = 2g_{\rho\pi\pi}^2 f_\pi^2$. This gives $a = 2$. Now, the $\rho \rightarrow \pi^+\pi^-$ gives $g = 4.3$. From the relation $m_\phi^2 = m_\rho^2(1 + 2c_V)$, one gets $c_V = 0.37$. On the other hand, the relation $m_{K^*}^2 = m_\rho^2(1 + c_V)$ gives $c_V = 0.34$. However, this does not change our phenomenological result significantly and we will use the former value of c_V . The experimental value of kaon and pion decay widths are related as $f_K/f_\pi = 1.22$ giving $c_A = 0.44$. The ratio of the decay widths $K^{*0} \rightarrow K^0\gamma$ and $K^{*\pm} \rightarrow K^\pm\gamma$ gives $c_{WZ} = -0.10$ [37, 38, 41].

Let us now calculate the temperature dependence of the pseudoscalar meson masses from this model. For this purpose we have to calculate certain polarisation functions. The corresponding diagrams are given in figure (4).

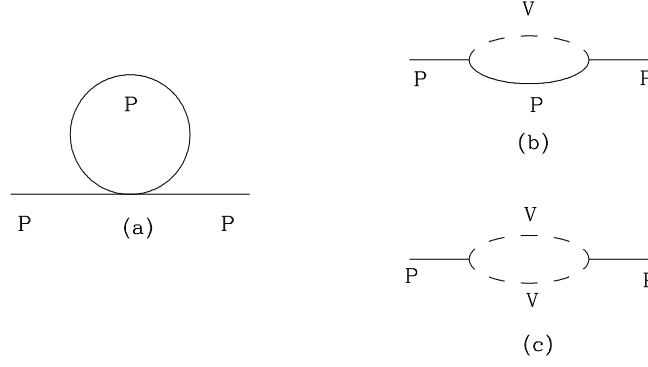


Fig. 4. Feynmann diagrams for the pseudoscalar meson polarisation function. P stands for pseudoscalar and V stands for vector meson.

The $P - P - P - P$ interactions give the tadpole diagrams. The contribution to self energy coming out from these diagrams are given by

$$\begin{aligned}
 \Pi_{1ps}(q) &= i \sum_{ps} g_{1ps} \int \frac{d^4 p}{(2\pi)^4} q^2 D_{ps}(p) \\
 &= i \sum_{ps} g_{1ps} \int \frac{d^4 p}{(2\pi)^4} q^2 \left[\frac{1}{p^2 - m_{ps}^2} - 2\pi i \delta(p^2 - m_{ps}^2) \sinh^2 \phi_{p_0} \right] \\
 &= \frac{2}{(2\pi)^2} q^2 \sum_{ps} g_{1ps} \int p^2 dp \frac{f_{ps}(E_{ps})}{E_{ps}}
 \end{aligned} \tag{25}$$

where g_{1ps} is the coupling for different pseudoscalar mesons, D_{ps} is the propagator for a pseudoscalar meson, $E_{ps} = \sqrt{p^2 + m_{ps}^2}$, \sum_{ps} is the sum over all the pseudoscalar mesons and f_{ps} , the Bose Einstein distribution function, is given by $f_{ps} = 1/(e^{E_{ps}/T} - 1)$

The $V - P - P$ interaction gives the $V - P$ loop. The corresponding self-energy is

$$\begin{aligned}
\Pi_{2ps}(q) &= i \sum_v \sum_{ps} g_{2ps}^2 \int \frac{d^4 p}{(2\pi)^4} q_\mu q_\nu D_{ps}(p) D_v^{\mu\nu}(q-p) \\
&= i \sum_v \sum_{ps} g_{2ps}^2 \int \frac{d^4 p}{(2\pi)^4} q_\mu q_\nu [g^{\mu\nu} - \lambda(q-p)^\mu (q-p)^\nu / m_v^2] \\
&\quad \times \left[\frac{1}{p^2 - m_{ps}^2} - 2\pi i \delta(p^2 - m_{ps}^2) \sinh^2 \phi_{p_0} \right] \\
&\quad \times \left[\frac{1}{(q-p)^2 - m_v^2} - 2\pi i \delta((q-p)^2 - m_v^2) \sinh^2 \phi_{(q-p)_0} \right] \\
&= \sum_v \sum_{ps} g_{2ps}^2 \frac{2}{(2\pi)^2} q^2 \int p^2 dp \left[\frac{f_{ps}(E_{ps})}{E_{ps}} \times \frac{(q_0^2 - m_v^2 + m_{ps}^2)}{(q_0^2 - m_v^2 + m_{ps}^2)^2 - 4q_0^2 E_{ps}^2} \right. \\
&\quad \left. + \frac{f_v(E_v)}{E_v} \times \frac{(q_0^2 + m_v^2 - m_{ps}^2)}{(q_0^2 + m_v^2 - m_{ps}^2)^2 - 4q_0^2 E_v^2} \right] \tag{26}
\end{aligned}$$

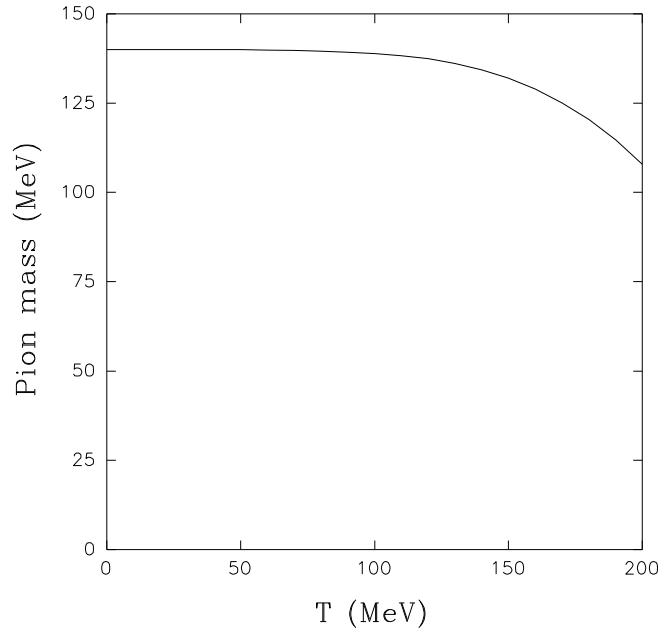


Fig. 5. Temperature dependence of pion mass.

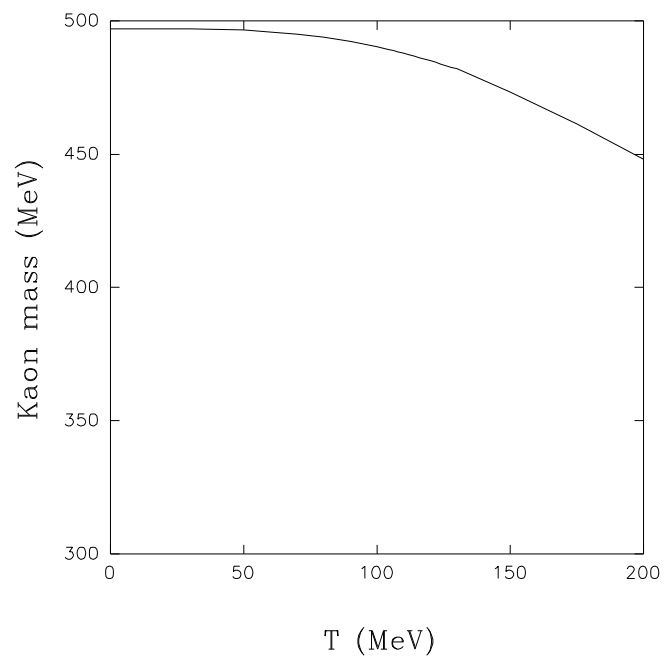


Fig. 6. Temperature dependence of kaon mass.

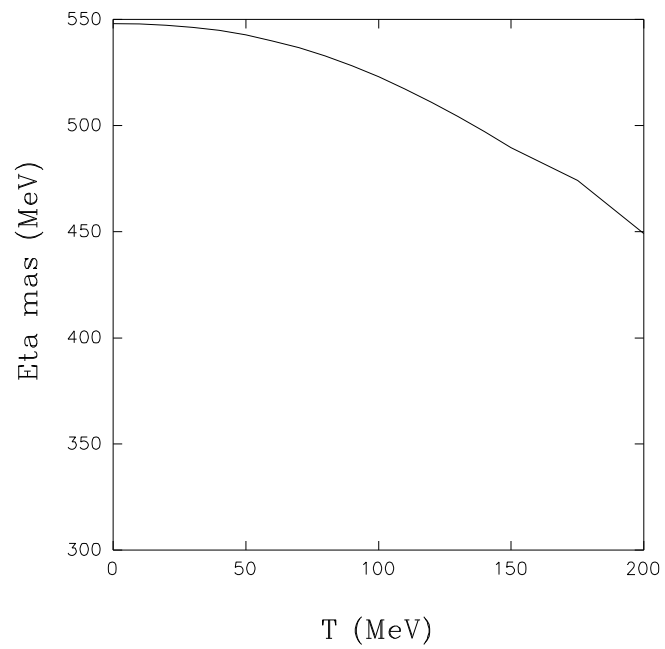


Fig. 7. Temperature dependence of eta mass.

The $V - V - P$ interaction amounts to the $V - V$ loop. The self-energy is

$$\begin{aligned}
\Pi_{3ps}(q) &= i \sum_v g_{3ps}^2 \int \frac{d^4 p}{(2\pi)^4} \epsilon_{\mu\nu\alpha\beta} p^\mu (q-p)^\nu D_v^{\alpha\alpha'}(p) \epsilon_{\mu'\nu'\alpha'\beta'} p^{\mu'} (q-p)^{\nu'} D_v^{\beta\beta'}(q-p) \\
&= i \sum_v g_{3ps}^2 \int \frac{d^4 p}{(2\pi)^4} \epsilon_{\mu\nu\alpha\beta} p^\mu (q-p)^\nu \epsilon_{\mu'\nu'\alpha'\beta'} p^{\mu'} (q-p)^{\nu'} \\
&\quad \times \left[g^{\alpha\alpha'} - \lambda p^\alpha p^{\alpha'} / m_v^2 \right] \left[g^{\beta\beta'} - \lambda (q-p)^\beta (q-p)^{\beta'} / m_v^2 \right] \\
&\quad \times \left[\frac{1}{p^2 - m_v^2} - 2\pi i \delta(p^2 - m_v^2) \sinh^2 \phi_{p_0} \right] \\
&\quad \times \left[\frac{1}{(q-p)^2 - m_v^2} - 2\pi i \delta((q-p)^2 - m_v^2) \sinh^2 \phi_{(q-p)_0} \right]
\end{aligned} \tag{27}$$

So the total self-energy for a pseudoscalar meson can be written as

$$\Pi_{ps} = \Pi_{1ps} + \Pi_{2ps} + \Pi_{3ps} \tag{28}$$

The temperature dependence of the effective mass of a pseudoscalar meson (m_{ps}^*) can be obtained from a self-consistent solution of the equation

$$m_{ps}^{*2} - m_{ps}^2 - \text{Re} [\Pi_{ps}(q_0 = m_{ps}^*, |\mathbf{q}| \rightarrow 0)] = 0 \tag{29}$$

The results have been plotted in figures (5-6).

In exactly the similar manner the temperature dependence of the vector meson masses may be calculated. Those results may be obtained in ref. [41, 42].

D Summary

Here we have discussed the in-medium hadron properties from two different models. The density dependence of ρ -mass and the $\rho - \omega$ mixing amplitude have been calculated from Walecka model. The effective mass of ρ -meson has been found to decrease and the change is consistent with the experimental findings. The $\rho - \omega$ mixing has been found to increase strongly with density which means that the $\omega \rightarrow \pi^+ \pi^-$ will be enhanced strongly in the medium. This will be experimentally tested very soon.

In section 3 we have studied the pseudoscalar meson masses from a low energy effective theory of QCD. All the pseudoscalar meson (π , K and η) masses are found to decrease with temperature.

In conclusion, the in-medium properties of hadrons have been calculated from two effective models. Some of the properties have been found to agree with the experimental findings. However, there are a large number of effective models which could not be described here. There is no way to select one particular model over the other. The search for a model which will reproduce all the hadronic properties successfully is still in progress.

Acknowledgement I would like to thank the organisers for inviting me in this workshop.

References

1. Chris Quigg, "Gauge Theories of the Strong, Weak and Electromagnetic Interactions" - The Benjamin/Cummings Publishing Company, USA, 1983.
2. M.Gell-Mann, Phys. Lett. **B8**, 214 (1964).
3. J.Alam, S.Raha and B.Sinha, Phys.Rep. **273**, 243 (1996).
4. C.Alcock, in "Quark-Gluon Plasma" (Springer Verlag 1989), Eds : B.Sinha, S.Pal and S.Raha.
5. W.Baade and F.Zwicky, Phys.Rev. **45**, 134 (1934).
6. J.D.Walecka, Ann.Phys. **83**, 491 (1974).
7. B.D.Serot and J.D.Walecka, Adv. Nucl. Phys. **16**, 1 (1986).
8. A.Bhattacharyya and S.K.Ghosh, Int. J. Mod. Phys. **7**, 495 (1998).
9. J.Piekarewicz and A.G.Williams, Phys. Rev. **C47**, 2462 (1993).
10. CERES collaboration, Th.Ulrich *et al.*, Nucl. Phys. **A610**, 313c (1996).
11. HELIOS Collaboration, M.Masera *et al.*, Nucl. Phys. **A590**, 93c (1995).
12. NA50 collaboration, E.Scomparin *et al.*, Nucl. Phys. **A610**, 331c (1996).
13. G.Q.Li, C.M.Ko and G.E.Brown, Phys. Rev. Lett. **75**, 4007 (1995).
14. G.E.Brown *et al.*, Nucl. Phys. **A343**, 295 (1995).
15. G.J.Lolos *et. al.*, Phys. Rev. Lett. **80**, 241 (1998).
16. G.M.Huber *et. al.*, Phys. Rev. Lett. **80**, 5285 (1998).
17. K.Saito, K.Tsushima and A.W.Thomas, Phys. Rev. **C55**, 2637 (1997).
18. K.Saito, A.W.Thomas and K.Tsushima, Phys. Rev. **C56**, 566 (1997).
19. A.Bhattacharyya, S.K.Ghosh and S.Raha, Phys. Rev. **C60**, 018202 (1999).
20. R.Machleidt, K.Holinde and Ch.Elster, Phys. Rep. **149**, 1 (1987).
21. S-L.Zhu, Phys. Rev. **C59**, 435 (1999).
22. L.M.Barkov *et.al.* Nucl.Phys. **B256** 365 (1985).
23. S.A.Coon and R.C.Barrett, Phys.Rev. **C36**, 2189 (1987).
24. H.B.O'Connel, B.C.Pearce, A.W.Thomas and A.G.Williams, Phys. Lett. **B354**, 14 (1995).
25. A.Bhattacharyya and S.Raha, Jr. of Phys. **G21**, 741 (1995).
26. A.Bhattacharyya, Mod. Phys. Lett. **A13**, 2585 (1998).
27. J.J.Sakurai, Currents and Mesons (University of Chicago Press, Chicago 1969).
28. V.de Alfaro *et al.*, Currents in Hadron Physics (North Holland Amsterdam, 1973).
29. M.Gourdkin, Phys.Rep. **11**, 29 (1979).
30. G't Hooft, Nucl.Phys. **B72**, 461 (1975); **B75**, 461 (1974).
31. E.Witten, Nucl.Phys. **B160**, 57 (1979).
32. T.H.R.Skyrme, Proc.R.Soc.London Ser. **A260**, 237 (1961); **A262**, 237 (1961).
33. T.H.R.Skyrme, Nucl.Phys. **B31**, 556 (1962).
34. E.Witten, Nucl.Phys. **B233**, 422,433 (1983).
35. J.Wess and B.Zumino, Phys.Lett. **B37**, 95 (1971).
36. A.Bhattacharyya and S.Raha, Phys.Lett. **B363**, 162 (1995).
37. A.Bramon, A.Grau and G.Pancheri, Phys. Lett. **B344**, 240 (1995).
38. A.Bramon, A. Grau and G.Pancheri, Phys. Lett. **B345**, 263 (1995).
39. T.Fujiwara *et al.*, Prog.Theor.Phys.Suppl. **73**, 926 (1985).
40. K.Kawarabayashi and M.Suzuki, Phys.Rev.Lett. **16**, 255 (1966); Riazuddin and Fayyazuddin, Phys. Rev. **147**, 1071 (1966).
41. A.Bhattacharyya, S.K.Ghosh, S.C.Phatak and S.Raha, Physical Review **C55**, 1463 (1997).
42. A.Bhattacharyya, J.Alam, S.Raha and B.Sinha, Int. Jr. Mod. Phys. **A12**, 5639 (1997).

Nuclear Structure effects in Nuclear Astrophysics

Radhey Shyam¹ and S.K. Dhiman¹

¹ Saha Institute of Nuclear Physics, Kolkata - 700 064, India.

² Department of Physics, Himachal Pradesh University, Shimla , India.

Abstract. Nuclear structure data are of crucial importance in order to address important astrophysical problems such as the origin of chemical elements, the inner working of our Sun, and the evolution of stars. We demonstrate this by investigating the ground state structure of ^8B and ^7Be nuclei within the Skyrme Hartree-Fock framework and by calculating the overlap integral of ^8B and ^7Be wave functions. The latter is used to calculate the astrophysical S factor (S_{17}) for the solar fusion reaction $^7\text{Be}(p, \gamma)^8\text{B}$.

A Introduction

Nuclear astrophysics research addresses some of the most fundamental questions in nature *e.g.*, the origin of the elements that make up our bodies and our world, and formation and evolution of the sun, the stars and the galaxies. There is an intimate connection between nuclear physics inputs and studies of these fascinating astrophysical phenomena. A diverse set of nuclear data is required to model the composition changes and energy release in astrophysical environments ranging from Big Bang to inner working of our own Sun to exploding stars. Theoretical studies as well as measurements of microscopic nuclear physics processes provide the foundation for models to understand various astrophysics phenomena. These models are now challenged by incredibly detailed observations from ground based and space based (*e.g.*, CHANDRA X-ray Observatory, Hubble Space Telescope) observational devices that give us an unprecedented view of the Cosmos

We shall demonstrate the role of the nuclear structure physics in nuclear astrophysics by considering the case of the Solar fusion reaction $^7\text{Be}(p, \gamma)^8\text{B}$, which is of great importance to the solar neutrino issue and to other related astrophysical studies since ^8B is the source of the high energy neutrinos from the sun that are detected in the SNO, Kamiokande and Homestake experiments [1–3]. Therefore, accurate determination of the cross section of this reaction at relative energies corresponding to solar temperatures (about 20 keV) is very crucial. In this energy region, the cross-section $\sigma_{p\gamma}(E_{cm})$ [which is usually expressed in terms of the astrophysical $S_{17}(E_{cm})$ factor] of the $^7\text{Be}(p, \gamma)^8\text{B}$ reaction is directly proportional to the high energy solar neutrino flux. A better knowledge of S_{17} is, therefore, important to improve the precision of the theoretical prediction of ^8B neutrino flux from present and future solar neutrino experiments.

$^7\text{Be}(p, \gamma)^8\text{B}$ reaction has been studied extensively both theoretically as well as experimentally [4–8, 10, 57]. S_{17} is determined either by direct measurements [11] or by indirect methods such as Coulomb dissociation [12] of ^8B on heavy targets and transfer

reactions in which ^8B is either the residual nucleus or the projectile nucleus [13–17]. Efforts have also been made to calculate the cross section of this reaction within the framework of the shell model and the cluster model [18–20]. The key point of these calculations is the determination of the wave functions of ^8B states within the given structure theory.

We have investigated the structure of ^8B in the framework of the Skyrme Hartree-Fock (SkHF) model which has been used successfully to describe the ground-state properties of both stable [21–24] as well as exotic nuclei [25–28]. The SkHF method with density-dependent pairing correlation and SLy4 interaction parameters has been successful in reproducing the binding energies and rms radii [27] in the light neutron halo nuclei ^6He , ^8He , ^{11}Li and ^{14}Be .

We solve spherically symmetric Hartree-Fock (HF) equations with SLy4 [29] Skyrme interaction which has been constructed by fitting to the experimental data on radii and binding energies of symmetric and neutron-rich nuclei. This has also been used in Ref. [28] to study the phenomenon of shape coexistence in semi-magic isotopes of Mg, S and Zr nuclei. In our calculations pairing correlations among nucleons have been treated within the BCS pairing method. We have, however, renormalized the parameter of the spin-orbit term of the SLy4 interaction so as to reproduce the experimental binding energy of the last proton in the ^8B nucleus [30]. A check on our interaction parameters was made by calculating binding energies and rms radii of ^7Be , ^7B , ^8Li and ^9C nuclei with the same set where a good agreement is obtained with corresponding experimental data. We calculate the root mean square (rms) radii for matter, neutron and proton distributions for ^8B . Using the overlap integral of HF wave functions for ^7Be and ^8B ground states, the rms radius of the valence p-shell proton in this nucleus has been determined which is expected to provide information about the proton halo structure in ^8B . The overlap integral has also been used to calculate the astrophysical S_{17} factor.

In the Skyrme Hartree-Fock formalism binding energies, densities, and single particle wave functions are obtained from a local energy functional. Skyrme force parameters are determined empirically by fitting the properties of the nuclear matter, of stable nuclei, and of neutron star [29]. Microscopically, the Skyrme functional corresponds to an expansion of the nuclear interaction up to the first order in momentum transfer [21]. The ground state properties of nuclei are derived self-consistently from the total energy functional of the nucleus.

In the Hartree-Fock method the mean field localizes the wave functions which breaks the translational invariance. This causes spurious contribution from the c.m. motion to the observables. One way of removing this problem is to use the projection-after-variation method in which the zero-point energy of nearly harmonic oscillation of the c.m. is subtracted from the mean-field energy functional.

B Results and discussions

B.1 Structure calculations

The values of various parameters of the *SLy4* Skyrme effective interaction as used in our calculations are given in [30]. It may be noted that we have renormalized the

strength of the spin-orbit term so as to reproduce the single proton separation energy of ${}^8\text{B}$. In the following the force with renormalized spin orbit force will be referred to as TH1 and that with the original one as TH2. With the same set of force parameters

Table 1. The comparison of theoretical binding energies for various nuclei calculated in self-consistent SkHF method with experimental data. The TH1 and TH2 represent theoretical results obtained with modified and original values of the (b_4) parameter of the SLy4 Skyrme force, respectively.

Nucleus	BE(MeV)		
	Expt.	Theor.	
		TH1	TH2
${}^7\text{Be}$	37.601	37.561	39.780
${}^7\text{B}$	24.720	24.262	25.931
${}^8\text{Li}$	41.278	41.034	44.098
${}^8\text{B}$	37.739	37.739	40.677
${}^9\text{C}$	39.716	39.035	37.416

we have calculated total binding energies and rms radii of light unstable nuclei, ${}^8\text{Li}$, ${}^8\text{B}$, ${}^7\text{B}$, ${}^7\text{Be}$, and ${}^9\text{C}$. Results for binding energies are presented in Table I where the corresponding experimental values are also shown. Binding energies calculated with TH1 and TH2 forces are shown in third and fourth columns of this table, respectively. It is clear that with the renormalized spin orbit force, our calculations reproduce the experimental binding energies of these nuclei quite well.

The rms radii for matter (r_m), neutron (r_n) and proton (r_p) distributions are presented in Table II for all the five isotopes. Also shown in this table are the matter, neutron, and proton radii (under the column "Expt") extracted by methods in which measured reaction (or interaction) cross sections are fitted by theoretical models having them as input parameters. The quantities listed under "Theory" column are the results of our calculations. Here r_m is obtained by summing the average of proton and neutron radii in every orbit weighted with occupation probabilities. We see that for all the isotopes r_m calculated with the modified force TH1 parameter is in better agreement with the corresponding values listed under the "Expt" columns as compared to that calculated with the original force TH2. In Fig. 1, we show distributions of matter, charge, neutron and proton densities (in the units of fm^{-3}) in the coordinate space. The density distribution has been obtained by folding the HF results for proton and neutron densities with the intrinsic charge density distribution of nucleons in Fourier-space by transforming the densities to form-factors. In actual calculations of the nuclear charge density, the c.m. correction effects are taken into account by unfolding the spurious vibrations of the nuclear c.m. in harmonic approximation. We note that nuclear charge and proton densities differ very slightly from each other. The key point of this figure is that the neutron and proton densities differ quite a bit from each other for distances larger than 3 fm, where the proton density develops a long tail. This is reminiscent of the situation

Table 2. Rms mass (r_m), proton (r_p) and neutron (r_n) radii for various nuclei. The TH1 and TH2 represents the theoretical results obtained with modified and original values of the (b_4) parameter of the SLy4 Skyrme force, respectively. Also shown, under the column "Expt", are the values of corresponding radii extracted by fitting the reaction or interaction cross sections by different theoretical methods as discussed in the text. We have defined $r_i = \langle r_i^2 \rangle^{1/2}$

Nucl.	rms radii(fm)								
	"Expt"			Theory					
				TH1			TH2		
	r_m	r_p	r_n	r_m	r_p	r_n	r_m	r_p	r_n
${}^7\text{Be}$	2.33 ± 0.02	-	-	2.49	2.63	2.29	2.32	2.46	2.12
${}^7\text{B}$	-	-	-	2.86	3.18	1.84	2.73	3.01	1.87
${}^8\text{Li}$	2.37 ± 0.02	2.26 ± 0.02	2.44 ± 0.02	2.54	2.29	2.67	3.01	2.98	3.02
${}^8\text{B}$	2.55 ± 0.08	2.76 ± 0.08	2.16 ± 0.08	2.57	2.73	2.27	2.84	2.96	2.73
	2.43 ± 0.03	2.49 ± 0.03	2.33 ± 0.03						
${}^9\text{C}$	2.42 ± 0.03			2.59	2.77	2.20	2.13	2.32	1.67

in the neutron halo nuclei where the neutron density distribution has a long tail. This observation supports the existence of a proton halo structure in ${}^8\text{B}$.

B.2 Valence proton radius in ${}^8\text{B}$ and Astrophysical S_{17} factor

We define an overlap function of the bound state wave functions of two nuclei B and A , where $B = A + p$ (p represents a proton and for our purpose in this paper, $A = {}^7\text{Be}$ and $B = {}^8\text{B}$), as

$$I_A^B(\mathbf{r}) = \int d\xi \Psi_{A I_A M_A}^*(\xi) \Psi_{B I_B M_B}(\mathbf{r}, \sigma_p, \xi), \quad (1)$$

where I_A and I_B are the total spins of nuclei A and B , respectively, and \mathbf{r} is the position of the proton with respect to the c.m. of nucleus A . σ_p is the spin variable of the proton, and ξ stands for the remaining set of internal variables which also include isospins. In this expression nuclear wave functions Ψ_A and Ψ_B are supposed to be properly translational invariant. The Hartree-Fock wave functions calculated in the previous section may not be so despite the fact that a c.m. correction factor has been incorporated in the energy functional. Corrections for the spurious c.m. motion should, therefore, be applied to the HF wave functions before using them in Eq. (1). Effects of such corrections on the one-particle overlap function calculated within the shell model have been studied by several authors [31, 32]. It is shown in [32] that this correction increases the one-particle overlap function (calculated with the shell model wave functions) in the asymptotic region (beyond 3 fm) by about 2-5 % for lighter nuclei and even less than this for the medium mass ones. It is likely that the situation will be more or less the same for the HF case. In the following we shall use the HF wave functions for ${}^8\text{B}$ and ${}^7\text{Be}$ as calculated in the previous section to evaluate our one-particle overlap function

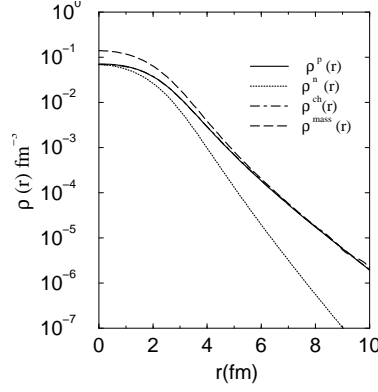


Fig. 1. Density distribution $\rho(r)$ for protons, neutrons, charge and mass in ${}^8\text{B}$ nucleus calculated with SkHF method.

with the understanding that conclusions drawn from this study may have an uncertainty of this rather small factor.

Eq. (1) can be written more rigorously as

$$I_A^B(\mathbf{r}) = \sum_{\ell j \mu} \langle I_A M_A j m | I_B M_B \rangle \langle \ell m - \mu s \mu | j m \rangle i^\ell R_{A\ell j}^B(r) Y_{\ell m - \mu}(\hat{r}) \chi_{s\mu}(\hat{\mathbf{r}})$$

where ℓ is the orbital angular momentum for the relative motion of proton with respect to nucleus A and s is the spin of the proton. Since the force parameter set TH1 is chosen to reproduce experimental one proton separation energy in ${}^8\text{B}$, the function $R_{A\ell j}^B(r)$ in Eq. (2) has the proper asymptotic behavior for this case. The same is not true for the parameter set TH2.

The overlap function for ${}^8\text{B}$ and ${}^7\text{Be}$ nuclei is used in the calculation of a asymptotic normalization constant which is related to the astrophysical factor S_{17} . It is also needed for the calculation of the valence proton density distribution which could be one more source of information about the existent of a proton halo structure in this nucleus. It should be noted that the overlap function is not an eigen function of the total Hamiltonian and it may or may not be normalized to unity.

The rms radius of the overlap function $R_{A\ell j}^B(r)$ corresponds to that of the ${}^7\text{Be} + p = {}^8\text{B}$ bound state (or of the valence proton) for a given ℓj combination. It can be written as

$$\langle r^2 \rangle_{{}^7\text{Be}-p} = N(0)^{-1} \int_0^\infty r^4 dr |R_{A\ell j}^B(r)|^2, \quad (3)$$

where

$$N(0) = \int_0^\infty r^2 dr |R_{A\ell j}^B(r)|^2. \quad (4)$$

Using HF wave functions calculated in the previous sections we get, $\langle r^2 \rangle_{{}^7\text{Be}-p}^{1/2} = 4.93$. Comparing our results with those of other authors (as listed in Table I of Ref. [8]) we

note that our results are in agreement with them within 10–20%. Thus, almost all these calculations appear to be in agreement with the fact that the valence proton has a large spatial extension in ^8B . One exception, however, is Ref. [33] where a relatively smaller value of 3.75 fm has been reported for the valence proton rms radius in ^8B . These authors have done their calculations by employing a two-body model with a Gaussian potential of range 1.90 fm which may not describe accurately the tail of the p-shell single proton wave function in ^8B .

We have estimated the contribution of the asymptotic part of the overlap wave function to the valence proton rms radius in ^8B in the following way (see, e.g., [8]). We define the ratio

$$C_1(R_{cut}) = \frac{\int_{R_{cut}}^{\infty} r^2 dr |R_{Alj}^B(r)|^2}{\int_0^{\infty} r^2 dr |R_{Alj}^B(r)|^2}, \quad (5)$$

$$C_2(R_{cut}) = \frac{N(R_{cut})^{-1} \int_{R_{cut}}^{\infty} r^4 dr |R_{Alj}^B(r)|^2}{N(0)^{-1} \int_0^{\infty} r^4 dr |R_{Alj}^B(r)|^2}, \quad (6)$$

where R_{cut} is a cut-off radius and $N(x)$ is as defined in Eq. (4) with x being the lower limit of the integration. C_1 and C_2 give contributions of the asymptotic part to the norm of the overlap function and to the rms radius of the valence proton, respectively. For $R_{cut} = 2.5$ fm which is the calculated value of the matter radius in ^7Be (see table II), we find $C_1(R_{cut})[C_2(R_{cut})] = 0.62(0.87)$. This indicates that the region outside the ^7Be core contributes up to 87% to the valence proton radius in ^8B and that the probability of finding a valence proton outside the ^7Be core nucleus is about 62%. For $R_{cut} = 4.0$ fm (beyond which the nuclear interaction becomes negligible) we get $C_1(R_{cut})[C_2(R_{cut})] = 0.32(0.65)$. This means that contributions to the valence proton rms radius are about 65% from the distances beyond 4 fm. These results provide further support to the existence of a proton halo structure in the ^8B nucleus. As remarked earlier, in these calculations we have assumed that ^7Be behaves as an inert core inside the ^8B nucleus. Consideration of the excitation of ^7Be core will not change these conclusions significantly [8, 34].

Next, we present results for the astrophysical S_{17} factor calculated within our model. In the region outside the core where range of the nuclear interaction becomes negligible ($r > 4.0$ fm), the radial overlap wave function $R(r)$ of the bound state can be written as

$$R_{Alj}^B(r) \simeq \bar{c}_{lj} W_{\eta, l+1/2}(2kr)/r, \quad (7)$$

where W is the Whittaker function, k the wave number corresponding to the single proton separation energy and η the Sommerfield parameter for the bound state in ^8B . In Eq. (7), \bar{c}_{lj} is the asymptotic normalization constant, required to normalize the radial overlap wave function in the ^8B nucleus to the Whittaker function in the asymptotic region. The S_{17} factor is related to the proton capture cross section as

$$S_{17}(E) = \sigma(E) E e^{(2\pi\eta(E))}. \quad (8)$$

It has been shown in ref. [13] that at the zero energy the S_{17} factor depends only on \bar{c}_{lj} and one can write [19, 20]

$$S_{17}(0) = \kappa \sum_j \bar{c}_{1j}^2, \quad (9)$$

In Ref. [19], κ ($= 37.8$) has been obtained by using a microscopic cluster model for the scattering states, while a value of 36.5 has been reported for this quantity in Ref. [20] using a hard sphere scattering state model. However, it has been argued in [19] that once the relevant integration distances are sufficiently enhanced in [20] the value of κ there comes out to be 37.2, which is in good agreement with that of the microscopic model. In our calculations, we have used our HF overlap function directly as an input

Table 3. SkHF results for asymptotic normalization coefficients ($\bar{c}_{\ell j}$), and astrophysical S -factors $S_{17}^A(0)$ and $S_{17}^B(0)$ and $S_{17}^C(0)$. S_{17}^A corresponds to results obtained by using the HF overlap function directly to a capture code while S_{17}^B and S_{17}^C to those obtained by using Eq. (9) with $\kappa = 36.5$ and 37.8, respectively.

	SkHF	
	TH1	TH2
$\bar{c}_{13/2}$	0.64	0.88
$\bar{c}_{11/2}$	0.34	0.29
$S_{17}^A(0)(eVb)$	22.0	35.3
$S_{17}^B(0)(eVb)$	19.5	31.3
$S_{17}^C(0)(eVb)$	20.2	32.4

into a capture code where the scattering states are described by pure Coulomb wave functions between ${}^7\text{Be}$ and p . Thus, within an inert ${}^7\text{Be}$ core approximation our results are parameter free. In Table III, $S_{17}^A(0)$ represents the astrophysical S -factor obtained by this method. We show results obtained by using overlap functions calculated with both TH1 and TH2 force parameters. We see that $S_{17}^A(0)$ obtained with TH1 force is quite close to its adopted value of $19.1^{+4.0}_{-1.0}$ eV b. On the other hand, that obtained with TH2 is quite large and well beyond the maximum limit of this value. We also show in this table values of asymptotic normalization coefficients and $S_{17}(0)$ obtained by using Eq. (9) with $\kappa = 36.5$ and 37.8 ($S_{17}^B(0)$ and $S_{17}^C(0)$), respectively). These results are in agreement with those obtained by our method within 10%.

C Summary and conclusions

In summary, in this paper we studied the structure of ${}^8\text{Li}$, ${}^8\text{B}$, ${}^7\text{B}$, ${}^7\text{Be}$, and ${}^9\text{C}$ nuclei within the Skyrme Hartree-Fock (SkHF) framework. We calculated binding energies, various densities distribution and rms radii for these nuclei. Using the same set of the force parameters, we obtain good agreements with experimental values of binding energies and rms matter radii for all these nuclei. We have calculated the overlap function $\langle {}^7\text{Be} | {}^8\text{B} \rangle$ from the SkHF wave functions which has been employed to obtain the radius of the valence proton in ${}^8\text{B}$ nucleus. The value of this quantity is found to be 4.76 fm which is almost two times larger than the matter radius of ${}^7\text{Be}$ core. This provides support to the possibility of ${}^8\text{B}$ having a one proton halo structure.

This overlap function has also been used to extract the asymptotic normalization coefficients for ${}^8\text{B} \rightarrow {}^7\text{Be} + p$. Using the overlap function calculated with the modified force we obtain an astrophysical S-factor of 22.0 eV b which lies within the adopted limits ($19.1^{+4.0}_{-1.0}$ eV b) of the near zero energy astrophysical S-factor. The values of S_{17} obtained by using the corresponding asymptotic normalization coefficients follow the similar trend. Our work clearly shows that proper nuclear structure input is vital in order to understand some very important issues in astrophysics.

Acknowledgment

This work is supported by the Department of Atomic Energy, (BRNS), (BARC), Mumbai, under contract no. 2001/37/14/BRNS/699.

References

1. J.N. Bahcall *Neutrino Astrophysics* (Cambridge University Press, 1989), J.N. Bahcall and M. Pinsonneault, Rev. Mod. Phys. **64** (1992) 885.
2. R. Davis, Prog. Part. Nucl. Phys. **32** (1994) 13, Eric G. Adelberger et al., Rev. Mod. Phys. **70** (1998) 1265.
3. S. Fukuda et al, Phys. Rev. Lett. **86** (2001) 5651, Q.R. Ahmad et al., **87** (2001) 071031, **89** (2002) 011301.
4. H. Esbensen and K. Hencken, Phys. Rev. **C61** (2000) 054606.
5. T. Barker et al., Phys. Rep. **289** (1997) 235.
6. R. Shyam and H. Lenske, Phys. Rev. **C57** (1998) 2427.
7. N.K. Timofeyuk, Nucl. Phys. **A632** (1998) 19.
8. F. Carstoiu, L. Trache, C.A. Gagliardi, R.E. Tribble and A.M. Mukhamedzhanov, Phys. Rev. **C63** (2001) 054310.
9. M.H. Simedberg et al., Phys. Lett. **B452** (1999) 1.
10. L.V. Grigorenko, B.V. Danilin, V.D. Efros, N.B. Shulgina and M.M. Zhukov, Phys. Rev. **C57** (1998) R2099.
11. B.W. Filippone, S.J. Elwyn, C.N. Davids, D.D. Koetke, Phys. Rev. Lett. **50** (1983) 412; Phys. Rev. **C28** (1983) 2222; F. Hammache et al., Phys. Rev. Lett. **80** (1998) 928; A.R. Jungmans et al., Phys. Rev. Lett. **88** (2002) 041101.
12. T. Motobayashi et al., Phys. Rev. Lett. **73** (1994) 2680; I. Motobayashi, Nucl. Phys. **A693** (2001) 258; N. Iwasa et al., Phys. Rev. Lett. **83** (1999) 2910; B. Davids, et al., Phys. Rev. **C63** (2001) 065806.
13. H.M. Xu, C.A. Gagliardi, R.E. Tribble, A.M. Mukhamedzhanov and N.K. Timofeyuk, Phys. Rev. Lett. **73** (1994) 2027.
14. G.A. Gagliardi et al., Nucl. Phys. **A682** (2001) 369.
15. A. Azhari et al., Phys. Rev. **C60** (1999) 055803.
16. W. Lui et al., Nucl. Phys. **A616** (1997) 131c; Phys. Rev. Lett. **77** (1996) 611.
17. J. J. Das et al., Nucl. Phys. **A746** (2004) 561c.
18. N.K. Timofeyuk, D. Baye, and P. Descouvemint, Nucl. Phys. **A620** (1997) 29.
19. A. Csoto, Phys. Rev. **C61** (2000) 037601; B.K. Jennings, S. Karataglidis, and T.D. Shoppa, Phys. Rev. **C58** (1998) 3711.
20. B.A. Brown, A. Costo, and R. Sherr, Nucl. Phys. **A597** (1996) 66.
21. J.W. Negele and D. Vautherin, Phys. Rev. **C5** (1972) 1472.

22. F. Quentin and H. Flocard, *Annu. Rev. Nucl. Part. Sci.* **28** (1978) 523.
23. J. Friedrich and P.-G. Reinhard, *Phys. Rev. C* **33** (1986) 335.
24. J. Dobaczewski, I. Hamamoto, W. Nazarewicz and J.A. Sheikh, *Phys. Rev. Lett.* **72** (1994) 981.
25. Yao-song Shen and Zhogzhon Ren, *Phys. Rev. C* **54** (1996) 1158.
26. X. Li and P. H. Heensen, *Phys. Rev. C* **54** (1996) 1617.
27. S. Mizutori, J. Dobaczewski, G. A. Lalazissis, W. Nazarewicz and P. G. Reinhard, *Phys. Rev. C* **61** (2000) 044326.
28. P. G. Reinhard, D.J. Dean, W. Nazarewicz, J. Dobaczewski, J.A. Maruhn and M.R. Strayer, *Phys. Rev. C* **60**, (1999) 014316.
29. E. Chabanat, P. Bonche, P. Haensel, J. Meyey and R. Schaeffer, *Nucl. Phys. A* **627**, 710(1997).
30. S.S. Chandel, S.K. Dhiman, and R. Shyam, *Phys. Rev. C* **68** (2003) 054320.
31. W. T. Pinkston, *Nucl. Phys. A* **269** (1976) 281; W. T. Pinkston and P. J. Iano, *Nucl. Phys. A* **330** (1979) 91.
32. R. Shyam and M. A. Nagarajan, *J. Phys. G: Nucl. Part. Phys.* **9** (1983) 901.
33. K. Riisager and J.S. Jensen, *Phys. Lett. B* **301** (1993) 6.
34. A.M. Moro, R. Crespo, F. Nunes and I.J. Thompson, *Phys. Rev. C* **66** (2002) 024612.

Mean-field Approach for Interacting Boson Models: New Applications

V.K.B. Kota*

Physical Research Laboratory, Ahmedabad 380 009, India

Abstract. Mean-field approach for the algebraic interacting boson models (*sd*IBM, *sdg*IBM, *sdpf*IBM, *sp*IBM, *pn*IBM, *sd*IBM- T , *sd*IBM- ST etc.) is briefly reviewed. Intrinsic states defined by the lowest Hartree-Bose mean-field deformed single particle state, give ground state shapes generated by the symmetry limits of IBM's and they are described with examples from *sd*IBM and *sdg*IBM. For deformed nuclei, defining excited bands using TDA and carrying out angular momentum projection, analytical results, valid to order $1/N$ where N is the boson number, for various observables are obtained. In addition, two new applications of the mean-field approach to IBM's are also discussed and they are: (i) regular structures generated by random interactions; (ii) quantum phase transitions exhibited by nuclei.

A Introduction

Starting with the *sd* interacting boson model (*sd*IBM) introduced by Arima and Iachello [1], i.e. *sd*IBM for quadrupole collective states with $U(6)$ spectrum generating algebra (SGA), large class of interacting boson models (IBM's) are introduced and developed to study different types of collective motion exhibited by even-even nuclei. Some of them are: (i) *sp*IBM or nuclear vibron model with $U(4)$ SGA for molecular resonances and two-body clusters [2]; (ii) *sdpf*IBM for GDR states with $U(9)$ SGA [3]; (iii) *sdg*IBM for quadrupole plus hexadecupole states with $U(15)$ SGA [4,5]; (iv) *sdpf*IBM for octupole states with $U(16)$ SGA [6]; (v) *sdgpf*IBM with $U(25)$ SGA [7]; (vi) *spp'*IBM or the $U(7)$ model for 3-body clusters in nuclei with $U(7)$ SGA [8]; (vii) *sd*IBM-2 or *pn*IBM with $U(12)$ SGA [9]; (viii) *sd*IBM-3 or *sd*IBM- T (here bosons carry $T = 1$ degree of freedom) with $U(18)$ SGA [10]; (ix) *sd*IBM-4 or *sd*IBM- ST (here bosons carry $(ST) = (10) \oplus (01)$ degree of freedom) with $U(36)$ SGA [11]. In this paper we will not deal with odd-A and odd-odd nuclei (the only exception is *sd*IBM- ST which also applies to odd-odd nuclei). Algebraic approach, in the various dynamical symmetries generated by the SGA's of IBM's, gives analytical results for observables. This has been extremely successful as analytical results provide a simple framework for confronting data and hence in establishing the applications of the various IBM's; see for example [1-11].

On the other hand, mean-field approach gives deeper information about the structures generated by the interacting boson models as they apply in the situations that go beyond the symmetry limits of the models. In addition, in the symmetry limits they

* E-mail: vkbkota@prl.ernet.in

give insights into the structures without using group theory. Intrinsic states (obtained by putting all the bosons in the lowest Hartree-Bose (**HB**) mean-field deformed single particle state) give ground state shapes generated by the symmetry limits of IBM's and also by a general hamiltonian. Intrinsic states are constructed for many IBM's (see [1, 12, 13] and references there in) and they are briefly discussed with examples from *sd*IBM and *sdg*IBM in Section 2. Going beyond the study of ground state shapes, for deformed nuclei, starting with a $K = 0$ intrinsic state, defining excited bands using TDA and carrying out angular momentum projection, **analytical results** for the hamiltonian expectation values, $B(E2)$'s, $B(M1)$'s etc. can be derived [14] that are valid to order $1/N$ where N is the boson number (full HB and RPA and TDA equations are also available in literature [15]). The $1/N$ method is briefly outlined in Section 3. Recent novel applications of the mean-field approach to IBM's are in the study of regular structures generated by random interactions [16, 17] and in the study of quantum phase transitions exhibited by nuclei [18, 19]. Overview of these applications form Sections 4 and 5 respectively. Finally Section 6 gives conclusions.

B Geometric shapes in IBM's

For any IBM it is possible to construct a lowest deformed single particle state in which one can put all the bosons. The resulting many particle state is called a intrinsic (or coherent) state. Then it is possible to write the Hamiltonian expectation value as a function of the parameters defining the intrinsic state. Now one can minimize this energy functional with respect to the parameters of the intrinsic state. This procedure (HB) gives the equilibrium shapes generated by a IBM hamiltonian. The basic problem here is to identify a general single particle state such that as the parameters vary one will generate different shapes (i.e no shape is repeated). Intrinsic states are constructed for (i) *sd*IBM [20]; (ii) *sp*IBM [21]; (iii) *sdg*IBM [4, 12]; (iv) *pn*IBM [22]; (iv) *spdf*IBM [23]; (v) *sd*IBM-*T* [24]; (vi) *sd*IBM-*ST* [13]. For illustration, we will elaborate some of the results for *sd*IBM and *sdg*IBM in the subsections 2.1 and 2.2 respectively.

B.1 Geometric shapes in *sd*IBM

Most general (1+2)-body hamiltonian, for *sd*IBM, conserving boson number and angular momentum is

$$\begin{aligned}
 H_{sdIBM} = & \epsilon_s \hat{n}_s + \epsilon_d \hat{n}_d + \frac{1}{2} V^0(sss)[(s^\dagger s^\dagger)^0 \cdot (\tilde{s}\tilde{s})^0] \\
 & + \frac{1}{2} V^0(ssdd)[(s^\dagger s^\dagger)^0 \cdot (\tilde{d}\tilde{d}) + h.c.]^0 + V^2(sdsd)[(s^\dagger d^\dagger)^2 \cdot (\tilde{s}\tilde{d})^2] \\
 & + \frac{1}{\sqrt{2}} V^2(sddd)[(s^\dagger d^\dagger)^2 \cdot (\tilde{d}\tilde{d})^2 + h.c.] + \sum_{L_0=0,2,4} \frac{1}{2} V^{L_0}(dddd)[(d^\dagger d^\dagger)^{L_0} \cdot (\tilde{d}\tilde{d})^{L_0}]
 \end{aligned} \tag{1}$$

where the ϵ 's are single boson energies and V 's are two-particle matrix elements. Using the (β_2, γ) parameters for a quadruple surface, most general intrinsic state for *sd*IBM

is [1, 20]

$$|N; \beta_2, \gamma\rangle = \left[N! (1 + \beta_2^2)^N \right]^{-1/2} \left\{ s_0^\dagger + \beta_2 \left[\cos \gamma d_0^\dagger + 2^{-1/2} \sin \gamma (d_2^\dagger + d_{-2}^\dagger) \right] \right\}^N |0\rangle \quad (2)$$

where $\beta_2 \geq 0$ and $0^\circ \leq \gamma \leq 60^\circ$. Now the equilibrium shape parameters (β_2^0, γ_0) are obtained by minimizing the expectation value of H_{sdIBM} in the intrinsic state (2), i.e. by using

$$E(N; \beta_2, \gamma) = \langle N; \beta_2, \gamma | H | N; \beta_2, \gamma \rangle ;$$

$$\frac{\partial E}{\partial \beta_2} = 0, \quad \frac{\partial E}{\partial \gamma} = 0 \Rightarrow (\beta_2^0, \gamma_0) .$$

Using the basic commutation relations $[b, f(b^\dagger)] = \frac{\partial f}{\partial b^\dagger}$, $[b^\dagger, f(b)] = -\frac{\partial f}{\partial b}$, the formula for $E(N, \beta_2, \gamma)$ for a general $sdIBM$ hamiltonian is easily obtained (second reference in [12] gives all the mathematical details for sd and sdg IBM's),

$$\begin{aligned} E(N, \beta_2, \gamma) &= \frac{N}{1 + \beta_2^2} [\epsilon_s + \beta_2^2 \epsilon_d] \\ &+ \frac{N(N-1)}{(1 + \beta_2^2)^2} \left[\frac{1}{2} V^0(ssss) + \frac{1}{\sqrt{5}} \beta_2^2 V^0(ssdd) + \beta_2^2 V^2(sdsd) \right. \\ &\left. - \frac{2}{\sqrt{7}} \beta_2^3 \cos 3\gamma V^2(sddd) + \frac{\beta_2^4}{2} \left\{ \frac{V^0(dddd)}{5} + \frac{2V^2(dddd)}{7} + \frac{18V^4(dddd)}{35} \right\} \right] \end{aligned}$$

A simpler hamiltonian that covers the three $sdIBM$ symmetry limits is

$$H(\zeta, \chi) = \epsilon_0 \left[(1 - \zeta) n_d - \frac{\zeta}{4N} Q^x \cdot Q^x \right], \quad Q^x = (d^\dagger \tilde{s} + s^\dagger \tilde{d})^2 + \chi (d^\dagger \tilde{d})^2 \quad (3)$$

Here ϵ_0 is a scale factor. Note that $\zeta = 0$ gives the $U(5)$ limit, $\zeta = 1, \chi = 0$ gives the $O(6)$ limit and $\zeta = 1, \chi = \pm \frac{\sqrt{7}}{2}$ gives the $SU(3)$ limit (in fact the + sign gives $\overline{SU(3)}$ limit [1, 19]). Then the energy functional is

$$\begin{aligned} E^{(\zeta, \chi)}(N, \beta_2, \gamma) / (\epsilon_0 N) &= \\ &\frac{\beta_2^2}{1 + \beta_2^2} \left[(1 - \zeta) - \left(\frac{\zeta}{4N} \right) (1 + \chi^2) \right] + \frac{5}{1 + \beta_2^2} \left(-\frac{\zeta}{4N} \right) \\ &+ \frac{(N-1)}{(1 + \beta_2^2)^2} \left(\frac{-\zeta}{4N} \right) \left[4\beta_2^2 - 4\sqrt{\frac{2}{7}} \chi \beta_2^3 \cos 3\gamma + \frac{2}{7} \chi^2 \beta_2^4 \right] \end{aligned} \quad (4)$$

Now it is seen easily that the $U(5)$ limit gives spherical ($\beta_2^0 = 0$, vibrational) shape, $SU(3)$ limit gives axially deformed ($\beta_2^0 \neq 0, \gamma_0 = 0^\circ$, rotational) shape and the $O(6)$ limit is γ -unstable ($\beta_2^0 \neq 0$ and E is independent of γ).

B.2 Geometric shapes in sdg IBM

The general sdg IBM ($U_{sdg}(15)$) intrinsic state [or coherent state (CS)] is,

$$|N, \{\alpha\}\rangle = [N!(1 + \alpha_2 \cdot \alpha_2 + \alpha_4 \cdot \alpha_4)^N]^{-1/2} \left[s^\dagger + \sum_{\mu} \alpha_{2\mu} d_{\mu}^\dagger + \sum_{\nu} \alpha_{4\nu} g_{\nu}^\dagger \right]^N |0\rangle \quad (5)$$

Removing the three orientation parameters (for rotationally invariant hamiltonians), we have in general a 11 - parameter CS [25]. The simpler CS used in the study of geometric shapes in sdg IBM is [12],

$$\begin{aligned} |N; \beta_2; \beta_4, \gamma\rangle = & [N! (1 + \beta_2^2 + \beta_4^2)^N]^{-1/2} \left\{ s_0^\dagger + \beta_2 [\cos \gamma d_0^\dagger + \right. \\ & \left. \sqrt{\frac{1}{2}} \sin \gamma (d_2^\dagger + d_{-2}^\dagger)] + \frac{1}{6} \beta_4 [(5 \cos^2 \gamma + 1) g_0^\dagger \right. \\ & \left. + \sqrt{\frac{15}{2}} \sin 2\gamma (g_2^\dagger + g_{-2}^\dagger) + \sqrt{\frac{35}{2}} \sin^2 \gamma (g_4^\dagger + g_{-4}^\dagger)] \right\}^N |0\rangle \quad (6) \end{aligned}$$

Note that $\beta_2 \geq 0$, $-\infty \leq \beta_4 \leq +\infty$ and $0^\circ \leq \gamma \leq 60^\circ$ respectively. For the four strong coupling limits $SU_{sdg}(3)$, $SU_{sdg}(5)$, $SU_{sdg}(6)$ and $O_{sdg}(15)$ of sdg IBM, the hamiltonian (which is always quadrupole - quadrupole plus hexadecupole - hexadecupole type), energy functional, equilibrium shape parameters and the equilibrium energy are derived [12, 26] (see also the second reference in [4]). For the first three limits they are given in Tables 1, 2 and 3. Some of the important results here are: (i) Non-axial shapes (γ different from 0° or 60°) are not possible in the dynamical symmetry limits although $E(N; \beta_2, \beta_4, \gamma)$ contain $\cos^2 3\gamma$ terms; (ii) for a general H_{sdgIBM} non-axial shapes are possible (this is unlike in sd IBM) and one such example is given in [27]; (iii) $SU_{sdg}(3)$ is deformed and $O_{sdg}(15)$ is γ -unstable just as in the $SU(3)$ and $O(6)$ limits respectively of sd IBM; (iv) $SU_{sdg}(5)$ limit admits two minima and hence in the sdg model it is in principle possible, with an additional variable (say angular momentum), to have shape phase transition (i.e the system can go from one minimum to another by varying the variable); (v) $SU_{sdg}(6)$ limit has three degenerate minima and hence it is possible to have shape coexistence in sdg IBM. It is seen that the three degenerate minima in $SU_{sdg}(6)$ limit correspond to quite different shapes (in fact one is prolate and the other two are oblate). **Thus unlike sd IBM, the sdg IBM admits shape phase transition and shape coexistence;** (vi) The CS results are used in the analysis of two nucleon transfer data and in various other applications by Kota and Devi; see [26] and the second reference in [4].

C Excited bands and the 1/N method

For deformed nuclei an appropriate method is to construct the intrinsic state $|(b_0^\dagger)^N\rangle$ for the ground $K = 0$ band (with bosons carrying angular momenta ℓ and $\sum_{\ell} x_{\ell 0}^2 = 1$),

$$|N; K = 0\rangle = (N!)^{-1/2} (b_0^\dagger)^N |0\rangle = (N!)^{-1/2} \left(\sum_{\ell} x_{\ell 0} b_{\ell 0}^\dagger \right)^N |0\rangle, \quad (7)$$

with the variational parameters obtained by minimizing the expectation value of H . The excited bands are obtained by diagonalizing H in the TDA basis $|\ell K\rangle = [(N-1)!]^{-1/2} b_{\ell K}^\dagger (b_0^\dagger)^{N-1} |0\rangle$ and then the excited K -bands are [28]

$$\begin{aligned} |N; K\rangle &= [(N-1)!]^{-1/2} b_K^\dagger (b_0^\dagger)^{N-1} |0\rangle \\ &= [(N-1)!]^{-1/2} \left(\sum_{\ell \geq K} x_{\ell K} b_{\ell K}^\dagger \right) (b_0^\dagger)^{N-1} |0\rangle \end{aligned}$$

Note that full HB+TDA equations are also available in literature [15]. However for IBM's, energy spectrum and transition matrix elements can be derived, in terms of the parameters x 's in Eqs. (9) and (10), in the states with L -projection, in analytical form to order $1/N$ (giving the name $1/N$ method) as shown in a series of papers by Kuyucak and Morrison. Using this method analytical results are derived for *sdg*IBM, *sdpf*IBM, *sd*IBM-2 etc. [14]. Here only some basic results are described to illustrate the $1/N$ method and further details are available in [14, 28].

Let us denote the intrinsic state for a K band by ϕ_K . The expectation value of H in the intrinsic state is $\langle \phi_K | H | \phi_K \rangle / \langle \phi_K | \phi_K \rangle$ and using the methods of Section 2, it is easy to derive expressions for this. They can be used in variation before angular momentum projection (**VBP**). Similarly in the L projected states the expectation value is,

$$\begin{aligned} \langle KL | H | KL \rangle &= \langle \phi_K | H P_{KK}^L | \phi_K \rangle / \langle \phi_K | P_{KK}^L | \phi_K \rangle \\ P_{MK}^L(\Omega) &= \frac{(2L+1)}{8\pi^2} \int D_{MK}^L(\Omega)^* R(\Omega) d\Omega \end{aligned} \quad (8)$$

Expressions for $\langle KL | H | KL \rangle$ can be derived for any K . Let us consider the $K=0$ band, with $\ell = 0, 2, 4, \dots$ and H in multipole form,

$$H = \sum_{\ell} \epsilon_{\ell} n_{\ell} + \sum_{k=2,4,\dots} \kappa_k T^k \cdot T^k, \quad T^k = \sum_{\ell, \ell'} t_{\ell, \ell'}^k \left(b_{\ell}^\dagger \tilde{b}_{\ell'} \right)^k. \quad (9)$$

Firstly $\langle \phi_{K=0} | P_{00}^L | \phi_{K=0} \rangle$ is given by

$$\langle \phi_{K=0} | P_{00}^L | \phi_{K=0} \rangle = \frac{2L+1}{2} \int d\beta \sin \beta d_{00}^L(\beta) \langle 0 | (b_0)^N e^{-i\beta L_y} (b_0^\dagger)^N | 0 \rangle \quad (10)$$

Then, with the rotated intrinsic boson b_R^\dagger ,

$$b_R^\dagger = e^{-i\beta L_y} b_0^\dagger e^{i\beta L_y} = \sum_{\ell, m} x_{\ell 0} d_{m0}^\ell(\beta) b_{\ell m}^\dagger \quad (11)$$

one has

$$\begin{aligned}
 \langle 0 | (b_0)^N e^{-i\beta L_y} (b_0^\dagger)^N | 0 \rangle &= N \sum_{\ell} x_{\ell 0} \frac{\partial b_R^\dagger}{\partial b_{\ell 0}^\dagger} \langle 0 | (b_0)^{N-1} e^{-i\beta L_y} (b_0^\dagger)^{N-1} | 0 \rangle \\
 &= \left\{ N \sum_{\ell} (x_{\ell 0})^2 d_{00}^{\ell}(\beta) \right\} \langle 0 | (b_0)^{N-1} e^{-i\beta L_y} (b_0^\dagger)^{N-1} | 0 \rangle \\
 &= (N!) [Z(\beta)]^N, \quad Z(\beta) = \sum_{\ell} (x_{\ell 0})^2 d_{00}^{\ell}(\beta)
 \end{aligned} \tag{12}$$

For large N a simpler form for $Z(\beta)$ is,

$$[Z(\beta)]^N = \left\{ \sum_{\ell} (x_{\ell 0})^2 \right\}^N e^{-\beta^2/\Gamma}, \quad \Gamma = 4/(aN) \quad \text{where} \quad a = \sum_{\ell} \ell(\ell+1) (x_{\ell 0})^2 \tag{13}$$

Then the expectation value of H [for variation before projection (**VAP**)] to order $1/N^2$ is,

$$\begin{aligned}
 \langle GS, L | H | GS, L \rangle &= N \left[E_0 + \frac{1}{N} \left(E_0 - \frac{E_1}{a} \right) - \frac{L(L+1)}{aN^2} \left(E_0 - \frac{E_1}{a} \right) \right] \\
 &+ \sum_{k=2,4,\dots} \kappa_k N^2 \left\{ A_{k0}^2 + \frac{1}{N} \left[A_{k0}^2 \left(1 + \frac{k(k+1)}{2a} \right) + C_k - \frac{2A_{k0}A_{k1}}{a} \right] \right. \\
 &\left. - \frac{L(L+1)}{aN^2} \left[A_{k0}^2 \left(2 + \frac{k(k+1)}{2a} \right) - \frac{2A_{k0}A_{k1}}{a} \right] \right\}, \\
 A_{kn} &= \sum_{\ell, \ell'} [\ell'(\ell'+1)]^n \langle \ell' 0 \ell 0 | k 0 \rangle t_{\ell', \ell}^k x_{\ell 0} x_{\ell' 0}, \quad a = \sum_{\ell} \ell(\ell+1) (x_{\ell 0})^2 \\
 c_k &= \sum_{\ell, \ell'} \frac{2k+1}{2\ell+1} (t_{\ell', \ell}^k x_{\ell 0})^2, \quad E_n = \sum_{\ell} [\ell(\ell+1)]^n \epsilon_{\ell} (x_{\ell 0})^2
 \end{aligned} \tag{14}$$

Similar expressions are derived for excited $K = 0 (\beta, \beta', \dots)$ and $K \neq 0$ bands for various IBM's. Also expressions are derived, in terms of the mean field coefficients $x_{\ell k}$, for a variety of observables which include $B(E2)$'s, $B(M1)$'s, g -factors, $E2/M1$ ratios, moment of inertia, $B(E4)$'s and so on. For example:

$$\begin{aligned}
 \langle GS, L_f || Q^2 || GS, L_i \rangle &= \left[N \sqrt{2L_i+1} \right] \langle L_i 0 \ 20 | L_f, 0 \rangle \times \\
 &\left[B_{00} + \frac{1}{N} \left(B_{00} - \frac{B_{10} - 3B_{00}}{a} \right) - \frac{L_i(L_f+1)}{aN^2} \left\{ B_{00} + \frac{F_1}{4a} \delta_{L_f, L_i} \right. \right. \\
 &\left. \left. - \frac{F_2}{12a} \delta_{L_f, L_i+2} \right\} \right]; \quad L_f = L_i \quad \text{or} \quad L_f = L_i + 2 \\
 B_{mn} &= \sum_{\ell', \ell} [\ell'(\ell'+1)]^m [\ell(\ell+1)]^n \langle \ell' 0 \ell 0 | 20 \rangle t_{\ell', \ell}^2 x_{\ell' 0} x_{\ell 0}, \\
 F_1 &= B_{20} - B_{11} - 10B_{10} + 12B_{00}, \quad F_2 = B_{20} - B_{11} + 6B_{10} - 12B_{00}
 \end{aligned} \tag{15}$$

$$\langle K, L+K \parallel T^K \parallel GS, L \rangle = [N(2L+1)(2-\delta_{K0})]^{1/2} \times$$

$$\langle L0 \parallel KK \parallel L+K, K \rangle \sum_{\ell, \ell'} \langle \ell K \parallel \ell' 0 \parallel KK \rangle t_{\ell, \ell'}^{(K)} x_{\ell K} x_{\ell' 0}$$

$$g(K, L) = g + g' \sqrt{\frac{5}{3}} \left[\frac{x_{40}^2}{(a/2)} + \frac{K^2}{L(L+1)} \left(-\frac{x_{40}^2}{(a/2)} + \frac{x_{4K}^2}{10} \right) \right] \quad (16)$$

$$B(M1; 0_{GS}^+ \longrightarrow 1_1^+) = \frac{3}{4\pi} (g')^2 \frac{N}{(a/2)} (x_{20} \ x_{40})^2 \quad (17)$$

The last two equations are for *sdg*IBM and the *M1* operator used is $T^{M1} = g\mathbf{L} + g' (g^\dagger \tilde{g})^1$. In Eq. (18), Q_μ^2 is same as T_μ^2 of Eq. (12).

Table 1. Group chain, hamiltonian, energy functional and the equilibrium shape parameters, in large N limit, for the $SU(3)$ limit of sdg IBM

$SU_{sdg}(3)$ Limit
$U_{sdg}(15) \supset SU_{sdg}(3) \supset O(3)$
$H_{SU_{sdg}(3)} = -a \left\{ \frac{4}{3} C_2(SU_{sdg}(3)) - C_2(O(3)) \right\} + b C_2(O(3))$ $= -a Q^2(s) \cdot Q^2(s) + b C_2(O(3))$
$Q_\mu^2(s) = 4\sqrt{\frac{7}{15}} \left(s^\dagger \tilde{d} + d^\dagger \tilde{s} \right)_\mu^2 - 11\sqrt{\frac{2}{21}} (d^\dagger \tilde{d})_\mu^2 + \frac{36}{\sqrt{105}} \left(d^\dagger \tilde{g} + g^\dagger \tilde{d} \right)_\mu^2$ $- 2\sqrt{\frac{33}{7}} (g^\dagger \tilde{g})_\mu^2$
$E_{SU_{sdg}(3)}(N; \beta_2, \beta_4, \gamma) =$ $\frac{-a N^2}{(1 + \beta_2^2 + \beta_4^2)^2} \left[\frac{448}{15} \beta_2^2 + \frac{384\sqrt{14}}{35} \beta_2^2 \beta_4 + \right.$ $\frac{352\sqrt{35}}{105} \beta_2^3 \cos 3\gamma + \frac{64\sqrt{35}}{21} \beta_2 \beta_4^2 \cos 3\gamma + \frac{3456}{245} \beta_2^2 \beta_4^2$ $\frac{1056\sqrt{10}}{245} \beta_2^3 \beta_4 \cos 3\gamma + \frac{484}{147} \beta_2^4 + \frac{192\sqrt{10}}{49} \beta_2 \beta_4^3 \cos 3\gamma$ $\left. \frac{880}{441} (4 - \cos^2 3\gamma) \beta_2^2 \beta_4^2 + \frac{400}{1323} (16 - 7\cos^2 3\gamma) \beta_4^4 \right]$ $\beta_2^0 = \sqrt{\frac{20}{7}}, \quad \beta_4^0 = \sqrt{\frac{8}{7}}, \quad \gamma^0 = 0^\circ$ $E_{SU_{sdg}(3)}(N; \beta_2^0, \beta_4^0, \gamma^0) = -\frac{64}{3} a N^2$

D Regular structures with random interactions: mean-field analysis for IBM's

Two-body random matrix ensembles (TBRE) defined over Hilbert spaces of various nuclear models [29] led to the discovery [30] that many of the regular features observed in low-lying levels and near the yrast line in nuclei can arise due to random interactions (with rotational symmetry) and this is opposed to the conventional ideas of using regular (or coherent) interactions like pairing etc. in the nuclear hamiltonian. For the first time Johnson, Bertsch and Dean in 1998 [30], using the shell model, noticed that random two-body interactions lead to ground states, for even-even nuclei, having spin 0^+ with very high probability. Later studies with random interactions revealed statistical predominance of odd-even staggering in binding energies, the seniority pairing gap, 0^+ , 2^+ , 4^+ , \dots yrast sequence, parity distribution in ground states etc. Similarly, Bijker and Frank [16] using the interacting boson model showed the 0^+ dominance also in sd and sp IBM's and also that random interactions generate vibrational and rotational structures with high probability in sd IBM. These unexpected results gave rise to a new field of research activity with random interactions in nuclei [31, 32]. The question is (as Zelevinsky and Volya [31] state): **do we understand well the physics generated by random interactions under constraints of rotational symmetry and what is the reason for empirical regularities in nuclei? The problem is not limited to nuclear physics. Atomic clusters, particles in traps, quantum dots, disordered systems, such as quantum spin glasses, are just a few examples where the same questions are to be answered.**

In the interacting boson models sp IBM and sd IBM, mean-field methods defined by the coherent states discussed in Section 2 explain in a succinct way the probability with which various angular momentum states appear as ground states with random one plus two-body interactions [16]. In an attempt to gain much deeper understanding into these regularities, very recently [17] considered is the extension of the spin zero ground state dominance to the irreducible representations of group-subgroup chains in the ground states of boson systems interacting by random forces.

With m bosons in \mathcal{N} single particle states, the SGA for a IBM is $U(\mathcal{N})$. Considering random Hamiltonians (maximum two-body) that are G scalars in $U(\mathcal{N}) \supset G \supset \dots \supset O(3)$ with $G \equiv O(\mathcal{N}_1) \oplus O(\mathcal{N}_2)$, $\mathcal{N}_1 + \mathcal{N}_2 = \mathcal{N}$ which appears in all the interacting boson models (IBM's) enumerated in Section 1, addressed is the question of with what probability a given $(\omega_1 \omega_2)$ irreducible representation (irrep) will be the ground state in even-even nuclei; $[\omega_1]$ and $[\omega_2]$ are the symmetric irreps of $O(\mathcal{N}_1)$ and $O(\mathcal{N}_2)$ respectively. There are in general, for $\mathcal{N} > 3$, three situation (ignoring the $\mathcal{N}_1 = \mathcal{N}_2 = 2$ example), : (i) $\mathcal{N}_1 \geq 3$ and $\mathcal{N}_2 = 1$; (ii) $\mathcal{N}_1 \geq 3$ and $\mathcal{N}_2 = 2$; (iii) $\mathcal{N}_1 \geq 3$ and $\mathcal{N}_2 \geq 3$. As all the details are available in [17], we will discuss only (iii). Here the group chains, for symmetric $U(\mathcal{N})$ irreps $\{N\}$ the irrep labels for other group algebras in the chains and their reductions (and also the $O(\mathcal{N}_1) \oplus O(\mathcal{N}_2)$ symmetry preserving H) are,

$$\left| \begin{array}{ccccccc} U(\mathcal{N}) \supset U(\mathcal{N}_1) \oplus U(\mathcal{N}_2) \supset O(\mathcal{N}_1) \oplus O(\mathcal{N}_2) \supset K \\ \{N\} \quad \{n_1\} \quad \{n_2\} \quad [\omega_1] \quad [\omega_2] \quad \alpha \end{array} \right\rangle$$

$$n_1 = 0, 1, 2, \dots, N; \quad n_2 = n - n_1$$

$$\omega_1 = n_1, n_1 - 2, \dots, 0 \text{ or } 1, \quad \omega_2 = n_2, n_2 - 2, \dots, 0 \text{ or } 1$$

Table 2. Group chain, hamiltonian, energy functional and the equilibrium shape parameters, in large N limit, for the $SU(5)$ limit of sdg IBM

$SU_{sdg}(5)$ Limit
$U_{sdg}(15) \supset SU_{sdg}(5) \supset O_{dg}(5) \supset O(3)$
$H_{SU_{sdg}(5)} = -\frac{20a}{3} \left\{ C_2(SU_{sdg}(5)) - \frac{1}{2} C_2(O_{dg}(5)) \right\}$ $+ b C_2(O_{dg}(5)) + c C_2(O(3))$ $= -\frac{80a}{3} \{ G^2 \cdot G^2 + G^4 \cdot G^4 \} + b C_2(O_{dg}(5)) + c C_2(O(3))$
$G_\mu^2 = \sqrt{\frac{1}{5}} \left(s^\dagger \tilde{d} + d^\dagger \tilde{s} \right)_\mu^2 - \frac{3}{14} (d^\dagger \tilde{d})_\mu^2 + \frac{6}{\sqrt{245}} (d^\dagger \tilde{g} + g^\dagger \tilde{d})_\mu^2$ $+ 2 \frac{\sqrt{198}}{14} (g^\dagger \tilde{g})_\mu^2$
$G_\mu^4 = \sqrt{\frac{1}{5}} \left(s^\dagger \tilde{g} + g^\dagger \tilde{s} \right)_\mu^4 + \frac{2}{7} (d^\dagger \tilde{d})_\mu^4 + \sqrt{\frac{55}{98}} (d^\dagger \tilde{g} + g^\dagger \tilde{d})_\mu^4$ $+ \sqrt{\frac{143}{980}} (g^\dagger \tilde{g})_\mu^4$
$E_{SU_{sdg}(5)}(N; \beta_2, \beta_4, \gamma) =$ $\frac{-16a N^2}{3(1 + \beta_2^2 + \beta_4^2)^2} \left[4\beta_2^2 + \frac{72}{7} \sqrt{\frac{2}{7}} \beta_2^2 \beta_4 + \frac{27}{98} \beta_2^4 + \right.$ $\frac{6}{7} \sqrt{\frac{10}{7}} \beta_2^3 \cos 3\gamma - \frac{60}{7} \sqrt{\frac{10}{7}} \beta_2 \beta_4^2 \cos 3\gamma - \frac{24}{49} \sqrt{5} \beta_2^3 \beta_4 \cos 3\gamma$ $\left(\frac{100 \cos^2 3\gamma + 78}{49} \right) \beta_2^2 \beta_4^2 - \frac{60 \sqrt{5}}{49} \beta_2 \beta_4^3 \cos 3\gamma + 4 \beta_4^2 +$ $\left. \left(\frac{-1400 \cos^2 3\gamma + 3641}{2646} \right) \beta_4^4 + \left(\frac{200 \cos^2 3\gamma + 124}{63 \sqrt{14}} \right) \beta_4^3 \right]$ $\beta_2^0 = \sqrt{\frac{10}{7}}, \quad \beta_4^0 = \sqrt{\frac{18}{7}}, \quad \gamma^0 = 60^\circ$ $E_{SU_{sdg}(5)}(N; \beta_2^0, \beta_4^0, \gamma^0) = -\frac{64}{3} a N^2$

Table 3. Group chain, hamiltonian, energy functional and the equilibrium shape parameters, in large N limit, for the $SU(6)$ limit of sdg IBM

$SU_{sdg}(6)$ Limit
$U_{sdg}(15) \supset SU_{sdg}(6) \supset Sp_{dg}(6) \supset O(3)$
$H_{SU_{sdg}(6)} = -16 a \left\{ C_2(SU_{sdg}(6)) - \frac{1}{2} C_2(Sp_{dg}(6)) \right\}$ $+ b C_2(Sp_{dg}(6)) + c C_2(O(3))$ $= -64 a \{h^2 \cdot h^2 + h^4 \cdot h^4\} + b C_2(Sp_{dg}(6)) + c C_2(O(3))$
$h_\mu^2 = -\sqrt{\frac{1}{6}} \left(s^\dagger \tilde{d} + d^\dagger \tilde{s} \right)_\mu^2 + \frac{5}{\sqrt{294}} (d^\dagger \tilde{d})_\mu^2 - \frac{9}{\sqrt{392}} (d^\dagger \tilde{g} + g^\dagger \tilde{d})_\mu^2$ $- \frac{\sqrt{33}}{14} (g^\dagger \tilde{g})_\mu^2$
$h_\mu^4 = -\sqrt{\frac{1}{6}} \left(s^\dagger \tilde{g} + g^\dagger \tilde{s} \right)_\mu^4 - \sqrt{\frac{45}{392}} (d^\dagger \tilde{d})_\mu^4 - \sqrt{\frac{55}{588}} (d^\dagger \tilde{g} + g^\dagger \tilde{d})_\mu^4$ $+ \sqrt{\frac{143}{392}} (g^\dagger \tilde{g})_\mu^4$
$E_{SU_{sdg}(6)}(N; \beta_2, \beta_4, \gamma) =$ $\frac{-64 a N^2}{(1 + \beta_2^2 + \beta_4^2)^2} \left[\frac{2}{3} \beta_2^2 + \frac{10}{21} \sqrt{\frac{2}{7}} \beta_2^3 \cos 3\gamma + \right.$ $\frac{54}{7 \sqrt{42}} \beta_2^2 \beta_4 - \frac{20}{7 \sqrt{14}} \beta_2 \beta_4^2 \cos 3\gamma + \frac{1}{12} \beta_2^4 -$ $\left. \left(\frac{100 \cos^2 3\gamma + 62}{63 \sqrt{42}} \right) \beta_4^3 + \frac{1}{6} \beta_2^2 \beta_4^2 + \frac{1}{12} \beta_4^4 + \frac{2}{3} \beta_4^2 \right]$
$SU(6) \text{ I} : \quad \beta_2^0 = \sqrt{\frac{25}{14}}, \quad \beta_4^0 = \sqrt{\frac{3}{14}}, \quad \gamma^0 = 0^\circ$
$SU(6) \text{ II} : \quad \beta_2^0 = \sqrt{\frac{8}{7}}, \quad \beta_4^0 = \sqrt{\frac{6}{7}}, \quad \gamma^0 = 60^\circ$
$SU(6) \text{ III} : \quad \beta_2^0 = \sqrt{\frac{1}{14}}, \quad \beta_4^0 = -\sqrt{\frac{27}{14}}, \quad \gamma^0 = 60^\circ$
$E_{SU_{sdg}(6)}(N; \beta_2^0, \beta_4^0, \gamma^0) = -\frac{64}{3} a N^2$

$$\begin{aligned}
& \left| \begin{array}{ccccc} U(\mathcal{N}) & \supset & O(\mathcal{N}) & \supset & O(\mathcal{N}_1) \oplus O(\mathcal{N}_2) \supset K \\ \{N\} & & [\omega] & & [\omega_1] & & [\omega_2] & & \alpha \end{array} \right\rangle \\
& \omega = N, N-2, \dots, 0 \text{ or } 1, \quad \omega_1 + \omega_2 = \omega, \omega-2, \dots, 0 \text{ or } 1 \\
H = & \frac{1}{N} [\alpha_1 C_1(U(\mathcal{N}_1)) + \alpha_2 C_1(U(\mathcal{N}_2))] \\
& + \frac{1}{N(N-1)} [\alpha_3 C_2(U(\mathcal{N}_1)) + \alpha_4 C_2(U(\mathcal{N}_2)) + \alpha_5 C_1(U(\mathcal{N}_1)) C_1(U(\mathcal{N}_2)) \\
& + \alpha_6 C_2(O(\mathcal{N})) + \alpha_7 C_2(O(\mathcal{N}_1)) + \alpha_8 C_2(O(\mathcal{N}_2))] \quad (18)
\end{aligned}$$

Generating random H 's by choosing the parameters in (22) to be zero centered independent Gaussian random variables with unit variance, for a 500 member ensemble, by constructing and diagonalizing the H matrix for boson numbers $N = 10 - 25$, it is found that $(\omega_1 \omega_2) = (00)$, $(N0)$ and $(0N)$ irreps to be ground states with $\sim 50\%$, $\sim 25\%$ and $\sim 25\%$ probability for spp' IBM with $(\mathcal{N}_1, \mathcal{N}_2) = (4, 3)$, for spd IBM with $(6, 3)$, sdg IBM with $(10, 5)$ and $(9, 6)$, $spdf$ IBM with $(10, 6)$, $sdgpf$ IBM with $(15, 10)$, sd IBM-3 with $(15, 3)$ and sd IBM-4 with $(3, 3)$, $(30, 6)$, $(18, 18)$ and $(15, 15)$. An extended mean-field theory with intrinsic bosons $y_0^\dagger = \frac{1}{\sqrt{p}} \sum_{i=1}^p b_{\ell_i, 0}^\dagger$, $\sum_{i=1}^p (2\ell_i + 1) = \mathcal{N}_1$ and $z_0^\dagger = \frac{1}{\sqrt{q}} \sum_{j=1}^q b_{\ell'_j, 0}^\dagger$, $\sum_{j=1}^q (2\ell'_j + 1) = \mathcal{N}_2$, explains the numerical results. Here the hamiltonian [with only the α_1 and α_6 terms in Eq. (22)], CS and the energy functional $E(\alpha)$ are,

$$\begin{aligned}
H = & \frac{1}{N} \cos \chi \hat{n}_2 + \frac{1}{N(N-1)} \sin \chi S_+ S_- , \\
S_+ = & S_+(1) - S_+(2) = \sum_{i=1}^p b_{\ell_i}^\dagger \cdot b_{\ell_i}^\dagger - \sum_{j=1}^q b_{\ell'_j}^\dagger \cdot b_{\ell'_j}^\dagger , \quad S_- = (S_+)^\dagger \\
|N \alpha\rangle = & \frac{1}{\sqrt{N!}} \left(\cos \alpha y_0^\dagger + \sin \alpha z_0^\dagger \right)^N |0\rangle \\
E(\alpha) = & \cos \chi \sin^2 \alpha + \frac{1}{4} \sin \chi \cos^2 2\alpha
\end{aligned}$$

The $\alpha = 0$ gives y -boson condensate with energy $E(\alpha = 0) \propto -\sin \chi \omega_1(\omega_1 + \mathcal{N}_1 - 2)$. Then the ground state irreps are $(\omega_1 \omega_2) = (00)$ with 25% and $(\omega_1 \omega_2) = (N0)$ with 12.5% probability. Similarly $\alpha = \pi/2$ gives z -boson condensate with energy $E(\alpha = \pi/2) \propto -\sin \chi \omega_2(\omega_2 + \mathcal{N}_2 - 2)$ and then the ground state irreps are $(\omega_1 \omega_2) = (00)$ with 25% and $(\omega_1 \omega_2) = (0N)$ with 12.5% probability. In the situation $\cos 2\alpha = \cot \chi$, cranking has to be done with respect to both $O(\mathcal{N}_1)$ and $O(\mathcal{N}_2)$. Evaluating moment of inertia, by an extension of the ordinary $O(3)$ cranking, gives $(N0)$ and $(0N)$ irreps will be ground states each with 12.5% probability. Combining all the results give, $(\omega_1 \omega_2) = (00)$, $(N0)$ and $(0N)$ irreps to be ground states with 50%, 25% and 25% probability in complete agreement with numerical findings. At present, regularities in energy centroids defined over irreps of various IBM symmetries are being studied and the first results are available in [33].

E Quantum phase transitions in IBM's

As Iachello and Zamfir state [18]: ‘Quantum phase transitions - that is phase transitions that occur at zero temperature as a function of a coupling constant - have become

very important in connection with condensed matter systems. The phase transition is observed by measuring an order parameter as a function of the control parameter. Quite often the order parameter can not be measured directly, in such a case a function of the order parameter is measured. The concept of quantum phase transitions can be used in mesoscopic systems, that is systems with finite number of particles N , such as nuclei, atomic clusters, molecules, finite polymers etc. The transitions in these systems are between shapes or geometric configurations.”

Starting with the sd IBM intrinsic state given by Eq. (2) and the corresponding energy functional $E^{(\zeta, \chi)}(N, \beta_2, \gamma)/(\epsilon_0 N)$ given by Eq. (6) [hereafter called $V^{(\zeta, \chi)}(N, \beta_2, \gamma)$] for general (1+2)-body H , it is seen that $\gamma_0 = 0^\circ$ for $0 \geq \chi \geq -\sqrt{7}/2$. Similarly $\gamma_0 = 60^\circ$ for $0 \leq \chi \leq \sqrt{7}/2$. Alternatively one can put $\gamma_0 = 0^\circ$ and take $\beta_2 > 0$ (prolate) for χ negative and $\beta_2 < 0$ (oblate) for χ positive. As the potential is either γ independent (for $\chi = 0$) or has a minimum at $\gamma = 0^\circ$, one can put $\gamma = 0^\circ$ and study V as a function of β_2 . Studying $V_{min}^{(\zeta, \chi)}(\beta_2)$ and its first and second derivatives with respect to ζ will give information regarding phase transitions. If the first derivative is discontinuous, we have first order phase transition and the second derivative is discontinuous, then second order phase transition. It is seen that:

(i) $U(5)$ to $SU(3)$ is first order, $U(5)$ to $O(6)$ is second order and for $O(6)$ to $SU(3)$ there is no phase transition [1]. More recent result, due to Jolie et al [19], is that $O(6)$ is not only a dynamical symmetry but also a critical point of prolate-oblate (i.e $SU(3)$ to $\overline{SU(3)}$) first order phase transition.

(ii) With $\gamma = 0^\circ$, the potential V is exactly [except for the $(1 + \beta_2^2)$ terms in the denominator - they are due to finite N] of the form considered by Landau, i.e. $V^{\zeta, \eta}(\beta_2) = \beta_2^2 + \zeta [(2 - \beta_2)^2 - \eta \beta_2^3]$, $\beta_2 \geq 0$. For $\eta = 0$, $V^\zeta(\beta_2^0) = 4\zeta$ for $\zeta \geq \frac{1}{4}$ and $(8\zeta - 1)/(4\zeta)$ for $\zeta \leq \frac{1}{4}$; note that $\beta_2^0 = 0$ or $\sqrt{(4\zeta - 1)/2\zeta}$. Clearly this system exhibits second order phase transition. Thus $\zeta^c = 1/4$ is the critical point (here the two minima are equivalent). For $\eta \neq 0$, there is first order transition and $\zeta^c \sim 32/(128 + 8\eta^2)$. The minimum in V appears for $\beta_2^0 = 0$ or for $\beta_2^0 = (3\eta/8) \pm (1/2)\sqrt{(9\eta^2/16) + 8(1 - 1/4\zeta)}$.

(iii) Landau theory is for $V \rightarrow \infty$ for $\beta_2 \rightarrow \infty$ but for IBM-1, $V(\beta_2)$ is finite for $\beta_2 \rightarrow \infty$. Therefore the phase transition will be smooth for finite N but the signatures remain. This is demonstrated [18] using the order parameters $\nu_1 = \langle 0_1 | n_d | 0_1 \rangle / N$ and $\nu_2 = \{\langle 0_2 | n_d | 0_2 \rangle - \langle 0_1 | n_d | 0_1 \rangle\} / N$ which are measurable. **Landau's theory of continuous phase transitions applies to IBM's and the phase diagram for sd IBM is now completely determined** [18, 19, 34].

(iv) Another important development, in this subject, is the introduction, by Iachello [35], of the so-called $E(5)$, $X(5)$ and $Y(5)$ symmetries at the critical points of phase transitions in sd IBM [$Z(5)$ is added to this list by Bonatsos et al]. They are in fact the solutions of the Bohr hamiltonian with $V(\beta_2, \gamma)$ appropriate for the phase transition points. It is also found that there are many other situations where the Bohr hamiltonian is solvable either completely or at least for the low-lying states [36].

Significantly, exploring the relationship between level crossings and quantum phase transitions, it is seen that sdg IBM symmetries with $O(14)$ give new features that are absent in sd IBM symmetries with $O(5)$ [34]. Thus, detailed studies of phase transitions in

*sdg*IBM are expected to give new insights into quantum phase transitions in mesoscopic systems and this is for future.

F Conclusions

Mean-field approach for the algebraic interacting boson models is briefly reviewed in this paper. Renewed interest in the mean-field methods is due to their usefulness in the study of two current problems of interest in nuclear structure: (i) regular structures generated by random interactions; (ii) quantum phase transitions exhibited by nuclei. Also emphasized throughout this paper is the role of *sdg*IBM developed in [4,5,12,26]: (i) *sdg*IBM gives rich variety of ground state shapes; (ii) its applications to nuclei with large boson numbers led to the development of the $1/N$ mean-field method; (iii) it is proved to be useful in the study of regular structures with random interactions; (iv) it is already demonstrated that this model gives new results for quantum phase transitions.

R

References

1. A. Arima and F. Iachello, Phys. Rev. Lett. **35**, 1069 (1975); F. Iachello and A. Arima, The Interacting Boson Model (Cambridge University Press, Cambridge, 1987).
2. F. Iachello, Phys. Rev. C **23**, 2778 (1981); H.J. Daley and F. Iachello, Ann. Phys. (N.Y.) **167**, 73 (1986).
3. D.J. Rowe and F. Iachello, Phys. Lett. **B130**, 231 (1983).
4. V.K.B. Kota, H. DeMeyer, J. Vander Jeugt, and G. Vanden Berghe, J. Math. Phys. **28**, 1644 (1987); Y.D. Devi and V.K.B. Kota, Pramana - J. Phys. **39**, 413 (1992).
5. V.K.B. Kota, Phys. Rev. C **53**, 2550 (1996); Y.D. Devi and V.K.B. Kota, Nucl. Phys. **A600**, 20 (1996); L. Wu and H. Toki, Phys. Rev. C **56**, 1821 (1997); B.L. Wang, Comm. Theo. Phys. **30**, 445 (1998); Y. Liu, D. Sun, and E.G. Zhao, Phys. Rev. C **59**, 2511 (1999); E.D. Davis, B.R. Barrett, and A.F. Diallo, Phys. Rev. C **59**, 200 (1999); S. Kuyucak and M. Sugita, Phys. Rev. C **59**, 3146 (1999).
6. J. Engel and F. Iachello, Phys. Rev. Lett. **54**, 1126 (1985); D. Kusnezov, J. Phys. A **23**, 5673 (1990); G.L. Long, T.Y. Shen, H.Y. Ji, and E.G. Zhao, Phys. Rev. C **57**, 2301 (1998); H.Y. Ji, G.L. Long, E.G. Zhao, and S.W. Xu, Nucl. Phys. **A658**, 197 (1999).
7. G.L. Long, W.L. Zhang, H.Y. Ji, and S.J. Zhu, Science in China A **41**, 1296 (1998).
8. R. Bijker and F. Iachello, Ann. Phys. (N.Y.) **298**, 334 (2002).
9. F. Iachello, Phys. Rev. Lett. **53**, 1427 (1984); P. Van Isacker, K. Heyde, J. Jolie, and A. Servin, Ann. Phys. (N.Y.) **171**, 253 (1986); V.K.B. Kota, Pramana-J. Phys. **60**, 59 (2003).
10. J.P. Elliott and A.P. White, Phys. Lett. **B97**, 169 (1980); V.K.B. Kota, Ann. Phys. (N.Y.) **265**, 101 (1998); J.E. García-Ramos and P. Van Isacker, Ann. Phys. (N.Y.) **274**, 45 (1999).
11. J.P. Elliott and J.A. Evans, Phys. Lett. **B101**, 216 (1981); V.K.B. Kota, Ann. Phys. (N.Y.) **280**, 1 (2000); P. Van Isacker and D.D. Warner, Phys. Rev. Lett. **78**, 3266 (1997).
12. Y.D. Devi and V.K.B. Kota, Z. Phys. **A337**, 15 (1990); Y.D. Devi, Ph. D. Thesis (Gujarat University, India, 1992).
13. J.E. García Ramos, J.M. Arias, J. Dukelsky, and P. Van Isacker, Phys. Rev. C **61**, 034305 (2000).
14. S. Kuyucak and I. Morrison, Phys. Rev. Lett. **58**, 315 (1987); Ann. Phys. (N.Y.) **181**, 79 (1988), **195**, 126 (1989); A.F. Diallo, E.D. Davis, and B.R. Barrett, Ann. Phys. (N.Y.) **222**, 159 (1993); Phys. Rev. C **59**, 3146 (1999).

15. J. Dukelsky, G.G. Dussel, R.P.J. Perrazo, S.L. Reich, and H.M. Sofia, Nucl. Phys. **A425**, 93 (1984); S. Pittel, J. Dukelsky, R.P.J. Perrazo, and H.M. Sofia, Phys. Lett. **B144**, 145 (1984).
16. R. Bijker and A. Frank, Phys. Rev. Lett. **84**, 420 (2000); Phys. Rev. C **64**, 061303 (2001), **65**, 044316 (2002).
17. V.K.B. Kota, High Energy Phys. & Nucl. Phys. (China), in press; nucl-th/0401038 (2004).
18. F. Iachello and N.V. Zamfir, Phys. Rev. Lett. **92**, 212501 (2004).
19. J. Jolie, P. Cejnar, R.F. Casten, S. Heinze, A. Linnemann, and V. Werner, Phys. Rev. Lett. **89**, 182502 (2002).
20. A.E.L. Dieperink, O. Scholten, and F. Iachello, Phys. Rev. Lett. **44**, 1747 (1980); J.N. Ginocchio and M. Kirson, Phys. Rev. Lett. **44**, 1744 (1980).
21. O.S. van Roosmalen and A.E.L. Dieperink, Ann. Phys. (N.Y.) **139**, 198 (1982); S. Levit and U. Smilansky, Nucl. Phys. **A389**, 56 (1982).
22. A.B. Balantekin and B.R. Barrett, Phys. Rev. C **32**, 288 (1985); R. Bijker, Phys. Rev. C **32**, 1442 (1985); A. Leviatan and M.W. Kirson, Ann. Phys. (N.Y.) **201**, 13 (1990); J.N. Ginocchio and A. Leviatan, Ann. Phys. (N.Y.) **216**, 152 (1992).
23. S. Kuyucak and M. Honma, Phys. Rev. C **65**, 064323 (2002); A.F. Diallo, B.R. Barrett, P. Navrátil, and C. Gorrichategui, Ann. Phys. (N.Y.) **279**, 81 (2000).
24. J.N. Ginocchio, Phys. Rev. Lett. **73**, 1903 (1994); J.E. García Ramos, J.M. Arias, J. Dukelsky, E. Moya de Guerra, and P. Van Isacker, Phys. Rev. C **57**, R479 (1998).
25. S.G. Rohozinski, Phys. Rev. C **56**, 165 (1997).
26. V.K.B. Kota and Y.D. Devi, in Symmetries in Science VII, edited by B. Gruber and T. Otsuka (Plenum, New York, 1994), p.307; in Perspectives for the interacting boson model, edited by R.F. Casten et al (World Scientific, Singapore, 1994), p. 335.
27. S. Kuyucak and I. Morrison, Phys. Lett. **B255**, 305 (1991).
28. S. Kuyucak and I. Morrison, Phys. Rev. C **38**, 2482 (1988); Prog. Part. Nucl. Phys. **28**, 391 (1992); S. Kuyucak, in Perspectives for the interacting boson model, edited by R.F. Casten et al (World Scientific, Singapore, 1994), p.143.
29. V.K.B. Kota, Phys. Rep. **347**, 223 (2001).
30. C.W. Johnson, G.F. Bertsch, and D.J. Dean, Phys. Rev. Lett. **80**, 2749 (1998).
31. V. Zelevinsky and A. Volya, Phys. Rep. **391**, 311 (2004).
32. Y.M. Zhao, A. Arima, and N. Yoshinaga, Phys. Rep. **400**, 1 (2004).
33. V.K.B. Kota, in Progress in Boson Research (Nova Science publishers, New York), in press.
34. J.M. Arias, J. Dukelsky, and J.E. García-Ramos, Phys. Rev. Lett. **91**, 162502 (2003); S. J. Dukelsky, J.M. Arias, J.E. García-Ramos, and S. Pittel, nucl-th/0310031 (2003).
35. F. Iachello, Phys. Rev. Lett. **85**, 3580 (2000), **87**, 052502 (2001), **91**, 132502 (2003); R.F. Casten and N. V. Zamfir, Phys. Rev. Lett. **85**, 3584 (2000), **87**, 052503 (2001); R. Krücken et al, Phys. Rev. Lett. **88**, 232501 (2002); C. Hutter et al, Phys. Rev. C **67**, 054315 (2003); D. Tonev et al, Phys. Rev. C **69**, 034334 (2004); E.A. McCutchan et al, Phys. Rev. C **69**, 024308 (2004); D. Bonatsos, D. Lenis, D. Petrellis, and P.A. Terziev, Phys. Lett. **B588**, 172 (2004).
36. L. Fortunato and A. Vitturi, J. Phys. **G29**, 1341 (2003); D. Bonatsos, D. Lenis, N. Minkov, P.P. Raychev, and P.A. Terziev, Phys. Rev. C **69**, 014302 (2004); G. Lévai and J.M. Arias, Phys. Rev. C **69**, 014304 (2004).

Recent Applications of Deformed Shell Model

R. Sahu

Physics Department, Berhampur University, Berhampur 760 007, India

A Introduction

Over the last several years, the deformed shell model (DSM) has been successfully applied to study the spectroscopy of nuclei in the d-s shell, lower pf shell, upper pf shell and in the rare-earth region. The deformed shell model calculations in a limited configuration space are essentially to approximate a full shell model calculation [1]. The HF approach in a limited configuration space is used to generate a deformed shell model basis, where a few low-lying configurations are then sufficient to give most of the important features and systematics of spectroscopic properties.

The details of the model are discussed in chapter II. The isospin projection (which is of interest due to the recent experimental study of $N=Z$ odd-odd nuclei where both isoscalar and isovector pairing becomes important) in DSM and its application to some of the $N=Z$ odd-odd and even-even nuclei are discussed in chapter III. The DSM model was also applied to study electro-weak processes like 2ν double beta decay, muon-electron conversion in the field of the nucleus and cold dark matter. These are discussed in chapters IV-VI. A brief conclusion is given in chapter VII.

B Deformed Shell Model

The details of the model have been described in many of our previous publications (see for example ref. [2]). In the Deformed Shell Model (DSM) (see [2]), for a given nucleus, starting with a model space consisting of a given set of single particle orbitals and effective two-body Hamiltonian, the lowest energy (axially symmetric) prolate and oblate intrinsic states are obtained by solving the HF single particle equation self-consistently. Then various excited intrinsic states are obtained by making particle-hole excitations over the lowest intrinsic state. A constrained HF calculation (tagged HF) is performed in each case. These intrinsic states do not have good angular momentum. Hence good angular momentum states are projected from each of these intrinsic states. For completeness, we give a few important steps. First the lowest energy prolate and oblate intrinsic states are obtained by solving the HF single particle equation self-consistently. Then various excited intrinsic states are obtained by making particle-hole excitations over the lowest intrinsic state. A constrained HF calculation (tagged HF) is performed in each case. These intrinsic states do not have good angular momentum. Hence good angular momentum states are projected from each of these intrinsic states. In general the good angular momentum states coming from different intrinsic states are not orthogonal to each other. Hence they are orthonormalized by performing a band mixing calculation.

Let the various intrinsic states obtained by solving the axially symmetric HF equation selfconsistently be denoted by $\chi_K(\mu)$ with μ distinguishing different intrinsic states with same K . Good angular momentum states are projected from each of these intrinsic states using the projection operator

$$P_{MK}^J = \frac{2J+1}{8\pi^2} \int D_{MK}^{J*}(\Omega) R(\Omega) d\Omega \quad (1)$$

The angular momentum projected states ϕ_{MK}^J obtained from different intrinsic states have to be orthogonalized since they may not be orthogonal to each other. For this purpose, we consider the overlap matrix

$$N_{K'\mu', K\mu}^J = \langle \phi_{MK'}^J(\mu') | \phi_{MK}^J(\mu) \rangle \quad (2)$$

For an orthonormal set of vectors, this matrix would be a unit matrix, whereas in the case of the non-orthogonal basis, it is not diagonal. Hence the matrix $N_{K'\mu', K\mu}^J$ is diagonalized and the resulting vectors can be written as

$$\Phi_M^J(\alpha) = \sum_{K\mu} S_{K\alpha}^J(\mu) \phi_{MK}^J(\mu) \quad (3)$$

where

$$S_{K\alpha}^J(\mu) = [n_M^J(\alpha)]^{-1/2} X_{K\alpha}^J(\mu) \quad (4)$$

with $X_{K\alpha}^J$ corresponding to the element of the unitary transformation matrix that diagonalizes the overlap matrix N^J and n_M^J denotes the eigenvalues of N^J . The functions $\Phi_M^J(\alpha)$ constitute an orthonormal set of vectors.

$$\langle \Phi_M^J(\nu) | H | \Phi_M^J(\nu') \rangle = \sum_{K\eta} \sum_{K'\eta'} S_{K\eta}^{J*}(\nu) S_{K'\eta'}^J(\nu') \langle \phi_{MK}^J(\eta) | H | \phi_{MK'}^J(\nu') \rangle \quad (5)$$

The composite spectrum of a nucleus is obtained by diagonalizing the Hamiltonian matrix in the basis of the these orthonormalized projected states. The overlap

$$B_K^J(\eta, \alpha) = \langle \phi_{MK}^J(\eta) | \Phi_M^J(\alpha) \rangle = \sum_{K_1\eta_1} S_{K_1\eta_1}^J(\alpha) N_{K\eta, K_1\eta_1}^J \quad (6)$$

gives the measure of the state $\phi_{MK}^J(\eta)$ projected from a given intrinsic state $\chi_K(\eta)$ that the eigenstate $\Phi_M^J(\alpha)$ contains. The larger the amplitude $|B_K^J(\eta, \alpha)|^2$, the more pronounced will be the characteristic of that parent intrinsic state in the state $\Phi_M^J(\alpha)$.

C Spectroscopy

In the last several years, the deformed shell model has been successfully used to study the spectroscopic properties of nuclei through out the periodic table. I will discuss the application of this model to $N = Z$ nuclei in the medium heavy region which are of present interest. With the development of radioactive ion beam facilities and large detector arrays, study of the the structure of heavy ($A \geq 44$) odd-odd $N=Z$ nuclei (also

N=Z even-even nuclei) near the proton drip line (even-though they have very short half lives) has become an area of intense research as these nuclei are expected to give new insights into neutron-proton (np) correlations that are hitherto unknown and as they are important for rp-process nucleosynthesis. With N=Z, unlike the case with identical particle pairing, there will be both isoscalar ($T = 0$) and isovector ($T = 1$) pairing and their competition is expected to give new physics. Already it is established by experiments that in odd-odd nuclei with $A \geq 42$ up to ^{86}Tc (except for ^{58}Cu) the ground states are $T = 1$ and there are indications that there will be delay in angular momentum alignments at high spins in the even-even nuclei in this region [3]. With rich 'new' structures expected, experiments are initiated for spectroscopy of these nuclei and for ^{62}Ga [4], ^{66}As [5], ^{70}Br [6] and ^{74}Rb [7] many $T = 0$ and $T = 1$ levels, which can be grouped into bands, are identified recently. On the other hand, inspired by large scale shell model, there are experiments with new data for $T = 0$ and $T = 1$ bands for lower pf -shell nuclei ^{46}V [8–10], ^{50}Mn [11–13] and ^{54}Co [14]. Going beyond N=Z odd-odd nuclei, there are attempts to identify band structures in even-even N=Z nuclei with $A > 64$ with emphasis on identifying new alignment properties at high-spins. There is now new data for ^{68}Se [15], ^{72}Kr , ^{76}Sr and ^{80}Zr [3, 16], ^{84}Mo and ^{88}Ru [17]. Although isospin assignment of the bands/levels in these nuclei is not available (except for the trivial situations, for example the low-lying members of the ground band will have $T = 0$), the excited $T = 1$ and $T = 2$ levels are known for $A=44\text{--}60$ N=Z even-even nuclei; see [18].

Recently DSM is extended to include isospin projection so that the band structures in N=Z odd-odd nuclei can be analyzed. This extended model is called DSM-T with T denoting isospin projection [19]. In its elementary version DSM-T is developed for T projection from quasi-deuteron configurations. Now we will discuss this briefly. For N=Z odd-odd nuclei, the lowest prolate and oblate HF intrinsic states the unpaired proton and neutron occupy the same HF single particle orbits and hence these are symmetric in space co-ordinates. Therefore these intrinsic states will have $T = 0$ (protons and neutrons in the other occupied orbits will have α -particle like structure with $T = 0$). If in an intrinsic state (say $\phi_{k_1}^p \phi_{k_2}^n$), the unpaired proton occupies the single particle orbit specified by the azimuthal quantum number k_1 and the unpaired neutron occupies the state k_2 , then one can also consider an intrinsic state where the occupancies of the unpaired nucleons are reversed. By taking a linear combination of these intrinsic states, one can construct intrinsic states which are symmetric (or antisymmetric) in space co-ordinates. Symmetric combination will have isospin $T = 0$ and the antisymmetric combination gives $T = 1$. Thus,

$$\begin{aligned} \frac{1}{\sqrt{2}} [\phi_{k_1}^p \phi_{k_2}^n + \phi_{k_2}^p \phi_{k_1}^n] &\Leftrightarrow T = 0 \\ \frac{1}{\sqrt{2}} [\phi_{k_1}^p \phi_{k_2}^n - \phi_{k_2}^p \phi_{k_1}^n] &\Leftrightarrow T = 1 \end{aligned} \quad (7)$$

Then good angular momentum states are projected from all the $T = 0$ intrinsic states and a band mixing calculation is performed as described above. Similar procedure is applied for the $T = 1$ intrinsic states. With this we get bands/levels with good $T = 0$ and thus DSM-T allows one to study $T = 0$ and $T = 1$ levels/bands in N=Z odd-odd nuclei.

DSM-T model with isospin projection for quasi-deuteron configurations is applied for the first time to the $A > 60$ nuclei ^{62}Ga and ^{66}As [19]. Later this model is also applied to ^{70}Br [20]. The experimentally observed low-lying $T = 0$ and $T = 1$ bands in the three nuclei are well described by the model. Moreover the results for ^{62}Ga are close to shell model results and those of ^{66}As to IBM-4 (for this nucleus shell model results are not available). In the calculations ^{56}Ni is taken as the inert core with the spherical orbits $2p_{3/2}$, $1f_{5/2}$, $2p_{1/2}$ and $1g_{9/2}$ as active orbits with energies 0.0, 0.77, 1.113 and 3 MeV respectively. The two body interaction matrix elements in this space are defined by a realistic G-matrix interaction with a phenomenologically adjusted monopole part as given by the Madrid-Strasbourg group (this is the MS interaction mentioned in the introduction). Similarly, in the lower pf shell, the DSM-T is applied to the nuclei ^{46}V and ^{50}Mn [21]. Here also, with good success the model is able to describe not only the low-lying $T = 0$ and $T = 1$ bands but also several higher lying levels/bands. For these nuclei, ^{40}Ca is taken as the inert core with the pf -shell orbitals $1f_{7/2}$, $2p_{3/2}$, $2p_{1/2}$ and $1f_{5/2}$ as active orbits. The well known KB3 interaction with single particle energies 0.0, 2.0, 4.0 and 6.5 MeV respectively [22, 23] is employed in the calculations. For illustration, here we will discuss briefly the results for ^{62}Ga only.

For ^{62}Ga nucleus, with ^{56}Ni core, there are six valence nucleons and the lowest HF intrinsic state consists of two protons and two neutrons occupying the lowest $k = 1/2^-$ state and the last unpaired odd proton and neutron occupying the next $k = 1/2^-$ state. The total isospin for this configuration is $T = 0$ as the odd proton and odd neutron, for $K = 1^+$, form a symmetric pair in the k -space (here and elsewhere in this paper symmetry in k -space means symmetry in space-spin co-ordinates as k contains both space (orbital) and spin co-ordinates). Particle-hole excitations over the lowest HF intrinsic state generate excited HF intrinsic states (both prolate and oblate states are considered in the calculations). There are nine low-lying 1p-1h and 2p-2h excited intrinsic states for ^{62}Ga and they are:

$$\begin{array}{lll}
 (i) & (1/2_1)^{2p,2n}(1/2_2)^{p\uparrow,n\downarrow} & K = 0, T = 0, 1 \\
 (ii) & (1/2_1)^{2p,2n}(1/2_2)^{p\downarrow,n\uparrow} & K = 0, T = 0, 1 \\
 (iii) & (1/2_1)^{2p,2n}(3/2_1)^{p\uparrow,n\uparrow} & K = 3, T = 0 \\
 (iv) & (1/2_1)^{2p,2n}(3/2_1)^{p\uparrow,n\downarrow} & K = 0, T = 0, 1 \\
 (v) & (1/2_1)^{2p,2n}(3/2_1)^{p\downarrow,n\uparrow} & K = 0, T = 0, 1 \\
 (vi) & (1/2_1)^{2p,2n}(1/2_2)^{p\downarrow}(3/2_1)^{n\uparrow} & K = 1, T = 0, 1 \\
 (vii) & (1/2_1)^{2p,2n}(1/2_2)^{n\downarrow}(3/2_1)^{p\uparrow} & K = 1, T = 0, 1 \\
 (viii) & (1/2_1)^{2p,2n}(1/2_2)^{p\uparrow}(3/2_1)^{n\uparrow} & K = 2, T = 0, 1 \\
 (ix) & (1/2_1)^{2p,2n}(1/2_2)^{p\uparrow}(3/2_1)^{n\downarrow} & K = 2, T = 0, 1
 \end{array}$$

Projecting isospin and carrying-out band mixing calculations, $T = 0$ and $T = 1$ bands are constructed and compared with data; see Fig. 1.

Finally, it should be mentioned that more detailed discussion of the comparison of $T = 0$ and $T = 1$ bands/levels and also the inter and intra band $B(E2)$'s and $B(M1)$'s in ^{62}Ga and ^{50}Mn are given in [19, 21].

In order to go beyond the simple T projection for quasi-deuteron configurations, one should consider T Projection for $(2p, 2n)$ System in four k orbits. Towards this end, let us consider four distinct orbits A , B , C and D in which two protons and two

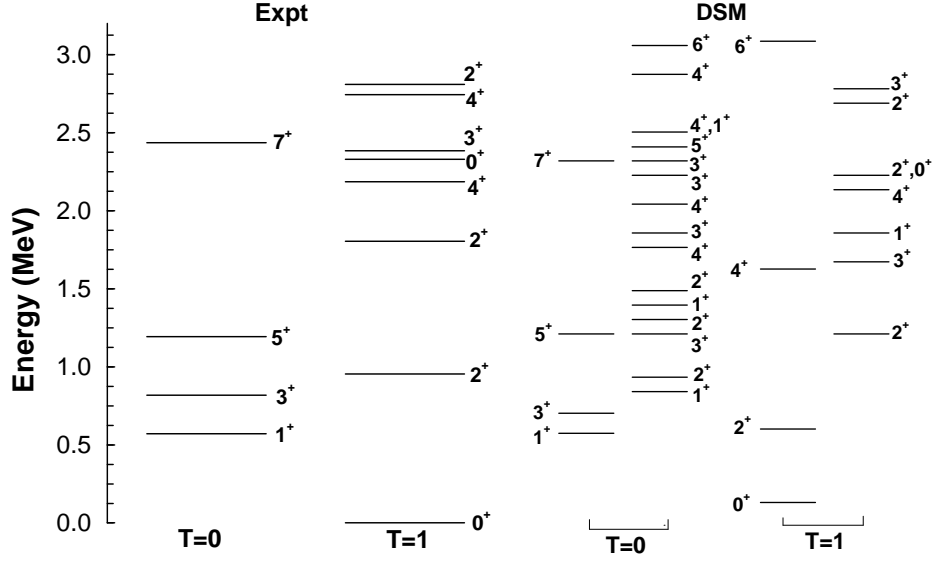


Fig. 1. $T = 0$ and $T = 1$ levels in ^{62}Ga obtained from DSM-T are compared with experimental data.

neutrons are distributed. Then there are six $(2p, 2n)$ states and they can be written as,

$$\begin{aligned}\Phi_1 &= \phi_A^p \phi_B^p \phi_C^n \phi_D^n & \Phi_2 &= \phi_A^p \phi_C^p \phi_B^n \phi_D^n \\ \Phi_3 &= \phi_A^p \phi_D^p \phi_B^n \phi_C^n & \Phi_4 &= \phi_B^p \phi_C^p \phi_A^n \phi_D^n \\ \Phi_5 &= \phi_B^p \phi_D^p \phi_A^n \phi_C^n & \Phi_6 &= \phi_C^p \phi_D^p \phi_A^n \phi_B^n\end{aligned}$$

In order to construct $(2p, 2n)$ states with good isospin, the T^2 matrix in the basis defined by the six states in (8) is constructed and diagonalized. For four particles the allowed isospin values are $(2, 1, 0)$ with T^2 eigenvalues 6, 2 and 0. As the Young tableaux corresponding to $T = 2, 1$ and 0 are $\{4\}$, $\{3, 1\}$ and $\{22\}$, from the symmetry group S_4 properties, it is easily seen that there must be one $T = 2$, three $T = 1$ and two $T = 0$ states. The T^2 matrix is constructed using,

$$\begin{aligned}T^2 &= \left(\sum_i t_i \right) \cdot \left(\sum_i t_i \right) \\ &= \sum_i t_i^2 + \sum_{i \neq j} t_i \cdot t_j \\ &= \sum_i (3/4) + 2 \sum_{i < j} t_i \cdot t_j \\ &= \sum_i (3/4) + 2 \sum_{i < j} \left\{ t_0^{i:1} t_0^{j:1} - t_1^{i:1} t_{-1}^{j:1} - t_{-1}^{i:1} t_1^{j:1} \right\}\end{aligned}\tag{8}$$

In (8) i is the particle index and t is the single particle isospin operator. In the last term in (8) the isospin operator is written in tensorial form. It should be noted that $t_1^1 = -\frac{1}{\sqrt{2}}t_+$ and $t_{-1}^1 = \frac{1}{\sqrt{2}}t_-$. With $|p\rangle = |\frac{1}{2}\frac{1}{2}\rangle$ and $|n\rangle = |\frac{1}{2}-\frac{1}{2}\rangle$, t_+ will change $n \rightarrow p$ and similarly t_- will change $p \rightarrow n$. Using this property and (8) the matrix for T^2 operator in the basis defined by (8) is,

$$T^2 = \begin{pmatrix} 2 & -1 & 1 & 1 & -1 & 0 \\ -1 & 2 & -1 & -1 & 0 & -1 \\ 1 & -1 & 2 & 0 & -1 & 1 \\ 1 & -1 & 0 & 2 & -1 & 1 \\ -1 & 0 & -1 & -1 & 2 & -1 \\ 0 & -1 & 1 & 1 & -1 & 2 \end{pmatrix} \quad (9)$$

Diagonalizing the matrix (9) gives the following six orthonormalized states with good isospin,

$$\begin{aligned} \Psi_1(T=0) &= \frac{1}{2} [\Phi_1 - \Phi_3 - \Phi_4 + \Phi_6] \\ \Psi_2(T=0) &= \frac{1}{2\sqrt{3}} [\Phi_1 + 2\Phi_2 + \Phi_3 + \Phi_4 + 2\Phi_5 + \Phi_6] \\ \Psi_1(T=1) &= \frac{1}{\sqrt{2}} [-\Phi_1 + \Phi_6] \\ \Psi_2(T=1) &= \frac{1}{\sqrt{2}} [-\Phi_2 + \Phi_5] \\ \Psi_3(T=1) &= \frac{1}{\sqrt{2}} [-\Phi_3 + \Phi_4] \\ \Psi(T=2) &= \frac{1}{\sqrt{6}} [\Phi_1 - \Phi_2 + \Phi_3 + \Phi_4 - \Phi_5 + \Phi_6] \end{aligned} \quad (10)$$

The good T states construction given by (10) can be used in the study of even-even $N=Z$ nuclei such as Ge(64), Se(68), Kr(72) and Sr(76). They can be used also for the lower pf-shell nuclei Ti(44), Cr(48) and Fe(52). For completeness let us add that the construction of good T states for $(2p, 2n)$ system becomes simple when there are only two or three orbits. As we can put only one proton or one neutron in a given orbit, for $(2p, 2n)$ system we need minimum of two orbits (in this discussion, orbits with k and $-k$ are treated as different orbits). With only two orbits (say A and B), only a $T=0$ state is possible and it is $[\phi_A^p \phi_A^n \phi_B^p \phi_B^n]^{T=0}$. With three orbits (say A , B and C) two states are possible and they are $\phi_A^p \phi_A^n \phi_B^p \phi_C^n$ and $\phi_A^p \phi_A^n \phi_C^p \phi_B^n$. Using them we can construct one $T=0$ and one $T=1$ states. Now we will apply Eq. (10).

Fischer et al [16], using Gammasphere, recently generated data for the yrast and near yrast bands (for spins up to 26^+) in ^{72}Kr . Besides the ground $K=0^+$ band, there is a side band starting from 3799 keV but the spins of this band are not established. However the 3799 keV level is found to decay to the yrast 6^+ level and the next 4758 keV level to the yrast 8^+ level. Similarly there is a band starting from 8747 keV with 16^+ decaying to yrast 14^+ level. There is also another 16^+ level in the same place. Unfortunately no $T=1$ or $T=2$ levels are identified by the experiments. We will see ahead that the band starting from 3799 keV could be a $T=1$ band. In order to first test DSM-T with four particle isospin projection (Eq. (10)), we present the results for ^{72}Kr .

For ^{72}Kr the interaction used is KBM as in [2]. The HF single particle spectrum for the lowest prolate configuration is $1/2_1^-$ (-9.44 MeV), $1/2_2^-$ (-5.53 MeV), $3/2_1^-$ (-5.53 MeV), $1/2^+$ (-3.43 MeV), $3/2^+$ (-1.58 MeV), $3/2_2^-$ (-1.23 MeV) etc. The oblate configurations which lie very low in energy (compared to prolate states) are neglected just as in the earlier studies of mass 80 nuclei [2]. Besides the lowest prolate configuration we have considered 20 excited prolate configurations and they are: (i) $(1/2_1^-)^{2p2n}(1/2_2^-)^{2p2n}(3/2^-)^{2p2n}(1/2^+)^{-\nu}(3/2^+)^{\nu}$ configurations giving $K = 1, 2$ with $\nu = p$ or n and they decompose into $T = 0, 1$; (ii) 2 protons and 2 neutrons in $1/2^+$ and $3/2^+$ orbits giving six $K = 0$, two $K = 1$, one $K = 2$, two $K = 3$ and one $K = 4$ configurations; (iii) 2 protons and 2 neutrons in $1/2^+$ and $3/2_2^-$ orbits giving six $K = 0$, two $K = 1$, one $K = 2$, two $K = 3$ and one $K = 4$ configurations. The $K = 2, 4$ states are pure $T = 0$ and the $K = 1, 3$ states can be decomposed into $T = 0, 1$ states. Similarly the six $K = 0$ states decompose into $T = 0, 1, 2$ states as given by Eq. (9). DSM-T calculations are performed using these 28 configurations and the results are compared with data in Fig. 2. Except for the position of the 2^+ level the ground $K = 0^+, T = 0$ band is well described upto 12^+ . All the levels of this band come mainly from the lowest prolate intrinsic state. However the mixing with other configurations increases with spin. The DSM-T gives a quasi- γ $K = 2^+, T = 0$ band starting from 2.075 MeV and it is not shown in the figure. Experimentally there is a band of states starting from 3.799 MeV and the decay of its lowest member to the yrast 6^+ indicates that it could be a 6^+ or 8^+ (assuming $E2$ decay). This is consistent with the observation that the next member of the band is found to decay to the yrast 8^+ level. DSM-T gives a band like structure with $6^+, 8^+, 10^+, 12^+$ etc. with $T = 1$ starting from 4.672 (the 6^+ and 8^+ are very close) and below this band there is no $T = 0$ band starting with 6^+ or 8^+ . Thus, comparing with the data it is plausible that the observed side band is the DSM-T predicted $T = 1$ band. Finally the model gives a $0^+, T = 2$ band starting from 6.374 MeV. So far no $T = 2$ levels are identified in ^{72}Kr and a search for them is clearly called for.

D 2ν Double Beta Decay

In recent years, there has been considerable interest in the study of nuclear double decay, both theoretically and experimentally. The recent review articles [24–26] give a detailed developments in the field in recent times. The double beta decay is a rare process in which the charge number of a nucleus changes by two units. Of particular interest is the neutrinoless double beta decay ($0\nu\beta\beta$ -decay) which involves the emission of two electrons and no neutrinos, and the two-neutrino double beta decay ($2\nu\beta\beta$ -decay) in which two electrons and two antineutrinos are emitted. The $0\nu\beta\beta$ -decay, which has not yet been observed, violates the lepton number conservation and has been predicted in some theories beyond the standard model [24–26]. In order to deduce the lepton number violating parameters of interest from the experimental lower limits on the half-life of $0\nu\beta\beta$ -decay, the corresponding nuclear transition should be calculated correctly. Hence one should first test the goodness of the nuclear model by calculating the $2\nu\beta\beta$ -decay (predicted by the Standard model), which is already well established experimentally for

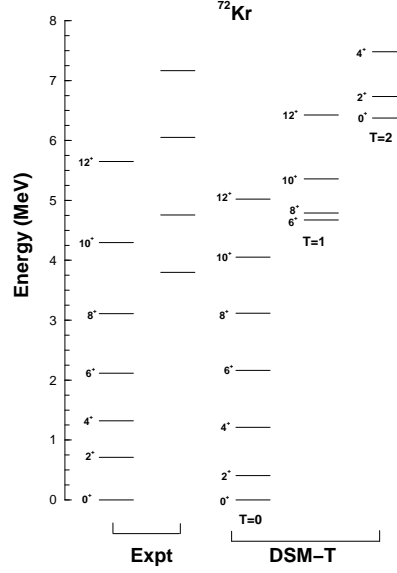


Fig. 2. $T = 0$ and $T = 1$ levels in ^{72}Kr obtained from DSM-T are compared with experimental data.

a couple of isotopes. Thus two neutrino double beta decay provides a testing ground for different nuclear models.

In view of the successes of the DSM in predicting many spectroscopic properties of nuclei, it would be quite interesting to study the $^{76}\text{Ge} \rightarrow ^{76}\text{Se}$ double beta decay within this model.

The Gamow-Teller matrix element $M_{GT}^{2\nu}$ for the $2\nu\beta\beta$ -decay is given by

$$M_{GT}^{2\nu} = \sum_m \frac{\langle 0_f^+ | \sigma\tau^+ | 1_m^+ \rangle \langle 1_m^+ | \sigma\tau^+ | 0_i^+ \rangle}{E_m - (E_i + E_f)/2} \quad (11)$$

where 0_i^+ and 0_f^+ are respectively the ground states 0^+ of initial and final nuclei with corresponding ground state energies E_i and E_f . 1_m^+ are the 1^+ states of the intermediate odd-odd nucleus and E_m are the energies of these 1^+ states. Since we restrict here only to the $2\nu\beta\beta$ -decay of ^{76}Ge , 0_i^+ corresponds to the lowest 0^+ state of ^{76}Ge , 0_f^+ the lowest 0^+ state of ^{76}Se and 1_m^+ corresponds to 1^+ states of the intermediate nucleus ^{76}As .

The nuclear wave functions $|0_i^+ \rangle$ and $|0_f^+ \rangle$ for the initial and final nuclei are obtained by projecting out good angular momentum states from the low-lying axially symmetric prolate HF intrinsic states of the corresponding nucleus and then performing a band mixing calculation for each nucleus separately. The DHF single particle orbits $|i \rangle$ obtained after solving the HF single particle equation self-consistently are related

to the basis states $|jk\rangle$ through the relation

$$|i\rangle = \sum_{j_i} c_{j_i k_i} |j_i k_i\rangle \quad (12)$$

Here j_i is the spherical single particle angular momentum and k_i is its projection along the symmetry axis. In the above equation, k_i is not summed over since we restrict ourselves to axial symmetry and hence k_i is a conserved quantity. The HF intrinsic states $\chi_K(\eta)$ are antisymmetrized product of the deformed single-particle orbits. It is easy to see that

$$\langle \chi_{K_1} | e^{-i\beta J_y} | \chi_{K_2} \rangle = \det [M_{ik}(\beta)] \quad (13)$$

where

$$M_{ik}(\beta) = \sum_j c_{jk} c_{jk'} d_{kk'}^j(\beta) \quad (14)$$

Now the reduced matrix element appearing in Eq. (11) can be evaluated using the formula

$$\begin{aligned} \langle \psi_{K_1}^{J_1}(\mu) | \sigma \tau^+ | \psi_{K_2}^{J_2}(\eta) \rangle &= \frac{2J_2 + 1}{2} \sqrt{\frac{2J_1 + 1}{N_{J_1 K_1} N_{J_2 K_2}}} \left[\begin{matrix} J_2 & 1 & J_1 \\ K_2 & \nu & K_1 \end{matrix} \right] \\ \int_0^\pi d\beta \sin\beta d_{K_1, K_2 + \nu}^{J_1} &< \chi_{K_1}(\mu) | e^{-i\beta J_y} \sigma_\nu \tau^+ | \chi_{K_2}(\eta) \rangle \end{aligned} \quad (15)$$

The quantity between the square bracket represents the Clebsch-Gordon coefficient. Since $\sigma \tau^+ = \sum_{\lambda=1}^n \sigma_1(\lambda) \tau_1^+(\lambda)$, the kernel reduces to the form

$$\begin{aligned} \langle \chi_{K_1}(\mu) | e^{-i\beta J_y} \sigma_\nu \tau^+ | \chi_{K_2}(\nu) \rangle &= \sum_{i,k=1}^n (-1)^{i+k} D_{i,k}^{n-1} \\ &\sum_{j_i, j_k} \frac{(-1)^{(3j_i - j_k - \nu)}}{(2j_k + 1)^{1/2}} c_{j_i m_i}^* c_{j_k m_k} d_{m_i, m_k + \nu}^{j_i} \\ &\left[\begin{matrix} j_i & 1 & j_k \\ m_k + \nu & -\nu & m_k \end{matrix} \right] \langle n_i l_i j_i \tau_i | \sigma_1 \tau_1^+ | n_k l_k j_k \tau_k \rangle \end{aligned} \quad (16)$$

Here $D_{i,k}^{n-1}$ is the determinant of rank $(n-1)$ of the matrix elements given by Eq. (14) obtained from the $n \times n$ determinant given in Eq. (13) by removing the i th row and k th column. It should be remembered that χ_{K_1} and χ_{K_2} correspond to HF intrinsic states of two different nuclei. The matrix element

$$\begin{aligned} \langle n_i l_i j_i \tau_i | \sigma_1 \tau_1^+ | n_k l_k j_k \tau_k \rangle &= (-1)^{l_k + j_i + 3/2} \sqrt{6(2j_i + 1)(2j_k + 1)} \\ &\left\{ \begin{matrix} 1/2 & l_k & j_k \\ j_i & 1 & 1/2 \end{matrix} \right\} \delta_{n_i n_k} \delta_{l_i l_k} \end{aligned} \quad (17)$$

In the above, the curly bracket represents six j symbol. The above matrix element is nonzero only if the bra-side corresponds to a proton and the ket-side to a neutron i.e. $\tau_i = 1$ and $\tau_k = -1$

We found that the DHF formalism provides a good description of the low-lying spectroscopic properties of ^{76}Ge and ^{76}Se . This gives us confidence regarding the wave functions of these nuclei. Let us now consider the energy denominator in the expression for Gamow-Teller matrix element in Eq. (11). The energies of the 0^+ ground states of ^{76}Ge and ^{76}Se obtained from the band mixing calculation and the projected energy of the lowest $K = 1^+$ state of ^{76}As are as follows:

$$-17.1 \text{ MeV } [^{76}\text{Ge}(0^+)], \quad -34.8 \text{ MeV } [^{76}\text{Se}(0^+)], \quad -25.0 \text{ MeV } [^{76}\text{As}(1^+)]. \quad (18)$$

Thus we see that the DHF is unable to reproduce correctly the relative energies of the three nuclei. The main reason is the neglect of Coulomb energy. The DHF was mainly used for studying the spectroscopic properties of medium heavy nuclei and Coulomb energy was never important. One way of taking into account the Coulomb energy is to raise the spherical proton single particle energies relative to neutron orbits. We have found that if we raise the proton single particle energies by 8.1 MeV in each nucleus, then we get more realistic relative position of the above considered three states. They are:

$$15.7 \text{ MeV } [^{76}\text{Ge}(0^+)], \quad 14.4 \text{ MeV } [^{76}\text{Se}(0^+)], \quad 16.7 \text{ MeV } [^{76}\text{As}(1^+)]. \quad (19)$$

It is worthwhile to notice that the shifting of the proton states by same amount in each nucleus has no influence on the value of the beta strength amplitudes and the energy denominator. In this case the $2\nu\beta\beta$ -decay matrix element M_{GT} is equal to 0.29 MeV^{-1} . This value is larger by about factor of 2 in comparison with the value 0.15 MeV^{-1} ($g_A = 1.25$) predicted by the $2\nu\beta\beta$ -decay experiment on ^{76}Ge [24]. It is mostly due to the underestimation of the value of energy denominator of M_{GT} . One can get correct relative position of the $^{76}\text{Ge}(0^+)$, $^{76}\text{Se}(0^+)$ and $^{76}\text{As}(1^+)$ levels, i.e. correct value of the energy denominator for the lowest energy state of the intermediate nucleus, if different shifting of the proton levels 8.2 MeV, 8.5 MeV and 7.9 MeV for ^{76}Ge , ^{76}As and ^{76}Se is considered, respectively. Then one get:

$$15.7 \text{ MeV } [^{76}\text{Ge}(0^+)], \quad 12.6 \text{ MeV } [^{76}\text{Se}(0^+)], \quad 17.3 \text{ MeV } [^{76}\text{As}(1^+)]. \quad (20)$$

These changes do not influence the value of the beta transition amplitudes in Eq. (11) but only on the value of energy denominator. For M_{GT} we obtain the value 0.09 MeV^{-1} .

E Muon-Electron Conversion in ^{72}Ge

The muon-electron conversion in nuclei, $(A, Z) + \mu_b^- \rightarrow e^- + (A, Z)^*$, is an important and challenging electroweak process [27–29] which violates the conservation of lepton-flavor quantum numbers L_μ and L_e by one unit. Recently, it has been the subject of considerable theoretical [28, 30, 31] and experimental [37–41] work. From the experimental attempts performed with the objective to “measure” the branching ratio $R_{\mu e}$ of this process, stringent limits on the lepton flavor violation (LFV) parameters have been obtained while significant improvements over these limits are expected in the near future by the new $\mu - e$ conversion experiments, i.e. SINDRUM II at PSI [37, 38],

MECO at BNL [39, 40], and PRIME at KEK [41]. On the other hand, the formulation of the $\mu^- \rightarrow e^-$ nucleon-level Lagrangian has been done [42] in terms of the nucleon effective fields in a Lorentz covariant form where all possible types of interactions, (pseudo)scalar, (axial)vector and tensor, are included. Furthermore, the one-body nuclear matrix elements of the basic nuclear-level operators resulting from this Lagrangian have been compactly formulated [32] and the many-body nuclear wave functions (with definite spin and parity) describing the low-lying nuclear excitations induced by the $\mu^- \rightarrow e^-$ operators have been deduced in the context of some nuclear methods (shell model, QRPA, RQRPA, etc.) for various nuclei [33–35]. In this presentation, we will discuss the calculation of $\mu \rightarrow e$ transition matrix element within our deformed shell model.

In order to write down at nuclear-level the relevant operators describing the assumed $\mu^- \rightarrow e^-$ mechanism, one starts from a nucleon-level Lagrangian. Here we use the general effective-Lagrangian written in a Lorentz covariant form with isospin structure as [42]

$$\begin{aligned} \mathcal{L}_{eff}^N = & \frac{G_F}{\sqrt{2}} \sum_{A,B,C,D} \left[j_\mu^A (\alpha_{AB}^{(0)} J_{(0)}^{B\mu} + \alpha_{AB}^{(3)} J_{(3)}^{B\mu}) + j^C (\alpha_{CD}^{(0)} J_{(0)}^D + \alpha_{CD}^{(3)} J_{(3)}^D) + \right. \\ & \left. + j_{\mu\nu} (\alpha_T^{(0)} J_{(0)}^{\mu\nu} + \alpha_T^{(3)} J_{(3)}^{\mu\nu}) \right], \end{aligned} \quad (21)$$

In Eq. (21) the symbols are: $A, B = \{A, V\}$, $C, D = \{S, P\}$, with S standing for scalar, V for vector, A for axial-vector, P for pseudo-scalar, and T for tensor interactions (the coefficients $\alpha_{lm}^{(k)}$ contain the couplings of the specific model [42]). The isoscalar $J_{(0)}$ and isovector $J_{(3)}$ nucleon currents are defined as

$$\begin{aligned} J_{(k)}^{V\mu} &= \bar{N} \gamma^\mu \tau_k N, \quad J_{(k)}^{A\mu} = \bar{N} \gamma^\mu \gamma_5 \tau_k N, \quad J_{(k)}^S = \bar{N} \tau_k N, \\ J_{(k)}^P &= \bar{N} \gamma_5 \tau_k N, \quad J_{(k)}^{\mu\nu} = \bar{N} \sigma^{\mu\nu} \tau_k N, \end{aligned}$$

where $k = 0, 3$ and $\tau_0 \equiv \hat{I}$. The leptonic currents, j_μ , are described in Ref. [42].

Then, the formulation of the nuclear $\mu^- \rightarrow e^-$ operators, is usually done within the impulse approximation, by carrying out a multipole decomposition on the hadronic current-density matrix elements. This multipole analysis (assuming CVC theory) leads to seven types of basic single-body multipole-operators (they are denoted as $T_{i,M}^J$, $i = 1, 2, \dots, 7$) [32]. These operators are given in terms of the projection functions

$$M_M^J(\mathbf{r}) = \delta_{LJ} j_L(\rho) Y_M^L(\hat{r}), \quad \mathbf{M}_M^{(L1)J}(\mathbf{r}) = j_L(qr) \mathbf{Y}_M^{(L1)J}(\hat{r}). \quad (22)$$

which involve the spherical Bessel functions $j_L(r)$ and the spherical Harmonics $Y_M^L(\hat{r})$ or the vector spherical Harmonics $\mathbf{Y}_M^{(L1)J}(\hat{r}) = \hat{q} \sum_{m,m'} \langle Lm1m' | JM \rangle Y_m^L(\hat{r})$. \hat{r} and \hat{q} are unit vectors in the directions of \mathbf{r} and \mathbf{q} , respectively. The magnitude of the three-momentum transfer $|\mathbf{q}|=q$ is related to the nuclear excitation energy E_x as,

$$q = m_\mu - \epsilon_b - E_x, \quad (23)$$

where m_μ is the muon mass, ϵ_b the muon atomic binding energy and E_x the excitation energy of the nucleus. Equation (23) shows that $\mu^- \rightarrow e^-$ operators are strongly momentum dependent.

The matrix elements of the fundamental single-particle operators obtained from the above decomposition procedure, T_i^{JM} , $1 = 1, 2, \dots, 7$, in a harmonic oscillator basis can be cast in closed analytical forms as [32]

$$\langle j_1 || \hat{T}^J || j_2 \rangle = e^{-y} y^{\beta/2} \sum_{\mu=0}^{n_{max}} \mathcal{P}_{\mu}^J y^{\mu}, \quad y = (qb/2)^2 \quad (24)$$

where

$$n_{max} = (N_1 + N_2 - \beta)/2. \quad (25)$$

where $N_i = 2n_i + l_i$ and $j_i \equiv (n_i l_i) j_i$. The integer β which appears in Eqs. (24) and (25) depends on the specific operator T_i^{JM} . The coefficients \mathcal{P}_{μ}^J are, in general, simple rational numbers for the diagonal matrix elements of Eq. (24), and square roots of simple rational numbers for the non-diagonal ones [32].

The deformed orbits $|\lambda\rangle$ entering the HF single particle equations are expanded to a chosen basis states $|j\rangle$ as, $|\lambda\rangle = \sum_j c_{j\lambda} |j\rangle$, where the expansion coefficients $c_{j\lambda}$ are determined via the iteration procedure. In the present work, the two-body interaction matrix elements available in the shell model representation are used. For the radial part of the basis states $|j\rangle$ we use spherical harmonic oscillator shell model states as, $|j\rangle \equiv |(nl)jk\tau\rangle$. In our axially symmetric solutions the orbits are eigenstates of the \hat{J}_z operator and the latter expansion is limited to states with a given k_{λ} , so as we have

$$|\lambda\rangle = \sum_j c_{jk_{\lambda}} |jk_{\lambda}\tau_{\lambda}\rangle \quad (26)$$

where j denotes the (spherical) single particle angular momentum and k_{λ} its projection along the symmetry axis (notice that k_{λ} is not summed over since this is a conserved quantity). In Eq. (26) the index τ_{λ} distinguishes proton and neutron orbits, but since $\mu - e$ conversion is a charge-preserving process, its operators do not mix proton and neutron states, and hence $|\lambda\rangle = \sum_j c_{jk_{\lambda}} |jk_{\lambda}\rangle$.

In the case of axially symmetric nuclear systems, the reduced matrix elements for any $\mu - e$ conversion operator, $\hat{O}_M^{(l,s)J} = \sum_{\lambda=1}^n \hat{T}_M^{(l,s)J}(\lambda)$, where $n = Z(N)$, for proton (neutron) states, rely on the formula

$$\langle \phi_{K_1}^{J_1}(\mu) || \hat{O}^{(l,s)J} || \phi_{K_2}^{J_2}(\eta) \rangle = \frac{2J_2 + 1}{2} \sqrt{\frac{2J_1 + 1}{N_{J_1 K_1} N_{J_2 K_2}}} \sum_{\nu} \left[\begin{matrix} J_2 & J & J_1 \\ K_2 & \nu & K_1 \end{matrix} \right] \int_0^{\pi} d\beta \sin\beta d_{K_1, K_2}^{J_1} \langle \chi_{K_1}(\mu) | e^{-i\beta J_y} \hat{O}_{\nu}^{(l,s)J} | \chi_{K_2}(\eta) \rangle. \quad (27)$$

In the latter equation, the square bracket $[]$ represents the Clebsch-Gordon coefficient and the matrix element of the kernel is written as [43]

$$\begin{aligned} \langle \chi_{K_1}(\mu) | e^{-i\beta J_y} \hat{T}_{\nu}^{(l,s)J} | \chi_{K_2}(\eta) \rangle &= \sum_{i,k=1}^n (-1)^{i+k} D_{i,k}^{n-1} \\ &\sum_{j_i, j_k} \frac{(-1)^{(3j_i - j_k - \nu)}}{(2j_k + 1)^{1/2}} c_{j_i m_i}^* c_{j_k m_k} d_{m_i, m_k + \nu}^{j_i} \\ &\left[\begin{matrix} j_i & J & j_k \\ m_k + \nu & -\nu & m_k \end{matrix} \right] \langle n_i l_i j_i | \hat{T}_{\nu}^{(l,s)J} | n_k l_k j_k \rangle \end{aligned} \quad (28)$$

This can be proved [43] by noting that,

$$\langle \chi_{K_1} | e^{-i\beta J_y} | \chi_{K_2} \rangle = \det [M_{il}(\beta)] \quad (29)$$

where

$$M_{il}(\beta) = \langle \lambda_i | \exp(-i\beta J_y) | \lambda_l \rangle = \sum_j c_{jk_i}^* c_{jk_l} d_{k_i k_l}^j(\beta). \quad (30)$$

In Eq. (28), $D_{i,k}^{n-1}$ stand for the determinants made of the matrix elements given by Eq. (30). They are determinant of rank $(n-1)$ obtained from the $n \times n$ determinant given in Eq. (29) by removing the i -th row and k -th column. The single particle reduced matrix element of the type $\langle (n_i l_i) j_i || \hat{T}^{(l,s)J} || (n_k l_k) j_k \rangle$ entering Eq. (28) are given in Eq. (24).

Because the coherent mode is the only potentially measured directly $\mu - e$ conversion channel (its rate is currently measured at the SINDRUM II [37] and MECO [39,40] detectors and is expected to be measured in the future PRIME experiment, at KEK (Japan) [36,41]), mostly the coherent contribution is employed for the estimation of the branching ratio $R_{\mu e}$. It is also used in combining nuclear physics inputs with experimental limits on $R_{\mu e}$, to put constraints on the LFV parameters entering the $\mu - e$ conversion effective currents in modern gauge theories [36,42].

The scalar and vector $g.s. \rightarrow g.s.$ transition matrix elements (if the couplings of the prevailing mechanism in the $\mu - e$ conversion are known), to a rather good approximation (depending on the properties of the nuclear target), can be determined by the proton (F_Z) and neutron (F_N) nuclear form factors [45]. In Table 1 we quote the results of F_Z and F_N for ^{72}Ge obtained with the deformed HF in the present work and those of previously used methods: Shell model (single Slater determinant) [44], normal QRPA [34] and renormalized QRPA [35]. We see that, the proton and neutron form factors, agree rather well among each other and with experiment, even though the value of the h.o. size-parameter used in the case of DHF ($b = 1.9 fm$) differs significantly from those of other methods.

The coherent matrix elements, M_{coh}^2 , in the photonic and W -boson exchange (non-photonic) mechanisms, obtained with the above calculations are also shown in Table 1. As can be seen, the results of DHF for the γ -exchange process, lie in-between those given by the other methods [34,35,44], but those for the W -exchange mechanisms are larger. Since, neutrons do not participate in the photonic mechanism, the DHF method gives larger neutron-contribution compared to other methods.

In this work we will perform detailed calculations for the dominant (scalar, vector and axial vector) $\mu - e$ matrix elements. Extensive results including contributions from other operators (for isotopes in the region $30 \leq Z \leq 60$, where the branching ratio $R_{\mu e}$ takes the largest value [36]), are available within QRPA treatments.

The incoherent $\mu - e$ matrix elements are of the form

$$S_\alpha = \sum_f \left(\frac{q_f}{m_\mu} \right)^2 \int \frac{d\hat{q}_f}{4\pi} |\langle J_\lambda^\pi, M | \Omega_\alpha | g.s. \rangle|^2, \quad f \equiv (J_\lambda^\pi, M). \quad (31)$$

In S_α (S_S for the scalar, S_V for the vector and S_A for the axial vector operators Ω_α) partial contributions coming from all excited states are summed over. Since the $|g.s.\rangle$ of ^{72}Ge nucleus corresponds to the lowest 0^+ level obtained from the lowest $K = 0^+$

intrinsic state, one important category of the states $|f\rangle$ will correspond to the excited levels projected from this $K = 0^+$ intrinsic state. The states $|f\rangle$, however, can in addition be deduced from the good angular momentum states projected out of other excited intrinsic states. In Table 2, the incoherent matrix elements listed, represent the sum of the contributions of all states (up to $J \sim 6^+$) produced as described in Sect. 3.1. We see that, the main incoherent rate originates from the excitations of the $g.s.$ band.

An interesting feature comes out of the calculations of the negative parity bands. In previous calculations, such excitations (especially the 1^- multi-polarities) provided a great portion of the incoherent strength. In the DHF results, the sum of the incoherent contributions of all negative parity states included in our model space, differs drastically from that obtained by other RPA methods. This can be attributed to the following reasons.

The incoherent rate which proceeds via the $J^\pi = 1^-$ excitations, comes in the DHF from the band (v), i.e. the $K = 1^-$ band. The in this way derived $J^\pi = 1^-$ excitation, is a relatively low-lying state only when a neutron is excited from the $g_{9/2}$ orbit. The 1^- state produced when a proton is excited from the $g_{9/2}$ orbit lies much higher. As a result, for the photonic mechanism (in which only protons contribute) the comparison is much worst than that for the non-photonic one (see Table 3). These characteristics are not in accord with QRPA results (both for vector and axial-vector matrix elements) [34] for which the $J^\pi = 1^-$ excitations offer in many nuclear systems the main contribution. The general picture of DHF incoherent results is rather similar to that of (spherical) shell model results [33].

We should stress, however, that the spectra derived by the DHF and QRPA methods, in general, differ radically and are obtained following different ways. Also, the size of the model space used in QRPA calculations, which, sometimes, plays significant role, is much larger than that used in our DHF calculations. The latter model space is limited like in shell model calculations [33]. In conclusion, the comparison of the incoherent contributions cannot be reasonably done state-by-state.

F Cold Dark Matter

We know that dark matter is needed to close the universe. One normally defines a parameter Ω given by $\Omega = \rho/\rho_c$ where ρ is the density of the universe and ρ_c is the critical density. One theoretically expects $\Omega \simeq 1$, while the usual baryonic matter gives $\Omega \leq 0.1$. In order to accommodate $\Omega \simeq 1$, non-luminous (dark) matter is needed. Two types of such matter have been considered. The first is composed of particles which were relativistic at the time of structure formation and constitutes the hot dark matter component (HDM). The other type is made up of particles which were non-relativistic at the time of freeze out and constitutes the cold dark matter component (CDM). The COBE data [47] suggest that CDM is at least 60%. There are also other analysis which suggest that there is no need for HDM and the situation can be adequately described by CDM. Since the nonexotic component can not exceed 40% of the CDM, there is room for the exotic weakly interacting massive particles (WIMP). In the currently favoured super-symmetric (SUSY) extensions of the standard model, the most natural WIMP candidate is the LSP, i.e. the lightest super-symmetric particle whose nature can be de-

^{72}Ge	Exper. Shell Model QRPA [35] RQRPA [35] DHF (this work)				
b_{ho} (fm)	–	2.04	2.07	2.07	1.90
F_Z	0.443	0.456	0.472	0.441	0.449
F_N	–	0.435	0.451	0.422	0.429
$M_{coh}^2(\gamma - exc.)$	200.9	212.9	169.9	199.1	206.0
$M_{coh}^2(W - exc.)$		595.8	477.1	558.9	623.2

Table 1. Proton, F_Z , and neutron, F_N , form factors, obtained with “spherical” and “deformed” models in the case of the ^{72}Ge nucleus. The corresponding coherent matrix elements for the $\mu - e$ conversion for photonic (γ -exchange) and non-photonic (W -exchange) mechanism are also shown.

DHF Excited States		Photonic Mechanism Non-Photonic Mechanism		
J^π	Origin	Vector	Vector	Axial-Vector
2^+	Lowest $K = 0^+$ g.s. band	0.997	6.245	0.0002
2^+	Gamma band	–	–	0.035
4^+	”	1×10^{-5}	0.001	–
0^+	First excited $K = 0^+$ band	4×10^{-4}	0.006	–
2^+	Gamma band	0.114	0.438	–
4^+	”	0.001	0.005	–
2^+	$K = 1^+$ band	0.018	0.073	0.005
3^+	$K = 1^+$ band	–	–	0.011
4^+	$K = 1^+$ band	–	2×10^{-4}	0.0002
3^-	Band (v)	0.0	0.001	1×10^{-5}
2^-	Band (vi)	0.016	–	0.178
3^-	Band (vi)	0.016	0.057	0.003
4^-	Band (vi)	0.016	–	0.0002
Total		1.157	6.826	0.201

Table 2. Incoherent transition matrix element of the $T^{(l,\sigma)J}$ operators for selected spin-isospin combinations. States not appearing in the first column contribute less than 10^{-3} for all components.

Mechanism	$S_V(\text{coh})$	$S_A(\text{coh})$	M_{coh}^2	$S_V(\text{inc})$	$S_A(\text{inc})$	M_{inc}^2	M_{tot}^2
γ -exchange	206.0	–	206.0	1.2	–	1.2	207.2
W -exchange	623.2	–	623.2	6.8	0.2	7.0	630.2

Table 3. Deformed HF results for coherent, incoherent ($M_{\text{inc}}^2 = S_V + 3S_A$) and total ($M_{\text{tot}}^2 = M_{\text{coh}}^2 + M_{\text{inc}}^2$) matrix elements in ^{72}Ge . The photonic and W -exchange diagrams are included.

scribed in most SUSY models to be a Majorana fermion, a linear combination of the neutral components of the gauginos and Higgsinos with mass greater than 30 GeV/ c^2 . The direct detection of such particles is thus of profound importance.

The detection of the LSP, which in the following is denoted by χ , is quite difficult, since this particle interacts extremely weakly with matter. The most interesting possibility for direct detection of the LSP is via the recoiling of the nucleus in the elastic channel. The LSP-nucleus differential cross section in the laboratory frame, $d\sigma(q, v)/dq^2$, where \mathbf{q} represents the momentum transfer to the nuclear target and v is the LSP velocity with respect to the earth which, if we neglect earth's rotation effects, is equal to the relative velocity of the LSP and the detector nucleus. Instead of \mathbf{q}^2 , one can use the variable $u = q^2 b^2/2 = M_A b^2 Q$ where M_A is the nuclear mass, b is the nuclear harmonic oscillator size parameter and Q the energy transfer to the nucleus. By neglecting the small vector contribution, we have

$$\frac{d\sigma(u, v)}{du} = \frac{1}{2}\sigma_0 \left(\frac{1}{m_p b} \right)^2 \frac{c^2}{v^2} \frac{d\sigma_{AS}(u, v)}{du} \quad (32)$$

with

$$\begin{aligned} \frac{d\sigma_{AS}}{du} = & (f_A^0 \Omega_0(0))^2 F_{00}(u) + 2f_A^0 f_A^1 \Omega_0(0) \Omega_1(0) F_{01}(u) \\ & + (f_A^1 \Omega_1(0))^2 F_{11}(u) + A^2 (f_S^0 - f_S^1 \frac{N-Z}{A})^2 |F(u)|^2 \end{aligned} \quad (33)$$

The above expression for the LSP-nucleus cross-section basically consists of two parts: the coherent part coming from the scalar interaction and the spin contribution coming from axial current. The coherent matrix elements can be easily be described in terms of the nuclear form factor but the evaluation of the spin matrix elements is more complicated. The spin structure function $F_{\rho\rho'}(u)$ with $\rho, \rho'=0,1$ are defined as

$$F_{\rho\rho'}(u) = \Sigma_{\lambda, \kappa} \frac{\Omega_{\rho}^{(\lambda, \kappa)}(u) \Omega_{\rho'}^{(\lambda, \kappa)}(u)}{\Omega_{\rho}(0) \Omega_{\rho'}(0)} \quad (34)$$

$$\Omega_{\rho}^{(\lambda, \kappa)}(u) = \sqrt{\frac{4\pi}{2J_i + 1}} \langle J_f \parallel \Sigma_{j=1}^A [Y_{\lambda}(\Omega_j) \otimes \sigma(j)]_{\kappa} j_{\lambda}(\sqrt{u} r_j) \times \omega_{\rho}(j) \parallel J_i \rangle \quad (35)$$

with $\omega_0(j) = 1$ and $\omega_1(j) = \tau_3(j)$. The calculated spin structure function for ^{73}Ge is given in fig. 3

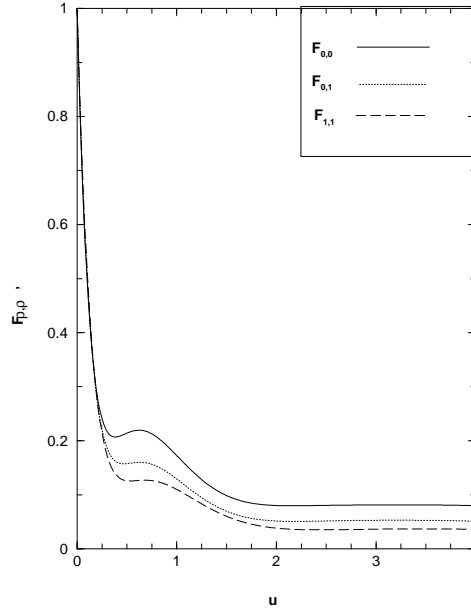


Fig. 3. The spin structure function $F_{\rho, \rho'}$ for ^{73}Ge .

G Conclusions

In this presentation, we have discussed the application of deformed shell model to different problems. The model was mainly used to study the spectroscopy of nuclei in the different regions of periodic table. In recent years, this model was applied to study the $N = Z$ nuclei in the medium heavy region with isospin projection. We have also applied this model to study other problems associated with weak interaction like (i) two neutron double beta decay (ii) muon-electron conversion in the field of the nucleus (iii) cold dark matter.

The author is thankful to DST (India) for financial support.

References

1. S.B. Khadikar, S.C.K. Nair and S.P. Pandya, Phys. Lett. **B36**, 290 (1971); S.B. Khadikar, D.R. Kulkarni and S.P. Pandya, Pramana **2**, 259 (1974)

2. R. Sahu and S.P. Pandya, Nucl. Phys. **A548**, 64 (1992); J. Phys. **G14**, L165 (1988); K.C. Tripathy and R. Sahu, J. Phys. **G20**, 911 (1994); Int. J. Mod. Phys. **E11**, 531 (2002).
3. S.M. Fischer et al, Phys. Rev. Lett. **87**, 132501 (2001).
4. S.M. Vincent et al, Phys. Lett. **B 437**, 264 (1998).
5. R. Grzywacz et al, Phys. Lett. **B 429**, 247 (1998); Nucl. Phys. **A682**, 41c (2001).
6. D.G. Jenkins et al, Phys. Rev. **C 65**, 064307 (2002); G. de Angelis et al, Eur. Phys. J. **A 12**, 51 (2001).
7. D. Rudolph et al, Phys. Rev. Lett. **76**, 376 (1996).
8. C. Friessner, N. Pietralla, A. Schmidt, I. Schneider, Y. Utsuno, T. Otsuka, and P. von Brentano, Phys. Rev. **C 60**, 011304 (1999).
9. S.M. Lenzi et al, Phys. Rev. **C 60**, 021303 (1999).
10. C.D. O'Leary, M.A. Bentley, D.E. Appelbe, R.A. Bark, D.M. Cullen, S. Ertürk, A. Maj, J.A. Sheikh, and D.D. Warner, Phys. Lett. **B 459**, 73 (1999).
11. A. Schmidt, I. Schneider, C. Friessner, A.F. Lisetskiy, N. Pietralla, T. Sebe, T. Otsuka, and P. von Brentano, Phys. Rev. **C 62**, 044319 (2000).
12. N. Pietralla et al, Phys. Rev. **C 65**, 024317 (2002).
13. C.D. O'Leary et al, Phys. Lett. **B 525**, 49 (2002).
14. I. Schneider, A.F. Lisetskiy, C. Friessner, R.V. Jolos, N. Pietralla, A. Schmidt, D. Weisshaar, and P. von Brentano, Phys. Rev. **C 61**, 044312 (2000).
15. S.M. Fischer et al, Phys. Rev. Lett. **84**, 4064 (2000).
16. S.M. Fischer, C.J. Lister, and D.P. Balamuth, Phys. Rev. **C 67**, 064318 (2003).
17. N. Marginean et al, Phys. Rev. **C 65**, 051303 (2002).
18. R.B. Firestone (ed. V.S. Shirley), Table of Isotopes, 8th edition, Vol. 1 (John Wiley, New York, 1996).
19. R. Sahu and V.K.B. Kota, Phys. Rev. **C 66**, 024301 (2002).
20. R. Sahu and V.K.B. Kota, in: Nuclear Models, Edited by V.K.B. Kota (Allied Publishers, New Delhi, 2002), p. 70.
21. R. Sahu and V.K.B. Kota, Phys. Rev. **C 67**, 054323 (2003).
22. A. Poves and A. Zuker, Phys. Rep. **70**, 235 (1981).
23. G. Martinez-Pinedo, A.P. Zuker, A. Poves, and E. Caurier, Phys. Rev. **C 55**, 187 (1997); E. Caurier, G. Martinez-Pinedo, F. Nowacki, J. Retamosa, and A. P. Zuker, Phys. Rev. **C 59**, 2033 (1999).
24. M. Moe and P. Vogel, Ann. Rev. Nucl. Part. Sci. **44** (1994) 247.
25. J. Suhonen and O. Civitarese, Phys. Rep. **300** (1998) 123.
26. A. Faessler and F. Šimkovic, J. Phys. **G 24**, 2139 (1998).
27. P. Scheck, Phys. Reports **44** (1979) 187.
28. Y. Kuno and S. Okada, *Rev. Mod. Phys.* **73** (2001) 151 .
29. J. Suhonen and O. Civitarese, *Phys. Rep.* **300** (1998) 123 .
30. T.S. Kosmas, *Nucl. Phys. A* **683** (2001) 443 .
31. T.S. Kosmas, The nuclear physics aspects of the exotic $\mu^- \rightarrow e^-$ conversion in nuclei, Invited talk at "3rd Intern. Workshop on Neutrino Factories based on Muon Storage Rings, NuFACT'01", Tsukuba, Japan, May 24-30, 2001; nucl-th/0108045.
32. T.S. Kosmas, *Prog. Part. Nucl. Phys.* **48** (2002) 307; V.Ch. Chasioti and T.S. Kosmas, *Czech. J. Phys.* **52** (2002) 467; nucl-th/0202062.
33. T. Siiskonen, J. Suhonen, and T.S. Kosmas, *Phys. Rev. C* **60** (1999) R 62501 ; *ibid* **62** (2000) 035502.
34. T.S. Kosmas, J.D. Vergados, O. Civitarese, and A. Faessler, *Nucl. Phys. A* **570** (1994) 637 ; T.S. Kosmas, A. Faessler, F. Šimkovic and J.D. Vergados, *Phys. Rev. C* **56** (1997) 526 .
35. J. Schwieger, T.S. Kosmas, and A. Faessler, *Phys. Lett. B* **443** (1998) 7 ; T.S. Kosmas, Z. Ren and A. Faessler, *Nucl. Phys. A* **665** (2000) 183 .

36. R. Kitano, M. Koike, and Y. Okada,
37. A. van der Schaaf, *Prog. Part. Nucl. Phys.* **31** (1993) 1; The SINDRUM II, Invited talk at [31].
38. P. Wintz, Status of $\mu - e$ conversion at PSI, Inv. talk at Work. on 'New initiatives in LFV and ν -oscillations with very intense muon and neutrino beams", Honolulu, USA, Oct. 2-6, 2000.
39. W. Molzon, *Spring. Trac. in Mod. Phys.* 163 (2000) 105.
40. J. Sculli, The MECO experiment, Invited talk at [38].
41. M. Aoki, the PRIME experiment, Invited talk at [31].
42. A. Faessler, T.S. Kosmas, S. Kovalenko, and J.D. Vergados, *Nucl. Phys. B* 587 (2000) 25 ; T.S. Kosmas, S. Kovalenko and I. Schmidt, *Phys. Lett. B* 511 (2001) 203 ; *ibid* 519 (2001) 78; F. Šimkovic, et al., *Phys. Lett. B* 554 (2002) 121 . *Phys. Rev. D* 66 (2002) 096002 .
43. R. Sahu and S.P. Pandya, *Nucl. Phys. A* 414 (1984) 240 ; R. Sahu and S.P. Pandya, *J. Phys. G* 14 (1988) L165 ; *Nucl. Phys. A* 529 (1991) 20 ; *Nucl. Phys. A* 571 (1994) 253 ; R. Sahu, F. Šimkovic, and A. Faessler, *J. Phys. G* 25 (1999) 1159 .
44. T.S. Kosmas and J.D. Vergados, *Phys. Lett. B* 217 (1989) 19 ; *Nucl. Phys. A* 510 (1990) 641 ; *Phys. Rep.* 264 (1996) 251 .
45. T.S. Kosmas and I.E. Lagaris, *J. Phys. G* 28 (2002) 2907 .
46. Ch.C. Moustakidis, *et al.*, in preparation.
47. G.F. Smoot et al., *Astrophys. J. Lett.* **396**, L1 (1992)

Hartree-Fock-Bogoliubov model application to double beta decay

P.K. Raina¹, A. Shukla¹, K. Chaturvedi², R. Chandra², J. Singh², P.K. Rath², S.K. Dhiman³, and J.G. Hirsch⁴

¹ Department of Physics, IIT Kharagpur-721302, India.

² Department of Physics, University of Lucknow, Lucknow-226007, India.

³ Department of Physics, H. P. University Shimla, Summerhill-171005, India.

⁴ Instituto de Ciencias Nucleares, Universidad Nacional and Autonoma de Mexico, A.P. 70-543 Mexico 04510 D.F.

A Introduction

The Neutrino was postulated by Wolfgang Pauli in 1930 and its first experimental observation confirmed by Reines and Cowan in 1956. Even after the 74 years of its postulation, the properties of neutrinos are not completely known and it auspiciously celebrates to be the most mysterious elementary particle. On the other hand, the characteristics of neutrinos, namely mass and nature (Dirac or Majorana character) play a key role in modern gauge field theories namely SM, GUTs, SUSYs, Sugras and String theories. The experimental search for neutrino mass can be classified as terrestrial and extra-terrestrial approaches. The terrestrial approach consists of accelerator and non-accelerator experiments. The π , τ -decay and neutrino oscillations are the accelerator experiments while tritium decay, neutrino oscillations at reactors, the neutrino decay at reactors and the nuclear double beta ($\beta\beta$) decay come under non-accelerator experiments. In the extra-terrestrial approach, the most promising ones are investigations of solar neutrinos, atmospheric neutrinos, neutrinos from supernovae explosions and the neutrino cosmic background radiation yet to be observed. Most significantly, the neutrino oscillation experiments convincingly show that neutrinos have a finite mass. However, in oscillation experiments only the differences in squares of the neutrino masses, $\Delta m_{ij}^2 = |m_i^2 - m_j^2|$, can be measured. Its existence, in turn, is causing a renaissance of enthusiasm in the experimentalists' community, which is expected to reach, in the next generation of experiments, the sensitivity corresponding to this mass scale. There are mainly two approaches - direct measurement of the electron neutrino mass through measurements near the end of the electron spectrum in (tritium) beta decay, and neutrinoless double beta decay. The KATRIN experiment currently being planned in Karlsruhe has a sensitivity of about 0.2eV close to the upper limit deduced (with assumptions) from cosmology of about 0.25eV. However, we also need to consider how to reach sensitivities of around 0.01eV. The most promising route seems to be neutrinoless double beta decay, which can potentially reach this sensitivity for a weighted average mass for the three neutrinos. Achieving this level of sensitivity presents several significant experimental and theoretical challenges, including exact knowledge of the nuclear matrix elements. Today, the double beta decay yields – besides proton decay – are the most

promising options to probe beyond standard model physics at energies beyond the reach of accelerator.

B Double Beta Decay And Its Implications

Double beta ($2\nu\beta\beta$) decay was first predicted by Goeppert-Mayer in 1935 as one of the rarest processes of the nature in which “... a metastable isobar can change into a more stable one by simultaneous emission of two electrons” [1]. Double beta decay, a second-order process of the weak interaction, is a spontaneous nuclear transition of an even-even nucleus in which the nuclear charge changes by two units while the mass number remains same. This remarkable $\beta\beta$ decay process can be characterized mainly by two modes, namely, the two neutrino double beta ($2\nu\beta\beta$) decay and the neutrinoless double beta ($0\nu\beta\beta$) decay.

$2\nu\beta\beta$ decay mode

1. Double Electron emission $(A, Z) \rightarrow (A, Z+2) + 2e^- + 2\nu_e$
2. Double Positron emission $(A, Z) \rightarrow (A, Z-2) + 2e^+ + 2\nu_e$
3. Positron emission/Electron capture $e^- + (A, Z) \rightarrow (A, Z-2) + e^+ + 2\nu_e$
4. Double electron capture $2e^- + (A, Z) \rightarrow (A, Z-2) + 2\nu_e$

$0\nu\beta\beta$ decay mode

1. Double Electron emission $(A, Z) \rightarrow (A, Z + 2) + 2e^-$
2. Double Positron emission $(A, Z) \rightarrow (A, Z-2) + 2e^+$
3. Positron emission/Electron capture $e^- + (A, Z) \rightarrow (A, Z-2) + e^+$
4. Double electron capture $2e^- + (A, Z) \rightarrow (A, Z-2)^*$

The process of Double Beta Decay can be regarded as a simultaneous transformation of two protons (neutrons) into two neutrons (protons), bound in the nucleus. The two modes of $\beta\beta$ decay can be distinguished from each other by the feature of the violation (or non-violation) of the lepton number (L) conservation. The two-neutrino $\beta\beta$ decay mode ($2\nu\beta\beta$) does not violate lepton number and is fully consistent with the standard model (SM) of electroweak theory. On the other hand Neutrinoless Double beta decay $0\nu\beta\beta$, which is far more interesting since it violates lepton number conservation, is not allowed in Standard Model. It was considered first by Racah in 1937 [2] and Furry in 1939 [3] as a tool to distinguish whether the neutrino is of Majorana (particle=antiparticle) [4] or Dirac (particle \neq antiparticle) type. Explicitly, if the antineutrino (neutrino) emitted in the first neutron (proton) decay is a Majorana particle, then it can be absorbed by another neutron (proton) which therefore leads to the $0\nu\beta\beta$ decay mode.

Werner Heisenberg postulated that pairing force renders the even-even nuclei (nuclei with even number of protons and even number of neutrons) more stable than the odd nuclei with broken pairs and thus the single beta decay transition from the even-even parent nucleus (A, Z) to the neighboring odd nucleus is energetically forbidden and the $\beta\beta$ decay to the daughter nucleus $(A, Z\pm 2)$ is the only possible decay channel. It was also seen that this process may occur even when single β decay is strongly suppressed due to a large change of spin.

There are very few nuclear systems which offer an opportunity to study it and nature isolates this very rare phenomenon with exceedingly tiny rates. Even then importance of double beta decay can be easily understood by the fact that the fascination in it continues from more than six decades and in this span of time, numerous reviews [5–8] have been published on it. Especially during the last decade enormous efforts have been put to study the double beta decay experimentally and some of them have successfully observed the $2\nu\beta\beta$ [9, 10] and also controversial observation of $0\nu\beta\beta$ for ^{76}Ge has been reported recently by Heidelberg-Moscow group claiming $m_{\nu e}=0.39$ eV [11] with $T_{1/2}^{0\nu} = 1.5 \times 10^{25}$ years. The significance of studying double beta decay lies in the fact that it directly addresses the question of lepton number conservation in weak interactions, as well as the related question of fundamental properties of neutrinos (such as whether the neutrino has mass and if it does, whether it is its own antiparticle i.e. is it a majorana particle), which has a very crucial role in modern gauge field theories and astrophysics. Today, the potential of double beta decay includes a broad range of topics that are equally relevant to particle physics and astrophysics, such as masses of heavy neutrinos, of sneutrinos, doubly charged Higgs bosons, R-parity violating SUSY, right-handed weak currents, compositeness, leptoquarks, left-right symmetric models, Dark matter search and tests of Lorentz symmetry and equivalence principle in the neutrino sector. Double beta decay has become indispensable nowadays for solving the problem of the neutrino mass spectrum and the structure of the neutrino mass matrix together with present and future solar and atmospheric neutrino oscillation experiments.

Experimental methods for detecting $\beta\beta$ decay can be classified broadly in to three categories. Geochemical measurements, Radiochemical measurements and Direct detection measurements. Geochemical measurements of total $\beta\beta$ decay half-lives are performed by measuring the abundance of daughter isotope accumulated in geologically old ore sample containing the parent isotope. In these experiments one determines the excess of daughter isotope that has accumulated over geologic times ($\sim 10^9$ years) in an ore sample, rich in the parent isotope. A really unambiguous proof for one or both modes of $\beta\beta$ decay and a clear way to discriminate between them can be provided by direct detection experiments. Direct detection measurements are performed by directly detecting positron pairs known to have been emitted at the same time and/or from the same point in the sample of parent isotope. Kinematical data on the positrons provides information on the mechanism (0ν , 2ν etc.) governing $\beta\beta$ decay. In direct detection experiments this fact is utilized that if $\beta^+\beta^+$ decay occurred within a thick sample of material, the positrons would stop and annihilate with the sample. Subsequently, four strongly correlated coincident 511-keV annihilation gamma rays would be emitted and this gamma ray signature of $\beta^+\beta^+$ decay can easily be detected by high purity detectors.

The half-lives of many $\beta^-\beta^-$ emitters are shorter, compared with the other modes, due to a larger available phase space. For this reason they were the natural choice for the experimental observation to start with. However, the experimental sensitivity of $\beta^-\beta^-$ decay mode gets limited because of the presence of electron background. On the other hand, from the experimental point of view, the $e^+\text{DBD}$ ($\beta^+\beta^+/\beta^+\text{EC}/\text{ECEC}$) modes are relatively easier to be separated from the background contaminations. Moreover, the e^+ DBD modes are also attractive due to the possibility to detect the coincidence

signals from four gamma-rays, two gamma-rays and one gamma-ray for $\beta^+\beta^+$, $\beta^+\text{EC}$ and ECEC modes respectively.

C Nuclear Structure aspects of Double Beta Decay

The extraction of information about neutrino mass is essentially dependent upon the prediction of nuclear matrix elements involved in these processes. The full Shell Model calculation is quite difficult and in QRPA approach unlike $2\nu\beta\beta$ decay, the $0\nu\beta\beta$ decay matrix elements are not greatly suppressed. The Variational models are the promising ones where the difficulties associated with other nuclear models can be overcome in most of the nuclei. All the $\beta^+\beta^+$ emitters are even-even nuclei, in which pairing of the nucleons play a crucial role. Most of them are deformed and the deformation degree of freedom is also important in describing the properties of these nuclei. Hence to study the double beta decay of these nuclei we need a framework where pairing and deformation degree of freedom can be dealt on equal footing in its formalism. The Projected Hartree-Fock-Bogoliubov (PHFB) model becomes the preferable choice to fulfill these needs.

Double Beta decay is not an isolated nuclear process and accumulation of vast amount of data concerning the level energies as well as electromagnetic properties permits us a rigorous and detailed critique of the ingredients of the microscopic framework that seeks to provide a description of nuclear $\beta\beta$ decay. However, most of the calculations of DBD transition matrix elements performed so far do not satisfy this criterion.

Pairing of like nucleons play an important role in all $\beta\beta$ decay emitters since they are even-Z and even-N nuclei. The nuclear structure in the mass region $A=70$ to 130 has been studied extensively theoretically as well as experimentally and it offers a nice example of shape transition. It is expected that deformation degrees of freedom will also play crucial role in the structure of nuclei involved in the study of $\beta\beta$ decay. Thus, it is desirable to have a framework for the study of $\beta\beta$ decay in which the pairing and deformation degree of freedom are treated on equal footing in its formalism. Therefore appropriate version of Hartree-Fock (Deformed Hartree-Fock or Hartree-Fock-Bogoliubov model) with proper residual interaction would be best suited for the study of $\beta\beta$ decay. Moreover, comparative study of the same philosophy (to establish the reliability of wavefunction by obtaining an overall agreement between a number of theoretically calculated spectroscopic properties before calculating NTME's) may be decisive in establishing the validity of nuclear model to evade the uncertainty of NTME's..

Although there has been very less experimental activity for determining the half-lives of $\beta^+\beta^+/\beta^+\text{EC}/\text{ECEC}$ modes even for the best candidate like but recently the interest has picked up particularly for few nuclei such as ^{78}Kr and ^{106}Cd and the limits are now quite close to theoretical predictions. It is expected that $2\nu\beta^+\beta^+/\beta^+\text{EC}/\text{ECEC}$ modes will be observed very soon. The most interesting nuclei for the experimental search are the ones with big conversion energy and a high isotopic abundance. Over the past few years several nuclear models have been employed to calculate the $2\nu\beta\beta$ and $0\nu\beta\beta$ decay transition matrix elements in two-nucleon (2n) mechanism. It has been observed that in all cases the $2\nu\beta\beta$ decay matrix elements are sufficiently quenched. Hence the main motive of all the theoretical calculations is to achieve the quenching of $M_{GT}^{2\nu}$ and to understand the physical mechanism responsible for the above mentioned

process. As mentioned the observation of $0\nu\beta\beta$ decay is controversial and has not been confirmed so far. Hence the models predict half-lives assuming a certain value for the neutrino mass or conversely extract various parameters from the observed limits of half-lives of the $0\nu\beta\beta$ decay. The reliability of the predictions can be judged a priori only from the success of the model in explaining various observed physical properties of nuclei.

Thus there are mainly two types of models usually employed to calculate 2ν and $0\nu\beta\beta$ decay nuclear transition matrix elements. One is the shell model and its variants. The second is the QRPA and extensions their of. Both the shell model and the QRPA model besides having their own limitations fail to fulfil the Ikeda sum rule. The small predictive power of QRPA and their extensions is the main motivation for us to seek an alternative description which might result in a more reliable approach for the study of nuclear double beta decay processes. The main message of all the calculations using various approaches is to obtain fair agreement between experimental results and theoretical calculations.

D Calculation of Double Beta Decay Transition Matrix Elements in PHFB framework

The theoretical formalism to calculate the half-lives of DBD modes has been given by Doi et al [12, 13] and Suhonen [14]. Hence, we briefly outline steps of the above derivations for clarity in notation following Doi et al. Details of the mathematical expressions used to calculate electromagnetic properties are given by Dixit et al. [15].

The two neutrino double beta decay is a second order process in the effective weak interaction and takes place within the standard model of electroweak unification. Therefore these processes which only involve left-handed currents give dominant contributions. The half-life of the $2\nu\beta\beta$ decay mode for the $0^+ \rightarrow 0^+$ transition is given by

$$[T_{\frac{1}{2}}^{2\nu}(0^+ \rightarrow 0^+)]^{-1} = G^{2\nu} |M_{2\nu}|^2 \quad (1)$$

where the integrated kinematical factor $G^{2\nu}$ can be calculated with good accuracy and the NTME $M_{2\nu}$ is given by

$$M_{2\nu} = \sum_N \frac{\langle 0^+ || \sigma\tau^\pm || I_N^+ \rangle \langle I_N^+ || \sigma\tau^\pm || 0^+ \rangle}{E_N - (M_I + M_F)/2} \quad (2)$$

The summation over intermediate states can be completed using the summation method and one finally obtains

$$M_{2\nu} = \sum_{\pi, \nu} \frac{\langle 0_F^+ || \sigma \cdot \sigma\tau^\pm \tau^\pm || 0_I^+ \rangle}{E_0 + \epsilon(n_\nu, l_\nu, j_\nu) - \epsilon(n_\pi, l_\pi, j_\pi)} \quad (3)$$

By assuming that the contributions from heavy neutrinos are small, the summation \sum_i is taken over only on light neutrinos ($m_i < 100$ MeV). The half-life for $0\nu\beta\beta$ decay

is obtained integrating over ϵ_1 and $\cos\theta_{12}$

$$\left[\tau_{\frac{1}{2}}^{0\nu} (0^+ \rightarrow 0^+) \right]^{-1} = \frac{W^{0\nu}}{\ln 2} = A^{(0)} \quad (4)$$

where

$$\begin{aligned} A^{(i)} = & C_{mm}^{(e)} \left(\frac{\langle m_\nu \rangle}{m_e} \right)^2 + C_{\lambda\lambda}^{(e)} \langle \lambda \rangle^2 + C_{\eta\eta}^{(e)} \langle \eta \rangle^2 + C_{m\lambda}^{(e)} \left(\frac{\langle m_\nu \rangle}{m_e} \right) \langle \lambda \rangle \\ & + C_{m\eta}^{(e)} \left(\frac{\langle m_\nu \rangle}{m_e} \right) \langle \eta \rangle + C_{\lambda\eta}^{(e)} \langle \lambda \rangle \langle \eta \rangle \end{aligned} \quad (5)$$

Here

$$C_{mm} = (M_{GT}^{(0\nu)})^2 (\chi_F - 1)^2 G_{01} \quad (6)$$

$$C_{m\lambda}^{(e)} = (M_{GT}^{(0\nu)})^2 (\chi_F - 1) [-S_e \chi_{2-} G_{03}^{(e)} + \chi_{1+} G_{04}^{(e)}] \quad (7)$$

$$C_{m\eta}^{(e)} = (M_{GT}^{(0\nu)})^2 (1 - \chi_F) [S_e \chi_{2+} G_{03}^{(e)} - \chi_{1-} G_{04}^{(e)} - S_\beta (\chi_{P'})_R G_{06}^{(e)}] \quad (8)$$

$$\begin{aligned} C_{\lambda\lambda}^{(e)} = & (M_{GT}^{(0\nu)})^2 [\chi_{2-}^2 G_{02}^{(e)} - \frac{1}{9} f_e (2S_e \chi_{1+} \chi_{2-} G_{03}^{(e)} - \chi_{1+}^2 G_{04}^{(e)})] \\ C_{\eta\eta}^{(e)} = & (M_{GT}^{(0\nu)})^2 [\chi_{2-}^2 G_{02}^{(e)} - \frac{1}{9} f_e (2S_e \chi_{1-} \chi_{2+} G_{03}^{(e)} + \chi_{1-}^2 G_{04}^{(e)}) \\ & - S_e \chi']_R G_{07}^{(e)} + \chi' \end{aligned} \quad (9)$$

and

$$\begin{aligned} C_{\lambda\eta}^{(e)} = & -2(M_{GT}^{(0\nu)})^2 [\chi_{2-} \chi_{2+} G_{02}^{(e)} - \frac{1}{9} f_e \{ S_e (\chi_{1+} \chi_{2+} + \chi_{1-} \chi_{2-}) G_{03}^{(3)} \\ & - \chi_{1+} \chi_{1-} G_{04}^{(e)} \}] \end{aligned} \quad (10)$$

Where S_e takes $S_e = +1$ for $\beta^+ \beta^+$ mode while $S_e = -1$ for the $\beta^+ \text{EC}$ mode, $S_\beta = +1$ for both $\beta^- \beta^-$ and $S_\beta = -1$ for both $\beta^+ \beta^+$ and $\beta^+ \text{EC}$ modes. The factor f_e is defined as

$$f_e = \begin{cases} 1 & \text{for } \beta^+ \beta^+ \text{ mode} \\ 1 - \frac{3\alpha}{2m_e R} & \text{for } \beta^+ \text{EC mode} \end{cases} \quad (11)$$

The nuclear transition matrix elements $M_{GT}^{(0\nu)}$ and ratios χ 's are given by

$$M_{GT}^{(0\nu)} = \langle H(r_{12}) (s_1 \cdot s_2) \rangle \quad (12)$$

$$\left\{ \begin{array}{c} \chi'_{GT} \\ \tilde{\chi}'_{GT} \end{array} \right\} = \left\langle \left\{ \begin{array}{c} -r_{12} H'(r_{12}) \\ \tilde{H}'(r_{12}) \end{array} \right\} (\sigma_1 \cdot \sigma_2) \right\rangle / (M_{GT}^{(0\nu)}) \quad (13)$$

$$\left\{ \begin{array}{c} \chi'_F \\ \tilde{\chi}'_F \end{array} \right\} = \left(\frac{g_V}{g_A} \right)^2 \left\langle \left\{ \begin{array}{c} H(r_{12}) \\ -r_{12} H'(r_{12}) \\ \tilde{H}(r_{12}) \end{array} \right\} \right\rangle / (M_{GT}^{(0\nu)}) \quad (14)$$

$$\chi'_T = \langle -r_{12} H'(r_{12}) S_{12} \rangle / M_{GT}^{(0\nu)} \quad (15)$$

$$\chi'_P = \left(\frac{g_V}{g_A} \right) \left\langle -\frac{1}{2} r_{+12} H'(r_{12}) i(s_1 - s_2) \cdot (r_{12} \times r_{+12}) \right\rangle / M_{GT}^{(0\nu)} \quad (16)$$

$$\chi'_R = \frac{g_V}{g_A} \frac{M^{('0\nu)}_R}{M^{('0\nu)}_{GT}} \quad (17)$$

where $M^{('0\nu)}_R = \langle -\frac{1}{2}m_e^{-1}H'(r_{12})\mathbf{r}_{12} \cdot (s_1 \times D_2 - s_2 \times D_1) \rangle$ and their combinations

$$\chi_{1\pm} = \chi'_{GT} - 6\chi'_T \pm 3\chi'_F, \quad \chi_{2\pm} = \tilde{\chi}_{GT} \pm \tilde{\chi}_F - \frac{1}{9}\chi_{1\pm} \quad (18)$$

Here $r_{nm} = r_n - r_m$, $r_{+nm} = r_n + r_m$ and $S_{nm} = (s_n \cdot \hat{r}_{nm})(s_m \cdot \hat{r}_{nm}) - \frac{1}{3}\sigma_n \cdot \sigma_m$. Here n and m refer to two nucleons which participate in the decay. The recoil matrix element $M^{('0\nu)}_R$ can be decomposed into central, tensor, momentum-dependent and spin-orbit parts.

$$M^{('0\nu)}_R = M_{RC} + M_{RT} + M_{RP} + M_{RLS} \quad (19)$$

$$M_{RC} = \langle H_{RC}(r_{12})\sigma_1 \cdot \sigma_2 \rangle \quad (20)$$

$$M_{RT} = \langle H_{RT}(r_{12})S_{12} \rangle \quad (21)$$

$$M_{RP} = \langle \frac{1}{4m_e M} H'(r_{12})\hat{r}_{12} \times P_{12} \cdot (\sigma_1 - \sigma_2) \rangle \quad (22)$$

$$M_{RLS} = \langle -\frac{1}{2m_e M r_{12}} H'(r_{12})I_{12} \cdot (\sigma_1 + \sigma_2) \rangle \quad (23)$$

The neutrino potential $H_{RC}(r)$ and $H_{RT}(r)$ are given by

$$H_{RC}(r) = \frac{\mu_\beta}{3m_e M} (4\pi\delta(r) - \frac{2\hat{A}}{\pi r^2} + \hat{A}^2 H(r)) \quad (24)$$

$$H_{RT}(r) = -\frac{\mu_\beta}{2m_e M} (\frac{3}{r}H'(r) - \frac{2\hat{A}}{\pi r^2} + \hat{A}^2 H(r)) \quad (25)$$

The centre of mass momentum \mathbf{P}_{nm} and relative orbital angular momentum \mathbf{l}_{nm} are given by

$$P_{nm} = p_n + p_m \quad l_{nm} = r_{nm} \times \frac{1}{2}(p_n - p_m) \quad (26)$$

Table 1. Experimental half-lives along with their theoretically calculated values for $2\nu\beta^-\beta^-$ decay of ^{100}Mo for $0^+ \rightarrow 0^+$ transition. The numbers corresponding to (a) and (b) are calculated for $g_A=1.25$ and 1.0 respectively.

Experiment			Theory		
Ref.	Projects	Half-life ($T_{1/2}^{2\nu}$)	Ref.	Models	Half-life ($T_{1/2}^{2\nu}$)
					(a) (b)
[46]	ITEP+INFN	$(7.2 \pm 0.9 \pm 1.8) \times 10^{18}$		PHFD	9.79×10^{18} 23.9×10^{18}
[45]	ITEP	8.5	[52]	SSDH	$8.97-7.15 \times 10^{18}$
[44]	UC-Irvin	$6.82^{+0.38}_{-0.53} \pm 0.68 \times 10^{18}$	[51]	SRQRPA	$(5.04-16800) \times 10^{18}$
[43]	LBL+MHC+ UNM+INEL	$7.6^{2.2}_{-1.4} \times 10^{18}$	[33]	SU(4)	4.11×10^{18} 10.03×10^{18}
[42]	NEMO	$(9.7 \pm 0.4 \pm 0.9) \times 10^{18}$	[34]	SSDH	3.27×10^{18} 7.99×10^{18}
[41]	LBL	$(9.7 \pm 4.9) \times 10^{18}$	[35]	SRPA(WS)	3.04×10^{19} 7.43×10^{18}
[40]	ELEGANTSV	$(11.5^{+3.0}_{-2.0}) \times 10^{18}$	[47]	SU(3)(SPH)	4.59×10^{18} 1.12×10^{19}
[39]	UC-Irvin	$(1.16^{+0.34}_{-0.08}) \times 10^{19}$	[47]	SU(3)(DEF)	9.09×10^{18} 2.22×10^{19}
[38]	INS Baksan	$(3.3^{+2.0}_{-1.0}) \times 10^{18}$	[29]	OEM	3.64×10^{19} 8.888×10^{19}
[5]	Average value	$(8.0 \pm 0.6) \times 10^{18}$	[36]	QRPA(EMP)	2.73×10^{18} 6.67×10^{18}
[37]	Average value	$(8.0 \pm 0.6) \times 10^{18}$	[50]	QRPA(EMP)	1.62×10^{18} 3.95×10^{18}
			[49]	QRPA	1.10×10^{18}
			[48]	QRPA	2.38×10^{18} 5.81×10^{18}

The two body transition operators are short ranged. Hence the q^2 dependence of the form factor should be retained, meaning there by

$$g_V \rightarrow g_V \left(\frac{\Lambda^2}{\Lambda^2 + k^2} \right)^2 \text{ and } g_A \rightarrow g_A \left(\frac{\Lambda^2}{\Lambda^2 + k^2} \right)^2 \quad (27)$$

with $\Lambda=850$ MeV. Thus δ and $1/r^2$ are modified as follows

$$\delta(r) \rightarrow \frac{1}{(2\pi)^3} \int dk e^{ik \cdot r} \left(\frac{\Lambda^2}{\Lambda^2 + k^2} \right)^4 \frac{I}{r^2} \rightarrow \frac{1}{4\pi} \int dk e^{ik \cdot r} \frac{1}{k} \left(\frac{\Lambda^2}{\Lambda^2 + k^2} \right)^4 \quad (28)$$

The finite size effect of a nucleon is neglected for all other transition operators as they are relatively long ranged or contribute negligibly for the $0\nu\beta\beta$ decay rate.

E Results and Discussions

Recently we [15, 16] carried out study of the double beta decay of $^{100}\text{Mo} \rightarrow ^{100}\text{Ru}$ for $0^+ \rightarrow 0^+$ and $2^+ \rightarrow 2^+$ transition and $^{106}\text{Cd} \rightarrow ^{106}\text{Pd}$, that has been investigated by many experimental groups as well as theoreticians by employing different theoretical frameworks. Here we present study of Double beta decay processes in the medium mass range for these two very potential candidates from experimental point of view.

The calculations for ^{100}Mo , ^{100}Ru , ^{106}Cd and ^{106}Pd nuclei have been performed in a valance space spanned by the $1p_{1/2}$, $2s_{1/2}$, $1d_{3/2}$, $1f_{5/2}$, $0g_{7/2}$, $0g_{9/2}$ and $0h_{11/2}$ for protons and neutrons orbits treating the doubly even nucleus ^{76}Sr as an inert core. The effective two-body interaction that has been used in the present calculation is the pairing plus Quadrupole-Quadrupole type [17]. The pairing part of the effective interaction may be written as

$$V_P = -\left(\frac{G}{4}\right) \sum_{\alpha\beta} S_{\alpha} S_{\beta} a_{\alpha}^{\dagger} a_{\bar{\alpha}}^{\dagger} a_{\bar{\beta}} a_{\beta} \quad (29)$$

where α denotes the quantum numbers ($nljm$). The state $\bar{\alpha}$ is same as α but with the sign of m reversed and S_{α} is the phase space factor $(-1)^{j-m}$. The $q-q$ part of the effective interaction is given by

$$V_{q,q} = -\left(\frac{\chi}{2}\right) \sum_{\alpha\beta\gamma\delta} \sum_{\mu} \langle \alpha | q_{\mu}^2 | \gamma \rangle \langle \beta | q_{-\mu}^2 | \delta \rangle \times (-1)^{\mu} a_{\alpha}^{\dagger} a_{\beta}^{\dagger} a_{\delta} a_{\gamma} \quad (30)$$

where the quadrupole operator q_{μ}^2 is written as $q_{\mu}^2 = \left(\frac{16\pi}{5}\right)^{1/2} r^2 Y_{\mu}^2(\theta, \varphi)$. The strength of the pairing interaction was fixed through the relation $G_p = (30/A)$ MeV and $G_n = (20/A)$ MeV which are same as used by Heestand et al to explain the experimental $g(2^+)$ data of some even-even Ge, Se, Mo, Ru, Pd, Cd and Te isotopes in Greiner's collective model. The strengths of the like particle components of the QQ interaction are taken as: $\chi_{pp} = \chi_{nn} = -0.0105$ MeV b^{-4} , where b is oscillator parameter. The strength of proton-neutron pn component of the QQ interaction χ_{pn} is varied so as to reproduce the experimentally observed excitation energy of the 2^+ state (E_{2^+}) as closely as possible. Thus for a given model space, SPE's, G_p , G_n and χ_{pp} , we have fixed χ_{pn} through the experimentally available energy spectra. These values for the strength of the QQ

Table 2. Experimental half-lives along with their theoretically calculated values for $2\nu\beta^+\beta^+/\beta^+\text{EC}/\text{ECEC}$ decay of ^{106}Cd for $0^+ \rightarrow 0^+$ transition. The numbers corresponding to (a) and (b) are calculated for $g_A=1.25$ and 1.0 respectively.

Mode of Decay	Experiment		Ref.	Model	Theory	
	Ref.	Half-life ($T_{1/2}^{2\nu}$) (in yrs.)			Half-life ($T_{1/2}^{2\nu}$) (in yrs.)	
					(a)	(b)
$\beta^+\beta^+$	[25]	$>45.0 \times 10^{18}$	Present	PHFB	307.58×10^{25}	777.71×10^{25}
	[24]	$>2.54 \times 10^{20**}$	[32]	SQRPA(l.b.)	5.38×10^{25}	13.6×10^{25}
	[23]	$>1.0 \times 10^{19*}$		SQRPA(s.b.)	6.16×10^{25}	15.58×10^{25}
	[22]	$>9.2 \times 10^{17}$	[31]	QRPA(AWS)	3.84×10^{25}	9.72×10^{25}
	[20]	$>5.0 \times 10^{17}$		QRPA(WS)	72.71×10^{25}	183.84×10^{25}
	[19]	$>2.6 \times 10^{17*}$	[23]	QRPA	3.3×10^{25}	8.33×10^{25}
					2.84×10^{25}	7.18×10^{25}
			[29]	QRPA	42.2×10^{25}	106.6×10^{25}
			[27]	QRPA	3.48×10^{25}	8.79×10^{25}
					6.93×10^{25}	17.52×10^{25}
$\beta^+\text{EC}$	[25]	$>1.2 \times 10^{18}$	Present	PHFB	77.925×10^{21}	197.03×10^{21}
	[24]	$>4.1 \times 10^{20}$	[32]	SQRPA(l.b.)	1.36×10^{21}	3.44×10^{21}
	[23]	$>0.66 \times 10^{19*}$		SQRPA(s.b.)	1.56×10^{21}	3.94×10^{21}
	[22]	$>2.6 \times 10^{17}$	[31]	QRPA(AWS)	0.98×10^{21}	2.49×10^{21}
	[19]	$>5.7 \times 10^{17*}$		QRPA(WS)	17.99×10^{21}	44.0×10^{21}
			[33]	SU(4)	13.39×10^{21}	33.86×10^{21}
			[30]	RQRPA(AWS)	1.62×10^{21}	4.098×10^{21}
				RQRPA(WS)	1.68×10^{21}	4.24×10^{21}
			[23]	QRPA(AWS)	0.83×10^{21}	2.11×10^{21}
				QRPA(WS)	0.72×10^{21}	1.82×10^{21}
			[29]	QRPA	4.1×10^{21}	10.4×10^{21}
			[28]	QRPA(AWS)	1.16×10^{21}	2.95×10^{21}
				QRPA(WS)	2.09×10^{21}	5.28×10^{21}
ECEC	[26]	$>1.0 \times 10^{18}$	Present	PHFB	97.59×10^{20}	246.76×10^{20}
	[25]	$>5.8 \times 10^{17}$	[32]	SQRPA(l.b.)	1.96×10^{20}	4.96×10^{20}
	[21]	$>5.8 \times 10^{17}$		SQRPA(s.b.)	2.6×10^{20}	6.57×10^{20}
			[31]	QRPA(AWS)	1.23×10^{20}	3.12×10^{20}
				QRPA(WS)	22.52×10^{20}	56.95×10^{20}
			[34]	SSDH	8.11×10^{20}	20.50×10^{20}
					22.00×10^{20}	55.62×10^{20}
			[33]	SU(4)	16.77×10^{20}	39.40×10^{20}
			[30]	RQRPA(AWS)	2.03×10^{20}	5.13×10^{20}
				RQRPA(WS)	2.10×10^{20}	5.31×10^{20}
			[23]	QRPA(AWS)	1.05×10^{20}	2.64×10^{20}
				QRPA(WS)	0.90×10^{20}	2.28×10^{20}
			[29]	QRPA	8.7×10^{20}	22.1×10^{20}
			[28]	QRPA(AWS)	1.46×10^{20}	3.69×10^{20}
				QRPA(WS)	2.62×10^{20}	6.61×10^{20}

Table 3. Experimental half-lives along with their theoretically calculated values for $0\nu\beta\beta$ decay of ^{100}Mo and ^{106}Cd for $0^+ \rightarrow 0^+$ transition.

Nuclei	Mode of Decay	Experiment		Theory		
		Ref.	Half-life	Ref.	Model	Half-life
^{100}Mo	$\beta^-\beta^-$	[55]	$>5.5 \times 10^{22}$	Present	PHFB	2.03×10^{24}
		[54]	$>1.6 \times 10^{21}$	[56]	QRPA	$(1.1-1.3) \times 10^{23}$
				[57]	QRPA	4.4×10^{23}
				[58]	QRPA	5.8×10^{23}
				[59]	QRPA	2.6×10^{23}
				[60]	QRPA	36.0×10^{26}
^{106}Cd	$\beta^+\beta^+$	[24]	$>2.4 \times 10^{20}$	Present	PHFB	13.21×10^{28}
		[25]	$>0.8 \times 10^{19}$	[32]	SQRPA	1.0×10^{28}
				[29]	QRPA	0.48×10^{28}
	$\beta^+\text{EC}$	[24]	$>3.7 \times 10^{20}$	Present	PHFB	90.05×10^{26}
		[25]	$>0.7 \times 10^{20}$	[32]	SQRPA	7.0×10^{26}
				[29]	QRPA	3.4×10^{26}

interaction are comparable to those suggested by Arima on the basis of an empirical analysis of the effective two-body interactions.

It is observed that PHFB results give nearly identical $M_{2\nu}$ value to those of Hirsch et al [47] in SU3(SPH) model. They are close to the experimental result given by De Silva et al for $g_A=1.25$ while for $g_A=1.0$, the $M_{2\nu}$ are in agreement with the results of NEMO. The calculated values given by other versions of QRPA by Stoica using SRPA(Ws) [35] are too low and those from Suhonen et al [36] are slightly on higher side. Further the value of $M_{2\nu}$ given by Hirsch et al using SU3(DEF) favors the results of NEMO for $g_A=1.25$.

Another case that we have very recently studied [18] is for the $0^+ \rightarrow 0^+ e^+\beta\beta$ ($\beta^+\beta^+$, $\beta^+\text{EC}$ and ECEC) decay of $^{106}\text{Cd} \rightarrow ^{106}\text{Pd}$. This transition has also been investigated by some experimental groups and also in different theoretical frameworks. In Table 2, we have compiled some of the latest available experimental and the theoretical results along with our calculated $M_{2\nu}$ and corresponding half-lives $T_{1/2}^{2\nu}$. Our calculated values are in reasonable agreement with the recently given QRPA results of Suhonen and Civitaressa [31] for all the three modes. The theoretical values of PHFB and SU(4) $_{\tau\sigma}$ [33] are in quite good agreement for the $\beta^+\text{EC}$ and ECEC modes. Further, we have observed that the np interactions viz a viz the deformations of the intrinsic ground states of ^{100}Mo , ^{100}Ru , ^{106}Cd and ^{106}Pd play important role in arriving at the appropriate nuclear matrix elements.

To summarize, it is clear that the validity of nuclear models presently employed to calculate the $M_{2\nu}$ cannot be uniquely established due to error bars in experimental results as well as uncertainty in g_A . Further work is necessary both on the experimental and theoretical front to judge the relative applicability, success and failure of various models used so far for the study of double beta decay processes. The quality of HFB wave functions has to be first tested by comparing the theoretically calculated results for

a number of spectroscopic properties of nuclei involved in double beta decay. Reliability of the intrinsic wave functions for calculation of $2\nu\ \beta\beta$ nuclear matrix elements, $M_{2\nu}$ has to be established. A reasonable agreement between the calculated and observed spectroscopic properties as well as the $2\nu\ \beta\beta$ decay rate of most of the nuclei in medium mass region makes us confident to employ the PHFB wave functions to the study of $0\nu\ \beta\beta$ decay.

References

1. Goeppert-Mayer, Phys. Rev. 48, 512 (1935).
2. G. Racah, Nuovo Cim.4, 322 (1937).
3. W. Fury, Phys. Rev. 56, 1184 (1939)
4. E. Majorana, Nuovo Cim.5, 171 (1937).
5. E. R. Elliott and P. Vogel, Annu. Rev Nucl. Part. Sci. 52, 115 (2002).
6. Faessler and F. Simkovic, hep-ph/9901215; J. Phys. G 24, 2139 (1998).
7. W. C. Haxton and G. J. Stephenson Jr., Prog. Part. Nucl. Phys. 12, 409 (1984).
8. K. Zuber, Phys. Rep 305, 295 (1998).
9. V. I. Tretyak, Y. G. Zdesenko, At. Data and Nucl. Data Tables 61, 43 (1995)
10. V. I. Tretyak, Y. G. Zdesenko, At. Data and Nucl. Data Tables 80, 83 (2002).
11. H. V. Klapador et al Modern Physics Letters A16, No. 37, 2409 (2001).
12. M. Doi, T. Kotani and E. Takasugi, Prog. Theo. Phys. Suppl. 83, 1 (1985).
13. M. Doi and T. Kotani, Prog. Theor. Phys. 87, 1207 (1992).
14. J. Suhonen and O. Civitarese, Phys. Rep. 300, 123 (1998).
15. B. M. Dixit, P. K. Rath and P. K. Raina, Phys. Rev. C65, 034311 (2002). Phys. Rev. C67, 059901 (2003).
16. K. Chaturvedi, B. M. Dixit, P. K. Rath and P. K. Raina, Phys. Rev. C67, 064317 (2003).
17. M. Baranger and K. Kumar, Nucl. PhysA110, 490(1968).
18. A. Shukla, P.K.Raina, R. Chandra P.K.Rath and J. G. Hirsch Eur. Phys. J. A 23, 235 (2005).
19. E. B. Norman and A. DeFaccio, Phys. Lett 148B, 31(1984).
20. L. W. Mitchell and P. H. Fisher, Phys. Rev C38, 895(1988).
21. A. Sh. Georgadze et al. Phys. At. Nucl 58, 1093 (1995).
22. F. A. Danevich et al., Z. Phys. A355, 433 (1996).
23. A. S. Barabash et al., Nucl. Phys. A604, 115 (1996).
24. P. Belli et al., Astroparticle Phys. 10, 115 (1999).
25. F. A. Danevich et al., Phys. Rev. C68, 035501 (2003).
26. K. Zuber Eur Phys J C (2003) (in Press)
27. A. Staudt, K. Muto, H. V. Klapdor-Kleingrothaus, Phys. Lett. 268B, 312 (1991).
28. J. Suhonen, Phys. Rev. C48, 574 (1993).
29. M. Hirsch, K. Muto, T. Oda, H. V. Klapdor- Kleingrothaus, Z. Phys. A347, 151 (1994).
30. J. Toivanen and J. Suhonen, Phys. Rev. C 55, 2314 (1997).
31. J. Suhonen and O. Civitarese, Phys. Lett. B 497, 221 (2001).
32. S. Stoica, and H.V. Klapdor-Kleingrothaus Eur. Phys. J. A17, 529 (2003).
33. O. A. Rumyantsev and M. G. Urin, Phys. Lett. B 443, 51 (1998).
34. O. Civitarese and J. Suhonen, Phys. Rev. C58, 1535 (1998).
35. S. Stoica, Phys. Lett. B350, 152 (1995).
36. J. Suhonen and O. Civitarese, Phys. Rev. C49, 3055 (1994).
37. A.S. Barabash, Czech. J. Phys. 52, 567 (2002).
38. S.I. Vasilev et al., JETP Lett. 51, 622 (1990); 58, 178 (1993).
39. S.R. Elliott, M.K. Moe, M.A. Nelson, M.A. Vient, J. Phys. G 17, S145 (1991).

40. H. Ejiri et al., J. Phys. G 17, 155 (1991).
41. A. Garcia et al., Phys. Rev. C 47, 2910 (1993).
42. D. Dassié et al., (NEMO collaboration), Phys.Rev.D 51, 2090 (1995).
43. M. Alston Garnjost et al., Phys. Rev. C 55, 474 (1997).
44. A. De Silva, M. K. Moe, M. A. Nelson and M. A. Vient, Phys. Rev. C 56, 2451 (1997).
45. V. D. Ashitkov et al., Phys. At. Nucl., 2044 (1999).
46. V. D. Ashitkov et al., JETP Lett. 74, 529 (2001).
47. J. G. Hirsch, O. Castanos, P. O. Hess and O. Civitarese, Phys. Rev. C 51, 2252 (1995).
48. J. Engel, P. Vogel, M.R. Zirnbauer, Phys. Rev. C 37, 731 (1988).
49. A. Staudt, K. Muto, H.V. Klapdor, Europhys. Lett. 13, 31 (1990).
50. A. Griths, P. Vogel, Phys. Rev. C 46, 181 (1992).
51. A. Bobyk, W.A. Kaminski, P. Zareba, Nucl. Phys. A 669 221 (2000).
52. F. Simkovic, P. Domin and S. V. Semenov, nucl-th/0006084.
53. S. Stoica, Phys. Rev. C 49, 2240 (1994).
54. A. S. Barbash et al. Phys. Lett. B 345, 408 (1995).
55. H. Ejiri et al. Phys. Rev. C 63, 065501 (2001).
56. S. Stoica and H. V. Klapdor-Kleingrothaus, Phys. Rev. C 63, 064304 (2001).
57. F. Simkovic, G. Pantis, J. D. Vergados, and A. Faessler, Phys. Rev. C 60, 055502 (1999).
58. C. Barbero, F. Krmpotic, A. Mariano, and D. Tadic, Nucl. Phys. A 650, 485 (1999).
59. F. Simkovic, J. Schwieger, G. Pantis, and A. Faessler, Found. Phys. 27, 1275 (1997).
60. G. Pantis, F. Simkovic, J. D. Vergados, and A. Faessler, Phys. Rev. C 53, 695 (1996).

A new symmetry for triton clustering in nuclei

Afsar Abbas*

Institute of Physics, Bhubaneswar-751005, India

Abstract. It is generally believed that quarks being confined inside nucleons should make their presence felt explicitly in nuclei only at higher energies. However it is shown here that the hole in the centre of 3H , 3He and 4He , the neutron halos in nuclei, the α - and other clustering effects in nuclei and the nuclear molecules all basically arise due to the same underlying quark effects. The role of triton clustering in very neutron rich nuclei is emphasized. All these require the concept of hidden colour states which arise from confinement ideas of QCD for the multi-quark systems. The cluster structure of the ground state and of the low-lying states of 6He , 6Li , 6Be and 8He is clarified. It is now known that in neutron rich nuclei, old magic numbers disappear and new ones appear. We show that nuclei with $(Z, N) = (6, 12), (8, 16), (10, 20), (11, 22)$ and $(12, 24)$ exhibit exceptional stability or magicity. As such these magic numbers appear in pairs. This correlation is shown here to be indicative of predominance of tritons in the ground state of these neutron rich nuclei. Thus ${}^{30}_{10}Ne_{20}$ has the structure of $10\,{}^3_1H_2$ in the ground state. It is shown here that this is due to fundamental symmetry arguments based on a new symmetry group $SU(2)_A$ christened as 'husospin'.

A Introduction (signature of quarks in ground state of nuclei)

It is a popular belief that nucleonic degrees of freedom are all that is required for a consistent description of the ground state and low energy properties of nuclei. It is shown here that there are specific nuclear effects wherein no way that one can do without invoking the quark degrees of freedom. A claim shall be made that only within the nucleonic and mesonic degrees of freedom these effects can just not be described consistently [1].

The effects that we shall concentrate upon are, the hole at the centre of 3H , 3He and 4He [2,3], the neutron halo nuclei [4], the clustering effects in nuclei [5] and the nuclear molecules [6]. As we shall see below, this would require an understanding of two or more nucleons strongly overlapping over a small region of $\leq 1\,fm$. This would necessarily imply a study of multi-quark states in regions $\leq 1\,fm$.

As we shall be discussing the structure of nuclei in the ground state, we should also have the structure of nucleons in the ground state as well. Hence we view the nucleon as consisting of 3 constituent quarks in the s-state. Note that though the r.m.s. radius of nucleon is 0.8 fm, it is a very diffuse system with matter distribution given by $\rho(r) = \rho_0 \exp(-mr)$ and hence matter extends significantly beyond 0.8 fm.

* Email: afsar@iopb.res.in

B Hidden colour in multi-quark configurations

Why does deuteron not have configurations where the two nucleons overlap strongly in regions of size $\leq 1\text{fm}$ to form 6-quark bags ? Why is deuteron such a big and loose system ? The reason has to do with the structure of the 6-q bags formed had the two nucleons overlapped strongly. As per the colour confinement hypothesis the 6-q wave function looks like [7] :

$$|6q\rangle = \frac{1}{\sqrt{5}}|1X1\rangle + \frac{2}{\sqrt{5}}|8X8\rangle \quad (1)$$

where '1' represents a 3-quark cluster which is singlet in colour space and '8' represents the same as octet in colour space. Hence $|8X8\rangle$ is overall colour singlet. This part is called the hidden colour because as per confinement ideas of QCD these octets cannot be separated out asymptotically and so manifest themselves only within the 6-q colour-singlet system. This part was found to be 80% and this would prevent the two nucleons to come together and overlap strongly [7]. Therefore the hidden colour would manifest itself as short range repulsion in the region $\leq 1\text{fm}$ in deuteron. So the two nucleons though bound, stay considerably away from each other [2,3].

The author had earlier obtained group theoretically the hidden colour components in 9- and 12-quark systems [2,3]. For the ground state and low energy description of nucleons we assume that $SU(2)_F$ with u- and d-quarks is required. Hence we assume that 9- and 12-quarks belong to the totally antisymmetric representation of the group $SU(12) \supset SU(4)_{SF} \otimes SU(3)_C$ where $SU(3)_C$ is the QCD group and $SU(4)_{SF} \supset SU(2)_F \otimes SU(2)_S$ where S denotes spin. Note that up to 12-quarks can sit in the s-state in the group $SU(12)$. The calculation of the hidden colour components for 9- and 12-quark systems requires the determination of the coefficients of fractional parentage for the group $SU(12) \supset SU(4) \otimes SU(3)$ [1,2] which becomes quite complicated for large number of quarks. The author found that the hidden colour component [1,2] of the 9-q system is 97.6% while the 12-q system is 99.8% ie. is almost completely coloured.

C On holes, halos and nuclear molecules

What is the relevance of these 9- and 12-quark configurations in nuclear physics ? The $A=3,4$ nuclei ${}^3\text{H}$, ${}^3\text{He}$ and ${}^4\text{He}$ have sizes of 1.7 fm, 1.88 fm and 1.674 fm respectively. Given the fact that each nucleon is itself a rather diffuse object, quite clearly in a size $\leq 1\text{fm}$ at the centre of these nuclei the 3 or 4 nucleons would overlap strongly. As the corresponding 9- and 12-q are predominantly hidden colour, there would be an effective repulsion at the centre keeping the 3 or 4 nucleons away from the centre. Hence it was predicted by the author [2,3] that there should be a hole at the centre of ${}^3\text{H}$, ${}^3\text{He}$ and ${}^4\text{He}$. And indeed, this is what is found through electron scattering.

Neutron halos have been discovered in several neutron rich nuclei like ${}^6\text{He}$, ${}^{11}\text{Li}$, ${}^{11}\text{Be}$, ${}^{14}\text{Be}$ etc. [4]. For example the rms radius of ${}^{11}\text{Li}$ is 3.2 fm while that of ${}^9\text{Li}$ is 2.3 fm. Hence in this halo nuclei it is believed that 2n are very loosely bound to a compact core of ${}^9\text{Li}$. So also the 2n in ${}^6\text{He}$ etc.

As to ${}^4\text{He}$ it is a very strongly bound system with binding energy of 28.29 MeV. It is a compact object of size 1.674 fm. Due to specific quark hidden colour state, as we discussed above, it has a hole of size $\sim 1\text{fm}$ at the centre. Thus it has a significantly higher density at the boundary and very small at the centre. Hence ${}^4\text{He}$ is like a tennis-ball. Add two more neutrons to ${}^4\text{He}$ to make it ${}^6\text{He}$, a bound system. This is like adding 2 neutrons to a tennis-ball nucleus. As the two neutrons approach the surface they will bounce off. A neutron halo would be manifested as these neutrons shall be kept significantly away from the core.

Macroscopically, as the density of the ${}^4\text{He}$ core is high on the boundary, any extra neutrons would not be able to penetrate as this would entail much larger density on ${}^4\text{He}$ surface than the system would allow dynamically. Microscopically, any penetration of extra neutron through the surface of ${}^4\text{He}$ would necessarily imply the existence of five or six nucleons at the centre. As already indicated due to the relevant SU(12) group only 12-quarks can sit in the s-state, which already is predominantly hidden colour. Any extra quarks hence would have to go to the p-orbital and in the ground state of nuclei, there is not sufficient energy to allow this. Hence the two neutrons are consigned to stay outside the ${}^4\text{He}$ boundary. In addition if at any instant the two neutrons come close to each locally the system would be like three nucleons overlapping and looking like a 9-q system. This too would be prevented by the local hidden colour repulsion.

Clusters, especially ${}^4\text{He}$ have an important role in nuclear structures [6]. These are crucial for light nuclei like ${}^8\text{Be}$, ${}^7\text{Be}$, ${}^6\text{Li}$, ${}^7\text{Li}$, ${}^{12}\text{C}$, ${}^{16}\text{O}$. Even for heavier nuclei like ${}^{20}\text{Ne}$, ${}^{24}\text{Mg}$, ${}^{28}\text{Si}$, ${}^{44}\text{Ti}$ and others they are important [6]. It is commonly stated that ${}^4\text{He}$ clusters are formed in nuclei because it is so strongly bound, ie. 28.29 MeV. Here we would like to point out that ${}^4\text{He}$ forms good clusters because in addition it has a hole at the centre so it is like a tennis-ball. The reason for resistance to inter-penetration of two α clusters would be hidden colour repulsion of the relevant 6-, 9- and 12-quark systems plus the fact that more than 12 quarks are not permitted in the lowest s- state in the group SU(12).

Let us treat ${}^{12}\text{C}$ as 3α cluster with the α 's sitting at the vertices of an equilateral triangle. Hidden colours would imply a depression in the central density of ${}^{12}\text{C}$. Indeed, from the density distribution determination by electron scattering, this is so in ${}^{12}\text{C}$. ${}^{16}\text{O}$ treated as 4α sitting at the vertices of a regular tetrahedron would, for the reasons stated above, too have a central density depression, again as seen in the electron scattering. Due to the central depression, ${}^{12}\text{C}$ and ${}^{16}\text{O}$ would appear tennis-ball like as well [1]. No wonder one observes nuclear molecules in C-C, C-O, O-O systems. The stability of nuclear molecules has to do with the bounciness of the C,O nuclei coupled with the fact that their large size is due to the largeness of the constituent clusters. Also obviously molecular structures would exist for nuclei ${}^{20}\text{Ne}$, ${}^{24}\text{Mg}$, ${}^{28}\text{Si}$ and ${}^{32}\text{S}$ [9,10]. Hence nuclear molecules [6] too arise basically due to quark effects [1].

Going through the binding energy systematics of neutron rich nuclei one notices that as the number of α 's increases along with the neutrons, each ${}^4\text{He} + 2n$ pair tends to behave like a cluster of two ${}^3_1\text{H}_2$ nuclei. Remember that though ${}^3_1\text{H}_2$ is somewhat less strongly bound (ie. 8.48 MeV) it is still very compact (ie. 1.7 fm), almost as compact as ${}^4\text{He}$ (1.674 fm). In addition it too has a hole at the centre. Hence ${}^3\text{H}$ is also tennis-ball like nucleus. This splitting tendency of neutron rich nuclei becomes more marked

as there are fewer and fewer of ${}^4\text{He}$ nuclei left intact by the addition of $2n$. Hence ${}^7\text{Li}$ which is ${}^4\text{He} + {}^3\text{H}$ with $2n$ becomes ${}^9\text{Li}$ which can be treated as made up of 3 ${}^3\text{H}$ clusters and should have hole at the centre. Similarly ${}^{12}\text{Be}$ consists of 4 ${}^3_1\text{H}_2$ clusters and ${}^{15}\text{B}$ of 5 ${}^3_1\text{H}_2$ clusters etc. Other evidences like the actual decrease of radius as one goes from ${}^{11}\text{Be}$ to ${}^{12}\text{Be}$ supports the view that it (ie ${}^{12}\text{Be}$) must be made up of four compact clusters of ${}^3\text{H}$.

Note that just as several light $N=Z$ nuclei with $A=4n$, $n=1,2,3,4 \dots$ can be treated as made up of n α clusters, in Table 1 we show several neutron rich nuclei which can be treated as made up of n ${}^3_1\text{H}_2$ clusters. We can write the binding energy of these nuclei as [1]

$$E_b = 8.48n + Cm \quad (2)$$

Here n ${}^3_1\text{H}_2$ clusters form m bonds and where C is the inter-triton bond energy. We notice from Table that this holds good and that the inter-triton cluster bond energy is approximately 5.4 MeV. This value seems to work for even heavier neutron rich nuclei. For example for ${}^{42}\text{Si}$ the inter-triton cluster energy is still 5.4 MeV. Notice that the geometry of these cluster structures of ${}^3\text{H}$ becomes more complex as the number increases but nevertheless still holds good. Thus all light neutron rich nuclei ${}^{3Z}_Z\text{A}_{2Z}$ are made up of Z ${}^3_1\text{H}_2$ clusters. The proton halo nuclei can also be understood in the same manner. Here another nucleus with a hole at the centre ${}^3_2\text{He}_1$ (binding energy 7.7 MeV, size 1.88 fm) would play a significant role.

Table 1. Neutron rich nuclei with inter-triton cluster bond energies

Nucleus	n	m	$E_B - 8.48n(\text{MeV})$	$C(\text{MeV})$
${}^9\text{Li}$	3	3	19.90	6.63
${}^{12}\text{Be}$	4	6	34.73	5.79
${}^{15}\text{B}$	5	9	45.79	5.09
${}^{18}\text{C}$	6	12	64.78	5.40
${}^{21}\text{N}$	7	15	79.43	5.29
${}^{24}\text{O}$	8	18	100.64	5.59

D Clusters in light nuclei

Cluster structure forms an important aspect of modern nuclear studies. It is generally believed that for the ground state and the low excited states of ${}^6\text{Li}$ (α -n-p) (or (α -d)) configuration is much more important than (h-t) (note: $h = {}^3\text{He}$) [eg. 8 (p.115), 9 (p.104)]. Most of the studies recently follow this line of (α -n-p) being significant for the ground state and the low-lying excitations [8,9]. Meanwhile there have been compelling experimental evidences which indicate that the (h-t) configuration for ${}^6\text{Li}$ cannot be ignored, and may be quite important [10]. It turns out that the two cluster configurations (α -d) and (h-t) are not mutually exclusive and that they can both be present as they are

not orthogonal either [8,11]. A few recent theoretical studies also support this view [14]. Recent experimental study of tri-nucleon cluster knockout for ${}^6\text{Li}$ favours simultaneously existing (α -d) and (h-t) structures [12]. The problem is that (α -d) and (h-t) configuration of ${}^6\text{Li}$ are not orthogonal and it is hard to give physical interpretation to the relative weights of these configurations [8,p.43].

In oscillator model the ground state of ${}^6\text{Li}$ is described by the following wave functions of equivalent forms [8,p.40, appendix C]

$$\psi_{gs}({}^6\text{Li}) = A\{\phi_0(\alpha)\phi_0(d)\chi(\alpha-d)\} = NA(\phi_0(t)\phi_0(h)\chi(t-h)) \quad (3)$$

Here $\chi(\alpha-d)$ and $\chi(t-h)$ are two oscillator quanta wave functions and $\phi_0(\alpha)$, $\phi_0(d)$, $\phi_0(t)$, $\phi_0(h)$ are the internal wave functions. The constant N is here to ensure that the two functions are equal to each other. The mathematical equivalence of the two can be easily demonstrated. Since they are the same, these can exist simultaneously and also note that these are not orthogonal [8]. None of this is changed even with the hard core of the Jastrow form in the two body interaction [8, p.113].

E Wounds due to multinucleon forces in nuclei

However, in the above mathematical proof, there is an underlying ansatz - which is that in the Schrodinger equation one need go only up to two-body interactions and ignore all many body forces like the Three Body Forces (3BF) V_{ijk} [6, p.1]. This was perhaps acceptable in the 60's but today we know that for A=3 nuclei 'h' and 't' there is no way we can obtain the binding energies and the rms radii for these nuclei without invoking some form of a simple or a more complicated 3BF may be active too. Let us accept that 3BF and 4BF are needed in a basic way for the study of light nuclei. These will manifest themselves in any physical situation where it would be essential to consider overlap of multi-nucleons.

Let the Hamiltonian for upto A=4 system be

$$H = \sum_i^A \frac{p_i^2}{2m} + \sum_{i<j}^A v_{ij} + \sum_{i<j<k}^A V_{ijk} + \sum_{i<j<k<l}^A V_{ijkl} \quad (4)$$

where v_{ij} , V_{ijk} and V_{ijkl} are NN, NNN and NNNN potentials respectively. For A=2 system only the first two terms would be present. While for A=3 system the NNN term would also be contributing. Only for A=4 system does the 4BF term contribute.

Now let us use this Hamiltonian to solve that A=2,3,4 body problems in nuclear physics. We may use the Quantum Monte Carlo method or some other method to obtain the best fits to all the relevant experimental quantities of these nuclei which are: ${}^2\text{H}$, ${}^3\text{H}$ and ${}^3\text{He}$ and ${}^4\text{He}$. Let us assume that we are able to do as good a job as possible. At the end of the day let the wave functions which provided these fits be $\psi_0(d)$, $\psi_0(t)$, $\psi_0(h)$ and $\psi_0(\alpha)$. (Note : d= ${}^2\text{H}$, t= ${}^3\text{H}$, h= ${}^3\text{He}$ and α = ${}^4\text{He}$)

Note that all these wave functions are solutions of Hamiltonian which have components not present in all of these. For example the A=4 case the wave function has "wounds" inflicted by the 4BF which are not present in the others. As such the wave

function for $A=4$ case has components which can not be reduced to any (2-body)-(2-body) or (3-body)-(1-body) wave functions. In the same manner the $A=3$ case have "wounded" wave functions unique to themselves and irreducible to any other system of wave functions. These 3BF and 4BF "wounds" in the wave functions in a way are unique signatures of their presence in $A=3$ and 4 systems. Hence due to the reasons indicated above the projection of the wave function $\phi_0(\alpha)\phi_0(d)$ on $\phi_0(t)\phi_0(h)$ would be zero. Hence the putative equivalence of different multi-clusters [8-11] for light nuclei and which forms the backbone of studies of nuclei at present is wrong and should be abandoned. Also on these physical ground that these two clusters : (α -d) and (h-t) should be orthogonal to each other.

F Ikeda-like diagrams for triton clustering in nuclei

It was suggested by Ikeda [13] that cluster like configurations would appear in light $A=4n$ self conjugate nuclei near the threshold energy for breakup into proper sub-nuclei. In our model here as triton clustering appears to be such a dominant effect for neutron rich nuclei [1], then quite clearly we should expect that for nuclei ${}^Z_Z A_{2Z}$ similar triton rich cluster structures would exist (for example ${}^9\text{Li}$ in the ground state is 3-t in triangular configuration). Therefore configurations with neutron rich nuclei would appear near the threshold energy for decay into corresponding relevant sub-nuclei. These Ikeda - like diagrams are here given in Figure 1. So as not to clutter the figure not all the relevant diagrams are shown here.

Recently exotic molecular states in ${}^{12}\text{Be}$ have been found [14]. This was in the study of breakup of ${}^{12}\text{Be}$ into ${}^6\text{He} + {}^6\text{He}$ and ${}^4\text{He} + {}^8\text{He}$. These molecular resonances can be understood in our model in terms of Ikeda-like diagrams given here. Thus we can treat this experiment to be confirming our prediction here also. Our unique prediction is the configurations ${}^9\text{Li} + t$ for ${}^{12}\text{Be}$ breakup.

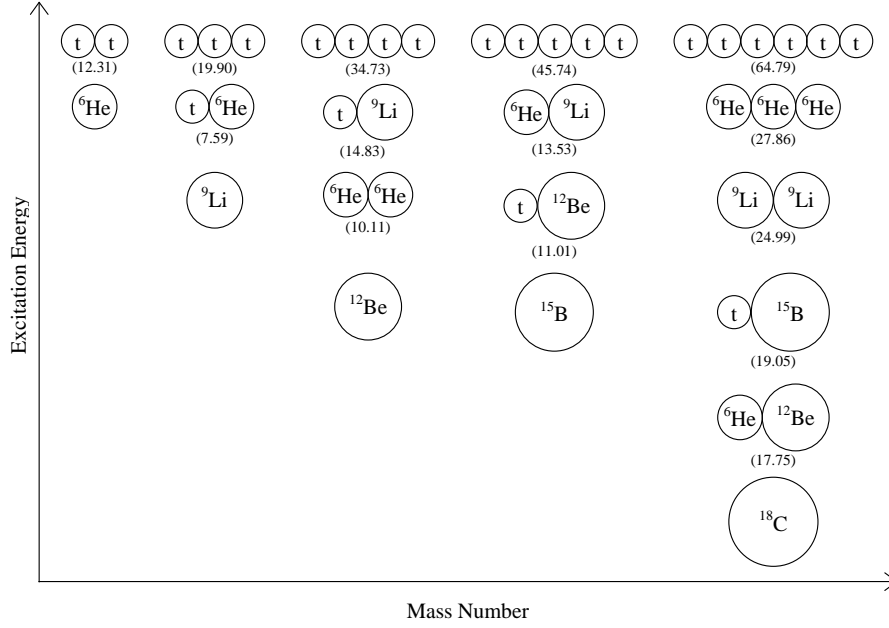
G Tetraneutron and the structure of ${}^8\text{He}$

While the nucleus ${}^6\text{He}$ seems to have a structure $\alpha + 2n$, with the two neutrons making up a clear cut halo structure around an inert α [15], the situation for ${}^8\text{He}$ is known to be more complicated [15]. What is the halo structure in ${}^8\text{He}$?

Two very different and independent experiment [16,17] reveal identity of structure for ${}^8\text{He}$. These seem to be ruling out the standard and canonical (but somewhat simplistic) $\alpha + 4n$ structure of ${}^8\text{He}$.

The first experiment [16] is that of the study of scattering of ${}^8\text{He}$ on ${}^4\text{He}$ with the aim of detecting the tetraneutronic structure of ${}^8\text{He}$. They considered a one step direct $4n$ transfer process and a two step sequential transfer process of $2n$ clusters proceeding through the intermediate ground state and the first excited 2^+ state (at 1.8 MeV) in ${}^6\text{He}$. Their DWBA calculations indicated that the two step $2n$ transfer is clearly more important than the one step $4n$ transfer. This experiment therefore clearly disfavors the $\alpha + 4n$ cluster structure of ${}^8\text{He}$ [16].

In the second experiment [17] they studied the two neutron transfer reactions $p({}^8\text{He}, t){}^6\text{He}_{gs}$ and $p({}^8\text{He}, t){}^6\text{He}^*(2^+)$ for the ground state and the first excited states of ${}^6\text{He}$

Fig. 1. Ikeda - like diagrams for neutron rich nuclei ${}^{3Z}_{Z}A_{2Z}$.

respectively. One expects that if the ground state of ${}^8\text{He}$ contains the subsystem ${}^6\text{He}$ mainly in the 0^+ state, then this would be preferentially populated in ${}^8\text{He}(p, t)$ reaction. Then it being a second order process, the cross section for the population of ${}^6\text{He}^*(2^+)$ would be considerably lower. Contrary to these expectations they found the cross section of the $p({}^8\text{He}, d){}^6\text{He}^*(2^+)$ reaction to be much higher than that of $p({}^8\text{He}, d){}^6\text{He}_{gs}$. One therefore concludes [17] that the ground state of ${}^8\text{He}$ contains subsystem ${}^6\text{He}$ in the excited state 2^+ with a large weight.

Hence what both these two experiments are showing is that ${}^8\text{He}$ has a two-tier structure with its ground state having ${}^6\text{He}$ in an the excited state (2^+ at 1.8 MeV). Therefore the structure of ${}^8\text{He}$ is very different from that of ${}^6\text{He}$. Note that in the excited state 2^+ the structure of ${}^6\text{He}$ may not remain pure $\alpha + 2n$ but may go over to another configuration - that of ${}^3\text{H} + {}^3\text{H}$ (ie $t+t$). And this is exactly what my model predicts [1].

H A double potential model for neutron halo nuclei

A unique feature is that for all the single neutron halo nuclei discovered so far the ground state spin has always been $\frac{1}{2}^+$. At present this is being interpreted as shifting and mixing of single particle levels in the shell model [18]. Here we make a novel suggestion of a double potential shell model which accounts for both the loose halo structure and its ground state spin.

Let us use the fact that the core is almost decoupled from the valence neutrons. In simple shell model we know the central potential follows rather closely the nuclear density distribution.

$$V = -V_0 \int_0^\infty \rho(r) r^2 dr \quad (5)$$

Let us put the empirical fact that the total density in a halo nucleus may be written as made up of a core and a halo part

$$\rho(r) = \rho_{core} + \rho_{halo} \quad (6)$$

And thus the total potential separates out as

$$V = V_{core} + V_{halo} \quad (7)$$

We suggest that these features are hinting at the existence of double potential for these nuclei. A schematic plot of such a double potential well is given in Figure 2. Let us take ${}^{11}_4\text{Be}_7$ as an example. Here as per empirical information ${}^{10}_4\text{Be}_6$ forms a core and a single neutron orbiting it in a loose halo around this core. We assume that the core ${}^{10}_4\text{Be}_6$ is built as per standard shell structure in the inner potential in Fig 1. The second potential structure assumes that it exists because there exists a primary inner potential. Now the last valence neutron fills the orbits in the second potential starting with the s-state. Hence its spin is $\frac{1}{2}^+$ which also is the spin of the whole nucleus ${}^{11}_4\text{Be}_7$. This is the situation in all the single neutron halo nuclei.

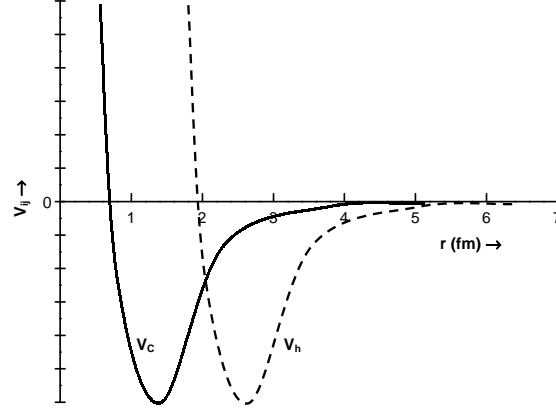
This picture predicts that as the lowest orbital in the second potential can absorb only upto two neutrons so halos should most likely be observed for upto two neutrons. If one wants to add more neutron one has to send it to the higher p- state.

I A new “nusospin” symmetry

Note that ‘n’ and ‘p’ are members of an isospin doublet. These combine together to give a bound triplet state (S=1, T=0), that is deuteron with a binding energy of 2.2 MeV. It has no excited states. The singlet state (S=0, T=1) is unbound by 64 keV. This being isospin partner of (n-n) (S=0, T=1) and (p-p) (S=0, T=1), all these are unbound.

Here we suggest a new symmetry in the same neutron rich nuclei [19]. Herein triton (“t”) ${}^3_1\text{H}_2$ helion (“h”) ${}^3_2\text{He}_1$ are treated as fundamental representations of a new symmetry group $SU(2)_A$ [19]. To distinguish it from isospin symmetry this new symmetry is christened as “nusospin”.

As above ‘h’ and ‘t’ are members of “nusospin”. Note that though both ‘n’ and ‘p’ are composites of three quarks these still act as elementary particles as far as low-energy excitations of nuclear physics are concerned. Only at relatively higher energies does the compositeness of ‘n’ and ‘p’ manifest itself. Similarly the binding energies of ${}^3\text{He}$ and ${}^3\text{H}$ are 7.72 MeV and 8.48 MeV respectively and also these two have no excited states. Hence for low-energy excitations, of a few MeV, we may consider these as elementary. Hence, we would expect for (h-t) the triplet (S=1, T=0) to be bound and singlet (S=0, T=1) to be unbound. Also, its isospin partners (h-h) (S=0, T=1) and (t-t) (S=0, T=1) would be unbound too.

Fig. 2. Schematic double well potential to explain the properties of halo nuclei

This means that (h-h) ($S=0$, $T=1$) being unbound would not mix with the bound (α -n-n) configuration of ${}^6\text{He}$ for the ground state. Similarly, the (t-t) ($S=0$, $T=1$) being unbound would not mix with the bound (α -p-p) ground state configuration of ${}^6\text{Be}$. Therefore, ${}^6\text{He}$ and ${}^6\text{Be}$ in its ground state and low excited states remain pure (α -N-N) configuration. However, things are different for ${}^6\text{Li}$. Here in ${}^6\text{Li}$ the (h-t) ($S=1$, $T=0$) configuration is bound with no other excited state. Being bound, it is close to the bound ground state of the orthogonal configuration (α -d). Thus for the ground state of ${}^6\text{Li}$ the two states (h-t) ($S=1$, $T=0$) and (α -d) ($S=1$, $T=0$) actually co-exist.

J Resolution of puzzles in light nuclei

Thus we expect that for the ground state of ${}^6\text{Li}$ ($S=1$, $T=0$), these two different cluster structures (α -d) and (h-t) would mix and repel. Thus, for the ground state wave function would be

$$\psi({}^6\text{Li}) = a\psi(\alpha - p - n) + b\psi(h - t) \quad (8)$$

with $a^2 + b^2 = 1$. The amplitude 'a' and 'b' would be found from best fits to suitable experiments. As per various studies one would expect 'a' to be more dominant for the ground state, but that 'b' is not negligible and actually should be quite significant [19].

If this be so, there should exist another higher-lying ($S=1, T=0$) orthogonal state in ${}^6\text{Li}$ with wave function

$$\psi^*({}^6\text{Li}) = b\psi(\alpha - p - n) - a\psi(h - t) \quad (9)$$

with 'a', 'b' the same as in $\psi({}^6\text{Li})$. Indeed, this state exists as the 5.65 MeV excited state in ${}^6\text{Li}$ [19] and we identify $\psi^*({}^6\text{Li})$ with this. So both the ground state and the 5.65 MeV states are mixed states of these two orthogonal cluster structures. Hence, rest of the low-lying states in ${}^6\text{Li}$ (as in ${}^6\text{He}$ and ${}^6\text{Be}$) should be of simple (α -N-N) structure.

Note that for $\psi(\alpha$ -p-n) amplitude 'a' is much larger than the $\psi(h$ -t) amplitude for the ground state and thus the $\psi(\alpha$ -p-n) or $\psi(\alpha$ -d) configuration would be much smaller than the corresponding $\psi(h$ -t) amplitude for the 5.65 MeV ($1+, 0$) state. The normal beta decay of ${}^6\text{He}$ proceeds almost entirely to the 1^+ ground state of ${}^6\text{Li}$ which as discussed is mainly of (α -d) configuration. The other beta-delayed deuteron emission in our picture goes almost entirely to the 5.65 MeV 1^+ state in ${}^6\text{Li}$. Therefore in our model the weakness in the intensity of the branch is mainly due to the small fraction of (α -d) existing in that state.

Fig. 3. Single neutron separation energy as a function of Z for fixed N

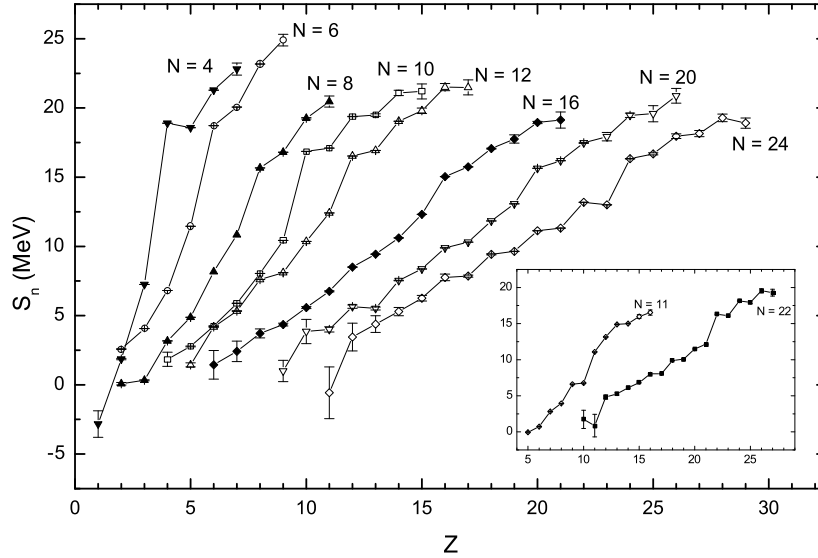


Fig. 4. Double neutron separation energy as a function of Z for fixed N

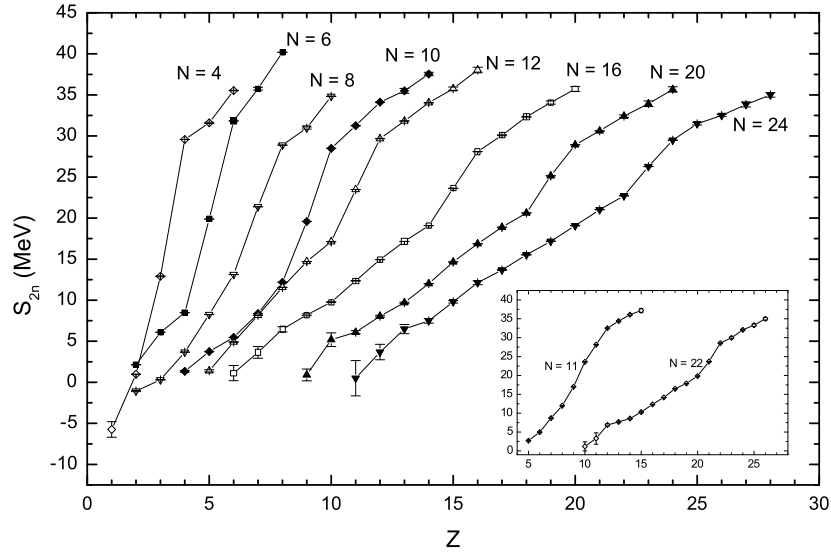


Fig. 5. Single neutron separation energy as a function of N for fixed Z

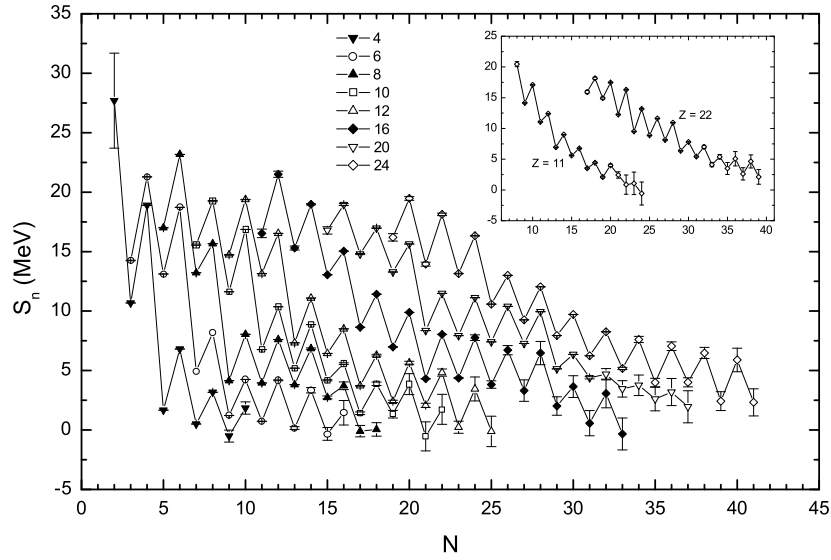


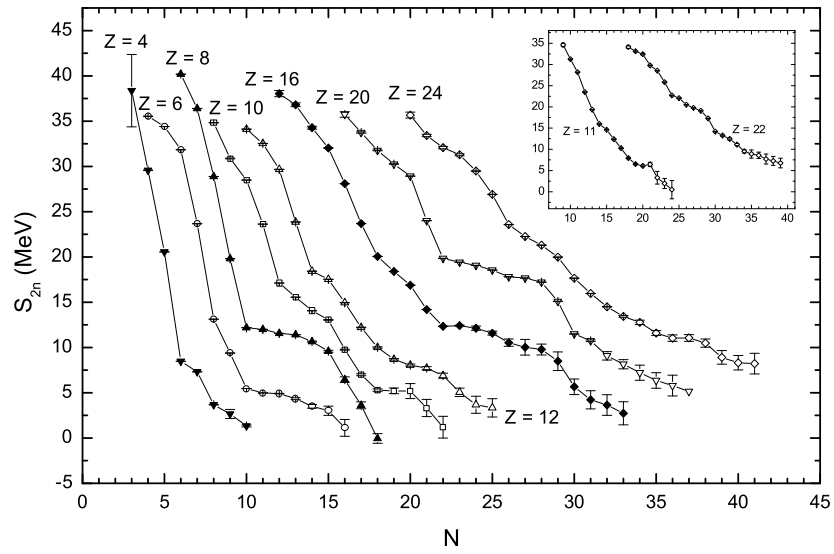
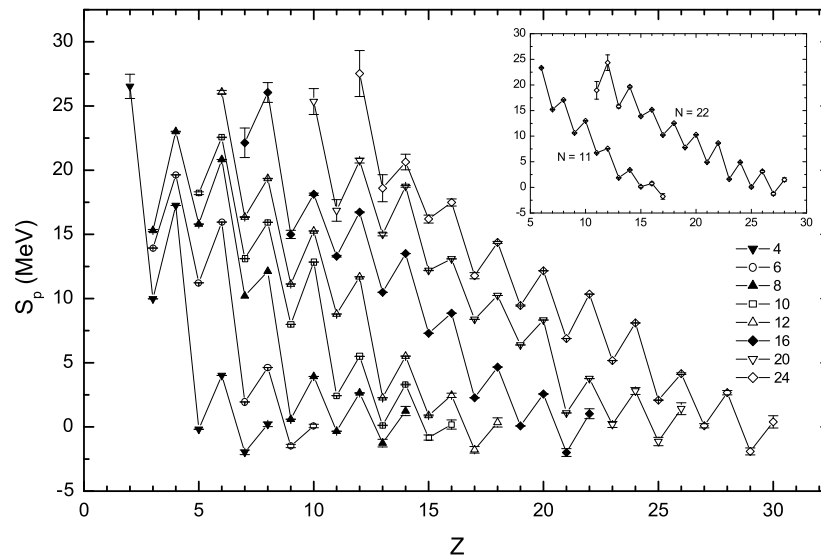
Fig. 6. Double neutron separation energy as a function of N for fixed Z **Fig. 7.** Single proton separation energy as a function of Z for fixed N 

Fig. 8. Double proton separation energy as a function of Z for fixed N

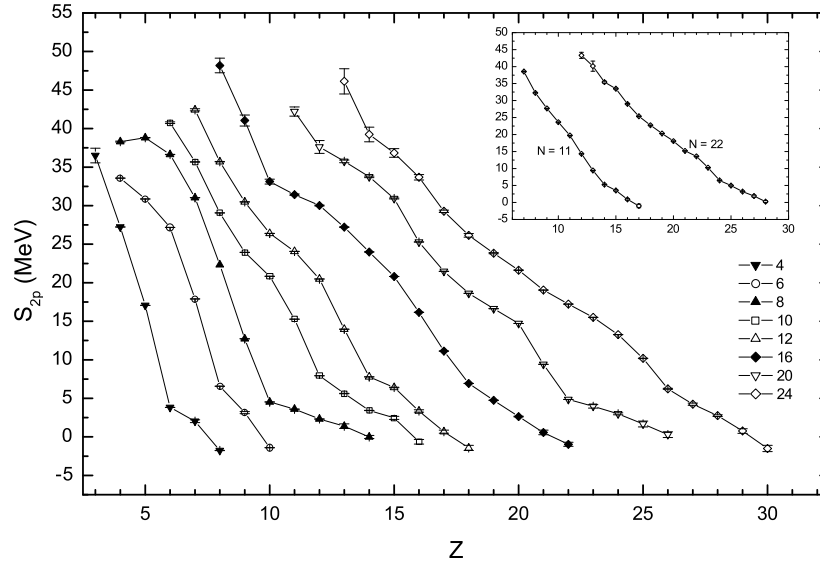


Fig. 9. Single proton separation energy as a function of N for fixed Z

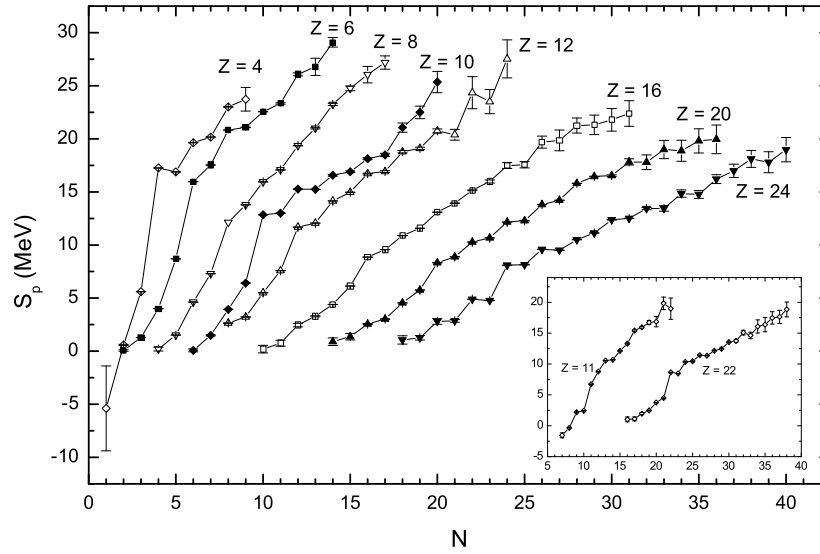
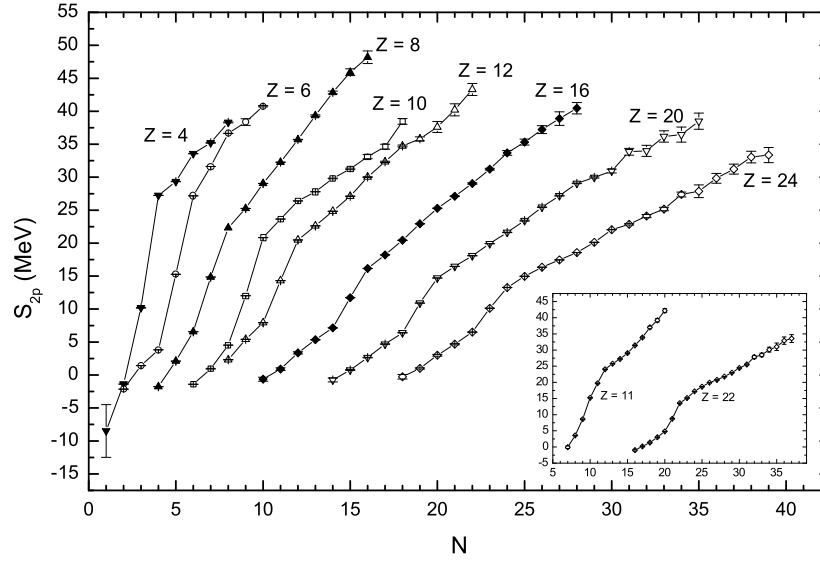


Fig. 10. Double proton separation energy as a function of N for fixed Z

K New magic numbers due to triton clustering in nuclei

It has recently been found that in nuclei the standard magic numbers may disappear and new ones may arise in an unanticipated manner as neutron number increases [18,19]. As indicated above triton ("t") ${}^3_1\text{H}$ helion ("h") ${}^3_2\text{He}$ are treated as fundamental representations of a new symmetry group $SU(2)_A$ called "nusospin" [19]. Even the isospin symmetry between neutron and proton is broken. So we expect that this new symmetry should be broken as well - in fact more so.

To see how this new symmetry is likely to manifest itself we look at other symmetry groups which are known to be broken. So in quark model we know that progressively the flavour symmetry groups $SU(2)$, $SU(3)$, $SU(4)$ etc for more number of quark flavours are broken more and more strongly. In fact $SU(5)$ for five quark flavours u, d, s, c and b quarks is very strongly broken. However it still manifests itself in particle physics. Its most clearly manifestation is in terms of representations of all the particles built up of any of these 5 quarks. So also in the case of our new symmetry in nuclei - $SU(2)_A$ this may be minimum expectation as well. Hence as already suggested [1,19] the particle representation of nuclei of the form ${}^{3Z}_Z A_{2Z}$ nuclei would be that of Z number of tritons.

So let us ask as to what this new symmetry "nusospin" $SU(2)_A$ has to tell us about new magicities. Clearly the fact that ${}^{3Z}_Z A_{2Z}$ nuclei are made up of Z number of tritons leads to new stability for them.

To discuss magicity one normally plots separation energies S_{1n} and S_{2n} as a function of neutron number N for a particular proton number Z or plot S_{1p} and S_{2p} as a function of Z for a particular N . We plot the separation energies a little differently. We plot S_{1n} and S_{2n} as a function of Z for a particular N . The same with S_{1p} and S_{2p} as a function of N for a particular Z . We shall find here that these new plots give useful and distinguishable information regarding stability and magicity in these light nuclei.

We plot separation energies for neutron number N and for proton number Z fixed separately at 4, 6, 8, 10, 11, 12, 16, 20, 22 and 24. For example Fig 1 and Fig 2 are respectively plots of S_{1n} and S_{2n} for fixed $N=4, 6, 8, 10, 11, 12, 16, 20, 22$ and 24 plotted as a function of Z . Figs 3 and 4 are respectively plots of S_{1n} and S_{2n} for fixed $Z=4, 6, 8, 10, 11, 12, 16, 20, 22$ and 24 as a function of N . Figs 5 and 6 plot S_{1p} and S_{2p} respectively for N fixed at the above set as a function of Z and Figs. 7 and 8 are S_{1p} and S_{2p} plotted respectively for Z fixed at the above set for different N . So what we have plotted are N fixed (isotoness) for S_{1n} , S_{2n} , S_{1p} and S_{2p} all as functions of Z and also for Z fixed (isotopes) S_{1n} , S_{2n} , S_{1p} and S_{2p} all as functions of Z .

The reader's attention is drawn to the extra-ordinary stability manifested by the plotted data for the proton and neutron pairs (Z,N) : (6,12), (8,16), (10,20), (11,22) and (12,24). In fact the Z,N pair (10,20) stands out as the best example of this. These new magicities present in the neutron rich sector for the pair (Z,N) where $N=2Z$.

What is the significance of this extraordinary stability or magicity for the nuclei ${}^{3Z}_{Z}A_{2Z}$? Quite clearly the only way we can explain the extra magicity for these $N=2Z$ nuclei is by invoking the significance of triton clustering in the ground state of these neutron rich nuclei. Thus ${}^{30}_{10}\text{Ne}_{20}$ has significant mixture of the This is a natural expectation due to the new "nusospin" symmetry.

L Future directions

We have found that the study of neutron rich nuclei has brought out the role of triton clustering in nuclei. It has led us to propose a new symmetry "nusospin" for the group $SU(2)_A$. As it arises within nuclei and competes with isospin symmetry of proton and neutron it is clear that it should have much significance in future studies in nuclei. A few possibilities:

1. It should be possible to understand how alpha arises near $N=Z$ line while as one goes away to neutron rich sector triton clustering becomes significant.
2. As "nusospin" is a fundamental symmetry even for $N=Z$ sector all three: alphas, tritons and helions should be significant,
3. The new symmetry predicts that for ${}^{3Z}_{Z}A_{2Z}$ nuclei because of triton clustering, while looking for superheavy nuclei one should look for nuclei with $N=2Z$ which are predicted to be more stable.
4. It is possible that one should be talking of triton stars. As per "nusospin" there should be a strong tendency for triton stars to be formed. In fact what may be believed to be neutron stars today may turn out to be triton stars under closer scrutiny.

Acknowledgement: I would like to thank Dr P Arumugam for the figures.

References

1. A. Abbas, *Mod. Phys. Lett. A* **16** (2001) 755
2. A. Abbas, *Phys. Letts.* **167 B** (1986) 150
3. A. Abbas, *Prog. Part. Nucl. Phys.* **20** (1988) 181
4. I. Tanihata, *J. Phys.* **G22** (1996) 157
5. P. E. Hodgson, *Z. Phys.* **A 349** (1994) 197
6. W. Greiner, J. Y. Park and W. Scheid, 'Nuclear Molecules', World Scientific Publishing Co. Ltd., Singapore, 1995.
7. V. A. Matveev and P. Sorba, *Lett. al Nuovo Cim.* **20** (1977) 435
8. K. Wildermuth and W. McClure, *Springer Tracts in Modern Physics* , **41** (1966), Springer Verlag, Berlin.
9. K. Langanke, *Adv. Nucl. Phys.* **21** (1994) 82.
10. F. Young, P.D. Forsyth and J.D. Marion. *Nucl. Phys.* **91**(1971) 209.
11. R.D. Amado and J.V. Noble, *Phys. Rev.* **C3** (1971) 2494.
12. J.P. Connelly, B.L. Berman, W.J. Briscoe, K.S.Dhuga, A. Mokhtari, D. Zubanov, H.P. Blok, R. Ent, J.H. Mitchell and L.Lapikas, *Phys. Rev.* **C57** (1998) 1569.
13. K. Ikeda, N. Takigawa and H. Horiuchi, *Suppl. Prog. Phys. (Japan) Extra* (1969) 464
14. M. Freer et. al., *Phys. Rev. Lett.* **82** (1999) 1383
15. I.Tanihata, D. Hirata, T. Kobayashi, S. Shimoura, K. Sugimoto and H. Toki, *Phys. Lett.* **B289** (1992) 261
16. R. Wolski, S. I. Sidorchuk, G. M. Ter-Akopian, A. S. Fomichev, A. M. Rodin, S. V. Stepantsov, W. Mittig, P. Roussel-Chomoz, H. Savajols, N. Alamanos, F. Auger, V. Lapoux, R. Raabe, Yu. M. Tchuvil'sky and K. Rusek, *Nucl. Phys.* **A 722** (2003) 55c
17. A. A. Korshennikov, *Nucl. Phys.* **A 722** (2003) 157c
18. I. Tanihata, *Nucl. Phys.* **A 682**, (2001) 114c
19. A. Abbas, *Mod. Phys. Lett. A* **19** No. 31 (2004) 2365

The Generator Coordinate Method and Role of Pauli Principle in the Structure of Light Nuclei

V.K. Sharma

Department of Physics, CCS University of Meerut, Meerut 250 004, India

Abstract. A general formalism is presented for the structure of light nuclei particularly ${}^7\text{Li}$ as an example within the framework of generator coordinate method (GCM), which is the coexistence of shell model and cluster aspects-a unique feature in light nuclei. The alpha-triton relative wave function and bremsstrahlung weighted cross-section with various nucleon exchange contributions are also calculated. It is noticed that the GCM take into account antisymmetrization properly and thus justify the role of Pauli principle in the structure of light nuclei. Various electromagnetic properties and RMS radii of ${}^7\text{Li}$ and other light halo nuclei is also obtained which is in close agreement with the experiment.

A Introduction

During the systematic investigation of atomic nuclei it was realised that their properties exhibit a large complexity and variety, ranging from single-particle features to many different kinds of collective features. For their description, various nuclear models have been developed, such as the liquid drop model, the compound nucleus model, the optical model, the direct interaction model, the various α -particle models, the shell model and its variations e.g. like the Hartree-Fock(HF) method, the BCS model, the Hartree-Fock-Bogolubov(HFB), the Boson Expansion methods, the Independent Boson Model(IBM), unified Bethe-Bruckner method, the Time-Dependent-Hartree-Fock(TDHF) method and other statistical models including the collective model. In HF method it is assumed that each nucleon of the nucleus moves independently in a potential field that is the sum of the interactions of this nucleon with all the other nucleons of the nucleus, averaged over the wave functions of those other nucleons. The effective nucleon-nucleon interaction from which the repulsive core has been removed can only be used in the calculations. In BCS model n-n, p-p pairing is considered like in BCS theory, as the correlation over single-particle features. The HFB is considered as HF with deformation and BCS pairing, also known as modified single-particle shell-model. In the boson expansion method the fermions space is mapped onto a different Hilbert space, a space of bosons as:

$$\begin{array}{c} \mathcal{H}_F \\ \text{Fock Space} \end{array} \longleftrightarrow \mathcal{H}_{\text{Phys}} \subset \begin{array}{c} \mathcal{H}_B \\ \text{Boson Space} \end{array} \text{(Mapping)}$$

The boson space is given by a boson vacuum $|0\rangle$ and boson creation B_μ^\dagger and annihilation B_μ operators as,

$$B_\mu |0\rangle = 0, \quad [B_\mu, B_{\mu'}] = 0, \quad [B_\mu^\dagger, B_{\mu'}^\dagger] = 0, \quad [B_\mu^\dagger, B_{\mu'}] = \delta_{\mu\mu'}.$$

In above models various possible ways are discussed for the motion of nucleons inside the nucleus. For example, in the compound nucleus model it is assumed that the nucleons interact so strongly with each other that any approximate independent motion of the nucleons inside the nucleus is not possible and therefore the motions of the nucleons are strongly correlated with each other. On the contrary in the shell-model it is assumed that the nucleons inside the nucleus in zero approximation move independently of each other. The idea of independent particles is accepted in almost all the models. It is quite natural to consider that the single-particle motion is governed by some average potential or mean field created by all the nucleons inside the nucleus. It is to be noted that the motion of the nucleons will be considerably different in the interior of the nucleus, where it is more or less force free and Pauli principle is important, from the one at the surface where the Pauli principle ceases to act and the particles feel a force of confining them to the interior of the nucleus. The single-particle model takes into account the individual nucleons. It therefore provides a microscopic description of the nucleus. This is certainly only an approximation to the exact nuclear many-body problem.

In 1937 John A. Wheeler had introduced the idea of resonating group method (RGM). In which it is assumed that *the nucleons in nuclei spend fraction of their time in various subgroups or clusters e.g. α -particle cluster*. One important idea of RGM is that, because of on the average attractive nature of the nuclear interaction relatively long range correlation exists in nuclei, which result in large probabilities of finding the nucleons group together and the nucleons are exchanged between one group to another. These groups are known as nuclear clusters. The RGM yielded results, which generally agreed with the experiment, but due to difficulties in computation this method is generally used to study only very light nuclear systems. With the remarkable success of the shell-model by Mayer and Jensen (1950,1951) and its generalization to the collective model by Bohr and Mottleson (1952), the cluster-model based on the RGM where the motions of the nucleons inside the nucleus are strongly correlated has completely overshadowed.

At the same time a method known as the generator coordinate method (GCM) by Hill-Wheeler (1953) and Griffin-Wheeler(1957) for the description of collective nuclear motion, is developed. This method is based on the viewpoint that *the nucleons in nuclei form various subgroups and nucleons of each subgroup move independently of each other like in the shell-model descriptions. The relative separation of shell-model potentials are known as the generator coordinate (GC)*.

The importance of Pauli principle is fully accepted in the light nuclear systems. This is mainly due to the Pauli principle which, via the antisymmetrization of the wave function, reduces the differences between various nuclear models, all of which had some success in predicting nuclear characteristics. Due to antisymmetrization the microscopic methods like RGM and GCM have some remarkable advantages desired for nuclear studies:

- Antisymmetrization is exactly taken into account.
- The centre-of-mass motion is treated correctly.
- Good quantum numbers can be introduced without any approximation.

- Asymptotically the clusters in RGM can be identified with real physical fragments, thus allowing for a natural approach to a microscopic collision theory.

These microscopic methods allow for a consistent, unified and successful description of bound, resonant and scattering states of a nuclear systems. A detailed and extensive account of these developments in GCM [1–3] and RGM [4] have been given in several basic books and reviews in the literature.

In light nuclear systems, the few-body techniques are increasingly becoming an important tool in various studies so as to provide valuable pieces of information, about the nucleon-nucleon interaction and nuclear structure such as halo structure as three-body systems and to understand the mechanism of various nuclear reactions. Some of the above informations are already obtained by solving few-nucleon problem. For example using MITRA three-body wave function, it is justified that the WHEELER'S fundamental idea (1937) of resonating group structure comes through the FEW-BODY DYNAMICS. The four-body system is the simplest one in the light nuclei and exhibit the structure different from the three-body system as it has been established that the co-existence of shell structure and cluster structure exists in light nuclei by SHARMA [5]. Therefore, it becomes necessary to consider the microscopic structure for four-nucleon system in terms of the exact FADDEEV-YAKUBOVSKY equations and its reduction within the framework of RGM which is also equivalent to the generator coordinate method. SASAKAWA [6] has also shown that his four-body equations are equivalent to the description that four nucleon system is the coexistence of shell-model and cluster-model, which is also the physical interpretation of the GCM.

In this paper we consider the microscopic structure of light nuclei such as ${}^7\text{Li}$, which is most recently [7] studied in the relativistic dissociation using photoemulsion technique, as an example within the framework of our GCM. Section 2 discuss the technique in detail itself. In Section 3 we discuss the role of Pauli principle in alpha-triton relative wave function and in the photodisintegration of ${}^7\text{Li}$. Section 4 give the detailed technique for the calculations of the electromagnetic properties of ${}^7\text{Li}$ including RMS radii of light halo nuclei. In Section 5 we present the summary and conclusion.

B Generator Coordinate Method

B.1 Basic Definitions and Two-Centre Generator Coordinate Function

The two-centre slater determinant wave function for ${}^7\text{Li}$ having alpha (α) and triton (t) configuration is a superposition of generator coordinate (GC) function of the form,

$${}^7\text{Li}\Phi_{\alpha+t}(\mathbf{x}_1, \mathbf{x}_3, \mathbf{x}_5, \mathbf{S}_1; \mathbf{x}_2, \mathbf{x}_4, \mathbf{x}_6, \mathbf{S}_2) = \frac{1}{\sqrt{7!}} \det \left[\prod_{i=1, \text{odd}}^{\leq 7} \phi_{\alpha_i}(\mathbf{x}_i, \mathbf{S}_1), \prod_{j=1, \text{even}}^{\leq 7} \phi_{\alpha_j}(\mathbf{x}_j, \mathbf{S}_2) \right] \quad (1)$$

where the single-particle wave function is given by

$$\phi_{\alpha_i}(\mathbf{x}_i, \mathbf{S}_j) = \phi_{n_i \ell_i m_i}(\mathbf{r}_i - \mathbf{S}_j) \chi_{m_{\sigma_i} m_{\tau_i}}(\boldsymbol{\sigma} \boldsymbol{\tau}) \quad (2)$$

Here the spatial function is taken as $(0s)^4$ for alpha and $(0s)^3$ for triton configuration and χ denotes the product of spin-isospin function with the single-particle spatial function in $(0s)$ orbital as

$$\phi_{n_i \ell_i m_i}(\mathbf{r}_i - \mathbf{S}_j) = [\beta_i/\pi]^{\frac{3}{4}} \exp[-\beta_i(\mathbf{r}_i - \mathbf{S}_j)^2] \quad (3)$$

We introduce the Jacobi coordinates for ${}^7\text{Li}$ as,

$$\xi_\alpha \equiv \begin{cases} \xi_{13} = \mathbf{r}_1 - \mathbf{r}_3 \\ \xi_{13,5} = (\mathbf{r}_1 + \mathbf{r}_3)/2 - \mathbf{r}_5 \\ \xi_{135,7} = (\mathbf{r}_1 + \mathbf{r}_3 + \mathbf{r}_5)/3 - \mathbf{r}_7 \\ \mathbf{R}_\alpha = (\mathbf{r}_1 + \mathbf{r}_3 + \mathbf{r}_5 + \mathbf{r}_7)/4 \end{cases} \quad ; \quad \xi_t \equiv \begin{cases} \xi_{24} = \mathbf{r}_2 - \mathbf{r}_4 \\ \xi_{24,6} = (\mathbf{r}_2 + \mathbf{r}_4)/2 - \mathbf{r}_6 \\ \mathbf{R}_t = (\mathbf{r}_2 + \mathbf{r}_4 + \mathbf{r}_6)/3 \end{cases} \quad (4)$$

and,

$$\mathbf{r} = \mathbf{R}_\alpha - \mathbf{R}_t, \quad \mathbf{R}_G = (4\mathbf{R}_\alpha + 3\mathbf{R}_t)/7 \quad ; \quad \mathbf{s} = \mathbf{S}_1 - \mathbf{S}_2, \quad \mathbf{S}_G = (4\mathbf{S}_1 + 3\mathbf{S}_2)/7. \quad (5)$$

Here \mathbf{R}_G and $\mathbf{S}_G = 0$ denote the total centre-of-mass (CM) of the intrinsic and generator coordinates respectively of the two subgroups alpha and triton of ${}^7\text{Li}$ nucleus.

The model Hamiltonian with the above basis configuration is of the form,

$$H = \left[-\frac{\hbar^2}{2m} \sum_{i=1}^7 \nabla_i^2 - T_{\text{CM}} \right] + \sum_{i < j}^7 V_{ij}^N + \sum_{i < j}^7 V_{ij}^C. \quad (6)$$

where two-body nuclear interaction is given by

$$V_{ij}^N = (w + m \mathbf{P}_{ij}^\sigma \mathbf{P}_{ij}^\tau) V^N(r_{ij}), \quad (7)$$

with

$$V_{ij}^N = V_a \exp[-(r_{ij}/a_1)^2] + V_r \exp[-(r_{ij}/a_2)^2]; \quad (8)$$

and coulomb potentials given as,

$$V_{ij}^C = \frac{1}{4} [1 + \tau_{iz}(i)][1 + \tau_{iz}(j)] (e^2/4\pi\epsilon_0) \frac{1}{|\mathbf{r}_i - \mathbf{r}_j|}, \quad (9)$$

where w and m denote the Wigner and the Majorana constants such that $w + m = 1$, \mathbf{P}_{ij}^σ (\mathbf{P}_{ij}^τ) are the spin (isospin) exchange operators and we have used Volkov V2 forces with coulomb forces represented in terms of gaussian form.

B.2 Matrix Elements of Normalization and Hamiltonian Matrix

The normalization matrix elements is defined by,

$$N(\mathbf{s}, \mathbf{s}') = \langle {}^7\text{Li} \Phi_{\alpha+t}(\mathbf{x}, \mathbf{s}) | \mathbf{I} | {}^7\text{Li} \Phi_{\alpha+t}(\mathbf{x}, \mathbf{s}') \rangle, \quad (10)$$

where the ${}^7\text{Li} \Phi_{\alpha+t}$ are the basis function (1) for equal H.O. width β and $(0s)$ single-particle wave function with different GC \mathbf{s} and \mathbf{s}' .

The normalization matrix is calculated as,

$$\begin{aligned} N(\mathbf{s}, \mathbf{s}') &= e^{-\frac{3}{7}\beta(s^2+s'^2)} \left[e^{\frac{12}{14}\beta\mathbf{s}\cdot\mathbf{s}'} - 3e^{\frac{5}{14}\beta\mathbf{s}\cdot\mathbf{s}'} + 3e^{-\frac{2}{14}\beta\mathbf{s}\cdot\mathbf{s}'} - e^{-\frac{9}{14}\beta\mathbf{s}\cdot\mathbf{s}'} \right] \\ &= \det[\langle \phi_\alpha | \phi_\beta \rangle] = \det[\mathbf{B}_{\alpha\beta}]. \end{aligned} \quad (11)$$

Here $\mathbf{B}_{\alpha\beta}$ is the overlap of the single-particle wave function of the normalization matrix.

Using Laplace expansion of determinant, we get the matrix elements of one-body operator as

$$\langle \phi | O^{(1)} | \phi \rangle = N(\mathbf{s}, \mathbf{s}') \sum_{\alpha=1}^7 \sum_{\beta=1}^7 \langle \phi_\alpha | O^{(1)} | \phi_\beta \rangle [\mathbf{B}^{-1}]_{\beta\alpha}. \quad (12)$$

Using above equation (11), the kinetic energy matrix can be easily shown as

$$T(\mathbf{s}, \mathbf{s}') = N(\mathbf{s}, \mathbf{s}') \left[\frac{9\hbar^2\beta}{2m} - \frac{3\hbar^2\beta^2}{14m}(\mathbf{s} - \mathbf{s}')^2 + \frac{3\hbar^2\beta^2}{4m}(\mathbf{s}\cdot\mathbf{s}')/(e^{\frac{\beta}{2}\mathbf{s}\cdot\mathbf{s}'} - 1) \right]. \quad (13)$$

Similarly, the matrix elements of the two-body operator is given by

$$\langle \phi | O^{(2)} | \phi \rangle = \sum_{\alpha<\beta}^7 \sum_{\gamma\delta}^7 \langle \phi_\alpha \phi_\beta | O^{(2)} | \phi_\gamma \phi_\delta \rangle C(\alpha\beta; \gamma\delta); \quad \alpha\beta \neq \gamma\delta \quad (14)$$

Using equation (14) the matrix elements of nuclear forces is obtained as,

$$\begin{aligned} V^N(\mathbf{s}, \mathbf{s}') &= \sum_{i<j}^7 \sum_{k\ell}^7 V_{ij;k\ell} C(ij; k\ell); \\ &= \sum_{i<j}^7 \sum_{k\ell}^7 \langle \phi_{\alpha_i} \phi_{\alpha_j} | \{ (w + m \mathbf{P}_{ij}^\sigma \mathbf{P}_{ij}^\tau) \{ V_a \exp[-(r_{ij}/a_1)^2] \\ &\quad + V_r \exp[-(r_{ij}/a_2)^2] \} | \phi_{\alpha_k} \phi_{\alpha_\ell} \rangle C(ij; k\ell). \end{aligned} \quad (15)$$

where the generalized cofactors $C(ij; k\ell)$ are given by

$$C(ij; k\ell) = N(\mathbf{s}, \mathbf{s}') [\mathbf{B}_{ki}^{-1} \mathbf{B}_{\ell j}^{-1} - \mathbf{B}_{kj}^{-1} \mathbf{B}_{\ell i}^{-1}]. \quad (16)$$

Similarly coulomb matrix elements are calculated.

B.3 Method of Angular Momentum and Parity Projection

The GCM wave function of ${}^7\text{Li}$ belonging to a definite total angular momentum J , its z-component M and parity Π is expected in terms of two-centre basis by

$${}^7\text{Li} \Psi_{\alpha+t}^{\text{JM}\Pi}(\mathbf{x}) = \sum_{\alpha} \int_0^\infty s^2 ds f_{\alpha}^{\text{JM}\Pi}(s) {}^7\text{Li} \Phi_{\alpha}^{\text{JM}\Pi}(\mathbf{x}, s); \quad (17)$$

where $\mathbf{x} \equiv (\mathbf{x}_1, \mathbf{x}_2, \mathbf{x}_3, \mathbf{x}_4, \mathbf{x}_5, \mathbf{x}_6, \mathbf{x}_7)$ and with s in magnitude only of eq (4), and α represents all the quantum numbers that are needed to specify the basis function completely.

The basis of the GC function are obtained by projecting the J, M and Π out of the GC function (1) as,

$${}^7\text{Li}\Phi_{\alpha}^{\text{JM}\Pi}(\mathbf{x}, s) = \mathbf{P}^{\Pi} \mathbf{P}_{\alpha}^{\text{JM}} {}^7\text{Li}\Phi_k(\mathbf{x}, s), \quad (18)$$

where Φ_k is of the form

$${}^7\text{Li}\Phi_{J_1 M_1, J_2 M_2}(\mathbf{x}, s) = [4!3!/7!]^{\frac{1}{2}} \mathcal{A}[\Phi_{J_1 M_1}(\mathbf{x}_1, \mathbf{x}_3, \mathbf{x}_5, \mathbf{S}_1)] [\Phi_{J_2 M_2}(\mathbf{x}_2, \mathbf{x}_4, \mathbf{x}_6, \mathbf{S}_2)]. \quad (19)$$

The effect of parity operator can be regarded as the inversion of \mathbf{s} , therefore the basis function (18) with definite parity Π can be rewritten as,

$${}^7\text{Li}\Phi_{\alpha}^{\text{JM}\Pi}(\mathbf{x}, s) = \mathbf{P}_{\alpha}^{\text{JM}} \left[\frac{1}{2C_{\Pi}} \{ {}^7\text{Li}\Phi_k(\mathbf{x}, s) + (-)^{\Pi} {}^7\text{Li}\Phi_k(\mathbf{x}, -s) \} \right], \quad (20)$$

where

$${}^7\text{Li}\Phi_k(\mathbf{x}, s) = \sum_{\Pi=\text{even}}^{\text{odd}} C_{\Pi} {}^7\text{Li}\Phi_k(\mathbf{x}, s), \text{ and } {}^7\text{Li}\Phi_k(\mathbf{x}, -s) = \sum_{\Pi=\text{even}}^{\text{odd}} (-)^{\Pi} C_{\Pi} {}^7\text{Li}\Phi_k(\mathbf{x}, s); \quad (21)$$

with

$$\sum_{\Pi=\text{even}}^{\text{odd}} |C_{\Pi}|^2 = 1, \quad \text{and} \quad \sum_{\Pi=\text{even}}^{\text{odd}} (-)^{\Pi} |C_{\Pi}|^2 = \langle {}^7\text{Li}\Phi_k(\mathbf{x}, s) | {}^7\text{Li}\Phi_k(\mathbf{x}, -s) \rangle. \quad (22)$$

The wave functions $\Phi_{J_1 M_1}$ and $\Phi_{J_2 M_2}$ are constructed so that they have no spurious CM motion with the equal H.O. width β of each subgroups of ${}^7\text{Li}$ i.e. alpha and triton, one can write eq (20) as

$${}^7\text{Li}\Phi_{J_1 M_1, J_2 M_2}(\mathbf{x}, s) = [4!3!/7!]^{\frac{1}{2}} \Phi_{\text{Li}}^{\text{CM}}(\mathbf{R}_G, \mathbf{S}_G) \otimes \mathcal{A} \left[(12\beta/7\pi)^{\frac{3}{4}} e^{-\frac{12\beta}{14}(\mathbf{r}-\mathbf{s})^2} \Phi_{J_1 M_1}(\zeta_{\alpha}) \Phi_{J_2 M_2}(\zeta_t) \right] \quad (23)$$

where

$$\Phi_{\text{Li}}^{\text{CM}}(\mathbf{R}_G, \mathbf{S}_G) = \left[\frac{7\beta}{\pi} \right]^{\frac{3}{4}} \exp \left[-\frac{7\beta}{2} (\mathbf{R}_G - \mathbf{S}_G)^2 \right]. \quad (24)$$

Here $\zeta_{\alpha}(\zeta_t)$ represent all the internal variables including spin-isospin of $\alpha(t)$.

Thus

$${}^7\text{Li}\Phi_{J_1 M_1, J_2 M_2}(\mathbf{x}, s) = \sum_{\substack{LM_L \\ J_{12} M_{12} JM}} \langle J_1 M_1 J_2 M_2 | J_{12} M_{12} \rangle \otimes \langle J_{12} M_{12} L M_L | J M \rangle Y_{LM_L}^*(\hat{s}) {}^7\text{Li}\Phi_{(J_1 J_2) J_{12} L}(\mathbf{x}, s), \quad (25)$$

where the angular momentum eigenstates are defined by

$${}^7\text{Li}\Phi_{(J_1 J_2) J_{12} L}(\mathbf{x}, s) = [4!3!/7!]^{\frac{1}{2}} \Phi_{\text{Li}}^{\text{CM}}(\mathbf{R}_G, \mathbf{S}_G) \mathcal{A} \left[(12\beta/7\pi)^{\frac{3}{4}} e^{-\frac{12\beta}{14}(\mathbf{r}-\mathbf{s})^2} \otimes 4\pi i_L [12\beta r s / 7] \{ \Phi_{J_1}(\zeta_{\alpha}) \Phi_{J_2}(\zeta_t) \}_{J_{12}} Y_L(\hat{r}) \}_{JM} \right] \quad (26)$$

Here \imath_L is the modified spherical Bessel function $\imath_L(z) = (-\imath)^L j_L(\imath z)$.

By inversion, we have

$${}^7\text{Li}_{(J_1 J_2) J_{12} L}(\mathbf{x}, s) = P_{(J_1 J_2) J_{12} L}^{\text{JM}} {}^7\text{Li}_{J_1 M_1, J_2 M_2}(\mathbf{x}, s), \quad (27)$$

where the projection operator is given by

$$P_{(J_1 J_2) J_{12} L}^{\text{JM}} = \sum_{\substack{M_1 M_2 \\ M_{12} M_L}} \langle J_1 M_1 J_2 M_2 | J_{12} M_{12} \rangle \langle J_{12} M_{12} L M_L | J M \rangle \int d\hat{s} Y_{L M_L}(\hat{s}). \quad (28)$$

Therefore eq(20) with parity projection becomes as,

$${}^7\text{Li}_{\alpha}^{\text{JM}\Pi}(\mathbf{x}, s) = \frac{1}{2C_{\Pi}} [1 + (-)^{\Pi+L}] P_{\alpha}^{\text{JM}} {}^7\text{Li}_{J_1 M_1, J_2 M_2}(\mathbf{x}, s), \quad (29)$$

Here α represents all the quantum numbers that are needed to specify the basis function completely. For ${}^7\text{Li}$, $L = 1$ and parity odd gives ground state doublet $J^{\Pi} = \frac{3}{2}^{-}, \frac{1}{2}^{-}$ since alpha is spin zero and triton spin $\frac{1}{2}$. Similarly, $L = 3$ with parity odd give excited state doublet $J^{\Pi} = \frac{7}{2}^{-}, \frac{5}{2}^{-}$.

B.4 Matrix Elements of Hamiltonian and Identity Operators in Projected Basis

The matrix elements in projected and unprojected basis are related as,

$$\begin{aligned} \begin{bmatrix} H_{\alpha\alpha'}^{\text{JM}\Pi}(s, s') \\ N_{\alpha\alpha'}^{\text{JM}\Pi}(s, s') \end{bmatrix} &= \langle {}^7\text{Li}_{\alpha}^{\text{JM}\Pi}(\mathbf{x}, s) | {}^H | {}^7\text{Li}_{\alpha'}^{\text{JM}\Pi}(\mathbf{x}, s') \rangle, \\ &= \frac{1}{2|C_{\Pi}|^2} [1 + (-)^{\Pi+L}] P_{\alpha}^{\text{JM}\dagger} P_{\alpha'}^{\text{JM}} \langle {}^7\text{Li}_{J_1 M_1, J_2 M_2}(\mathbf{x}, s) | {}^H | {}^7\text{Li}_{J_1 M_1, J_2 M_2}(\mathbf{x}, s') \rangle, \\ &= \frac{1}{2|C_{\Pi}|^2} [1 + (-)^{\Pi+L}] \delta_{\alpha\alpha'} \int d\hat{s} Y_{L M_L}^*(\hat{s}) \int d\hat{s}' Y_{L M_L}^*(\hat{s}') \begin{bmatrix} H(s, s') \\ N(s, s') \end{bmatrix}. \end{aligned} \quad (30)$$

The matrix elements of H and I operators are expanded in terms of spherical harmonics and using orthogonality conditions of spherical harmonics, we get the relationship between projected and unprojected basis as

$$\begin{bmatrix} H_{\alpha\alpha'}^{\text{JM}\Pi}(s, s') \\ N_{\alpha\alpha'}^{\text{JM}\Pi}(s, s') \end{bmatrix} = \frac{1}{2|C_{\Pi}|^2} [1 + (-)^{\Pi+L}] \delta_{\alpha\alpha'} (4\pi) \begin{bmatrix} H_{L M_L}(s, s') \\ N_{L M_L}(s, s') \end{bmatrix}. \quad (31)$$

The matrix elements are calculated in terms of modified spherical Bessel function as used in the definition of basis function.

B.5 Numerical Solution of Griffin-Hill-Wheeler Equation: Generator Coordinate Amplitudes and Energies

The GCM wave function of ${}^7\text{Li}$ is the superposition of the GC function (1) with respect to the generator coordinate s as (see eq 26),

$${}^7\text{Li}_{\alpha+t} \Psi(\mathbf{x}) = \int d\mathbf{s} f_{\alpha+t}(s) {}^7\text{Li}_{\alpha+t} \Phi(\mathbf{x}, s) \quad (32)$$

Here $\mathbf{x} \equiv (x_1, x_2, x_3, x_4, x_5, x_6, x_7)$, the f is known as the generator coordinate amplitude and obtained by determining the eigenfunctions of the Hamiltonian by the variational principle,

$$\delta \frac{\langle \Psi | H | \Psi \rangle}{\langle \Psi | \Psi \rangle} = 0. \quad (33)$$

Substituting (32) in (33) and using above angular momentum and parity projection, we get the Griffin-Hill-Wheeler(GHW) equation as

$$4\pi \int_0^\infty ds' s'^2 [H_L^{JMP}(s, s') - E N_L^{JMP}(s, s')] f_L^{JMP}(s') = 0 \quad (34)$$

Here we have dropped in the subscript of f_α^{JMP} (i.e. $\alpha \equiv (J_1 J_2) J_{12} L$) the quantum numbers other than L , because the kernels of the equation are dependent on L only. For normalized generator coordinate amplitudes the condition is

$$4\pi \int_0^\infty ds \int_0^\infty ds' s'^2 f_L^{JMP}(s) N_L^{JMP}(s, s') f_L^{JMP}(s') = 1. \quad (35)$$

The GHW equation (34) in the projected basis can be represented an algebraic eigenvalue problem as

$$\sum_{j=1}^N [H_L^{JMP}(s_i, s_j) - E N_L^{JMP}(s_i, s_j)] F_L^{JMP}(s_j) = 0; \quad i, j = 1, 2, \dots, N. \quad (36)$$

The set of linear equations (36) can be expressed in a matrix form as

$$[H_{ij}] [F_j] = E [N_{ij}] [F_j]; \quad i, j = 1, 2, \dots, N. \quad (37)$$

where H and N are the $|N \times N|$ matrices and F is the $|N \times 1|$ column matrix. This method of discretization can simplified the calculation of various other physical quantities, e.g. electromagnetic properties, form factors etc and various nucleon exchange effects. In the solution of (37), we can distinguish two types of problems:

- One must take a sufficient number of points in order to obtain a good convergence.
- One must not take too many points as this will lead to very small eigenvalues of the normalization matrix.

With the above problems in the numerical solution of eq (37), two different methods have been proposed for calculating the values of the generator coordinate s_i . The first method is suggest by Mihailovic' and Poljsak in which the points of discretization of eq (37) are obtained by optimizing the normalization matrix. the eigenvalues of the normalization matrix are chosen in such a way so that the evaluation of the matrix $N^{-1}H$ could not become inaccurate numerically.

The second method is proposed by Caurier as the consistent way for the variational determination of the values s_i . The first set of points s_i are chosen in such a way that the eigenvalue of eq (37) in Born-Oppenheimer approximation be a minimum. The second set of points are chosen in such a way that the second lowest eigenvalue be a minimum.

One goes on in the same way to determine the third set of points etc. in this way one constructs a cauchy series for the desired eigenstate of hamiltonian.

For the stability of the results one can evaluate the energy differences (for the r -th iteration)

$\|E^{(r)} - E^{(r-1)}\|$ and the Cauchy criterion $\|\Psi^{(r)} - \Psi^{(r-1)}\| = \sqrt{2[(1 - \text{Re}(\langle \Psi^{(r)} | \Psi^{(r-1)} \rangle))]}$, which is easily computed with

$$\langle \Psi^{(r)} | \Psi^{(r-1)} \rangle = \sum_{i=1}^r \sum_{j=1}^{r-1} F_i^{(r)} N(s_i, s_j) F_j^{(r-1)}. \quad (38)$$

Similarly, for coupled system of equations above treatment can be generalized.

C Role of Palui Principle in the Structure of Light Nuclei

C.1 Nucleon Exchange Effects in Alpha-Triton Relative Wave function

The relative motion wave function between alpha(α) and triton(t) is defined by the method of overlap integrals [8] as,

$$u_{\alpha+t} = [7!/4!3!]^{\frac{1}{2}} \int {}^7\text{Li} \Psi_{\alpha+t}(\mathbf{r}, \xi_\alpha, \xi_t) \Phi_\alpha^{(\text{in})}(\xi_\alpha) \Phi_t^{(\text{in})}(\xi_t) d\xi_\alpha d\xi_t \quad (39)$$

where \mathbf{r} is the relative coordinate between alpha and triton and ξ_α and ξ_t are the internal Jacobi coordinates (4) for normalized intrinsic wave functions of $\Phi_\alpha^{(\text{in})}$ (alpha) and $\Phi_t^{(\text{in})}$ (triton) in the virtual decay of ${}^7\text{Li}$ nucleus. Using the GCM wave function of ${}^7\text{Li}$ (17), the relative wave function (39) can be written in terms of the GC amplitude f^{JMI} , which is the weight function satisfying the Griffen-Hill-Wheeler equation (34), as

$$u_{\alpha+t}^{\text{JMI}}(\mathbf{r}) = [7!/4!3!]^{\frac{1}{2}} \sum_{\substack{\text{Spin} \\ \text{Isospin}}} \int d\xi_\alpha d\xi_t f^{\text{JMI}}(s) {}^7\text{Li} \Phi_{\alpha+t}(\mathbf{r}, \xi_\alpha, \xi_t, s) \otimes \chi_{\alpha+t}(\sigma\tau) \Phi_\alpha^{(\text{in})}(\xi_\alpha) \chi_\alpha(\sigma\tau) \Phi_t^{(\text{in})}(\xi_t) \chi_t(\sigma\tau) \quad (40)$$

where superscripts denote the particular states of ${}^7\text{Li}$ ($J^\pi = \frac{3}{2}^-$), χ ' are the spin-isospin factors and s is the separation between the two harmonic oscillator wells known as the generator coordinate.

The generator coordinate (GC) function occurring in the integrand of eq (40) is the form of $|7 \times 7|$ Slater determinant which is expanded by Lapalace expansion into 35 terms of $|4 \times 4| \otimes |3 \times 3|$ -type determinants. The nonzero determinant products are only eight terms and describe as follows:

$$\begin{aligned} \text{no-nucleon exchange } {}^{(0)}\Phi &: (1357)(246), \\ \text{one-nucleon exchange } {}^{(1)}\Phi &: -(2357)(146), -(1367)(245), -(1457)(236), \\ \text{two-nucleon exchange } {}^{(2)}\Phi &: (2457)(136), (2367)(145), (1467)(235), \\ \text{three-nucleon exchange } {}^{(3)}\Phi &: -(2467)(135). \end{aligned} \quad (41)$$

In terms of various nucleon exchange products (41), $\Phi_{\alpha+t}$ in (40) becomes as,

$$\Phi_{\alpha+t} = \frac{1}{\sqrt{7!}} [{}^{(0)}\Phi - 3 {}^{(1)}\Phi + 3 {}^{(2)}\Phi - {}^{(3)}\Phi]. \quad (42)$$

With the use of the Jacobi coordinates the eight terms (41) can be calculated in terms of the GC function (42) as

$$\begin{aligned} \Phi_{\alpha+t}(\mathbf{x}, \mathbf{s}) &= \Phi_{\alpha+t}(\mathbf{r}, \boldsymbol{\xi}_\alpha, \boldsymbol{\xi}_t, \mathbf{s}) \chi_{\alpha+t}(\boldsymbol{\sigma}\boldsymbol{\tau}), \\ &= \left[\left(\frac{\beta}{\pi} \right)^4 \right]^{\frac{3}{4}} \exp \left[-\frac{\beta}{2} \sum_{i=1, \text{odd}}^{\leq 7} (\mathbf{r}_i - \mathbf{S}_1)^2 \right] \\ &\quad \otimes \left[\left(\frac{\beta}{\pi} \right)^4 \right]^{\frac{3}{4}} \exp \left[-\frac{\beta}{2} \sum_{j=1, \text{even}}^{\leq 7} (\mathbf{r}_j - \mathbf{S}_2)^2 \right] \chi_{\mathbf{r}\boldsymbol{\sigma}\boldsymbol{\tau}}. \end{aligned} \quad (43)$$

Here $\mathbf{x} \equiv (\mathbf{r}, \boldsymbol{\sigma}, \boldsymbol{\tau})$ with

$$\begin{aligned} \chi_{\mathbf{r}\boldsymbol{\sigma}\boldsymbol{\tau}} &= \frac{1}{\sqrt{7!}} \det \left[e^{-\frac{\beta}{14}s^2} e^{-\frac{\beta}{14}\mathbf{s} \cdot \mathbf{r}_1} \chi_{n\downarrow}(1), \chi_{p\uparrow}(3), e^{-\frac{\beta}{14}s^2} e^{-\frac{\beta}{14}\mathbf{s} \cdot \mathbf{r}_5} \chi_{n\uparrow}(5), \chi_{p\downarrow}(7); \right. \\ &\quad \left. \otimes e^{\frac{\beta}{14}s^2} e^{\frac{\beta}{14}\mathbf{s} \cdot \mathbf{r}_2} \chi_{n\uparrow}(2), \chi_{p\uparrow}(4), e^{\frac{\beta}{14}s^2} e^{\frac{\beta}{14}\mathbf{s} \cdot \mathbf{r}_6} \chi_{n\downarrow}(6) \right] \end{aligned} \quad (44)$$

The GC function (43) can easily be rewritten in the following form

$$\Phi_{\alpha+t}(\mathbf{x}, \mathbf{s}) = \Phi_{7\text{Li}}^{\text{CM}}(\mathbf{R}_G, \mathbf{S}_G) [\Phi_{\alpha+t}^{\text{rel}}(\mathbf{x}, \mathbf{s}) \Phi_{\alpha}^{(\text{in})}(\boldsymbol{\xi}_\alpha) \Phi_t^{(\text{in})}(\boldsymbol{\xi}_t)] \chi_{\mathbf{r}\boldsymbol{\sigma}\boldsymbol{\tau}}, \quad (45)$$

where the centre-of-mass wave function is defined by eq (24) and,

$$\Phi_{\alpha+t}^{\text{rel}}(\mathbf{x}, \mathbf{s}) = \left[\frac{12\beta}{7\pi} \right]^{\frac{3}{4}} \exp \left[-\frac{12\beta}{14} (\mathbf{r} - \mathbf{s})^2 \right], \quad (46)$$

$$\begin{aligned} \Phi_{\alpha}^{(\text{in})}(\boldsymbol{\xi}_\alpha) &= \left[\frac{1}{4} \left(\frac{\beta}{\pi} \right)^3 \right]^{\frac{3}{4}} \exp \left[\frac{\beta}{2} \left(\frac{1}{2} \xi_{13}^2 + \frac{2}{3} \xi_{13,5}^2 + \frac{3}{4} \xi_{135,7}^2 \right) \right], \\ \Phi_t^{(\text{in})}(\boldsymbol{\xi}_t) &= \left[\frac{1}{3} \left(\frac{\beta}{\pi} \right)^2 \right]^{\frac{3}{4}} \exp \left[\frac{\beta}{2} \left(\frac{1}{3} \xi_{24}^2 + \frac{2}{3} \xi_{24,6}^2 \right) \right], \end{aligned} \quad (47)$$

and the spin-isospin function of alpha (or triton) is given by

$$\chi_{\alpha \text{ or } t}(\boldsymbol{\sigma}\boldsymbol{\tau}) = \frac{1}{\sqrt{4! (\text{or } 3!)}} \det \left[\sum_{i=1}^4 (\text{or } 3) \chi_{m_{\sigma_i} m_{\tau_i}}(\boldsymbol{\sigma}_i \boldsymbol{\tau}_i) \right]. \quad (48)$$

Here all the functions are normalized to unity. The centre-of-mass wave function $\Phi_{7\text{Li}}^{\text{CM}}$ is factored out explicitly in the definition of relative wave function $u_{\alpha+t}^{\text{JMII}}(\mathbf{r})$. taking all above consideration into account the normalized relative motion P-wave function, using the ground state of ${}^7\text{Li}$ ($J^\Pi = \frac{3}{2}^-$; $L = 1, S = \frac{1}{2}$) and after angular momentum projection, can be written as

$$u_{\alpha+t}^{\text{JMII}}(\mathbf{r}) = \sum_{M_L \mu} u_{L=1}^{\text{JMII}}(r) [\langle LM_L \frac{1}{2} \mu | \text{JM} \rangle Y_{LM_L}(\hat{\mathbf{r}})], \quad (49)$$

where the radial alpha-triton relative wave function with various nucleon exchange contributions is given by

$$u_{L=1}^{JMI} = {}^{(0)}u_{\alpha+t}^{JMI} - {}^{(1)}u_{\alpha+t}^{JMI} - {}^{(2)}u_{\alpha+t}^{JMI} + {}^{(3)}u_{\alpha+t}^{JMI}; \quad (50)$$

with (ν) -nucleon exchange contributions (i.e. $\nu = 0, 1, 2, 3$; $\nu_{\max} = 3$) are given in terms of modified Bessel functions $i_{L=1}(z)$ as,

$${}^{(\nu)}u_{\alpha+t}^{JMI}(r) = \sqrt{4\pi} \binom{\nu_{\max}}{\nu} \left[\frac{12\beta}{7\pi} \right]^{\frac{3}{4}} e^{-\frac{6\beta}{7}r^2} \int_0^\infty ds s^2 f_{L=1}^{JMI}(s) e^{-\frac{6\beta}{7}s^2} e^{\frac{\beta}{2}\nu(1-\frac{7\nu}{24})s^2} i_{L=1}\left(\frac{\beta}{2}|\frac{12}{7}-\nu|\right). \quad (51)$$

Here the weight function $f_{L=1}^{JMI}$ in the numerical form is obtained by considering the size $\beta = 0.5 \text{ FM}^{-2}$ which has given right separation energy and all other electromagnetic properties as in Section 4.

The asymptotic form of the alpha-triton relative wave function (50) can also be written in terms of a Whittaker function as,

$$\lim_{r \rightarrow \infty} u_{L=1}^{JMI} = C \frac{\sqrt{2K}}{r} W_{-\eta, L+\frac{1}{2}}(2Kr), \quad (52)$$

where K is related to separation energy E , and η the Coulomb parameter:

$$\frac{\hbar^2 K^2}{2\mu_{\alpha t}} = E; \quad \eta = \frac{Z_1 Z_2 e^2 \mu_{\alpha t}}{\hbar^2 K}.$$

The alpha-triton relative motion P-wave function ($L = 1$) with various nucleon exchange terms with proper sign (50) are plotted in Fig. 1. The dotted curves are the contributions to the total relative wave function $u(r)$, obtained by separately calculating the various nucleon exchange terms given by eq (51), viz, no-nucleon exchange ${}^{(0)}u$, one-nucleon exchange ${}^{(1)}u$, two-nucleon exchange ${}^{(2)}u$, three-nucleon exchange ${}^{(3)}u$ terms. The full solid curve $u(r)$ represents the total alpha-triton relative motion wave function which becomes negative for relative separation r of the two clusters less than 2 FM. This is due to the influence of the Pauli principle and the nature of the nuclear forces. The important facts about the nuclear forces are that they are short range (~ 2 FM), strongly attractive over most of the range, but at very short-range they become strongly repulsive. On the other hand the effect of the Pauli principle in a usual system of nuclear dimensions is to allow low-energy nucleons to move relatively undisturbed throughout the nuclear volume, because these nucleons may not be scattered into other already occupied energy levels. It is clear from Fig. 1 that when the relative distance between alpha and triton is small, the Pauli principle plays an important role as shown by various nucleon exchange contributions to the total alpha-triton relative wave function $u(r)$ (full curve) which becomes negative at less than 2 FM i.e. due to the strong Pauli repulsion.

C.2 Nucleon Exchange Contributions in the Photodisintegration of ${}^7\text{Li}$

A great deal of work on the photodisintegration of light nuclei has been done following the sum-rule formalism due to Levinger and Bethe(1950). The first sum-rule calculations for lithium nucleus have been performed by Lodhi and Wood(1982) for the

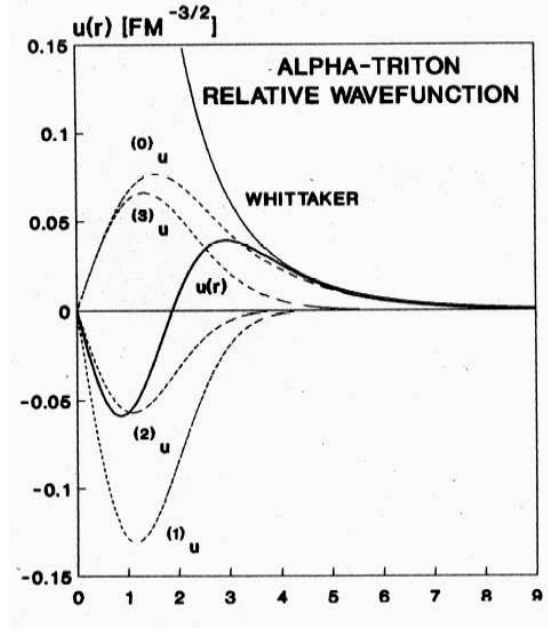


Fig. 1. Alpha-triton relative wavefunction

integrated bremsstrahlung weighted cross section for the dipole transitions using the resonating group method wave function of ${}^6\text{Li}$. It is observed that the bremsstrahlung cross-section is sensitive to the details of the wave function.

The GCM wave function of ${}^7\text{Li}$ (32) with angular momentum projection is given by

$$\Psi_{\alpha+t}^{JMI}(\mathbf{x}) = \sum_{M_L \mu} \langle L M_L \frac{1}{2} \mu | J M \rangle \int d\hat{s} f_L^{JMI}(s) Y_{L M_L}(\hat{s}) \Phi_{\mu}^{JMI}(\mathbf{x}, s) \quad (53)$$

where the GC function $\Phi_{\mu}(\mathbf{x}, s)$ is given by eq. (42) and the generator coordinate amplitude $f_{(L=1)}^{JMI}$ is obtained by solving the Griffin-Hill-Wheeler equation (34).

Following Dellafiore and Brink, we have for the total bremsstrahlung weighted cross-section as,

$$\sigma_b = \frac{4\pi^2}{3} \frac{e^2}{\hbar c} \left[\frac{NZ}{A} \right]^2 \langle \mathbf{R}_{pn}^2 \rangle, \quad (54)$$

where the operator \mathbf{R}_{pn} is defined in terms of $\mathbf{R}_{p(n)}$, the centre-of-mass of the Z (N) numbers of protons (neutrons) in the nucleus A with $\mathbf{R}_{pn} = \mathbf{R}_p - \mathbf{R}_n$. The expectation value \mathbf{R}_{pn}^2 is obtained in the GCM wave function of ${}^7\text{Li}$ (53) and can be expressed as

$$\langle \mathbf{R}_{pn}^2 \rangle = \int d\hat{s} \int d\hat{s}' f_{L=1}^{JMI}(s) Y_{LL}(\hat{s}) \langle \mathbf{R}_{pn}^2 \rangle_{s,s'} f_{L=1}^{JMI}(s') Y_{LL}(\hat{s}'), \quad (55)$$

with

$$\langle \mathbf{R}_{\text{pn}}^2 \rangle_{s,s'} = \frac{\langle \Phi_{\mu}^{\text{JMH}}(\mathbf{x}, \mathbf{s}) | [Z^{-1} \sum_i \frac{1}{2}(1 + \tau_{iz}) \mathbf{r}_i - N^{-1} \sum_j \frac{1}{2}(1 - \tau_{jz}) \mathbf{r}_j]^2 | \Phi_{\mu}^{\text{JMH}}(\mathbf{x}, \mathbf{s}') \rangle}{\langle \Phi_{\tau_{\text{Li}}}^{\text{CM}}(\mathbf{R}_{\text{G}}, \mathbf{S}_{\text{G}}) | \Phi_{\tau_{\text{Li}}}^{\text{CM}}(\mathbf{R}_{\text{G}}, \mathbf{S}'_{\text{G}}) \rangle} \quad (56)$$

where $\Phi_{\tau_{\text{Li}}}^{\text{CM}}(\mathbf{R}_{\text{G}}, \mathbf{S}_{\text{G}})$ is the normalized centre-of-mass wave function of ${}^7\text{Li}$ given by eq (24). The GC function occurring in the integrand of eq (56) is the form of $|7 \times 7|$ Slater determinant which is expanded into 35 terms of $|4 \times 4| \otimes |3 \times 3|$ -type determinants (41).

Substituting \mathbf{R}_{pn} and GC functions with various nucleon-exchange products (42) into (56) and integrating over all the internal variables with the summation on spin-isospin functions, we get

$$\langle \mathbf{R}_{\text{pn}}^2 \rangle_{s,s'} = \langle \mathbf{R}_{\text{pn}}^2 \rangle_{s,s'}^{(0)} - 3 \langle \mathbf{R}_{\text{pn}}^2 \rangle_{s,s'}^{(1)} + 3 \langle \mathbf{R}_{\text{pn}}^2 \rangle_{s,s'}^{(2)} - \langle \mathbf{R}_{\text{pn}}^2 \rangle_{s,s'}^{(3)} \quad (57)$$

where for ν -nucleon exchange contributions (i.e. $\nu = 0, 1, 2, 3$), we get

$$\langle \mathbf{R}_{\text{pn}}^2 \rangle_{s,s'}^{(\nu)} = \left[\frac{126}{\beta} + (\mathbf{s} + \mathbf{s}')^2 + 7\nu \left\{ \left(1 - \frac{7\nu}{24}\right) s'^2 - \frac{\mathbf{s} \cdot \mathbf{s}'}{6} \right\} \right] \exp \left[-\frac{3\beta}{7} (\mathbf{s} - \mathbf{s}')^2 - \frac{\beta}{2} \nu \mathbf{s} \cdot \mathbf{s}' \right]. \quad (58)$$

Substituting the partial waves expansions of (58) into (56) and in eq (55), we get total bremsstrahlung weighted cross-section (σ_{b}) equal to 5.341 mb which is in close agreement with the experimental value 5.224 mb and various nucleon-exchange contributions are as follows:

$$\begin{aligned} \sigma_{\text{b}} &= \sigma_{\text{b}}^{(0)} - \sigma_{\text{b}}^{(1)} - \sigma_{\text{b}}^{(2)} + \sigma_{\text{b}}^{(3)}, \\ &= 10.887 - 8.394 - 3.176 + 0.024 \\ &= 5.341 \end{aligned} \quad (59)$$

The bremsstrahlung weighted cross-section with various nucleon exchange contributions are calculated using the H.O. width parameter $\beta = 0.5 \text{ FM}^{-2}$ for ${}^7\text{Li}$ ground state ($L = 1, S = \frac{1}{2}; J^{\pi} = \frac{3}{2}^{-}$). Our calculation suggests that the nucleon exchange contributions due to Pauli principle plays a significant role in the total bremsstrahlung cross-section. As far as the comparison of the predicted total cross-section with the available experimental value is concern it depends entirely on the range of incoming photon energy in such photonuclear reaction. It is desirable to extend the energy range of the incident photons so that better values for the bremsstrahlung weighted cross-section could be obtained.

D GCM for Electromagnetic Form Factors, RMS Radii and Moments

D.1 General Formalism in Terms of Density

In this subsection we recapitulate the various formulae for nuclear moments and charge form factors already developed in the Born approximation to calculate charge and magnetic form factors and RMS radius of ${}^7\text{Li}$ within the framework of our GCM.

The nuclear charge, (convection) current, and (spin) and (orbital) magnetization density operators are modified by the finite size of the nucleons and by relativistic effects, and are given by

$$\rho^{\text{Op}}(\mathbf{r}) = \sum_{i=1}^A \frac{1}{2} [1 + \tau_{iz}] f_{\text{ch}}^{\text{n}}(\mathbf{r} - \mathbf{r}_i) + \sum_{i=1}^A \frac{1}{2} [1 - \tau_{iz}] f_{\text{ch}}^{\text{n}}(\mathbf{r} - \mathbf{r}_i); \quad (60)$$

(normalized to Z)

$$\mathbf{j}_c^{\text{Op}} = \sum_{i=1}^A \frac{1}{2} [1 + \tau_{iz}] f_{\text{ch}}^{\text{p}}(\mathbf{r} - \mathbf{r}_i) \frac{\mathbf{p}_i}{m} + \sum_{i=1}^A \frac{1}{2} [1 - \tau_{iz}] f_{\text{ch}}^{\text{n}}(\mathbf{r} - \mathbf{r}_i) \frac{\mathbf{p}_i}{m}, \quad (61)$$

$$\begin{aligned} \mu_s^{\text{Op}} &= \frac{1}{2m} [\mu_p \sum_{i=1}^A \frac{1}{2} [1 + \tau_{iz}] f_{\text{mag}}^{\text{p}}(\mathbf{r} - \mathbf{r}_i) \boldsymbol{\sigma}_i + \mu_n \sum_{i=1}^A \frac{1}{2} [1 - \tau_{iz}] f_{\text{mag}}^{\text{n}}(\mathbf{r} - \mathbf{r}_i) \boldsymbol{\sigma}_i], \\ \mu_o^{\text{Op}} &= \frac{1}{2m} [\sum_{i=1}^A \frac{1}{2} [1 + \tau_{iz}] f_{\text{ch}}^{\text{p}}(\mathbf{r} - \mathbf{r}_i) (\ell_i^{\text{Op}})_{\text{sym}} + \sum_{i=1}^A \frac{1}{2} [1 - \tau_{iz}] f_{\text{ch}}^{\text{n}}(\mathbf{r} - \mathbf{r}_i) (\ell_i^{\text{Op}})_{\text{sym}}]. \end{aligned} \quad (62)$$

Here m being the nucleon mass and A is the total number of nucleons in the nucleus, $\boldsymbol{\tau}$ and $\boldsymbol{\sigma}$ are the isospin and spin Pauli matrices. The proton and neutron static magnetic moments are: $\mu_p = 2.793 \text{ n.m.}$ and $\mu_n = -1.913 \text{ n.m.}$ respectively. The f 's are the spatial distribution function about the centers of the nucleons or equivalently the Fourier transforms of the realistic normalized nucleon electromagnetic form factors.

The proton (neutron) charge and magnetic form factors are given by,

$$F_{\text{ch}}^{\text{p}}(\mathbf{q}) = G_{\text{ES}}(q^2) + G_{\text{EV}}(q^2), \quad (63)$$

$$F_{\text{ch}}^{\text{n}}(\mathbf{q}) = G_{\text{ES}}(q^2) - G_{\text{EV}}(q^2); \quad (64)$$

and

$$F_{\text{mag}}^{\text{p}}(\mathbf{q}) = \frac{1}{(1 + \kappa_p)} [G_{\text{MS}}(q^2) + G_{\text{MV}}(q^2)], \quad (65)$$

$$F_{\text{mag}}^{\text{n}}(\mathbf{q}) = \frac{1}{\kappa_n} [G_{\text{MS}}(q^2) - G_{\text{MV}}(q^2)], \quad (66)$$

with

$$G_{\text{ES}}(q^2) = 0.5 \left[\frac{2.50}{(1 + q^2/15.7)} - \frac{1.60}{(1 + q^2/26.7)} + 0.10 \right] \quad (67)$$

$$G_{\text{EV}}(q^2) = 0.5 \left[\frac{1.16}{(1 + q^2/8.19)} - 0.16 \right]; \quad (68)$$

and

$$G_{\text{MS}}(q^2) = 0.44 \left[\frac{3.33}{(1 + q^2/15.7)} - \frac{2.77}{(1 + q^2/26.7)} + 0.44 \right] \quad (69)$$

$$G_{\text{MS}}(q^2) = 0.2.353 \left[\frac{1.11}{(1 + q^2/8.19)} - 0.11 \right]; \quad (70)$$

where the normalization conditions of the form factors as $F_{\text{ch}}^{\text{p}}(0) = 1$, $F_{\text{ch}}^{\text{n}}(0) = 0$; and $F_{\text{mag}}^{\text{p}}(0) = 1$, $F_{\text{mag}}^{\text{n}}(0) = 1$ gives $\kappa_p = 1.793$ and $\kappa_n = -1.913$ respectively.

For elastic scattering the form factors are given by

$$F_{\text{ch}}^2(q) = \sum_{L=0, \text{even}}^{\leq 2J} |F_L^{\text{ch}}(q)|^2 \quad (71)$$

and

$$F_{\text{mag}}^2(q) = \sum_{L=1, \text{odd}}^{\leq 2J} |F_L^{\text{mag}}(q)|^2 \quad (72)$$

Here the form factors for multipolarity L with $\hat{J} = (2J + 1)^{\frac{1}{2}}$ are given by

$$F_L^{\text{ch}}(q) = (4\pi)^{\frac{1}{2}} [\hat{Z}\hat{J}]^{-1} < JJ00 | JJ > i^L \int_0^\infty r^2 j_L(qr) \rho_L(r) dr, \quad (73)$$

and

$$F_L^{\text{mag}}(q) = \sqrt{3/2} [(L+1)/(2L+1)]^{\frac{1}{2}} F_{L-1}^{\text{mag}}(q) + \sqrt{3/2} [L/(2L+1)]^{\frac{1}{2}} F_{L+1}^{\text{mag}}(q); \quad (74)$$

with

$$F_{LL'}^{\text{mag}}(q) = (4\pi)^{\frac{1}{2}} [(\mu/2m)\hat{J}]^{-1} < JJ10 | JJ > i^{L'} \int_0^\infty r^2 j_{L'}(qr) \mu_{LL'}(r) dr; \quad L' = L \pm 1, \quad (75)$$

D.2 Electromagnetic Form factors, RMS Radii and Moments in Generator Coordinate Method

The electromagnetic form factors of ${}^7\text{Li}$ can be expressed as

$$F_{\text{ch}}(\mathbf{q}) = \int d\mathbf{s} \int d\mathbf{s}' f_L(s) Y_{LL}(\hat{s}') F_{\text{ch}}(\mathbf{q}, \mathbf{s}, \mathbf{s}') f_L(s') Y_{LL}^*(\hat{s}'), \quad (76)$$

$$F_{\text{mag}}(\mathbf{q}) = \int d\mathbf{s} \int d\mathbf{s}' f_L(s) Y_{LL}(\hat{s}') F_{\text{mag}}(\mathbf{q}, \mathbf{s}, \mathbf{s}') f_L(s') Y_{LL}^*(\hat{s}'); \quad (77)$$

where

$$F_{\text{ch}}(\mathbf{q}, \mathbf{s}, \mathbf{s}') = F_{\text{c}}^{\text{p}}(\mathbf{q}, \mathbf{s}, \mathbf{s}') F_{\text{ch}}^{\text{p}}(\mathbf{q}) + F_{\text{c}}^{\text{n}}(\mathbf{q}, \mathbf{s}, \mathbf{s}') F_{\text{ch}}^{\text{n}}(\mathbf{q}), \quad (78)$$

$$F_{\text{mag}}(\mathbf{q}, \mathbf{s}, \mathbf{s}') = F_{\text{spin}}^{\text{p}}(\mathbf{q}, \mathbf{s}, \mathbf{s}') F_{\text{mag}}^{\text{p}}(\mathbf{q}) + F_{\text{spin}}^{\text{n}}(\mathbf{q}, \mathbf{s}, \mathbf{s}') F_{\text{mag}}^{\text{n}}(\mathbf{q}) \\ + F_{\text{orbital}}^{\text{p}}(\mathbf{q}, \mathbf{s}, \mathbf{s}') F_{\text{ch}}^{\text{p}}(\mathbf{q}) + F_{\text{orbital}}^{\text{n}}(\mathbf{q}, \mathbf{s}, \mathbf{s}') F_{\text{ch}}^{\text{n}}(\mathbf{q}); \quad (79)$$

where $F_{\text{ch}, \text{mag}}^{\text{p}, \text{n}}(\mathbf{q})$ are the proton and neutron charge and magnetic form factors and $F_{\text{c}, \text{spin}, \text{orbital}}^{\text{p}, \text{n}}$ are given by [9]:

$$F_{\text{c}}^{\text{p}, \text{n}} = \frac{< \Phi_\mu | \sum \frac{1}{2} (1 \pm \tau_{iz}) \exp(i\mathbf{q} \cdot \mathbf{r}_i) | \Phi_\mu >}{< \Phi_G | \exp(i\mathbf{q} \cdot \mathbf{R}_G) | \Phi_G >}. \quad (80)$$

and

$$F_{\text{spin}}^{\text{p,n}} = \frac{\langle \Phi_\mu | \sum \frac{1}{2} (1 \pm \tau_{iz}) (\mu_{\text{p,n}}/2m) \exp(i\mathbf{q} \cdot \mathbf{r}_i) | \Phi_\mu \rangle}{\langle \Phi_G | \exp(i\mathbf{q} \cdot \mathbf{R}_G) \sigma_{iz} | \Phi_G \rangle}, \quad (81)$$

$$F_{\text{orbital}}^{\text{p,n}} = \frac{\langle \Phi_\mu | \sum \frac{1}{2} (1 \pm \tau_{iz}) (\mu_{\text{p,n}}/2m) \exp(i\mathbf{q} \cdot \mathbf{r}_i) (\ell_{iz})_{\text{sym}} | \Phi_\mu \rangle}{\langle \Phi_G | \exp(i\mathbf{q} \cdot \mathbf{R}_G) | \Phi_G \rangle}, \quad (82)$$

Here $\Phi_G(\mathbf{R}_G)$ is the centre-of-mass of ${}^7\text{Li}$ given by eq (24), and σ_{iz} and $(\ell_{iz})_{\text{sym}}$ are the z -components of the Pauli spin matrices and orbital angular momentum operator in units of \hbar in symmetrical form.

Using above formalism for ${}^7\text{Li}$ where $J = \frac{3}{2}$, various electromagnetic form factors, RMS radii and moments are calculated using the following formule:

The charge and magnetic form factors (71) and (72) are given as,

$$F_{\text{ch}}^2(q) = |F_0^{\text{ch}}(q)|^2 + |F_2^{\text{ch}}(q)|^2, \quad (83)$$

$$F_{\text{mag}}^2(q) = |F_1^{\text{mag}}(q)|^2 + |F_3^{\text{mag}}(q)|^2, \quad (84)$$

and plotted as in Fig. 2.

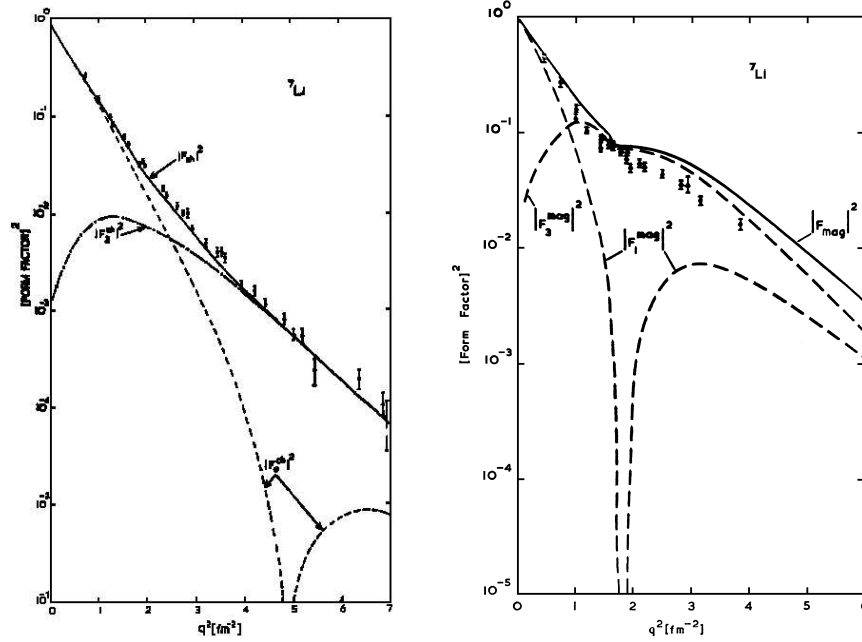


Fig. 2. Charge Form Factor and Magnetic Form Factor

Table 1. The S-Factor and Electromagnetic Properties of ${}^7\text{Li}$ in GCM with Volkov V2 Forces and others

Properties	Experimental Value	GCM	RGM (TANG)	RGM (ARIMA)
$\langle r_c^2 \rangle^{\frac{1}{2}}$ [FM]	2.35 ± 0.10 2.39 ± 0.03 2.405 ± 0.02 2.41 ± 0.10 2.55 ± 0.07	2.42	2.44	2.35 2.55
Q [e.FM ²]	-3.40 ± 0.60 -3.66 ± 0.03 -3.70 ± 0.08 -4.10 -4.44	-3.67	-3.70	-3.50 -4.41
B(E2) [e ² .FM ⁴]	6.70 ± 0.20 7.40 ± 0.10 7.42 ± 0.14 8.30 ± 0.60 8.9 ± 0.60	6.698	7.55	6.61 10.57
$\langle r_m^2 \rangle^{\frac{1}{2}}$ [FM]	2.70 ± 0.15 2.98 ± 0.05	2.83	—	2.81 3.04
μ [μ_N]	3.256424 ± 0.20	3.149	3.148	3.15 3.16
Ω [μ_N .FM ²]	$ 9.3 \pm 0.40 $	9.66	—	-8.71 -10.45
B(M1) [μ_N^2]	2.48 ± 0.12	2.057	2.17	2.17 2.16
S(0) [Kev-b] ${}^3\text{He}(\alpha, \gamma){}^7\text{Be}$	0.31 ± 0.03 0.53 ± 0.03 54 ± 0.04 0.58 ± 0.03 0.63 ± 0.04	0.59	0.56 0.598	0.51 0.50

Table 2. RMS Radii for Halo Light Nuclei in GCM with Volkov V2 Forces

Nucleus Model	B.E. [MeV]	R _p [FM]	R _n [FM]	R _m [FM]	ΔR _{np} [FM]	R _{ch} [FM]
⁶ He (^α +nn) (J ^π =0 ⁺ , T=1)	GCM -28.89 EXP -27.98	1.95 1.72	2.49 2.59	2.32 2.33	0.53 0.87	2.07
⁶ Li (^α +np) (J ^π =1 ⁺ , T=0)	GCM -27.26 EXP -31.99	2.34 2.32	2.34 2.32	2.34 2.32	0.0 0.0	2.46 2.46
⁶ Be (^α +pp) (J ^π =0 ⁺ , T=1)	GCM -25.67	2.53	1.98	2.36	0.55	2.66
⁷ Li (^α + ³ H) (J ^π = $\frac{3}{2}^-$, $\frac{1}{2}^-$, T= $\frac{1}{2}$)	GCM -38.31 EXP -39.25	2.29 2.29	2.40 2.40	2.35 2.35	0.11 0.11	2.42 2.42
⁷ Be (^α + ³ He) (J ^π = $\frac{3}{2}^-$, $\frac{1}{2}^-$, T= $\frac{1}{2}$)	GCM -36.69 EXP -37.60	2.41 2.38	2.31 2.27	2.37 2.33	0.10 0.11	2.54
⁸ Be (^α +α) (J ^π =0, T=0)	GCM -56.79	2.48	2.48	2.48	0.0	2.60

The RMS charge radius and quadrupole moment is given as

$$\langle r^2 \rangle_{\text{ch}} = -6(d/dq^2)F_0^{\text{ch}}(q)|_{q^2=0}, \quad (85)$$

$$Q = -15(\frac{4}{5})^{1/2} \langle JJ20|JJ \rangle Z(d/dq^2)F_0^{\text{ch}}(q)|_{q^2=0}, \quad (86)$$

The magnetic dipole moment and octupole moment are obtained from the relation,

$$\begin{aligned} \mu &= 2m \int \mu_z(\mathbf{r}) d\mathbf{r} \\ \mu &= 2m F_{\text{mag}}(\mathbf{q} = 0), \end{aligned} \quad (87)$$

$$\Omega = -15(\frac{7}{2})^{1/2} \langle JJ10|JJ \rangle^{-1} \langle JJ30|JJ \rangle \mu (d/dq^2)F_3^{\text{mag}}(q)|_{q^2=0}, \quad (88)$$

It is interesting to note as shown in Table 1 that in general the volkov V2 forces with $\beta = 0.5\text{FM}^{-2}$ yields the optimum binding energy for ${}^7\text{Li}$ also yields the best values of the charge and magnetic properties including the astrophysical S-factor unlike other RGM calculations and in close in agreement with the experiment.

We have also calculated the matter and charge RMS radii of six, seven and eight nucleon systems including halo nuclei using the same H.O. width parameter $\beta = 0.5\text{FM}^{-2}$ within the GCM as in Table 2 which are also in close agreement with experiment.

E Summary and Conclusion

To summarise, we have considered the microscopic structure for light nuclei in the framework of GCM by calculating various electromagnetic properties, RMS radii, alpha-triton relative wave function and bremsstrahlung weighted cross-section with various nucleon exchange terms, which also justify the role of Pauli principle in light nuclear systems. It is shown that our GCM has a physical interpretation as the coexistence of shell-model and cluster aspects-a unique feature in light nuclei, which also justified by the exact Few-Body Dynamics,

In conclusion, we can say that the GCM is a powerful technique to understand the structure of light nuclei including recently observed halo nuclei.

References

1. D. M. Brink, *Proc. of the Int. School of Physics, "Enrico Fermi" Course 36*, edited by C. Block, Academic Press, New York, (1966) p 247.
2. C. W. Wong, *Phys. Rep.*, **15C** (1975) 285.
3. P. Ring and P. Schuck, *The Nuclear Many-Body Problem*, Springer-Verlag, Berlin Heidelberg New York, (1980) 389.
4. K. Wildermuth and Y. C. Tang, *A Unified Theory of the Nucleus*, Vieweg, Braunschweig, (1977).
5. V. K. Sharma, *Developments of Nuclear Cluster Dynamics*, edited by Y. Akaishi *et al*, World Scientific, Singapore (1989) 50.

6. T. Sasakawa, Phys. Rev., **19** (1979) 1473.
7. M. I. Adamovich *et al* , J. Phys. G: Nucl. Part. Phys. Rev., **30** (2004) 1479.
8. V. K. Sharma, PRAMANA, **51** (1998) 733, and other references.
9. V. K. Sharma and M. A. Nagarajan, J. Phys. G: Nucl. Phys. , **10** (1984) 1703, and other references.

Nuclear saturation in non-relativistic and relativistic theories

L. Satpathy

Institute of Physics, Sachivalaya Marg, Bhubaneswar - 751 005, India.

Abstract. The saturation properties of infinite nuclear matter reflected integrally the nature of nucleon-nucleon interaction and thereby determine the observable properties. If nuclei and dynamics of stellar evolution understanding of these properties, starting from nucleon-nucleon interaction has been a long standing goal of nuclear physics since the early days beginning around 1940. The present status of our understanding of these properties in non-relativistic and relativistic many-body theories, the used two-body force has been found to be inadequate to reproduce these properties, and the introduction of 3-body force is expected to remove the remaining discrepancies and make the calculations agree empirical values. The relativistic theories are still in the process of development. It is premature to conclude that saturation properties of nucleon matter is satisfactorily solved taking relativistic effect into account.

A Introduction

Saturation properties of infinite nuclear matter (INM) are the key fundamental properties which determine the observable properties of nuclei, and quite importantly also the dynamics of the stellar evolution. Understanding of these properties starting from nucleon-nucleon interaction, has been a long-standing goal of nuclear physics since the early days beginning around 1940. The shell structure of atom is quite understandable. However the reality of shell structure in nuclei and the success of shell model in the description of nuclei is not easily comprehensible. There is no central agency at the centre of the nucleus unlike in the atom, which can make the nucleons move in close orbits. Why shell model works - is a fundamental question. The complexity of nucleon-nucleon interaction with its repulsive hard core, short range, state dependence and tensor component etc. should give rise to an effective interaction in INM capable of describing its saturation properties and then gets the stamp of validity for use in the study of nuclear structure with shell playing the pivotal role. The three properties of INM known as its saturation properties are E/A , ρ , K_∞ are the energy per nucleon, density and compression modulus respectively. In the E/A versus ρ curve shown schematically in Fig. 1, the lowest point 'O' defines the saturation point with the empirical values $(E/A) = -16$ MeV and $\rho \simeq 0.17$ nucl/fm⁻³. The third property is the compression modulus K_∞ which is essentially the curvature at the saturation point. Its value is not yet definitely known and is expected to lie in the range 200 to 350 MeV. One is mostly concerned with the first two properties in the context of saturation. The aim of all nuclear many-body theories is to obtain the binding energy=16 MeV for the saturation density $\rho = 0.17$ nucl/fm³ starting with realistic nucleon-nucleon interaction. In this talk we will review

how far relativistic and non-relativistic theories have succeeded in describing these saturation properties of INM. It has been prompted by the assertion of many practitioners of relativistic mean field theorists that this problem has been satisfactorily solved in relativistic theory which is far from truth.

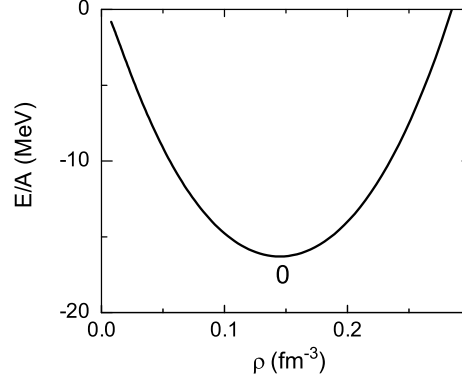


Fig. 1. Schematic diagram showing energy per nucleon E/A of infinite nuclear matter versus density ρ .

B Non-relativistic approach

Historically, Euler [1] made the first attempt to calculate the saturation properties of INM in second order perturbation theory taking a two-body potential of Gaussian shape. However, after the discovery of the singular nature [2] of the two nucleon potential ('hard core') at short distances in 1950, the inadequacy of the conventional perturbation theory for the calculation of saturation properties was recognized. So special many-body theories had to be developed. Brueckner, Levinson and Mahmoud [3] were the pioneers in initiating a new theory, which was improved and enriched further by Bethe [4] and Goldstone [5]. Jastrow [6] suggested an alternative method based on the application of the variational principle to the many-body problem. A brief outline of these two microscopic many-body approaches, and the present status, in regard to the prediction of nuclear matter properties is given below.

B.1 Brueckner-Bethe approach

Consider a system of ' A ' nucleons confined in a large box of volume Ω , that obey the non-relativistic Schrödinger equation. The Hamiltonian for such a system is given by,

$$H = -\sum_i \frac{\hbar^2}{2m} \nabla_i^2 + \sum_{i<j} V_{ij}, \quad (1)$$

where V_{ij} is a realistic two-body potential. The hard core repulsive component of V gives rise to strong correlation in the motion of a pair of nucleons. The basic aim is to find out the effective interaction G seen by the two nucleons when they are interacting inside the nuclear medium. Further, since the nuclear system is a low-density system, the probability of a third or more nucleons coming simultaneously close to a given correlated pair is small. In this situation, the interactions of a pair of nucleons to all order of perturbation theory, has overriding importance than the terms that need the presence of more than two Fermi sea nucleons. Therefore, it is considered proper to assume that during the collision of two nucleons, all others continue to remain undisturbed with constant momentum in nuclear matter. At first instance, the cluster of three and more number of nucleons are neglected and one makes the independent pair approximation [7], also called two-hole line approximation, under which the effective interaction G is defined as

$$\langle ij | G | kl \rangle = \langle ij | V | kl \rangle - \sum_{ab > F} \frac{\langle ij | V | ab \rangle \langle ab | G | kl \rangle}{E_{ijab}}. \quad (2)$$

The summation has to take into account the Pauli exclusion principle. So the single particle states a and b lie above the Fermi level F , and the pairs of states $(i, j), (k, l)$ lie in the Fermi sea. The energy denominator depends upon the single particle energy e_α and is given as

$$E_{ijab} = e_a + e_b - e_i - e_j,$$

The single-particle energies e_i of the states occupied in the Fermi sea are required to satisfy the Brueckner Hartree-Fock (BHF) equation [8],

$$e_i \delta_{ij} = \langle i | -\frac{\hbar^2}{2m} \nabla^2 | j \rangle + \sum_{j < F} \langle ij | G | ij \rangle, \quad (3)$$

The many-body ground state energy is then,

$$E_0 = \sum_i \langle i | -\frac{\hbar^2}{2m} \nabla^2 | i \rangle + \sum_{i < j} \langle ij | G | ij \rangle. \quad (4)$$

To solve the key equation (2), which is called Bethe-Goldstone equation, it is necessary to define the energies e_a and e_b of the single particle states above the Fermi sea. Since these states lie high above the Fermi level, being the high momentum Fourier components, induced by the strongly repulsive short-range part of V . One usually takes the energies of these states to be just the kinetic energies;

$$e_a = -\frac{\hbar^2}{2m} k_a^2 \quad (5)$$

The above scheme for the ground state energy is exact under two-hole line approximation, *i.e.* no three and higher particle clusters are included in the definition of G

given by Eq. (2). Although it was envisaged in the early period, subsequently it was realized that many-particle clusters, in particular the three- and four-particle clusters are important and must be taken into account. Further, the convergence of the Brueckner-Goldstone expansion, in terms of the number of hole lines has to be ensured. The pioneering role played by the Bethe school in this regard, needs hardly to be stressed. A simultaneous development which complemented this effort and provided a great boost in the Brueckner-Bethe (BB) perturbation calculation is a series of study initiated by Pandaripande [9], using constrained variational method. A number of good review articles on BB approach [10, 11] are available in literature which may be consulted by the readers.

B.2 Variational approach

The wave function for a system of ‘ A ’ particles can be written as a Slater determinant,

$$\Phi = \frac{1}{\sqrt{A!}} \det \phi_i(x_j), \quad (6)$$

where ϕ_i ’s are plane wave states.

Unlike in the BB approach, such a wave function has been considered inadequate as a unperturbed wave function to be used at the starting point for the description of a strongly interacting system like nuclear matter. Following Jastrow ansatz [12], a variational trial wave function is constructed in the form

$$\Psi_v = F\Phi, \quad (7)$$

where F represents the correlation induced by the complicated two-body potential. It is generally chosen to be the product of two-body correlation function $f(r_{ij})$.

$$F = \prod_{i < j}^A f(r_{ij}). \quad (8)$$

The $f(r_{ij})$ are functions of a set of variational parameters. Using Ψ_v as a variational trial wave function, the energy,

$$E_v = \frac{\langle \Psi_v | H | \Psi_v \rangle}{\langle \Psi_v | \Psi_v \rangle}, \quad (9)$$

is minimized by varying the parameter set and thus an upper bound to the ground state energy E_0 is obtained. The expectation value E_v involves a diagrammatic cluster expansion, analogous to the Mayer expansion in the statistical mechanics of interacting system. The two-particle cluster energy can be calculated exactly; the three and higher order clusters are evaluated using Fermi hyper-netted chain - single operator chain (FHNC - SOC) approximation. The details of this method can be seen in the review articles by Day [13] and by Pandaripande and Wiringa [14].

B.3 Status of saturation property calculation

A great deal of effort, spanning over a period of more than 15 years commencing since 1970, has been made to check the goodness of Brueckner-Bethe theory through comparative studies carried out in the framework of above variational method, also called the hyper-netted chain theory. It is now believed that Brueckner-Goldstone expansion is convergent in terms of number of hole lines. The calculations of Day [15, 16], and Day and Wiringa [17] for some realistic potentials have demonstrated it. In Fig. 2, the convergence of BB results in terms of the hole line expansion, is shown for the Argonne V_{14} potential [18]. The curves marked with BB1, BB2 and BB3 denote the results obtained with two-, three- and four-hole line approximations respectively. The error bars show the estimated uncertainties in the calculation. Near the saturation, the three-hole line diagrams contribute about 5-6 MeV and the four-hole line ones about 1 MeV. Thus they are not negligible. This result supports the view that the BB theory is convergent.

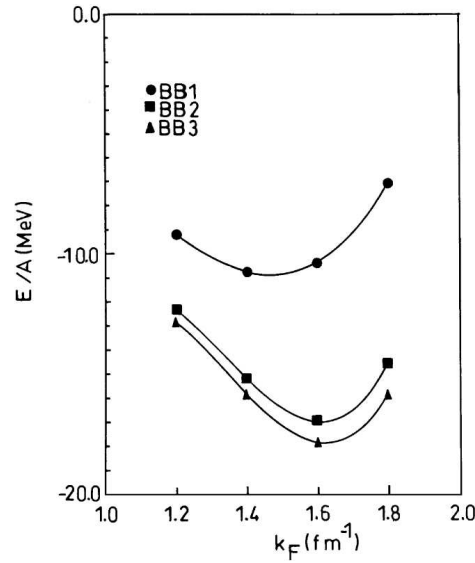


Fig. 2. Energy per nucleon E/A of nuclear matter versus Fermi momentum k_F in two-hole line (BB1), three-hole (BB2) and four-hole line (BB3) approximations calculated in Brueckner-Bethe approach using Argonne V_{14} potential (from Ref. [17]).

The results of many-body calculation obtained for various realistic modern potentials compiled by Brokmann and Machleidt [19] are presented in Table 1, and the corresponding saturation points are shown in Fig. 3. A general feature is that, out of the two properties E/A and ρ , if one is closer to the empirical value the other is far off. The results form a pattern called Coester band. It is clear that, the lowest order approximation (two-hole line) is not adequate. When contributions due to three- and four-hole line are taken into account, one obtains an improved Coester band. However, the results are

still far from the empirical saturation point. At this stage, it was felt that with realistic two-body interaction, there is no more scope to improve the result in BB theory and get agreement with the empirical saturation point.

Table 1. Nuclear matter saturation properties E/A and k_F as predicted for various NN potentials with two-hole line approximation. The results show in the square brackets are the ones obtained when the three- and four-hole line contributions are added. P_D is the predicted %-D state of the deuteron (from Ref. [19]).

Potential	Reference ^a	P_D %	E/A (MeV)	k_F (fm ⁻¹)	Reference ^b
HJ	[20]	7.0	-7.2	1.27	[15]
BJ	[21]	6.6	-8.5[-14.2]	1.36[1.48]	[15]
RSC	[22]	6.5	-10.3 ^c [-17.3]	1.40 ^c [1.52]	[15, 23]
V ₁₄	[18]	6.1	-10.8[-17.8]	1.47[1.62]	[17]
Paris	[24]	5.8	-11.2[-17.7]	1.51[1.63]	[17, 24]
HM1	[25]	5.8	-11.8[-16.9]	1.48[1.56]	[17, 25]
Sch	[26]	4.9	-20.2	1.85	[25]
UNG	[27]	4.4	-23.3	1.87	[25]
(Bonn)C	[28]	5.6	-12.1	1.54	[28]
(Bonn)B	[28]	5.0	-14.0	1.61	[28]
(Bonn)A	[28]	4.4	-17.1	1.74	[28]

^aReferences to the potentials.

^bReferences for the nuclear matter calculations.

^cUsing OBEP for $J \geq 3$.

The possible deficiency of BB theory was searched with great care by carrying out comparative studies in the hyper-netted chain theory. However, extensive calculations in the latter theory show that, the results are in fair agreement with the BB theory predictions. In Fig. 4, the results of Day and Wiringa [17] for the saturation properties of nuclear matter obtained with the realistic two-body Argonne V_{14} potential [18] in both the methods are compared. The solid line corresponds to the calculation in BB theory, and the dotted lines on either side are drawn taking into account the estimated uncertainties in the calculated values. The variational calculation has been done taking two different forms of the kinetic energy, namely, the Pandaripande-Bethe (PB) and the Jackson-Feenberg (JF) forms [29]. The results obtained are shown as filled circles and crosses respectively. The uncertainties in the variational calculation are of similar magnitude as in BB calculation. Taking this into account, Day and Wiringa have concluded that, these two methods agree reasonably well with predicted saturation points of -17.8 MeV at 1.6 fm^{-1} for the BB theory, and -16.6 MeV at 1.7 fm^{-1} for the variational method. Further this calculation shows that, both the methods, used to their full potential, have quantitatively failed to explain the saturation with realistic two nucleon potential.

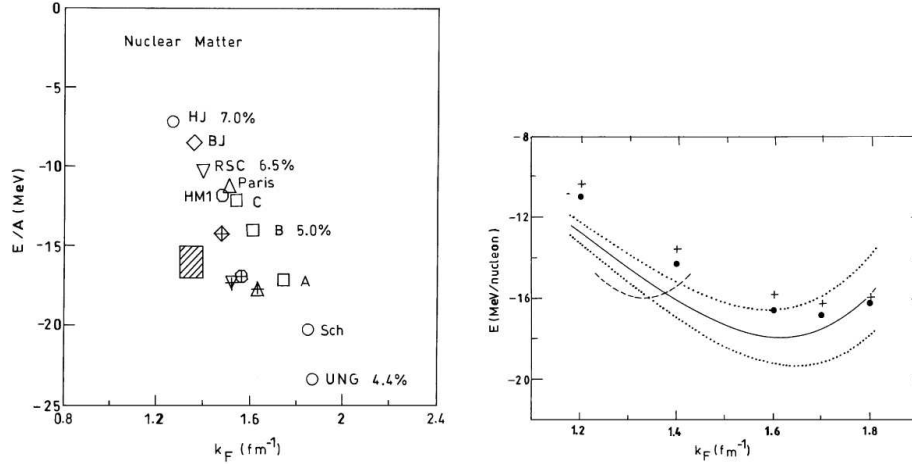


Fig. 3. Nuclear matter saturation for various potentials (see Table 1). Open symbols denote saturation point obtained in the two-hole line approximation; symbols with a cross stand for corresponding predictions when three- and four-hole line contributions are included. Percent number refer to the D-state probability of the deuteron as predicted for the corresponding potential. The shaded rectangle denotes the empirical value of the saturation, (from Ref. [19]).

Fig. 4. Energy of nuclear matter as a function of Fermi momentum. The solid line denotes the fit to the Bruckner-Bethe energy; the dotted lines show their estimated uncertainties. The data and crosses stand for the variational JF and PB energies respectively (from Ref. [17]). Empirical saturation curve with a binding energy of 16 MeV at 1.33 fm^{-1} and an incompressibility 210 MeV is shown as dashed line.

C Many-body theory with mesonic degrees of freedom

Thus extension of many-body theory including other effects was clearly needed. One conceivable direction of extension is to include the mesonic degrees of freedom explicitly in the many-body theory. In low energy nuclear physics, their presence is clearly manifested in the electro-magnetic properties of nuclei. The magnetic moments of neutrons and protons are substantially different from those of the Dirac values. The pion-nucleon scattering cross-section is dominated by a broad resonance at 300 MeV. This is the $\Delta(1232)$ isobar which plays important role in the N-N scattering at low and intermediate energies. Therefore, totally freezing-out the mesonic degrees of freedom in the many-body problem may be too simplistic. Being conscious of this fact, many groups [30–33] in the past, have attempted to develop a many-body theory for the composite system of nucleons and mesons. (For a recent review on the subject, the Ref. [28] may be seen). Introduction of the additional degrees of freedom due to mesons and isobar has essentially produced two effects in nuclear matter; namely the medium effect on the two-nucleon interaction and the contribution from many-body force. Both these

effects are substantial, however, they are of opposite sign. The medium effect has been found to be repulsive, while the contribution from the many-nucleon force is attractive. Thus, they tend to cancel without significantly affecting the saturation properties [28]. This may be the reason why the traditional picture of nuclear system with two-body force and nucleonic degrees of freedom is largely successful. Thus no improvement in the saturation properties of INM through the introduction of meson degrees of freedom was possible.

D Saturation properties in relativistic theory

Another direction, along which the nuclear many-body theory could evolve towards perfection, is the relativistic aspect of nuclear physics. Since 1970, this branch of nuclear physics developed with considerable pace when Clark et al. [34] proposed a new method called Dirac phenomenology to describe high energy proton-nucleus scattering. In this approach, a Dirac equation with a strong attractive (scalar) and repulsive (vector) potential is solved, and the solution is used to fit quantitatively the spin observable in the above reaction, which cannot be described well by the Schrodinger equation. Simultaneously, the relativistic mean field theory for nuclei developed by Miller and Green [35], Serot and Walecka [36], and Brockmann [37] produced impressive success. Inspired by these developments, Shakin and co-workers [38] made a relativistic extension of many-body Brueckner theory called Dirac-Brueckner theory. This was further improved by Brockmann and Machleidt [39], and by ter Harr and Malfliet [40]. There is no scope for comprehensive discussion on this topic here. It will suffice for our purpose to state, the main results of this approach *i.e.*, it could account quantitatively the remaining discrepancy between empirical saturation point and the conventional many-body theory result, obtained with the realistic two-body interaction discussed above. The results of Brockmann and Machleidt on the saturation properties can be seen in Fig. 3. Thus, the Dirac-Brueckner approach could reproduce the empirical saturation properties of nuclear matter. It has to be noted that, this theory in its present form is not considered a complete theory. There are many criticisms [41–44]. As yet, only lowest order G-matrix calculation has been carried out in this approach. The higher order contributions have to be calculated and the convergence has to be shown. Further, for consistency, both the positive and negative energy states have to be taken into account on equal footing in the calculation. Thus, the relativistic many-body theory is still in the process of development, and we cannot regard at this stage that the problem of saturation properties of nuclear matter is satisfactorily solved taking relativistic effect into account.

E Saturation in non-relativistic theory with three-body force

At the present time, a three-body force is being favoured as additional physical effect to be included in the non-relativistic theory, to compensate the deficiency encountered so far in the saturation of nuclear matter. The idea of three-body force is quite old in nuclear physics. However, it has acquired greater importance lately because of the failure of two-body interaction to quantitatively describe the saturation and the properties

of few body systems. Its contribution to the saturation property has also been considered before [10, 45–48] But its proper treatment using a reliable many-body method has been accomplished [49] only lately in 1980s. The measure source of this force has been considered to be due to two-pion exchange. Lagaris and Pandaripande [49, 50] argued that the three body potential can be expressed in the form

$$V_{123} = \sum_l \sum_{\text{cyc}} U_l u_l(r_{12}) u_l(r_{13}) P_l(\cos\theta_i), \quad (10)$$

where U_l are the strength parameters, $u_l(r)$ are functions of inter-particle distances, θ_i are the inner angles of the triangle ($\mathbf{r}_1, \mathbf{r}_2, \mathbf{r}_3$) and \sum_{cyc} represents a sum of three terms defined by the cyclic permutation of the indices 1, 2 and 3. In a model calculation, they added the above three-body potential to the realistic V_{14} potential and carried out variational calculation to show that saturation can be described. They varied the strength U_l to get the best overall fit to the binding energy, the saturation density, and incompressibility of nuclear matter. The details can be seen in Ref. [50]. This is phenomenological and clearly unsatisfactory. With only V_{14} potential, the saturation is found with $k_F \simeq 1.7 fm^{-1}$ and $E/A = -17.5 MeV$, while with the addition of three nucleon interaction the empirical values $k_f = 1.33 fm^{-1}$ and $E/A = -16 MeV$ could be fitted.

F Conclusion

Recently there has been considerable progress in the determination of three nucleon force at a fundamental level using proton-deuteron and neutron-deuteron scattering data in the framework of various field theoretic models [51] and chiral-perturbation theory [52]. With this development, it is hoped, the saturation problem will be solved and our understanding of nuclear dynamics will be firm. More than 60 years of effort has been put in describing the saturation properties of INM in non-relativistic theory. The theoretical method for such study has been well perfected over these years. In the relativistic approach the theoretical method needs to be perfected before drawing any conclusions.

References

1. H. Euler, Z. Phys. 105 (1937) 553.
2. R. Jastrow, Phys. Rev. 79 (1950) 389; Phys. Rev. 81 (1951) 165.
3. K. A. Bruckner, C. A. Levinson and H. M. Mahmoud, Phys. Rev. 95 (1954) 217.
4. H. A. Bethe, Phys. Rev. 103 (1956) 1353.
5. J. Goldstone, Proc. R. Soc. (London) A239 (1957) 267.
6. R. Jastrow, Phys. Rev. 98 (1955) 1479.
7. L. C. Gomes, J. D. Walecka, and V. F. Weisskoff, Ann. Phys. (N.Y.) 3 (1958) 241.
8. H. A. Bethe, B. H. Brandow and A. G. Petschek, Phys. Rev. 129 (1963) 225.
9. V. R. Pandaripande, Nucl. Phys. A174 (1971) 641; Nucl. Phys. A181 (1972) 33.
10. H. A. Bethe, Ann. Rev. of Nucl. Sc. 21 (1971) 93.

11. B. D. Day, Rev. Mod. Phys. 39 (1967) 719; J. P. Jeukenne, A. Lejeune, and C. Mahaux, Phys. Rep. 25 (1976) 83; J. W. Negele, Rev. Mod. Phys. 54 (1982) 913.
12. R. Jastrow, Phys. Rev. 98 (1955) 1479.
13. B. D. Day, Rev. Mod. Phys. 50 (1978) 495.
14. V. R. Pandaripande and R. B. Wiringa, Rev. Mod. Phys. 51 (1979) 821.
15. B. D. Day, Phys. Rev Lett. 47 (1981) 226.
16. B. D. Day, Phys. Rev C 24 (1981) 1203.
17. B. D. Day and R. B. Wiringa, Phys. Rev. C 32 (1985) 1057.
18. R. B. Wiringa, R. A. Smith and T. L. Ainsworth, Phys. Rev. C 29 (1984) 1207.
19. R. Brockmann and R. Machleidt, Phys. Rev. C 42 (1990) 1965.
20. T. Hamada and I. D. Johnson, Nucl. Phys. 34 (1962) 382.
21. H. A. Bethe and M. B. Johnson, Nucl. Phys. A230 (1974) 1.
22. R. V. Reid, Ann. Phys. (N.Y.) 50 (1968) 411.
23. R. Machleidt, Ph. D. thesis, University of Bonn, (1973) (unpublished).
24. M. Lacombe et al., Phys. Rev. C 21 (1980) 861.
25. K. Holinde and R. Machleidt, Nucl. Phys. A247 (1975) 495.
26. G. Schierholz, Nucl. Phys. B40 (1972) 335.
27. T. Ueda, M. Nack and A. E. S. Green, Phys. Rev. C 8 (1973) 2061.
28. R. Machleidt, Adv. Nucl. Phys. 19 (1989) 189.
29. J. G. Zabolitzky, Phys. Rev. A16 (1977) 1258.
30. C. B. Dover and R. H. Lemmer, Phys. Rev. 165 (1968) 1105.
31. W. D. Brown, R. D. Puff and L. Wilets, Phys. Rev. C 2 (1970) 331.
32. J. D. Walecka, Ann. Phys. (N.Y.) 83 (1974) 491.
33. D. Schutte, Nucl. Phys. A221 (1974) 450.
34. B. C. Clark, R. L. Mereer, D. G. Ranehall, and A. M. Saperstein, Phys. Rev. C 7 (1973) 466.
35. L. D. Miller and A. E. S. Green, Phys. Rev. C 5 (1972) 241.
36. B. D. Serot and J. D. Walecka, Adv. Nucl. Phys. 16 (1986) 1.
37. R. Brockmann, Phys. Rev. C 18 (1978) 1510.
38. M. R. Anastasio, L. S. Celenza, W. S. Pong and C. M. Shakin, Phys. Rep. 100 (1983) 327.
39. R. Brockmann and R. Machleidt, Phys. Lett. 149B (1984) 283.
40. B. ter Harr and R. Malfleit, Phys. Rep. 149 (1987) 207.
41. G. E. Brown, W. Weise, G. Baym and J. Speth, Comments Nucl. Part. Phys. 17 (1987) 39.
42. J. W. Negele, Comments Nucl. Part. Phys. 14 (1985) 303.
43. E. D. Cooper and B. K. Jennings, Nucl. Phys. A458 (1986) 717.
44. M. Thies, Phys. Lett. 166B (1986) 23.
45. S. Drell and K. Huang, Phys. Rev. 91 (1963) 1527.
46. G. E. Brown, A. M. Green and W. J. Gerace, Nucl. Phys. A115 (1968) 435.
47. G. E. Brown, and A. M. Green, Nucl. Phys. A137 (1969) 1.
48. B. H. J. McKellar and R. Rajaraman, Phys. Rev. C 3 (1971) 1877; S. A. Coon, M. D. Scadron, P. C. McNamee, B. R. Barrett, D. W. E. Blatt and B. H. J. McKeller, Nucl. Phys. A317, (1979) 242.
49. I. E. Legaris, and V. R. Pandaripande, Nucl. Phys. A359 (1981) 349.
50. J. Carlson, V. R. Pandaripande and R. B. Wiringa, Nucl. Phys. A401 (1983) 59.
51. W. Gloeckle, H. Witala, D. Hueber, H. Kamada and J. Golak, Phys. Rep. 274 (1996) 107; S. A. Coon and M. T. Pena, Phys. Rev. C 48, (1993) 2559.
52. J. L. Friar, D. Hueber and U. van Kolck, nucl-th/9809065 .

Giant Dipole Resonance in Hot and Rotating Nuclei

P. Arumugam^{1*}, A. Ganga Deb², and S.K. Patra¹

¹ Institute of Physics, Sachivalaya Marg, Bhubaneswar - 751 005, India

² Department of Physics, Sonepur College, Subarnapur-767017, Orissa, India.

Abstract. We present here the method of calculating giant dipole resonance (GDR) observables in hot and rotating nuclei. We employ a macroscopic approach towards GDR in which the GDR observables are related to the nuclear shapes. Shape calculations were done using cranked Nilsson-Strutinsky method (CNSM) extended to finite temperature and spin. The GDR built on the states determined by NS method are studied with a macroscopic model comprising anisotropic harmonic oscillator potential with separable dipole-dipole interaction. Methods to parameterize the free energy, such as the Landau theory, for easier evaluation of thermal fluctuations are discussed along with a scheme to evaluate thermal fluctuations with full CNSM. Variation of GDR width as a function of temperature and spin is discussed. The results obtained are confronted with the experimental data wherever available. Applicability of the Landau theory at low temperature and at high spins is scrutinized. The Jacobi transition at high spins and hyperdeformed structures are studied.

A Introduction

Iso-vector giant dipole resonance commonly termed as GDR is one among the fundamental modes of excitations in nuclei caused by the photons [1]. In a microscopic picture, GDR can be understood in terms of particle-hole excitations often called $p - h$ doorway resonance [2, 3]. Alternatively, macroscopic approaches couple the GDR to the shape of the nuclei [4–7]. The GDR spectrum could effectively reflect the structure of nuclear state on which GDR is built. For hot rotating nuclei, GDR serves as a unique probe to obtain the structure information. Hence GDR studies of nuclei as a function of both temperature (T) and spin (I) has been an interesting and important area of research in nuclear structure physics. The domain of GDR spreads rapidly over different areas of theoretical and experimental interest. For instance, from the GDR γ -decay, it was possible to extract the information of lifetime of hot super-heavy system such as ^{272}Hs [8]. By populating the isomeric states in the decay of the GDR better information about the isomers could be extracted [9]. The measurement of GDR gamma rays from highly excited nuclei could be utilized [10] to check the level density prescriptions. In general, the GDR observations provide us information about the geometry as well as the dynamics of nuclei even at extreme limits of temperature, spin and isospin. Several experiments have been carried out recently [11–14] to study the influence of angular momentum and temperature, by observing the gamma rays from the GDR states from hot rotating nuclei. The behavior of GDR width as a function of temperature has been an

* Email: aru@iopb.res.in

interesting phenomenon and the GDR measurements at extreme spins render information about highly deformed structures. Recent developments in theoretical [7, 15–17] and experimental [11–14] fronts could throw more light in our understanding of hot rotating nuclei. However, several key issues remain to be well understood [18]. One among them is the variation of GDR width (Γ_{GDR}) as a function of T and I .

In the ground state, the GDR observables, primarily the Γ_{GDR} can be directly related to the equilibrium deformation (β). For hot and rotating nuclei the Γ_{GDR} is influenced primarily by three factors viz., a) change in β , b) due to thermal shape fluctuations the averaged deformation ($\bar{\beta}$) may increase which leads to the increase of Γ_{GDR} with increasing T and c) coriolis splitting of GDR components may increase Γ_{GDR} at higher spins. Among the above factors, the thermal fluctuations are observed to be more dominant. Hence, as the temperature increases, Γ_{GDR} increases irrespective of the trend of β (which in most of the cases would be decreasing). In observations at fixed T , Γ_{GDR} was found to follow the trend of β and $\bar{\beta}$. In this case we observe that the gross structure effects do survive thermal fluctuations and changes in the equilibrium shape could be probed by the GDR [20]. However, in any case, there is a direct correlation between $\bar{\beta}$ and Γ_{GDR} and few explicit relations could be derived [17, 21].

At low temperatures when fluctuations are not very dominant, the averaged shape ($\bar{\beta}$) could well reflect the changes in the equilibrium shape (β). Hence it would be interesting to carry out investigations in such cases where better and clear correlations between Γ_{GDR} and β do exist. With recent experimental techniques, few low T measurements have been made [11, 12] and the data could not be explained by conventional thermal fluctuation calculations. At low T , microscopic effects such as shell and pairing effects could make important contributions [7, 15, 16]. Hence care should be taken while applying the theories which were successful in the high T regime. One among the major concern in this regard is the applicability of free energy parameterizations such as Landau theory [5, 22] which were employed to do timesaving calculations. In a previous work [7], some of the authors have presented a simple theoretical framework for calculating GDR observables without employing the shape parameterizations. In Ref. [23] we have brought out the discrepancies in applying the shape parameterizations at low T and high spins. In the present work, we study in detail the shape transitions in few selected medium heavy mass nuclei with an emphasis on the low T behaviour of these nuclei.

In the next section, we present our theoretical framework in an illustrative way comprising the details about temperature dependance of shell corrections. In section III, we have discussed our results for few selected nuclei along with the experimental data wherever available. The conclusions drawn are laid in section IV.

B The Formalism

The details of our theoretical formalism for studying giant dipole resonance can be found in Refs. [7, 23]. Here we present an outline of that in an illustrative way. The formalism can be explained in three folds with models for 1) shape calculations, 2) relating the shapes to GDR observables and 3) considering the shape fluctuations due to

thermal effects. The important details of these three parts are presented in the following subsections.

B.1 Cranked Nilsson-Strutinsky method at finite temperature

In this approach [7, 23], the total free energy (F_{TOT}) at fixed deformation is calculated using the expression

$$F_{\text{TOT}} = E_{\text{RLDM}} + \sum_{p,n} \delta F . \quad (1)$$

Expanding the rotating liquid-drop energy E_{RLDM} and writing shell corrections in rotating frame [24] leads to

$$F_{\text{TOT}} = E_{\text{LDM}} + \sum_{p,n} \delta F^\omega + \frac{1}{2} \omega (I_{\text{TOT}} + \sum_{p,n} \delta I) . \quad (2)$$

The angular velocity ω is tuned to obtain the desired spin given by

$$I_{\text{TOT}} = \mathfrak{I}_{\text{rig}} \omega + \delta I . \quad (3)$$

The liquid-drop energy (E_{LDM}) is calculated by summing up the Coulomb and surface energies corresponding to a triaxially deformed shape defined by the deformation parameters β and γ . The rigid-body moment of inertia ($\mathfrak{I}_{\text{rig}}$) is calculated with surface diffuseness correction [7]. δF and δI are the shell corrections corresponding to free energy and spin respectively. To calculate the shell corrections, we use the triaxially deformed Nilsson model together with the Strutinsky's prescription. The single-particle energies (e_i) and spin projections (m_i) are obtained by diagonalizing the triaxial Nilsson Hamiltonian in cylindrical representation upto first twelve major shells. At finite temperatures the free energy in rotating frame is given by

$$F^\omega = \sum_{i=1}^{\infty} e_i^\omega n_i - T \sum_{i=1}^{\infty} s_i , \quad (4)$$

where s_i are the single-particle entropy and n_i are the occupation numbers which follow Fermi-Dirac distribution given by

$$n_i = \frac{1}{1 + \exp\left(\frac{e_i^\omega - \lambda}{T}\right)} . \quad (5)$$

The chemical potential λ is obtained using the constraint $\sum_{i=1}^{\infty} n_i = N$, where N is the total number of particles. The total entropy $S = \sum_{i=1}^{\infty} s_i$ can be represented in terms of occupation numbers as

$$S = - \sum_{i=1}^{\infty} [n_i \ln n_i - (1 - n_i) \ln(1 - n_i)] . \quad (6)$$

The shell correction is given in terms of the single particle level density as [7,32]

$$\delta F^\omega = F^\omega - \tilde{F}^\omega = \int_{-\infty}^{\lambda} e g(e) de - \int_{-\infty}^{\tilde{\lambda}} e \tilde{g}(e) de . \quad (7)$$

where $g(e) = \frac{d\mathcal{N}(e)}{de}$ is the single particle level density and $\mathcal{N}(e)$ is the total number of particles that can be accommodated by the energy levels with their energy $\leq e$. λ and $\tilde{\lambda}$ are the chemical potentials corresponding to the discrete and smooth single particle distributions respectively. λ and $\tilde{\lambda}$ can be calculated using the constraints $\mathcal{N}(\lambda) = N$ and $\tilde{\mathcal{N}}(\tilde{\lambda}) = N$ respectively. We can also write

$$g(e) = \left. \frac{d\mathcal{N}(\lambda)}{d\lambda} \right|_{\lambda=e} = \sum_{i=1}^{\infty} \left. \frac{dn_i(e_i^\omega, \lambda)}{d\lambda} \right|_{\lambda=e} . \quad (8)$$

From Eqs.(5) and (8), we can write the temperature dependent single particle level density as

$$g(e) = \sum_{i=1}^{\infty} \frac{1}{4T \cosh^2[(e^\omega - e_i)/2T]} . \quad (9)$$

From the above relation, it is clear that with the inclusion of temperature the effective energy spectrum is no longer discrete as we allow the level density to vary smoothly with its peaks at discrete levels corresponding to zero temperature. Hence for hot nuclei the effective single-particle spectrum can be thought as a quasi-continuum whose smoothness increases with temperature. This smoothing of energy levels due to temperature is illustrated in Fig. 1b.

The natural way of applying Strutinsky averaging to the level density is to convolute $g(e)$ with the averaging function

$$\tilde{g}(e) = \frac{1}{\gamma_s} \int_{-\infty}^{\infty} \tilde{f}\left(\frac{e - e'}{\gamma_s}\right) g(e') de' . \quad (10)$$

We use the averaging function

$$\tilde{f}(x) = \frac{1}{\sqrt{\pi}} \exp(-x^2) \sum_{m=0}^p C_m H_m(x) , \quad (11)$$

where $C_m = (-1)^{m/2}/(2^m(m/2)!)$ if m is even and $C_m = 0$ if m is odd; $x = (e - e_i^\omega)/\gamma_s$, γ_s is the smearing parameter satisfying the plateau condition $d\tilde{F}/d\gamma_s = 0$; p is the order of smearing and $H_m(x)$ are the Hermite polynomials. When $T = 0$, $g(e')$ is a delta function and we get

$$\tilde{g}(e) = \sum_{i=1}^{\infty} \tilde{f}(x) . \quad (12)$$

The above relation can be treated as a representative of a Strutinsky smoothed spectrum as illustrated in Fig. 1c. At $T = 0$, we can consider the shell correction energy (7) to be the difference between the energies calculated using, the discrete spectrum (Fig.

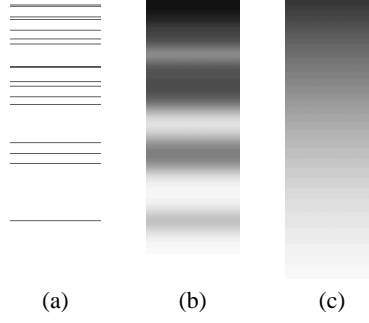


Fig. 1. (a) A typical single-particle energy spectrum. (b) Simulation of thermal effect on smoothing of the single-particle spectrum (a) at a temperature 0.5 MeV. (c) Simulation of Strutinsky smoothing of the single-particle spectrum (a). Now the shell correction comes from the difference between (b) and (c) which will always be less than that between (a) and (c). At higher temperatures, (b) and (c) will be similar leading to the disappearance of shell correction. (In cases (b) and (c) the level densities (9) and (12) are plotted with white representing zero and full black representing values ≥ 1.254 shades of grey are used to represent intermediate values).

1a) and the Strutinsky smoothed spectrum (Fig. 1c). At finite temperature one has to consider the difference between the temperature smoothed spectrum (Fig. 1b) instead of the discrete spectrum (Fig. 1a).

Increasing the temperature will result in the increase of the width of the function (9) and subsequently will make the level density to vary smoothly with respect to the single particle energy. This situation is well explained by Fig. 2, in which the temperature dependent single-particle level density (9) is plotted as a function of single-particle energy. It is clearly seen in the figure that around $T = 3$ MeV the level density ceases to fluctuate. This form of $g(e)$ at high temperature is very similar to the Strutinsky smoothing function $\tilde{f}(x)$. In this case, the Strutinsky smoothed spectrum and the effective single-particle spectrum are much similar and hence there is no difference between the two terms in Eq. (7). This illustrates the vanishing of shell correction at high temperatures.

The function (9) is very similar to a Gaussian and we have our Strutinsky smeared single-particle level density as a Gaussian with curvature correction. The relation between the two smoothing quantities is given by [25]

$$T \approx 0.472 \gamma_s . \quad (13)$$

If we have γ_s in the order of the inter-shell spacing ($\hbar\omega$), the above relation suggests that temperatures above half of the inter-shell spacing will wash out shell corrections. The critical temperatures obtained using expression (13) are given in Fig. 3. It is evident from the figure that the critical temperature is high for lower mass nuclei and strongly depend on smearing parameter γ_s .

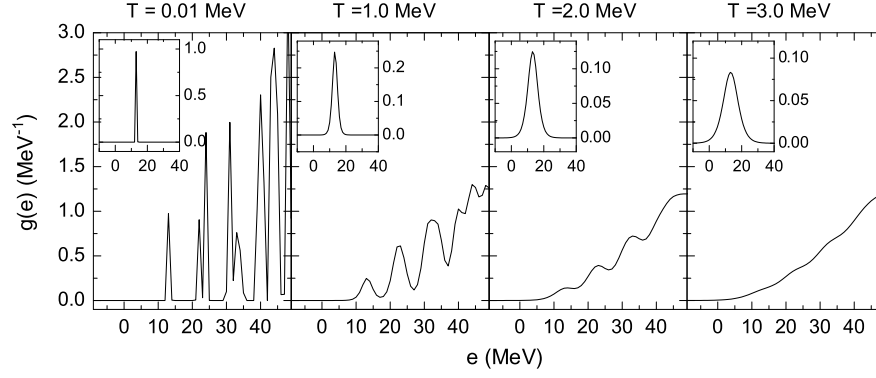


Fig. 2. Temperature dependent single-particle level densities at different temperatures. The curves in the insets are the first component of $g(e)$ (9). It is evident that the rise in temperature leads to an increase in the width of the components and hence leads to a smooth energy spectrum.

Substituting Eq. (10) in the expression for \tilde{F} in Eq. (7), and using Eq. (4), we have [26, 32]

$$\tilde{F}^\omega = \sum_i e_i^\omega \tilde{n}_i - T \sum_i \tilde{s}_i + \gamma_s \int_{-\infty}^{\infty} \tilde{f}(x) x \sum_i n_i(x) dx, \quad (14)$$

where

$$\tilde{n}_i = \int_{-\infty}^{\infty} \tilde{f}(x) n_i(x) dx, \quad (15)$$

$$\tilde{s}_i = \int_{-\infty}^{\infty} \tilde{f}(x) s_i(x) dx. \quad (16)$$

The integrals appearing in Eq. (14) are evaluated numerically using the Hermite-Gauss quadrature. The plateau conditions are observed to be well satisfied with the third term in the right of Eq. (14). We observe that in most of the cases the plateau is more clear for the values of $\gamma_s = 1.6$ and $p = 6$.

For the spin distribution, the Strutinsky smoothed spin can be derived in a similar way leading to the expression $\tilde{I} = \sum_{i=1}^{\infty} m_i \tilde{n}_i$ and hence the shell correction for spin is

$$\delta I = \sum_{i=1}^{\infty} m_i n_i - \sum_{i=1}^{\infty} m_i \tilde{n}_i. \quad (17)$$

B.2 Macroscopic method for GDR

The nuclear shapes are related to the GDR observables using a model [7, 27] comprising an anisotropic harmonic oscillator potential with separable dipole-dipole interaction. The Hamiltonian describing the model is given by

$$H = H_{av} + H_{int}, \quad (18)$$

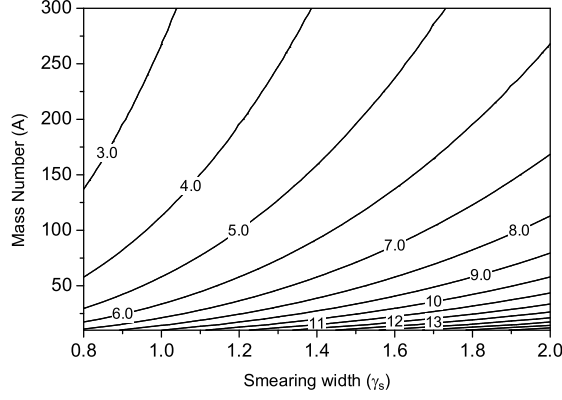


Fig. 3. Upper limits for critical temperatures (in MeV) as a function of mass number and smearing width (in units of oscillator frequency $\hbar\omega_0$).

where H_{av} is the average potential corresponding to the triaxial harmonic oscillator and H_{int} represents the effective dipole interaction.

$$H_{av}(\Omega) = \sum_{\nu=1}^A h_{\nu}(\Omega) , \quad (19)$$

where

$$h(\Omega) = \frac{p^2}{2m} + \frac{m}{2} (\omega_x^2 x^2 + \omega_y^2 y^2 + \omega_z^2 z^2) - \Omega l_z , \quad (20)$$

$L_z = \sum_{\nu=1}^A l_z(\nu)$ is the operator of rotation about the z axis and Ω is the cranking frequency. The effective dipole interaction has the form

$$H_{int} = \eta \sum_{i=x,y,z} \frac{m\omega_i^2}{2A} \left[\sum_{\nu=1}^A \tau_3^{(\nu)} x_i(\nu) \right]^2 , \quad (21)$$

where $\tau_3^{(\nu)}$ is the third projection of the Pauli isospin matrix and η is a parameter that characterizes the isovector component of the neutron and proton average field. The frequencies of the GDR in a rotating nucleus can be obtained by diagonalizing analytically the Hamiltonian (18) with the effective interaction (21) within the framework of the standard random-phase-approximation. Including the splitting of the GDR frequencies due to rotation, the final set of GDR frequencies in laboratory frame are obtained as [27]

$$\tilde{\omega}_z = (1 + \eta)^{1/2} \omega_z , \quad (22)$$

$$\begin{aligned} \tilde{\omega}_2 \mp \Omega = & \left\{ (1 + \eta) \frac{\omega_y^2 + \omega_x^2}{2} + \Omega^2 + \frac{1}{2} [(1 + \eta)^2 (\omega_y^2 - \omega_x^2)^2 \right. \\ & \left. + 8\Omega^2 (1 + \eta) (\omega_y^2 + \omega_x^2)]^{\frac{1}{2}} \right\}^{\frac{1}{2}} \mp \Omega , \end{aligned} \quad (23)$$

$$\tilde{\omega}_3 \mp \Omega = \left\{ (1 + \eta) \frac{\omega_y^2 + \omega_x^2}{2} + \Omega^2 - \frac{1}{2} [(1 + \eta)^2 (\omega_y^2 - \omega_x^2)^2 + 8\Omega^2 (1 + \eta) (\omega_y^2 + \omega_x^2)]^{\frac{1}{2}} \right\}^{\frac{1}{2}} \mp \Omega, \quad (24)$$

All these five frequencies do not exist for all nuclei. The number of existing frequencies depends on the shape of the nucleus [27, 28]. One have five GDR components corresponding to the frequencies, $\tilde{\omega}_1$, $\tilde{\omega}_2 - \Omega$, $\tilde{\omega}_2 + \Omega$, $\tilde{\omega}_3 - \Omega$ and $\tilde{\omega}_3 + \Omega$, for collectively rotating triaxial nuclei. For prolate nuclei ($\omega_x = \omega_y > \omega_z$) rotating about an axis perpendicular to its symmetry axis, all the above five frequencies will exist. But for oblate nuclei ($\omega_x = \omega_y < \omega_z$) rotating about its symmetry axis, as shown first by Hilton in Ref. [28], only two frequencies, namely, $\tilde{\omega}_1$ and $\tilde{\omega}_2 - \Omega = \tilde{\omega}_3 + \Omega$ will exist and thus all effects due to rotation vanish and only those purely due to deformation will be left. For the spherical nuclei ($\omega_x = \omega_y = \omega_z$), which comes under the later category, one gets only one frequency namely $\tilde{\omega}_1 = \tilde{\omega}_2 - \Omega = \tilde{\omega}_3 + \Omega$.

By the semi classical theory of the interaction of photons with nuclei, the shape of a fundamental resonance in the absorption cross-section is that of the Lorentz curve

$$\sigma(E_\gamma) = \sum_i \frac{\sigma_{mi}}{1 + (E_\gamma^2 - E_{mi}^2)^2 / E_\gamma^2 \Gamma_i^2} \quad (25)$$

where Lorentz parameters E_m , σ_m and Γ are the resonance energy, peak cross-section and full width at half maximum respectively. Here i represents the number of components of the GDR and is determined from the shape of the nucleus. It is to be noted that these Lorentz lines are non-interfering, but Γ_i is assumed to depend on energy. The energy dependence of the GDR width can be approximated by [29]

$$\Gamma_i \approx 0.026 E_i^{1.9}. \quad (26)$$

The peak cross section σ_m is given by

$$\sigma_m = 60 \frac{2}{\pi} \frac{NZ}{A} \frac{1}{\Gamma} 0.86(1 + \alpha). \quad (27)$$

The parameter α which takes care of the sum rule is fixed at 0.3 for all the nuclei. In most of the cases we normalize the peak with the experimental data and hence the choice of α has less effect on the results. The other parameter η varies with nucleus so that the ground state GDR centroid energy is reproduced. The choice for different nuclei are given in table 1.

Table 1. Choice of the parameter η used in GDR calculations

Nuclei	η	Nuclei	η
Ca, Ti	2.1	Er	3.0
Zr, Sn	2.6	Au	3.2
Eu	2.8	Hg, Pb	3.4

B.3 Shape Fluctuations

The relation between nuclear shape and GDR cross section is not straightforward especially in hot nuclei where large-amplitude thermal fluctuations of the nuclear shape play an important role [30]. Hence, for a meaningful comparison of experimental and theoretical values, the thermal shape fluctuations should be taken care properly. In the case of hot and rotating nuclei there can be fluctuations in the orientation of the nuclear symmetry axis with respect to the rotation axis. The general expression for the expectation value of an observable \mathcal{O} incorporating both thermal and orientation fluctuations is given by [5, 31]

$$\bar{\mathcal{O}} = \langle \mathcal{O} \rangle_{\beta, \gamma, \Omega} = \frac{\int \mathcal{D}[\alpha] e^{-F(T, I; \beta, \gamma, \Omega)/T} (\hat{\omega} \cdot \mathcal{I} \cdot \hat{\omega})^{-3/2} \mathcal{O}}{\int \mathcal{D}[\alpha] e^{-F(T, I; \beta, \gamma, \Omega)/T} (\hat{\omega} \cdot \mathcal{I} \cdot \hat{\omega})^{-3/2}}, \quad (28)$$

where $\Omega = (\phi, \theta, \psi)$ are the Euler angles specifying the intrinsic orientation of the system, $\hat{\omega} \cdot \mathcal{I} \cdot \hat{\omega} = I_{x'x'} \cos^2 \phi \sin^2 \theta + I_{y'y'} \sin^2 \phi \sin^2 \theta + I_{z'z'} \cos^2 \theta$ is the moment of inertia about the rotation axis $\hat{\omega}$ given in terms of the principal moments of inertia $I_{x'x'}$, $I_{y'y'}$, $I_{z'z'}$, and the volume element $\mathcal{D}[\alpha] = \beta^4 |\sin 3\gamma| d\beta d\gamma \sin \theta d\theta d\phi$.

In a parametrization based on the Landau theory of phase transitions, developed by Alhassid *et al* [22], the free energy is expanded in terms of certain temperature dependent constants which are to be extracted by fitting with the free energy calculations at fixed temperatures from the NS method. The extended Landau theory [7, 22] includes expansion upto sixth power of β given by

$$F(T, \omega = 0; \beta, \gamma) = F_0 + F_2 \beta^2 + F_3 \beta^3 \cos 3\gamma + F_4 \beta^4 + F_5 \beta^5 \cos 3\gamma + F_6^{(1)} \beta^6 + F_6^{(2)} \beta^6 \cos^2 3\gamma + \dots, \quad (29)$$

where F_0, F_2, \dots are the temperature dependent Landau parameters, which are obtained by least square fitting to the free energy surfaces calculated by the NS method. The general expression for moment of inertia $I_{z'z'}$ is given by

$$I_{z'z'} = I_0 + I_1 \beta \cos \gamma + I_2^{(1)} \beta^2 + I_2^{(3)} \beta^2 \sin^2 \gamma + I_3^{(1)} \beta^3 \cos 3\gamma + I_3^{(2)} \beta^3 \cos \gamma + I_4^{(1)} \beta^4 + I_4^{(2)} \beta^4 \cos 3\gamma \cos \gamma + I_4^{(3)} \beta^4 \sin^2 \gamma. \quad (30)$$

The constants I_0, I_1, \dots are also evaluated using the fitting procedure. It is enough to calculate $I_{z'z'}$ for rotations around a principal axis z' and the other moments of inertia are then given by

$$\begin{aligned} I_{x'x'}(T; \beta, \gamma) &= I_{z'z'}(T; \beta, \gamma - 2\pi/3), \\ I_{y'y'}(T; \beta, \gamma) &= I_{z'z'}(T; \beta, \gamma + 2\pi/3). \end{aligned} \quad (31)$$

Once the fits involving free energy and moment of inertia are made for the non-rotating case, the calculations can be extended to higher spins using the relation [5]

$$F(T, I; \beta, \gamma, \Omega) = F(T, \omega = 0; \beta, \gamma) + \frac{(I + 1/2)^2}{2 \hat{\omega} \cdot \mathcal{I} \cdot \hat{\omega}}. \quad (32)$$

Hence this theory offers an economic parameterization to study the hot rotating nuclei. We have employed Landau theory in its extended form as given in Refs. [7, 22] and for the fitting of Landau constants we use the least squares method.

We perform the thermal fluctuation calculations exactly by computing the integrations in Eq. (28) numerically with the free energies (1) and the cross sections (25) being calculated exactly at the integration (mesh) points. Thus we could avoid using any parametrization and consequent fitting, however, neglecting the orientation fluctuations. The orientation fluctuations are not expected to play significant role while studying the scalar observables such as the Γ_{GDR} and cross sections [6, 7]. The free energy, GDR cross section and width at any given spin is obtained by tuning the cranking frequency to get the desired spin. The thermal fluctuation calculations are performed with 1) the liquid-drop model (LDM) free energies and Landau theory, 2) NS free energies and Landau theory and 3) exact CNSM free energies evaluated at given T and I .

C Results and Discussions

The results of our calculations for GDR in several hot and rotating nuclei can be found in Refs. [7, 19, 23]. Here we present few typical cases with more details. First we investigate nuclei with strong deformation in the ground state as we could see the effect of shape transitions as a function of spin and temperature. As representative cases, we study $^{160,166}\text{Er}$ for which experimental data are available. The calculated GDR cross-sections for $^{160,166}\text{Er}$ along with the experimentally observed cross sections are presented in Fig. 4. From this figure, it is clear that there is no significant difference between the results of exact and Landau calculations. This is because of the weak nature of shell effects in $^{160,166}\text{Er}$ at the measured temperatures.

Both the nuclei have a well deformed prolate shape $\beta = 0.37$; $\gamma = -120^\circ$ for ^{160}Er and $\beta = 0.41$; $\gamma = -120^\circ$ for ^{166}Er at the ground state. At $T = 1.2$ MeV and $I = 12\hbar$, the most probable shape is primarily influenced by the temperature as a consequence of the weakening of shell effects. This situation is illustrated in Fig. 5. Due to increase of temperature, the single particle levels start diffusing, leading to a continuum in which the nucleus behaves classically. On the other hand, the spin induces a shape transition towards a non-collective oblate shape via the spherical shape, even in a rotating liquid drop. Hence both the temperature and spin drive these nuclei towards a spherical shape.

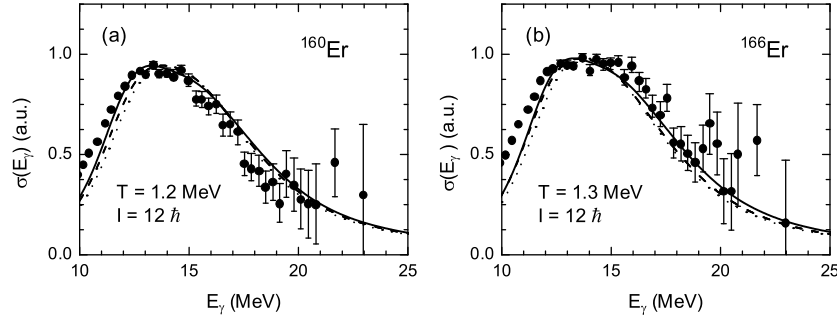


Fig. 4. GDR cross sections for the nuclei $^{160,166}\text{Er}$ in comparison with experimental data [33].

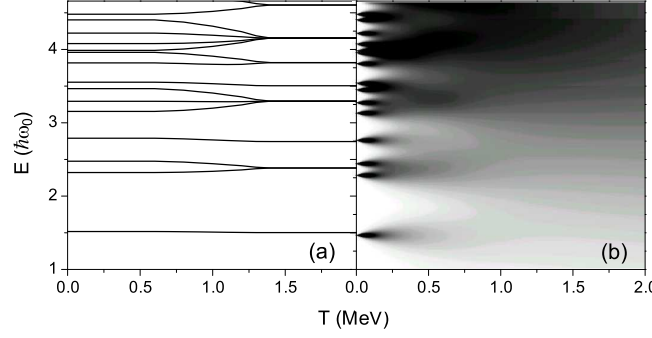


Fig. 5. Simulation of the effect of temperature on the single-particle energy spectrum. The shadings in the right panes is done in a similar way as in Fig. 1b. As the temperature increases the discrete single-particle spectrum starts diffusing to a continuum and hence leading to a classical description finally resulting in a spherical shape.

However the experimental data is well explained by a two Lorentzian fit showing a finite deformation. This splitting (or broadening) of GDR line-shape could be understood to be due to thermal fluctuations which allows the non-equilibrium shapes to contribute.

Eventhough the experimental data is well understood in terms of shape fluctuations, the data could not directly represent the shape transitions happening in these nuclei. The GDR cross sections could not be easily related to the equilibrium shapes [30] as it was done in the ground states. The correlations between the shape and GDR observables are well established [20] to be prominent in spite of thermal fluctuations. For example comparison between the behaviour of Γ_{GDR} with spin in the nuclei $^{106,110}\text{Sn}$ and ^{176}W clearly suggest that the shape transitions are well represented by the Γ_{GDR} [20]. A very direct relation between the averaged shapes and Γ_{GDR} is recently derived [17]. However it has to be noted that the GDR could probe shape transitions only if the change in $\bar{\beta}$ is noticeable or rather swift. This swift change in $\bar{\beta}$ in many cases is well suppressed by the fluctuations. Here we show that use of shape parametrizations as well could suppress the sharp changes in $\bar{\beta}$. In Fig. 6 we present the potential energy surfaces (PES) of ^{166}Er at different T and I . At $T = 0.5 \text{ MeV}$, $I = 0\hbar$, the exact calculations suggest that the $\bar{\beta}$ is close to its ground state value. At $I = 10\hbar$, due to the centrifugal effects there is a quenching in the prolate deformation. At higher spins, contributions from high deformations lead to the increase in $\bar{\beta}$. These sharp changes in the averaged shapes are totally missing in the Landau results. Moreover the trajectory of $(\bar{\beta}, \bar{\gamma})$ is very different from the exact calculations. This discrepancy at low temperature is inherent with the Landau parametrization [23]. At higher temperatures we see that the Landau calculations do well in par with exact calculations. Also we see that due to strong fluctuations at higher T , the variation in $(\bar{\beta}, \bar{\gamma})$ is very less.

At $T = 0.5 \text{ MeV}$ we see that the shell effects are stronger keeping intact the well deformed prolate shape. At $T = 1.0 \text{ MeV}$, we observe a spread in the first minimum due to the weakening of shell effects and at $T = 1.5 \text{ MeV}$ the shell effects almost loses its sting as we see a PES resembling a LDM picture. It is instructive to see how well

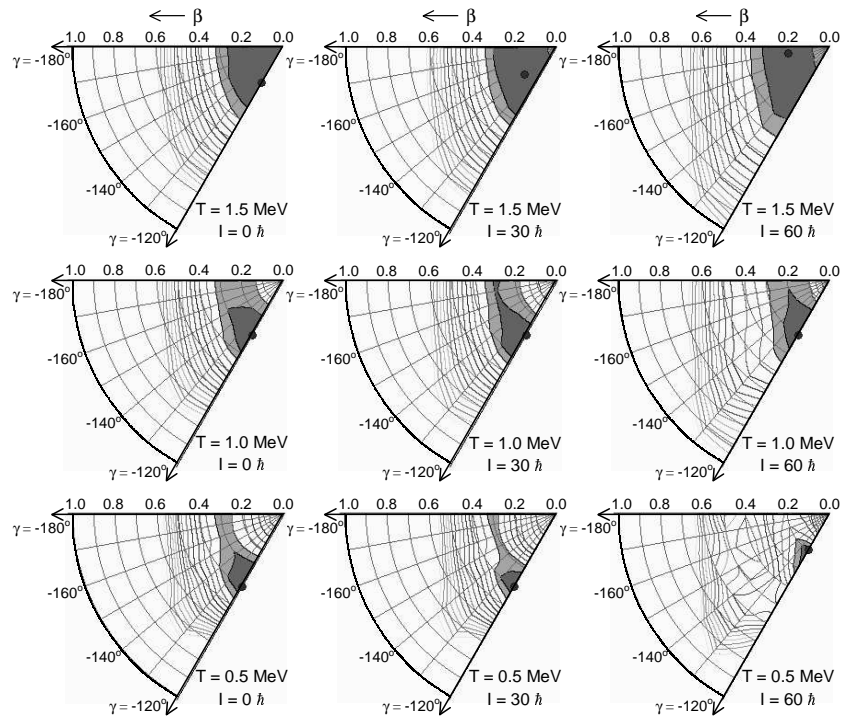


Fig. 6. Potential energy surfaces of the nucleus ^{166}Er at different spins and temperatures. The contour line spacing is 1 MeV. The equilibrium shape is represented by filled circle and the first two minima are shaded.

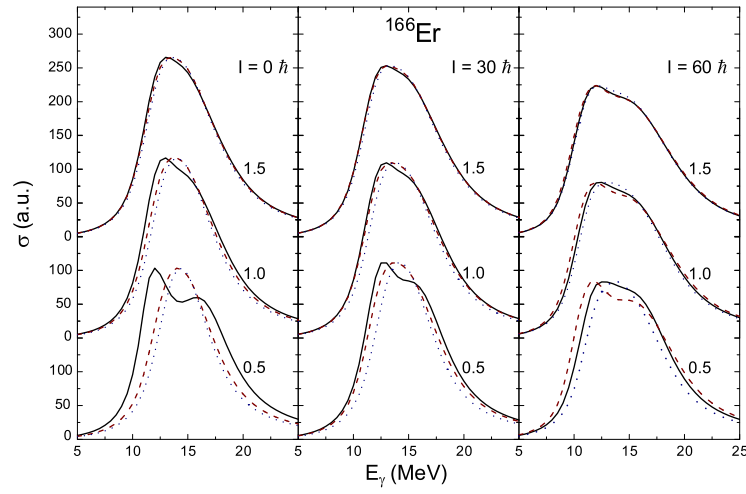


Fig. 7. GDR cross sections for the nucleus ^{166}Er at different spins and temperatures. The solid, dashed and dotted lines represent results of exact, Landau and LDM calculations respectively. The numbers given to the right of GDR curves are the corresponding temperatures given in MeV.

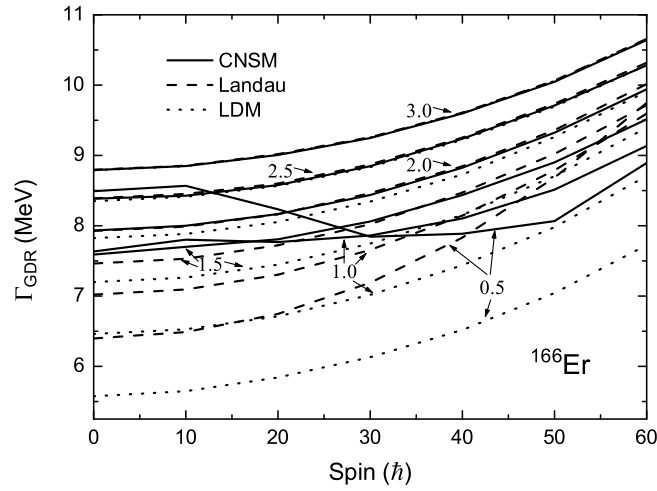


Fig. 8. GDR width for the nucleus ^{166}Er as a function of spin at different temperatures. The numbers near the curves are the corresponding temperatures given in MeV.

these shape effects are reflected in GDR cross sections. The results of our GDR cross section calculations are shown in Fig. 7. The shape transitions at $T = 0.5$ MeV are well reflected in the GDR curves. At $T = 0.5$ MeV, $I = 0\hbar$, the GDR curve is well split. As discussed previously this splitting can arise from two cases viz., a) the well deformed equilibrium shape, b) the dominance of thermal fluctuations. Comparison of the exact result with Landau and LDM results suggest ruling out of the latter case. If it is due to fluctuations alone, then the Landau and LDM results also should have shown the broadening. At $T = 0.5$ MeV, $I = 60\hbar$, the Landau results suggest a broader curve. This also could be understood due to difference in the β values. At $T = 1.0$ MeV the discrepancy between different methods is marginal which is washed out at $T = 1.5$ MeV.

The calculated Γ_{GDR} at different T are presented in Fig. 8 as a function of spin. At $T = 0.5$ MeV, the difference in Γ_{GDR} values obtained from Landau and exact calculations are of the order upto 2 MeV in few cases. The spin-dependence at low T could not be reproduced even qualitatively by the Landau calculations. This is due to the fact that the spin-dependence of the shell correction energy is not taken care by the Landau parametrization. At $T = 1.0$ MeV, the difference goes upto ~ 0.6 MeV along with the discrepancy in spin-dependence. At $T = 2.0$ MeV, the Landau results go well with exact calculations and at $T = 2.5$ MeV all the results reach the LDM values.

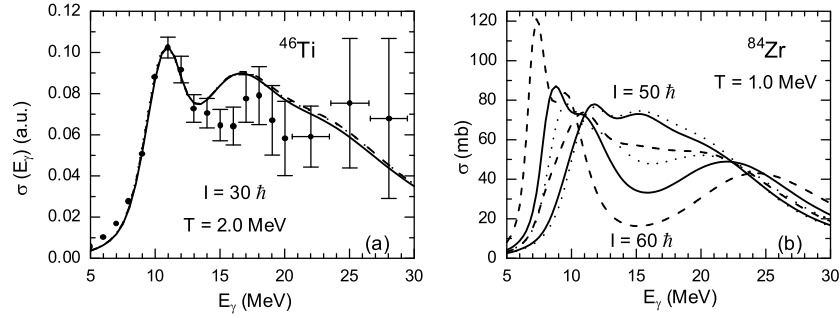


Fig. 9. GDR cross-sections at high spins for ^{46}Ti at $T = 2.0$ MeV and for ^{84}Zr at $T = 1.0$ MeV. Different lines carry same meaning as in Fig. 1. In the left panel experimental data from Ref. [35] also are given.

In the region of critical spin also we test our formalism by applying it to explain the Jacobi transition (JT) in the nucleus ^{45}Sc which is established by experiment [36] and theory [37]. JT is a sudden phase transition occurring at high angular momentum leading to a transition from non-collective oblate shape to a triaxial collective shape which is close to a prolate shape. This transition is analogous to the Jacobi transition occurring in gravitating rotating stars. JT in ^{46}Ti could precisely be identified in a recent observation [35] with proper spin gating. As we see in Fig. 9, our calculations could reasonably explain the data. Such observations are expected to be made in other regions also. It

has been proposed [7] that in neutron-deficient Zr isotopes, spin-driven shell effects are stronger favouring the JT leading to highly deformed shapes at lower temperatures. In these isotopes the JT occurs at around 10 units of spin prior to the maximum sustainable spin [38]. Interestingly, in these cases JT at $T = 0$ leads to hyperdeformed states with $\beta \sim 0.9$. These states could survive thermal fluctuations at low temperatures [7]. In Fig. 9, we show the GDR cross-sections at $T = 1.0$ MeV. It is evident from Fig. 9 that, in certain nuclei at higher spins the spin-driven shell effects may play vital role even at $T \sim 1$ MeV. In the case of Zr isotopes our study, with proper inclusion of spin-driven shell effects, suggests that the shell effects are vital enough at low T (~ 0.5 MeV) to overcome the thermal fluctuations and hence could still favour hyperdeformed states.

D Concluding Remarks

We have presented our macroscopic approach towards GDR with the details involved. Thermal shape fluctuations are treated with and without shape parameterization. Shape transitions in $^{160,164,166}\text{Er}$ are discussed and the inadequacy of Landau parameterization is brought out at low temperature and high spin. Jacobi transition in ^{44}Ti and Zr isotopes are discussed. Experimentally observed GDR properties at different temperature and spin could be well understood by our calculations. We have showed that if the fluctuations are treated exactly, then in spite of thermal fluctuations, GDR observables could very well reflect the shape transitions at low temperature. Any complete description of nuclei at low T should comprise pairing correlations. Work is in progress to incorporate them in our framework. Besides neglecting the role of pairing correlations, our low T calculations clearly bring out the discrepancy in using shape parameterizations and suggest that GDR could effectively probe sharp transitions in spite of thermal fluctuations. This observation is true at very high spin and hence predicts the survival of hyperdeformed structures at low temperatures.

References

1. K.A. Snover, *Annu. Rev. Nucl. Part. Sci.* **36**, 545 (1986); J.J. Gaardhøje, *Annu. Rev. Nucl. Part. Sci.* **42**, 483 (1992).
2. V. Baran, M. Colonna, M. Di Toro, A. Guarnera, V. N. Kondratyev, and A. Smerzi, *Nucl. Phys.* **A599**, 29 (1996).
3. N.D. Dang, K. Tanabe, and A. Arima, *Phys. Lett.* **B445**, 1 (1998); *ibid*, *Nucl. Phys.* **A645**, 536 (1999).
4. M. Gallardo, M. Diebel, T. Døssing, and R.A. Broglia, *Nucl. Phys.* **A443**, 415 (1985).
5. Y. Alhassid, *Nucl. Phys.* **A649**, 107c (1999).
6. W.E. Ormand, P.G. Bortignon and R.A. Broglia, *Nucl. Phys.* **A614**, 217 (1997).
7. P. Arumugam, G. Shanmugam and S.K. Patra, *Phys. Rev. C*, 054313 (2004).
8. A. Maj *et al*, *Acta Phys. Pol.* **B26**, 417 (1995).
9. N. Tsoneva, Ch. Stoyanov, Yu.P. Gangrsky, V.Yu. Ponomarev, N.P. Balabanov, and A.P. Tonchev, *Phys. Rev. C* **61**, 044303 (2000).
10. I. Diószegi, I. Mazumdar, N.P. Shaw, and P. Paul, *Phys. Rev. C* **63**, 047601 (2001).
11. P. Heckman *et al*, *Phys. Lett.* **B555**, 43 (2003).
12. F. Camera *et al*, *Phys. Lett.* **B560**, 155 (2003).

13. A. Bracco, *Acta Phys. Pol.* **B34**, 2163 (2003).
14. S.K. Rath *et al*, *Phys. Rev. C* **67**, 024603 (2003).
15. N.D. Dang and A. Arima, *Phys. Rev. C* **68**, 044303 (2003).
16. A.N. Storozhenko, A.I. Vdovin, A. Ventura and A.I. Blokhin, *Phys. Rev. C* **69**, 064320 (2004).
17. D. Kusnezov, and W.E. Ormand, *Phys. Rev. Lett.* **90**, 042501 (2003).
18. M. Thoennessen, *Nucl. Phys. A* **731**, 131 (2004).
19. P. Arumugam, A. Ganaga Deb and S.K. Patra, *Acta Phys. Pol. B* (In press).
20. A. Bracco *et al*, *Nucl. Phys.* **A599**, 83c (1996).
21. S. F. Mughabghab and A. A. Sonzogni, *Phys. Rev. C* **65**, 044620 (2002)
22. Y. Alhassid and B. Bush, *Nucl. Phys.* **A549**, 12 (1992).
23. P. Arumugam, A. Ganaga Deb and S.K. Patra, arxiv:nucl-th/0410075.
24. K. Neergaard, V.V. Pashkevich and S. Frauendorf, *Nucl. Phys.* **A262**, 61 (1976).
25. L.G. Moretto, *Phys. Lett.* **B38**, 393 (1972).
26. M. Brack and P. Quentin, *Nucl. Phys.* **A361**, 35 (1981).
27. G. Shanmugam and M. Thiagasundaram, *Phys. Rev. C* **37**, 853 (1988); **C 39**, 1623 (1989).
28. R.R. Hilton, *Z. Phys. A* **309**, 233 (1983).
29. P. Carlos, R. Bergere, H. Beil, A. Lepretre and A. Veyssiere, *Nucl. Phys.* **A219**, 61 (1974).
30. Y. Alhassid and B. Bush, *Nucl. Phys.* **A509**, 461 (1990).
31. Y. Alhassid and B. Bush, *Nucl. Phys.* **A531**, 39 (1991).
32. G. Shanmugam and P. Arumugam, *Pramana - J. Phys.* **57**, 223 (2001).
33. J.J. Gaardhøje, C. Ellegaard, and B. Herskind, *Phys. Rev. Lett.* **53**, 148 (1984).
34. M. Kmiecik, et al., *Nucl. Phys. A* **674**, 29 (2000).
35. A. Maj, et al., Arxiv:nucl-ex/0302004 (2003).
36. M. Kicinska Habior, K.A. Snover, S.A. Behr, C.A. Gossett, Y. Alhassid and N. Whelan, *Phys. Lett. B* **308**, 225 (1993).
37. Y. Alhassid and N. Whelan, *Nucl. Phys.* **A565**, 427 (1993).
38. A.J. Sierk, *Phys. Rev. C* **33**, 2039 (1986).

Energy dependence of Lane potential and effective mass splitting

T.R. Routray*, A. Pradhan, and B. Behera

P.G. Department of Physics, Sambalpur University, Jyoti Vihar, Burla - 768019, Sambalpur, Orissa.

Abstract. Momentum dependence of the isospin part of nuclear mean field is analyzed with general effective interactions with specific reference to Skyrme and Gogny interactions. Two contrasting trends of momentum dependence are observed, i.e., one in which the isospin part of nuclear mean field decreases and another where it increases with increase in momentum. Using a simple parametrization of the energy density based on a single Yukawa form of exchange interaction the complete equation of state (EOS) of asymmetric nuclear matter (ANM) as well as neutron and proton mean field properties are analyzed. Properties of beta-stable $n + p + e + \mu$ matter calculated with this EOS of ANM are also used to study neutron star properties.

A Introduction

The equation of state (EOS) of asymmetric nuclear matter (ANM) under extreme conditions is a subject of current interest for its connections and implications to physical phenomena beyond standard nuclear physics such as astrophysical phenomena like supernova explosion and neutron star structure. The most important quantity in the calculation of EOS of ANM is the isospin part of nuclear mean field $u_\tau(k, \rho)$ as function of momentum k and total nucleon density $\rho = \rho_n + \rho_p$. Properties of ANM such as energy per particle, chemical potentials, pressure and incompressibility are determined by the behaviour of $u_\tau(k, \rho)$ around the Fermi surface $k = k_f$. The isospin part of nuclear mean field at Fermi surface $u_\tau(k = k_f, \rho)$ is directly connected with the density dependence of nuclear symmetry energy $J_\tau(\rho)$. The high density behaviour of $J_\tau(\rho)$ is very important for the understanding of many astrophysical phenomena such as chemical composition and related mechanism in the process of formation of neutron stars [1-9]. The momentum and density dependence of $u_\tau(k, \rho)$ also plays a very crucial role in the simulation of dynamical evolution of high energy heavy-ion collisions with radioactive ion beams using isospin dependent transport models. The growing experimental facilities to study nuclear reactions induced by high energy intense radioactive ion beams and their analysis in terms of transport model calculations have provided an opportunity for the first time to explore the EOS of highly asymmetric dense nuclear matter experimentally [10-20]. However, the progress in this direction seems to be rather low and the momentum and density dependence of $u_\tau(k, \rho)$ is still largely unknown [10,11,18] particularly at high density and at high momentum. On the other hand, many

* E-mail: trrl@rediffmail.com

theoretical approaches have been made to study the EOS of ANM and to estimate the momentum and density dependence of the isospin part of nuclear mean field $u_\tau(k, \rho)$. These include Dirac-Brueckner-Hartree-Fock (DBHF) calculations [21-26], Brueckner-Hartree-Fock (BHF) approximation to Brueckner-Bethe-Goldstone (BBG) calculations [27-29], variational methods [30-32] and relativistic mean field (RMF) approximations [11,33-36]. Besides these microscopic approaches, phenomenological effective interactions have also been used extensively to study the EOS and mean field properties of asymmetric nuclear matter [37-41] because of the simplicity of the calculations involved. In the simulations of dynamical evolution of high energy heavy ion collisions using isospin dependent transport models, usually very simple parametrizations of the energy density are used [10,17,18]. The high density behaviour of nuclear symmetry energy $J_\tau(\rho)$ as well as momentum and density dependence of the isospin part of the nuclear mean field $u_\tau(k, \rho)$ predicted by these different theoretical model calculations are rather extremely diverge and even contradicting. All theoretical results on the high density behaviour of $J_\tau(\rho)$ which is directly connected with the behaviour of $u_\tau(k, \rho)$ around the Fermi surface $k = k_f$ can be roughly classified into two groups; i.e., a group where $J_\tau(\rho)$ increases monotonically and another where it decreases after attaining a maximum value and then ultimately becomes negative with increasing density. Similarly, all theoretical predictions on the momentum dependence of the isospin part of nuclear mean field $u_\tau(k, \rho)$ can also be classified into two distinct opposite groups depending on whether $u_\tau(k, \rho)$ decreases or increases with increase in momentum k [11].

The purpose of the present work is to study the EOS of ANM and to analyze the momentum dependence of the isospin part of nuclear mean field $u_\tau(k, \rho)$ using parametrizations of the energy density based on general density dependent finite range effective interactions. The simplicity of the energy density allows analytical calculations of the isospin part of nuclear mean field and other properties of ANM.

B Momentum dependence of the isospin part of nuclear mean field and neutron and proton effective masses

In the present work we consider four different effective interactions to describe the EOS of asymmetric nuclear matter (ANM), namely, the direct and the exchange effective interactions between like and unlike nucleons; $v_d^l(r)$, $v_d^{ul}(r)$, $v_{ex}^l(r)$ and $v_{ex}^{ul}(r)$. These effective interactions are averaged over angles, spins and isospins of the two interacting nucleons and depend on the separation distance 'r' between them as well as on the total nucleon density $\rho = \rho_n + \rho_p$ of ANM. The neutron and proton densities ρ_n and ρ_p are generated by single particle Fermi-Dirac momentum distribution functions

$$\rho_\tau = \int f_T^\tau(\mathbf{k}) d^3k \quad \tau = n, p \quad (1)$$

The energy density functional in asymmetric nuclear matter $H_T(\rho_n, \rho_p)$ obtained from the effective interactions mentioned earlier can be expressed as

$$\begin{aligned}
H_T(\rho_n, \rho_p) = & \int [f_T^n(\mathbf{k}) + f_T^p(\mathbf{k})] (c^2 \hbar^2 k^2 + M^2 c^4)^{1/2} d^3 k \\
& + \frac{1}{2} (\rho_n^2 + \rho_p^2) \int v_d^l(r) d^3 r + \rho_n \rho_p \int v_d^{ul}(r) d^3 r \\
& + \frac{1}{2} \iint [f_T^n(\mathbf{k}) f_T^n(\mathbf{k}') + f_T^p(\mathbf{k}) f_T^p(\mathbf{k}')] g_{ex}^l(|\mathbf{k} - \mathbf{k}'|) d^3 k d^3 k' \\
& + \frac{1}{2} \iint [f_T^n(\mathbf{k}) f_T^p(\mathbf{k}') + f_T^p(\mathbf{k}) f_T^n(\mathbf{k}')] g_{ex}^{ul}(|\mathbf{k} - \mathbf{k}'|) d^3 k d^3 k' \quad (2)
\end{aligned}$$

Here we have assumed relativistic relation between momentum and kinetic energy to include possible relativistic effects at high temperature and at high density in an approximate way. The momentum dependent interactions $g_{ex}^{l,ul}(|\mathbf{k} - \mathbf{k}'|)$ are Fourier transform of the respective exchange interactions $v_{ex}^{l,ul}(r)$,

$$g_{ex}^{l,ul}(|\mathbf{k} - \mathbf{k}'|) = \int e^{i(\mathbf{k} - \mathbf{k}') \cdot \mathbf{r}} v_{ex}^{l,ul}(r) d^3 r \quad (3)$$

The neutron and proton mean fields $u_T^{n,p}(\mathbf{k}, \rho, Y_p)$ can be derived as the respective functional derivatives of the interaction part of the energy density $H_T(\rho_n, \rho_p)$. The more important quantity in the studies of EOS of ANM is however the difference between neutron and proton mean fields; $u_T^{n-p}(\mathbf{k}, \rho, Y_p) = u_T^n(\mathbf{k}, \rho, Y_p) - u_T^p(\mathbf{k}, \rho, Y_p)$ expressed as a function of momentum k , total nucleon density $\rho = \rho_n + \rho_p$ and proton fraction $Y_p = \rho_p / \rho$. For the energy density in ANM given in eqn. (2) one can obtain $u_T^{n-p}(\mathbf{k}, \rho, Y_p)$ in the form

$$\begin{aligned}
u_T^{n-p}(\mathbf{k}, \rho, Y_p) = & (1 - 2Y_p) \rho \int [v_d^l(r) - v_d^{ul}(r)] d^3 r \\
& + \int [f_T^n(\mathbf{k}') - f_T^p(\mathbf{k}')] [g_{ex}^l(|\mathbf{k} - \mathbf{k}'|) - g_{ex}^{ul}(|\mathbf{k} - \mathbf{k}'|)] d^3 k' \quad (4)
\end{aligned}$$

We now introduce the dimensionless quantity $\frac{M}{\hbar^2 k} \frac{\partial u_T^{n-p}(\mathbf{k}, \rho, Y_p)}{\partial k}$,

$$\begin{aligned}
\frac{M}{\hbar^2 k} \frac{\partial u_T^{n-p}(\mathbf{k}, \rho, Y_p)}{\partial k} = & \frac{M}{\hbar^2 k} \frac{\partial}{\partial k} \left[\int [f_T^n(\mathbf{k}') - f_T^p(\mathbf{k}')] \right. \\
& \left. [g_{ex}^l(|\mathbf{k} - \mathbf{k}'|) - g_{ex}^{ul}(|\mathbf{k} - \mathbf{k}'|)] d^3 k' \right] \quad (5)
\end{aligned}$$

It is important to note that $\frac{M}{\hbar^2 k} \frac{\partial u_T^{n,p}(\mathbf{k}, \rho, Y_p)}{\partial k}$ are directly connected to the neutron and the proton effective masses as functions of k , ρ and Y_p . As evident from eqn. (5) $\frac{M}{\hbar^2 k} \frac{\partial u_T^{n-p}(\mathbf{k}, \rho, Y_p)}{\partial k}$ has a very complicated dependence on temperature T , momentum k , total nucleon density ρ and proton fraction Y_p for finite range interactions. However, in the limit of very large k when we can approximate $g_{ex}^{l,ul}(|\mathbf{k} - \mathbf{k}'|)$ inside the integral in eqn. (5) by $g_{ex}^{l,ul}(k)$ this quantity simplifies to

$$\frac{M}{\hbar^2 k} \frac{\partial u_T^{n-p}(\mathbf{k}, \rho, Y_p)}{\partial k} \xrightarrow{k \rightarrow \infty} (1 - 2Y_p) \frac{M \rho}{\hbar^2 k} \left[\frac{dg_{ex}^l(k)}{dk} - \frac{dg_{ex}^{ul}(k)}{dk} \right] \quad (6)$$

This result is very important in the sense that it is independent of temperature and is directly proportional to neutron-proton asymmetry parameter $(1 - 2Y_p) = (\rho_n - \rho_p)/\rho$. If the asymptotic behaviour of $\frac{M}{\hbar^2 k} \frac{\partial u_T^{n-p}(\mathbf{k}, \rho, Y_p)}{\partial k}$ is positive it implies that $\frac{M}{\hbar^2 k} \frac{\partial u_T^n(\mathbf{k}, \rho, Y_p)}{\partial k} \geq \frac{M}{\hbar^2 k} \frac{\partial u_T^p(\mathbf{k}, \rho, Y_p)}{\partial k}$ and the neutron effective mass is less than the proton effective mass for given values of k , ρ and Y_p and the other way around for negative values of $\frac{M}{\hbar^2 k} \frac{\partial u_T^{n-p}(\mathbf{k}, \rho, Y_p)}{\partial k}$ for large k .

For the Gogny effective interactions the behaviour of $\frac{M}{\hbar^2 k} \frac{\partial u_T^{n-p}(\mathbf{k}, \rho, Y_p)}{\partial k}$ for large k can be calculated analytically and the result can be written as,

$$\frac{M}{\hbar^2 k} \frac{\partial u_T^{n-p}(\mathbf{k}, \rho, Y_p)}{\partial k} \xrightarrow{k \rightarrow \infty} (1 - 2Y_p) \frac{M\rho}{2\hbar^2} \sum_{i=1,2} \alpha_i^5 \left(\frac{W_i}{2} + B_i \right) \exp(-\alpha_i^2 k^2/4) \quad (7)$$

For large values of k the contribution coming from the long range part of Gogny effective interactions ($\alpha=1.2$ fm) can be safely ignored compared to the contributions from the short range part ($\alpha=0.7$ fm). Thus the sign of $(\frac{W_1}{2} + B_1)$ for the short range part of Gogny effective interactions will determine whether asymptotically for large k the neutron effective mass is above the proton effective mass or the other way around. Among the different sets of Gogny effective interactions used by Blaizot *et al.* [42] the parameter $(\frac{W_1}{2} + B_1)$ is positive for D1S and D250 and therefore asymptotically for large k the proton effective mass goes above the neutron effective mass. On the other hand, $(\frac{W_1}{2} + B_1)$ is negative for D1, D260, D280 and D300 and as a result the neutron effective mass goes above the proton effective mass asymptotically for large k . In case of Skyrme type parametrizations of the EOS in ANM the quantity $\frac{M}{\hbar^2 k} \frac{\partial u_T^{n-p}(\mathbf{k}, \rho, Y_p)}{\partial k}$ defined in eqn. (5) has a very simple structure,

$$\frac{M}{\hbar^2 k} \frac{\partial u_T^{n-p}(\mathbf{k}, \rho, Y_p)}{\partial k} = (1 - 2Y_p) \frac{M}{4\hbar^2} [t_2(2x_2 + 1) - t_1(2x_1 + 1)] \rho \quad (8)$$

which is not only proportional to neutron-proton asymmetry parameter $(1 - 2Y_p)$ but is also independent of temperature T and momentum k . The sign of the parameter $B = [t_2(2x_2 + 1) - t_1(2x_1 + 1)]$ will determine whether the proton effective mass is above the neutron one or the other way around. For all Skyrme parametrizations with $x_1 = x_2 = 0$ the value of B is negative. Other Skyrme parametrizations such as SGII [43], RATP [44], SkP [45], SKX [46], SKXm [46] and SkSC [46] have also negative values of the parameter B . In all these cases the neutron effective mass is above the proton effective mass irrespective of temperature, momentum and density. On the other hand, the SLy-type Skyrme parametrizations SLya and SLyb [37] give positive values of the parameter B and in these cases the proton effective mass is above the neutron one. For Skyrme parametrizations such as SkSC4 and T6 for which $x_1 = x_2 = -0.5$ the parameter B vanishes and the neutron and proton effective masses are identical.

In connection with the splitting of neutron and proton effective masses in asymmetric nuclear matter (ANM) as discussed for Skyrme and Gogny type effective interactions above, it may be mentioned here that all theoretical results based on different microscopic calculations mentioned earlier can be roughly classified in to two groups; one in which the neutron effective mass goes above the proton effective mass and the

other showing a splitting in the opposite direction. The results obtained from BHF calculations with realistic nucleon-nucleon interaction [28-29] exhibit a splitting where the neutron effective mass goes above the proton effective mass. On the other hand, the results obtained in the microscopic relativistic Dirac-Brueckner calculations [26] as well as relativistic mean field (RMF) approximation using quantum hadrodynamics (QHD) [33,38] exhibit opposite type of splitting of neutron and proton effective masses. Since the behaviour of $\frac{M}{\hbar^2 k} \frac{\partial u_T^{n,p}(k, \rho, Y_p)}{\partial k}$ is proportional to the total nucleon density ρ and the neutron-proton asymmetry parameter $(1 - 2Y_p)$, the splitting of neutron and proton effective masses mentioned above may be small around normal nuclear matter density ρ_0 [35] and therefore, can be neglected in finite nuclei where the neutron-proton asymmetry $(1 - 2Y_p)$ is rather small. However, this difference in neutron and proton effective masses may be quite relevant for transport properties of energetic nucleons in highly asymmetric dense nuclear matter that can be formed in high energy heavy-ion collisions with radioactive ion beams. As we have seen above, both for Skyrme and Gogny type effective interactions the sign of this splitting in neutron and proton effective masses depends on the choice of interaction parameters connected with the exchange part of the effective interaction and the puzzle can only be resolved by a detailed analysis of transport properties of energetic nucleons in highly asymmetric dense nuclear matter.

For finite range effective interactions the temperature evolution of neutron and proton mean fields $u_T^{n,p}(k, \rho, Y_p)$ is built upon its zero temperature version $u^{n,p}(k, \rho, Y_p)$ in the process of self-consistent evaluation of neutron and proton single particle momentum distribution functions $f_T^{n,p}(\mathbf{k})$. In view of this it is very important to note how $u^{n,p}(k, \rho, Y_p)$ depends on k , ρ and Y_p . At zero temperature the distribution functions $f_T^{n,p}(\mathbf{k})$ are given by step functions and the zero temperature version of eqn. (4) can be expressed as,

$$u^{n,p}(k, \rho, Y_p) = (1 - 2Y_p)\rho \int [v_d^l(r) - v_d^u(r)] d^3r + \int \left[\rho_n \frac{3j_1(k_n r)}{k_n r} - \rho_p \frac{3j_1(k_p r)}{k_p r} \right] [v_{ex}^l(r) - v_{ex}^u(r)] d^3r, \quad (9)$$

where j_0 and j_1 are spherical Bessel functions of order 0 and 1 respectively and $k_\tau = (3\pi^2 \rho_\tau)^{1/3}$, ($\tau = n, p$) are the Fermi momenta in ANM. The direct part of $u^{n,p}(k, \rho, Y_p)$ is proportional to $(1 - 2Y_p)$, the proportionality factor being a function of total density ρ . The exchange part is also roughly proportional to $(1 - 2Y_p)$ and the proportionality factor can be approximated in terms of a Taylor expansion of the exchange part about $Y_p = 1/2$,

$$u^{n,p}(k, \rho, Y_p) = (1 - 2Y_p)\rho \left[\int [v_d^l(r) - v_d^u(r)] d^3r + \int j_0(kr)j_0(k_f r) [v_{ex}^l(r) - v_{ex}^u(r)] d^3r \right], \quad (10)$$

We now introduce the isospin part of nuclear mean field $u_\tau(k, \rho)$ through the relation,

$$u_\tau(k, \rho) = \frac{u^{n-p}(k, \rho, Y_p)}{2(1 - 2Y_p)} \\ = \frac{\rho}{2} \left[\int [v_d^l(r) - v_d^{ul}(r)] d^3r + \int j_0(kr)j_0(k_f r) [v_{ex}^l(r) - v_{ex}^{ul}(r)] d^3r \right] \quad (11)$$

A common problem which frequently arises in comparing the momentum dependence of the isospin part of nuclear mean field $u_\tau(k, \rho)$ derived from different effective interactions is the difference in the density dependence of the nuclear symmetry energy $J_\tau(\rho)$ for these interactions. In view of this it is desirable to separate out the density dependence of $J_\tau(\rho)$ from the isospin part of nuclear mean field $u_\tau(k, \rho)$. The nuclear symmetry energy $J_\tau(\rho)$ is usually defined through the relation,

$$J_\tau(\rho) = \frac{1}{8\rho} \left[\frac{\partial^2 H(\rho, Y_p)}{\partial Y_p^2} \right]_{Y_p=1/2} \quad (12)$$

Here, $H(\rho, Y_p)$ is the energy density in asymmetric nuclear matter at zero temperature as function of total nucleon density ρ and proton fraction Y_p . For the simple form of energy density $H(\rho, Y_p)$ used in this work, the nuclear symmetry energy defined in eqn.(12) can be calculated analytically and the result can be put in the form,

$$J_\tau(\rho) = \frac{\hbar^2 k_f^2}{6m} \left[\left(\frac{M^*(k, \rho)}{M} \right)^2 + \frac{\hbar^2 k^2}{M^2 c^2} \right]_{k=k_f}^{-1/2} + \frac{\rho}{4} \int [v_d^l(r) - v_d^{ul}(r)] d^3r \\ + \frac{\rho}{4} \int [v_{ex}^l(r) - v_{ex}^{ul}(r)] j_0^2(k_f r) d^3r \quad (13)$$

where, $M^*(k, \rho)/M$ is the zero-temperature nucleon effective mass in symmetric nuclear matter (SNM) as function of momentum and density. The isospin part of the nuclear mean field $u_\tau(k, \rho)$ in eqn. (11) can be connected to the nuclear symmetry energy $J_\tau(\rho)$ obtained in eqn. (13) through the relation,

$$u_\tau(k, \rho) = 2J_\tau(\rho) - \frac{\hbar^2 k_f^2}{3m} \left[\left(\frac{M^*(k, \rho)}{M} \right)^2 + \frac{\hbar^2 k^2}{M^2 c^2} \right]_{k=k_f}^{-1/2} \\ + \frac{\rho}{2} \int [v_{ex}^l(r) - v_{ex}^{ul}(r)] [j_0(kr) - j_0(k_f r)] j_0(k_f r) d^3r \quad (14)$$

For nonrelativistic relation between momentum and kinetic energy the $\frac{\hbar^2 k^2}{M^2 c^2}$ term in eqn. (14) drops out. It is evident from eqn. (14) that different $u_\tau(k, \rho)$ sharing the same behaviour around $k = k_f$ over a wide range of density but having quite different momentum dependence for k away from k_f will lead to almost same results for properties like energy per particle, neutron and proton chemical potentials, pressure and incompressibility in ANM. However, these different $u_\tau(k, \rho)$ can lead to significantly different predictions on experimental observables sensitive to transport properties of energetic nucleons in highly asymmetric dense nuclear matter [12-14].

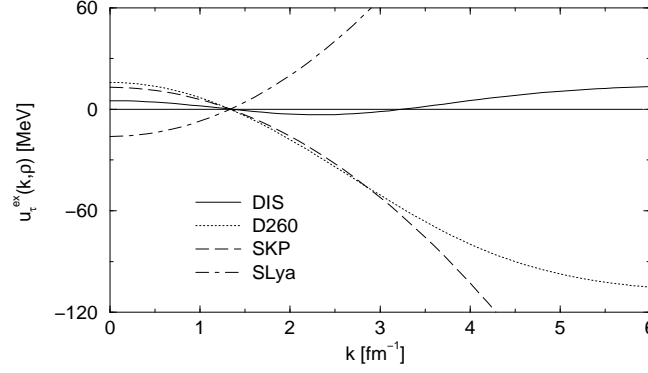


Fig. 1. $u_{\tau}^{ex}(k, \rho)$ shown as a function of momentum k for Skyrme and Gogny effective interactions

We now focus on the momentum dependence of the isospin part of nuclear mean field. For this purpose we concentrate on the last term in eqn. (14),

$$u_{\tau}^{ex}(k, \rho) = \frac{\rho}{2} \int [v_{ex}^l(r) - v_{ex}^{ul}(r)] [j_0(kr) - j_0(k_f r)] j_0(k_f r) d^3r \quad (15)$$

This can be calculated analytically for Gogny effective interactions and result is given by

$$u_{\tau}^{ex}(k, \rho) = -\frac{1}{3\pi^{1/2}} \sum_{i=1,2} \left(\frac{W_i}{2} + B_i \right) \left[\frac{x_i^2}{z_i} \left\{ e^{-(z_i - x_i)^2/4} - e^{-(z_i + x_i)^2/4} \right\} - x_i(1 - e^{-x_i^2}) \right] \quad (16)$$

For the Skyrme parametrization it has a very simple form,

$$u_{\tau}^{ex}(k, \rho) = \frac{1}{16} [t_2(2x_2 + 1) - t_1(2x_1 + 1)] (k^2 - k_f^2) \rho \quad (17)$$

Eqns. (16) and (17) clearly demonstrate the difference in the high momentum behaviour of $u_{\tau}(k, \rho)$ for Skyrme and Gogny type effective interactions. While for Skyrme parametrization $u_{\tau}(k, \rho)$ either increases or decreases monotonically with increase in k , it approaches a definite value

$$u_{\tau}^{ex}(k \rightarrow \infty, \rho) = \frac{1}{3\pi^{1/2}} \sum_{i=1,2} \left(\frac{W_i}{2} + B_i \right) x_i(1 - e^{-x_i^2}) \quad (18)$$

in the limit of $k \rightarrow \infty$ for Gogny parametrizations. In fig. 1 the functional $u_{\tau}^{ex}(k, \rho)$ is shown as a function of momentum k at normal density ρ_0 for two Skyrme parametrizations SLya and SKP as well as for two different Gogny parametrizations DIS and D260. This figure clearly exhibits the fact mentioned earlier that the momentum dependence of the isospin part of nuclear mean field predicted by different theoretical calculations are rather extremely diverge and even contradicting. While $u_{\tau}^{ex}(k, \rho)$ increases monotonically for the Skyrme parametrization SLya it decreases monotonically for SKP with

increase in momentum. On the other hand, $u_\tau^{ex}(k, \rho)$ for the Gogny interaction D260 exhibits a decreasing trend with increase in momentum and for large k it approaches a definite negative value: -108.68 MeV. The variation of $u_\tau^{ex}(k, \rho)$ with momentum for the Gogny interaction D1S is rather different from the three other interactions shown in fig. 1. In this case $u_\tau^{ex}(k, \rho)$ has a value 5.1 MeV at $k = 0$ and with increase in k it gradually decreases, becomes negative and attains a minimum value -3.23 MeV at $k = 2.3 \text{ fm}^{-1}$ and then gradually increases with further increase in k and approaches a value 14.61 MeV in the limit of $k \rightarrow \infty$.

It is important to note that a decreasing trend of momentum dependence of the isospin part of nuclear mean field corresponds to $[M^*/M]_n > [M^*/M]_p$ whereas an increasing trend corresponds to $[M^*/M]_p > [M^*/M]_n$. In order to illustrate it more explicitly we extend our earlier studies of momentum dependence of nuclear mean field in symmetric nuclear matter (SNM) [49] to the domain of asymmetric nuclear matter (ANM). Assuming that the form of interactions between like and unlike nucleons are the same and they differ only in their strength factors, the energy density used in SNM can be extended to the case of ANM as,

$$\begin{aligned}
 H_T(\rho_n, \rho_p) = & \int [f_T^n(\mathbf{k}) + f_T^p(\mathbf{k})] (c^2 \hbar^2 k^2 + M^2 c^4)^{1/2} d^3 k \\
 & + \frac{1}{2} \left[\frac{\varepsilon_0^l}{\rho_0} + \frac{\varepsilon_\gamma^l}{\rho_0^{\gamma+1}} \left(\frac{\rho}{1+b\rho} \right)^\gamma \right] (\rho_n^2 + \rho_p^2) \\
 & + \left[\frac{\varepsilon_0^{ul}}{\rho_0} + \frac{\varepsilon_\gamma^{ul}}{\rho_0^{\gamma+1}} \left(\frac{\rho}{1+b\rho} \right)^\gamma \right] \rho_n \rho_p \\
 & + \frac{\varepsilon_{ex}^l}{2\rho_0} \iint [f_T^n(\mathbf{k}) f_T^n(\mathbf{k}') + f_T^p(\mathbf{k}) f_T^p(\mathbf{k}')] g_{ex}(|\mathbf{k} - \mathbf{k}'|) d^3 k d^3 k' \\
 & + \frac{\varepsilon_{ex}^{ul}}{2\rho_0} \iint [f_T^n(\mathbf{k}) f_T^p(\mathbf{k}') + f_T^p(\mathbf{k}) f_T^n(\mathbf{k}')] g_{ex}(|\mathbf{k} - \mathbf{k}'|) d^3 k d^3 k'. \quad (19)
 \end{aligned}$$

The parameters b , γ and the range of the exchange interaction α are same as in the case of SNM [49] and the strength parameters ε_0 , ε_γ and ε_{ex} split into two channels namely, ε_0^l (ε_0^{ul}), ε_γ^l (ε_γ^{ul}) and ε_{ex}^l (ε_{ex}^{ul}) for interactions between like (unlike) nucleons subject to the conditions,

$$\varepsilon_0^l + \varepsilon_0^{ul} = 2\varepsilon_0, \quad \varepsilon_\gamma^l + \varepsilon_\gamma^{ul} = 2\varepsilon_\gamma \quad \text{and} \quad \varepsilon_{ex}^l + \varepsilon_{ex}^{ul} = 2\varepsilon_{ex} \quad (20)$$

For the energy density given in eqn.(19), the functional $u_\tau^{ex}(k, \rho)$ in eqn. (15) assumes a simpler form,

$$u_\tau^{ex}(k, \rho) = \frac{(\varepsilon_{ex}^l - \varepsilon_{ex}^{ul})}{2\rho_0 \int f(r) d^3 r} \int [j_0(kr) - j_0(k_f r)] j_0(k_f r) f(r) d^3 r \quad (21)$$

where $f(r)$ is the form of the finite range exchange interaction, ε_{ex}^l and ε_{ex}^{ul} are strengths of exchange interactions between like and unlike nucleons subject to the condition in eqn.(20). The values of the two parameters namely strength ε_{ex} and range α of exchange interaction in SNM are fixed by using an optimisation procedure so as to give a reasonable account of momentum dependence of the nuclear mean field in SNM over a wide

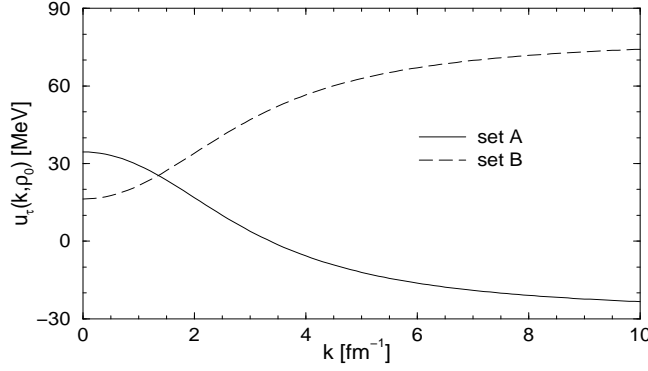


Fig. 2. $u_\tau(k, \rho_0)$ shown as function of momentum k for exchange parameter sets A and B with $J_\tau(\rho_0)=30$ MeV and $M^*(k = k_{f_0}, \rho_0)/M = 0.67$.

range of momentum as demanded by optical model fits to nucleon-nucleus scattering data [49]. Both the parameters obtained in this way for the Yukawa form of exchange interaction are $\varepsilon_{ex} = -121.8$ MeV and $\alpha = 0.4044$ fm. A complete calculation of momentum dependence of the isospin part of nuclear mean field will require the knowledge of three additional parameters namely ε_0^l , ε_γ^l and ε_{ex}^l . However, at normal nuclear matter density we can make use of standard values of $J_\tau(\rho_0)$ and $M^*(k = k_{f_0}, \rho_0)/M$ and examine the momentum dependence of $u_\tau(k, \rho_0)$ for different representative combinations of the exchange parameter ε_{ex}^l and ε_{ex}^{ul} . The momentum dependence of $u_\tau(k, \rho_0)$ for the Yukawa form of exchange interaction is shown in fig. 2 for two sets of exchange strength parameters

$$(A) \varepsilon_{ex}^l = \varepsilon_{ex}/3, \varepsilon_{ex}^{ul} = 5\varepsilon_{ex}/3, \quad \text{and} \quad (B) \varepsilon_{ex}^l = 5\varepsilon_{ex}/3, \varepsilon_{ex}^{ul} = \varepsilon_{ex}/3 \quad (22)$$

For this purpose we have assumed a standard value of nuclear symmetry energy $J_\tau(\rho_0)=30$ MeV and the value of $M^*(k = k_{f_0}, \rho_0)/M$ has been taken as 0.67 from our earlier study of EOS of SNM [49]. It is observed that the two different sets of exchange strength parameters A and B exhibit quite contradicting momentum dependence of the isospin part of nuclear mean field. While $u_\tau(k, \rho_0)$ decreases with increase in momentum for set-A, it increases for set-B and the two curves intersect at $k = k_{f_0}$. This contradiction in momentum dependence of the isospin part of nuclear mean field will however become less and less pronounced with decrease in the absolute value of $(\varepsilon_{ex}^l - \varepsilon_{ex}^{ul})$.

The momentum dependence of $u^{n-p}(k, \rho_0, Y_p)$ at different proton fractions Y_p , calculated by using eqns. (11) and (21) for the two different sets of exchange parameters A and B are shown in figs. 3(a) and 3(b) respectively. The two different sets A and B considered in fig. 3 exhibit contrasting trends of momentum dependence of neutron and proton mean fields. It is interesting to note that in fig. 3(a) a crossing point occurs for $u^{n-p}(k, \rho_0, Y_p)$ at $k=3.3$ fm⁻¹, where it vanishes and then becomes negative with further increase in k , and the isospin effect on the difference between neutron and proton mean fields as a function of Y_p is inverted. Such inversion of the isospin effect at a crossing point is observed in BHF calculations using realistic nucleon-nucleon interactions [28-29] and also in the work of Li *et. al.* [12] mentioned earlier in this section.

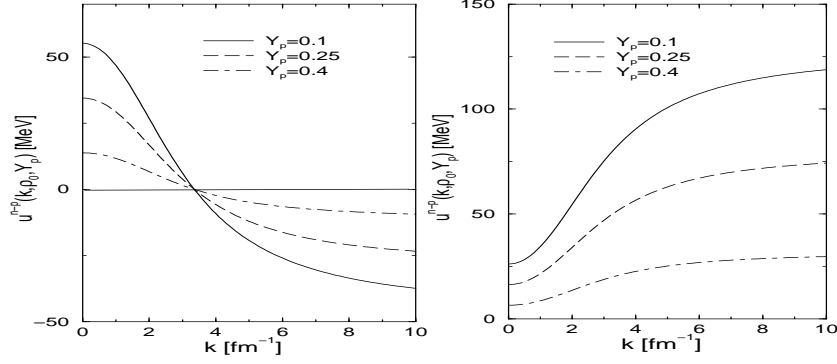


Fig. 3. $u^{n-p}(k, \rho_0, Y_p)$ is shown as function of momentum k in ANM having $\rho = \rho_0$ and $Y_p = 0.1, 0.25$ and 0.4 for the two sets of exchange parameters; A (left panel fig. 3(a)) and B (right panel fig. 3(b)) with $J_\tau(\rho_0) = 30$ MeV and $M^*(k = k_{f_0}, \rho_0)/M = 0.67$.

However, it is worth noticing that such a crossing point can appear only if $u_\tau(k, \rho)$ vanishes at some value of momentum k and ultimately approaches a negative asymptotic value in the limit of $k \rightarrow \infty$, similar to the one shown in fig. 2 for the exchange parameters set A. On the other hand, the difference between neutron and proton mean fields as a function of momentum for the set-B in fig. 3(b), becomes more and more repulsive with increase in k and approaches higher and higher asymptotic values with decrease in the proton fraction Y_p in the limit of $k \rightarrow \infty$.

C Fixation of additional parameters, equation of state of beta-stable $n + p + e + \mu$ matter and neutron star properties

As evident from eqn. (19), pure neutron matter (PNM) and symmetric nuclear matter (SNM) at same total nucleon density and temperature constitute the two extremes of asymmetric nuclear matter (ANM) with $Y_p = 0$ and $Y_p = 1/2$ respectively. The relationships among the strength parameters given in eqn. (20) clearly show that a complete description of EOS of ANM is exactly equivalent to separate descriptions of EOS of SNM and PNM. In view of this, we now focus on the EOS of PNM to fix up the additional parameters involved. In the absence of any experimental/empirical constraints we use simple physical considerations based on the fact that PNM should not be bound at any density and that SNM is supposed to be the lowest energy state of ANM. We, therefore, impose the following two conditions

$$P^n(\rho) > 0, \quad K^n(\rho) = 9 \frac{dP^n(\rho)}{d\rho} > 0. \quad (23)$$

$$e^n(\rho) > e(\rho), \mu^n(\rho) > \mu(\rho), P^n(\rho) > P(\rho), K^n(\rho) > K(\rho) \text{ and } (v^n/c) > (v/c). \quad (24)$$

It may be mentioned here that for the simple parametrization of energy density considered here, it is not possible to prevent violation of all the constraints in eqn. (24). In

Table 1. Values of $J_\tau(\rho_0)$ and $J'_\tau(\rho_0)$ in MeV for different EOS in ANM having minimum isospin dependence where, the symbols have their usual meanings

γ		ε_{ex}^l [MeV]						
		0	$\varepsilon_{ex}/3$	$2\varepsilon_{ex}/3$	ε_{ex}	$4\varepsilon_{ex}/3$	$5\varepsilon_{ex}/3$	$2\varepsilon_{ex}$
1/2	$J_{\tau}(\rho_0)$	27.7	28.4	29.1	29.8	30.6	31.4	32.2
	$J'_{\tau}(\rho_0)$	21.9	23.2	24.4	25.6	27.0	28.3	29.6
1/3	$J_{\tau}(\rho_0)$	28.5	29.0	29.5	30.0	30.5	31.0	31.5
	$J'_{\tau}(\rho_0)$	22.95	23.8	24.6	25.4	26.2	27.0	27.8
1/6	$J_{\tau}(\rho_0)$	30.1	30.1	30.1	30.1	30.1	30.1	30.2
	$J'_{\tau}(\rho_0)$	24.7	24.8	24.8	24.8	24.8	24.9	25.0
1/12	$J_{\tau}(\rho_0)$	31.5	31.0	30.5	30.1	29.7	29.3	29.1
	$J'_{\tau}(\rho_0)$	26.1	25.5	24.9	24.4	23.9	23.3	22.95

particular the constraint $(v^n/c) > (v/c)$ is violated at higher densities. Since density of matter in the interior of neutron stars is estimated to be $8\rho_0 - 10\rho_0$ we demand that the constraint $(v^n/c) > (v/c)$ must be satisfied at least up to a density $10\rho_0$. For a given strength in the range $\varepsilon_{ex}^l = 0$ to $2\varepsilon_{ex}$, we vary the other two parameters ε_0^l and ε_γ^l and look for the complete domain of allowed EOS according to the constraints in eqns.(23) and (24). This procedure leads to an EOS in ANM having minimum isospin dependence in the sense that out of all admissible EOS, this one has the lowest values of nuclear symmetry energy $J_\tau(\rho_0)$ and its first derivative $J'_\tau(\rho_0) = [\rho dJ_\tau(\rho)/d\rho]_{\rho=\rho_0}$ at normal density ρ_0 . The values of $J_\tau(\rho_0)$ and $J'_\tau(\rho_0)$ corresponding to these EOS having minimum isospin dependence are listed in table-1 for different values of ε_{ex}^l and γ . It may be seen from the results in table-1 that minimum values of $J_\tau(\rho_0)$ are in the range 28-32 MeV which are in good agreement with the empirical values quoted in the literature [50]. In the remaining part of this work we shall be restricting to these EOS having minimum isospin dependence. It is also observed from table-1 that the minimum values of $J_\tau(\rho_0)$ and $J'_\tau(\rho_0)$ increase with increase in the strength of ε_{ex}^l for $\gamma > 1/6$ and the other way around for $\gamma < 1/6$. For the particular case of $\gamma = 1/6$ the minimum values of $J_\tau(\rho_0)$ and $J'_\tau(\rho_0)$ are almost stationary at 30.1 MeV and 24.8 MeV respectively when ε_{ex}^l changes from 0 to $2\varepsilon_{ex}$. In view of this, all these EOS with $\gamma = 1/6$ and ε_{ex}^l in the range 0 to $2\varepsilon_{ex}$ will lead to almost same results for properties like energy per particle, chemical potentials, pressure and incompressibility in zero-temperature ANM as well as PNM over a wide range of density. However, all these EOS will give rise to quite different momentum dependence of the isospin part of nuclear mean field $u_\tau(k, \rho)$ and can therefore lead to different predictions on experimental observables sensitive to transport properties of energetic nucleons in highly asymmetric dense nuclear matter [12-14].

It may be noticed from table-1 that for the specific case of $\varepsilon_{ex}^l = \varepsilon_{ex}$, the isospin part of nuclear mean field $u_\tau(k, \rho)$ is momentum independent and the minimum values of $J_\tau(\rho_0)$ for all values of γ considered are almost stationary at 30 MeV, whereas the minimum values of $J'_\tau(\rho_0)$ increase slowly with increase in the exponent γ . The high density behaviour of $J_\tau(\rho)$ for four different EOS with $\gamma = 1/12, 1/6, 1/3$ and $1/2$ but

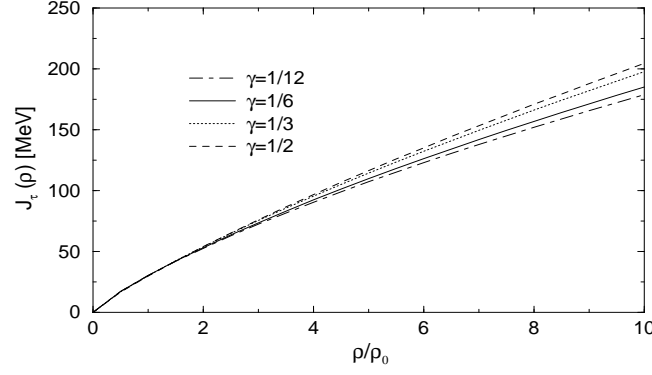


Fig. 4. $J_\tau(\rho)$ plotted as function of density ρ for different values of $\gamma = 1/12, 1/6, 1/3$ and $1/2$ but for the same value of exchange strength parameter $\varepsilon_{ex}^l = \varepsilon_{ex}$ for interaction between like nucleons.

having the same value of $\varepsilon_{ex}^l = \varepsilon_{ex}$ are shown in fig. 4. The calculated curves of $J_\tau(\rho)$ as a function of density for these EOS are almost same up to a density $\rho = 2.5 \rho_0$. However, at higher densities these curves gradually become more and more stiff with density for increasing values of the exponent γ . It may be worth mentioning here that the trend of high density behaviour of nuclear symmetry energy $J_\tau(\rho)$ is very much controversial and all theoretical results can be roughly classified into two groups [18,19,51,52], i.e., a group where $J_\tau(\rho)$ increases monotonically and another in which it decreases after attaining a maximum value and then ultimately becomes negative with increasing density. High density behaviour of $J_\tau(\rho)$ is very crucial for the understanding of many important astrophysical phenomena. In particular, an increasing $J_\tau(\rho)$ will lead to a relatively more proton rich neutron star, whereas, a decreasing $J_\tau(\rho)$ would make the neutron star almost a pure neutron matter at high densities. As a result of this, chemical composition and cooling mechanisms in the process of formation of neutron stars will all be different for the two different types of high density behaviour of nuclear symmetry energy mentioned above [3,4,18]. It may be emphasized here that imposition of the physical constraints in eqn.(24) rules out a decreasing trend of $J_\tau(\rho)$ at higher densities in the present work. However, the actual high density behaviour of nuclear symmetry energy can only be ascertained from a detailed analysis of transport properties of energetic nucleons in highly asymmetric dense nuclear matter that can be formed in high energy heavy-ion collisions with radioactive ion beams.

The core of a neutron star is expected to be formed by an uncharged mixture of neutrons, protons, electrons and muons in equilibrium with respect to the weak interaction (beta-stable $n + p + e + \mu$ matter). Equilibrium for the reactions $n \Leftrightarrow p + e^-$ and $n \Leftrightarrow p + \mu^-$ requires that

$$[\mu^n(\rho, Y_p) - \mu^p(\rho, Y_p)] = \mu^e(\rho, Y_e) = \mu^\mu(\rho, Y_\mu) \quad \text{with } Y_p = Y_e + Y_\mu \quad (25)$$

In this equation $\rho = \rho_n + \rho_p$, $Y_p = \rho_p/\rho$, $Y_e = \rho_e/\rho$, $Y_\mu = \rho_\mu/\rho$ and ρ_i ($i=n, p, e, \mu$) are the densities of respective particles. In this work, the electron and muon chemical potentials and the leptonic contributions towards EOS of beta-stable $n + p + e + \mu$

Table 2. Properties of both maximum mass M_{\max} and $1.4M_{\odot}$ neutron star calculated with three different EOS of ANM having minimum isospin dependence with $\gamma = 1/12$, $1/6$ and $1/3$ but same value of $\varepsilon_{ex}^l = 4\varepsilon_{ex}/3$. The different symbols representing neutron star properties in the first column have their usual meanings.

Neutron star properties	Maximum mass neutron-star			1.4 M_{\odot} neutron-star		
	$\gamma=1/12$	$\gamma=1/6$	$\gamma=1/3$	$\gamma=1/12$	$\gamma=1/6$	$\gamma=1/3$
$\rho_c(\text{fm}^{-3})$	1.42	1.35	1.2	0.63	0.58	0.52
R(km)	9.6	9.82	10.14	11.32	11.58	11.99
M(M_{\odot})	1.74	1.79	1.87	1.4	1.4	1.4
A(10^{57})	2.41	2.48	2.61	1.86	1.86	1.86
$E_{\text{bind}}(10^{53}\text{erg})$	5.06	5.28	5.7	2.96	2.91	2.84
Z_{surf}	0.467	0.469	0.482	0.255	0.247	0.235

matter have been approximated by their relativistic Fermi-gas expressions, whereas, the respective baryonic parts have been calculated from the EOS of asymmetric nuclear matter (ANM) described earlier. The calculated EOS of beta-stable $n + p + e + \mu$ matter have been used to study neutron star properties by solving the Tolman-Oppenheimer-Volkoff (TOV) equation. As expected it is found that energy density and pressure in beta-stable $n + p + e + \mu$ matter over a wide range of density, as well as neutron star properties are almost same for the two different EOS in ANM with $\gamma = 1/6$ and exchange parameter sets A and B . To examine the effect of nuclear matter incompressibility on neutron star properties, calculations have been done for the three different EOS of ANM with $\varepsilon_{ex}^l = 4\varepsilon_{ex}/3$ and $\gamma = 1/12$, $1/6$ and $1/3$ using their respective minimum values of $J_{\tau}(\rho_0)$ and $J_{\tau}^l(\rho_0)$ given in table-1. The neutron star properties calculated for the three different values of γ mentioned above are listed in table-2 for the maximum mass M_{\max} and standard $1.4M_{\odot}$ neutron star models.

An important quantity related to the cooling mechanisms in the formation of neutron star is the threshold density ρ_{urca} at which direct Urca process starts. For beta-stable $n + p + e + \mu$ matter, the condition for direct Urca process is $Y_n^{1/3} \leq Y_p^{1/3} + Y_e^{1/3}$ and/or $Y_n^{1/3} \leq Y_p^{1/3} + Y_{\mu}^{1/3}$ where $Y_n = \rho_n/\rho$ is the neutron fraction. The threshold density ρ_{urca} calculated for the three values of γ , namely, $1/12$, $1/6$ and $1/3$ are respectively found to be 0.522 fm^{-3} , 0.487 fm^{-3} and 0.441 fm^{-3} respectively. These calculated values of ρ_{urca} are less than the respective central densities ρ_c for the neutron star properties listed in table-2 which shows that direct Urca process leading to rapid cooling in the process of formation of neutron star is allowed in all the three cases $\gamma = 1/12$, $1/6$ and $1/3$.

The effect of increasing incompressibility in nuclear matter on neutron star properties as evident from the results of maximum mass neutron star model listed in table-2 is to decrease the central density ρ_c and to increase the radius R , maximum mass M_{\max} and the total baryon number A . This is in agreement with the findings of Prakash *et. al.* [7]. Moreover, the results of neutron star properties listed in table-2 obtained with the three different values of the exponent γ for both the maximum mass M_{\max} and the stan-

standard $1.4M_{\odot}$ neutron star models agree quite well with those referred to in the literature [30,37,53,54].

References

1. J.M. Lattimer, M. Prakash, *Astrophys. J.* 550 (2001) 426.
2. M. Prakash, et. al., *Phys. Rep.* 280 (1997) 1.
3. J.M. Lattimer, C.J. Pethick, M. Prakash, P. Haensel, *Phys. Rev. Lett.* 66 (1991) 2701.
4. K. Sumiyoshi, H. Toki, *Astrophys. J.* 422 (1994) 700
5. C.H. Lee, *Phys. Rep.* 275 (1996) 255.
6. S. Kubis, M. Kutschera, *Acta Phys. Pol. B* 30 (1999) 2747.
7. M. Prakash, T.I. Ainsworth, J.M. Lattimer, *Phys.Rev.Lett.* 61 (1988) 2518.
8. L. Engvik et.al., *Astrophys. J.* 469 (1996) 794.
9. M. Kutschera, J. Niemiec, *Phys. Rev. C* 62 (2000) 025802.
10. Lie Wen Chen, Che Ming Ko, Bao-An li, *Phys.Rev. C* 69 (2004) 054606.
11. J. Rizzo, M. Colonna, M. Di Toro, V. Greco, *Nucl. Phys. A* 732 (2004) 202.
12. B.A. Li, C.B. Das, S. Das Gupta, C. Gale, *Nucl. Phys. A* 735 (2004) 563.
13. C.B. Das, S. Das Gupta, C. Gale, B.A. Li, *Phys. Rev. C* 67 (2003) 034611.
14. B.A. Li, C.B. Das, S. Das Gupta, C. Gale, *Phys. Rev. C* 69 (2004) 011603(R).
15. M. Colonna, M. Di Toro, G. Fabri, S. Maccarone, *Phys. Rev. C* 57 (1998)1410.
16. B.A. Li, C.M. Ko, W. Bauer, Topical review, *Int. J. Mod. Phys. E* 7 (1998)147.
17. P. Danielewicz, R. Lacey, W.G. Lynch, *Science* 298 (2002) 1592.
18. B.A. Li, *Phys.Rev.Lett.* 88 (2002) 192701.
19. B.A. Li, *Nucl. Phys. A* 708 (2003) 365.
20. The DOE/NSF Nuclear Science Advisory Committee Opportunities in Nuclear Science, April, 2002.
21. B. ter Haar, R. Malfliet, *Phys. Rev. Lett.* 59 (1987) 1652; R. Malfliet, *Nucl. Phys. A* 488 (1988) 721c.
22. L. Engvik, M. Hjorth-Jensen, E. Osnes, G. Bao, E. Ostgaard, *Phys.Rev.Lett.* 73 (1994) 2650.
23. H. Hubber, F. Weber, M.K. Wiegel, *Phys. Rev. C* 51 (1995) 1790.
24. C.H. Lee, T.T.S. Kuo, G.Q. Li, G.E. Brown, *Phys. Rev. C* 57 (1998) 3488.
25. N. Frlich, H. Baier, W. Bentz, *Phys. Rev. C* 57 (1998) 3447.
26. F de Jong, H. Lenske, *Phys. Rev. C* 57 (1998) 3099.
27. I. Bombaci, U. Lombardo, *Phys. Rev. C* 44 (1991) 1892.
28. W. Zuo, I. Bombaci, U. Lombardo, *Phys. Rev. C* 60 (1999) 024605.
29. I. Bombaci in: B.A. Li and W. Udo Schrder (Eds.) *Isospin Physics in Heavy-Ion Collisions at Intermediate Energies*, Nova Science Publishers, Huntington, NY, 2001, p. 35.
30. R.B. Wiringa, V. Fiks, A. Fabrocini, *Phys. Rev. C* 38 (1988) 1010.
31. A. Akmal, V.R. Pandharipande, *Phys. Rev. C* 56 (1997) 2261.
32. G.B. Bordbar, M. Modarres, *Phys. Rev. C* 57 (1998) 714.
33. B. Liu, V. Greco, V. Baran, M. Colonna, M Di Toro, *Phys. Rev. C* 66 (2002) 045201.
34. V. Greco, F. Matera, M. Colonna, M Di Toro, G. Fabri, *Phys. Rev. C* 63 (2001) 035202.
35. V. Greco, M. Colonna, M. Di Toro, G. Fabri, F. Matera, *Phys. Rev. C* 64 (2001) 045203.
36. V. Greco, V. Baran, M. Colonna, M. Di Toro, T. Gaitanos, H.H. Wolter, *Phys. Lett. B* 562 (2003) 215.
37. E. Chabanat, P. Bonche, P. Haensel, J. Mayer, R. Schaeffer, *Nucl. Phys. A* 627 (1997) 710.
38. K. Kolehmainen, M. Prakash, J.M. Lattimer, J. Treiner, *Nucl. Phys. A* 439 (1985) 535.
39. H.M. M.Mansour, M. Hammad, M.Y. M.Hassan, *Phys. Rev. C* 56 (1997) 1418.
40. S.J.Lee, A.Z.Mekjian, *Phys.Rev. C* 63 (2001) 044605.

41. D. Bandyopadhyay, C. Samanta, S.K. Samaddar, J.N. De, Nucl. Phys. A 511 (1990) 1.
42. J.P.Blaizot, J.F.Berger, J.Decharge, M.Girod, Nucl.Phys. A591 (1995) 435.
43. N.V.Giai, H.Sagawa, Nucl.Phys. A371 (1981) 1.
44. M.Rayet, M.Arnoold, F.Tondeur, G.Paulus, Astron. Astrophys. 116 (1982) 183
45. J.Dobaczewski, H.Flocard, J.Treiner, Nucl.Phys. A422 (1984) 103.
46. B.A.Brown, Phys.Rev.C 58 (1998) 220.
47. Y.Aboussir, J.M.Pearson, A.K.Dutta, R.C.Nayak, M.Farine, Nucl.Phys. A528 (1992) 155.
48. F. Tondeur, M. Brack, M. Farine and J.M. Pearson, Nucl.Phys. A420 (1984) 297.
49. B. Behera, T.R. Routray, B. Sahoo, R.K. Satpathy, Nucl. Phys. A 699 (2002) 770.
50. W.D. Mayers, W.D. Swiatecki, Ann. Phys. 84 (1973) 186; J. M.Pearson, Y. Aboussir, A.K. Dutta, R.C. Nayak, M. Farine, F. Tondeur, Nucl. Phys. A 528 (1991) 1; P. Miller, J.R. Nix, At. Data and Nucl. Data Tables 39 (1988) 219; P. Miller, W.D. Mayers, W.J. Swiatecki, J. Treiner, At. Data and Nucl. Data Tables 39 (1988) 225; W.D. Mayers, W.J. Swiatecki, T. Kodama, L.J. El-Jaick, E.R. Hiff, Phys. Rev. C 15 (1989) 189.
51. B.A. Brown, Phys. Rev. Lett. 85 (2000) 5296.
52. J. Margueron et. al., Nucl-th/0110026.
53. A. Akmal, V.R. Pandharipande, D.G. Ravenhall, Phys. Rev. C 58 (1998) 1804.
54. J. Rikovska Stone, P.D. Stevenson, J.C. Miller, M.R. Strayer, Phys. Rev. C 65 (2002) 064312.

Author Index

- Abbas, A. 241
Ansari, A. 1, 46
Arumugam, P. 82, 288

Behera, B. 305
Bhagwat, A. 56
Bhattacharyya, A. 170

Centelles, M. 82
Chakrabarty, S. 107
Chandra, R. 228
Chaturvedi, K. 228

Deb, A.G. 288
Dhiman, S.K. 185, 228

Gambhir, Y.K. 14
Gangopadhyay, G. 70
Gupta, R.K. 31

Hirsch, J.G. 228

Kota, V.K.B. 194

Patra, S.K. 31, 82, 288
Phatak, S.C. 162
Pradhan, A. 305

Raina, P.K. 228
Rath, P.K. 228
Routray, T.R. 305

Sahu, P.K. 137, 153
Sahu, R. 209
Satpathy, L. 277
Sharma, B.K. 82
Sharma, V.K. 257
Shukla, A. 228
Shyam, R. 185
Singh, J. 228

Viñas, X. 82